EWEA 2015 PARIS
EUROPE'S PREMIER WIND ENERGY EVENT

Scientific Proceedings

EWEA Annual Conference and Exhibition
Paris, France

IN PARTNERSHIP AND SUPPORTED BY:

Syndicat des Énergies Renouvelables
eawe european academy of wind energy
France Energie Eolienne
GWEC Global Wind Energy Council

EVENT AMBASSADORS:

EDF energies nouvelles
ENERCON ENERGY FOR THE WORLD
GE Renewable Energy

ORGANISED BY:

EWEA THE EUROPEAN WIND ENERGY ASSOCIATION

EWEA 2015
PARIS
EUROPE'S PREMIER **WIND ENERGY EVENT**

Scientific Proceedings

Publisher:
European Wind Energy Association (EWEA)

Responsible:
Alice Rosmi
Rue d'Arlon 80, B-1040 Brussels, Belgium
Tel: +32 2 213 1811 Email: ewea@ewea.org

Printed by:
Artoos

9 782930 670003

Scientific committee

Sandrine Aubrun, Université d'Orléans – France
Frede Blaabjerg, Aalborg University – Denmark
Ervin Bossanyi, DNV GL – Norway
Carlo Bottasso, Technische Universität München, – Germany
Ndaona Chokani, ETH Zürich – Switzerland
Maurizio Collu, Cranfield University – UK
Boris Conan, Ecole Centrale de Nantes – France
Antonio Crespo, Universidad Politécnica de Madrid – Spain
Alvaro Cuerva, Universidad Politécnica de Madrid – Spain
Iain Dinwoodie, University of Strathclyde – UK
Gudmund Eiksund, Norwegian University of Science and Technology (NTNU) – Norway
Ole Endrik Vestøl Endrerud, UiS – Norway
Pawel Gancarski, National Renewable Energy Centre (CENER) – Spain
Gregor Giebel, DTU Wind Energy – Denmark
Sugoi Gomez Iradi, National Renewable Energy Centre (CENER) – Spain
Emilio Gomez-Lazaro, Universidad de Castilla La Mancha – Spain
Nikos Hatziargyriou, National Technical University of Athens – Greece
Jan Helsen, BruWind – Belgium
Peter Jamieson, Univeristy of Strathclyde – UK
Georges Kariniotakis, MINES ParisTech – France
Athanasios Kolios, Cranfield University – UK
Han Lindeboom, IMARES – Netherlands
Jakob Mann, DTU Wind Energy – Denmark
Denis Matha, University of Stuttgart – Germany
Julio Melero, Fundacion CIRCE – Spain
Karl Merz, SINTEF – Norway
Angel Molina-Garcia, Universidad Politécnica de Cartagena – Spain
Michael Muskulus, Norwegian University of Science and Technology (NTNU) – Norway
Jannie Sønderkær Nielsen, Aalborg University – Denmark
Tor Anders Nygaard, Insitute for Energy Technology – Norway
Stavros Papathanassiou, National Technical University of Athens – Greece
John Dalsgaard Sørensen, Aalborg University – Denmark
David Schlipf, University of Stuttgart – Germany
Carlos Simao Ferreira, TUDelft – Netherlands
Bernhard Stoevesandt, Fraunhofer IWES – Germany
Mareike Strach-Sonsalla, Fraunhofer IWES – Germany
Kirsten Tracht, BIME, University of Bremen – Germany
Jeroen van Beek, The von Karman Institute for Fluid Dynamics – Belgium
Gerard van Bussel, TUDelft – Netherlands
Jan Willem van Wingerden, TUDelft – Netherlands
Simon Watson, University College Cork – Ireland
Thomas Welte, Sintef – Norway
Wei Jun Zhu, DTU – Denmark

Foreword

On behalf of the European Academy of Wind Energy (EAWE) and the European Wind Energy Association (EWEA), we have the pleasure of presenting the Scientific Proceedings of the EWEA 2015 Conference in Paris.

EWEA's annual conference has included a Science & Research Track since 2007. This track has served both as a platform for engineers and scientists to present their latest results, and has tried to engage the audience and the presenters in in-depth technical discussions and exchange of ideas. In our opinion, it has demonstrated that European wind energy research benefits from the synergy between industrial and academic research. It is a very lively discipline that supports the industry in developing novel competences and relevant solutions, while adhering to strict research standards. The sessions in the scientific track have been characterized by novelty, care for details, and scientific excellence.

In contrast to previous years, for EWEA2015 the Scientific Track has been merged with the General Track, such that most sessions during the conference now feature both scientific and industry presentations. The main benefit to the audience is that this allows for covering more diverse topics, with 36 sessions in total. These sessions were jointly developed by the Scientific and Industry Topic Leaders from the 400+ abstracts received. Conference delegates will thereby be exposed to both the latest ideas and analyses from academia as well as to the latest experiences and developments from industry. As in previous years, the individual sessions were carefully prepared to showcase highlights of current academic thinking and industry practice, striking a balance between international experts and the new generation of upcoming young researchers. Although the Scientific Track has been discontinued, abstracts could be either submitted as a general or as a scientific abstracts, and presentations are clearly marked as scientific in case of the latter.

These proceedings include the full papers of all oral, scientific presentations given during the conference sessions; these were selected due to their novelty, relevance and interest to a general audience. In addition, a poster session has been organized for works of a more technical nature. The full papers of both the oral presentations and of all posters from the Science & Research Track are also available in the online proceedings at: **www.ewea.org/annual2015/conference/conference-proceedings/**

The European Academy of Wind Energy (EAWE) is responsible for organizing the review process for scientific contributions, has contributed to develop the sessions, and provides scientific chairs for all sessions. All papers were peer-reviewed by a Scientific Committee, consisting of scientists from EAWE member institutes and their associates. Each abstract received a review by at least two of these experts. We thank all authors for their willingness to take part in this procedure, and the reviewers for their hard work alongside their daily business.

EWEA is responsible for the organisation and logistics of the conference, and we thank their highly professional staff and their associates for the excellent collaboration.

Assoc. Prof. Dr. Sandrine Aubrun
Université d'Orléans
Editor of the EWEA 2015 Scientific Proceedings
President of the European Academy of Wind Energy (EAWE)

Prof. Dr. Jakob Mann,
Technical University of Denmark (DTU)
Editor of the EWEA 2015 Scientific Proceedings
Past-President of the European Academy of Wind Energy (EAWE)

Prof. Dr. Michael Muskulus
Norwegian University of Science and Technology (NTNU)
Chair of the Scientific Committee and Editor of the EWEA 2015 Scientific Proceedings
Past-President of the European Academy of Wind Energy (EAWE)

Organised by:

Review and selection of papers:

Table of contents

1. Turbine Technology

Table of contents

Table of contents

4. O&M & Logistics

5. Resource assessment

Table of contents

6. Integrating wind power into the electricity market

The table of content mentions presenting authors at EWEA 2015.
Names of all authors are included in the full papers.

Design of monopiles for multi-megawatt wind turbines at 50 m water depth

Wilfried Njomo Wandji
DTU Wind Energy
wilw@dtu.dk

Anand Natarajan
DTU Wind Energy
anat@dtu.dk

Nikolay Dimitrov
DTU Wind Energy
nkdi@dtu.dk

Thomas Buhl
DTU Wind Energy
thbu@dtu.dk

Abstract:

The design of a monopile substructure for wind turbines of 10 MW capacity installed at 50 m water depth is presented. The design process starts with the design of a monopile at a moderate water depth of 26 m and is then up scaled to a 50 m water depth. The baseline geometry is then modified to specific frequency constraints for the support structure. The specific design requirements including the soil boundary conditions of this large diameter monopile has been described and fully coupled hydro-aero-servo elastic simulations are performed for ultimate limit state design. Soil plasticization is also considered. Analyses have shown that the design of large diameter monopile is not a straightforward extrapolation process, but it requires specific checks and iterations. An appropriate design scheme is proposed with perturbation analysis for robustness.

Keywords: Multi-megawatt wind turbines, large diameter monopile, deep water, ultimate design

1 Introduction

Offshore wind energy is moving towards larger turbines and into deeper waters. However, the wind energy industry is relatively recent and needs continuous improvements to its design practices. Two paths are used to improve wind energy productivity: reliability and more powerful wind turbines. The crossroads of these paths places the problem at the edges of the state of the art.

Indeed, wind turbines with rated capacity of 10 MW are being developed [1]. Their sizes necessitate suitable support structures that can withstand the engendered loads and last the intended life. Plus, their capacity needs enough wind resources to be fully exploited. This obliges that multi-megawatt turbines should be located in sites where wind resources are abundant. For this reason, recent potent sites have been found at deep waters (50+ m). They are able to provide enough wind resources as required by 10 MW wind turbines, but they also add to the challenge related to support structures.

Facing this challenge, space frame substructures have been proposed. However, their manufacturing process is daunting. In addition, there is a need to maintain the strength and stiffness requirements at the lowest possible cost [2]. In particular, a jacket structure has been proposed within the INNWIND.EU project [3] for a 10 MW turbine at 50 m water depths, but it has been extremely challenging to ensure jacket durability for 25 years with respect to its fatigue limit state. Besides the space frame solution, floating support structures are also a potential solution, but are economical at greater water depths over 100 m [2].

A monopile substructure solution at 50 m water depth is gaining more and more traction, due to the fact that its manufacturing process just consists of rolling and welding and its small footprint eases its transportation and its installation. This technology has been employed in many wind farms up to 30 m water depths composed usually of 2 to 5 MW wind turbines. For wind farms that combine larger wind turbines and deeper waters, significant design adaptation of the monopile is necessary to ensure structural integrity and cost effective manufacturing. Upscaling from present designs at lower water depths cannot be regarded as a straightforward process because of specific design requirements for large diameter monopiles.

The present paper proposes a preliminary design for large diameter monopiles at 50 m water depth. The study departs from current practices (middle size monopile) to accomplish its objectives. Precise design constraints are stated and large diameter monopile specifics are presented. Once a final design is obtained, perturbation study is carried out, drawing additional conclusions.

2 Fully coupled aero-hydro-servo-elastic analysis

In addition to the controller, three media (air, sea, and soil) concurrently act on a given offshore wind turbine mounted on monopile. To ensure that all ambient interactions are adequately considered, a fully coupled design loads computation has been performed using the aero-hydro-servo-elastic software package HAWC2 [4].

HAWC2 utilizes a multibody formulation which couples different elastic bodies together. Bodies are composed of Timoshenko beam [5] finite elements whereby their stiffness, mass and damping are assembled into the governing equations of motion, whose solution is obtained using the Newmark-β method [6]. The damping coefficients are adjusted using Rayleigh coefficients to obtain desired damping ratios for the global structure. Blade Element Momentum (BEM) theory is employed for the rotor subjected to aerodynamics.

The turbulent wind field in the aeroelastic simulations is defined using the Mann model [7]. Tower shadow and aerodrag on all exposed elements are also accounted for. Random Gaussian 10-minute realizations are simulated over 11 mean wind speed bins between cut-in and cut-out wind speeds, and one mean wind speed related to the extreme load case. Each mean wind speed has been linked to a particular sea state.

The wave height is modeled based on a JONSWAP spectrum at the expected value of significant wave height and spectral peak period at each mean wind speed. Wave kinematics are computed according to the irregular Airy model with Wheeler stretching [8]. The hydrodynamic forces are computed based on the Morison equation [8] evaluated from water surface to seabed.

Below the seabed, soil-structure interaction is modeled as beam-on-nonlinear Winkler foundation with uncoupled responses of axial friction (t-z) and lateral force (p-y). American Petroleum Institute [9] recommends an algorithm to obtain p-y and t-z curves. Although [9] suggests using load-displacement behavior at unit tip, in the present study the nonlinear spring is replaced by a joint, restrained for vertical displacement and yaw rotation.

3 Site conditions, structure, and design constraints

In this study, the site conditions are taken from those described in [3]. The soil is made of superimposed sand layers of various properties each. The complete description of the adopted soil properties can be found in [3]. Above the soil, sea states are defined according to the atmospheric conditions (Table 1). Considering the JONSWAP wave spectrum, 95 % of the wave energy is realized under 0.225 Hz in the critical case. The off-resonance range related to wave excitation is hence restricted to above 0.225 Hz.

Table 1: Metocean conditions [3]

Wind speed [m/s]	Turbulence Intensity [%]	Significant height, Hs [m]	Peak period, Tp [s]
5	43.85	1.140	5.820
7	33.30	1.245	5.715
9	27.43	1.395	5.705
11	23.70	1.590	5.810
13	21.12	1.805	5.975
15	19.23	2.050	6.220
17	17.78	2.330	6.540
19	16.63	2.615	6.850
21	15.71	2.925	7.195
23	14.94	3.255	7.600
25	14.30	3.600	7.950
42.73	11.00	9.400	13.700

The DTU 10 MW reference wind turbine (DTU 10 MW RWT) [1] is used as mounted on a monopile substructure, whose design is sought. The tower is made of steel whose density is taken as 8500 kg/m^3 to account for the mass of secondary structures. Based on the rotor speeds, the corresponding Campbell diagram is drawn in Figure 1. This figure shows that 1P, 3P and 6P ranges are respectively in hertz [0.099, 0.158], [0.300, 0.480] and [0.600, 0.960].

The monopile is considered as made of hollow cylinder rolled from a steel plate of 7850 kg/m^3 whose characteristic strength is 500 MPa, which corresponds to high-strength steel. The monopile safety is assumed to be of component class 3. It can be fully defined by its outer diameter (D), wall thickness (t) and length. Its length consists of the part within the transition piece (26 m), the submerged part (50 m), and the embedded part below the soil level whose length is to be defined. The design of the monopile is carried out based on the constructability and mass minimization. The following conflicting design aspects are analysed:

- larger outer diameter and smaller wall thickness lead to lighter piles and are easy to roll manufacture;
- larger outer diameter leads to large bending stiffness, but also to higher wave loads;
- smaller outer diameter leads to larger wall thickness and to deeper piles, but with reduced wave loading.

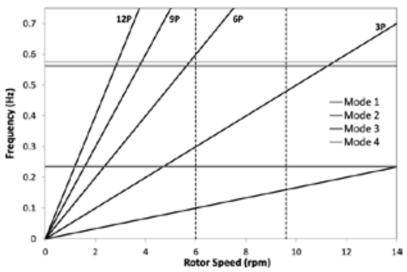

Figure 1: Campbell diagram

Practically, an upper limit of 10.00 m has been set for outer diameter in order to limit fluid-shaft interactions and to resort to large hammer. The selected wall thickness should withstand the stresses generated during pile-driving. In the absence of detailed analyses or past experiences, API (2005) [9] recommends that the minimum wall thickness should be taken as:

$$t\,[mm] = 6.35 + \frac{D\,[mm]}{100} \quad (1)$$

In order to ease the rolling process, the wall thickness is restricted within the range [1, 1.1] times its recommended minimum value.

Besides the constructability and stability criteria, the monopile should also possess stiffness such that deformations are limited. In that respect, Krolis et al (2010) [10] have adopted a maximum displacement at the mudline of 120 mm and a maximum toe deflection of 20 mm. They found that these limitations can be fulfilled with embedded pile length between 5.3D and 4.4D for 3.0 MW turbines, and between 5.0D and 3.3D for 5.0 MW turbines.

In addition, the resulting design should provide enough dynamic stiffness such that the first frequencies of the overall structure lie between [0.225, 0.300] and [0.480, 0.600] in hertz. This requirement is important to minimize the fatigue effects generated by the vibrations, which are due to wind, wave, and rotor excitation during the structure lifetime.

4 Standard monopile at 26 m sea depth

The overall aim of this study is to determine the characteristic monopile properties so that the full structure has its first natural frequencies outside the resonance ranges. In order to achieve this target, the 10 MW wind turbine has been considered placed at a mean water depth of 26 m as a starting point. A corresponding monopile has been designed to fit the natural frequency requirements. As a first trial, a pile of 8.0 m outer-diameter and 100 mm wall thickness has been extruded from 26 m above mean water level till 50 m (= 6.25D) below the seabed i.e. a total of 102 m. The hub height above mean sea level is maintained at 119 m.

The steps required to tune the first natural frequencies outside resonance ranges are made by adjusting the wall thickness and the embedded depth of the monopile. From the initial design estimate, one parameter is varied and modal analysis is carried out with each of its value. The obtained natural frequencies are then checked against the admissible frequency range. Once a minimum satisfying value of the said parameter is obtained, it is set constant and another parameter is now varied till its minimum value that also satisfies the frequency requirement. This iterative process is repeated for all parameters.

Table 2: Wall thickness adjusting for 26 m sea depth

Wall thickness [mm]	Eigen frequencies [Hz]			
	Mode 1	Mode 2	Mode 3	Mode 4
90	0.224	0.227	0.544	0.584
100	0.229	0.232	0.545	0.584
120	**0.238**	**0.242**	**0.546**	**0.585**

The wall thickness has been fine-tuned to a value of about 120 mm as shown in Table 2 because the lower wall thickness cases of 100 mm and below provides a design too close to the resonance frequency boundary. Further, considering this wall thickness, the embedded length has been adjusted. Table 3 shows that a satisfying value is 30 m.

Table 3: Embedded length below soil using a wall thickness t = 120 mm

Embedded length [m]	Eigen frequencies [Hz]			
	Mode 1	Mode 2	Mode 3	Mode 4
25.00	0.218	0.221	0.548	0.580
30.00	**0.227**	**0.230**	**0.548**	**0.587**
50.00	0.238	0.242	0.546	0.585

As a result of this process, a monopile of 8.0 m outer diameter, 120 mm wall thickness and 30 m embedded length satisfies the frequency requirement for the DTU 10 MW RWT placed at 26 m water depth.

5 Specificity of large diameter monopile

The model as described above works well for small to medium water depths but for greater depths, closer attention needs to be given to the structural stiffness distribution, influence of wave diffraction and soil-structure interaction.

For a given turbine moving from moderate to deep water, the longer cantilever length requires a wider monopile to provide enough stiffness to maintain the natural frequencies above that of wave excitation. However, it can be beneficial to distribute the added stiffness along the whole length by modifying the tower dimensions.

Furthermore, the wave diffraction phenomenon (for pile diameters greater than 20% of the wave length) for a vertical cylinder extending from the sea bottom through the free surface is proposed by MacCamy and Fuchs (1954) [11] as a correction for the inertia coefficient in the Morison equation at each metocean state.

Another factor to be taken into consideration is the soil-structure interactions wherein several issues are associated. For example, the p-y curve traditionally used has been developed for slender monopiles with up to approximately 2 m diameter ([12], [13]).

6 Geometry design

When placed at 50 m water depth, an initial monopile design estimate would be a cylinder with outer diameter of 10.0 m, wall thickness of 120 mm, and embedded length of 30 m, similar to what was achieved in the earlier design, but with a wider diameter. An iterative process similar to the one above is carried out.

Here, the outer diameter and the corresponding tower geometry are selected having in mind the necessary stiffness distribution along the structure height. This implies a thinner monopile but a wider tower. Table 4 shows adjustments of the outer diameter. In this table, diameter 10.0 m satisfies the resonance frequency requirements whereas diameter 9.5 m does not. Although the value of 9.5 m is found unsatisfactory in comparison to 10.0 m, the former is chosen and change is done on the tower geometry to compensate (Table 5). Table 6 shows that with the new tower, named B, there is a possibility to decrease monopile's wall thickness. Finally, a wall thickness of 110 mm is obtained. A value of 100 mm for wall thickness satisfies the frequency criterion but violates the minimum thickness as calculated by Eq. (1). The whole process as well as the obtained results is illustrated in Figure 2.

Table 4: Outer diameter adjustment with Tower A

Outer diameter [m]	Eigen frequencies [Hz]			
	Mode 1	Mode 2	Mode 3	Mode 4
9.50	**0.218**	**0.267**	**0.548**	**0.564**
10.00	0.225	0.227	0.549	0.565

Table 5: Tower selection

Tower type and mass [t]	Eigen frequencies [Hz]			
	Mode 1	Mode 2	Mode 3	Mode 4
A: 426.293	0.218	0.267	0.548	0.564
B: 511.131	**0.239**	**0.241**	**0.563**	**0.576**

Table 6: Wall thickness adjustment with Tower B

Wall thickness [mm]	Eigen frequencies [Hz]			
	Mode 1	Mode 2	Mode 3	Mode 4
110	**0.234**	**0.236**	**0.563**	**0.575**
120	0.239	0.241	0.563	0.576

By changing the tower from A to B, a global material save is made: from 3525.591 t to 3211.254 t. Plus, the rolling effort is preserved as wall thickness moves from 120 mm to 110 mm; the required driving power is made smaller; and the wave loads have been decreased. For next paragraphs, outer diameter of 9.5 m, wall thickness of 110 mm, embedded length of 30 m and Tower B are considered.

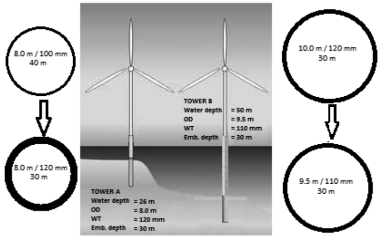

Figure 2: Design evolution

7 Characteristic curves

The global performance of the present design needs to be checked against that of the DTU 10 MW RWT. Generated power and aero rotor thrust as obtained from steady conditions are used as comparison criteria. The steady conditions are achieved by the application of steady wind whose speed linearly goes from cut-in to cut-out speed in 2500 s.

Figure 3 and Figure 4 respectively illustrate the curves of the generated power and of the aero rotor thrust plotted against the reference curves. These figures show that the present design performs as good as the reference as the curves almost superimpose each other.

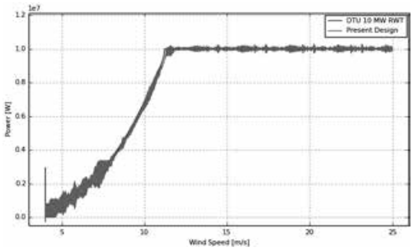
Figure 3: Power curve

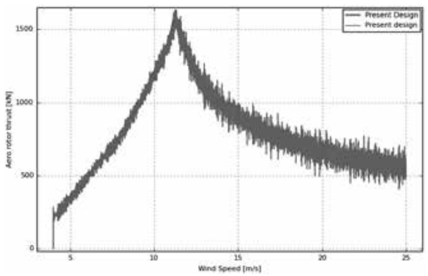
Figure 4: Aero rotor thrust curve

8 Ultimate limit state

8.1 Design load cases

The design at ultimate limit state has considered the model with articulated pile tip and shaft friction. Two load cases have been used here according to IEC 61400-3 [14]:

- DLC 1.3: six wind seeds for each of 11 wind speed bins have been applied each with no yaw error. Waves were aligned along wind direction. That makes 11 × 6 = 66 scenarios.
- DLC 6.2a: 42.73 m/s wind has been applied along 24 directions: from 0^0 to 345^0 in 15^0 steps. Waves were directed along wind direction with ±30^0 yaw error. With no active controller, the structure was loaded with an extreme current (1.2 m/s) of parabolic type at 0^0. Blades were pitched at 90^0 with no dynamic induction. This leads to a total of 24 × 3 = 72 scenarios.

8.2 Ultimate loads and deformation

Typical resultant shear force and bending moment curves are illustrated in Figure 5. In this figure, loads reach their maximum values in the embedded part. At about 7 m under the mudline, the moment value is maximal and the shear force is zero. At about 21 m depth in the soil, the monopile experiences maximal shear force. That location corresponds to zero-crossing point as it can be seen in Figure 6, which depicts a typical lateral displacement curve of the pile embedded portion. At that point, the monopile does not move laterally.

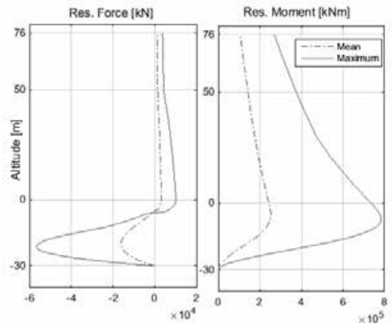

Figure 5: Typical resultant force and moment

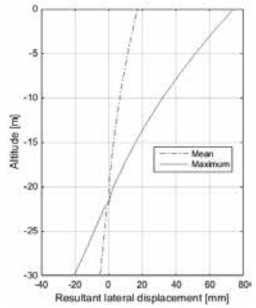

Figure 6: Typical lateral displacement

8.3 Stress check

Based on the internal forces and moments, maximum von Mises stresses are obtained for various sections along the pile portion going from mean water level to the tip. Three directional stresses have been combined according to the von Mises yield criterion: they are the axial stress, the circumferential stress, and the shear stress. Further details can be found in [15].

Figure 7 illustrates the design maximum von Mises stress distribution together with the steel design strength. The maximum design stress is about 251.9 MPa for a utilization factor of 72 %. This proves that the thickness is enough to withstand ultimate loads.

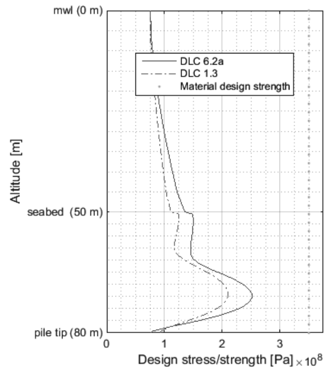

Figure 7: Design maximum von Mises Stresses

8.4 Deformation

The maximal displacement at the mudline is about 81 mm and the maximal tip deflection 22 mm. These values are globally acceptable with respect to the design constraints set above. However, as shown in Figure 8, the soil yield strength has been exceeded in approximately the first 10 meters from seabed. This value is intolerable as it represents one third of the foundation depth. The yielded zone shall be reduced. The perturbation analysis below investigates the possibilities for achieving this reduction.

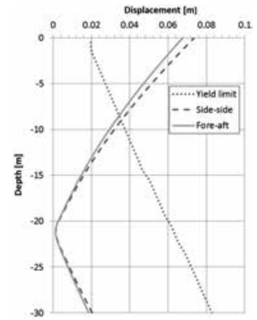

Figure 8: Elastic/Plastic zones

9 Investigation of perturbations

Holding the above design as baseline, five perturbation cases are considered for perturbation analysis. In addition to the baseline, the five other cases consist of:

- Baseline – The toe is modeled as a joint with restrained yaw and vertical motions. The contribution of the axial skin friction is accounted for. The monopile has a wall thickness of 110 mm, and is 26 m deep embedded into the soil whose internal friction angle is 35º.
- Perturbation A – Toe boundary condition. The pile tip is fixed, i.e. all degrees of freedom are restrained.
- Perturbation B – Axial skin friction contribution. The contribution of skin friction to the pile axial equilibrium has been annihilated.
- Perturbation C – Deeper pile. The embedded length of the pile has been changed from 30 m to 50 m.
- Perturbation D – Thicker wall. The wall thickness has been increased to 150 mm.
- Perturbation E – Soil friction angle. The soil around the pile is set denser; its internal angle has been improved from 35º to 38º.

The effects of each of these perturbations are investigated in terms of dynamic stiffness, deflections and yielded zone, and ultimate loads.

9.1 Dynamic stiffness

The dynamic stiffness is measured in terms of eigenfrequencies of the whole structure. As depicted in Figure 9, modal analysis results show that the respective modal frequencies are insignificantly different one from others. This observation reveals that none of the perturbation meaningfully influences the structure dynamic stiffness.

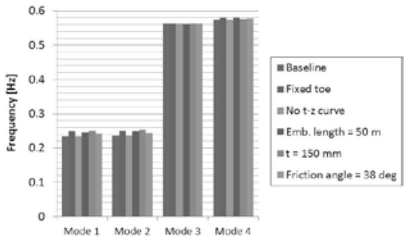

Figure 9: Modal frequencies for different perturbation

9.2 Deflection and plastic zone

However, Figure 10 shows some differentiation about the behavior of the perturbations regarding pile deflection. On the one hand, the skin friction contribution or the wall thickness increase does not bring any improvement. Their respective deformed shapes are similar to that of the baseline. On the other hand, fully fixing the toe or deepening the monopile leads to milder deformations (below 40 mm in each direction), and substantially reduces the yielded zone to about 5 m. On Figure 11, with the new internal friction angle, deformations have also decreased (between 40 and 60 mm in each direction). Considering the corresponding yield limit, the yielded zone is now about 7 m.

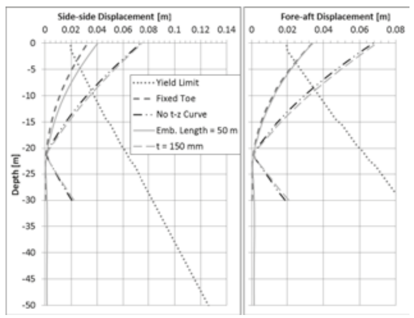

Figure 10: Deflection and yielded zones (Perturb. A, B, C, D)

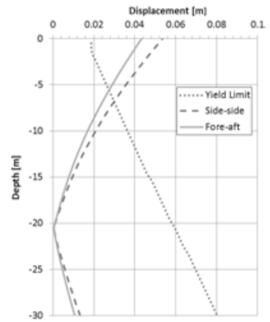

Figure 11: Deflection and yielded zones (Perturb. E)

9.3 Bill of material

Table 7 recapitulates the material mass used for each perturbation and for the baseline. It shows mass increase of 35.78% for the wall thickness change, and 18.87% for the length increase compared to the baseline mass. The other perturbations have the same mass as that of the baseline.

Table 7: Bill of quantities

Case	Baseline	A, B, E	C	D
Mass [t]	2700	2700	3210	3666
Rel. diff. [%]	-	0.00	18.87	35.78

9.4 Ultimate load

The maximum ultimate loads are given in Table 8 and in Table 9. They represent the load maxima obtained for each perturbation and for the baseline at the interface and at the mudline. They do not necessary occur simultaneously. It can be seen that these loads are respectively of the same ranges except the torsional moment from the deep pile case. This exceptional load value is more than twice the value of the other cases.

Table 8: Characteristic representative loads at interface – Deviation from the baseline

	Fres [kN]	Fz [kN]	Mres [kNm]	Mz [kNm]
Baseline	3500	13000	290000	-38000
Pert. A	0.0%	0.0%	3.4%	36.8%
Pert. B	0.0%	0.0%	0.0%	-234.2%
Pert. C	-2.9%	7.7%	-3.4%	-415.8%
Pert. D	-2.9%	0.0%	3.4%	-218.4%
Pert. E	2.9%	0.0%	3.4%	36.8%

Table 9: Characteristic representative loads at mudline – Deviation from the baseline

	Fres [kN]	Fz [kN]	Mres [kNm]	Mz [kNm]
Baseline	11000	40000	730000	-38000
Pert. A	0.0%	0.0%	2.7%	39.5%
Pert. B	9.1%	0.0%	0.0%	-236.8%
Pert. C	9.1%	0.0%	8.2%	-442.1%
Pert. D	0.0%	17.5%	2.7%	-221.1%
Pert. E	9.1%	0.0%	5.5%	39.5%

9.5 Discussion

Although all the cases (perturbations and baseline) have similar dynamic stiffness, they demonstrate different performance with respect to lateral deformations. This observation reveals that a design, exclusively based on dynamic stiffness, may be misleading. A thorough design process should continue till soil plasticization check as some perturbations have exhibited unchanged performance.

In particular, increasing the wall thickness does not bring any improvement. On the contrary, it introduces additional inconveniences. For example, it adds on to the total mass and requires more rolling effort. Consequently, the total cost will be increased. Similarly, shaft friction contribution happens to be non-influential. This may be due to the fact that the vertical degree of freedom has been restrained. Further investigations on axial skin friction may be carried out with a pile tip unrestrained in all directions.

Fixing all toe degrees of freedom produces a positive effect. However, the monopile toe is factually fixed if it is rooted into a rock, for example. If this is not the actual circumstance, this modeling approach may lead to misrepresentative results. In this case, results show that the best solution is to lengthen the monopile. Deepening the monopile increases the mass to some extend but significantly enhances the design. However, a drawback is the increase of torsional moment in the structure. It is expected that the account for the soil torsional resistance (M-θ curve) can contribute to mitigate this shortcoming.

10 Conclusion

In conclusion, the design of monopile for multi-megawatt wind turbines at 50 m water depth is carried out. The process started with the design of a monopile at 26 m water depth. Then, its upscaling has served as baseline geometry for 50 m water depth. The specificity of large diameter monopile has been stated and implemented. Analyses have shown that (i) the initial tower was not apposite for the design constraints; and (ii) a large amount of soil got plasticized.

With a new tower, five perturbation cases have been considered. Their examinations reveal that a design exclusively based on avoiding resonant frequency may not be thorough. An appropriate design scheme for large diameter monopile, however, could be extracted from the assessments. Indeed, the geometry that satisfies the resonant frequency range criterion is a good starting point. Attention should be taken to distribute the stiffness along the structure: a change of the tower properties can be necessary. The design is completed by setting a sufficient length that gives desired deflection shape.

Updating the pile length leads to increase of torsional moment. Further studies need to investigate how the consideration of soil torsional resistance can affect this observation. In addition, accounting for tip-displacement relationship might also reveal salient conclusions, namely about the influence of the skin friction. Finally, more detailed soil-structure interaction can also be regarded. This includes coupled load-displacement relationships, gapping phenomena and cyclic behavior.

Acknowledgements

The research leading to these results has received funding from the European Community's 7th Framework Programme FP7-ENERGY-2012-1-2STAGE under grant agreement No. 308974 (INNWIND.EU) and also from the Danish Energy Agency EUDP project titled, "Offshore wind turbine reliability through complete loads measurements", project no. 64010-0123. The financial support is greatly appreciated.

References

[1] Bak C, Zahle F, Bitsche R, Kim T, Yde A, Henriksen LC, Andersen PB, Natarajan A, Hansen MH. "Design and performance of a 10 MW wind turbine". http://www.innwind.eu/-/media/Sites/innwind/Publications/Deliverables/DeliverableD1,-d-,21ReferenceWindTurbinereport_INNWIND,-d-,EU.ashx?la=da

[2] Jonkman JM, Buhl Jr ML. "Loads analysis of a floating offshore wind turbine using fully coupled simulation". WindPower 2007 Conference & Exhibition Los Angeles, California, June 3–6, 2007.

[3] Von Borstel T. "INNWIND Design Report Reference Jacket", Ramboll. 2013. http://www.innwind.eu/-/media/Sites/innwind/Publications/Deliverables/DeliverableD4,-d-,31_20131030_INNWIND,-d-,EU.ashx?la=da

[4] Larsen TJ, Hansen AM. How 2 HAWC2, the user's manual. DTU Wind Energy: Risoe, 2014.

[5] Przemieniecki JS. Theory of matrix structural analysis. McGraw-Hill, 1968.

[6] Chopra AK. Dynamics of structures. Prentice-Hall: Upper Saddle River, N.J., 2011.

[7] Mann J. "The spatial structure of neutral atmospheric surface-layer turbulence". Journal of Fluid Mechanics 1994; 273:141–168.

[8] Chakrabarti SK. Handbook of Offshore engineering. Elsevier: Oxford, 2005, Vol. 1.

[9] American Petroleum Institute. Recommended practice for planning, designing and constructing fixed offshore platforms—Working stress design. API RP 2A-WSD, 2005.

[10] Krolis VD, van der Zwaag GL, de Vries W. "Determining the embedded pile length for large-diameter monopiles". Marine Technology Society Journal 2010; 44(1): 24-31.

[11] MacCamy RC, Fuchs RA. Wave forces on piles: A diffraction theory. Corps of Engineers 1954.

[12] Pradhan DL. Development of P-Y Curves for Monopiles in Clay using Finite Element Model Plaxis 3D Foundation. Master Thesis NTNU 2012.

[13] Bekken L. Lateral behaviour of large diameter offshore monopile foundations for wind turbines. TU Delft Master Thesis 2009.

[14] The international Electrotechnical Commission: Wind Turbines – Part 3: Design requirements for offshore wind turbines, IEC 61400-3 Ed 1, 2009.

[15] Koukoura C. Validated loads prediction models for offshore wind turbines for enhanced component reliability. DTU PhD Thesis 2014.

Comparative Study of the Design Methods for Large Diameter Offshore Monopiles

Azadeh Attari[1], Gerry Murphy[2], Paul Doherty[1]

1: Gavin & Doherty Geosolutions Ltd. (GDG), Beech Hill Office Campus, Clonskeagh, Dublin 4, Ireland
2: Department of Civil Engineering, University College Dublin, Belfield, Dublin 4, Ireland

Abstract

The conventional method of determining the lateral resistance of piles by using the load-displacement (p-y) springs has been initially developed for the oil&gas industry, and is based on the behaviour of piles at much smaller diameters compared to those common today in the offshore wind industry. The large diameter monopiles are expected to mobilise higher resistances in soil due to the contribution of rigid body behaviour. Hence, it is generally believed that the conventional methods underestimate the capacity of these monopiles. In the absence of abundant full-scale test data for supporting this theory and determining the extent of divergence between the predicted vs. actual capacity, this study employs Finite Element modelling for predicting the lateral resistance of monopiles with variable diameters. A comparative study is undertaken to investigate the disparity in the capacity of monopiles determined using numerical vs. analytical methods. The impact of the design method on the estimated lateral capacity of large diameter monopiles is discussed, as well as the impact of monopile diameter on the accuracy of conventional design approaches.

Key words XL monopiles, Lateral capacity, Plaxis, p-y curves, Offshore wind

1. Introduction

Monopiles comprise a large share of the offshore wind market and are likely to be the most preferred type of foundation for the offshore wind turbines in the future developments. Their simple design makes them suitable for standardisation of the manufacturing process, as well as quicker and cheaper installation procedures. These features are of high importance, as the offshore wind industry strives to lower the Levelised Cost Of Energy (LCOE) in order to be competitive with the fossil-fuel sources of energy.

The current guidelines for designing laterally-loaded monopiles rely mostly on the methods developed for oil&gas industry, and are based on the behaviour of small diameter piles (1 to 2 m). It is known that, as the pile dimensions shift towards the larger diameters common in the wind industry, the rigid body behaviour becomes more prominent, leading to an increase in the lateral resistance. Taking into account this excess resistance in the geotechnical design of monopile foundations can lead to more economical designs and potential cost savings. It has been advised that the range of application of monopiles, most importantly in terms of the suitable water depths can be increased through the use of optimised and more accurate design methods which are tailored to the specifications of the offshore wind industry [1].

In recent years Finite Element Modelling (FEM) has been used to further analyse the response of laterally loaded monopiles. Kim and Jeong (2011) [2], Fan and Long (2005) [3], and Byrne et al. (2015) [4] discussed several methods of calculating P-y curves using the results of FEM. Fan and Long (2005) found that the P-y response of the piles in sands was not sensitive to the EI stiffness of the pile, as in the API guidelines, but the ultimate soil resistance had a non-linear relationship with the pile diameter. This was also found to be the case by Kim and Jeong (2011). The analysis also concluded that the ultimate soil resistance was increased significantly with increased horizontal earth pressure and soil dilatancy –none of which are directly considered in the API method.

Bekken (2009) [5] compared the mobilised lateral resistance of the soil as estimated using the API and the Finite Element method for two model monopiles with diameters of D=1.0m and D=4.3m. The analysis found that the API design method overestimates the initial soil stiffness as was also observed by Achmus et al. (2009) [6] and Lesny et al. (2007) [7]. Recently, FEM analysis has also led to the proposal of modified numerical approaches for the design of stiff laterally loaded monopiles as discussed by Thieken et al. (2015) [8] and Byrne et al. (2015) [4].

Haiderali and Madabhushi (2013) [9] reported a numerical study on monopiles with 5m and 7.5m diameter installed in soft clay. Based on comparison of p-y curves back-calculated from the numerical model with those derived using the conventional approaches for soft clay, they concluded that the API method underestimates the lateral capacity of large diameter monopiles in soft clay, and yield an overly conservative design. Van Buren and Muskulus (2012) [10] discussed the shortcomings of the conventional p-y curve methods in detail and proposed a method for incorporating more advanced models, which account for the effects of nonlinearities, dynamic behaviour and damping of the soil, into the wind turbine substructure design procedure.

This paper aims at investigating the efficiency of conventional methods for analysing the lateral capacity of XL monopiles in the dense sand profiles and under loading scenarios corresponding to the larger capacity wind turbines which are expected for future developments in the offshore wind industry. The analyses have been performed with the assumption of static loading for the comparative evaluation which was the purpose of the current study. However, it should be noted that the design of wind turbine substructures is usually governed by the fatigue limit state, which cannot be reliably assessed using a static analysis. Taking into account the dynamic behaviour of monopiles and the degradation of soil due to cyclic loading are important considerations when making realistic assessments of the fatigue life of the structure.

At present there is no lateral test data for piles in the range of 4-6m for which the code is currently being applied which is resulting in growing scepticism about the validity of the design code. When examining the design of offshore wind turbine foundations a validation of stiff piles with low slenderness ratios is needed. The slenderness ratio and bending stiffness of the steel pile will have a significant effect on the initial stiffness response of the structure as discussed in Doherty et al (2012) [11]. The API methods [12] for calculating the ultimate soil resistance (p_u) assumes a frictionless pile-soil interface and therefore a Rankine type failure. However, in reality the pile wall is neither perfectly rough nor perfectly smooth. Therefore, it is reasonable to assume that the pile will exhibit some degree of friction as the sand flows around the pile shaft. The current design codes also neglects the shear resistance mobilised along the pile shaft due to the rotation of the pile and the additional shear component at the pile base [13]. The stiff failure of the pile consists of rotation of the pile about a point of zero deflection near the base of the pile. As the pile fails, the rotation will also result in additional passive and active earth pressures beneath the point of rotation which are also disregarded in the API design methodology. Achmus et al. (2009) [6] found that for large diameter rigid monopiles the resistance of the pile tip will have a significant effect on the pile capacity compared to long slender piles. As these components of resistance due to the rigid pile behaviour are not accurately included in the API RP2A it is largely uncertain how the method prescribed in the code can be extrapolated to larger pile diameters.

2. Model Geometries

Four different variations of monopile geometries were considered, with diameters ranging from 5.0 to 9.5m (representative of the current designs as well as the anticipated future developments). The embedment length of the monopiles varies in order to maintain a constant L/D ratio of 5 in all the models. This slenderness ratio was adopted by giving consideration to the common geometries used to date for offshore wind monopiles as discussed in [11]. The wall thickness has been considered to remain constant along the length of the pile. Even though this is not a realistic assumption in real projects, the influence of variation of thickness of monopile on its lateral resistance was not included in this analysis, in order to limit the model variables. Table 1 provides a summary of the four model piles considered.

Table 1 Geometry of the model piles

Model No.	Diameter (m)	Embedded length (m)	Thickness (m)
1	5.0	25.0	0.08
2	6.5	32.5	0.08
3	8.0	40.0	0.08
4	9.5	47.5	0.08

2.1 Loads

Considering the trend in recent offshore wind farm developments towards implementing larger turbines, located further offshore in deeper water sites, the model piles have been analysed using the loads corresponding to 8MW turbine, and at 40m water depth. The focus of this study is on the interaction of soil and the monopile and the accuracy of the p-y curves for predicting the mobilised lateral soil resistance. Therefore, the effect of hydrodynamic forces and the axial loads resulting from the weight of turbine and monopile have not been considered in the analysis. The 8 MW model turbine developed by the LEANWIND consortium [14] has been used in this study (Table 2).

Table 2 Loads and characteristics for the 8MW LEANWIND turbine

Horizontal Force (H)	2743 kN
Vertical Force (V)	4704 kN
Hub Height	110 m
Moment at pile head (M)	411450 kN.m
Tower mass	558 Tonnes

The design of LEANWIND 8MW turbine is primarily based on the publicly available data relating to the Vestats V164-8.0 MW turbine [15]. Scaling between the NREL 5MW and the DTU 10MW turbine models have been conducted with the application of engineering judgement to make up for the unavailable information. The LW turbine design has been validates by DNV-GL using an internal turbine engineering tool, Turbine Architect [16].

2.2 Soil Profiles

Generic soil profiles were utilised in this study to represent the North Sea layered dense sand deposits. A relative density of 80% was assumed (as a typical dense sand deposit) and synthetic CPT profiles were generated using Eq.1 (re-arrangement of the formulation proposed by [17]). This results in CPT profiles where the q_c values are consistently increasing with the depth of the soil.

$$q_c = \sqrt{\sigma_v' \times \sigma_{atm}} \exp(3.73 D_r + 2.52) \qquad \text{Eq.1}$$

Various guidelines and empirical equations have been proposed for determining the strength parameters from the CPT profiles, e.g. Robertson and Cabal (2015) [18]. In this study the equations proposed by [19] and [20] were employed to determine the friction angle (φ) and dilation angle (ψ) of the sand from the q_c values. The in-situ soil stress states (OCR, K_0 and $K_{0,NC}$) were calculated using the procedure proposed by [21] and [22]. Depending on the required accuracy, a number of soil layers are considered and average strength parameters are determined for each layer. A saturated unit weight of 18 kN/m^3, was assumed for the soil, along with a constant volume friction angle (φ_{cv}') of 30 degrees. The detailed approach for determining the soil parameters is explained elsewhere [23].

2.3 Plaxis Soil Model

The Hardening Soil (HS) model has been used for modelling the soil deposit in the 3D Finite Element software PLAXIS. The hardening soil model, unlike the Mohr-Coulomb elastic perfectly plastic model, does not fix the yield surface in the principal stress space, but rather allows for plastic straining of the material, by considering the hyperbolic stress-strain curve presented in Figure 1 [24]. More information about this model can be found in [25].

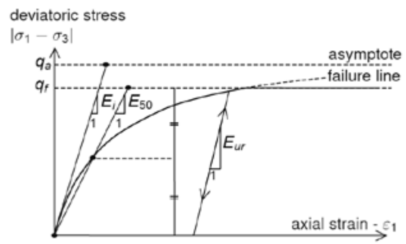

Figure 1 Hyperbolic stress-strain relation in primary loading [24]

Application of this model requires knowledge of the initial stiffness of the soil (E_{oed}), the secant stiffness (E_{50}), and the modulus of elasticity for unload-reload (E_{ur}). Kulhawy and Mayne (1990) [20] have proposed correlations for determining the moduli of elasticity of the soil based on q_c and relative density. Using these correlations, the profiles of variation of the three parameters with the depth of soil are obtained.

Several layers of soil have been considered, each 2m deep, and the corresponding values of E_{oed}^{ref}, E_{50}^{ref}, E_{ur}^{ref} have been calculated for each layer, as the input of the Plaxis software. These parameters have been determined by back-calculating the following power function curves (Eq 2 to Eq 4) which are used by the Plaxis software to determine the stress-dependent stiffness of the soil elements [26].

$$E_{oed}^{ref} = E_{oed} / \left(\frac{c \cos\varphi - \frac{\sigma'_3}{K_0} sin\varphi}{c \cos\varphi + p^{ref} sin\varphi} \right)^m \qquad \text{Eq 2}$$

$$E_{50}^{ref} = E_{50} / \left(\frac{c \cos\varphi - \sigma'_3 sin\varphi}{c \cos\varphi + p^{ref} sin\varphi} \right)^m \qquad \text{Eq 3}$$

$$E_{ur}^{ref} = E_{ur} / \left(\frac{c \cos\varphi - \sigma'_3 sin\varphi}{c \cos\varphi + p^{ref} sin\varphi} \right)^m \qquad \text{Eq 4}$$

Figure 2 illustrates the synthetic stiffness profiles as generated by the Plaxis software along the depth of the monopiles (in the Strain Hardening soil model).

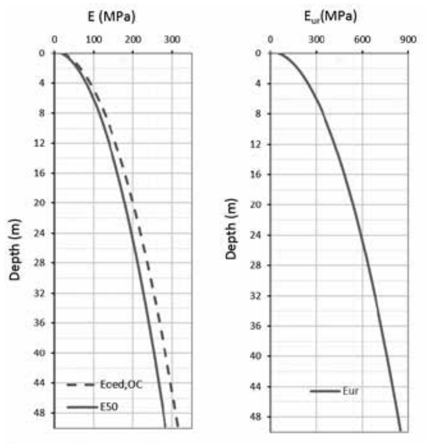

Figure 2 Profiles of the soil stiffness generated in the Plaxis model in the in-situ condition

3. Methodology

Using the synthetic soil profiles, the four model piles have been analysed under the effect of lateral loads resulting from the 8.0MW LEANWIND turbine. The mobilised lateral resistance of the soil is estimated using the p-y curves, depending on the deflection of the soil at the corresponding depth. In this study, two different methods have been employed for constructing the p-y curves and predicting the deflection curves along the piles. The results have then been compared with the numerical results obtained from analysis of the model piles using Plaxis 3D software.

3.1 API method

The most widely used method of obtaining p-y curves for lateral loading of piles is the method proposed by API (2011) [12]. The API method is based on the method proposed by Reese et al. (1974) [27], and the modifications suggested by O'Neill and Murchison (1983) [28], and adopts a hyperbolic equation for determining the p-y curves (Eq. 5).

$$P = A \times p_u \times \tanh\left(\frac{kH}{A\,p_u} \times y\right) \qquad \text{Eq. 5}$$

In this equation, A is a factor to account for the cyclic/static loading conditions, p_u is the ultimate bearing capacity at the specified depth of H, k is the initial modulus of subgrade reaction (dependent on the friction angle), and y is the lateral deflection of soil at the corresponding depth.

The API formulation has been calibrated by back-analysis of the experimental data obtained in small-scale piles under lateral loads [29], and is reported to have underestimated the initial stiffness of piles compared to the full-scale monitoring results based on Eigen frequency estimation [30]. The LPile software was used for analysing the model piles listed in Table 1, using the suggested API approach.

3.2 Finite Element modelling

Plaxis 3D have been employed for performing the finite element analyses. Determining the soil properties has been conducted according to the method explained in the previous section, and the input parameters in the Hardening Soil (HS) model have been determined for the various soil layers. The monopile structure was generated by inserting a cylindrical shaft into the Plaxis structures space. The surfaces of the cylinder were then decomposed into several simple surfaces, and were modelled using a plate structure. The final horizontal load at the corresponding height of the turbine relative to the seabed (150m) was imposed on this model in 20 consecutive steps. The model dimensions were selected in order to prevent boundary effects influencing the failure zone around the foundation (Figure 3). The equivalent weight of turbine and tower (as listed in Table 2) are imposed at the top of the piles as a uniformly distributed stress.

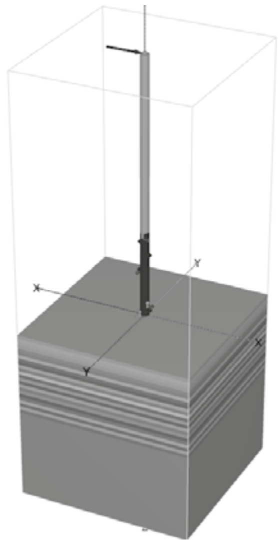

Figure 3 The Plaxis model of pile and the soil mass

4. Results and discussion

The deflection curves obtained from the three explained methods are presented in Figure 4. It can be seen that application of the API method in the smallest model pile (D=5m) resulted in smaller deflections at the upper section of the pile, compared to the results of the numerical model. As the pile diameter increases, the deflections predicted using the API approach become larger than the numerically determined values.

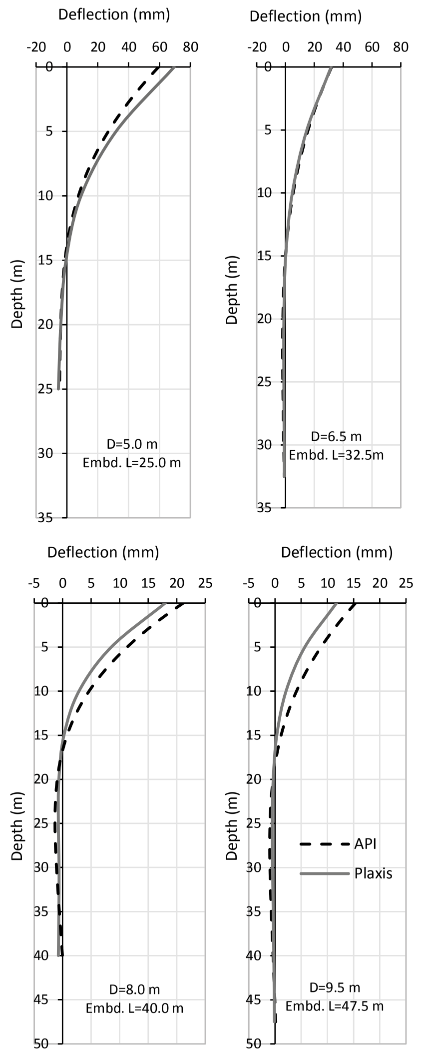

Figure 4 Lateral deflection of the model piles predicted using different methods

This trend can be explained by giving consideration to the range of stresses developed in the soil as a result of the applied turbine loads. The stiffness of soil in the hardening soil model (Figure 1) depends on the range of stresses the mass of soil undergoes. The considerable softening of the soil in the vicinity of the 5m diameter monopile modelled using Plaxis occurs as a result of the large stresses induced by application of the loads equivalent to an 8MW turbine. This has counteracted the contribution of rigid body behaviour of the monopile, resulting in an overall lateral capacity lower than that predicted using the API approach. Figure 5 illustrates the extent of formation of the hardening points in the models with various diameters and at the ultimate stage of loading. It can be seen that in the 5m diameter monopile, all the soil elements in the vicinity of monopile have entered the hardening phase.

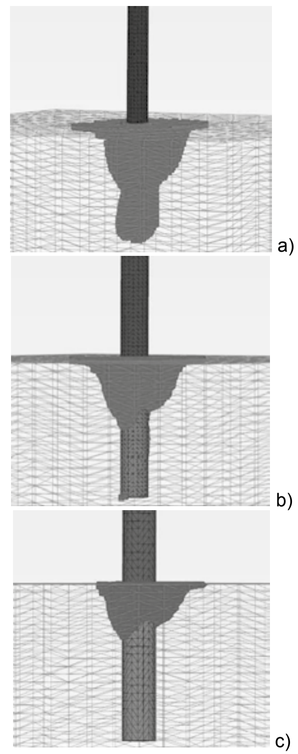

Figure 5 Formation of hardening soil elements at the final stage of loading: a) D=5.5m, b) D=6m, c) D=8.5m

Comparison of the deflection curves of the 5m diameter monopile, obtained using the Plaxis and API methods, at various reduced load steps also revealed that as the horizontal load applied to the model decreases, the response predicted using the numerical model becomes stiffer when compared to the response from the API approach. This shows that the accuracy of the API approach for realistic prediction of the monopile behaviour is not only dependent on the diameter of the monopile, but also on the range of stresses that the loading conditions induce in the soil. While at lower stress levels the API method overestimates the monopile deflections, resulting in the API method being prone to overestimating the lateral capacity at larger stress levels, leading to un-economical designs.

Comparison of the deflection curves obtained from the numerical vs. analytical methods for other monopile diameters can also confirm this. Figure 6 shows the reduction in the head deflection of the monopile estimated using Plaxis vs. the conventional API approach $(100 \times \frac{\Delta_{API}-\Delta_{Plaxis}}{\Delta_{API}})$. It can be seen that while in the smallest model (D=5m) the deflections predicted by the numerical approach are higher than the API method, as the diameter of the monopile increases the cost-benefits of the numerical analysis becomes more clear, resulting in 15% reduction in the head deflection in the 8m diameter monopile and 24% reduction in the 9.5m diameter monopile. As the monopile behaviour becomes further distinct from the flexible, bending dominated behaviour of small-diameter piles, and the contribution of shear in the lateral resistance becomes more significant, the efficiency of accurate FE analyses over the conventional approaches becomes more considerable. Considering that the recent developments in the offshore wind industry are shifting towards wind farms with larger capacity turbines and increased water depths, the need for soil-structure interaction models that can predict the behaviour of structure under the more demanding service loads, with higher certainty becomes clear.

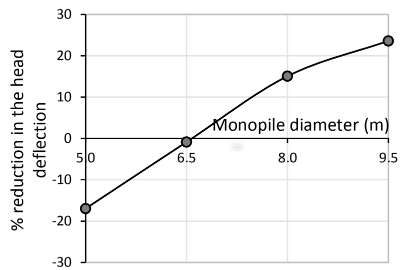

Figure 6 Percent reduction in the estimated head deflection$(100 \times \frac{\Delta_{API}-\Delta_{Plaxis}}{\Delta_{API}})$

Considering the significant contribution of initial stiffness in the results of the numerical model, it is expected that the application of the Hardening Soil model with small-strain stiffness (HSsmall) would result in even stiffer responses from the numerical model and consequently, more considerable disparity between the Plaxis and the API approach (at fixed service loads), shifting the graph of Figure 6 further upwards.

5. Conclusion

A comparative study was conducted to evaluate the accuracy of conventional p-y methods for reliable prediction of the lateral capacity of XL monopiles (D=5m to D=9.5m) in dense sand deposits. In the absence of full-scale test results, FE modelling of the XL monopiles is believed to be the most accurate indicator of their behaviour in the field, and has been used as the basis of the comparison. Plaxis 3D software and the hardening soil model were employed for the purpose of modelling.

The p-y method as proposed by the API was found to overestimate the lateral capacity of the monopile with 5m diameter. However, this was not the case for the larger diameter monopiles. It was observed that as the diameter increases, the head deflections predicted by the numerical approach become smaller compared to those obtained using the API approach. This suggests that the cost-benefits resulting from the application of more refined models will be more significant in the larger diameter monopiles.

It is expected that the enhanced capability of the HSsmall soil model in capturing the initial stiffness of the soil results in even smaller head deflections, and hence a larger disparity between the results obtained from API and the numerical methods.

Acknowledgement

The research leading to these results has been conducted as part of the LEANWIND project, which has received funding from the European Union Seventh Framework Programme under the agreement SCP2-GA-2013-614020.

References

[1] D. Kallehave, B. Byrne, C. LeBlanc and K. K. Mikkelsen, “Optimization of monopiles for offshore wind turbines,” Philosophical Transactions of the Royal Society of London A: Mathematical, Physical and Engineering Sciences, vol. 373, no. 2035, 2015.

[2] Y. Kim and S. Jeong, “Analysis of soil resistance on laterally loaded piles based on 3D soil–pile interaction,” Computers and Geotechnics, 38(2), 248–257, 2011.

[3] C. Fan and J. H. Long, “Assessment of existing methods for predicting soil response of laterally loaded piles in sand,” Computers and Geotechnics, 32(4), 274–289, 2005

[4] B. W. Byrne, H. J. McAdam, G. T. Burd, C. M. Houlsby, L. Martin, D. M. Zdravković, et al., “New design methods for large diameter piles under lateral loading for offshore wind applications,” Frontiers in Offshore Geotechnics III, 2015.

[5] L. Bekken, “Lateral behavior of large diameter offshore monopile foundations for wind turbines,” Dissertation, Delft University of Technology, 2009.

[6] M. Achmus, Y. S. Kuo, and K. Abdel-Rahman, “Behavior of monopile foundations under cyclic lateral load,” Computers and Geotechnics, 36(5), 725–735, 2009.

[7] K. Lesny, S., Paikowsky, and A. Gurbuz, “Scale effects in lateral load response of large diameter monopiles,” Proceedings of Sessions of Geo-Denver: Contemporary Issues In Deep Foundations, (158), 2007.

[8] K. Thieken, M. Achmus, and K. Lemke, “Evaluation of a new p-y approach for piles in sand with arbitrary dimensions,” Frontiers in Offshore Geotechnics III, 2015.

[9] G. S. P. Madabhushi and A. E. Haiderali, “Evaluation of the py Method in the Design of Monopiles for Offshore Wind Turbines,” Offshore Technology Conference, Texas, USA, 2013.

[10] E. Van Buren and M. Muskulus. “Improving pile foundation models for use in bottom-fixed offshore wind turbine applications,” Energy Procedia 24, 363-370, 2012.

[11] P. Doherty and K. Gavin, “Laterally loaded monopile design for offshore wind farms,” Energy 165, EN1, 2011.

[12] API (American Petroleum Institute), Washington DC, USA: API Publishing Services, 2011.

[13] I. P. Lam, “Diameter Effects on p-y Curves,” Deep Marine Foundations - A Perspective on the Design and Construction of Deep Marine Foundations, 2009.

[14] C. Desmond, “Description of an 8MW reference turbine”, LEANWIND Internal report, University College Cork, 2015.

[15] Vestas, “Offshore V164-8.0 MW, V112-3.3 MW,” Vestas Wind Systems, Available online: [http://pdf.directindustry.com/pdf/vestas/offshore-v164-80-mw-v112-33-mw/20680-310439.html]

[16] L. Blonk, W. Haans, “Technical note: LEANWIND 8MW benchmark to TEST TA data,” DNV-GL – Energy, May 2015.

[17] M. Jamiolkowski, D. LoPresti and M. Manassero, “Evaluation of relative density and shear strength of sands from Cone Penetration Test and Flat Dilatometer Test;” Soil Behaviour and Soft Ground Construction, American Society of Civil Engineers, Reston, Va., 2001.

[18] P. K. Robertson and K. L. Cabal, “Guide to Cone Penetration Testing for geotechnical engineering,” Gregg Drilling and Testing, Inc., CA, 2014.

[19] M. D. Bolton, “The strength and dilatancy of Sands,” Geotechnique 36, 65–78, 1986.

[20] F. Kulhawy, and P. W. Mayne, “Manual on estimating soil properties for foundation design”, No. EPRI-EL-6800. Electric Power Research Inst., Palo Alto, CA (USA); Cornell Univ., Ithaca, NY (USA). Geotechnical Engineering Group, 1990.

[21] P. W. Mayne and F. Kulhawy, “K\ do-OCR relationships in soil,” Journal of the Geotechnical Engineering Division 108.6, 851-872, 1982.

[22] P. W. Mayne, “Stress-strain-strength-flow parameters from enhanced in-situ tests,” in: Proceedings of the International Conference on In-Situ Measurement of Soil Properties & Case Histories, Bali, Indonesia, 27–48, 2001.

[23] G. Murphy, “Experimental testing of hybrid monopile foundations using prototype scaled models and finite element analysis,” PhD Thesis, University College Dublin, 2016. [See Also: Murphy, Igoe, Doherty and Gavin. (2016), “FE modelling of stiff laterally loaded monopiles using in-situ site investigation and scaled model testing,” in review, 2016.]

[24] Plaxis, “Material Manual,” Plaxis, 2013.

[25] T. Sanchez, A. Vermeer and P. Bonnier, “The hardening soil model: formulation and verification,” in Proceedings of the International Symposium beyond 2000 in Computational Geotechnics, Amsterdam, the Netehrlands, 1999.

[26] R. Brinkgreve, E. Engin and W. Swolfts, “Plaxis 3D material models manual,” Plaxis, 2012.

[27] L. C. Reese, W. R. Cox, and F. D. Koop, “Analysis of laterally loaded piles in sand,” Proceedings of the offshore technology conference, Houston, TX, paper OTC 2080, 1974.

[28] M. W. O'Neill, J. M. Murchison, “An evaluation of p-y relationships in sands,” report to American Petroleum Institute, Houston, TX, USA: University of Houston, 1983.

[29] S. K. Suryasentana and B. M. Lehane, “Numerical derivation of CPT-based p-y curves for piles in sand,” Geotechnique, 64(3), 186-194, 2014.

[30] D. Kallehave, C. LeBlanc Thilsted, & M. A. Liingaard, “Modification of the API P-y formulation of initial stiffness of sand,” In: P. Allan, et al. eds. Offshore Site Investigation and Geotechnics: Proceedings of the 7th International Conference. London: Society for Underwater Technology, 465-472, 2012.

Prediction of dynamic response of semi-submersible floating offshore wind turbine using Morison based theory

Shining Zhang*[1] and Takeshi Ishihara[2]
[1,2]Department of Civil Engineering, School of Engineering, The University of Tokyo, Japan

Abstract

A fully coupled nonlinear simulation tool (CAsT) using Morison based theory was developed to predict dynamic response of Floating Offshore Wind Turbine (FOWT). Performance of the simulation tool in prediction of dynamic response to sea states was validated through one water tank experiment in this paper. Besides, hydrodynamic coefficients were evaluated from numerical simulation and were validated with another water tank experiment. Significance of radiation damping, axial Froude-Krylov force on slender members and dynamic behavior of mooring system were investigated and clarified. In addition, systematic comparison of results from FAST and CAsT was carried out and discussed in this research.
Keywords: Floating Offshore Wind Turbine, Dynamic response, Morison equation, Radiation damping, Froude-Krylov force, Mooring tension

1. Introduction

Three main types of floating foundations, namely spar foundation, semi-submersible foundation, and tension leg platform(TLP) foundation can be applied to floating wind turbines in waters deeper than 30m. Accurate evaluation of hydrodynamic force and the way of modeling mooring system are significant in prediction of dynamic response of FOWT to current, wave and combination of these two. In evaluation of hydrodynamic loads, Morison equation and potential flow theory are widely used. Sethuraman *et al*.[1] examined the hydrodynamic response of a floating spar wind turbine under regular and irregular waves with full Morison equation[2] using the industry standard time-domain modelling tool, OrcaFlex. Numerical model and simulation results were validated with a 1:100 scale model in water tank test. Browning *et al*.[3] validated the performance of simulation tool FAST which is developed by National Renewable Energy Laboratory (NREL) using potential flow theory through a 1:50 scale spar-type floating offshore wind turbine model. Kvittem *et al*. [4] examined the dynamic response of a single semi-submersible wind turbine based on different hydrodynamic models-Morison equation and potential flow theory. From the foregoing, numerical model using potential flow theory for spar-type and semi-submersible support system has been validated through water tank test. However, potential flow theory accounts for the Froude-Krylov forces and diffraction effects for large and rigid body but distributed hydrodynamic loads on each immersed component of FOWT cannot be predicted which is necessary for fatigue design of platform. In contrast to potential flow theory, Morison equation is well known to predict in-line hydrodynamic force (normal force) on slender members and it can be used to evaluate distributed loads on each immersed member which makes it possible to capture high-order resonance of flexible floating system due to nonlinear wave loads (Phuc and Ishihara[5]). Phuc & Ishihara[5] and Waris & Ishihara[6] used a modified Morison equation to analyze the dynamic response of a semi-submersible FOWT, nevertheless, the difference between simulation and water tank test demonstrates that conventional Morison equation needs to be further investigated and expanded to provide much more accurate prediction of dynamic response since sufficient accuracy in prediction of dynamic response is indispensable for cost-effective design of FOWT. Basically, Morison equation is limited to slender structures. Apart from that, conventional Morison equation assumes small relative motion and radiation damping could be ignored as a result, but outgoing wave might be generated by the remarkable motion of FOWT and in this sense evaluation of significance of radiation damping is needed. Secondly, only in-line force acting on platform could be evaluated with conventional Morison equation, but axial loads along members, like heave plate in vertical direction might be crucial for heave response. To cope with this, Ishihara *et al.* [5,7] put forward a Morison-like equation using dynamic pressure to account for hydrodynamic axial loads on heave plates. However, axial force on the other slender members (such as braces) were ignored at that time. Whether this portion can be ignored or not is needed to be investigated and confirmed with validation through water tank experiment. From what mentioned above, the significance of radiation damping and axial force on those slender members are not clear for semi-submersible FOWT and therefore it is necessary to investigate and clarify the effects of radiation damping and axial force on dynamic response of FOWT.

Mooring system is critical for station-keeping of FOWT in sea states. A comprehensive literature review in terms of dynamic modeling and quasi-static modeling of mooring system can be found in the research by M. Hall *et al*.[8,9]. Quasi-static model in the form of either force-displacement relationships or analytical solutions for catenary cables in static equilibrium is commonly used in simulation tools because of computational efficiency, such as FAST (v8.08)[10] and Bladed (v4.6)[11]. It is thought to be conservative approach to predict dynamic motion of platform and the tension in mooring line. However, in order to achieve cost effective design for the floating system, much more accurate prediction of mooring tension by using dynamic model is necessary.

The outline of this paper is as follows. Numerical model is described in section 2, encompassing equation of motion, hydrodynamic loads, numerical scheme and wave theory. Section 3 briefly introduces the setup of 1/50 scale water tank experiment and covers validation of finite element method (FEM). Section 4 aims to discuss dynamic response of FOWT to various load cases and the paper is finalized with conclusions in Section 5.

2. Numerical model

A finite element scheme with beam, truss and spring type elements is developed to calculate dynamic response of full coupled wind turbine, support platform and mooring system. The time domain analysis enables the FEM to efficiently capture nonlinear characteristics of system. Morison equation is implemented to evaluate the hydrodynamic load on platform and mooring system. Non-hydrostatic model proposed by Waris and Ishihara[6] is used to evaluate hydrostatic force. In this model, not only the motion of platform itself but the wave elevation is considered in calculating the change of hydrostatic force. Nonlinear restoring load from mooring system of floating platform can be estimated from either quasi-static model[12] or dynamic model.

2.1 Equation of motion

The general non-linear time domain equations of motion for the coupled wind turbine and support platform system can be written as

$$[M]\{\ddot{X}\}+[C]\{\dot{X}\}+[K]\{X\}=\{F\} \qquad (1)$$

Where, $\{F\}=\{F_\gamma\}+\{F_\beta\}+\{F_H\}+\{F_R\}+\{F_G\}$

$[M]$, $[C]$ and $[K]$ are mass matrix, damping matrix and stiffness matrix of system respectively. $\{X\}$, $\{\dot{X}\}$ and $\{\ddot{X}\}$ are unknown displacements in six degree of freedom and their time derivatives. $\{F\}$ is the total external force changing with time, including gravitational force $\{F_\gamma\}$, buoyancy force $\{F_\beta\}$, hydrodynamic force $\{F_H\}$, restoring force (hydrostatic force) $\{F_R\}$, and force from mooring line system $\{F_G\}$.

2.2 External force

The term of gravitational force $\{F_\gamma\}$ includes loads from wind turbine, platform and mooring line. $\{F_\beta\}=\rho g\forall$ represents the buoyance force from Archimedes' Principle and is nonzero only for vertical heave-displacement platform DOF of the support platform. It balances with the gravitational force and tension in mooring line when platform is at rest.

2.2.1 Hydrodynamic force

Morison equation is well known in estimation of wave exciting force on slender bottom-mounted cylinders. The equation assumes total in-line forces exerted by unbroken surface waves can be represented by linear superposition of two components, namely: inertia force and drag force. An inertia force is proportional to the local flow acceleration as well as the mass displaced by the cylinder. A drag force is proportional to the signed square of the instantaneous flow velocity. When the body moves instantaneously in an oscillatory flow, the relative flow velocity and acceleration should be taken into consideration. The in-line hydrodynamic force on a segment of cylinder can be written in Morison equation as following relative form:

$$\{F_H\}=\rho_w(C_M-1)\forall(\dot{\boldsymbol{u}}-\ddot{X})+\rho_w\forall\dot{\boldsymbol{u}}+\frac{1}{2}\rho_w C_d A(\boldsymbol{u}-\dot{X})|\boldsymbol{u}-\dot{X}| \qquad (2)$$

Where first term in right of Eq. (2) account for diffraction effects and second term is Froude-Krylov force due to undisturbed waves while the third terms is viscous drag force. ρ_w is density of water; $\boldsymbol{u}$ and $\dot{\boldsymbol{u}}$ are vector of undisturbed fluid-particle velocity and acceleration respectively; $\{X\}$, $\{\dot{X}\}$ and $\{\ddot{X}\}$ are vector of support platform displacement and their time derivatives; $\forall$ is the displaced volume of fluid by each segment when the support platform is in its undisplaced position; A is cross-sectional area; C_M and C_d are inertia coefficient and drag coefficient respectively which depends on

Keulegan-Carpenter number $K_C = u_{max}T/D$, frequency parameter $\beta = D^2/\nu T$ and relative roughness etc. Where u_{max} is the maximum water particle velocity, T is incident wave period, D is diameter of cylinder and ν is the kinematic viscosity of water.
In order to effectively increase the hydrodynamic damping in heave direction and reduce heave response[13,14,15], appendage such as a disk (heave plate) are commonly added to the keel of a vertical cylinder such as the disk used in WindFloat and heave plate employed in Fukushima MIRAI[7]. Ishihara *et al*.[7] proposed a Morison like equation to evaluate hydrodynamic force on heave plate in axial direction. Hydrodynamic force acting on a heave plate is formulated using modified Morison equation as given below,

$$\{F_z\} = \rho_w(C_{Mz}-1)\forall_z(\dot{w}-\ddot{X}_3)+\frac{1}{2}\rho_w C_{dz}A_C(w-\dot{X}_3)\left|w-\dot{X}_3\right| + \frac{\pi}{4}D_h^2 p_b - \frac{\pi}{4}(D_h^2-D_c^2)p_t \quad (3)$$

Where, C_{Mz} is the added mass coefficient in the heave direction, $\forall_z$ is volume of heave plate, $\dot{w}$ is the vertical wave particle acceleration, $\ddot{X}_3$ is the heave acceleration of the heave plate, C_{dz} is the drag coefficient in the heave direction, A_c is the cross-sectional area of the heave plate in the Z-direction, w is the vertical wave particle velocity, $\dot{X}_3$ is the heave velocity of the heave plate, D_h is the diameter of the heave plate, D_c is the diameter of the upper column (which is placed on top of the heave plate), and p_b and p_t are the dynamic pressure acting on the bottom and top faces of the heave plate. Dynamic pressure at position z in regular wave is evaluated using Airy theory.

2.3 Numerical Model

Motion of equation in numerical solution is rewritten as follows

$$([M]+[M_a])\{\ddot{X}\}+([C]+[C_{Add}])\{\dot{X}\}+[K]\{X\}=\{F\} \quad (4)$$

Where $[M_a]=\rho_w(C_M-1)\forall$ is added mass in Eq.(2), $[C_{Add}]$ is additional damping, which can be used to account for radiation effect from outgoing wave generated by motion of FOWT itself, $[C]$ is the structural damping matrix which is estimated using Rayleigh damping as follows,

$$[C]=\alpha([M]+[M_a])+\beta[K] \quad (5)$$

$$\alpha = 2\omega_1\omega_2\left(\frac{\omega_1\zeta_2-\omega_2\zeta_1}{\omega_1^2-\omega_2^2}\right), \beta = 2\left(\frac{\omega_1\zeta_1-\omega_2\zeta_2}{\omega_1^2-\omega_2^2}\right) \quad (6)$$

Where ω_1,ω_2 and ζ_1,ζ_2 are natural frequency and damping for heave and pitch modes. Numerical scheme is summarized in Table 1.

Table 1: Description of the finite element numerical scheme

Dynamic analysis	Newmark- β method
Formulation	Total Lagrangian formulation
Convergence	Newton-Raphson Method
Damping estimation	Rayleigh damping
Element type	Beam / Truss element
Hydrodynamic force	Morison equation
Restoring force	Non-Hydrostatic Model
Mooring force	Quasi-static/Dynamic model

2.4 Wave theory

Linear Airy wave is used in regular wave condition to provide water particle velocity and acceleration for Morison equation. Wheeler stretching is employed to account for the kinematics of water particle above mean water level.

As for the dynamic response of FOWT to irregular wave, JONSWAP wave spectra was used both in simulation tool and water tank experiment. The spectrum is given as

$$S(f)=\alpha_* H_S^2 T_P^{-4} f^{-5}\exp\left\{-1.25(T_P f)^{-4}\right\}\gamma^{\exp\left\{-\frac{(T_P f-1)^2}{2\sigma^2}\right\}} \quad (7)$$

$$\alpha_* = \frac{0.0624}{0.230+0.0336\gamma-0.185/(1.9+\gamma)} \quad (8)$$

Where, f is wave frequency (Hz), H_S is significant wave height, T_P is peak wave period, γ is peak factor and σ is shape factor ($\sigma=0.07$ for $f\le(1/T_P)$ and $\sigma=0.09$ for $f>(1/T_P)$).

3. Description of water tank experiment

Two water tank experiments were carried out in this research. One was used to validate performance of CFD in evaluation of viscous drag coefficient. The another water tank experiment was utilized to validate performance of in-house code CAsT in prediction of dynamic response of FOWT to sea states.

3.1 Towing experiment

To obtain viscous drag coefficient, towing experiment was conducted. A 1/50 scale Froude platform based on 2MW Fukushima MIRAI FOWT was tested in Mitsui Engineering & Shipbuilding Co., Ltd. in 2015 (Japan). Dimension of water tank is 100m(length)×5m(width)×2.65m(depth), water depth set up in the experiment is 1.7m. Figure 1(a) exhibits the scaled model in towing experiment. Towing experiment was conducted with three different speed- 0.2m/s, 0.5m/s and 1.0m/s. Dimension of platform is shown in Figure 2. Origin of the coordinate is located above center column and still water level is where Z equals to zero.

In the towing experiment, platform was attached to the towing vehicle through one instrument known as force balance which is used to measure the three-components force (Fx, Fy and Mx) acting on platform while vehicle is moving with one constant speed. One minute data at least was measured in each case and then the averaged force was used to evaluate equivalent C_d^D. Equivalent C_d^D identified from experiment is defined in following way

$$C_d^D = \frac{F_D}{0.5\rho U^2 S} \quad (9)$$

where F_D is total drag force experienced by whole platform, ρ is the water density (9807N/m^3), U is the towing speed, S is the characteristic area. In case of scaled model, S (=0.3216m^2)is the projected area from components in YZ plane including center column (0.0469m^2), three side columns with heave plates (0.1896m^2), two pontoons downstream (0.0463m^2) and three braces (0.0388m^2).

3.2 Dynamic response test in water tank experiment

A 1/50 scale Froude model based on 2MW Fukushima MIRAI FOWT was tested in National maritime Research Institute (Japan) to validate the performance of in-house code CAsT in prediction of dynamic response of FOWT to sea states. Dimension of water tank is 40m(length) ×27m(width) ×2m(depth) and water depth set up in the experiment is 1.7m. Figure 1(b) shows the scaled model in water tank test and three video markers on the platform and tower were used to record the motion of platform in 6DOFs. Six mooring lines are distributed symmetrically along XZ plane as shown in Figure 2. The information of chain consisting mooring line is summarized in Figure 3 and Table 2.

The platform DOFs translated in the X, Y, and Z directions are called surge, sway and heave; and rotations about X, Y and Z axes are called roll, pitch and yaw respectively. Origin of the coordinate is located above center column and still water level is where Z equals to 0.

Cases conducted in the simulation and experiment are shown in

Table 3. Case 1 was conducted to determine the initial position of the platform and tension in the mooring line. Besides, it was used to verified the initial state in the simulation. Cases 2.x were carried out to determine the natural period and damping ratio of floating system in each DOF. Case 3 was conducted to analyze the response amplitude operators (RAOs) of platform in regular wave. Case 4 was employed to test the transient response in irregular wave. In case 3 and case 4, the wave propagates along positive X-axis.

(a): Towing experiment (b): Response test

Figure 1: Images of water tank experiments

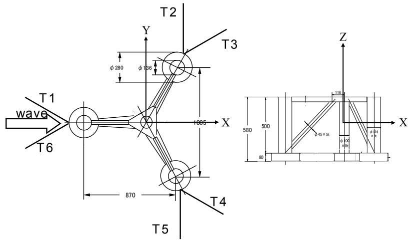

Figure 2: Plan (left) and Side (right) view of the floating system (units:mm)

Figure 3: Image of chain consisting mooring line

Table 2: Gross chain properties

Material	Nominal Diameter d	Length P	Spacing W	Weight in air (Exp.)	Weight in water (Exp.)
steel	mm	mm	mm	kg/m	kg/m
	3	24	5	0.146	0.127

Table 3:Definition of cases in experiment and simulation

Cases	Conditions	Description
case 1	Still water	Static equilibrium test
case 2.1	Still water	Free decay test in Surge, Sway, Heave, Roll, Pitch and Yaw
case 2.2	Still water	
case 2.3	Still water	
case 2.4	Still water	
case 2.5	Still water	
case 2.6	Still water	
case 3	Regular wave	H=0.06m; T=1.6~3.0sec.
case 4	Irregular wave	Hs=0.06m; Tp=1.34sec.

4. Results and discussion

4.1 Identification of hydrodynamic coefficients using numerical simulation

To use Morison based theory to evaluate hydrodynamic loads on the platform, hydrodynamic coefficients, namely viscous drag coefficient (C_d^D) and inertia coefficient (C_M) have to be determined firstly. Reference value from data base[16,17] is one way of confirming C_d^D and C_M , but effect of interaction between individual members cannot be evaluated from the data base which will result in inaccurate C_d^D and C_M . Alternatively, numerical simulation provides one possibility to evaluate those hydrodynamic coefficients.

To evaluate inertia coefficient, program AQWA(ANSYS) based on potential theory was used in this paper. Equivalent C_M in horizontal direction is obtained based on the added mass in surge direction evaluated from AQWA. C_M in vertical direction is same as that in horizontal direction expect for heave plate. The axial added mass coefficient for heave plate shown in Table 4 is resulted from fitting the total added mass in heave direction from AQWA simulation. Due to limitation of potential theory itself, AQWA cannot be used to evaluate viscous drag coefficient. Alternatively, program FLUENT(ANSYS) was used to estimate C_d^D in this research.

To evaluate C_d^D , Large-eddy simulation (LES) in FLUENT was adopted in this paper to simulate flow field around platform. From numerical simulation, equivalent C_d^D in horizontal direction was estimated to be 0.86 which matches well with that (0.84) obtained from experiment.

Drag coefficient in axial direction for heave plate is in accordance to what identified in water tank experiment as shown in the research by A. Robertson *et al*.[18].

As for mooring system in dynamic model, added mass coefficient and drag coefficient for mooring line are taken from DNV[19]. It should be noted that recommended Cd (2.4) of studless chain is defined by nominal diameter of the chain. In this paper, mooring line is modeled as cylindrical members and C_d^m is estimated to be 1.2 as a result. It is believed that effects of drag force on mooring line should be considered if quasi-static model is used to deal with mooring system. In this research, the drag force on mooring line is evaluated mathematically, and then the equivalent C_d^Q considering contribution of force on mooring line could be expressed in following way,

$$C_d^Q = C_d^D + C_D^{Mooring-line} = \frac{F_D^{Platform}}{0.5\rho U^2 S} + \frac{F_D^{Mooring-line}}{0.5\rho U^2 S} \quad (10)$$

Where $C_d^D, C_D^{Mooring-line}$ are equivalent viscous drag coefficient of platform and mooring line respectively. $F_D^{Platform}$, $F_D^{Mooring-line}$ are drag force on platform and mooring line respectively. $F_D^{Platform}$ is evaluated by numerical simulation and $F_D^{Mooring-line}$ is evaluated in following way by using C_D=2.4.

$$F_D^{Mooring-line} = \sum_{i=1}^{N} F_i = C_D \frac{1}{2}\rho U_i^2 D L_i \quad (11)$$

Where F_i is the force on segment i , C_D is drag coefficient of studless chain (2.4), U_i is velocity of water on segment i which follows sub-surface current velocity profile with standard power law exponent α (1/7), D is nominal diameter of the chain (0.003m), L_i is length of projected segment i in vertical direction.

As a result, $C_D^{Mooring-line}$ equals to 0.19. Then equivalent C_d^Q used in quasi-static model is estimated to be

$C_d^Q = C_d^D + C_D^{Mooring-line} = 0.86 + 0.19 = 1.05$.

Hydrodynamic coefficients for floating system are summarized in Table 4.

Table 4:Hydrodynamic coefficients for floating system

Part	Description		Value
Platform	Added mass coefficient in normal direction	C_M	1.835
	Drag coefficient (quasi-static model)	C_d^Q	1.05
	Drag coefficient (dynamic model)	C_d^D	0.86
	Axial added mass coefficient for heave plate	C_{Mz}	$4\pi\rho(D/2)^3/(3\forall_z)$
	Drag coefficient in axial direction for heave plate	C_{dz}	4.8
Mooring line	Added mass coefficient in normal direction	C_M^m	2.0
	Drag coefficient in normal direction	C_d^m	1.2

4.2 Verification of FEM model

Full FEM of scaled FOWT is shown in Figure 4. In quasi-static model, only platform (73 elements), tower (11 elements) and rotor including blades (33 elements)were simulated with FEM. In dynamic model, each mooring line was molded with 50 truss elements as shown in Figure 4.

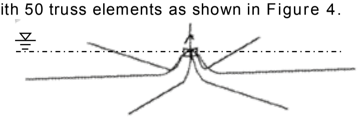

Figure 4: Image of full FEM of scaled FOWT

Natural period of floating system and damping ratio calculated from cases 2.x are listed in Figure 5 and Figure 6. It can be found from Figure 5 that there is negligible difference in terms of natural period between quasi-static and dynamic model. And the resulting natural period from simulation matches well with that confirmed in the water tank experiment which ensures the reliability of established floating system. From Figure 6, one can conclude that dynamic model contributes much more damping than quasi-static model, especially in DOF of yaw which is due to hydrodynamic damping and friction between contacted mooring segments and seabed. It should be highlighted here that radiation damping effect has been taken into account in all cases 2.x which make damping ratio in surge and sway approximate with that in the experiment. The significance of radiation damping effect will be investigated and clarified in section 4.3 by using free vibration in sway direction.

According to the results from potential theory by FAST(V8.08), one can find natural period in surge, sway and heave direction matched well with the experimental data, while roll and pitch natural period were underestimated and natural period in yaw mode was overestimated. FAST underestimated damping ratio in DOF of yaw which is due to the same reason as argued in the quasi-static model implemented in CAsT.

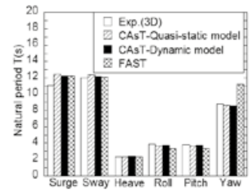

Figure 5: Natural period of floating system in 6 DOF

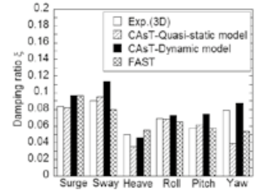

Figure 6: Damping ratio of floating system in 6 DOF

4.3 Significance of radiation damping in free vibration

Morison equation is well known in estimation of hydrodynamic load on bottom-mounted structures. Even though relative form is employed in modified Morison equation (Eq.2 and Eq.3) to expand its application to floating structures, it still overlooks wave-radiation load. The radiation loads are brought about as the platform radiates waves away from itself (i.e., it generates outgoing waves). It can be ignored only if the motions of the platform are very small, otherwise wave-radiation damping should be taken into consideration. It should be stressed here that radiation problem has been separated from the diffraction problem in Morison equation and the wave-radiation loads are independent of the incident waves. The frequency dependence of the hydrodynamic-added damping from potential flow theory means that damping coefficients depend on the oscillation frequency of the particular mode of floating platform motion. And the platform is assumed to oscillate at the same frequency as the incident wave frequency. Therefore, the frequency dependent radiation damping coefficient can be used in regular incident wave and irregular incident wave conditions.

To simplify the problem, one unique linear radiation damping coefficient in each mode rather than frequency dependent matrices was evaluated and employed in Morison equation. This is reasonable because frequency dependent radiation damping coefficient is stable within concerned wave periods.

Equivalent linear radiation damping $[C_{Rdm}]$ can be estimated based on the frequency dependent added damping resulted from potential flow theory. In this paper, $[C_{Rdm}]$ is evaluated by following way.

$$[C_{Rdm}] = \frac{\int_{f_1}^{f_2} C_r(f_i)df_i}{f_2 - f_1} \quad (12)$$

Where $C_r(f_i)$ is wave frequency dependent added damping in each mode, $[f_1, f_2]$ is the possible wave frequency (units: Hz) range scaled from specified sea field.

For the conducted experiment, $[f_1, f_2]$ is[0.33Hz, 0.625Hz].Then resulting $[C_{Rdm}]$ is estimated to be 4.1Kg/s in surge and sway mode. Added damping in the other modes are negligible.

Morison equation after introducing proposed linear radiation damping model reads

$$\{\boldsymbol{F}_H\} = \rho_w(C_M - 1)\forall(\dot{\boldsymbol{u}} - \ddot{\boldsymbol{X}}) + \rho_w\forall\dot{\boldsymbol{u}} + \frac{1}{2}\rho_w C_d A(\boldsymbol{u} - \dot{\boldsymbol{X}})|\boldsymbol{u} - \dot{\boldsymbol{X}}| - [C_{Rdm}]\dot{\boldsymbol{X}} \quad (13)$$

Figure 7 exhibits measured and predicted time series of sway motion in case 2.2 in condition of quasi-static model. Damping ratio identified from measurement was estimated to be 9.0%. Without radiation damping effect, predicted damping ratio was only 5.35% while it increased to be 9.46% when radiation damping was introduced. Error in terms of damping ratio prediction was reduced from -40.5% to 5.2%. Therefore, effect of radiation damping on translational modes is significant in free vibration. Not unexpected, in the situation where wave loads are primary, the effect of radiation damping is minimal. From the figure, one can also find that FAST yields good agreement in terms of natural period and amplitude because radiation damping is taken into account automatically from diffraction analysis.

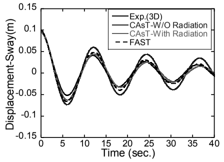

Figure 7: Time series of sway motion in case 2.2.

4.4 Significance of axial force on dynamic response

Recall that Morison equation is limited to calculate the in-line hydrodynamic force which is perpendicular to the cylinder. Ishihara *et al.*[7] put forward a Morison-like equation(Eq.3) using dynamic pressure to account for the Froude-Krylov loads on axial-direction along members for heave plates. However, Froude-Krylov loads on the other slender members (such as braces) were ignored at that time. The significance of those forces will be investigated and be clarified from what follows.

Figure 8 shows measured and predicted dynamic RAOs and phase difference between motion and incident wave in case 3. Due to the limitation of equipment used in experiment, maximum of incident wave period is 2.8s which covers the possible wave range in real site. In site measurement, wave region is estimated to be scaled down between 1.0s and 2.0s in operational condition. The dynamic response of FOWT to regular wave periods higher than 2.0s is important as well for the reason that long wave component in irregular wave such as case 4 could excite heave and pitch resonance which will impact tension in mooring line significantly. Therefore, accuracy of prediction in higher wave period is needed to be ensured. It was found that dynamic motion to regular wave were improved when axial Froude-Krylov force on slender members were considered, especially in heave RAO. It should be noted here that phase difference between incident wave and dynamic motion were improved as well after taking that axial force into consideration. Accuracy in prediction of this phase difference is considerably crucial for evaluation of hydrostatic force in vertical direction because hydrostatic force is dependent on both incident wave height and resulting heave motion itself.

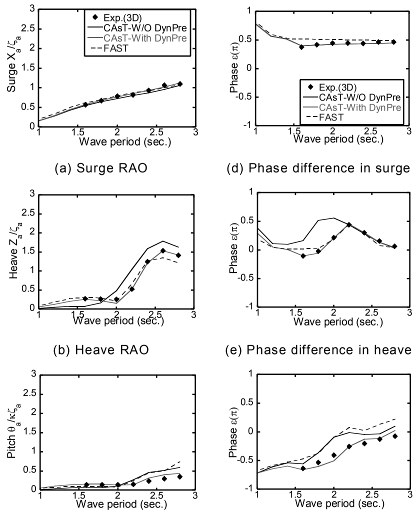

Figure 8: Dynamic RAO and phase difference between motion and incident wave in case 3. $\zeta_a = H/2$, X_a, Z_a and θ_a are amplitude of motion in surge, heave and pitch. W/O DynPre indicates Froude-Krylov force on slender members in axial direction is omitted, With DynPre indicates Froude-Krylov force on slender members in axial direction is considered.

To further explain the significance of axial Froude-Krylov force acting on slender members, components of the external force in Eq.1 were extracted to conduct detailed comparison. The buoyance force, gravity load and steady mooring force will be cancelled out in vertical direction, thus only hydrodynamic and hydrostatic force will be discussed here. Figure 9 exhibits time series of hydrodynamic force Fz in case 3 with wave period of 2.0s. From the figure one can find each component of the force does not change so much after considering axial Froude-Krylov force on slender members. However, the phase difference between hydrodynamic (F_{Hz}) and hydrostatic force (F_{Rz}) changes dramatically which will lead to remarkably different total force on the platform. From Figure 9(b) , one can find resulting total force Fz in case of T=2.0s is decreased after taking account of axial Froude-Krylov force which yields reduced heave motion. As for cases in other wave periods, same analysis can be conducted. Main contributions of fluctuation of total force on platform are from hydrodynamic (F_{Hz}) and hydrostatic force (F_{Rz}). Combination of those two could make the resulting motion amplified or reduced in one specified wave period because there is certain phase differences between hydrodynamic force and hydrostatic force.

To sum up, when axial Froude-Krylov force acting on slender member ends is considered, underestimation of dynamic response in heave and pitch direction in low wave period range is solved. In addition, the overestimation of dynamic response in high wave period range is resolved. Furthermore, phase difference in all sea states were improved as a result as shown in Figure 8.

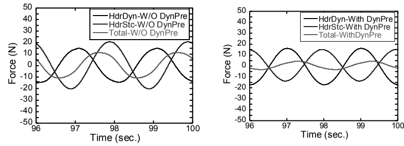

(a) without axial F-K force (b) with axial F-K force

Figure 9: Time series of hydrodynamic F_{Hz}, hydrodynamic F_{Rz} and total Fz in case 3 (T=2.0s) with and without consideration of axial Froude-Krylov (F-K) force

Figure 10(a) depicts power spectrum density (PSD) of incident wave (case 4) which used in CAsT and FAST. From the figure, one can find that incident wave in CAsT and FAST can be used to represent the wave condition in water tank experiment except for a small amount underestimation in low wave frequency region([0,0.4Hz]) in which FAST underestimates the wave energy much more. Figure 10 (b),(c) and (d)exhibits measured and predicted PSD of dynamic response in surge, heave and pitch respectively. In PSD of pitch motion, the peak at around 0.26Hz corresponds to natural pitch frequency of floating system and the resonance phenomenon was excited by low wave frequency components in irregular wave. The peak at around 0.75 Hz corresponds to peak period of incident wave and the predicted wave-induced response was improved since the underestimation of predicted dynamic RAO in low wave period region was solved after axial Froude-Krylov load on slender members is taken into account as shown in Figure 8. Compared with PSD of heave and pitch in CAsT, FAST underestimates the amplitude much more in the wave frequency range [0,0.4Hz] for the reason that FAST underestimates the wave energy in this wave region much more as indicated in Figure 10(a). The small amount of difference in the PSD of incident wave especially in low wave frequency region between CAsT and experimental data is needed to be solved in future study since the long wave period is crucial for prediction of tension in mooring system. Consequently, the dynamic response of FOWT is expected to be improved as well.

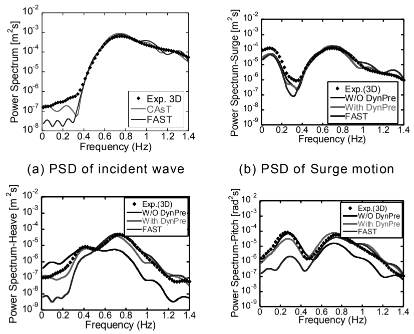

(c) PSD of Heave motion (d) PSD of Pitch motion

Figure 10: Power spectrum of incident wave and dynamic response of motion to irregular wave in case4.

4.5 Significance of dynamic behavior of mooring system on tension prediction

Provided translational motion in sway direction and rotational motion in roll direction is negligible, tension in T1, T2 and T3 are identical with the tension in T6, T5 and T4 respectively due to symmetric arrangement of mooring line as shown in Figure 2. Thus only tension in T1, T2 and T3 will be discussed. Figure 11 exhibits measured and predicted time series of tension within T1 using quasi-static model and dynamic model respectively in case 3 (T=2.4s). Initial tension in each mooring line is removed in the total tension and only the fluctuation of tension is remained and shown in Figure 11. It should be noted here that the tension from simulation is under condition of that dynamic pressure effect has been considered on all immersed members. From the Figure 11(a), one can find that predicted tension T1 is overestimated and predicted crest in tension lags behind what measured in experiment. In addition, harmonic response in tension was observed in measured data which was not reproduced by quasi-static model. It should be stressed here that even though the mooring system is coupled with platform and wind turbine, overestimated amplitude of tension has negligible effect on prediction of hydrodynamic response of floater since fluctuated tension is proved to be sufficiently small compared with the fluctuation of hydrodynamic force on platform which makes the quasi-static model be acceptable to be used to predict dynamic response of floating platform. From the Figure 11(b), one can find amplitude of tension from simulation matched well with that from experiment. In addition, harmonic components in the tension were reproduced successfully by using dynamic model. The reason why harmonic components were observed in experiment and could be reproduced in simulation is that nonlinear viscous drag force is dominant in total hydrodynamic force acting on mooring line.

Figure 12 shows measured and predicted tension RAO and phase difference between tension and incident regular wave in mooring line T1, T2 and T3. Phase difference shown in the figure is normalized by π. It was found that quasi-static model overestimates tension RAO of T1 by 56% while dynamic model in CAsT only yields 14% difference compared with measured tension. Even though dynamic model in CAsT still overestimates the tension in T2 and T3 in some extent, it is proved to be conservative in the design of mooring system. But the improved accuracy will contribute cost reduction in design process. The predicted tension RAO using FAST is consistent with that in CAsT using quasi-static model. The little difference is due to the discrepancy of dynamic motion predicted by CAsT and FAST as exhibited in Figure 8.

Recognized that influence of dynamic behavior of mooring line is significant in evaluation of tension amplitude and drag force is dominant in total hydrodynamic loads on mooring line, one should realize that drag coefficient of chain consisting mooring line is a key parameter in dynamic analysis of mooring system.

5. Conclusions

Effects of radiation damping, axial Froude-Krylov force on slender members and dynamic behavior of mooring system were investigated using Morison based theory in this paper. Main conclusions are as follows,

1. Potential flow based theory is proved to be sufficiently accurate in evaluation of inertia coefficient, but drag coefficient cannot be obtained because of inviscid assumption in potential flow theory. Alternatively, the distributed drag coefficient was evaluated using CFD in this paper and the equivalent value was validated by water tank experiment.

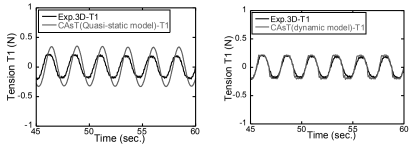

(a) Quasi-static model (b) dynamic model

Figure 11: Measured and predicted time series of tension within T1 in case 3 with wave period 2.4sec.

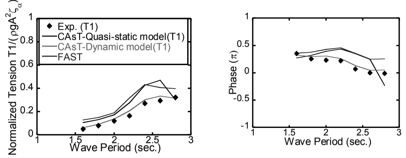

(a) Tension RAO-T1 (d) Phase difference in T1

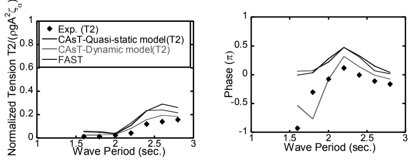

(b) Tension RAO-T2 (e) Phase difference in T2

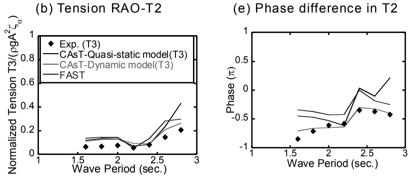

(c) Tension RAO-T3 (f) Phase difference in T3

Figure 12: Measured and predicted tension and phase difference between tension and incident regular wave by using quasi-static model, dynamic model and FAST.

2. Radiation damping plays an important role in free decay test. Without radiation damping effect, predicted damping ratio in DOF of sway was 5.35% and with radiation damping effect it was predicted to be 9.46%. Error in terms of damping ratio prediction was reduced from -40.5% to 5.2%. But, in the situation where wave loads are primary force the role of radiation damping is minimal.

3. Froude-Krylov loads on slender members are crucial in prediction of dynamic response of FOWT to regular wave. Conventional Morison based theory is enhanced. Consequently, in irregular wave, wave-induced response was improved in low wave period region as well.

4. Predicted tension by using quasi-static model was overestimated by 56% in T1. Dynamic model gave only 14% difference between measured and predicted tension. Thus, inertia and nonlinear damping force on mooring system has to be considered when evaluate tension in mooring lines.

5. FAST yields good agreement with experiment in prediction of natural period of surge, sway and heave DOF, but it underestimates pitch natural period. FAST is capable of predicting dynamic motion of platform in regular wave, but tension in mooring line is overestimated considerably since inertia and nonlinear damping force are ignored in the quasi-static model it implemented.

Acknowledgement

This research is funded by Ministry of Economy, Trade and Industry, Japan. I wish to express my deepest gratitude to the concerned parties for their assistance and contribution in this research.

References:

[1] Latha Sethuraman, Vengatesan Venugopal. Hydrodynamic response of a stepped-spar floating wind turbine:Numerical modelling and tank testing. Rnewable Energy 52(2013) 160-174.

[2] J. R. Morison, M. P. O'Brien, J. W. Johnson and S. A. Schaaf. The force exerted by surface waves on piles. J.Petrol.Tech., A.I.M.E., Vol.189,1950.

[3] J.R. Browning, J. Jonkman, A. Robertson and A.J. Goupee. Calibration and Validation of a Spar-Type Floating Offshore Wind Turbine Model using the FAST Dynamic Simulation Tool. Conference paper (National Renewable Energy Laboratory (U.S.)); NREL/CP-5000-56138,2012.

[4] Marit I. Kvittem, Erin E. Bachynski, and Torgeir Moan. Effects of hydrodynamic modelling in fully coupled simulations of a semi-submersible wind turbine. Energy Procedia 24 (2012) 351-362.

[5] P.V. Phuc, T. Ishihara, A study on the dynamic response of a semi-submersible floating offshore wind system part 2: Numerical simulation, in: Proceedings of the international Conferences of Wind Engineering 12, Cairns, Australia, 2007.

[6] M. B. Waris and T. Ishihara. Dynamic response analysis of floating offshore wind turbine with different types of heave plates and mooring systems by using a fully nonlinear model. Coupled Systems Mechanics, Vol. 1, No. 3 (2012) 247-268.

[7] T. Ishihara, K. Kagaya, Y. Kikuchi. Dynamic Analysis of Floating Offshore Wind Turbine System Considering Combined Hydrodynamic Loadings. EWEA OFFSHORE 2013. PO.ID 133.

[8] M. Hall, B. Buckham and C. Crawford. Evaluating the importance of mooring line model fidelity in floating offshore wind, Wind Energy.2014;17:1835–1853

[9] M.Hall , A. Goupee. Validation of a lumped-mass mooring line model with DeepCwind semisubmersible model test data. Ocean Engineering 104 (2015) 590–603

[10] FAST version 8.08, NREL,2014.

[11] Bladed version 4.6, DNV·GL,2014.

[12] J. M. Jonkman. Dynamics of Offshore Floating Wind Turbines- Model Development and verification. Wind Energy. 2009; 12:459-492. DOI 10.1002/we.347

[13] L. Tao,S. Cai. Heave motion suppression of a spar with a heave plate. Ocean Engineering 31 (5), 669-692,2004

[14] H.A. Haslum, and O. M. Faltinsen. Alternative Shape of Spar Platforms for Use in Hostile Areas. Offshore Technology Conference, OTC10953, Houston, Texas, 1999.

[15] L. Tao, K. Y. Lim and K. Thiagarajan. Heave Response of Classic Spar With Variable Geometry. Journal of Offshore Mechanics and Arctic Engineering, Vol.126, 90-95,2004

[16] Hermann Schliching. Boundary-Layer Theory[M]. New York: Mcgraw-Hill Book Company,1979.

[17] A Review of Added Mass and Fluid Inertia Forces, Naval Civil Engineering Laboratory, Port Hueneme, California, January 1982

[18] A. Robertson, J. Jonkman, M. Masciola, H. Song, A. Goupee, A. Coulling and C. Luan. Definition of the Semisubmersible Floating System for Phase II of OC4. Technical Report. NREL/TP-5000-60601, Golden, Colorado, September 2014.

[19] DNV (2010a). DNV Recommended Practice DNV-RP-C205. Environmental Conditions and Environmental loads.

Evaluation of the performance of a Navier-Stokes and a viscous-inviscid interaction solver in trailing edge flap simulations

John Prospathopoulos, jprosp@fluid.mech.ntua.gr
Giorgos Papadakis, papis@fluid.mech.ntua.gr
Alexis Theofilopoulos, atheofi@yahoo.gr
Theofanis Tsiantas, th.tsiantas.mech.ntua@gmail.com
Vasilis Riziotis, vasilis@fluid.mech.ntua.gr
Spyros Voutsinas, spyros@fluid.mech.ntua.gr

National Technical University of Athens, 9 Heroon Polytechniou, 15780, Zografou, Athens, Greece

Abstract:

Trailing edge flap is one of the most common flow control devices aiming at reducing the loads on the wind turbine blades. From the modelling point of view the dynamic character of flap introduces challenges, including unsteady flow phenomena and moving/deformable meshes. In the present paper airfoils with flapping trailing edge are simulated using two different computational tools, one viscous-inviscid interaction code and one compressible Navier-Stokes code. The predictions of the codes for static and dynamic flap situations are compared to the existing measurements. In the static flap cases, predictions of both models were satisfactory in the linear region. In free transition the better predictions of the drag coefficient by the viscous-inviscid interaction code are attributed to the different transition model. In the dynamic flap cases, combined with a harmonic pitching motion of the airfoil, part of the differences emanates from the fact that the actual (measured) flap angle deviates from the nominal one as reported by the experimenters.

Keywords: Trailing edge flap simulation, viscous-inviscid interaction, CFD, transition models.

1 Introduction

Lifetime of large wind turbines depends on the aerodynamic and structural loads experienced during operation. Most of these loads exhibit periodic variation in multiples of the rotational frequency. To minimize these loads, control systems should be able to reduce the fluctuations of the aerodynamic loads or add damping to the structural modes. On the other hand the aerodynamic performance of the airfoils along the blade span should be maximized. Flow control devices, such as trailing edge (TE) flaps or vortex generators, aim at mitigating the fatigue loads and improving the aerodynamic performance of an airfoil. In the framework of AVATAR.EU FP7 project the effect of flow control devices on large wind turbine blades is investigated.

In the present paper, trailing edge flap is investigated using simulations by two in-house computational tools developed at NTUA. The first is the Foil1w viscous-inviscid interaction code [1] and the second is the MaPFlow compressible Navier-Stokes solver [2]. Two different cases with available experimental data were chosen: The first refers to static TE flap for which steady state simulations are performed. For that case, the experimental data are taken from the measurements of the TL190-82 airfoil performed in the course of the European UPWIND project at the wind tunnel of the Institute of Aerodynamics and Gas Dynamics (IAG), University of Stuttgart [3]. The second case refers to dynamic TE flap for which unsteady state simulations are performed. In that case the experimental data are taken from measurements on NACA0012 carried out by Krzysiak and Narkiewicz in the trisonic N-3 wind tunnel located at the Institute of Aviation Warsaw, Poland [4].

2 Numerical models

Foil1w: Foil1w is a viscous-inviscid interaction code developed at NTUA. The potential flow part is simulated by singularity distributions along the airfoil geometry and the wake. The wake is represented by vortex particles which are allowed to freely move with the local flow velocity.

The viscous flow solution is obtained by solving the unsteady integral boundary layer equations defined by Drela [5] with unknowns the displacement thickness, the momentum thickness and the amplification factor (laminar part) or the shear stress coefficient (turbulent part) through which C_D is determined. The viscous-inviscid coupling is achieved through a transpiration velocity distribution along the airfoil surface that represents the mass flow difference over the boundary layer height between the real viscous flow and the equivalent inviscid flow.

The boundary layer equations are discretized using finite differences and the final set of the non-linear equations are solved simultaneously using the Newton-Raphson algorithm. The boundary layer solution is supplemented by a transition prediction model based on the e^N spatial amplification theory [6] and by a dissipation closure equation for the maximum shear stress coefficient over the turbulent part.

MaPFlow: MaPFlow is a multi-block MPI enabled compressible solver equipped with preconditioning in regions of low Mach flow [7]. The discretization scheme is cell centered and makes use of the Roe approximate Riemann solver for the convective fluxes. In space the scheme is 2nd order accurate defined for unstructured grids and applies the Venkatakrishnan's limiter [8]. Also in time the scheme is second order and implicit introducing dual time stepping for facilitating convergence. The solver is equipped with the Spalart-Allmaras (SA) and the k-w SST eddy viscosity turbulence models.

Regarding transition, the correlation γ-Re_θ model of Menter [9] has been implemented. The γ-Re_θ is a two transport equation model for the intermittency and the momentum thickness Reynolds number. It utilizes local variables easily computed in each cell and does not need boundary layer definition and parameters.

3 Simulation of Trailing Edge flap

3.1 Static TE flap cases

For the TL190-82 airfoil (Figure 1), static TE flap deflections from -10 to 10 degree are simulated in clean and tripped conditions at a Reynolds number of $2.5{\cdot}10^6$. MaPFlow used an O-type mesh of 150000 cells generated by ICEM CFD. The non-dimensional distance of the first node from the wall is less or equal to 10^{-5}. Foil1w can use only sharp airfoil profiles, so the original blunt airfoil profile is made sharp by modifying the aft of the original shape and discretized with a number of 100 panels. Clean conditions are simulated with free transition modeling, whereas tripped conditions are simulated with fully turbulent and fixed transition modeling by MaPFlow and Foil respectively.

Figure 1: Articulated TE flap for the TL190-82 airfoil

The predictions of the lift and drag coefficients are compared with the measurements in Figures 2,3. In clean conditions, both models predict lift well in the linear region. The fact that Foil1w predicts drag better than MaPFlow suggests that the e^N transition model identifies the transition locations more accurately than the γ-Reθ model. Differences among predictions appear at higher AoAs and are more pronounced in the post-stall region. In general, stall is predicted at higher AoAs compared to the measurements. Tripping appears to have a drastic effect on the measurements by shifting stall to lower AoA. This effect is less pronounced in the predictions which present larger deviations from the measurements compared to clean conditions.

In tripped conditions, the predictions of MaPFlow are closer to the measurements, in terms of both lift and drag. As expected the more advanced CFD model predicts friction more accurately than the boundary layer model in turbulent flow conditions.

3.2 Dynamic TE flap cases

Dynamic TE flap cases of the NACA0012 airfoil refer to a Reynolds number of 1.63 10^6. A rigid trailing edge flap is implemented with a length 20% of the airfoil chord. The reduced frequency of the airfoil pitching motion is $k_A = 0.021$, while the flap oscillation has a double frequency, $k_F = 0.042$. The angle of attack (pitch angle) and the flap deflection are governed by the equations

$$a=a_m+\Delta\alpha\ \sin(2k_A t)\ , \qquad (1)$$

$$\beta=\beta_m+\Delta\beta\ \sin(2k_F t-\varphi) \qquad (2)$$

where α_m and β_m are the mean values of the angle of attack and flap deflection, $\Delta\alpha$ and $\Delta\beta$ are the amplitudes of the airfoil and flap harmonic movement respectively and φ is the phase shift between the airfoil and the flap angle.

In all simulated cases $\alpha_m=4^o$, $\Delta\alpha=6$, $\beta_m=0^o$ *and* $\Delta\beta=5^o$ is considered while the effect of varying φ on aerodynamic loads is investigated. It is noted that positive pitching angle is the one that leads to nose up motion of the airfoil (increasing angles of attack) while positive flap deflection angle is the one obtained when the flap moves downwards.

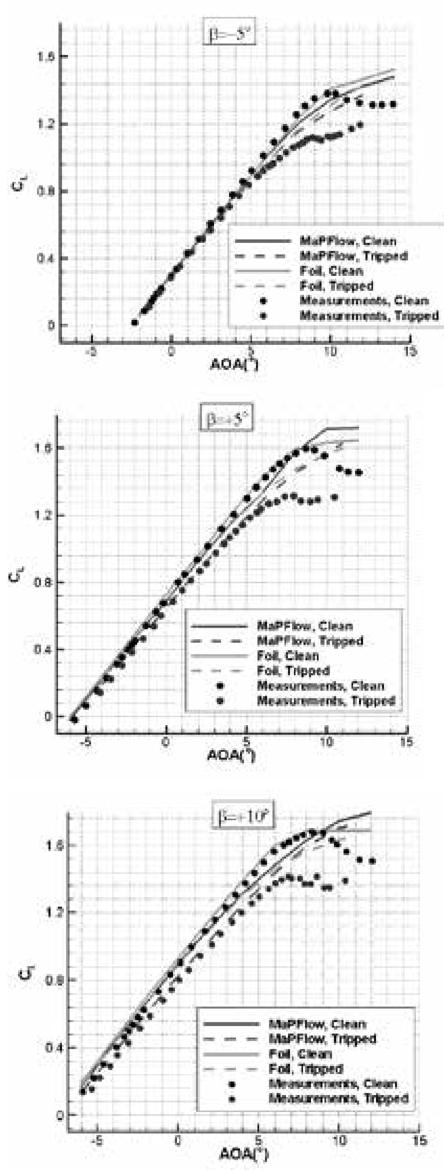

Figure 2: C_L polars for TE static flap, TL190-82 airfoil, Re=2.5·10[6]. Flap angle takes the values -5°, +5° and +10°. Clean conditions correspond to free transition and tripped conditions correspond to fixed transition

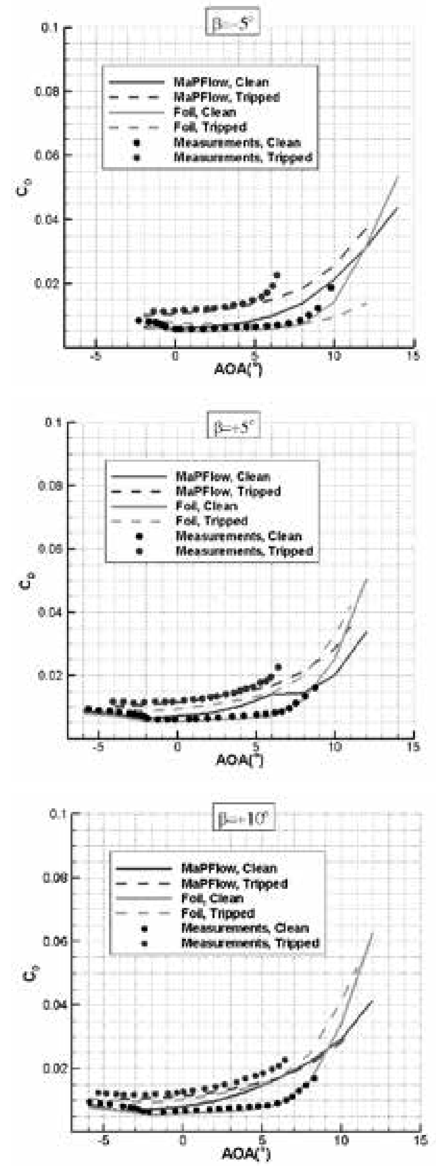

Figure 3: C_D polars for TE static flap, TL190-82 airfoil, Re=2.5·10[6]. Flap angle takes the values -5°, +5° and +10°.. Clean conditions correspond to free transition and tripped conditions correspond to fixed transition

MaPFlow uses a C-type mesh of 88000 cells generated by ICEM CFD (Figure 4) and performs fully turbulent simulations. One flapping period is discretized using 720 time steps. The code runs initially for constants AoA= α_m and flap angle= β_m until a steady state solution is reached and then the harmonic variations of both angles are imposed. A periodic solution is achieved after 6 flapping periods. Foil1w considers fixed transition at 5% chord from the leading edge. One flapping period is discretized using 400 time steps and convergence is achieved again after 6 flapping periods.

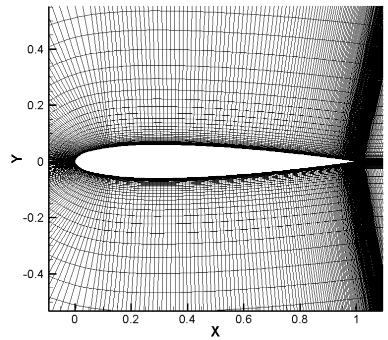

Figure 4: Computational mesh around the NACA0012 airfoil

The different test cases refer to different phase shifts between the airfoil pitching motion and the flap angle. Figure 5 shows the variation of the flap angle with the angle of attack for φ=148°, φ=206° and φ=298°. Measurements deviate from the nominal values provided by Equations (1),(2) possibly due to elastic deformations occurred during the experimental campaign or delay/errors in the response of the actuators controlling the motion of the airfoil and the flap. In order to fit the measured airfoil phase /flap relative motion, Nestor [10] suggested corrections to the phase shift from φ=148° to φ=135°, from φ=206° to φ=196° and from φ=298° to φ=280°. The double frequency of the flap movement results in the appearance of two loops, one corresponding to a whole flap cycle when AoA is positive and another one corresponding to a whole flap cycle when AoA is negative.

In order to estimate the effect of the phase shift correction, as suggested by Nestor, to the predictions, some initial simulations are performed with Foil1w. In Figure 6, the modified C_L, C_M loops for φ=148° are compared with those of φ=135° which is the corrected phase shift. Differences with measurements have been decreased suggesting that an even better correlation with the measured flap angle may result in a better and more fair comparison

.

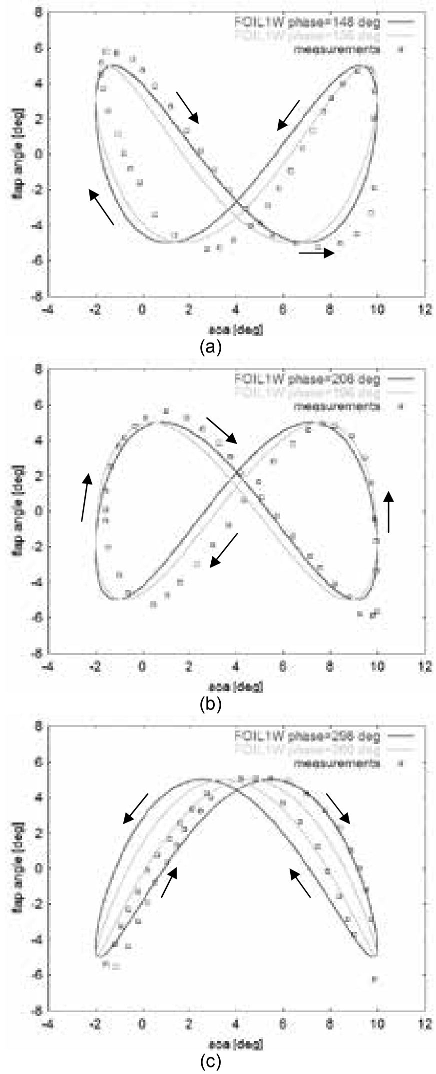

Figure 5: Theoretical and measured variation of the flap angle with the angle of attack (i.e. pitching angle) for (a) φ=148°, (b) φ=206° and (c) φ=298°. Nestor [12] suggested phase corrections from 148° to 135°, from 206° to 196° and from 298° to 280° in order to fit the measured airfoil / flap relative motion

For the comparison between predictions and measurements, the corrected phase shift is adopted. In Figures 7,8, the predicted C_L, C_M loops are presented. The overall shape of the loops is reproduced by both models, however, lift is generally overpredicted and moment is underpredicted. Larger differences are observed at the positive AoAs and are responsible for the overestimation in the slope of the double loop (C_L-AoA diagrams, Figure 7). A part of these differences can be attributed to the deviation of the measured flap angles from the theoretical values or to the 3D effects related to the experiment, such as the creation of stall cells along the blade model.

For example, in Figure 5a, it can be observed that during the upstroke measured flap angles are lower than the nominal (positive AoA, negative flap), reducing the lift. A similar observation can be made in Figure 5b, where the measured values of the flap deflection are again more downwards than the theoretical used in the simulations, when the airfoil is in the downstroke phase (negative AOA, negative flap). Estimation of the 3D effect on the slope of the lift loops could be made by comparing predicted and measured lift polars at static TE flaps. However, no measurements have been reported for static TE flap.

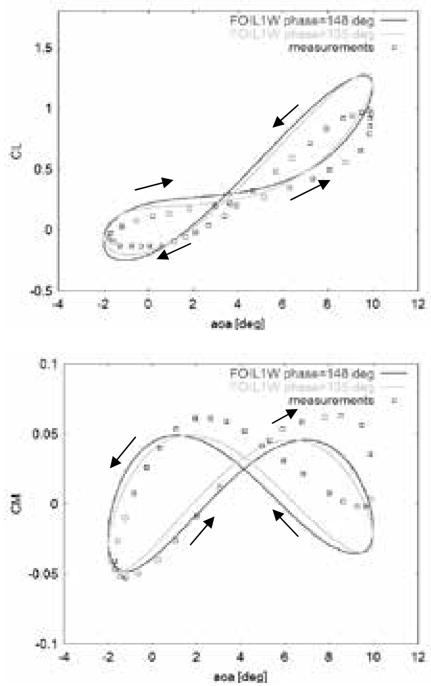

Figure 6: Modification in C_L, C_M coefficients predicted by Foil1w when the phase shift is corrected from 148° to 135°

It should be noted that Foil1w predictions are closer to the measurements compared to those of MaPFlow. One possible reason is that MaPFlow used fully turbulent simulation instead of fixed transition. On the other hand, there are no experimental data for drag, which is expected to be better predicted using the k-ω SST turbulence model implemented in MaPFlow.

4 Conclusions

Several static and dynamic TE articulated flap cases were simulated by two solvers, the MaPFlow CFD solver using the k-ω SST turbulence model, and the viscous-inviscid interaction Foil1w model using the e^N transition model. Regarding the static TE cases, numerical models give acceptable C_L errors in the linear region. In free transition cases, the e^N transition model showed a better behavior than the γ-Reθ transition model, probably because it predicts the transition locations more accurately. The location of the $C_{L,\,max}$ was not well reproduced by the numerical models. Therefore, in the post-stall region the predicted errors were almost doubled compared to those found in the linear region. In the tripped condition cases, drag was better predicted by the fully turbulent simulations of the CFD code using the k-ω SST model.

Regarding the dynamic TE flap cases (along with a harmonic movement of the airfoil), the measured flap angle deviated from the one obtained from the theoretical relationships to be used as input to the simulations. This is a first reason for the differences between predictions and measurements of the lift and moment coefficients. Although the correction suggested by Nestor partly improved the correlation with the experimental data, an even more accurate representation of the input flap angle must be sought. One way to do this is by approximating the flap angle variation by a Fourier series in which higher order harmonics are retained. A first attempt was made for the φ=206° case as shown in Figure 9. The flap representation is much closer to the measured one (six coefficients of the Fourier series are retained in this case), and the Foil1w C_L, C_M predictions have been considerably improved. C_L comes close to the measurements during the downstroke of the airfoil at positive flap angles, while C_M comes close to the measurements again during the downstroke of the airfoil but at negative flap angles. More simulations using both Foil1w and MaPflow codes must be performed to evaluate the effect of a more accurate flap angle representation on the predictions.

Another reason for the differences between predictions and measurements could be the 3D effects, such as the creation of stall cells along the blade model. Nevertheless, the comparison is encouraging because the shape of the lift and momentum variations was well reproduced and the mean level was predicted satisfactorily in many cases.

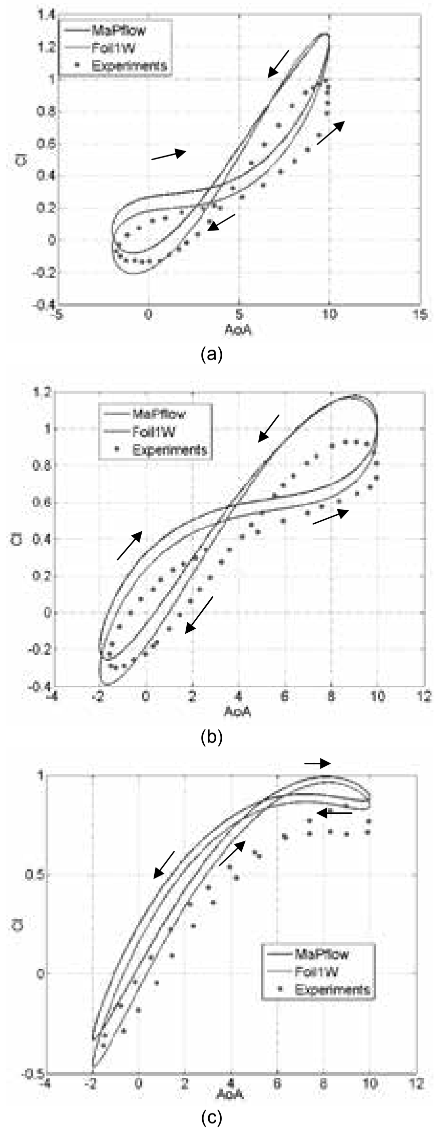

Figure 7: Comparison of predicted C_L coefficients with measurements. Phase shift is (a) 135°, (b) 196° and c) 280°

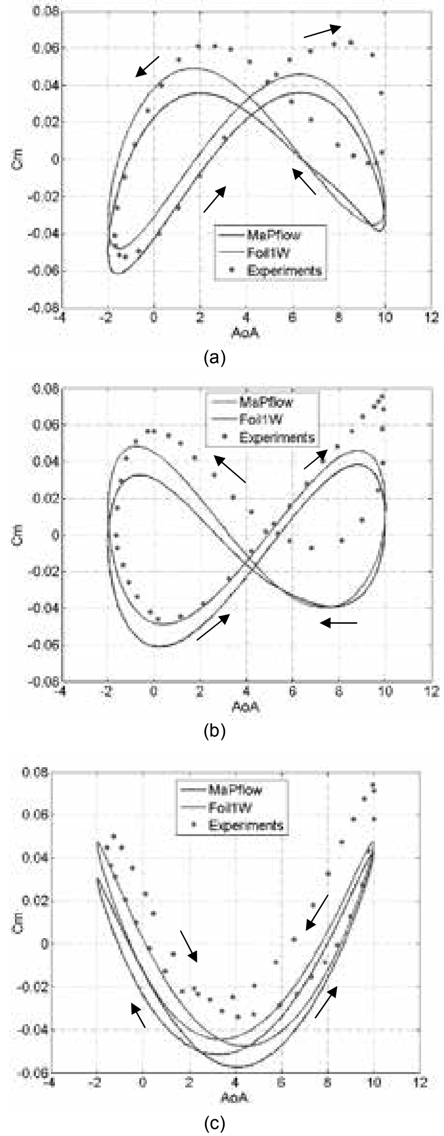

Figure 8: Comparison of predicted C_M coefficients with measurements. Phase shift is (a) 135°, (b) 196° and c) 280°

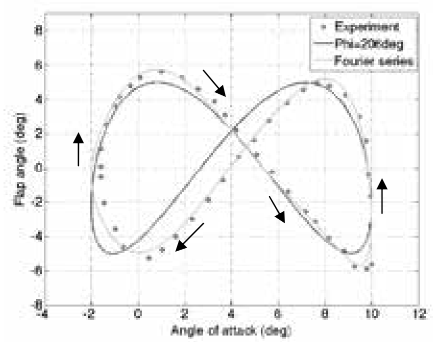

(a)

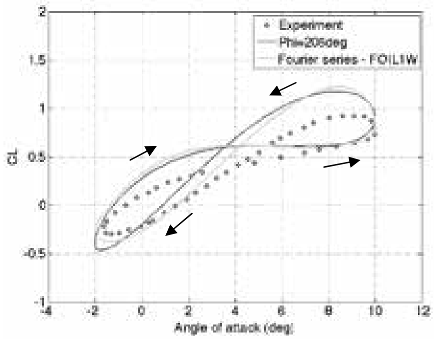

(b)

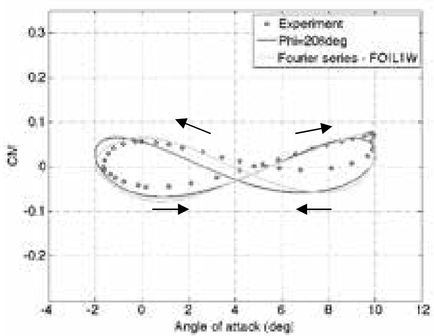

(c)

Figure 9: Representation of the flap angle variation using Fourier series and predicted C_L, C_M by Foil1w. Comparison with the predictions derived by the nominal flap angle variation: (a) Flap angle variation, (b) C_L and (c) C_M

Acknowledgment

The research leading to a part of these results has received funding from the European Community's Seventh Framework Programme under grant agreement No. 2013- 608396 (AVATAR.EU)

References

[1] Riziotis V.A. and Voutsinas S.G., 2008, "Dynamic stall modelling on airfoils based on strong viscous–inviscid interaction coupling", *International Journal for Numerical Methods in Fluids* 56 2 185-208

[2] Papadakis G. and Voutsinas S.G., 2014, "In view of accelerating CFD simulations through coupling with vortex particle approximations" in: *The Science of Making Torque from Wind Journal of Physics: Conference Series*, IOP Publishing Copenhagen pp. 012126

[3] Lutz T. and Wolf A., 2010, "Aerodynamic and acoustic design of wind turbine airfoils with trailing-edge flap" in Proceedings of DEWEK 2010, DEWI, Germany.

[4] Krzysiak, A. and Narkiewicz, N. "Aerodynamic loads on airfoil with trailingedge flap pitching with different frequencies". *Journal of aircraft*, 43:407-418, 2006

[5] Drela M, Giles M., "Viscous–inviscid analysis of transonic and low Reynolds number airfoils". *AIAA Journal* 1987; 25(10):1347–1355

[6] van Ingen JL., "A suggested semi-empirical method for the calculation of the boundary layer transition region". *Report VTH-74*, Department of Aerospace Engineering, Delft University of Technology, 1956.

[7] Papadakis G. and Voutsinas S.G, "In view of accelerating CFD simulations through coupling with vortex particle approximations", in: *The Science of Making Torque from Wind Journal of Physics: Conference Series*, IOP Publishing Copenhagen pp. 012126, 2014

[8] Venkatakrishnan V. "On the accuracy of limiters and convergence to steady state solutions", AIAA Paper 93-0880, 1993

[9] Robin B. Langtry, Florian R. Menter: "Correlation-Based Transition Modeling for Unstructured Parallelized Computational Fluid Dynamics Codes", AIAA Journal, Vol. 47, No. 12, December 2009..

[10] Nestor Ramos Garcia, "Unsteady Viscous-Inviscid Interaction Technique for Wind Turbine Airfoils", PhD Thesis, DTU Department of Mechanical Engineering, April 2011.

Testing of a new morphing trailing edge flap system on a novel outdoor rotating test rig

Helge A. Madsen, Thanasis K. Barlas, Tom Løgstrup Andersen

Aeroelastic Design group, Wind Energy department, Technical University of Denmark (DTU)

hama@dtu.dk

Abstract

The morphing trailing edge system or flap system, CRTEF, has been developed over the last 10 years at DTU Wind Energy. After a promising wind tunnel test of the system in 2009 the INDUFLAP project has been carried out from 2011-2014 to transfer the technology from laboratory to industrial manufacturing and application.
To narrow the gap between wind tunnel testing and full scale prototype testing we developed the rotating test rig. The overall objectives with the rotating test rig are: 1) to test the flap system in a realistic rotating environment with a realistic g-loading; 2) to measure the flap performance in real turbulent inflow and 3) to test the flap system in a realistic size and Reynolds number when comparing with full scale applications..
The rotating test rig consists of a 2.2m blade section attached to a 10m boom and mounted on a 100kW turbine platform. It was installed in June 2014 and a short measurement campaign was conducted in the autumn 2014.
An important result of testing the flap system on the rotating test rig was operation of the flap system up to 30 rpm. which a g-loading of 9-10g comparable with the conditions on a 2-3MW turbine.
Another important result was the measured performance of the flap system. We found that about 5.0deg. flap angle gives the same load change as 1deg. pitch. This is somewhat lower than simulations have shown which are in the range of 2 to 3 deg. flap angle to 1deg. pitch angle for a 15% flap. The realistic, turbulent inflow is probably a major cause of this lower performance.

Keyword

CRTEF: Controllable Rubber Trailing Edge Flap
Flap testing
Morphing airfoil
Rotating test rig
Pressure measurements

1. Introduction

Considerable research on SMART blade technology has been conducted for more than 10 years and has shown big potentials for load reduction on MW turbines using distributed control for alleviation of the fluctuating loads along the blade span [1]. However, the requirements by the wind turbine industry of robust actuator solutions where the strongest specifications mean no metal and electrical parts in the blades have so far limited the use of the smart blade technology on wind turbines.
The development and testing of the morphing trailing edge flap system to be presented in the present paper, also called the Controllable Rubber Trailing Edge Flap (CRTEF), was initiated in 2006. The first prototype was tested in the laboratory in 2008 and in late 2009 wind tunnel measurements in the Velux wind tunnel in Denmark were conducted on a blade section of 1.9m span and 1m chord with a 15% trailing edge flap system [2]. From 2011 to 2014 the INDUFLAP project, funded by the Danish national funding board EUDP, was conducted with the overall aim to transfer the technology from laboratory conditions to industrial manufacturing and application [3]. An important part of this work was the testing of the flap system on an outdoor rotating test rig in order to reduce the gap in test conditions between wind tunnel testing and full scale testing on a MW turbine.
In the present paper the developed flap technology will first be briefly described. Then the design and construction of the rotating test rig will be presented followed by a section with results from a few weeks test campaign in the autumn 2014

2. The developed flap technology – the CRTEF system

2.1 The flap actuation concept

The initial flap concept studies back in 2006 led to the design of the so-called Controllable Rubber Trailing Edge Flap (CRTEF) which comprises a morphing trailing edge manufactured in an elastic material with a number of voids inside. Their geometry are designed so that pressurizing some or all of the them will create a deflection of the flap.
In an actual design shown in Figure 1 the

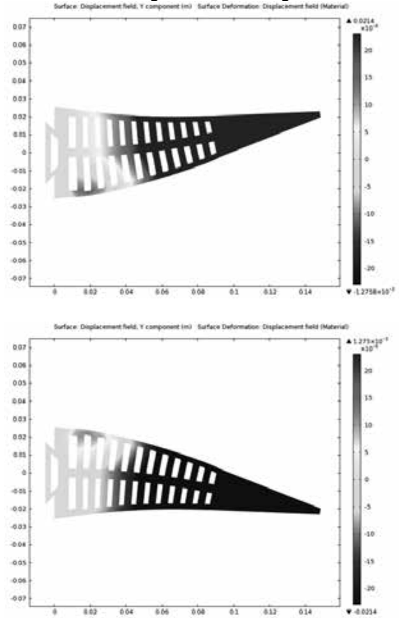

Figure 1 – Deflection of the flap by pressurizing the lower and upper layer of voids, respectively.

voids are orientated in the spanwise direction in two layers which is a design suited for manufacturing by extrusion. Pressurizing the lower layer will give an upward deflection as shown in the upper part of Figure 1. Likewise, pressurizing the upper row of voids will give a downward deflection as shown in the lower part of Figure 1.

2.2 Flap design and manufacturing

During the above mentioned INDUFLAP project carried out by DTU Wind Energy in cooperation with the two industrial partners Hydratech and Rehau a flap design well suited for manufacturing in an extrusion process was developed. It consist of three main parts; a passive, load carrying part as shown in Figure 2 and two actuation parts containing the voids as shown in Figure 3 where they are assembled with the passive part.

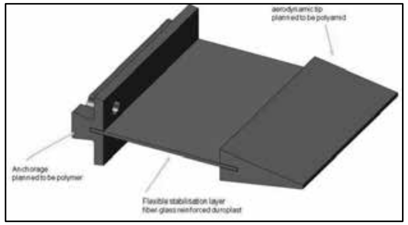

Figure 2 – The passive, load carrying part of the flap system.

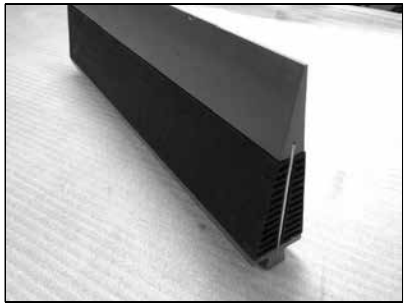

Figure 3 – The two actuation flap elements assembled with the load carrying part.

The manufacturing of the 2m long actuation parts was performed by Rehau in a continuous thermoplastic extrusion process in form of a quasi endless 12 chamber hollow profile using the santoprene material. For manufacturing the sealed ends of the hollow profiles, a special method of a contact welding process was developed.

2.3 Flap integration into the blade and overall blade design

The integration of the flap system into the blade is an important part of the concept. It should allow an easy mounting of the flap so that a possible replacement of the flap segments can be carried out without any heavy tools and equipment. If a spanwise length of e.g. 3m is chosen it should be possible for two technicians climbing on the blade to dismantle a flap segment and mount a new one. Further, if the extrusion process is used for manufacturing the flaps, they will have a constant chord. It is therefore proposed to use different sizes of flaps along the blade span with passive, 3D mold manufactured flaps in between to enable a more continues blade planform. By passive flaps are meant flaps that don´t have voids and they can therefore easily be manufactured in a full 3D geometry, e.g. by a molding process, with variable chord length so they can be inserted between the active flaps with constant chord and thus give a smoother planform distribution.
One overall blade design could therefore be a blade manufactured without the last about 10% of the trailing edge region along the whole span. On the inboard part of the blade with the thick airfoils this would form the flat back airfoils commonly used to improve aerodynamic performance of thick airfoils.
From e.g. 1/3 of the radius and to the tip, passive and active flap sections could then be mounted. During the INDUFLAP project [3] the attachment elements shown in Figure 4 were developed. A big advantage of the design is that it will reduce the requirements for blade trailing edge finishing a lot as the rest material from the gluing does not need to be removed. It also enables a fast attachment of the flap to the blade and in the lab. it took less than a minute to mount the 2m flap on a blade section as shown in Figure 5.

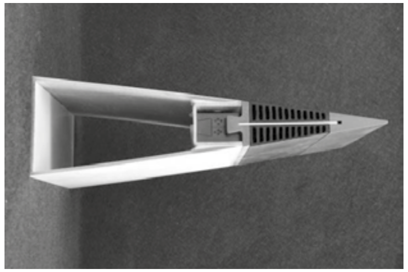

Figure 4 – The flap attachment to the blade.

Figure 5 – Demonstration in the lab. of mounting the 2m flap on a blade section.

3. The rotating test rig

At an early stage of development of the flap system wind tunnel tests were carried out in 2009 to verify the aerodynamic response characteristics of the system [1]. Pressure measurements were carried out on a blade section of 1.9m span, 1m chord and with a 15% CRTEF system in the VELUX wind tunnel in Denmark. The unsteady aerodynamic response characteristics were derived showing a characteristic time constant of about 100ms.
However, there is big step from wind tunnel testing on a stationary blade section to full scale turbine application and therefore a so-called rotating test rig has been developed in the INDUFLAP project [3].

The idea behind the test rig is that the testing should be as close as possible to the rotating environment on the real turbine. So exposing the flap system to a g-loading comparable with the conditions on the fullscale turbine is one of the main objectives but also measuring the flap performance in unsteady inflow conditions as on the real turbine operating in the atmospheric boundary layer is another important aim. Finally it is desirable that the size of the flap is not that far from full scale.
It is expected that testing the flap system on the rotating rig will reduce the time for prototype testing on a full scale turbine where the costs for a test hour are several times bigger than for a test hour on the rotating test rig.

3.1 Rotating test rig design

To fulfill the above requirements to the test set-up we designed the rotating test rig comprising: 1) a blade section of 2.2m span and about 1m chord with aerodynamic shaped end caps; 2) a 10m pitchable boom where the blade section is attached to the one end and a counterweight at the other end and 3) a turbine platform where the boom is mounted on the shaft instead of a normal rotor, Figure 6.
The basic platform for the rotating test rig is the 100kW Tellus turbine positioned at the old turbine test site at DTU, Campus Risoe. The original three bladed rotor has been taken down, Figure 7 and a new 100kW full

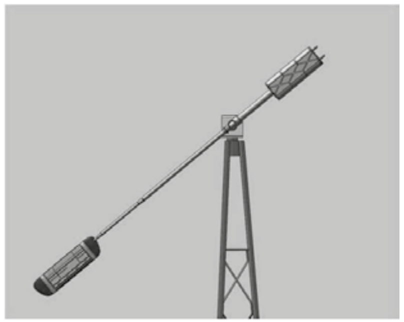

Figure 6 – Sketch of the rotating test rig.

variable speed drive was installed so the rotational speed with the boom mounted is controllable between 0 and 60 rpm.

Figure 7 – The 100kW Tellus turbine is used at the platform for the rotating test rig.

3.2 Blade section design and manufacturing

The blade section has the NACA0015 aerofoil shape and a constant chord length of 1m. The overall concept consists of a spanwise 2.2 meter long wing section covered with side pods in each end giving a total length of 3.4 meter. The blade section is built up on an inner aluminum structure covered with two shells of glass-epoxy composite material, Figure 8 and Figure 9. The aluminum structure consists of an 110mm hollow tube, two rib structures and a U-profile web. The aluminum parts were welded together.
The tube makes it possible to mount and dismount the wing section on a boom and the U-profile web at the trailing edge is for fixation of different morphing flap systems.

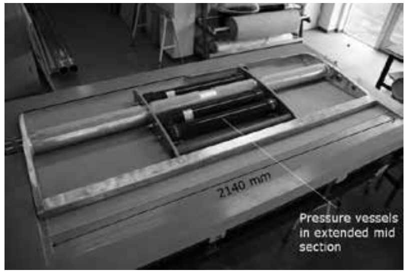

Figure 8 – The inner aluminium structure of the blade section.

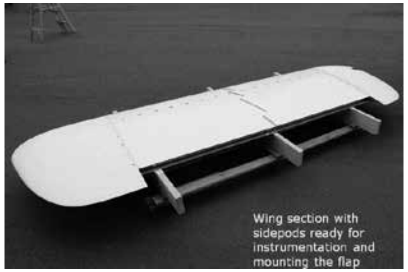

Figure 9 – The blade section ready for instrumentation and mounting the flap system.

3.3 Boom design and installation

The boom is built up of four thin-walled tubular sections (three of aluminium alloy 6082 and one of steel St52) and the connection pieces and flanges between them, Figure 10. The blade section is attached with a 100mm diameter rod sliding into the tube in the blade section Figure 8.

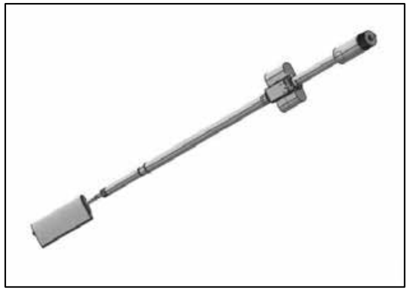

Figure 10 – The boom design.

The boom is fully pitchable so that a combined pitch and flap control can be investigated.
The boom with the blade section and flap system was installed in June 2014, Figure 11, and the test rig was ready for measurements in September 2014, Figure 12.

Figure 11 – Installation of the boom and blade section in June 2014.

Figure 12 – Rotating test rig ready for measuring.

3.4 Pneumatic system for flap actuation

Pressurizing the voids can be done either by a hydraulic or a pneumatic system or by a combination of the two systems. The choice of system depends e.g. on the requirements for the actuation time constant and on how strong the restrictions are on having valves/wires in the blade.
In the present case a first option has been a pneumatic system developed and implemented by Hydratech Industries which were one of the industrial project partners in the INDUFLAP project.
A compressor at the hub supplies pressurized air into 3 accumulators which are the black tubes mounted in the blade section shown in Figure 8. They have three different pressure levels: low, medium, and high. A series of 3 switches per flap side ('positive'-upper, negative'-lower) control which of the three pressure levels is connected to the flap voids (on-off). A fourth switch per flap side controls the release of pressure. Controlling the switch valves allows for dynamic control of the pressure in the voids and therefore the flap deflection. The pressure at the flap inlets, the switches, the accumulators and the compressor are measured using pressure transducers.

3.5 Instrumentation

Besides the advantages by the rotating test rig mentioned above, one other major advantage by testing the flap system on a blade section is that it is possible to install a surface pressure measurement system which would be very complicated to implement on a full scale blade. By measuring the pressure distribution, the instantaneous aerodynamic loading can be derived and the performance of the flap system investigated.
The installed pressure system comprised 59 pressure holes distributed along the chord at the mid span position and additional 16 pressure taps at the 25% chordwise position to monitor the spanwise load distribution. The pressure taps were connected to two 64 channel Scannivalve pressure scanners mounted inside the blade section.

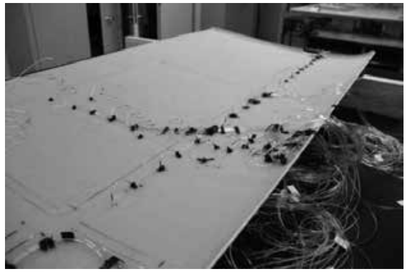

Figure 13 – Pressure taps installed on the suction side at the mid span position and along the span at 25% chord from the leading edge.

Besides the pressure measurements several accelerometers and strain gauges were mounted on the boom and the nacelle. In order to correlate the pressure measurements to the unsteady inflow, two five hole pitot tubes were mounted on the leading edge with the sensor head about ½m in front of the leading edge, Figure 14. A meteorology mast was positioned about three rotor diameters west of the test rig where wind speed and direction was measured in several heights. In total, 196 data channels are recorded.

Figure 14 – The blade section with the CRTEF flap system. Inflow measured with two five hole pitot tubes.

3.6 Calibration of the flap deflection correlated to actuation pressure

It was not possible to measure the flap deflection directly with a sensor (e.g. a strain gauge built into the flap) on the rotating test rig and therefore a calibration in the lab. correlating the flap deflection to the pressure in the voids has been used. The calibration set-up shown in Figure 15 was used. A laser sensor measured the flap deflection and the supply pressure in the two layers of voids was likewise measured. An example on how the flap deflection correlates with the pressure is shown in Figure 16. It is seen that there is a close correlation between pressure and deflection although there might be minor hysteresis effects.
The result of the calibration was 1.85 deg./bar to the one side and 1.48 deg./bar to the other side.

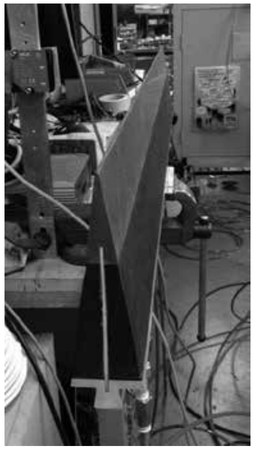

Figure 15 – Set-up for calibrating the flap deflection correlation to pressure in the voids.

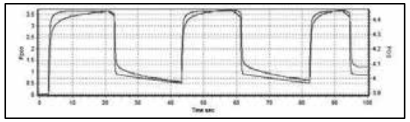

Figure 16 – Example of flap deflection calibration correlating the activation pressure (blue curve) to the flap deflection (red curve – [Volt]).

4. Experimental results

An important result of testing the flap system on the rotating test rig was operation of the flap system up to 30 rpm. which combined with a 10m radius gives a g-loading of 9-10g which is the same range as the system will be exposed to on a 2-3MW turbine.
Then during the relative short measurement period that was available for the first measurement campaign on the rotating test rig in the autumn 2014 the focus was on characterization of the flap performance using prescribed flap variations. An example is showed in Figure 17 where the flap angle was changed with 10 deg. each

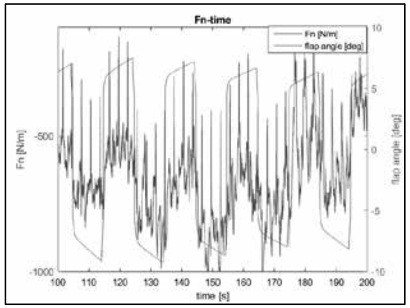

Figure 17 – The normal aerodynamic load force on the blade section (blue curve) for a flap angle variation of total 10 deg. (red curve) each 10 sec.

10s. The aerodynamic normal force integrated from the measured pressure distribution is seen to change with the flap angle. The unsteadiness in the inflow due to the turbulence and tower shadow is also clearly seen in the aerodynamic loading. This makes the visibility of the flap action more unclear. It should be noted that the tower shadow is quite strong in this case due to downwind operation of the rotor during this particular test.
One way of characterizing the flap performance was carried out in the following way. A few 10min. time series were measured at a constant rotational speed of 20 rpm. with a square change pattern of the flap angle with a period of 10s. as shown in Figure 18. The flap angle variation was not completely symmetrical around 0deg. but the mean total amplitude was around 15deg when using the time sequencies marked with red and blue, respectively, in Figure 18. To achieve a wide range of inflow angles the pitch setting was changed from one 10min. time series to the next.
The normal force loading was derived from the pressure data and then binned on the measured inflow angle derived from the five hole pitot tube measurements, Figure 19. From that figure we can now derive that the average change in normal force due to a degree change in flap angle is about 32% of the average change in normal force due to a degree change in inflow angle.

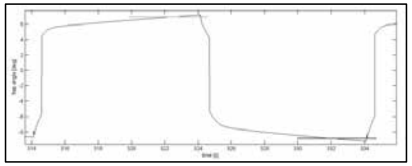

Figure 18 – A square pattern change of flap angle with a period of 10s.

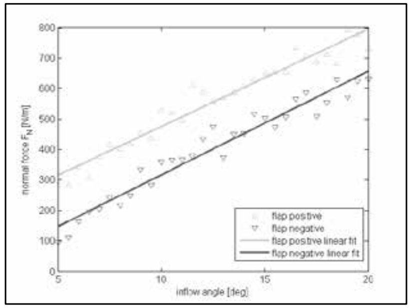

Figure 19 – Normal force data for extreme flap positions plotted against inflow angle. Data averaged every 0.5deg inflow angle.

The calibration and interpretation of the inflow angle is the uncertain parts of the above analysis. Another way of characterizing the flap performance would be to derive the lift and drag coefficients for different flap angles on basis of the measured aerodynamic loading from the pressure measurements and using the inflow angle and the relative velocity from the five hole pitot tube to derive these non-dimensional coefficients. However, this is not a straight forward data reduction for turbulent, unsteady inflow data and in particular due to the low aspect ratio of the blade section and how this influence the local inflow angle.
Therefore another measure of the flap performance is presented. Often we are interested in comparing the capability of the flaps to change the loading with the well known control by pitching the whole blade section.
The result of this analysis is shown in Figure 20 where the normal force is plotted for a number of different pitch settings and again for the same data set as used in Figure 19
The data show a considerable scatter due to the changes in wind speed but deriving the mean normal force for the different pitch settings a clear effect of the flaps are seen. From these mean data we can derive that the total about 15deg. change in flap angle gives almost the same change in aerodynamic loading as 3.0deg. change in pitch. This means that the lift change from about 5 deg. flap angle is the same as for one degree pitch.
This is somewhat less than simulations typically have shown which are in the range of 2 to 3 deg. flap angle to 1 deg. pitch angle for a 15% flap, Troldborg 2005 [4]. The turbulent, unsteady inflow is probably a major cause of this lower performance.

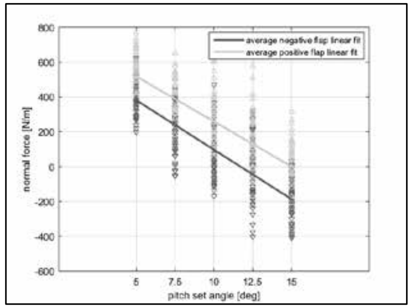

Figure 20 – the normal force on the blade section for plus/minus 5 deg. flap angle as function of the pitch setting of the flap angle.

5. Conclusion

The morphing trailing edge system or flap system, CRTEF, has been developed over the last 10 years at DTU Wind Energy. After a promising wind tunnel test of the system in 2009 the INDUFLAP project has been carried out from 2011-2014 to transfer the technology from laboratory to industrial applications. During that work a flap design was developed where the manufacturing is done in an extrusion process using the santrophene material for one of the components.

To narrow the gap between wind tunnel testing and full scale prototype testing we developed the rotating test rig. The overall objectives with the rotating test rig are: 1) to test the flap system in a realistic rotating environment with a realistic g-loading; 2) to measure the flap performance in real turbulent inflow and 3) to test the flap system in a realistic size and realistic Reynolds number.

The rotating test rig consists of a 2.2m blade section attached to a 10m boom and mounted on a 100kW turbine platform. It was installed in June 2014 and a short measurement campaign was conducted in the autumn 2014. Instantaneous aerodynamic loading in a cross section of the blade was derived from pressure measurements providing detailed insight into the unsteady flap response.

An important result of testing the flap system on the rotating test rig was operation of the flap system up to a 30 rpm. which combined with a 10m radius gives a g-loading of 9-10g which is comparable to the conditions on a 2-3MW turbine.

Another important result was the measured performance of the flap system. As the blade section has a low aspect ratio we have chosen to compare the flap load response with the pitch load response as the pitch is the normal control system. We found that about 5 deg. flap angle gives the same load change as 1 deg. pitch. This is somewhat less than simulations have shown in the past which are in the range of 2 to 3 deg. flap angle to 1 deg. pitch angle for a 15% flap. The realistic, turbulent, inflow is probably a major cause of this lower performance.

Acknowledgements

The presented research and development work was partly carried out within the project “Industrial adaptation of a prototype flap system for wind turbines” which was been funded by the Danish development and demonstration programme EUDP under contract J.nr. 64010-0458.

References

[**1**] Barlas, T. K. and van Kuik, G. A. M., Review of state of the art in smart rotor control research for wind turbines, Progress in Aerospace Sciences — 2010, Volume 46, Issue 1, pp. 1-27, 2010.

[**2**] Madsen, H. A., Andersen, P. B., Andersen, T. L., Bak C. and Buhl, T., The potentials of the controllable rubber trailing edge flap (CRTEF). Proceedings of EWEC 2010, Warsaw, Poland, 2010.

[**3**] Madsen, H.Aa et al., Towards an industrial manufactured morphing trailing edge flap system for wind turbines,Proceedings of the EWEC 2014, Barcelona, Spain, 2014.

[**4**] Troldborg, N 2005, 'Computational study of the Risø-B1-18 airfoil with a hinged flap providing variable trailing edge geometry' Wind Engineering, vol 29, no. 2, pp. 89-113.

Field Testing of LIDAR Assisted Feedforward Control Algorithms for Improved Speed Control and Fatigue Load Reduction on a 600 kW Wind Turbine

Avishek A. Kumar, Ervin A. Bossanyi, Andrew K. Scholbrock, Paul A. Fleming, Matthieu Boquet, Raghu Krishnamurthy

Abstract

A severe challenge in controlling wind turbines is ensuring controller performance in the presence of a stochastic and unknown wind field, relying on the response of the turbine to generate control actions. Recent technologies such as LIDAR, allow sensing of the wind field before it reaches the rotor.

In this work a field-testing campaign to test LIDAR Assisted Control (LAC) has been undertaken on a 600-kW turbine using a fixed, five-beam LIDAR system. The campaign compared the performance of a baseline controller to four LACs with progressively lower levels of feedback using 35 hours of collected data.

The collected data indicates that utilising measurements from multiple range gates on a pulsed LIDAR system can result in rotor averaged wind speed (RAWS) estimates with greater levels of correlation with wind speed at the rotor than using a single range gate. The LACs showed higher levels of speed control performance with significantly reduced levels of pitch activity and generally lower levels of tower excitation. Although the loading spectrum for the test turbine was dominated by responses at twice the rotor speed (2P) and the first tower fore-aft natural frequency, the reduction is likely to show greater relative significance on typical full-sized turbines, which show lower excitation levels due to harmonic clashes.

A. A. Kumar is a Control Engineer with DNV GL - Energy, Auckland, New Zealand (phone: +64-9-414-5572; fax: +64-9-414-5573; e-mail: avishek.kumar@dnvgl.com).

E. A. Bossanyi is a Senior Principal Researcher with DNV GL - Energy, Bristol, UK (phone: +44-203-816-4270; e-mail: ervin.bossanyi@dnvgl.com).

A. K. Scholbrock is a Field Test Engineer at the National Wind Technology Center, Golden, CO 80401, USA (phone: +1-303-384-7181; fax: +1-303-384-6950 ; e-mail: andrew.scholbrock@nrel.gov).

P. A. Fleming is a Senior Engineer at the National Wind Technology Center, Golden, CO 80401, USA (phone: +1-303-384-7181; fax: +1-303-384-6918 ; e-mail: paul.fleming@nrel.gov).

M. Boquet is Lead of Science and Application at Leosphere-Avent, Paris, France (e-mail: mboquet@leosphere.com).

R. Krishnamurthy a Science and Application Engineer at Leosphere-Avent, Paris, France (e-mail: rkrishnamurthy@leosphere-avent.com).

I. Introduction

A severe challenge in controlling wind turbines is ensuring controller performance in the presence of a stochastic and unknown wind field, relying on the response of the turbine to generate control actions. Recent technologies such as LIDAR, allow sensing of the wind field before it reaches the rotor. This information allows controllers to work in an anticipatory mode, potentially improving control performance [1] and leading to reduced costs of energy through load reduction and reduced actuator usage.

A number of methods have been researched using simulation studies to exploit preview wind information ranging from basic [2] and advanced [3]–[5] feedforward algorithms to model predictive control methods [6]–[8]. Although most methods have been tested in simulation on models of various fidelity, feedforward controllers have begun to be field tested on full-scale turbines [9]–[11].

In this work we present the results of field testing a feedforward control algorithm that utilises LIDAR measurements on a full-scale wind turbine. This work contributes the first set of public field tests of a feedforward controller in conjunction with a five-beam pulsed LIDAR system. This paper makes use of approximately 35 hours of data in a range of wind conditions and multiple controller tunings to show the impact on rotor speed control, pitch actuator usage and tower loading from LAC.

II. Approach

A. CART2 Wind Turbine

Testing has been conducted on the Controls Advanced Research Turbine (CART2) wind turbine at the National Wind Technology Center in Colorado, USA. The CART2, a two-bladed variable-speed, variable-pitch turbine with a 42.7-m rotor diameter [2], is nominally rated at 600 kW, however, for the purposes of this study, the turbine has been de-rated to 128 kW to maximise the time during which pitch control is active because the measurements took place during a period of low wind speeds. The resulting set points for rated rotor speed, generator speed and generator torque were set at 24 rpm, 1036 rpm and 1182 Nm, respectively.

B. LIDAR System

The preview wind information used for control was obtained by a nacelle-mounted LIDAR system created by Avent LIDAR Technology. The Avent five-beam LIDAR unit uses a pulsed LIDAR with five fixed beams, each capable of sampling the line-of-sight (LOS) wind speed at up to 10 ranges simultaneously. The LIDAR is mounted on the nacelle facing upwind, as shown schematically in Fig. 1 and on-site in Fig.2. The LIDAR also processes the LOS data to return the current RAWS estimate, wind shear estimate and wind direction estimate for each range gate. The RAWS is defined as the mean wind speed over the rotor swept area at a defined plane (not necessarily at the rotor).

For the purposes of this testing campaign, the feedforward control algorithm makes use of the RAWS data from three range gates focused at 50 m, 65 m and 80 m. These gates correspond to covering the centre and approximately 63%-100% of the rotor radius using a beam angle of 15° from horizontal.

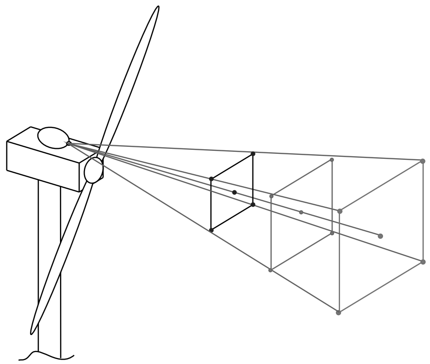

Figure 1. LIDAR mounting and scanning schematic. Red lines indicate LIDAR beams, green dots indicate scan points, dashed lines indicate orientation axis and dash-dot lines indicate range gate plane.

C. Baseline Feedback Controller

The CART2 was de-rated to have a rated wind speed of 8 ms^{-1} (128-kW rated power) in order to function in the pitch control regime as much as possible for this study. The CART2 has separate generator torque and blade pitch controllers to maintan the required rotor speed. The generator torque is applied as a function of filtered generator speed, attempting to track the optimal power coefficient until the rotor speed is 19.2 rpm, after which the torque is

Figure 2. Avent five-beam LIDAR sytem mounted on the CART2. (Photo Credit: Lee Jay Fingersh, NREL 33621.)

increased linearly until it saturates at 1182 Nm coinciding with a rotor speed of 22.9 rpm. The pitch controller becomes active to regulate the rotor speed to 24 rpm once the turbine reaches maximum torque. This speed is obtained at wind speeds of approximately 8 ms^{-1}. The controller is implemented as a gain-scheduled PI controller using the filtered generator speed as feedback, typical of full-scale wind turbines.

D. Feedforward Controller

The feedforward controller is designed to use preview wind measurements to assist the feedback controller in speed control, with the aim of achieving higher levels of speed control performance and/or reduced levels of pitch activity. We approximate the entire wind disturbance acting on the rotor by a RAWS at the rotor plane (V) and focus on rejecting low frequency aspects of the disturbance. We can then apply a static control law based on the steady-state blade pitch as a function of RAWS. This method has been shown to be successful at reducing rotor speed variance in both field testing and simulation [9], [10]. The control law moves the pitch actuators pre-emptively to the correct steady-state pitch angle for the incoming wind field through the following algorithm:

$$\dot{\theta}_{FF}(t) = \frac{\hat{\theta}_{ss}(V(t+\tau)) - \hat{\theta}_{ss}(V(t))}{\tau},$$

where $\dot{\theta}_{FF}$ is the feedforward pitch rate, $\hat{\theta}_{ss}$ is the steady-state pitch angle for a given wind speed and τ is the look-ahead time (LAT). The feedforward control signal is then added to the feedback signal as shown in Fig. 3.

The LIDAR system used for this study provides an estimate of the RAWS at three range gates $V(t+\tau+T)$, where T is the time-to-rotor (TTR) determined by:

$$T = \frac{D_i}{V_c} - \varepsilon,$$

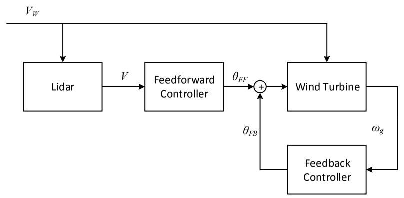

Figure 3. Schematic of pitch control architecture. V_w is the wind field, V is the LIDAR-estimated RAWS data, θ_{FF} is the feedforward pitch angle, θ_{FB} is the feedback pitch angle and ω_g is the generator speed.

where D_i is the distance between the rotor plane and the focus plane of range gate i, V_c is the convection speed and ε represents any processing delays. The convection speed is determined by low-pass filtering $V(t+\tau)$. The TTR decreases on each controller time step and when a RAWS estimate has a TTR equalling the LAT or has reached the rotor (TTR of 0) it is low-pass filtered (to avoid discontinuities caused by combining data from multiple range gates) and used in the feedforward algorithm.

III. Results

To analyse the control performance, the CART2 was run in a de-rated state, cycling between LAC and Baseline control every 5 minutes. Data was binned into contiguous 45-second samples in which the minimum rotor speed was above 23 rpm (96% rated) and the minimum generator torque was 1000 Nm, both indicating above-rated operation with pitch action. The sample length choice was based on a trade-off between environmental condition distribution (wind speed, turbulence intensity and number of samples) and the ability to analyse spectral responses at lower frequencies. Each chunk was processed to return environmental data, speed control performance, pitch actuator duty and structural loading metrics. Data was gathered with the LAC using feedback gains of 100%, 75%, 38% and 10% of Baseline gains (LAC100, LAC75, LAC38, and LAC10). A summary of data volumes is given in Table I and distributions according to wind speed and turbulence intensity are illustrated in Fig. 4. The analysis presented in this paper used more than 35 hours of data.

TABLE I. RECORDED DATA VOLUMES

Gains	Baseline 45-s Chunks	LAC 45-s Chunks
100%	137	110
75%	197	234
38%	54	43
10%	1423	614

Data from LAC100, LAC75 and LAC38 shows similar distributions and volumes to the baseline controller during their respective periods of operation, whereas LAC10 shows much lower levels of data collected compared to the baseline. Overall, the amount of data collected from LAC10 is still much greater than the other controller tunings.

A. Rotor Average Wind Speed Reconstruction Performance

The Avent LIDAR system is able to sample winds at multiple distances in front of the turbine. RAWS reconstructions taken closer to the turbine are likely to have a higher correlation to the "true" RAWS at the rotor plane. However, because the plane is closer, the sample points at the range gate are closer to the centre of the rotor, possibly losing data from spatial turbulence acting at the edge of the rotor. Using multiple gates can allow larger correlations while still maintaining adequate rotor coverage.

A wind speed estimator (WSE) was used to give the closest approximation to the "true" RAWS, which is used to test the coherence of RAWS estimated reconstructed from LIDAR signals. The estimator takes the following form:

$$V_{WSE|k+1} = AV_{WSE|k} + K(\alpha_{k+1} - \hat{\alpha}_{k+1})$$

where:

^ denotes an estimated value;

k is the time step index;

V_{WSE} is the wind speed estimate;

α is the rotor acceleration;

A is the state transition matrix; and

K is the estimator gain.

The linearised error dynamics of this estimator are defined by:

$$\Delta e_{k+1} = (A - KC)\Delta e_k$$

where:

$$e = \alpha_{k+1} - \hat{\alpha}_{k+1};$$

Given that in quasi-steady-state conditions the following relation is held:

$$P = \frac{1}{2}\rho A_r C_p(\omega, V, \theta)V^3$$

where:

P is the mechanical power from the rotor;

ρ is the air density;

A_r is the rotor area;

C_p is the power coefficient;

ω is the rotor speed;

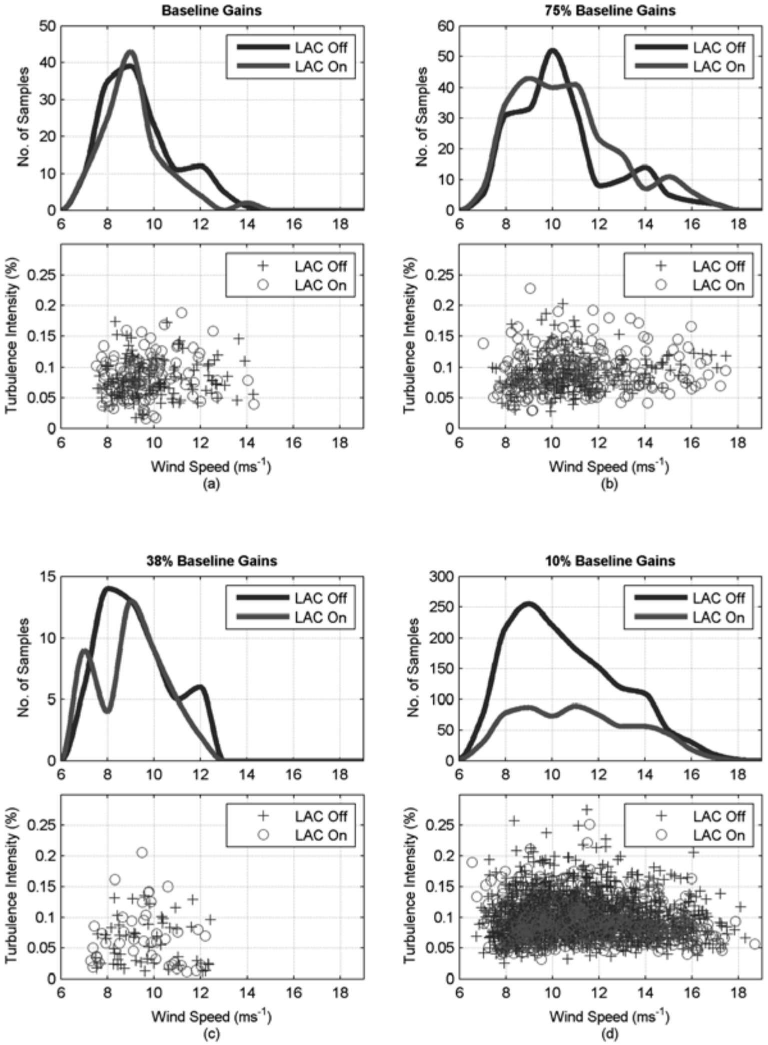

Figure 4. Data wind speed distribution according to mean wind speed for each controller setting.

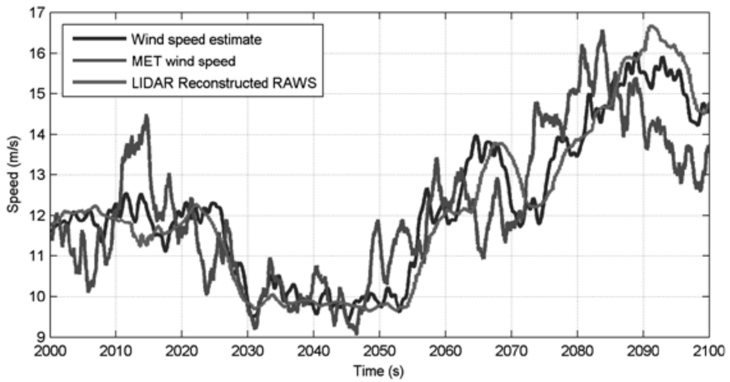

Figure 5. Time series sample of meteorological mast wind speed measurement, V_{WSE} and V.

V is the rotor effective wind speed; and

θ is the mean blade pitch angle,

we get:

$$C = \frac{\partial \alpha}{\partial V} = \left(\frac{\rho A_r}{2 J_R \omega}\right)\left(\frac{\partial C_p(\omega, V, \theta)}{\partial V} V^3 + 3C_p(\omega, V, \theta)V^2\right)$$

By modelling the wind as a step input, A = 1, the estimator gain can be described in terms of an approximate time constant, τ , for the error dynamics:

$$K = \frac{\frac{1}{\tau} + 1}{C},$$

τ is set to 1 s for this study. C is recalculated online, allowing K to be updated each time step. In this realisation, the wind speed estimate is adjusted until the estimated and measured rotor accelerations match.

To find α, we differentiate and low-pass filter the measured rotor speed with time. The low-pass filter is a second-order, Butterworth filter with a natural frequency of 3 rads^{-1} and a damping ratio of 0.707.

To find $\hat{\alpha}$, we use the torque imbalance equation for a rigid drivetrain:

$$\hat{\alpha} = \frac{0.5 \rho A_r \mu C_p(\omega_k, V_{k-1}, \theta_k) V_{k-1}{}^3 - N Q_{g|k} \omega_k}{J_R \omega_k}$$

where:

Q_A is the aerodynamic torque;

Q_g is the generator torque;

N is the gearbox ratio;

μ is the drivetrain efficiency; and

J_R is the rotor inertia.

C_p can be found by interpolating over a lookup table of C_p as a function of pitch angle and tip-speed ratio. The resulting RAWS estimate, V_{WSE}, will show a lag relative to the "true" RAWS due to filtering. This lag will be similar to the lag from LIDAR-reconstructed RAWS signals because the latter is also filtered with a time constant of 1 s.

WSE outputs have been checked against meteorological (met) mast measured data and LIDAR reconstruction data; a time series sample is given in Fig. 5. The met mast is positioned 80 m away from the CART2 with an anemometer at the CART2's hub height (36.5 m). Due to the changing wind directions, the phasing between the RAWS and met mast measurements will be somewhat random, but the magnitude trends coincide very well. The LIDAR-reconstructed RAWS and the WSE reconstructions also coincide well, with slight phasing error.

Fig. 6 shows a magnitude squared coherence between $V_{WSE}(t)$ and $V(t)$ as reconstructed using data from each range gate individually and using data from all range gates together for a 200-minute data sample. The results demonstrate that combining data from all the gates results in the best performance, slightly outperforming data from Range Gate 1 above 0.1 Hz. The levels of coherence from Range Gate 1 are close to the combination of all range gates; this is likely due to the relatively large rotor coverage at a short focus distance, 63% and 50 m, respectively. As turbine sizes increase, we would expect a greater trade-off between LIDAR range and rotor scan area (assuming similar beam angles), amplifying the benefits of combining LIDAR measurements from multiple distances.

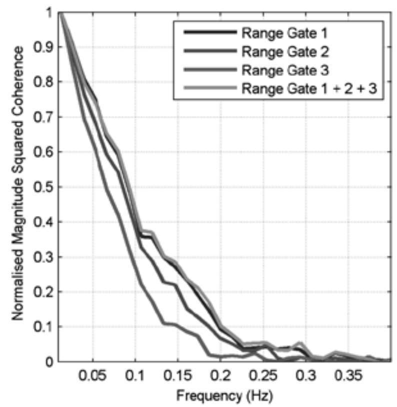

Figure 6. Magnitude squared coherence between $V_{WSE}(t)$ and $V_L(t)$ using different range gates.

B. Controller Performance

Rotor speed spectral response is the primary performance metric used in this study, chosen because the control algorithm is designed to assist the speed controller. The average normalised power spectral densities (PSDs) of the rotor speed for each controller are given in Fig. 7. LAC100 already shows a reduction in speed variance relative to the Baseline below 0.075 Hz, with a 19% reduction in peak spectral response (PSR). This frequency coincides with relatively high levels of coherence between the actual RAWS and the estimated RAWS (Fig. 5). Surprisingly, detuning to LAC75 actually shows a further reduction in relative rotor speed variance (64% reduction in PSR); this may indicate that the baseline gains are not necessarily optimal for rotor speed control on the de-rated turbine. Detuning further to LAC38 shows that the speed control performance begin to deteriorate — albeit slightly, at 58% reductions in PSR relative to the Baseline. The final detune to LAC10 shows that we have detuned enough for the speed control performance to fall and cause a 55% increase in PSR. Unfortunately, it was not possible to obtain a finer resolution of controller gains to determine the level at which speed control levels were at parity with the Baseline.

The reduction in controller gains from LAC100 to LAC10 resulted in decreasing levels of actuator usage beyond 0.1 Hz as expected (Fig. 8). Although overall levels of pitch rate activity fall dramatically beyond 0.1 Hz, the relative contribution of pitching at 1P (0.4 Hz), 2P and the tower first fore-aft modal frequency (0.87 Hz) is still relatively high until LAC38. In terms of speed control, it is a very positive result to see that the speed control performance of LAC75 and LAC38 outperforms the baseline even though actuator usage levels have fallen.

The final piece of analysis of this campaign was to determine the impact of the reduced pitching levels on thrust-related fatigue damage. Fig. 9 shows the spectral response of the tower base fore-aft moment under different controller tunings. The results show that as the controller is detuned, the tower response between 0.13 Hz and 0.6 Hz shows less activity. However, the plots also show that the spectral response is dominated by activity at the tower natural frequency (0.87 Hz), which sits very close to 2P (0.8 Hz), with a much smaller peak at 1P. Fig. 7 (a)-(c) and Fig. 9 (a)-(c) show that the pitching around 1P and 2P for LAC100, LAC75 and LAC38 results in similar relative tower response levels at 1P and 2P despite the reduction in pitching away from these frequencies. LAC10, which showed very low levels of 1P and 2P pitching, shows much lower levels of 1P and 2P response levels relative to the Baseline (Fig. 9 (d)); however, the tower will be consistently excited at 2P because the CART2 is a two-bladed turbine.

Tower loading is further quantified in Fig. 10, which presents maximum, minimum and mean damage equivalent load (DEL) results for each operating condition and controller tuning. DELs were calculated using a rainflow counting algorithm with a 1-Hz cycle and an inverse S-N slopes of 4 [12]. Note that:

- The DEL comparisons have been taken with 45-s chunks, they do not include the lower end of the turbulence spectrum; and
- The wind conditions for each calculation have not been binned according to similar turbulence intensity levels.

With that in mind, LAC100 and LAC75 show no clear tower load reduction trends relative to the Baseline. LAC38 shows reductions in the 10-ms^{-1} and 11-ms^{-1} wind speed bins where a significant portion of data is collected, and an increase at 12 ms^{-1} where there is much less data. LAC10, on the other hand, shows a clear trend in the reduction of tower base DELs at all wind speeds above 8 ms^{-1} relative to the baseline. This indicates that the reduction in pitch actuation at 1P and 2P in addition to the general mid-high frequency pitching reductions have resulted in lower fatigue damage levels.

These results indicate that LAC can achieve comparable speed control with reduced levels of pitch activity. The reduction in pitch activity resulted in tower spectral response reductions, and if targeted correctly, these reductions can imply reductions in tower base DELs. Although the CART showed a strong tower response at 1P, 2P and tower first fore-aft frequency, turbines typically operate with a larger gap between rotor harmonics and structural frequencies, and controllers are typically tuned to avoid resonance at rotor harmonics, meaning that the relative impact on baseline loading levels from LAC could be much more significant on a more typical turbine.

IV. Conclusions

A field-testing campaign to test LAC has been undertaken on a 600-kW turbine using a fixed five-beam LIDAR system. The campaign compared the performance of a baseline controller relative to four LACs with progressively lower levels of feedback using 35 hours of collected data.

The collected data demonstrates that utilising measurements from multiple range gates on a pulsed LIDAR system can result in RAWS estimates with greater levels of correlation to wind speed at the rotor than using a single range gate. The benefits are likely to be more pronounced on implementations with larger rotors wherein each scanning range has a trade-off between distance and rotor coverage.

The LACs showed higher levels of speed control performance until controller gains had been reduced to 10% of baseline levels. The speed control was achieved with significantly reduced levels of pitch activity and generally lower levels of tower excitation.

LAC tower base DEL levels were consistently reduced relative to baseline levels once pitch activity at rotor harmonic frequencies and tower frequencies was sufficiently reduced (LAC10); however, at these controller gain levels, speed control performance was poorer than baseline levels. However, the CART2 loading spectrum was dominated by responses at 2P and the first tower fore-aft natural frequency, indicating that the response reduction is less significant for this turbine. The reduction is likely to be more significant with typical full-sized turbines, which show lower excitation levels due to harmonic clashes.

Acknowledgments

This work was supported by the U.S. Department of Energy under Contract No. DE-AC36-08GO28308 with the National Renewable Energy Laboratory. Funding provided by the DOE Office of Energy Efficiency and Renewable Energy, Wind and Water Power Technologies Office.

The authors would also like to acknowledge the contribution of Samuel Davoust, formerly of Avent Lidar technology, for his assistance during the initial stages of this project.

References

[1] E. A. Bossanyi, A. A. Kumar, and Hugues-Salas, "Assessment of Turbine Mounted LIDAR for Control Applications," in *EWEA*, 2012.

[2] D. Schlipf, E. Bossanyi, C. E. Carcangiu, T. Fischer, T. Maul, and M. Rossetti, "LIDAR assisted collective pitch control," UPWIND Deliverable D5.1.3Stuttgart, 2006.

[3] F. Dunne, L. Y. Pao, A. D. Wright, E. Simley, and B. Jonkman, "Adding Feedforward Blade Pitch Control for Load Mitigation in Wind Turbines : Non-Causal Series Expansion , Preview Control , and Optimized FIR Filter Methods," in *49th AIAA Aerospace Sciences Meeting*, 2011.

[4] J. Laks, L. Y. Pao, A. Wright, N. Kelley, and B. Jonkman, "Blade Pitch Control with Preview Wind," in *48th AIAA Aerospace Sciences Meeting*, 2010.

[5] D. Schlipf and P. Cheng, "Flatness-based feedforward control of wind turbines using Lidar," in *Proceedings of the 19th World Congress of the International Federation of Automatic Control*, 2014.

[6] L. C. Henriksen, "Model Predictive Control of Wind Turbines," Technical University of Denmark, 2012.

[7] A. A. Kumar, "Multivariable Control of Wind Turbines for Fatigue Load Reduction in the Presence of Nonlinearities," The University ofAuckland, Auckland, 2011.

[8] D. Schlipf, L. Y. Pao, and C. Po Wen, "Comparison of feedforward and model predictive control of wind turbines using LIDAR," in *Decision and Control (CDC), 2012 IEEE 51st Annual Conference on*, 2012, pp. 3050–3055.

[9] A. K. Scholbrock, P. A. Fleming, L. J. Fingersh, A. D. Wright, D. Schlipf, and F. Haizman, "Field Testing LIDAR Based Feed-Forward Controls on the NREL Controls Advanced Research Turbine Preprint," in *51st AIAA Aerospace Sciences Meeting*, 2013.

[10] D. Schlipf, P. Fleming, and F. Haizmann, "Field testing of feedforward collective pitch control on the CART2 using a nacelle-based lidar scanner," in *The Science of Making Torque from Wind*, 2012, vol. 2.

[11] P. A. Fleming, A. K. Scholbrock, A. Jehu, S. Davoust, E. Osler, a D. Wright, and A. Clifton, "Field-test results using a nacelle-mounted lidar for improving wind turbine power capture by reducing yaw misalignment," *J. Phys. Conf. Ser.*, vol. 524, Jun. 2014.

[12] DNVGL, *Bladed 4.5 User Manual*. 2013.

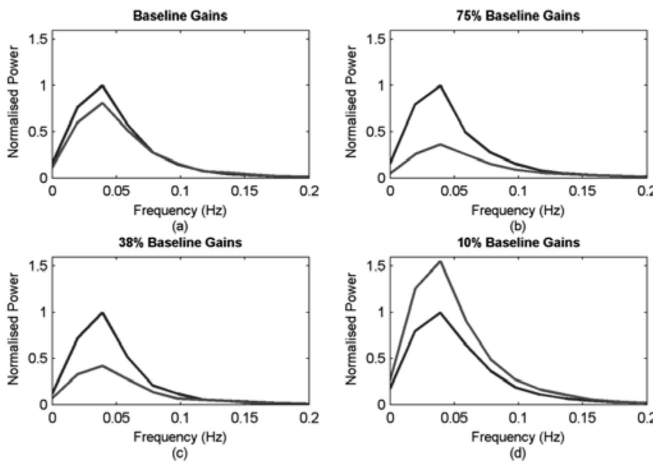

Figure 7. PSD of rotor speed with different LAC tunings vs the Baseline controller binned by wind speed. Blue – Baseline, Green – LAC.

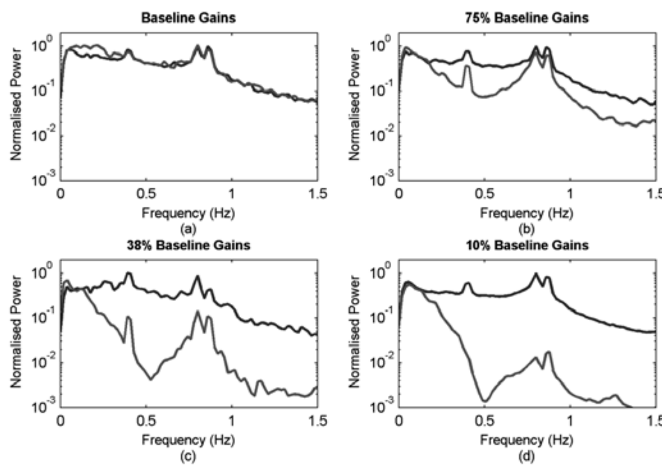

Figure 8. PSD of pitch rate with different LAC tunings compared to the Baseline controller binned by wind speed. Blue: Baseline; Green: LAC.

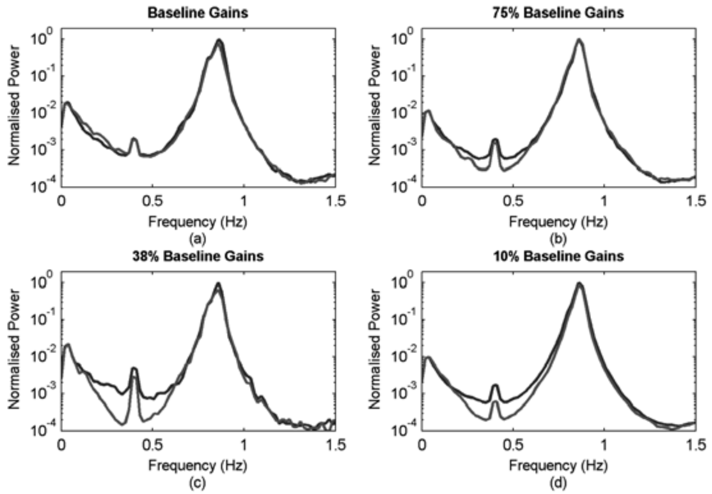

Figure 9. PSD of tower base fore-aft moment with different LAC tunings compared to the Baseline controller binned by wind speed. Blue: Baseline; Green: LAC.

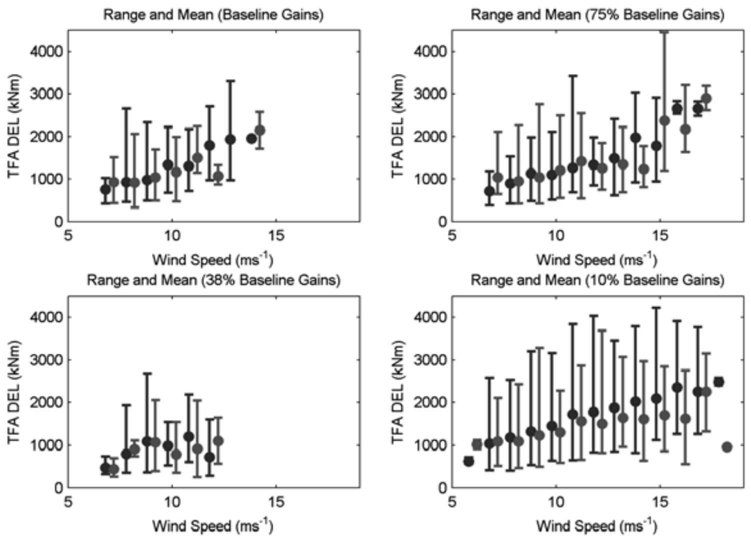

Figure 10. Tower base fore-aft DEL with different LAC tunings compared to the Baseline controller binned by wind speed. Markers indicate range and mean of data in each wind speed bin. Blue: Baseline; Green: LAC.

An Adaptive Data Processing Technique for Lidar-Assisted Control to Bridge the Gap between Lidar Systems and Wind Turbines

David Schlipf[1,2], Paul Fleming[2], Steffen Raach[1], Andrew Scholbrock[2], Florian Haizmann[1], Raghu Krishnamurthy[3], Matthieu Boquet[3], and Po Wen Cheng[1]

[1]Stuttgart Wind Energy (SWE) @ Institute of Aircraft Design, University of Stuttgart, Germany.
[2]National Renewable Energy Laboratory (NREL), Boulder, Colorado, USA.
[3]Avent Lidar Technology, Orsay, France.

Abstract

This paper presents first steps toward an adaptive lidar data processing technique crucial for lidar-assisted control in wind turbines. The prediction time and the quality of the wind preview from lidar measurements depend on several factors and are not constant. If the data processing is not continually adjusted, the benefit of lidar-assisted control cannot be fully exploited or can even result in harmful control action. An online analysis of the lidar and turbine data is necessary to continually reassess the prediction time and lidar data quality.

In this work, a structured process to develop an analysis tool for the prediction time and a new hardware setup for lidar-assisted control are presented. The tool consists of an online estimation of the rotor effective wind speed from lidar and turbine data and the implementation of an online cross-correlation to determine the time shift between both signals. Further, we present initial results from an ongoing campaign in which this system was employed for providing lidar preview for feedforward pitch control.

1 Introduction

For wind turbines, wind is the energy source as well as the main disturbance to the wind turbine control system. The control system has to balance competing control objectives: increasing the energy yield while reducing the structural loads. However, traditional feedback controllers are only able to react to the disturbance of the inflowing wind field after it has already impacted the turbine. With the recent development of lidar technology, the information about incoming disturbances can be made available ahead of time and used for feedforward control. A comprehensive overview of lidar-assisted control can be found in [1].

In an initial field testing on the two- and three-bladed Controls Advanced Research Turbines (CART2 and CART3 at the National Wind Technology Center in Boulder, Colorado), a collective pitch feedforward controller using lidar wind disturbance preview was able to reduce the rotor speed variation [2, 3]. However, this reduction cannot be directly converted into a reduction of the levelized cost of energy (LCOE). Thus, one of the long-term research challenges identified by the European Academy of Wind Energy is the transformation from scientific proof-of-concept to studies that provide a measurable benefit of lidar-assisted control [4]. A first study shows an LCOE reduction of 6.5% for large offshore wind turbines [5].

Lidars are only able to measure the wind speed along the line-of-sight (LOS) of the laser beam. Multiple LOS measurements can be put together to form a general wind field, with a longitudinal wind speed, as well as horizontal and vertical shear. Additionally, these wind speed measurements are taken upstream of the wind turbine, and as the wind travels toward the wind turbine, it will change due to the turbulence in the atmosphere. A coherence measurement between the lidar wind measurement and the rotor effective wind speed measured by the wind turbine helps to quantify the turbulent wind evolution. Higher and higher coherence values will lead to further and further improvements in the controller's ability to use the lidar preview information for feedforward control. An example of this is in [6], where simulation studies showed that improving the coherence will lead to improvements in feedforward control for load reductions.

Having a high coherence between the lidar measured wind speed and the rotor effective wind speed is quite challenging, as the coherence has to take into account the lidar measurement techniques as well as the turbine dynamics. From an industrial standpoint, lidars and wind turbines come from different manufacturers and have their own individual data acquisition systems. Additionally, due to the multi- and interdisciplinary character of the problem, there is a gap in knowledge: on the one hand, a thorough understanding of lidar measurement principles and limitations is mandatory for providing usable signals to the control system. On the other hand, detailed knowledge about wind turbine dynamics and controls are necessary to determine which signals can be used for preview control. These challenges make it hard for lidars and wind turbines to relate to one another in order to effectively enhance the turbine control system with lidar wind preview. Instead, a centralized system—developed by a joint project between industry and research institutions—which has access to real-time data from both the wind turbine and the lidar, would be better suited to close the gap between lidars and wind turbines.

A consortium of NREL, SWE, and the lidar manufacturer Avent Lidar Technology started to test advanced lidar-assisted control on the CART2 in January 2015. The same lidar-turbine combination has been used in an previous campaign [7]. A new adaptive data processing technique independent from lidar and turbine control software and hardware was developed during this campaign. The improved setup and the combination of lidar- and turbine-specific knowledge enables a comparison of the rotor-effective wind estimates from turbine and lidar data. With a cross-correlation calculated in real time, the lidar estimate can be aligned with the turbine's reaction via a graphical user interface (GUI). The feedforward control action can be applied to the turbine with the desired preview time, which improves the overall control performance.

This system was then used to provide a feedforward pitch update to the feedback controller, and a campaign to assess the improvement in performance from the baseline controller was performed. Initial results from this campaign are provided to show the value of the approach.

2 Approach

As discussed in the introduction, this paper presents a system for producing an accurate wind preview that can be used for maximally effective feedforward control of wind turbines.

In this section, we present the approach taken for designing this complete system, from the design of the feedforward controller that will apply the lidar signal, the development of the data processing that produces the signal, and the stages of refinement and implementation that would be expected in an industrial application.

2.1 Structured Code Development for Lidar-Assisted Control

The code development for lidar-assisted control is structured in five stages: feedforward controller development, data processing development, real-time environment development, hybrid simulations, and field testing.

1. *Feedforward Controller Development*: Assuming perfect wind preview, the feedforward controller is first designed and tested using the Simplified Low Order Wind turbine (SLOW) model [8] with only 2 degrees-of-freedom (rotor and tower motion). In this case, the simulation model is identical to the controller design model and the control performance should be as desired. Then, the same wind is used in simulations with an aeroelastic model (FAST [9]) to test the robustness of the controller against model uncertainties. Figure Figure 1 shows simulations with the FAST model for an extreme operating gust (EOG). The feedforward controller is able to reduce the impact of wind speed changes to the rotor speed following its design objective [10]. Figure 2 (left) shows a diagram of the SLOW model.

2. *Data Processing Development*: In the previous stage, the feedforward controller was designed to perform well assuming perfect wind preview. In this stage, we develop the data processing that will be used given realistic lidar measurement of the wind. Using the FAST model, we now simulate the turbine operating in a turbulent wind field, rather than a uniform flow, which can be easily represented by a single velocity. A lidar simulator [11] is used to scan the incoming wind field. The data is condensed to an estimate of

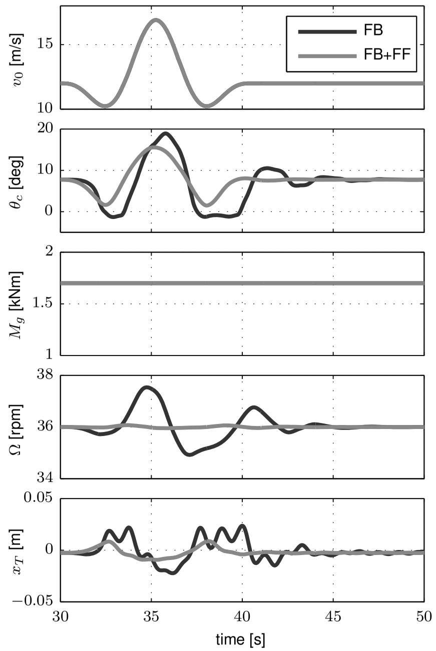

Figure 1: Reaction to an EOG at 12 m/s: Feedback only (dark blue) and with additional feedforward (light blue).

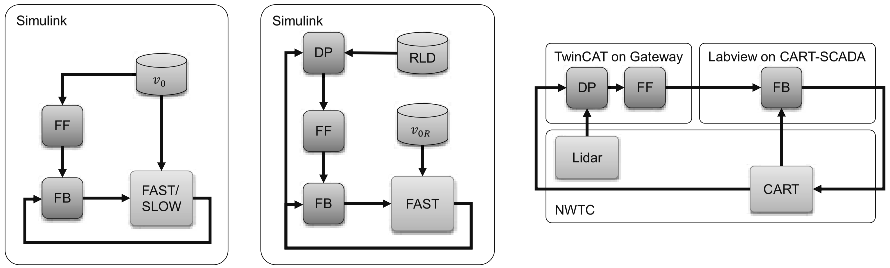

Figure 2: Code development. Stage 1 (left): Simulation within Simulink with perfect wind preview; the rotor-effective wind v_0 disturbs the turbine and the feedforward controller (FF) is designed to assist the feedback controller (FB). Stage 4 (center): Hybrid Simulations within Simulink; the rotor-effective wind speed from field test turbine data v_{0R} and simultaneously measured field test raw lidar data (RLD) are used to adjust the data processing (DP). Stage 5 (right): Field Testing; the DP and FF are compiled for TwinCAT on the Gateway and the FB for Labview on the CART-SCADA.

the rotor-effective wind speed, filtered, and transferred to the feedforward controller. The data processing can be evaluated by comparing the correlation between the lidar estimate and the real rotor-effective wind speed to a correlation model [12, 13]. Simulations are done over the full operation range to test the robustness of the controller against measurement uncertainties.

3. *Real-Time Environment Development*: The data processing system and the feedforward controller are compiled to be used within a real-time capable frame (TwinCAT) on a separate computer (referred in this work as "Gateway"). The same simulations from Stage 2 are done and thus allow a direct verification of the real-time environment.

4. *Hybrid Simulations*: Effects such as the wind evolution can be included [14] in simulations, but effects such as measurement errors and changing lidar data quality are difficult to simulate. Thus, the approach of the Hybrid Simulations [15] is used to adjust the lidar data processing and feedforward controller: The rotor-effective wind speed is extracted from real turbine data [16] and together with simultaneously measured lidar data used for simulations, as shown in Figure 2 (center).

5. *Field Testing*: Finally, following the above iterations, the Gateway is connected to the actual lidar and turbine controller, as shown in Figure 2 (right).

The approach has several advantages:

- The feedforward controller, the data processing, and the real-time environment are developed independently. Thus, the data processing can be combined with different feedforward controllers.
- Each stage has a defined goal. This helps to develop several controllers in parallel.

Figure 3: The Avent 5-Beam installed on the nacelle of the CART2 at the NWTC. (Photo Credit: Lee Jay Fingersh, NREL 33621)

- The code is developed in the control-engineer-friendly Simulink environment and is organized in one single library. Thus, adjustments can be directly transferred to other stages.

2.2 Hardware Setup for Lidar-Assisted Control

The CART2, located at the National Wind Technology Center (NWTC), is a 600-kW turbine heavily instrumented with sensors. A control system (CART-SCADA) was developed and implemented in Labview by NWTC engineers running at 400 Hz, containing a dynamic link library (DLL) compiled from the Simulink-based feedback controller.

The Avent 5-Beam pulsed system was installed on the nacelle of the CART2 (see Figure 3) and measures at 10 distances in front of the rotor. At each distance, five line-of-sight measurements are taken sequentially within 1.25 seconds and are transferred to the CART-SCADA via an Ethernet connection in real time.

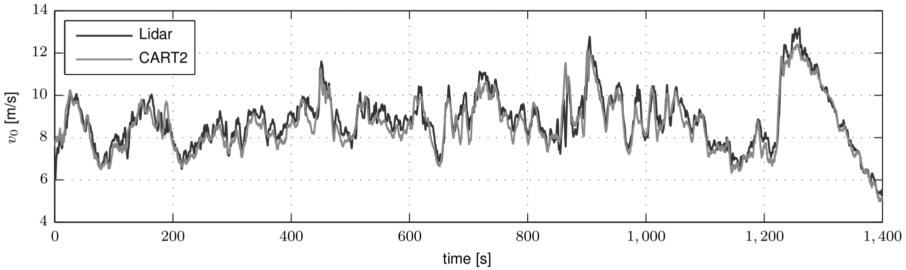

Figure 4: Rotor effective wind speed: from CART2 data (light blue) and lidar data (dark blue).

The data processing and feedforward controller are realized on the Gateway, which is a deterministic, real-time capable industrial PC and is connected to the CART-SCADA via an Ethernet connection. The lidar data is condensed into an estimate of the lidar-measured rotor-effective wind speed. Additionally, the Gateway receives turbine data, including rotor speed, blade pitch angle, and rotor shaft torque, to obtain the turbine-measured rotor-effective wind speed. The Gateway provides its feedforward update signals to the CART-SCADA, and the CART-SCADA can independently choose whether or not to use the signals in order to provide robust operation.

A separate computer connected to the Gateway visualizes the processed data and offers a way to directly interact with the Gateway via a GUI. Further, the feedforward control action (blade pitch, generator torque, desired rotor speed) are compared to measured data. Additionally, the software provides the possibility of adjusting parameters used for the online cross-correlation that will be described in the next section.

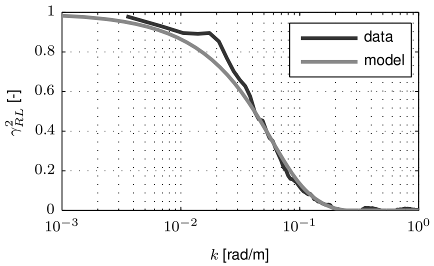

Figure 5: Coherence between the lidar and turbine estimate of the rotor-effective wind speed: From data of Figure 4 (dark blue) and from analytic correlation model (light blue).

3 Results

3.1 Correlation Study

Similar to previous work, the rotor effective wind speed estimated from the raw lidar data and from the turbine reaction has been compared before the feedforward controller was applied. Figure 4 compares both signals in the time domain. Larger trends, such as the gust at the end of the period, are very well detected by the lidar.

This is confirmed by Figure 5, which compares both signals in the frequency domain: for small wavenumbers (large turbulent eddies) the coherence is close to one (1 means perfect correlation), and for larger wavenumbers (smaller turbulent eddies) the coherence γ^2_{RL} is going toward zero (0 means no correlation). The correlation is verified by the analytical model [12]. The longitudinal decay parameter for the wind evolution was set to 0.2 based on the detected value from [17].

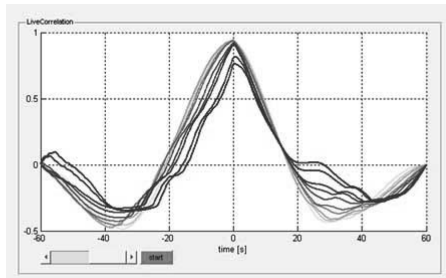

Figure 6: Cross-Correlation between the lidar and turbine estimate of the rotor-effective wind speed over the last 10 s: Newest (dark blue) and oldest (light blue) data.

The detected correlation is used to design an adaptive filter, which adjusts the cut-off-frequency depending on the mean wind speed. In future work, the adaptation needs to be extended to detect changes in the correlation and adjust the filter accordingly.

3.2 Online Calculation of Cross-Correlation

The feedforward control inputs are calculated based on the lidar estimate of the rotor-effective wind speed and sent to the CART-SCADA with an adjustable preview time before the wind disturbance reaches the turbine. This timing is crucial and the lidar estimate needs to be aligned with the rotor-effective wind speed from the turbine data. The preview time of the lidar estimate is based on Taylor's Frozen Turbulence Hypothesis and calculated by dividing the measurement distance by the mean wind speed. Changes in the preview can be due to the changing impact of the induction zone or inaccuracies in Taylor's hypothesis or the measurement distance.

On the Gateway, the timing is evaluated online by calculating the cross-correlation between the rotor-effective wind speed from lidar and turbine data. The normalized cross-correlation gives a measure of the similarity of the estimation and the timing of the estimation. An example of the online cross-correlation over the last 10 seconds is given in Figure 6. The timing can be adjusted manually by shifting the lidar preview via the GUI, and the changes can be observed in real time. During the ongoing field testing, an offset of 1 second was identified and corrected.

3.3 Initial Results of Field Testing

Finally, a field-campaign was conducted in which the baseline feedback pitch controller was augmented by the lidar-preview feedforward pitch update. Because the lidar preview measurement was shown to have good coherence to turbine measurements and was robust over time, the feedback controller could be detuned to maximize the benefit of using lidar feedforward. Detuning the feedback controller allows the feedforward controller to handle the lower wind disturbance frequencies, up to the coherence limit, which should be the optimal combination.

The field test is set up so that the controller cycles between 5 minutes of running the normal baseline feedback controller and 5 minutes of combined a feedforward and detuned feedback controller as described above. By cycling in this way, the two controllers are tested in wind conditions that are as similar as possible.

Currently, field tests have been run intermittently over several months, across a range of seasons and atmospheric conditions. While still somewhat initial, the data is already demonstrating promising trends. To analyze the data, we process each 5-minute data file as follows. The first 30 seconds of each file are ignored, to allow the change in performance of transitioning from one controller to another to be established. The remaining time is divided in 45-second continuous chunks and processed. For each chunk, statistics such as mean and standard deviation are computed for all signals, and for signals related to fatigue, a damage equivalent load (DEL) is likewise computed.

We first consider the speed-regulation performance of the lidar-enhanced controller compared to the baseline. The collective pitch controller regulates the rotor speed to the rated setpoint. The first question to answer is how has our modification affected this performance.

Figure 7 compares the performance of speed regulation. Note that for the plots, the statistics computed from the 45-second chunks have been binned by wind speed, and for each wind speed and controller the mean value and standard error of the mean are computed. First, in Figure 7 (left), the standard deviation of the rotor speed is compared across the collected 45-second chunks of data. From this plot, it appears that the speed regulation performance has not been impacted, which is the desired result. Had lidar feedforward been ineffective, detuning the feedback controller would have significantly worsened and rotor speed variation would have increased. Figure 7 (right) plots the frequency of occurrence of each per-chunk maximum rotor speed. While the highest observed rotor speeds did occur with the lidar-enhanced controller, there is not much noticeable change in performance. Finally, Figure 8 (left) shows the pitch rate standard deviation, which indicates the amount of pitch activity. Here, it is clear the lidar-enhanced controller is achieving similar results in speed-control with significantly less pitch actuation when compared to the feedback-only controller. Because the feedback controller can only react after a wind event, it would normally need to pitch more aggressively than a controller that previews the upcoming wind event and can begin acting ahead of time.

Additionally, the standard deviation of the tower acceleration in Figure 8 (right) is reduced. We can now compare the controllers in terms of the fatigue loads by plotting the per-chunk DEL statistics. Because collective pitch is most tightly coupled to fatigue loads related to rotor thrust, we focus on those—specifically blade flap bending moment and tower fore-aft bending moment.

The comparison of flap bending is shown in Figure 9 (left). Although additional data collection in higher winds would greatly aid in drawing conclusions, a reduction in this load is evident in wind speeds above rated. Fore-aft tower bending, shown in Figure 9 (right), is significantly reduced by the experimental controller.

4 Conclusion and Outlook

In this work a solution is presented that allows the data processing and feedforward control to be independently calculated of the lidar system and the turbine controller. This setup allows robust operation of the wind turbine and intensive calculations on time scales different from the feedback control loop.

Further, the setup provides the possibility to determine not only the rotor-effective wind speed estimate

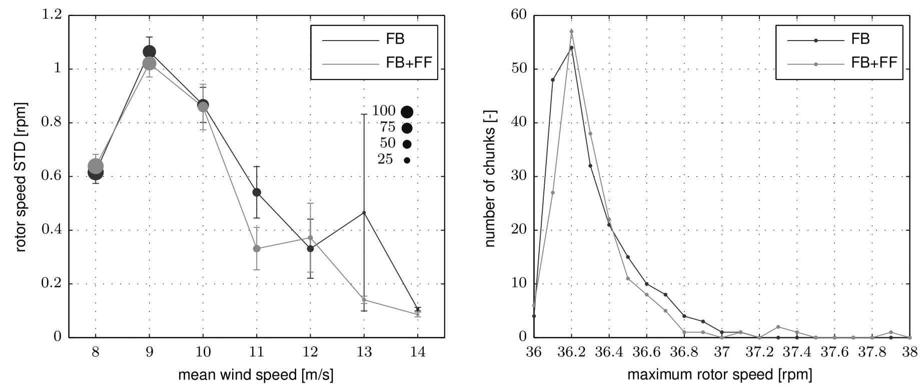

Figure 7: Comparing controller effects on rotor speed regulation. Left: standard deviation of rotor speed. The points are the mean value for each bin, while the error bars indicate the standard error of the mean. Right: frequency of occurrence of each per-chunk maximum rotor speed.

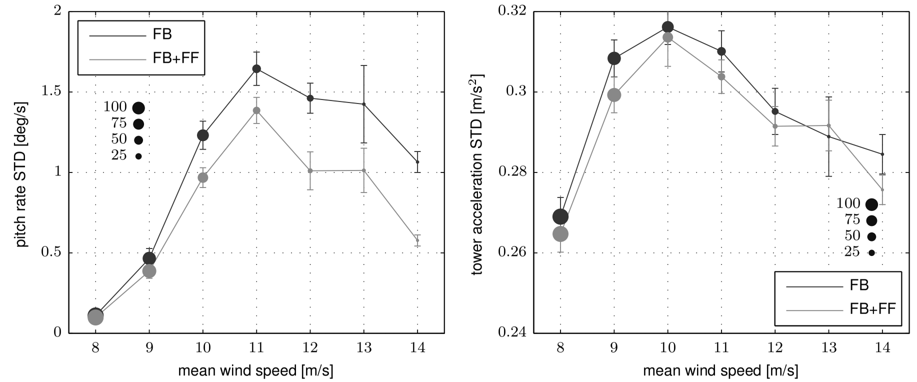

Figure 8: Comparing controller on standard deviation of pitch rate (left) and tower acceleration (right). The points are the mean value for each bin, while the error bars indicate the standard error of the mean.

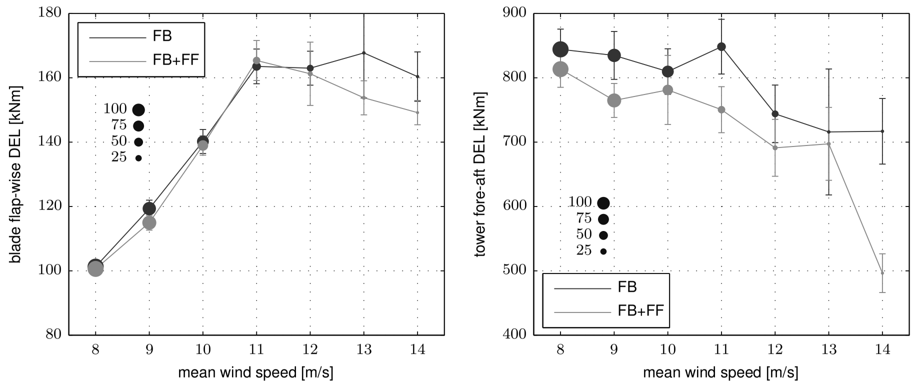

Figure 9: Comparing controller effects on loads. Blade flap-wise bending (left) and tower fore-aft bending (right). The points are the mean value for each bin, while the error bars indicate the standard error of the mean.

H∞ Based Gain Scheduled Robust Control for Load Mitigation in a Commercial 3 MW Wind Turbine

Iciar Font
Alstom Renovables
iciar.font@power.alstom.com

Aron Pujana-Arrese
IK4-IKERLAN
APujana@ikerlan.es

Asier Diaz de Corcuera
IK4-IKERLAN
ADiazCorcuera@ikerlan.es

Carlo-Enrico Cancangiu
Alstom Renovables
carlo-enrico.carcangiu@power.alstom.com

Joseba Landaluze
IK4-IKERLAN
JLandaluze@ikerlan.es

Abstract

The design and analysis of different robust control strategies applied to a commercial 3 MW wind turbine are presented in this paper. An exhaustive simulation analysis is developed with the proposed robust controllers and they are compared to the baseline controller – LTI based – installed in a commercial wind turbine by means of Key Performance Indicators (KPIs). The family of linear models extracted from a high-fidelity aeroelastic code is used to design the robust controllers and this software package is also used to perform a full set of calculations including both extreme and fatigue load cases.

Keywords: Robust Control, Load Mitigation, Commercial Wind Turbine, H∞ Control, Controller Interpolation, LMI Interpolation

1 Introduction

In the last years, the incessant increase of size of wind turbines, combined with an increment of the structure complexity for offshore wind turbine designs, has introduced new challenges in the control systems. These control systems have to be more complex to match tight design specifications in terms of loads and performance. Such design targets have often opposite trends, for instance lighter mechanical structures with lower resonance frequencies are required but loads must be kept limited, and the best trade-off must be found. In this way, the number of control objectives has increased and, due to coupling of variables and components of wind turbines, the present tendency of the control strategy design is to use multi-objective and multivariable schemes. Several applications of advanced multivariable control techniques – such as robust control – are found in the literature, and some of them have also been field-tested in wind turbine prototypes [2].

In previous work of the authors [1][4][5] gain-scheduled (GS) robust controllers were designed for the public 5 MW 'upwind' wind turbine model. The controllers obtained had a higher capacity to adapt their behaviour according to the different operating points in wind turbine non-linear systems, therefore they improved closed loop performance, compared to Linear Time Invariant (LTI) controllers. Bearing in mind that those GS robust controllers are based on high-order H∞ controllers, used interpolation methods implicate an important contribution in the LTI control interpolation field due to the mathematical calculation convergence problems.

Figure 1: ALSTOM's wind turbine

Recently, robust control techniques have been applied to a commercial multi-megawatt wind turbine (Fig. 1) and this paper focuses on the results achieved. The controllers were designed according to design procedures presented in [4] and [5]. The different robust controllers obtained were integrated in the control code and in the control hardware. As a previous step before field-testing, the robust controllers have been tested by Hardware in the Loop (HIL). To consolidate the results presented in this paper with field data, an experimental test campaign will be carried-out at the real wind turbine in the coming months.

This paper compares the different control structures based on robust control theory and designed for a multi-megawatt commercial wind turbine against its LTI based baseline controller. The comparison of these controllers has been developed by means of simulations in a high-fidelity aeroelastic code. Four control structures are analyzed, named BCS (Baseline Control Structure), RCS1 (Robust Control Structure 2), RCS2 (Robust Control Structure 2) and RCS3 (Robust Control Structure 3). In the case of the control structure RCS2 two controllers are considered: RCS2a without tower side-to-side compensation and RCS2b with this compensation. The comparison is made by means of Key Performance Indicators (KPIs).

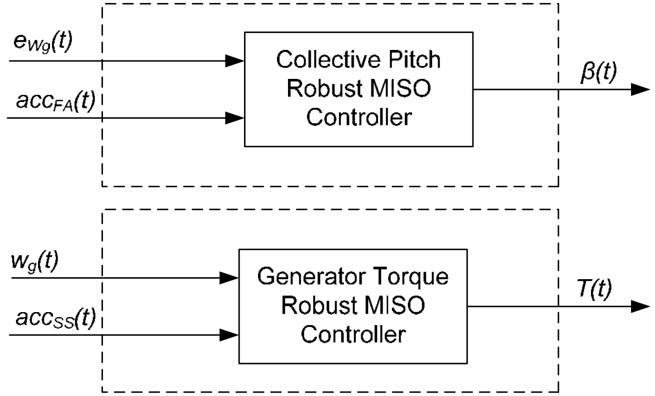

Figure 2: General view of the robust control structure in the above rated control zone

2 Controllers

The four control structures developed for the commercial wind turbine (BCS, RCS1, RCS2 and RCS3) are briefly described in next sub-sections.

The control objectives for the novel proposed robust control algorithms are as follows: 1) improving the regulation of the generator speed, 2) mitigating the wind effect on the tower fore-aft and side-to-side first modes and 3) damping the drive train mode – both with the main objectives of mitigating the loads in the wind turbine –, and 4) improving the generation of electric power. Fig. 2 shows a general view of the robust control structure used in this work, which is based on two multivariable collective pitch and generator torque controllers. Finally the tower fore-aft compensation was not activated in any of the robust controllers and the tower side-to-side compensation was not considered in the RCS2a controller, but it was in the other robust controllers.

In the robust controller structure RCS1 a unique collective pitch H∞ controller is designed for the whole above rated zone [4]. The robust control structures RCS2 and RCS3 are based on three collective pitch H∞ controllers, designed with the same structure of the RCS1 controller but for three operating points in the above rated zone, corresponding to wind speeds of 13 m/s, 19 m/s and 25 m/s, and covering, covering robust stability up to cut out wind speed. The main goal is to improve the

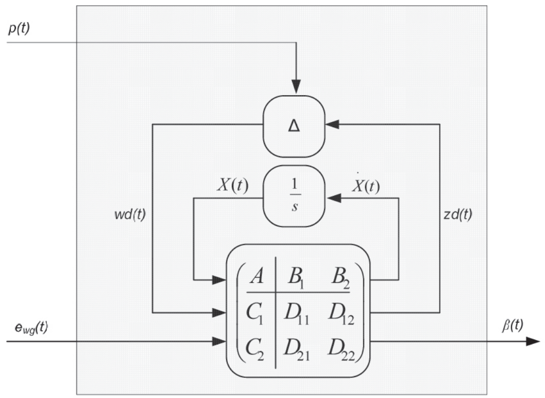

Figure 3: RCS2: Upper LFT representation of the gain-scheduled robust pitch controller

regulation of the generator speed achieved with the LTI pitch control designed in RCS1. In RCS2 the interpolation of these three controllers has been developed with a gain-scheduling of the controller's state space matrices by polynomials approximations [5], where the controller is represented by Linear Fractional Transformation (LFT). In RCS3 a more sophisticated interpolation method solving a complex a Linear Matrix Inequalities (LMI) system [5], which guarantees the closed loop stability during the transitions, has been used.

2.1 Baseline controller (BCS)

Controller based on the classical control design proposed by Bossanyi in [3]. This control design considers uncoupled monovariable pitch angle and generator torque control loops and the controllers are based on gain-scheduled Proportional-Integral (PI) controllers and filters. This controller is a mature and well-tuned controller of the commercial wind turbine.

2.2 Robust controller 1 (RCS1)

Basically, the designed control strategy consists of two robust H∞ multi-input single output (MISO) controllers (Fig. 2).

The first MISO (Multi-Input Single-Output) controller is a generator torque controller which reduces the wind effect in the drive train and tower side-to-side first modes. This works in all operating zones, although the basis in the below rated zone – to follows the optimum power coefficient curve – is the same as in the baseline BSC controller. The other MISO controller, the collective pitch angle MISO controller, is designed for the operating point corresponding to a mean speed of 15 m/s and regulates the generator speed at the nominal value.

Taking into account that this is a unique controller for the whole above rated zone, limited performance levels were expected, balancing the large robustness of the controller.

2.3 Robust controllers 2 (RCS2a and RCS2b)

The generator torque control is the same as the MISO generator torque controller used in the RCS1 controller. For the collective pitch controller, in order to overcome the performance limitation of using a unique H∞ MISO controller for the whole above rated zone, three basic H∞ controllers are designed with the same structure of the RCS1 controller but for three operating points, corresponding to wind speeds of 13 m/s, 19 m/s and 25 m/s. Each basic controller is valid only for a stability robust region and therefore the controller must be changed according to the region in the above rated zone. The change of controllers can be performed either gradually by interpolation or by switching. Switching might produce instability and interpolation is preferred. In the RCS2 control structure the interpolation of the three LTI H∞ controllers is based on the gain-scheduling of the coefficients of the three LTI controller's state-space matrices [5]. The stability in all trajectories of the above rated zone is not guaranteed in the control design with this LFT represented gain-scheduled controller, but it should be guaranteed by means of extended simulations. Fig. 3 shows the upper LFT representation of the gain-scheduled robust pitch controller, where the coefficients of the state space matrices are interpolated with a first order polynomial approximation. The varying parameter is named *p*(t) and it varies according to the present pitch angle.

As mentioned, with the RCS2 robust control structure two controllers were designed: RCS2a, without tower side-to-side compensation and RCS2b, with tower side-to-side compensation.

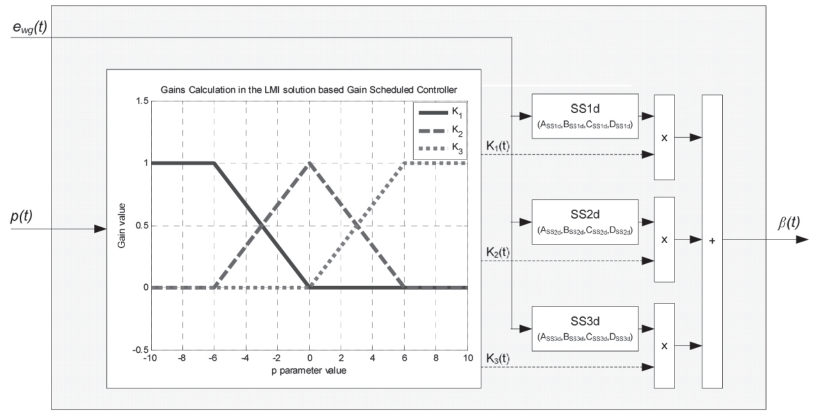

Figure 4: RCS3: Structure of the LMI solution based gain-scheduled pitch control

2.4 Robust controller 3 (RCS3)

The generator torque control is not changed from the RCS2 robust control structure to this control structure. However, the interpolation of the three collective H∞ pitch controllers diverges from RCS2. It is based on solving a Linear Matrix Inequalities (LMI) system to represent it in a new gain scheduled scenario (see Fig. 4). The collective pitch angle control signal is calculated from the contribution of the new three calculated discretized controllers, represented in state space: SS1d, SS2d and SS3d. These are calculated solving the LMI system and their frequency response is the same as in the three H∞ controllers used. However, SS1d, SS2d and SS3d are prepared to be interpolated by the three gains. The stability is guaranteed in all points of the parameter trajectory of the

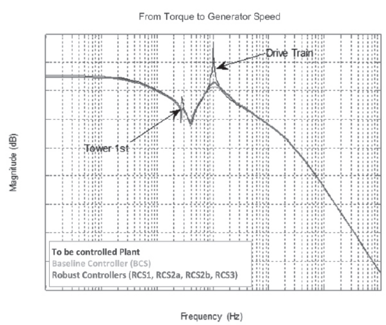

Figure 5: Drive train mode compensation of baseline and robust controllers

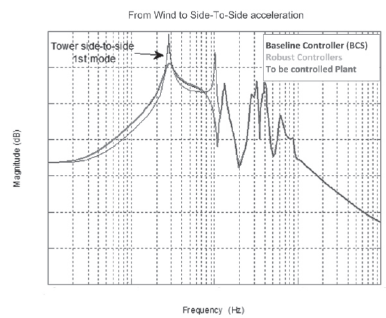

Figure 6: Tower side-to-side compensation

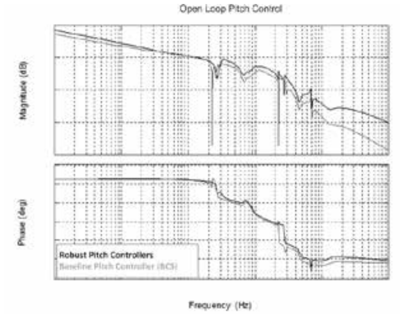

Figure 7: Effect of robust controllers on pitch plants compared to the baseline controller

control zone considered in the design process [5].

As examples of the robust designs, Fig. 5 shows the Bode diagram from the generator torque to the generator speed for the baseline controller when the drive train damper is not activated and activated, and the case of the robust controllers, where the generator torque loop is the same for the four controllers. As observed the compensation of the drive train mode is less aggressive with the robust controllers. Fig. 6 shows the Bode diagram between the wind speed and the tower side-to-side acceleration. As observed, the generator torque loop of the RCS1, RCS2b and RCS3 robust controllers compensates the 1st tower side-to-side mode, which is not performed with the baseline BCS and RCS2a controllers. Related to differences obtained with the pitch control loops of the different controllers, Fig. 7 shows the Bode diagram of the open loop pitch control of the RCS3 controller compared to the baseline controller. As observed, in general the robust controller has more pitch activity in medium-high frequencies.

3 Result Comparison

Some simulations have been performed in a high-fidelity aeroelastic code with the five controllers.

Load Cases DLC1.1, DLC1.2, DLC1.3, DLC1.4, DLC1.5, DLC1.6, DLC1.7, DLC1.9, DLC2.1a, DLC2.1b, DLC2,2 and DLC4.2 of the standard IEC 61400-1:1999 [6] have been considered.

The results obtained with the different controllers are compared by means of KPIs (Key Performance Indicators) of main coordinate systems. The four robust controllers are evaluated in comparison to the baseline controller BCS. Performance is evaluated by means of KPIs of ‘over speed’, ‘Annual Energy Yield (AEY)’, ‘tower clearance’ and ‘pitch duty’ values. Fatigue loads are assessed with KPIs of Tower Base Mx and My, Blade Root Mflap and Medge, and Stationary Hub Mx, My and Mz. Finally, for the evaluation of ultimate loads, KPIs of Tower Base Mxy, maximum and minimum Blade Root Mflap and Medge, and Stationary Hub Mx and Myz are taken into account.

Next subsections present some results, which appear summarized in Table 2.

3.1 Performance

3.1.1 Time domain results

As an example of results in the time domain, Fig. 8 shows the generator speed, generator torque, blade pitch angle and electric power signals for a power production wind with a mean speed of 18 m/s by using the four analyzed controllers. As observed, the generator speed is better controlled with the robust controllers. The pitch angle and the generator torque signals are very similar with all the controllers. Similar results are obtained with other turbulent wind speeds. Generator speed regulation and electrical power regulation improve with the GS robust controllers.

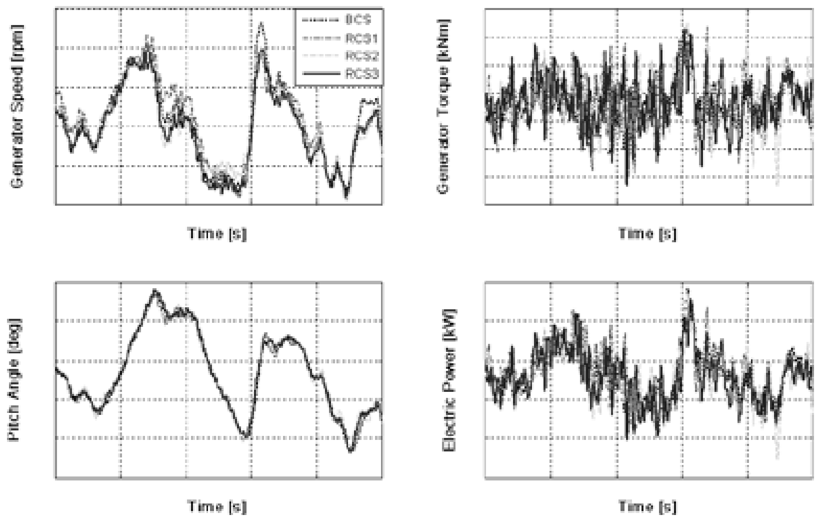

Figure 8: Comparison results for the four controllers with a turbulent production wind at 18 m/s

3.1.2 Annual Energy Yield

Using the power production simulations (DLC1.2) KPIs of the Annual Energy Yield (AEY) weighted with a Weibull distribution (hours/year) was calculated. Fig. 9 shows the results obtained with the robust controllers compared to the baseline controller. As observed, the AEY decreases with the RCS1 controller: this is because being a unique pitch controller for the whole above rated zone, the performance is optimized for the nominal operation point considered for the design – 15 m/s – and it gets worse when moving away from this optimum point. AEY increases 0.3% and 0.2% with the RCS2 and RCS3 controllers.

The increments are especially relevant in the range 6-14 m/s because one of the basic H∞ controllers considered was developed to be optimum at 13 m/s. In high wind speeds the results with the robust controllers are worse in general due to the characteristics of the interpolation techniques.

Power Curve [kW]					
Mean Wind	BCS (%)	RCS1	RCS2a	RCS2b	RCS3
4	100	✓ 0.0%	✗ -0.1%	✗ -0.1%	✗ -0.1%
6	100	✗ 0.0%	✓ 0.1%	✓ 0.1%	✓ 0.1%
8	100	✗ -0.3%	✓ 0.2%	✓ 0.2%	✓ 0.2%
10	100	✗ -0.5%	✓ 0.6%	✓ 0.6%	✓ 0.4%
12	100	✗ -0.3%	✓ 0.5%	✓ 0.5%	✓ 0.3%
14	100	✗ -0.2%	✓ 0.1%	✓ 0.1%	✗ -0.3%
16	100	✓ 0.0%	✓ 0.1%	✓ 0.1%	✗ -0.2%
18	100	✓ 0.2%	✓ 0.1%	✓ 0.2%	✗ -0.1%
20	100	✗ -0.1%	✗ -0.3%	✗ -0.3%	✗ -0.3%
22	100	✗ -0.2%	✗ -0.4%	✗ -0.5%	✗ -0.2%
24	100	✗ -1.5%	✗ -0.8%	✗ -0.8%	✗ -0.8%
AEY [kWh/year]	100	✗ -0.3%	✓ 0.3%	✓ 0.3%	✓ 0.2%

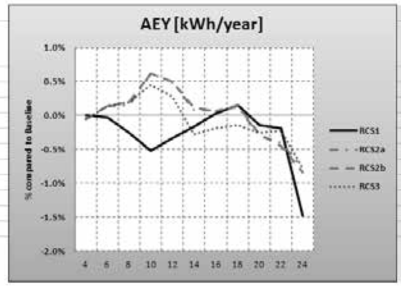

Figure 9: KPI Table for Annual Energy Yield in comparison to BCS controller

Tower Base My (m = 4)					
Mean Wind	BCS (%)	RCS1	RCS2a	RCS2b	RCS3
4	100	✓ -1.4%	✓ -0.4%	✓ -0.4%	✓ -0.4%
6	100	✓ -0.3%	✓ -0.1%	✓ -0.1%	✓ -0.1%
8	100	✓ -2.4%	✗ 2.3%	✗ 1.9%	✗ 1.9%
10	100	✗ 0.1%	✓ -1.3%	✓ -1.0%	✓ -3.1%
12	100	✓ -2.4%	✓ -4.6%	✓ -3.3%	✓ -3.3%
14	100	✗ 2.0%	✓ -2.1%	✓ -2.3%	✗ 1.7%
16	100	✓ -9.5%	✗ 4.2%	✗ 3.1%	✓ -3.4%
18	100	✓ -9.9%	✗ 6.5%	✗ 5.4%	✓ -6.8%
20	100	✗ 0.5%	✗ 8.9%	✗ 6.4%	✓ -5.1%
22	100	✗ 2.0%	✗ 4.8%	✗ 2.7%	✓ -1.8%
24	100	✗ 7.7%	✗ 2.4%	✗ 0.2%	✓ -9.2%
TOTAL	100	✓ -1.2%	✗ 1.7%	✗ 1.2%	✓ -1.7%

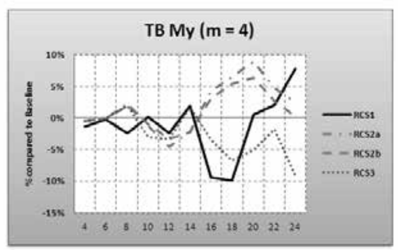

Figure 10: KPI Table for Tower Base My in fatigue comparison to BCS controller

Mean Wind	BCS (%)	RCS1	RCS2a	RCS2b	RCS3
Blade Root Mflap (m = 9)					
4	100	✗ 0.2%	✗ 0.3%	✗ 0.3%	✗ 0.3%
6	100	✗ 1.1%	✗ 3.2%	✗ 3.2%	✗ 3.2%
8	100	✗ 0.6%	✗ 1.3%	✗ 0.0%	✗ 0.2%
10	100	✗ 2.1%	✗ 1.5%	✗ 1.5%	✗ 0.7%
12	100	✗ 1.8%	✓ -2.4%	✓ -2.1%	✓ -3.8%
14	100	✗ 2.3%	✓ -0.2%	✓ -0.3%	✗ 4.1%
16	100	✗ 3.4%	✗ 3.8%	✗ 3.3%	✗ 5.3%
18	100	✓ -1.3%	✗ 3.4%	✗ 3.3%	✓ -0.1%
20	100	✓ -4.9%	✗ 0.0%	✓ -0.2%	✓ -2.7%
22	100	✗ 2.3%	✗ 4.5%	✗ 4.7%	✗ 3.4%
24	100	✓ -4.8%	✗ 2.9%	✗ 2.7%	✗ 3.0%
TOTAL	100	✗ 0.5%	✗ 1.7%	✗ 1.5%	✗ 1.6%

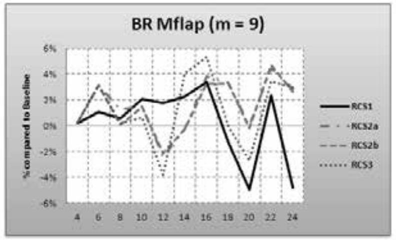

Figure 11: KPI Table for Blade Root Mflap in fatigue comparison to BCS controller

3.2 Mechanical loads

3.2.1 *Fatigue loads*

Simulations were performed in the DLC1.2 case with all controllers for turbulent production wind files between 4 and 24 m/s. After that, Key Performance Indicators (KPIs) were calculated for the main coordinate systems and compared with the baseline controller BCS.

Fig. 10 shows the comparison table for the fatigue of Tower Base My variable. As a result, after calculating Damage Equivalent Loads (DEL) weighted with a Weibull distribution, this load decreases 1.2% with the RCS1 controller and 1.7% with the RCS3 controller but it increases up to 1.7% with the RCS2 controllers. This increment with the RCS2 control structure is due to an increment of the pitch activity around the first tower fore-aft mode, whose frequency is close to the 1P frequency.

Fig. 11 and Fig. 12 show the comparison tables for the fatigue of Blade Root Mflap and Medge coordinate systems. As observed, the Mflap load increases with the four controllers at low and intermediate wind speeds and it decreases especially with the controller RCS1 at high wind speeds. In the end, the total equivalent load increases with the three controllers, 0.5%, 1.7%, 1.5% and 1.6% respectively. The Medge fatigue load increases quite a lot with the controller RCS1 at high wind speeds and it remains very similar with the RCS2 and RCS3 controllers. In the end, the total equivalent load increases 0.3% for the controller RCS1 and 0.1% for the RCS2b and RCS3 controllers. As observed, the activation of the tower side-to-side first mode damping channel in the above rated zone has not influence in this load. The higher activity of the robust controllers – see 'pitch duty' in Table 2 and Fig. 7 – has negative effects on the Blade Root loads.

As an example of a load which degenerates with the new controllers, Fig. 13 shows the case of the Stationary Hub Mx variable. In this case the load increases, especially when the tower side-to-side compensation is activated and at high wind speeds. The equivalent load increases 4.4% for RCS1 controller, 2.9% for RCS2b controller and 3.0% for RCS3 controller. However, the load increment is only 0.2% in the case of the RCS2a controller. The design of the drive train damper using robust control techniques is less aggressive than the one used in the baseline controller (Fig. 5), and this may justify this small divergence versus baseline. As a conclusion, the activation of the tower side-to-side first mode damping channel increases this fatigue load due to its generator torque contribution. As observed, the increments increase with the wind speed for the three robust controllers with tower side-to-side compensation.

Mean Wind	BCS (%)	RCS1	RCS2a	RCS2b	RCS3
Blade Root Medge (m = 9)					
4	100	✓ -0.1%	✓ 0.0%	✓ 0.0%	✓ 0.0%
6	100	✗ 0.2%	✓ -0.2%	✓ -0.2%	✓ -0.2%
8	100	✗ 0.2%	✗ 0.2%	✗ 0.2%	✗ 0.2%
10	100	✗ 0.0%	✗ 0.7%	✗ 0.7%	✗ 0.4%
12	100	✗ 0.0%	✓ -0.7%	✓ -0.5%	✓ -0.8%
14	100	✗ 0.7%	✓ -0.2%	✓ -0.1%	✗ 0.6%
16	100	✓ 0.0%	✓ -0.2%	✗ 0.2%	✗ 0.1%
18	100	✗ 0.7%	✓ -0.3%	✓ -0.3%	✗ 0.5%
20	100	✗ 2.3%	✗ 0.4%	✗ 0.5%	✗ 1.0%
22	100	✗ 0.4%	✗ 0.7%	✗ 0.5%	✓ -1.0%
24	100	✗ 2.6%	✗ 0.7%	✗ 1.0%	✗ 0.9%
TOTAL	100	✗ 0.3%	✗ 0.0%	✗ 0.1%	✗ 0.1%

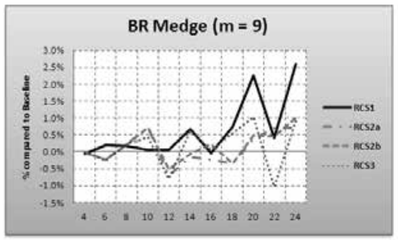

Figure 12: KPI Table for Blade Root Medge in fatigue comparison to BCS controller

Mean Wind	BCS (%)	RCS1	RCS2a	RCS2b	RCS3
Stationary Hub Mx (m = 3)					
4	100	✗ 2.6%	✗ 2.1%	✗ 2.1%	✗ 2.0%
6	100	✗ 0.1%	✗ 1.2%	✗ 1.2%	✗ 1.2%
8	100	✗ 0.3%	✗ 0.9%	✗ 1.1%	✗ 1.1%
10	100	✗ 0.4%	✗ 0.5%	✗ 0.8%	✗ 0.5%
12	100	✗ 3.1%	✓ -3.2%	✓ -1.9%	✓ -0.5%
14	100	✗ 1.2%	✗ 1.2%	✗ 5.2%	✗ 2.9%
16	100	✗ 5.5%	✓ -1.7%	✗ 6.4%	✗ 5.2%
18	100	✗ 11.1%	✓ -1.6%	✗ 9.0%	✗ 7.6%
20	100	✗ 23.3%	✗ 1.2%	✗ 15.6%	✗ 17.0%
22	100	✗ 37.8%	✗ 2.9%	✗ 23.9%	✗ 27.3%
24	100	✗ 41.9%	✗ 4.6%	✗ 24.5%	✗ 24.9%
TOTAL	100	✗ 4.4%	✗ 0.2%	✗ 2.9%	✗ 3.0%

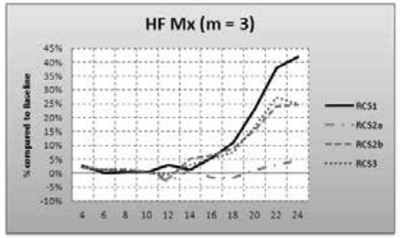

Figure 13: KPI Table for Stationary Hub Mx in fatigue comparison to BCS controller

3.2.2 *Ultimate loads*

One of the main advantages of using robust control techniques is the capability for adapting closed loop shapes by means of weighting functions and therefore to improve the bandwidths of the control loops compared to the baseline controller's ones. The effects of an improvement in bandwidths could be observed especially in ultimate load cases, which are very important when evaluating the performance of a wind turbine with a specific controller.

After taking into account all DLC cases simulated the extreme loads were evaluated for the coordinate systems under analysis. Table 1 shows the results obtained with the four robust controllers in comparison to the baseline controller. With the controller RCS1 ultimate loads improve in all coordinate systems except in Blade Root Medge, where loads increase 1% compared to the baseline case. The decrement in Tower Base Mxy is very significant (4.9%). This improvement is much higher than improvements obtained with the GS robust controllers: the reason is that the worst case is an emergency stop DLC case in combination with a coherence gust where the pitch bandwidth of the RCS1 controller has very positive effects.

Stationary Hub Myz increases 3.2% with the RCS2b controller and only 0.5% with the RCS2a controller. Influence of the tower side-to-side compensation can be observed also in Stationary Hub Mx and Tower Base Mxy, but in some cases loads improve and in others do not compared to the baseline BSC controller. With the RCS2 control structure the loads on the other coordinate systems decrease, but in general less than with the RCS1 controller.

With the RCS3 controller all of the ultimate loads improve, being the improvement relevant in maximum Blade Root Mflap (2.4%), maximum Blade Root Medge (1.6%) and Stationary Hub Mx (1%).

3.3 Summary

Table 2 shows a summary of the KPI values obtained for the four robust controllers in comparison to the baseline controller.

	Tower Base	Blade Root				Stationary Hub	
	TB Mxy	BR Mflap (3 blades)		BR Medge (3 blades)		HF Mx	HF Myz
	AbsMax	Max	Min	Max	Min	AbsMax	AbsMax
RCS1	✓ -4.9%	✓ -1.1%	✓ -2.8%	✗ 1.0%	✗ 1.0%	✓ -3.0%	✓ -0.9%
RCS2a	✓ -0.7%	✓ -0.5%	✗ 0.2%	✓ -1.3%	✓ -0.5%	✓ -0.7%	✗ 0.5%
RCS2b	✓ -0.3%	✓ -1.3%	✗ 0.2%	✓ -1.3%	✓ -0.3%	✓ 0.0%	✗ 3.2%
RCS3	✓ -0.6%	✓ -2.4%	✓ -0.3%	✓ -1.6%	✓ -0.9%	✓ -1.0%	✓ -0.3%

Table 1: KPI of ultimate loads in comparison to BCS controller

KPI analysis		BCS [%]	RCS1 [%]	RCS2a [%]	RCS2b [%]	RCS3 [%]
Fatigue Loads	Tower Base Mx (m=4)	100	✓ -15.6	✗ 4.0	✓ -15.6	✓ -15.5
	Tower Base My (m=4)	100	✓ -1.2	✗ 1.7	✗ 1.2	✓ -1.7
	Blade Root Mflap (m=9)	100	✗ 1.5	✗ 1.7	✗ 1.5	✗ 1.6
	BladeRootMedge (m=9)	100	✗ 0.1	✓ 0.0	✗ 0.1	✗ 0.1
	Stat. Hub Mx (m=3)	100	✗ 2.9	✗ 0.2	✗ 2.9	✗ 3.0
	Stat. Hub My (m=3)	100	✗ 0.2	✗ 0.2	✗ 0.2	✓ 0.0
	Stat. Hub Mz (m=3)	100	✓ -0.2	✓ -0.2	✓ -0.2	✓ -0.5
Extreme Loads	Tower Base Mxy	100	✓ -0.3	✓ -0.7	✓ -0.3	✓ -0.6
	Blade Root Mflap (max)	100	✓ -1.3	✓ -0.5	✓ -1.3	✓ -2.4
	Blade Root Mflap (min)	100	✗ 0.2	✗ 0.2	✗ 0.2	✓ -0.3
	BladeRootMedge (max)	100	✓ -1.3	✓ -1.3	✓ -1.3	✓ -1.6
	BladeRootMedge (min)	100	✓ -0.3	✓ -0.5	✓ -0.3	✓ -0.9
	Stat. Hub Mx	100	✓ 0.0	✓ -0.7	✓ 0.0	✓ -1.0
	Stat. Hub Myz	100	✗ 3.2	✗ 0.5	✗ 3.2	✓ -0.3
Annual Energy Yield		100	✓ -0.3	✗ 0.3	✗ 0.3	✗ 0.2
OverSpeed		100	✓ -0.2	✓ 0.0	✗ 0.1	✗ 0.6
Tower Clearance		100	✓ -1.3	✗ 0.8	✗ 0.8	✓ 0.0
Pitch Duty		100	✗ 59.8	✗ 13.6	✗ 13.8	✗ 17.8

Table 2: Summary KPI Table

Related to fatigue loads, the results are very similar except in cases where the robust controllers introduce new features: Tower Base Mx is improved considerably when the robust controllers include in the torque loop the tower side-to-side compensation – all controllers except the RCS2a controller –. Tower Base My improves slightly with the RCS1 and RCS3 controllers. It must be remarked as well as a negative feature that Stationary Hub Mx increases with the robust controllers having the tower side-to-side compensation activated, due to the extra generator torque contribution from that compensation feature. No relevant conclusions to be extracted on the other coordinate systems.

Ultimate loads improve in general with all controllers. With the RCS3 controller loads are improved in all the coordinate systems under analysis, especially in Blade Root Mflap, Blade Root Medge and in Stationary Hub Mx. With the controllers RCS2 the results are also fairly good but there is an important load increment (3.2%) in Stationary Hub Myz with the RCS2b controller.

In relation to AEY (Annual Energy Yield), maximum speed and tower clearance, the results are very similar to the values obtained with the baseline BCS controller. However, AEY improves 0.3% and 0.2% with RCS2 – RCS2a and RCS2b – and RCS3 respectively. The tower side-to-side compensation has not any influence on AEY (same results with RCS2a and RCS2b controllers).

The pitch duty, which is an indicator of the pitch activity, increases considerably with the three controllers, especially with the RCS1 controller (59.8%) due to the limited performance obtained with a unique controller for the whole above rated zone. The increment is lower (13.6%, 13.8% and 17.8%) with RCS2 and RCS3 controllers due to the adaptability to the operating points of the gain scheduling. In general multivariable controllers lead to increase the pitch activity.

4 Conclusions

This paper presents a comparison of different robust controllers, designed for a commercial Alstom's 3 MW wind turbine, to its baseline controller. The family of linear models, extracted from a linearization process in a high-fidelity aeroelastic code, is used to design the proposed collective pitch and generator torque robust controllers. Also, this software package is used to develop the battery of simulations for the calculations of the extreme and fatigue load cases and to determine the values of the KPIs (Key Performance Indicators).

As expected, the use of gain-scheduled collective pitch control based on the interpolation of three H_∞ controllers improves the response of the loop in this control zone due to a better adaptability of the controller to the wind turbine operating points. The two methods analyzed to develop the interpolation are based on the gain-scheduling of the controller's state space matrices by polynomials approximations or solving Linear Matrix Inequalities (LMI) systems. In the first one, the stability is not guaranteed in the control design and it has to be demonstrated with simulations in the non-linear closed loop. However, the stability in the second method is guaranteed because it is considered in the formulation of the LMI system.

The generator speed regulation is improved with the gain-scheduled controllers in the above rated zone and, inherently, the electric power production is regulated in the above rated control zone with more accuracy near the nominal value of 3 MW. Also, a generator torque control loop to mitigate the wind effect in the tower side-to-side first mode is proposed and analyzed for this commercial Alstom's wind turbine.

Overall, the results obtained from this study are very promising in terms of loads and performance. Load levels are generally aligned with the baseline controller, and even allowing some extra load reduction, which is a good result considering that the baseline is a mature turbine product. In addition, it is expected that the robust control approach, being intrinsically multi-objective and multivariable, is particularly suitable for complex systems such as offshore floating wind turbine.

The work presented in this paper is the first fundamental step for the implementation of advanced robust controllers in real commercial wind turbines. Moreover, the robust controllers have been integrated into the whole control software package and validated through HIL, confirming the capability of the current control hardware to work with such high ordered state-space represented controllers. The next step consists in performing a comprehensive field test campaign, in order to complete the validation cycle and make this solution available for industrial applications

5 Learning Objectives

The Alstom's control code is now prepared to work with these multi-variable robust controllers in LTI or GS based control scenarios. A simulation validation is shown in this work to see the real performance levels of different robust controllers in a commercial Alstom's 3 MW wind turbine compared to the baseline control strategy. This is an important first step in the process to field-test these controllers in the commercial wind turbine.

6 Acknowledgements

The material used in this article was partly supported by the Spanish Ministry of Economy and Competitiveness and European FEDER funds (research project DPI2012-37363-C02-02).

7 References

[1] Diaz de Corcuera, A., A. Pujana-Arrese, J.M. Ezquerra, A. Milo and J. Landaluze. 2014. "Design of Robust Controllers for Load Reduction in Wind Turbines"*. Book chapter in the book Wind Turbine Control and Monitoring,* edited by Springer.

[2] Fleming, P. A., J.W. van Wingerden and A.D. Wright. 2012. "Comparing State-Space Multivariable Controls to Multi-SISO Controls for Load Reduction of Drivetrain-Coupled Modes on Wind Turbines through Field-Testing". AIAA wind energy symposium. January 2011. Nashville (USA).

[3] Bossanyi, E.A. 2010. "Work Package 5 – Control systems: Final report. European Upwind Project Report". www.upwind.eu (downloaded on February 2013).

[4] Diaz de Corcuera A., A. Pujana-Arrese, J.M. Ezquerra, E. Segurola and J. Landaluze. 2012. "H_∞ Based Control for Load Mitigation in Wind Turbines". Energies 2012, 5, 938-967.

[5] Pujana-Arrese, A., A. Diaz de Corcuera, P. Fernandez, J.M. Ezquerra, A. Milo and J. Landaluze. 2014. "Analysis of two interpolation methods of H infinity controllers for robust wind turbine control". EWEA 2014, Barcelona (Spain).

[6] IEC 61400-1:1999(E), Wind Turbine Generator Systems – Part 1: Safety Requirements, Second edition. International Technical Commission. Bought by: IKERLAN S COOP, W0673826.

Systematic Tuning of Fixed-Structure Speed and Active Tower Damping Controllers using H∞-Norm Criteria in the Frequency Domain

Martin Shan, Boris Fischer, Peter Loepelmann

Fraunhofer IWES Kassel,
Department Control Engineering, Email: martin.shan@iwes.fraunhofer.de

Abstract

This paper considers how structured H∞-control design based on a given wind spectrum can be used as a systematic, transparent and efficient way for tuning the parameters of fixed-structure controllers for rotor speed control and active tower damping for a horizontal-axis wind turbine using collective pitch actuation.

Keywords: Pitch Control, Active Tower Damping, H∞

1 Introduction

If collective pitch is used for both rotor speed control and active tower damping of a wind turbine, control design effectively becomes a multivariable problem. Speed control and axial tower motion are highly coupled, as changes in pitch angle always influence both the aerodynamic thrust and the aerodynamic torque acting on the rotor. Modern control design methods, in principle, can optimize both control loops in parallel once the overall optimization criterion is defined, e.g. [1]. This, however, requires proper weighting of different control objectives as a starting point, which in many cases is not obvious. As a consequence, the problem of controller parameter tuning is often shifted towards tuning of weighting matrices or weighting functions.

Furthermore, the resulting MIMO-controllers are not very comprehensible and, depending on the control design model, may be of high order. In practice, this can cause problems for gain scheduling or pitch actuator saturation / controller switching between part- and full-load operation.

It is common practice in industry to design separate control loops for speed control and tower damping. The controller structure typically consists of simple PID schemes or filters that are designed in an iterative process. In many cases, an existing speed controller is augmented with an additional control loop for active tower damping [2]. Clearly, this approach will not result in an optimal controller parameterization regarding both speed control and tower fatigue objectives.

The approach taken in this paper is to apply a pragmatic multivariable control design to a controller with predefined, i.e. fixed structure. The advantages of a simple and comprehensible controller structure should be combined with those of a systematic multivariable control design.

The results and conclusions presented in this paper have been derived for the well-known 5 MW NREL reference wind turbine [3]. However, similar results have been observed also for models of different multi-MW wind turbines.

2 Formulation of Control Objectives in the Frequency Domain

The assumed control objective in this study is:

For a given wind spectrum,

- **minimize the fatigue damage related to the fore-aft tower base bending moment**
- **while keeping the rotor speed deviations below a defined threshold**
- **and keeping pitch speed and pitch acceleration below given limits**

Since information on the wind field is typically given in the frequency domain, an H∞-norm based approach is chosen. The original control objectives, which are actually time domain criteria, are translated into weighting functions. While some authors propose "black-box" numerical optimization of weighting function parameters, see e.g. Ozdemir [4], in this paper the dependency between weighting function parameters and the original control objectives should be made transparent. For this purpose, tower bending fatigue and maximum speed deviations must be related to the frequency domain properties of the wind turbine, i.e. the shape of the closed-loop transfer functions.

As described in [5], fatigue due to tower fore-aft bending can be estimated directly based on the power spectral density (PSD) of the bending moment signal, using the Dirlik-method [6].

Also, the maximum speed deviations can be estimated based on the PSD of the generator speed signal using the Rice-method for estimating the probability distribution of maximum amplitudes of a normally distributed signal [7]. In this paper, the value of 2 times the amplitude corresponding to 95% in the cumulated probability distribution was used as (conservative) estimation for the maximum rotor speed deviation from mean in a 600 s time series.

The evaluation of controllers with regard to the control objective formulated above can thus conveniently be carried out on the basis of PSDs. As long as the assumption that the turbine behaves linearly is valid, these PSDs can be calculated directly from the transfer function and the assumed wind spectrum without any time domain simulations, see e.g. [2]. Thus, optimizations are computationally very efficient. Note that the linear system assumption will be violated for large deviations from the operating point and especially if the transition between full-load and part-load is considered. However, for optimizing the controller for individual operating points in the full-load region of the wind turbine, the approach is considered to be very useful.

3 Wind Turbine Model for Control Design

In this paper, a linearized model for only one operating point at 18 m/s mean wind speed is considered for control design. As we consider only full-load operation, the generator torque was assumed to be constant and pitch speed reference was used as single control input.

In order to reduce complexity and calculation time for the full-order H∞-control design, the linear control design model was derived from a 40^{th} order reference wind turbine model by model reduction using modal condensation. For full-order and structured H∞-design, an 18^{th}-order wind turbine model was found to be sufficient, which describes the relevant system dynamics up to approximately 4 Hz, including

- 1^{st} and 2^{nd} tower bending modes fore-aft
- 1^{st} flapwise blade bending collective and whirling modes
- 2^{nd} flapwise blade bending collective mode
- 1^{st} drivetrain mode coupled with edgewise collective blade bending

If the model is further reduced, the interaction between tower and blade bending modes is not properly described.

To be more accurate, however, the resulting transfer functions, step responses and frequency domain performance indicators are computed based on the more detailed linear model of order 40.

4 H∞-Reference Control Design

H∞-control design in this paper is considered in the interpretation of shaping closed loop transfer functions. In the first step, full-order H∞-control design is carried out as a reference, using the *hinfsyn*-function in MATLAB [8].

By means of suitable weighting functions, it is possible to define an upper bound for the magnitude of transfer functions from wind speed to generator speed, denoted as $N_{Om}(j\omega)$, and from wind speed to tower top acceleration $N_{aT}(j\omega)$. The schematic of the control design model combined with weighting functions is shown in Figure 1. The applied types of weighting functions are shown in Figure 9 as inverse bode magnitude plots and will be discussed in the following.

Weighting function for generator speed

The first idea was to put a threshold k_{WOm} on the transfer function $N_{Om}(j\omega)G_{Wind}(j\omega)$, where $G_{Wind}(j\omega)$ is a transfer function describing the wind turbulence spectrum. The type of the transfer function was chosen according to [9] and the parameter adjusted to fit the magnitude to the square root of the considered PSD of wind speed variations. The corresponding weighting function would thus be k_{WOm}*$G_{Wind}(j\omega)$. However, while for this choice there is a tight correlation between weighting function gain factor k_{WOm} and the resulting bandwidth of speed deviations, it was found that this specific weighting function did not result in minimum tower bending fatigue.

Instead, the observation was made that weighting functions crossing the open loop transfer function G_{Om} with zero slope, in general, result in smaller tower bending fatigue. For this reason, an inverse weighting function as shown in Figure 9 (a) was chosen, having proportional behavior around the desired controller bandwidth and derivative behavior at low frequencies, resulting in zero steady-state speed deviation of the closed-loop system. The first corner frequency is denoted as $f_{c,WOm}$. At a frequency of 0.8 Hz, the slope again changes to 20 dB/decade to avoid interaction with higher frequency modes of the wind turbine.

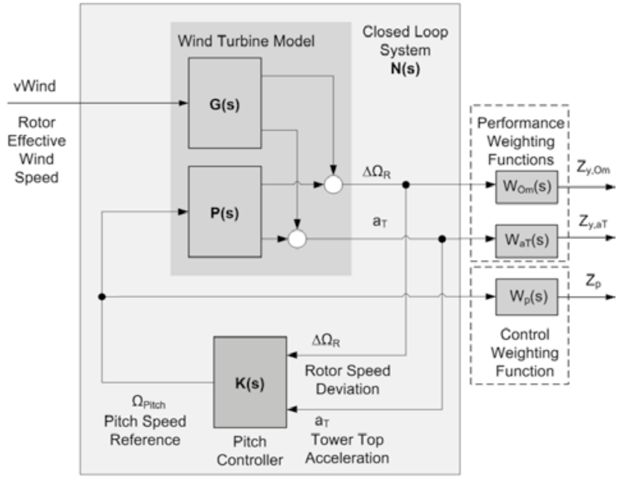

Figure 1: Augmented Model Scheme considered for control design

The free parameters of the inverse weighting function are thus corner frequency $f_{c,WOm}$ and the gain in the horizontal part k_{WOm}.

Considering Figure 8, if tower bending fatigue is compared for different controllers with equal maximum generator speed deviation (Rice-estimate), it turns out that controllers with small values of $f_{c,WOm}$ achieve lower values of tower bending fatigue damage.

As a consequence, a pure D-controller acting on pitch rate reference (or a pure P-controller acting on the pitch angle reference) seems to be most suitable if steady-state rotor speed deviations can be tolerated. If zero steady-state error is required, a desired time compensation constant for the steady state error can be specified. In the following it will be assumed that $f_{c,WOm}$ is set to a defined value corresponding to a comparably large time constant of 10s.

Weighting function for tower top acceleration

For tower top acceleration, a simple constant k_{WaT} is used as inverse weighting function, see Figure 9 (b). The aim is to attenuate the peak in the transfer function from wind speed to tower top acceleration, which corresponds to an active damping of the tower fore-aft-motion.

Weighting function for pitch speed

The aim of this weighting function is to represent the actuator limits in terms of pitch speed and pitch acceleration. Furthermore, it should provide sufficient roll-off to the controller for higher frequencies in order to avoid interaction with high-order structural modes and noise, and to increase robustness against model uncertainties. Additionally, it was observed that proper bandwidth limitation is effective to avoid the calculation of unstable controllers by the *hinfsyn* function.

The inverse of the chosen weighting function is shown in Figure 9 (c). In the low frequency region, the requirement to limit the pitch speed results in

$$W_p(j\omega) = G_{Wind}(j\omega) / \Omega_{Pitch,max} \qquad (1)$$

Here the maximum pitch speed $\Omega_{Pitch,max}$ was assumed to be 5 deg/s.

For higher frequencies, two zeros are placed in order to limit the bandwidth of the pitch controller. The bandwidth of the inverse transfer function was chosen at approximately 2 Hz to roll off above the first flapwise blade bending mode.

Influence of weighting function parameters on tower bending fatigue and maximum speed deviation

In the following, the weighting function for pitch speed is considered as fixed, while the gains k_{WOm} and k_{WaT} of the weighting functions for generator speed and tower acceleration are considered as free parameters for control design. One of the advantages of the control design using parametric weighting functions is the interpretation of these free parameters in terms of upper limits on transfer functions. To illustrate this, a number of H∞-controller calculations have been carried out on a grid in the 2-dimensional parameter space [k_{WOm}, k_{WaT}]. For the resulting controllers, the dependency of maximum speed deviations and tower bending fatigue damage on the maximum magnitude values of $N_{Om}(j\omega)$ and $N_{aT}(j\omega)$ have been investigated.

For that purpose, the parameters k_{WOm} and k_{Wat} have been reduced stepwise beginning from starting values $k_{WOm,0}$, $k_{Wat,0}$. These starting values can be interpreted as absolute upper bounds on the magnitude of the transfer functions $N_{Om}(j\omega)$, $N_{aT}(j\omega)$. For $k_{Wat,0}$ the natural choice is to set the starting value to the maximum of the open-loop transfer function from wind speed to tower top acceleration $G_{aT}(j\omega)$. This means, the controller should not reduce the damping in comparison to the open loop. Regarding the speed control loop, an upper bound for $|N_{Om}|$ can be easily found from the admissible maximum speed deviation, as shown below.

For every H∞-controller computation, the function *hinfsyn* returns a performance value γ which is smaller than 1 if all specifications in terms of weighting functions have been met. For $\gamma > 1$ this is not the case and some closed loop transfer functions exceed the weighting functions. The lower limit of the parameter space is thus given by the combinations [k_{WOm}, k_{WaT}] that result in $\gamma = 1$, forming the border to the parameter region that is not feasible in terms of actuator limits or robustness requirements.

The dependency of the Rice estimate for maximum generator speed deviation on the maximum magnitude of the transfer function $N_{Om}(j\omega)$ is shown in Figure 2. Here, the relation is quite clear: a reduction in max$|N_{Om}|$ - as expected - will result in a proportional reduction of the maximum speed deviation. There is almost no dependency on max$|N_{aT}|$. If the slope of the linear dependency is known, the maximum value of $k_{WOm,0}$ as upper bound on k_{WOm} can thus be directly derived from the maximum admissible speed deviation.

Considering the dependency of tower bending fatigue damage D_{MYT} on the individual maxima of $|N_{Om}(j\omega)|$, $|N_{aT}(j\omega)|$ the relation is shown by the color map in Figure 3. The red dots denote the calculated controllers. For constant max $|N_{Om}|$, a decrease in max$|N_{aT}|$ will result in reduced fatigue damage. On the other hand, for constant max$|N_{aT}|$, also a decreasing max$|N_{Om}|$ will result in reduced fatigue damage. In the considered case, the minimum is located on the lower border of the plane which is determined by the condition $\gamma = 1$, and is thus mainly influenced by the pitch speed weighting function. Since max$|N_{aT}|$ and max$|N_{Om}|$ are not independent of each other, the optimum trade-off has to be found. Especially, for the NREL wind turbine, it is not true in any case that a more aggressive active tower damping (reduced max$|N_{aT}|$) will result in lower tower bending fatigue as it might mean an increase in max $|N_{Om}|$. Also relaxing the speed controller will not in any case result in lower fatigue loads.

For finding the optimum set of weighting function parameters, the most transparent way, as described above, is to apply H∞-control design for all parameter points [k_{WOm}, k_{WaT}] on a sufficiently dense grid in the feasible region.

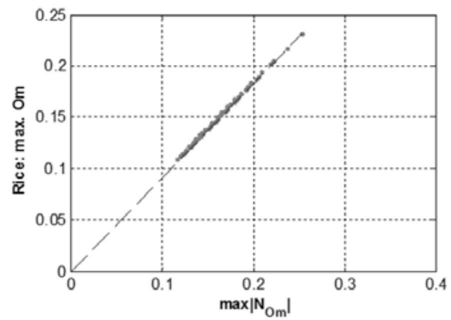

Figure 2: Dependency of Rice estimate for maximum speed deviation on the maximum of the transfer function $N_{Om}(j\omega)$

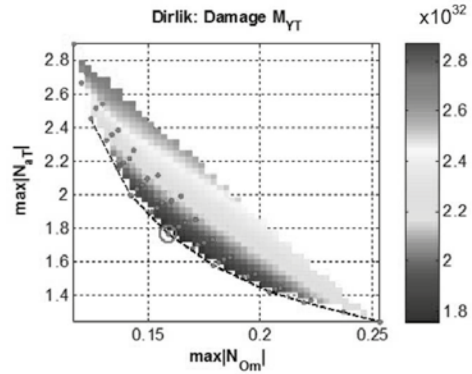

Figure 3: Dependency of tower bending fatigue damage on the maxima of transfer functions $N_{Om}(j\omega)$ and $N_{aT}(j\omega)$, red dots: calculated controllers, black dashed line: border γ=1 in the [max $|N_{Om}|$, max$|N_{aT}|$] plane, red circle: controller with minimum D_{MYT}

The simple algorithm is as follows:

(1) Start with $k_{WOm} = k_{WOm,0}$, $k_{WaT} = k_{WaT,0}$.

(2) Reduce k_{WaT} in sufficiently small steps, until $\gamma > 1$. Calculate the H∞-controller and evaluate D_{MYT} for each point.

(3) Reduce k_{WOm} by one step. If $\gamma > 1$, stop.

(4) Repeat steps (2) and (3) until stop.

(5) Select the controller for the grid point with minimum D_{MYT}.

The whole procedure can be easily automated. The gridding approach is feasible as each controller calculation and evaluation takes only a few seconds. For the grid, in the present case, a logarithmic step size for Δk_{WOm}, Δk_{WaT} of 1dB was found to be reasonable.

Even faster solution is possible by applying a numerical search algorithm, e.g. Nelder-Mead-Simplex. The regions $k_{WOm} > k_{WOm,0}$, $k_{WaT} > k_{WaT,0}$ and $\gamma > 1$ can be excluded from the search area by suitable penalty offsets.

5 Fixed-Structure Control Design

In the second step, structured H∞-control design was carried out. The idea was to use the optimum H∞-controller described in the previous section as a reference and find a fixed-structure controller that is sufficiently close.

For that purpose, the *hinfstruct* function in Matlab was used [8], which applies non-smooth optimization to find the free parameters of a prescribed controller structure. Especially, the same weighting functions for specifying the control design objectives can be used for the H∞-design. Refer to [10] for more detailed information on the method.

As supported by experience, it was found that the speed control objectives can be achieved by a simple PD-controller, where an additional 2nd-order low-pass filter was applied for roll-off in the high frequency region.

For the tower damping controller, it was not possible to identify a transparent transfer function structure, e.g., a bandpass filter. Instead, a state space model with free parameters was assumed. The order of this model was increased, until the *hinfstruct* algorithm provided sufficient agreement with the H∞-reference controller. It was found that a 5th-order state space model is sufficient to meet the design objectives, however, the pitch speed weighting function had to be relaxed somewhat by shifting the roll-off to higher frequencies.

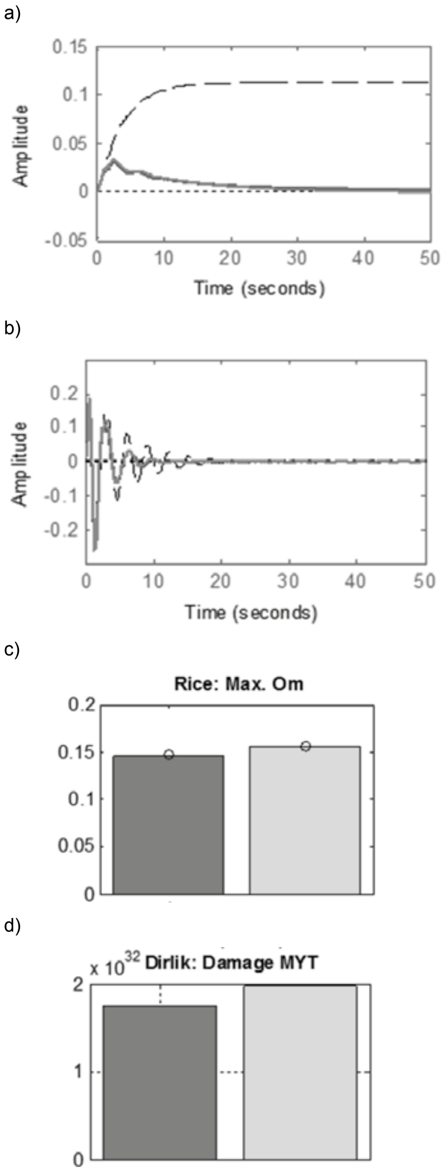

Figure 4: Performance comparison of H∞ (red) and fixed-structure controller (green): (a) step response wind speed to rotor speed; (b) step response wind speed to tower top acceleration fore-aft; (c) max. speed deviation (Rice), (d) tower base fore-aft bending fatigue damage (Dirlik)

The comparison with the H∞-controller is shown in Figure 4 in terms of performance and in Figure 9 regarding the resulting transfer functions. For the fixed-structure controller, it is interesting to see that although the step response and the result of fatigue estimation are very similar, the transfer function of the tower damping part of the calculated *hinfstruct*-controller is quite different from that of the H∞-controller, compare Figure 10.

6 Tower Damping Controller without Tower Acceleration Measurement

The H∞-design methodology was also used to design a controller for speed control and active tower damping based on solely the generator speed input. This is possible, in theory, since the H∞-controller includes a full model of the plant and the tower acceleration is observable in the generator speed.

However, if similar performance specifications were used, as have been for the controllers in the previous sections, the *hinfsyn*-algorithm calculated controllers with unstable poles. These controllers are clearly not practicable for use in real wind turbines. With relaxed speed controller specifications, still it was possible to find stable controllers that provide active tower damping. These controllers, however, proved to be unstable in nonlinear simulations. A possible explanation was found by considering the robust stability for higher frequency unstructured uncertainty, as will be discussed in Section 8.

All controllers considered in this paper are then listed in Table 1.

7 Verification with nonlinear Simulations

For verification of the control design results, nonlinear simulations have been carried out with the IWES in-house wind turbine simulation tool WTsim [11]. This simulation tool is implemented in MATLAB/Simulink. It includes a structural dynamics description comparable to the full order linear model, which is scheduled with operational point, as well as a nonlinear aerodynamic model based on a state-of-the-art BEM implementation.

In order to make the time domain simulations fully comparable with the linear model predictions of the control design, a homogeneous wind field was applied. Furthermore, the tower shadow was disabled. A turbulence intensity of 10% at 18 m/s mean wind speed was assumed, leading to considerable deviations from the steady-state operational point of the wind turbine model. Only a single turbulence seed of 600s duration was simulated, leaving some room for statistical uncertainty in the time domain results.

The comparison of the results for fatigue damage related to the tower base fore-aft bending moment M_{YT} and rotor speed deviations are shown in Figure 5 and Figure 6. It can be concluded that there is good agreement with the linear model predictions, even though only one turbulence seed was simulated. The decrease in tower bending fatigue by means of active tower damping as well as the deviations in rotor speed are well predicted by the linear control design procedure, as compared to the nonlinear simulation results.

Table 1: Overview of considered controllers

Controller	Order	Description
K_{ref}	2	Reference Speed controller with same speed controller settings as K_{struct}
K_{struct}	7	Fixed structure controller, PD speed controller and 5th order tower damping controller
K_{hinf}	22	H∞-controller with generator speed and tower acceleration input
$K_{hinf,Om}$	23	H∞-controller with only generator speed input

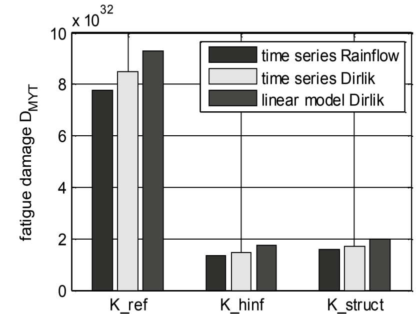

Figure 5: Comparison of tower base bending fatigue D_{MYT} for nonlinear simulation (time series) and linear model prediction.

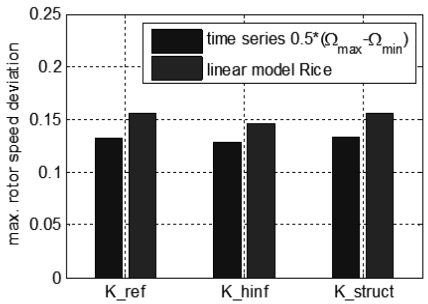

Figure 6: Comparison of maximum rotor speed deviation for nonlinear simulation (time series) and linear model prediction.

8 Robust Stability Analysis

In order to evaluate the robust stability of the four different controllers discussed above, two uncertainty descriptions have been considered:

1. **Multiplicative output uncertainty margin MMO:**

Here, the perturbed plant P_p is described by

$$P_p = (I+\mathrm{diag}(\Delta_{Om}, \Delta_{aT}))P_0 \quad (2)$$

where Δ_{Om}, Δ_{aT} are complex perturbations at the generator speed and tower acceleration outputs of the nominal turbine model P_0.This is a structured uncertainty which would cover for instance uncertainties in the damping of the tower and blade bending modes. Equivalently to the classical gain and phase margin for SISO systems, multivariable output margins MMO can be calculated that provide the value of gain and phase variations which can be tolerated independently on both outputs [12].

2. **Normalized coprime factor uncertainty NCFM:**

This is a fairly general description for unstructured uncertainty, which has proven useful in practical applications [13]. The key statement is that the maximum singular value of the expression

$$M = [K^T\ I]^T (I+P_0K)^{-1} M_L^{-1} \quad (3)$$

is a measure for the unstructured combined input / output uncertainties Δ_M , Δ_N in the perturbed plant

$$P_p = (M_L+\Delta_M)^{-1}(N_L+\Delta_N) \quad (4)$$

that can be tolerated without losing closed-loop stability, where $P_0 = M_L^{-1}N_L$ is a left coprime factorization of the nominal plant P_0.

Overview of robustness measures

For the current control problem, we consider the MMO as a useful measure of uncertainty for frequencies up to the first flapwise blade-bending eigen-frequency, whereas the NCFM is additionally evaluated as a measure for tolerated unstructured uncertainty. NCFM is considered only for frequencies larger than the first tower eigen-frequency.

Table 2 shows an overview of MMO multivariable output gain and phase margins. As can be seen, all considered controllers show very similar results regarding the MMO. This is somewhat unexpected, especially for K_{ref} which includes no active tower damping. It was observed, however, that the MMO is mainly influenced by the speed control loop and the minimum value occurs just below the first tower bending eigen frequency.

On the other hand, the robustness regarding unstructured uncertainty as described by the NCF is quite different, as can be seen in Table 3 and Figure 7. Especially the H∞-controller without acceleration measurement provides poor robustness to unstructured plant variation in the frequency region close to the first flapwise blade bending mode.

Future research is required for improving the understanding of the stability measures and considering also robust performance aspects.

Table 2: Comparison on multivariable output gain and phase margins for the considered controllers

	MMO Gain tol [dB]	MMO Phase tol [°]	MMO Freq [Hz]
K_{ref}	7.1	42	0.23
K_{struct}	7.0	41	0.22
K_{hinf}	6.7	40	0.25
$K_{hinf,Om}$	6.6	40	0.20

Table 3: Comparison of minimum NCF gain (for frequencies > 0.3 Hz) and the corresponding frequencies for the considered controllers

	NCF Margin	NCF Freq [Hz]
K_{ref}	0.074	1.68
K_{struct}	0.059	9.09
K_{hinf}	0.0047	1.24
$K_{hinf,Om}$	0.0014	1.02

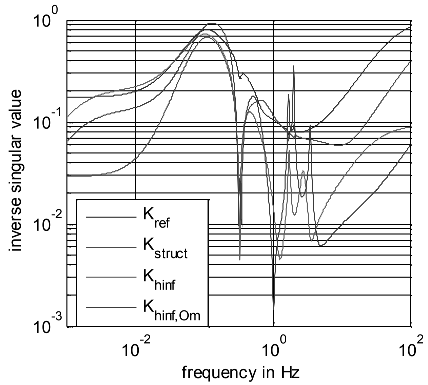

Figure 7: Inverse max. singular value of M in Eq. (3) for the different controllers as a measure for the NCF margin at different frequencies

9 Summary and Conclusions

A pragmatic multivariable approach for parallel design of rotor speed control and active tower damping is proposed. The control design is carried out in the frequency domain and provides a high level of transparency to the control engineer. In detail, the following conclusions can be drawn:

- H∞-criteria can be conveniently used to formulate relevant pitch control objectives in the frequency domain. If speed controllers with sufficiently large compensation time constants for the steady state error are applied, the maximum magnitude of the transfer function from wind speed to generator speed is directly related to the maximum values of speed deviations for a given turbulence spectrum.
- Unfortunately, such a direct link between weighting function and time domain control objective was not found for the tower bending fatigue damage. Here, the minimum results from a trade- off between tight speed control and active tower damping, which can be found, e.g., by applying a numerical search algorithm on weighting function gain parameters. In comparison to direct controller parameter optimization, however, the H∞-approach allows to restrict the search area by considering upper bounds on the closed-loop transfer functions.
- If both generator speed and tower top acceleration feedback are used, structured control design can achieve similar results as full order H∞-controllers. The prescribed controller structure, however, is more transparent and easier to handle in a practical arrangement including gain scheduling and handling of actuator saturations. It has also been shown to provide more robustness to unstructured uncertainty in the higher frequency region.
- For the speed controller, D-control (acting on pitch speed reference) seems to be most effective to minimize tower bending fatigue while restricting speed deviations to a prescribed threshold.
- For the full order H∞-control design, in principle, both speed control and active tower damping would be possible using only generator speed feedback. For robustness reasons, however, omission of the tower top acceleration feedback is not recommended.

10 Future Work

In this work, only one full-load operational point of the turbine was considered. If required, however, the approach can be easily extended to a number of operating points. Especially for the fixed order control design, gain-scheduling between the different controllers is then quite straightforward because of the low order and the transparency of the prescribed controller structure.

One of the open points is the inclusion of unsymmetrical effects like spatial turbulence and 3p harmonic excitation into the fatigue load prediction in the frequency domain. These effects have been omitted in this study but will lead to deviations.

Acknowledgement

The presented research was partly carried out in the joint research project „ELBA – control systems for the reduction of extreme loads at large-scale wind turbines" (0325731A) funded by the German Federal Ministry for Economic Affairs and Energy.

Gefördert durch:

Bundesministerium für Wirtschaft und Energie

aufgrund eines Beschlusses des Deutschen Bundestages

References

[1] M. Geyler and P. Caselitz: *Robust multivariable pitch control design for load reduction on large wind turbines*. Journal of Solar Energy Engineering, 130(3):031014, 2008.

[2] W. E. Leithead, S. Dominguez: *Analysis of tower/blade interaction in the cancellation of the tower fore-aft mode via control*. Proc. EWEC 2004, London, UK.

[3] J. Jonkman, S. Butterfield, W. Musial, and G. Scott: *Definition of a 5 MW Reference Wind Turbine for Offshore System Development*, National Renewable Energy Laboratory, Technical Report NREL/TP-500-38060, February 2009

[4] A. A. Ozdemir: *Preview Control for Wind Turbines.*, dissertation submitted to the faculty of the graduate school of the university of Minnesota, August 2013

[5] P. Ragan, L. Manuel: *Comparing estimates of wind turbine fatigue loads using time-domain and spectral methods.* Wind Engineering, Vol. 31(2), pp. 83— 99, 2007.

[6] T. Dirlik: *Application of computers in fatigue analysis,* PhD-Thesis submitted to the department of engineering, University of Warwick Coventry, England, 1985.

[7] S. O. Rice, *Mathematical Analysis of Random Noise: Part III*, Bell Systems Technical Journal, vol. 1945, no. 24, pp. 46–156. 1945

[8] MATLAB, robust control system toolbox, http://de.mathworks.com/products/robust/

[9] *Von Karman Wind Turbulence Model*, MATLAB documentation, aerospace blockset: http://de.mathworks.com/help/aeroblks/vonkarmanwindturbulencemodelcontinuous.html

[10] P. Gahinet and P. Apkarian: *Decentralized and Fixed-Structure H∞ Contol in MATLAB*, 50th IEEE Conference on Decision and Control and European Control Conference (CDC-ECC), 2011

[11] B. Jasniewicz, M. Geyler: *Wind turbine modelling and identification for control system applications*, in: Scientific proceedings of the EWEA 2011, Bruxelles, Belgium, pp. 280-283.

[12] Blight, J.D., R.L. Dailey, and D. Gangsass, *Practical control law design for aircraft using multivariable techniques*, International Journal of Control, Vol. 59, No. 1, 1994, pp. 93-137

[13] D. McFarlane, K.Glover, *Robust Controller Design using Normalized Coprime Factor Plant Descriptions*, Vol 138 of Lecture Notes in Control and Information Sciences, Springer-Verlag, Berlin, 1990.

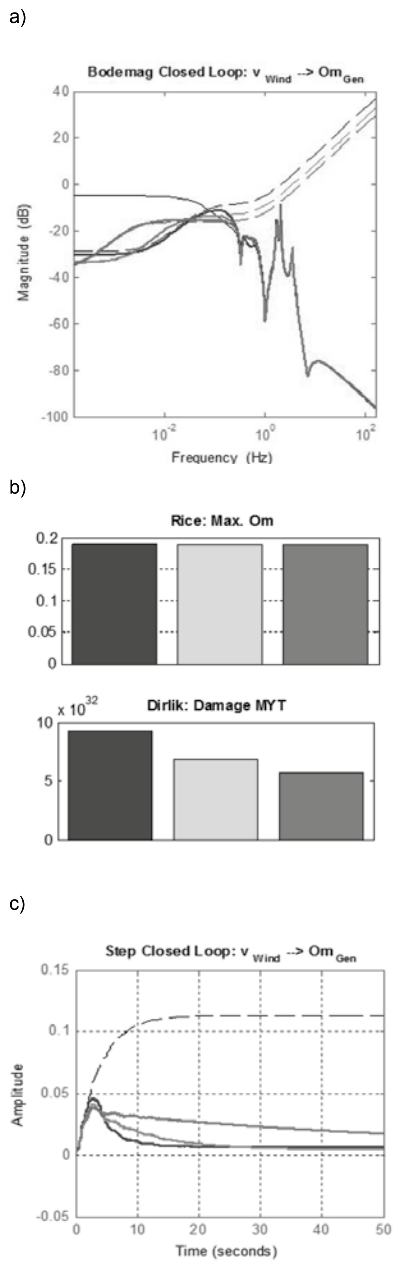

Figure 8: Comparison of three different H∞-controllers with the same maximum speed deviation: (a) Bode Magnitude Plot from wind speed to rotor speed, black line: open loop; (b) estimates of maximum rotor speed deviation (Rice) and tower bottom bending fatigue damage (Dirlik); (c) step responses from wind speed to rotor speed; black dashed line: open loop

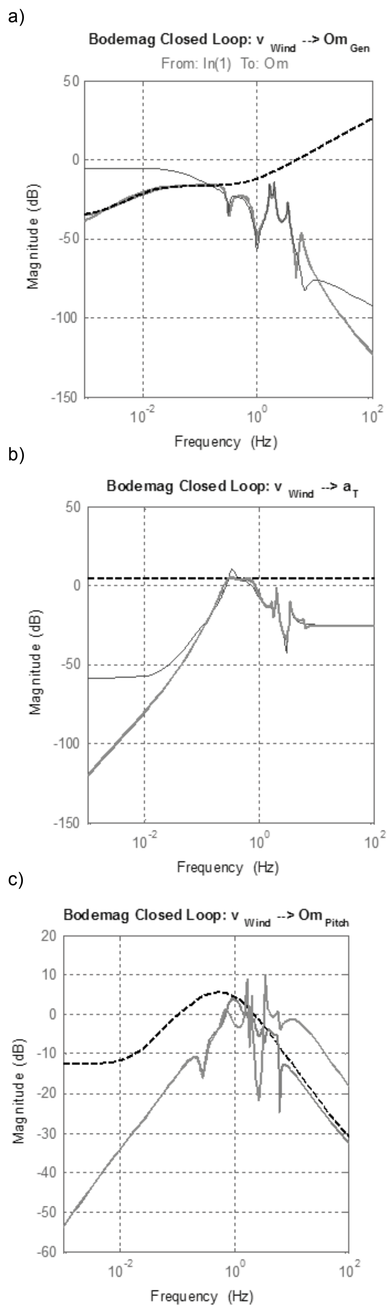

Figure 9:(left) Bode Magnitude Plots of open loop and closed loop, comparison of H∞- and fixed-structure controller:

(a) from wind speed to generator speed;

(b) from wind speed to tower top acceleration fore-aft;

(c) from wind speed to pitch speed

blue: open loop, black dashed: inverse weighting functions, red: closed loop H∞-controller, green: closed loop fixed-structure controller

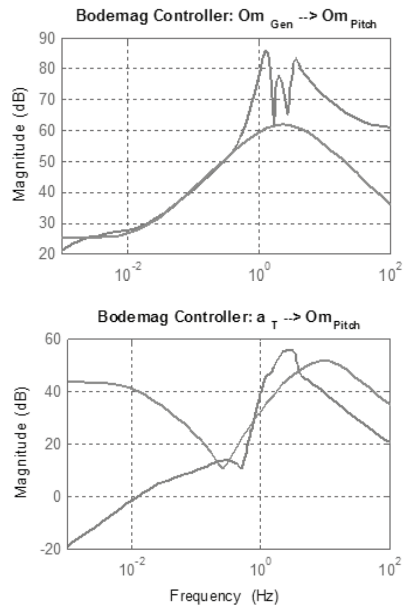

Figure 10: Bode Magnitude Plots of H∞ (red) and fixed-structure controller (green); speed controller (top) and active tower damping controller (bottom).

New Bearingless PM Machine with Magnet and Core Modules for Large Direct-Drive Wind Turbines

Deok-je Bang[1,*], Wook Hwang[1], Ji-Won Kim[1], Pil-Wan Han[1], Chan-Nyeong Heo[2], Seon-Hwan Hwang[2]

[1]Electric Motor Research Center, Korea Electrotechnology Research Institute
[2]Department of Electrical Engineering, Kyungnam University

[*]E-mail: djbang@keri.re.kr / deokje.bang@gmail.com

Abstract:

The aim of this paper is to verify both the magnetic circuit analysis model of a permanent magnet (PM) machine with magnet and iron core modules and the control algorithm of a bearingless PM machine with the modules and double-sided air-gap configuration for large direct-drive wind turbines. The proposed magnet and core modules and bearingless PM machine configurations enable to facilitate manufacture and maintenance and to reduce bearing failures. The magnetic circuit analysis model is verified by both the measurements of the flux density and the induced voltage of a downscaled machine in a no-load case, and the three-dimensional analyses (3D FEA) to identify the torque in a load case. The main windings of the machine are used to simultaneously control both the torque and the bearing force in the air-gap between the rotor and the stator. The torque and the air-gap length of the machine are controlled by the control q-axis and d-axis currents, respectively. In order to verify the control algorithm, the downscaled PM machine is used and the new bearingless machine control concept is achieved experimentally in generator mode.

Keywords: Bearingless, Module, PM, Generator, Direct-drive

1. Introduction

In wind turbines, bearing failures have been a continuing problem and a significant proportion of all failures. Bearing-related downtime is among the highest of all components of wind turbines. [1] The location of wind turbines is moving offshore because of higher wind speeds and less turbulence, and limited space to install the turbines on land and onshore. However, to access offshore is difficult thus the wind turbines with high reliability and availability are required offshore. Direct-drive wind generators have been discussed as the generator type with higher energy yield than geared generators. However, direct-drive generators require large diameter, which results in large mass and high cost, in order to get high torque rating compared to geared generators. To construct direct-drive generators with large diameter as a single module (one-body structure) is disadvantageous in terms of manufacture and maintenance. It is thus necessary to significantly reduce both bearing failures and mass, and to facilitate manufacture of large direct-drive wind generators.

In order to reduce bearing loads and bearing wear that cause bearing failures, the reduction of an unbalanced magnetic pull (UMP) for the ocean generator has been discussed in [2]. To reduce bearing failures of large wind generators, the use of magnetic bearings, bearingless drive or hydraulic bearings could be an alternative instead of the use of mechanical bearings [3][4]. In order to reduce the mass of large direct-drive wind generators, different generators such as an ironless permanent magnet (PM) generator with a spoke structure, a PM generator with the bearings close to the air gap, and a high temperature superconducting generator (HTSG) [5][6][7]. In order to facilitate manufacture and maintenance of large direct-drive wind generators, it is required that a modular construction easily produced, assembled, transported and installed [3].

In previous researches by the author [8][9], a new generator concept, ring-shaped direct-drive bearingless PM wind generator with a buoyant rotor as shown in Figure 1, has been proposed as a solution to reduce the structural mass and bearing failures. The total mass of the proposed generator for 10 MW direct-drive wind turbines has been estimated at 235 tonnes rated at 8.6 rpm, which is comparable with the mass of HTSG, 230 tonnes rated at 8.6 rpm [9] and 225 tonnes rated at 8.1 rpm [10].

In this paper, it is focused on verifying both the magnetic circuit analysis model and the control algorithm of the proposed bearingless PM machine with magnet and core modules. This paper begins with a description of the new ring-shaped direct-drive bearingless PM wind generator with a buoyant rotor and double-sided air-gaps. Second, the configuration and feature of magnet and iron core modules of the proposed machine is described, and the magnetic circuit analysis model of the proposed machine is developed. Third, the proposed control algorithm for the bearingless PM generator is described. Next, the magnetic circuit analysis model is verified by the three-dimensional finite element analyses (3D FEA) and the experiments of a downscaled machine. The control algorithm to simultaneously control both the torque and the bearing force of the machine with double-sided air-gaps is discussed and implemented by the experiments in generator mode.

2. New ring-shaped direct-drive bearingless PM generator with a buoyant rotor and double-sided air-gaps

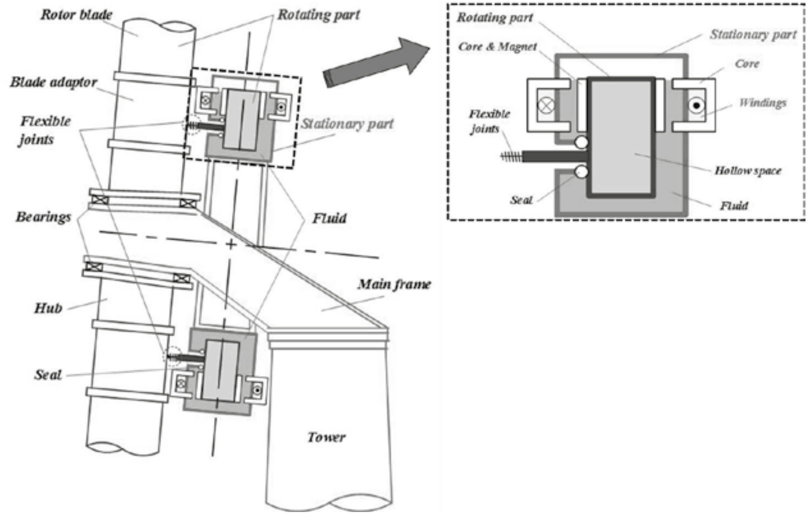

Figure 1: Sketch of new ring-shaped bearingless PM generator with a buoyant rotor and double-sided air-gaps

Conventional direct-drive generators have disadvantages such as large mass and difficulties in manufacture, assembly, transport, installation and repair. These disadvantages raise their cost. When a component of a conventional generator fails, the generator systems cease operation. The failure of large scale generator systems is more serious than the failure of small scale generator systems. In order to overcome these disadvantages of large direct-drive generators, the following concepts have been discussed by the author in previous researches.

- Bearingless generator that would enable a significant reduction of the downtime related with bearing failures
- A ring-shaped generator without a shaft and without torque arms
- Buoyant rotor structure to easily support a heavy structure, to reduce the structural mass and to provide flexibility in supporting a heavy structure
- Modular structure of rotor and stator which is easy to assemble, transport, install and repair
- Multi-sets of three-phases generators to continue electricity production in case of failure in a few components

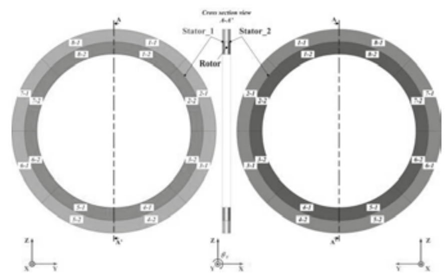

Figure 2: Conceptual construction of ring-shaped generator with multi-sets of 3-phase double-sided configuration

The construction of the buoyant rotating part and the stationary part of the new ring-shaped direct-drive bearingless generator is represented in Figure 1. In order to make the rotor afloat, we could remind the principle of buoyancy:

- A body wholly or partly immersed in a fluid is buoyed up by a buoyant force equal to the mass of the fluid displaced by the body.

This principle does not mean we need more fluid than the mass of the body in order to make the body afloat. Thus it is possible to make the rotor afloat with less mass of fluid than the mass of the rotor. For more

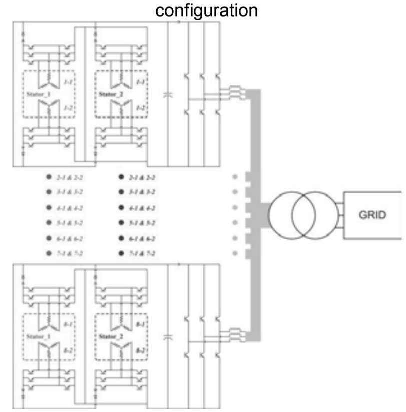

Figure 3: Conceptual construction of power converters of ring-shaped generator with multi-sets

information about the new generator, please refer to the previous researches [8][9]. Figure 2 depicts the conceptual construction of a ring-shaped generator with multi-sets of 3-pahse double-sided configurations. Multi-sets of the generator's converter system are represented in Figure 3, which shows that each stator set has its own converter set. The number of the rotor and stator sets can be changed depending on the applications.

3. New PM machine with magnet and iron core modules

3.1 Machine configuration

This section describes on a new configuration of PM machine with magnet and core modules. In order to fix the magnets on the iron cores in the conventional configuration, bonding is widely used. However, when bonding magnets to affix iron cores, the magnets can detach as shown in Figure 4. In order to avoid the detachment of magnets and to facilitate manufacturing of the rotor with magnets and iron cores, a new configuration of magnets and iron cores is proposed as shown in Figure 5. The parts with grey color are non-ferromagnetic parts to assemble magnets and iron cores. The configuration in Figure 4(a) is modified to the configuration segmented as Figure 5(a). The

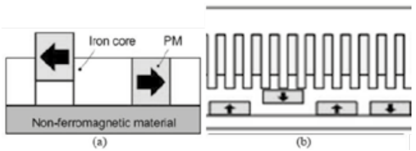

Figure 4: Bonded magnets to affix iron cores

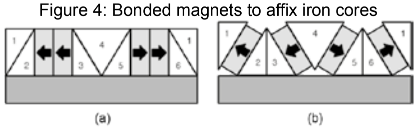

Figure 5: New magnet and core modules

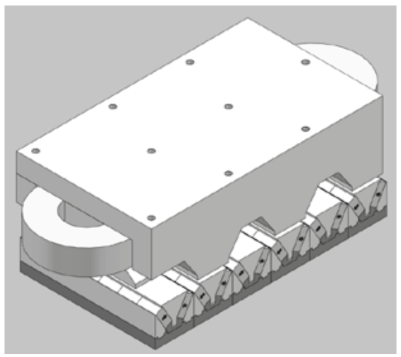

Figure 6: 3D sketch of PM machine with claw poles and new magnet and core modules

magnet and iron core segment are rearranged as in Figure 5(b). This new configuration allows for an increase in the volume of magnets while maintain the pole pitch length without increasing the volume of the iron cores. The configuration in Figure 5(b) makes easier mass-production and can be used for both the longitudinal flux PM machine and the transverse flux PM machine. Figure 6 depicts a sketch of the proposed flux-concentrating PM machine with the configuration of single-sided, single-winding, racetrack-shaped windings, claw poles, multiple-modules of magnets and cores and multiple-slots per phase. The yellow racetrack-shaped structure represents the copper winding. The sky blue hexahedra with black arrows represent the PMs.

3.2 Magnetic circuit modelling

Electromagnetic reluctances in every pole pair are the same and repetitive, and the electromagnetic reluctances in a pole are symmetrical with the reluctances in the next pole. Therefore, the equivalent circuit of electromagnetic reluctances in one pole is considered for the magnetic circuit analysis model.

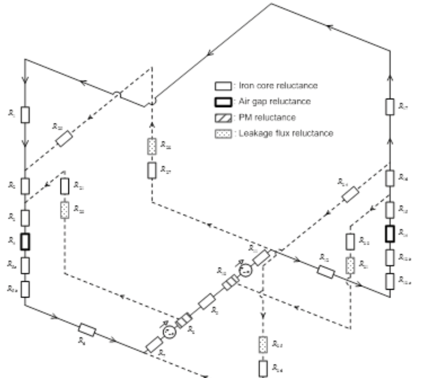

Figure 7: Equivalent circuit of magnetic reluctances

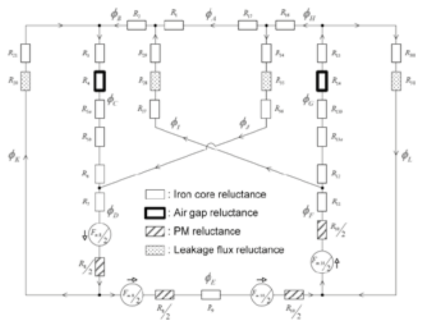

Figure 8: Modified equivalent circuit of magnetic reluctances of the proposed PM generator

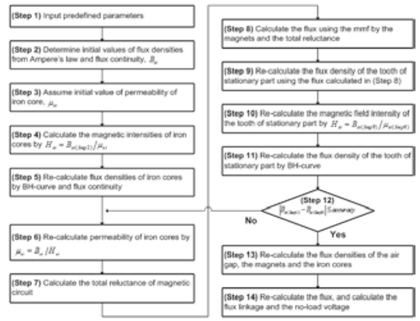

Figure 9: Process to determine the flux density, the flux, the flux linkage and the no-load induced voltage of the magnetic circuit of the proposed PM generator

Figure 7 illustrates the equivalent circuits of the reluctance model of the PM generator. The white rectangles represent iron core reluctances, and the white rectangles with bold lines represent air gap reluctances. The blue rectangles hatched represent PM reluctances and the red rectangles dotted represent leakage flux reluctances. In order to formulate the flux equations of the equivalent circuit in Figure 7, the equivalent circuit is modified as Figure 8. The procedure to determine the flux density, the flux, the flux linkage and the no-load induced voltage of a magnetic circuit including nonlinear characteristics is made as the following steps represented in Figure 9.

4. New bearingless machine concept

4.1 Conventional bearingless machine concept

As discussed in previous research, a significant feature of the bearingless machine compared to the electric machine with the magnetic bearing is that the bearing winding is integrated into the electric machine. Conventional bearingless machine drives need to control both the torque with torque winding and the

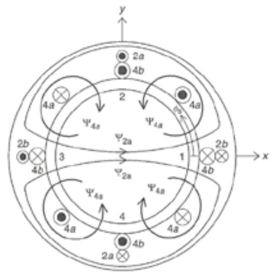

Figure 10: 4-pole and 2-pole winding arrangements of a primitive bearingless drive [Chiba 2005]

bearing force with bearing winding. In order to achieve extensive decoupling between the generators of the torque and the bearing forces, those windings are designed with different numbers of poles as shown in Figure 10. In the case of large direct-drive machines, the mass of the rotating part is large. Thus it is expected that the power consumption of producing the bearing force, for supporting the rotating part against the gravity, will be large for large direct-drive wind generators.

4.2 Proposed bearingless machine concept

The proposed ring-shaped bearingless machine discussed in this paper does not need the power consumption to support the rotating part against the gravity because the part is supported by the buoyancy force. Additionally the new bearingless drive concept needs only one winding to produce both the torque and the bearing force to control the air-gap length.

In this paper, an algorithm of phase angle shift is applied for the proposed bearingless PM machine in order to control the air-gap length by controlling the normal forces between the rotor and stator. Using the results of the 3D-FEA, the variation of those forces can be represented as a function of phase shift angle, rotor position, air-gap length and magneto-motive force by currents. The normal force at 6mm air-gap length could

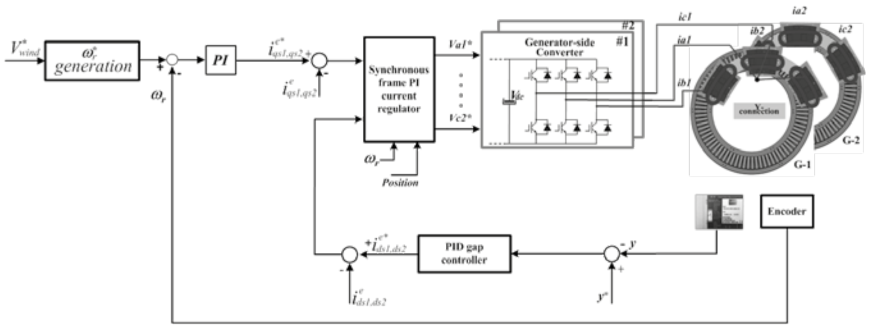

Figure 11: Control block diagram of the bearingless PM machine

be controlled to be larger than the force at 2mm air-gap length by shifting the phase angles and by changing the magneto-motive forces. Therefore, it is possible to achieve the air-gap controls of both sides to be equal when the air-gap 1 is not equal with air-gap 2. The control block diagram for the air-gap control and the rotor position control is represented as Figure 11. The air-gap length reference is produced by the proportional-integral-derivative (PID) controllers. After operating the gap controller, the currents to control the air-gap length are generated by shifting the phase angles. These signals are added to the outputs of the PI speed controller. The phase currents to control the normal forces and the air-gap length can be written as (1) and (2) as a function of the phase shift angle θ_{shift}.

$$I^*_{abc\_left} = I^*_{mag} \cdot \sin\left(\theta + n \cdot \frac{2\pi}{3} + \theta_{shift}\right) \quad (1)$$

$$I^*_{abc\_right} = -I^*_{mag} \cdot \sin\left(\theta + n \cdot \frac{2\pi}{3} - \theta_{shift}\right) \quad (2)$$

Where, n is 0 for A-phase, 1 for B-phase and -1 for C-phase.

5. Verification of the proposed bearingless PM machine

5.1 Magnetic circuit analysis model

Figure 12 depicts the tangential and axial views of the PM machine with dimensional parameters. The electromagnetic dimensions and parameters of the machine are given in Table 1. In order to identify the thrust force and the normal force of the machine in terms of air-gap length, current and rotor position, the 3D-FEA is done. The model for the 3D-FEA model is depicted as Figure 13. The 3D-FEA results of the thrust force and the normal force as a function of current and rotor position are represented for different air-gap length, 2mm and 6mm, in Figure 14 and Figure 15, respectively.

In order to verify the analysis model in no-load case, the air gap flux density and the no-load induced

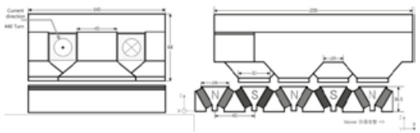

Figure 12: Tangential and axial views of the generator with dimensional parameters

Air gap length (mm)	4
Pole pitch (mm)	40
Magnet length (mm)	8
Pole width (mm)	32
Height of primary part (mm)	68
Width of winding window (mm)	30
Height of secondary part (mm)	36.5
Axial length of pole (mm)	40

Table 1: Electromagnetic dimensions and parameters

voltage calculated by the model are compared with those obtained by the measurements. The peak flux density in the air gap of 4 mm length is calculated to 0.93 T, and the flux density measured is 0.924 T. In the analysis model at the same air gap length, 4 mm and the speed of 0.25 m/s, the peak no-load induced voltage per a phase is calculated to 18.96 V, and the voltage measured is 18.73 V. In order to verify the analysis model in load case, the thrust force per a

- **No-load case**

	Calculation	Measurement	Remark
Peak flux density in the air gap	0.93 [T]	0.924 [T]	at 4 [mm] air gap
Peak no-load induced voltage per two pole pairs	18.96 [V]	18.73 [V]	at 4 [mm] air gap & 0.25 [m/s] speed

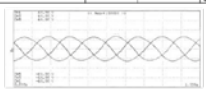

- **Load case**

	Calculation	3D FEA	Remark
Force per two pole pairs	1057 [N]	903 [N]	at 4 [mm] air gap & 6000 [AT]

$$F = E\frac{I_{mm}}{v_g} = \left(\frac{\pi b_{sr}}{\sqrt{2}\tau_p}\right) p N_{coil} B_{p,mm} l_s v_s \frac{I_{mm}}{v_g} = \left(\frac{\pi b_{sr}}{\sqrt{2}\tau_p}\right) p N_{coil} B_{p,mm} l_s I_{mm}$$

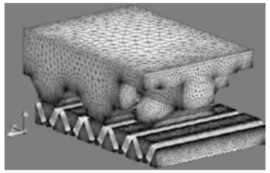

Figure 13: Mesh model of the proposed PM machine for 3D FEA

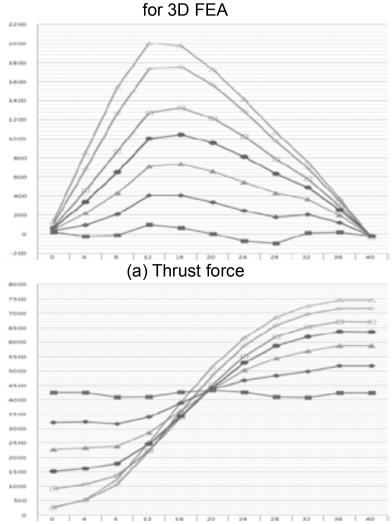

(a) Thrust force

(b) Normal force

Figure 14: Thrust force and normal force at 2mm air-gap length by 3D-FEA

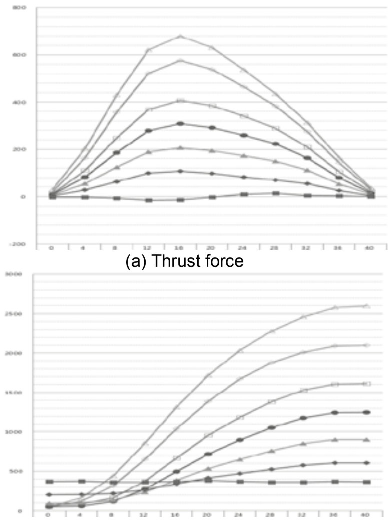

(a) Thrust force

(b) Normal force

Figure 15: Thrust force and normal force at 6mm air-gap length by 3D-FEA

phase (two pole pairs) is calculated to 1057 N, and the force obtained by the 3D-FEA is 903 N. Building the downscaled PM machine to the rotating type, the mean diameter of the rotor is 1.16 m and the designed air gap length is 4 mm. The stators consist of 2-sides of 3-sets (phases). The designed torque and power at 4 mm air gap length and 1 m/s (16.4 rpm) speed are 3.14 kNm and 5.4 kW, respectively.

5.2 Control of proposed bearingless machine

In order to verify the concept of the proposed bearingless PM machine, the experimental setup can be constructed as shown in Figure 16. The mean diameter of the machine is 1.16m. The machine consists of multiple-modules of the stator and the rotor, and a hinge with roller mechanism is set on between the bottom of rotor and the stationary part. As the first step to verify the bearingless machine control concept, the air gap lengths are set to 9 mm for both sides. Figure 17 depicts the experimental set up built with two inverters for the generators located in upper side and the driving motors located in lower side, instruments and control PC. In the experiments the speed of the rotor is 16.4 rpm (1 m/s). The q- and d-axis currents and the air gap length are controlled and measured in both no-load case and load case. Figure 18 represents that the air gap length is controlled without consuming the d-axis current to control the flux and the bearing force in the both cases. Thus it has been achieved to verify the proposed bearingless machine control concept in generator mode as the first step. In further researches, the authors will continue to verify the bearingless machine with increasing power rating.

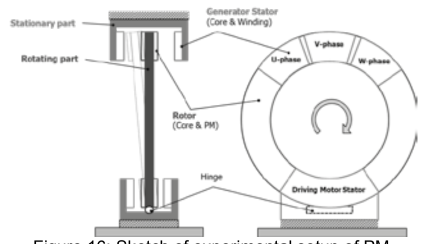

Figure 16: Sketch of experimental setup of PM generator with multiple-modules

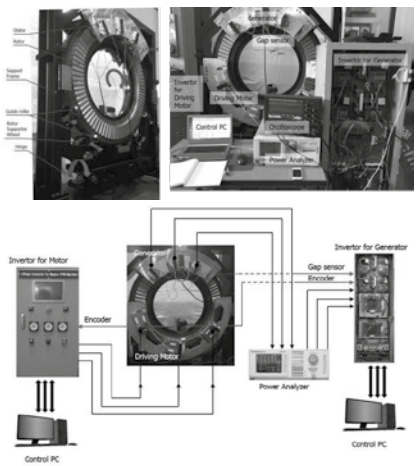

Figure 17: Experimental setup built

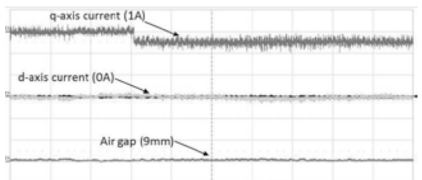

Figure 18: Experimental results of q-axis and d-axis currents, and air-gap length in the control at 1m/s speed

6. Conclusions

This paper discussed on a new modular construction of magnets and iron cores that enables to facilitate manufacture and maintenance of PM generators for large direct-drive wind turbines. A new concept of the bearingless PM machine with the modular construction and the double-sided air-gaps has been discussed to reduce bearing failures for large direct-drive wind generators. The magnetic circuit analysis model of the machine with the modular construction has been verified by the experiment and 3D FEA. The control algorithm of the double-sided bearingless PM machine with the modular construction has been verified experimentally in the generator mode. The maximum displacement of the air gap length in generator mode was 0.4 mm which is about 4% of the air gap length, 9mm in operating at 16.4 rpm (1 m/s) speed without consuming the d-axis current to control the bearing forces. In further researches, the proposed bearingless generator with a buoyant rotor will be designed to apply for the floating vertical axis wind turbines (VAWT). In this application, the sealing mechanism may not be required.

References

[1] J. Ribrant and L.M. Bertling, "Survey of Failures in Wind Power Systems with Focus on Swedish Wind Power Plants during 1997-2005", IEEE Transactions on Energy Conversion, Vol. 22, pp.167-173, 2007.

[2] J.K.H. Shek, D.G. Dorrell, M. Hsieh, D.E. Macpherson and M.A. Mueller, "Reducing bearing wear in induction generators for wave and tidal current energy devices", IET Conference on Renewable Power Generation, pp.1-6, 2011.

[3] D. Bang, H. Polinder, G. Shrestha and J.A. Ferreira, "Promising direct-drive generator system for large wind turbines", EPE Journal, Vol. 13, pp.7-13, September 2008.

[4] G. Shrestha, H. Polinder, D. Bang and J.A. Ferreira, "Structural flexibility: A solution for weight reduction of large direct-drive wind turbine generators", IEEE Trans. Energy Conversion, Vol. , Issue:99, pp.1-9, 2010.

[5] E. Spooner, P. Gordon, J.R. Bumby and C.D. French, "Lightweight, ironless-stator, PM generators for direct-drive wind turbines" , IEE Proc.-Electr. Power Appl., Vol. 152, No. 1, pp. 17-26, January 2005.

[6] S. Engström and S. Lindgren, "Design of NewGen direct-drive generator for demonstration in a 3.5 MW wind turbine", EWEC (European Wind Energy Conference & Exhibition, Milan, Italy, May 7-10 2007.

[7] G. Snitchler, B. Gamble, C. King and P. Winn, "10MW class superconductor wind turbine generators", IEEE Trans. on Applied Superconductivity, Vol. 21, No. 3, June 2011, pp. 1089-1092.

[8] D. Bang, H. Polinder, J.A. Ferreira and S.S. Hong, "Structural mass minimization of large direct-drive wind generators using a buoyant rotor structure", in Proc. 2010 IEEE Energy Conversion Congress and Exposition, Atlanta, Georgia, September 12-16 2010.

[9] D. Bang, G.W. Jang, S.H. Hwang, P.W. Han, J.W. Kim, D.H. Koo, H. Polinder and J.A. Ferreira, "New bearingless generator with buoyant rotor for large direct-drive wind turbines", in Proc. EWEA 2014, Barcelona, Spain, March 10-13 2014.

[10] A. Pujana, J.M. Merino, G. Sarmiento, S. Sanz, I. Marino and J.L. Vilate, "Design, optimization and integration of a direct drive superconducting generator for large wind turbines", in Proc. EWEA 2014, Barcelona, Spain, March 10-13 2014.

Potential of MgB_2 superconductors in direct drive generators for wind turbines

Asger B. Abrahamsen[1], Dong Liu[2], Niklas Magnusson[3] and Henk Polinder[2].

[1]DTU Wind Energy, Technical University of Denmark, Denmark.

[2]Electrical Sustainable Energy Department, Delft University of Technology, The Netherlands.

[3]SINTEF Energy Research, Norway

Abstract

Topologies of superconducting direct drive wind turbine generators are based on a combination of superconducting wires wound into field coils, copper armature windings, steel laminates to shape the magnetic flux density and finally structural materials as support. But what is the most optimal topology for superconducting wind turbine generators?

This question is investigated by assuming some unit cost of the different materials and then minimizing the cost of the active materials of a 10 MW and 9.65 rpm direct drive wind turbine generator intended to be mounted in front of the INNWIND.EU King-Pin concept nacelle. A series of topologies are investigate by adding more iron components to the generator, such as rotor back iron, field winding pole, magnetic teeth and armature back iron. This method is used to investigate 6 topologies and to determine the optimal cost of the different topologies by using the current cost of 4 €/m for the MgB_2 wire from Columbus Superconductors and also a possible future cost of 1 €/m if a superconducting offshore wind power capacity of 10 GW has been introduced by 2030 as suggested in a roadmap. The obtained topologies are compared to what is expected from a permanent magnet direct drive generators and the further development directions are discussed.

Finally an experimental INNWIND.EU demonstration showing that the current commercial MgB_2 wires can be wound into functional field coils for wind turbine generators is discussed.

Keywords

Superconducting generator, direct drive, wind turbine, cost optimization, MgB_2, INNWIND.EU, MgB_2 coil demonstration

1. Introduction

Superconducting electrical machines have been investigated since the successful manufacturing of the NbTi wire, which is made of many filaments of the superconducting NbTi metal alloy enclosed in a copper matrix. The NbTi wire has developed gradually since the 1960s and a series of machines were investigated until the 1980s [1], but a serious barrier for commercialization was the need for liquid helium for cooling the machines to 4 K (-269 ^{o}C) and the challenging thermal insulation. Today NbTi is used heavily in about 20000 Magnetic Resonance Imaging (MRI) Scanners in hospitals around the world [2]. The critical temperature, T_c, is 9.8 K, the critical current density, J_c, is approximately 2000 A/mm^2 at 4.2 K & 10 T and finally the unit cost is about 0.4 €/m [3].

In 1986 a new class of ceramic superconductors was discovered and since these superconductors become superconducting at a much higher temperature they are called high-temperature superconductors (HTSs). They can be cooled with liquid nitrogen, boiling at 77 K (-196 ^{o}C) and this relatively high temperature was believed to facilitate commercialization of superconducting machines for power generation and ship propulsion[4]. The higher operation temperature also allowed for the use of closed-cycle helium based cooling machines, which only need electricity and not a supply of a cryogenic liquid such as liquid helium or liquid nitrogen. The processing of the HTS wires is however expensive and the unit cost is in the order of 30 €/m [3] with current densities of 200 A/mm^2 at 20-30 K and 1-3 T [5].

In 2001 it was discovered that the simple metal alloy MgB_2 became superconducting at a temperature of 39 K (-234 ^{o}C). This temperature is high enough to still use the close-cycle cooling machines and MgB_2 therefore holds the potential to be a cheaper alternative than the high temperature superconductors for many superconducting applications[3]. MgB_2 provides a compromise between a reasonable super-conducting current density J_e ~ 100-200 A/mm^2 in 1-2 Tesla and an operation temperature in the range 15-25 K [3]. MgB_2 wires have been developed and are offered by only two manufacturers today: Columbus Superconductors SpA [6] and Hyper Tech Research Inc [7]. The unit cost of the MgB_2 is shown in table 1.

2 Superconducting wind turbine generators

The application as a compact high torque and slow speed generator for direct drive wind turbines was identified as a shift from ship propulsion and into the wind sector by American Superconductors (AMSC). The 10 MW SeaTitan turbine from AMSC is based on their high temperature superconducting tape [8]. Several other companies and research institutions have also proposed wind turbine generators based on the HTS[9,10] as well as both NbTi[11,12] and MgB_2 wires[13].

There are basically two philosophies behind the design of superconducting generators:

1) The high current density of the superconducting wire is used to make field coils with no iron cores that produced a magnetic flux density, which is exceeding the saturation flux density of the usual magnetic steel.

2) The high current density of the superconductor is used to magnetize conventional magnetic steel providing as closed a magnetic flux path as possible of the generator.

A consequence of option 1) is that more superconducting wire is needed to provide the amp-turns for producing the needed magnetic flux of the machine and secondly the magnetic flux density at the superconducting winding will be several teslas, which is suppressing the critical current density of the superconductor. The thermal insulation of the superconducting coil might be more simple. This philosophy is well suited for the cheap NbTi wire and has been applied by GE in a 10 MW design [11], which basically transfers the MRI technology to the wind turbine generator. AMSC has also applied philosophy 1) for the SeaTitan generator [8].

The second option is quite close to the normal way of building generators, because the only function of the superconducting winding is to provide very compact amp-turns in a relatively low magnetic field. However, the use of magnetic steel in the center of the superconducting field coils increases the cold mass and result in longer cool-down times as well as larger forces acting inside the thermal insulation. One may however consider to position the magnetic steel outside the cryostat at room temperature. This will provide an almost closed magnetic flux path and the challenge is then to construct the thermal insulation of the superconducting coils.

This second option was originally proposed by Technalia for a 10 MW MgB_2 turbine and is investigated in the FP7 project SUPRApower [13], in their case with a slotless armature winding. This salient-pole concept with HTS has been investigated more extensively for wind turbine applications [9].

In this paper it is investigated how the cost of the active materials can be reduced by increasing the amount of iron in a series of superconducting machine topologies. This will provide useful input for the final design of the cryogenic cooling system, because the thermal insulation will be very different for the two philosophies outlines above.

2.1 MgB_2 model generator

In order to investigate the impact of the amount of iron in the machine a general generator pole model was described in the finite element code

COMSOL as shown in figure 1. First the main topology T4-T9 is chosen by specifying the materials which the different parts of the generator are made of according to table 1. The topology T4 consists of an air-cored superconducting field winding supported by non-conducting glass fiber material, G10. The armature winding is also of the air-cored type in order to reduce the magnetic flux ripple, which is causing AC losses in the superconductor. Only the Armature winding back material is chosen to be magnetic steel to confine the magnetic flux inside the machine. The subsequent topologies T5-T9 are obtain by choosing the field back, the field pole piece and the armature teeth to also be made of magnetic steel [14].

Figure 2 shows the critical current density of a number of MgB_2 tapes from Columbus superconductors, which is used for a INNWIND.EU coil demonstration [15]. The question is at what magnetic flux density and temperature it is best utilized. The magnetic steel used for the generator is standard steel for electrical machines.

2.2 Generator topology optimization

The topology optimization routine is checking if the operational current density *J* of the superconducting windings are at least 25 % lower than the critical current shown in figure 2 using 2D FE calculations taking into account the non-linear saturation of the steel laminates for a given generator configuration. Then the length of the generator is determined to match the torque requirement of the turbine and the cost of the active materials is determined from the active masses and the assumed unit costs from table 1. If the cost of a topology configuration is lower than the previous then this is used for further optimization [14].

Material	Unit cost [€/kg]
MgB_2 wire (MgB2) 3.0 mm x 0.7 mm (m = 16.7 kg / km)	4 €/m → 1 €/m 240 → 60
Copper (Cu)	15
Steel laminates (Fe)	3
Glass-fiber (G10)	15
Permanent Magnet(PM)	50-75

Table 1: Unit cost of active material of MgB_2 superconducting generator [14].

Figure 3 shows a series of magnetic flux density maps of the topologies (T4 to T9) with an increasing amount of iron in the generators as well as the cost of the active material after the minimization. It is seen that more iron in the flux path of the magnetic circuit reduces the amount of superconductor needed. Thus the total cost is decreasing from about 1800 k€ for T4 to 800 k€ for the iron based topology T9. By using the permanent magnet unit cost in table 1 then the cost of the PM materials is expected to be in the order of 350 k€- 525 k€ by assuming a usage of 7 tons PM for a 10 MW turbine [16]. This is the same order of magnitude as the iron based MgB_2 machines indicating that the two technologies will be quite similar from an active material cost perspective.

2.3 Supply chain investigation

The MgB_2 wire is however not a mature technology and it is relevant to ask what is expected to happen with the wire cost in the future in case it will be used more. Figure 4 shows a suggestion to a scenario of how to introduce 10 GW of superconducting offshore capacity compared to the current capacity and future predictions [17]. The basic idea is to introduce the first 10 MW turbine around 2020, but then to scale up the production of superconducting turbines considerable in order to have approximately 10 GW by 2030. From figure 3 it can be determined that 200-60 km of MgB_2 wire is needed for a 10 MW machine for the topologies T4-T9 with a wire unit cost of 4 €/m. This will result in a wire demand of about 60000 – 200000 km up until 2030. The current production volume of Columbus superconductors is about 3000 km per year [6], whereby the lower limit can be met with only a limited investment. The cost of the wire is however also expected to decrease if the scenario of figure 4 is realized and a lower level of 1 €/m could be considered. Using such a unit cost and running the optimization for the T4-T9 topologies result in the second set of active material costs marked with * in figure 3. The active material cost will then decrease from about 1000 k€ to 600 k€ going from T4-T9 and the MgB_2 usage will be 340-100 km. In figure 4 the MgB_2 wire usage is shown in terms of tons of wire and is compared to the usage of PM for a permanent magnet direct drive.

3. Discussion

It might seems like the MgB_2 generator would become cheaper than the PM, but it should be remembered that the cost of the cryogenic cooling system have still not been included. A first attempt to include the cryogenic costs have been done for a warm iron cored field winding similar to the T9 topology and it was shown that the amount of MgB_2 wires needed could be reduced from 100 km in the analysis above to about 20 km for the entire 10 MW generator [18]. An evaluation of the Levelized Cost of Energy (LCoE) of the INNWIND.EU 10 MW reference turbine holding such a MgB_2 generator indicated a relative decrease in the order of ΔLCoE ~ - 0.4 % ± 2 % as compared to a medium speed drive train [19]. The uncertainty in the LCoE is estimated by the uncertainties in the cryogenic cooling and generator structural support design.The INNWIND.EU reference turbine used for the analysis has a power rating of 10 MW provided by a 178 m diameter rotor elevated to a hub height of 119 m [20]. The turbine is designed for the wind class Ia with an average wind speed of 10 m/s representing an offshore environment with a water depth of 50 m. The turbine is installed on a jacket foundation [21] and the reference drive train is of the medium speed type scaled from 4 MW to 10 MW [22]. The evaluation of the LCoE of different INNWIND.EU turbines are done by combining the cost estimates for the blades, the drive train, the tower and the foundation adding an estimate for the operation and maintenance (OPEX) and then deviding the total cost by the Annual Energy Production (AEP) of the different concepts taking the partial load efficiency into account [23, 24].

It is found that the SCDD 10 MW generator [25] can reach a full load efficiency of 96.5 % [19], which is reduced to about 94.9 % when including the losses of the power electronics [26]. This is basically the same effeciency as the medium speed drive train in [22]. The SCDD is expected to have a constant loss of about 50 kW used to run the cryocoolers even when the wind speed is below the cut-in wind speed of 4 m/s. Using the class Ia wind distribution one can estimate that this condition is found in 1550 hours per year and correspond to a loss of 77.5 MWh per year, which is 0.2 % of AEP. Thus this loss will have an impact similar to the estimated LCoE, but is believed to be included the uncertainty estimate of the LCoE. The cost of the SCDD is estimated to be similar to the medium speed drive train as analysed in 2012 using prices of permanent magnets ranging from 60 – 150 €/kg [22]. It is however shown by Schmidt and Vath in [22] that the medium speed drive train only shows a small sensitivity to the PM price due to the presence of the gearbox. Thus the cost comparison is believed to be resonable.

The above analysis indicates that the superconducting MgB_2 wind turbine generators have the potential to become as cheap as the PM direct drive, but further analysis and experimental demonstration is needed to clarify if any issues with reliability and availability of the superconducting wind generator will make the PMDD superior.

Before a 10 MW MgB_2 generator can be realized the coil winding technology must be established at an industrial scale. Figure 5 shows the design of a MgB_2 race track coil in the INNWIND.EU project [15]. A challenge with the MgB_2 wire is that the tension along the wire must not exceed 110 MPa, because interfaces between the MgB_2 grains will break and the critical current will be permanently reduced. Work is ongoing to calculate the thermal stress building up in the coil as it is cooled to 15-20 K and the additional stress from the Lorentz force. The winding of the double pan-cake coils is ongoing and the testing of the magnet is expected in the spring of 2016 to provide high field experimental data on the wire properties as they are integrated into a large race track coil.

4. Conclusion

The cost analysis shows that the cheapest MgB_2 direct drive generator will have as much iron as possible in the magnetic circuit and is pointing to the salient pole generator concept introduced by the SUPRApower project [13]. The cost analysis also indicate that the MgB_2 direct drive generator will have a hard time to compete with the permanent magnet direct drive in terms of active material cost if the philosophy is to use a lot of iron in the generator and to only expect lower MgB_2 cost in the future. An additional improvement of the critical current density of the wires must probably also have to be considered as suggested by Hypertech proposing a 5-fold increase of the critical current density in some years [27].

A roadmap of introducing 10 GW of superconducting offshore turbines is used to argue that the volumes of MgB_2 wire needed is not too far from what Columbus Superconductors can produce in EU, but the small number of possible suppliers of MgB_2 wires will probably be considered a risk in the supply chain. On the other hand the MgB_2 technology is lifting the potential dependence on Rare Earth Elements(REE), which has previously been considered a major supply chain risk for the production of $R_2Fe_{14}B$ permanent magnets. From figure 5 it can be seen that 10 GW of PMDD will correspond to about 7000 tons of PM material over a period of 10 years.

Finally demonstrations of coil winding techniques are needed to mature the MgB_2 technology for the wind sector and the INNWIND.EU MgB_2 racetrack coil demonstration is expected to provide experimental data on the wires in coils and for verification of finite element models of coils for further generator design.

Acknowledgement

The research leading to these results has received funding from the European Community's Seventh Framework Programme FP7-ENERGY-2012-1-2STAGE under grant agreement No. 308974 (INNWIND.EU).

References

[1] Bumpy JR, "Superconducting electrical rotating machines", Clarendon Press, Oxford, 1983.

[2] RADEBAUGH R, " Refrigeration for Superconductors", Proceedings of the IEEE, VOL. 92, NO. 10, OCTOBER 2004, p 1719.

[3] Jensen BB, Mijatovic N, Abrahamsen AB, "Development of superconducting wind turbine generators", Renewable Sustainable Energy, vol. 5, p. 023137, 2013.

[4] Barnes PN, Sumption MD and Rhoads GL," Review of high power density superconducting generators: Present state and prospects for incorporating YBCO windings", Cryogenics 45 (2005) 670–686.

[5] Superpower, web site: www.superpower-inc.com/. Visited October 2015.

[6] Columbus Superconductors, Web site: www.columbussuperconductors.com, visited May 2015.

[7] Hyper Tech Research, http://www.hypertechresearch.com/ . Visited October 2015.

[8] SeaTitan data sheet: http://www.amsc.com/documents/seatitan-10-mw-wind-turbine-data-sheet/ . Visited october 2015.

[9] Nyanteh Y, Schneider N, Netter D, Wei B and Masson PJ, "Optimization of a 10 MW Direct Drive HTS Generator for Minimum Levelized Cost of Energy", IEEE TRANSACTIONS ON APPLIED SUPERCONDUCTIVITY, VOL. 25, NO. 3, JUNE 2015, 5203504.

[10] Ecoswing (Horizon 2020 project), web site: ecoswing.eu/ . Visited October 2015.

[11] Fair R et. al., "Superconductivity for Large Scale Wind Turbines", DOE final report DE-EE0005143 (2012).

[12] J. Wang *et. al.*, "Design of a Superconducting Synchronous Generator with LTS Field Windings for 12 MW Offshore Direct-Drive Wind Turbines," IEEE Trans. Ind. Electron., vol. 0046, no. c, pp. 1-1, 2015.

[13] Marino I, et. al., "Superconducting light generator for large offshore wind turbines", EWEA (European Wind Energy Association) Offshore 2013, Frankfurt, Germany, 19-21 November 2013.

[14] Liu D, Polinder H, Abrahamsen AB and Ferreira JA, "Comparison of 10 MW Superconducting Generator Topologies for Direct-Drive Wind Turbines", IEEE International Electric Machines & Drives Conference (IEMDC) 2015.

[15] Abrahamsen AB, Magnusson N, Jensen BB, Liu D, Polinder H, "Design of an MgB2 race track coil for a wind generator pole demonstration", Journal of Physics: Conference Series 507 (2014) 032001.

[16] Li H, Chen Z, Polinder H, "Optimization of Multibrid Permanent-Magnet Wind Generator Systems", IEEE TRANSACTIONS ON ENERGY CONVERSION24, 82 (2009).

[17] Abrahamsen AB and Jensen BB, "Superconducting Direct Drive Wind Turbine Generators: Advantages and Challenges", Wind Energy Conversion Systems. Technology and Trends - 2012, pp. 53-80.

[18] Liu D, Polinder H, Magnusson N, Schellevis J and Abrahamsen AB, "Ripple Field AC Losses in 10 MW Wind Turbine Generators with a MgB2 Superconducting Field Winding", Submitted to EUCAS 2015.

[19] INNWIND.EU deliverable D1.24 "PI-based Assessment of the Results of WP2-WP4. Ongoing Integration Action", Submitted October 2015. www.innwind.eu

[20] Bak C *et. al.*, "Description of the DTU 10 MW Reference Wind Turbine", INNWIND.EU deliverable D1.21, www.innwind.eu/Publications/Deliverable-reports (Visited October 2015).

[21] Borstel T v, " Design Report – Reference Jacket", INNWIND.EU deliverable D4.31, www.innwind.eu/Publications/Deliverable-reports (Visited October 2015).

[22] Schmidt S and Vath A, "Comparison of Existing Medium-speed Drive Train Concepts with a Differential Gearbox Approach", paper presented at EWEA 2012.

[23] Chaviaropoulos P and Natarajan A, "Definition of Performance Indicators (PIs) and Target Values", INNWIND.EU deliverable D1.22, www.innwind.eu/Publications/Deliverable-reports (Visited October 2015).

[24] Chaviaropoulos PK, Karga I, Harkness C and Hendriks B, , "PI-based assessment of innovative concepts (methodology)", INNWIND.EU deliverable D1.22, www.innwind.eu/Publications/Deliverable-reports (Visited October 2015).

[25] Abrahamsen AB, Magnusson N, Liu D, Stehouwer E, Hendriks B. and Polinder H, "Design study of a 10 MW MgB2 superconductor direct drive wind turbine generator", Poster PO 336, EWEA annual event 2014.

[26] Deng F et. al., "Converter Designs based on New Components and Modular Multilevel Topologies", INNWIND.EU deliverable D3.32, www.innwind.eu/Publications/Deliverable-reports (Visited October 2015).

[27] Kalsi SS, "Superconducting Wind Turbine Generator Employing MgB_2 Windings Both on Rotor and Stator", IEEE TRANSACTIONS ON APPLIED SUPERCONDUCTIVITY, VOL. 24, NO. 1, FEBRUARY 2014 p. 5201907

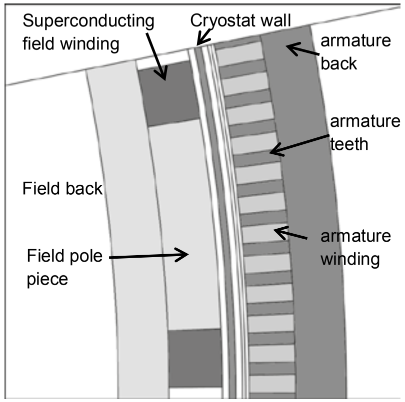

Figure 1. Model layout of a generator pole with the following components from left to right: field winding back, superconducting coil, field pole piece, air gab, cryostat wall, armature windings, armature teeth and armature back.

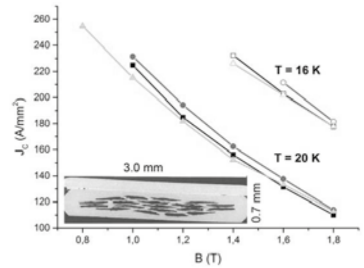

Figure 2. Critical current density of 3 different MgB_2 superconductor wires as function of operational magnetic flux density at different temperatures. **Inset:** Cross section image of the tape. MgB_2 filaments (black) are enclosed in anickel matrix and a copper strip is soldered on top.

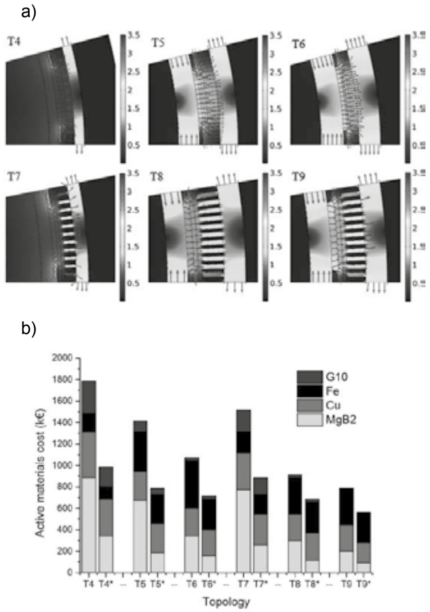

Figure 3. **a)** Topologies of 10 MW direct drive wind turbine generator with an increasing amount of iron components included in the design of the rotor and armature configuration (T4: iron behind armature, T5: add rotor back iron, T6: add field coil iron pole, T7: iron teeth for support of armature, T8: add rotor back iron and T9: add field coil iron pole) [14]. Topologies T1-3 have no back iron of the armature and has been omitted due to high cost. **b)** Active material cost of topologies after minimizing the cost for a D = 6.0 m generator intended as front mounted on the INNWIND.EU king-pin nacelle configuration [25]. The solutions indicated with a star is assuming that the price of the MgB_2 wire is reduced to 1 €/m from the current level of 4 €/m [14].

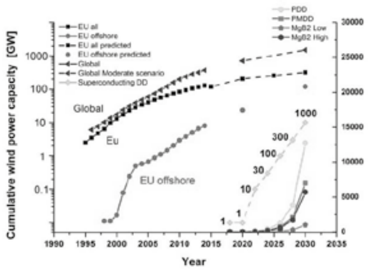

Figure 4. Scenario for market introduction of 10 GW superconducting wind turbines (green) in comparison with the past and expected future development of installed wind power capacity for all of EU (black) and offshore (red). The needed supply of permanent magnet (PM) material and MgB_2 wire are plotted with reference to the right hand axis by assuming a usage of 700 kg PM /MW for the direct drive and 10-35 km MgB_2 / MW for the superconducting MgB_2 direct drive generators.

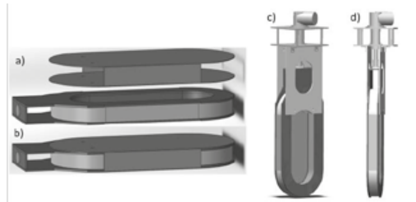

Figure 5. Illustration of INNWIND.EU superconducting race track coil demonstration based on a stack of 10 double pan-cake coils of MgB_2 superconducting wire with a 3.0 mm x 0.7 mm cross section. **a)** A stainless steel cover is fitted around the MgB_2 race track coil (gray) and enclosed between copper plates (brown) to provide the cooling at the circular end-plate (blue). The straight section of the coil is 0.5 m and the inner opening is 0.3 m. **b)** Assembled race track coil with the thermal and mechanical support. **c)** Mounting of the MgB_2 race track coil by hanging it inside a cryostat with the outer wall holding the top plate at room temperature. A cryocooler cold head is inserted into the cryostat wall and cools down a radiation shield (lower plate) to about 70 K. The coil is hanging in two glass fiber plates (yellow) and is supported by two rods going through the coil and a glass fiber support inside the coil. **d)** The second stage of the cryocooler coldhead is cooling the thermal support of the coil (blue circle of b) to the operation temperature of 10-20 K.

Alternative Wind Turbine Drive Train with Power Split and High-speed Generators

Cristian Andrei[1] **Simon Serowy[2]** **Friederike Barenhorst[2]**

Björn Riemer[1] **Ralf Schelenz[2]** **Kay Hameyer[1]**

[1]Institute of Electrical Machines (IEM), RWTH Aachen University
Schinkelstraße 4, 52062 Aachen, Germany

[2]Institute for Machine Elements and Machine Design (IME), RWTH Aachen University
Schinkelstraße 10, 52062 Aachen, Germany

1. Abstract

Conventional wind turbines (WTs) have large weight and size, reliability issues and show potential for efficiency increase at partial load. This paper describes an alternative 6 MW WT drive train, which uses the power split concept to enable its high-speed generators to operate in their optimal operating point. A design with more carry-over parts is possible, which reduces maintenance time and leads to an efficient manufacturing process. The system is also redundant when individual drive trains fail. Different gearbox configurations and generator topologies are evaluated for the proposed concept and an operating strategy is developed.

2. Keywords

Wind power generation, wind turbine drive train, power split gearbox, permanent magnet synchronous machine, high-speed generator.

3. Wind Turbine Concepts

Today's wind energy market displays a variety of drive train topologies with different generator concepts, which impose different challenges on the gearboxes and power converters [1].

Direct driven WTs are designed with no gearbox, which results in low speeds and high torques at the generator. The generators are commonly synchronous machines with high pole pair numbers. Their excitation is realized on the rotor with an electrical winding or with permanent magnets. These generators are large, heavy, challenging to transport and require a high amount of copper for the windings. In case of permanent magnet excitation, rare earth magnets are required, which represent a financial insecurity, due to the price fluctuations over the last years [2].

Further established WT concepts are based on medium-speed (100 – 400 rpm) or high-speed (up to 2,000 rpm) generators. Medium-speed generators are also synchronous machines (most common with permanent magnets). Usually they are integrated with an one- or a two-stage gearbox. This results in a more compact construction compared to direct driven generators [3]. However, higher maintenance and an increased cost factor, due to the design with gearbox and the use of permanent magnets, are still an issue. Both direct driven and medium-speed generators require a full power converter for the adjustment of the grid frequency, due to dynamic operation with fluctuating wind conditions. This adds to the overall costs, because of the relatively high prices of the power electronics components.

WTs with high-speed generators mostly use doubly-fed induction machines combined with a three-stage gearbox. For this concept the stator is directly coupled to the grid and the frequency adjustment is realized by a converter in the rotor winding system. Disadvantages of this concept are the reduced speed variability and the fault-prone gearbox. Being a mature technology, this is nevertheless the most cost-effective concept on the market.

Additional alternative concepts have also been developed. Clipper's Liberty is a 2.5 MW WT with a similar construction to the concept proposed in this paper [4]. The gearbox consists of two spur gear stages and the power is split between four permanent magnet synchronous generators, which rotate at 1,133 rpm. For the individual drive trains, the power is split and then summated in the gearbox from two different power paths. This mechanical redundancy has led to significant issues in the gearbox.

Another WT gearbox configuration with power split is the Multi Duored concept from Winergy [5]. This gearbox uses spur gear stages for an eight-fold power split with subsequent four-fold power summation, leading to only two outputs. The combination of power split and power summation and the exclusive use of spur gears yields a high number of carry-over parts, but also leads to a large weight (62 t for 6.5 MW).

Today's available WT concepts do not take full advantage of the modularity and redundancy of a drive train with power split, or the material and cost reduction of high-speed electrical machines. In order to achieve these goals, an alternative drive train is proposed and its development is described in the following sections. The potential of an efficiency increase over a wide operating range at partial load (especially below 30 % rated power) is shown, where typical efficiencies of conventional WTs drop significantly to under 80 %, irrespective of the used concept [6], [7].

4. Proposed Drive Train

Figure 1 illustrates the concept of the 6 MW WT drive train with six 1 MW high-speed (5,000 rpm) generators and a four-stage gearbox with power split. The gearbox in Figure 1 consists of one spur and three planetary gear stages and realizes the power split in the first stage. The generator is designed as a permanent magnet synchronous machine (PMSM). These gearbox and generator topologies are described in sections 5 and 6, alongside other configurations that were also considered in the development process.

The gearbox used for this concept needs a higher transmission ratio compared to conventional configurations. Higher losses due to the higher transmission ratio can be compensated by an optimized operating strategy and the benefits of the high-speed machines. The targeted higher speed results in an increased power density, which leads to a considerable reduction of weight and size of the generators. Furthermore this reduces the amount of active magnetic material and decreases investment costs. The design with multiple identical generators enables the utilization of more carry-over parts. These parts are at the same time smaller and more lightweight due to the power split configuration. As a result increased economic efficiency in production and improvements in maintenance can be achieved. Mechanical power split with subsequent electrical power summation on the grid side is also a more robust solution, than a purely mechanical split and summation of the power inside the gearbox. A certain redundancy of the system is given as well, since energy will still be produced, even when one or more generators fail.

5. Gearbox Configurations

The predesigned gearbox concepts for the high-speed multi-generator drive train are basically similar to the structure of conventional WT gearboxes. They are built as a combination of planetary and spur gear stages. The planetary stages are considered exclusively in the two-shaft mode (drive: planet carrier, driven: sun shaft) in order to restrict the solution space. With the use of planetary gears a compact space with high power density and high transmission ratios can be obtained. To implement the power split to six generators, a spur gear is used. Since the intended rated speed of the generators is 5,000 rpm, the gearbox needs to have a transmission ratio higher than 1:400. To realize this ratio, only gearbox concepts with four gear stages are considered. In order to develop a modular configuration, the gearbox concepts consist of standard and independent gear stages, joined together through couplings. In case of a malfunction the faulty gearbox component can thus be completely replaced and the downtime of the WT can be reduced.

Different gearbox concepts have been developed and evaluated in order to determine the best solution for this drive train concept. In a multi-level rating scheme there have been four concepts identified for the further examination. Depending on the requirements for space and durability, shafts, bearings and gears are dimensioned based on the rated load

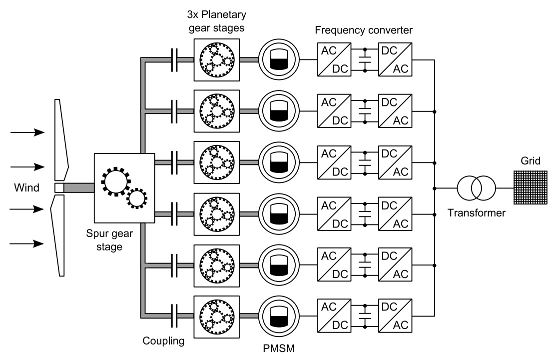

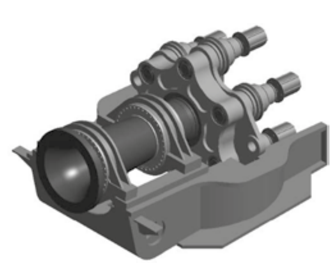

Figure 1: Concept and CAD model of the proposed alternative WT drive train.

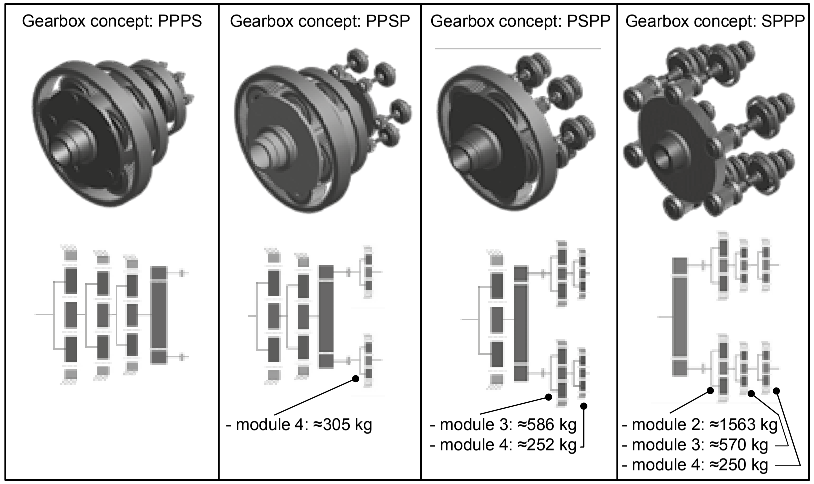

Figure 2: Studied gearbox concepts.

Gearbox concept	PPPS	PPSP	PSPP	SPPP
Weight (Gears, shaft, bearings)	≈ 47 t	≈ 49 t	≈ 45 t	≈ 40 t
Size (Width × length)	3.4 × 3.4 m	3.4 × 3.4 m	3.4 × 3.2 m	4.2 × 3 m
Total number of parts	90	193	275	370
Number of different parts	28	31	30	31
Modularity	3.21	6.23	9.17	11.94

Table 1: Comparison of different gearbox concepts.

for these four gearbox concepts (see Figure 2). The four gearbox configurations in Figure 2 consist of three planetary stages (P) and a spur gear stage (S). The concepts differ in the position of the spur gear stage and thus the power split in the gearbox.

A challenge of these gearbox concepts is the shaft bearing for the spur gear used to realize the power split. Switchable couplings are designated behind the power split, which are opened or closed depending on the input power. The generators are ramped up to the synchronous speed before the couplings are activated, which reduces the wear. Positive fit and frictionally engaged couplings, both dry- and wet-running, are evaluated for this application. While a coupling is opened the associated spur gear output shaft is rotating anyway, because the gearing is still in operation. Though the shaft is not transmitting power – other than the friction in the bearings – the tooth forces in this operational state are quite low. The bearings are pre-stressed with an initial tension, in order to reduce the operating risk of the bearings below minimum load. This initial tension is 2 % of the load rating for the used tapered roller bearings [8].

The developed concepts are rated regarding space, weight, modularity and efficiency. To give a statement on the modularity of the different concepts, a parameter is introduced that rates the total number of identical parts to the number of different parts. The result is the average number of used elements in the entire gearbox. The higher this parameter is, the higher is the modularity of the concept. Only the parts from the bottom level of the bill of materials are considered to be single parts. Only shafts, bearings, planet carrier and gears are regarded.

In Table 1 the four gearbox concepts are compared. The use of planetary gear units in the first three stages leads to a compact gear design with a low modularity. The concept with power split in the first stage stands in direct contrast to this structure. For this concept six individual 1 MW gear trains, each with three planetary stages, are arranged after the first stage. This leads to a very modular gearbox structure, increases the number of identical parts and reduces the mass of the individual components. The remaining concepts provide the power split in the second and third stage, respectively.

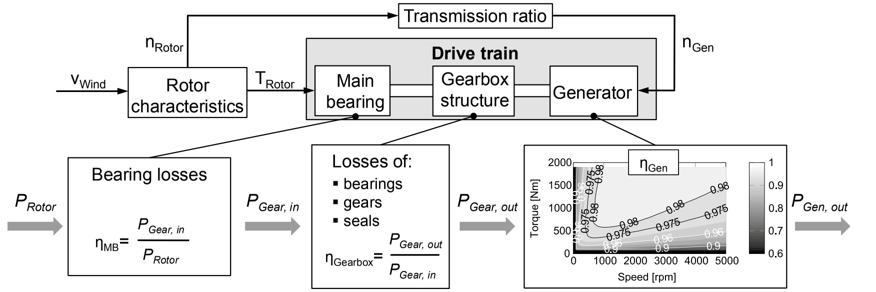

Figure 3: Structure of the efficiency calculation model.

The comparison of the four gearbox concepts regarding their efficiency is carried out on a system level. In order to perform efficiency calculations for the entire drive train – including main bearing, gearbox with six-fold power split and generators – an AMESim model of the entire system is created (see Figure 3). The main bearing is designed as a fixed-floating bearing system, as it is typically used in WT drive trains with four point suspension. For the developed gearbox structures, the used seals, bearings and gear parameters are implemented in the model. The generators are modeled based on the efficiency map of the PMSM described in section 6.

To calculate the efficiency the power losses of every component are determined for all operating points of the gearbox based on analytic equations. These power losses are – regarding the bearings and gears – both load-dependent and -independent. The bearing losses are calculated for the main bearing and other bearings used in the gearbox, according to established calculation methods [8].

There are commonly hydrodynamic and friction losses occurring in the tooth contact. In the used calculation model these friction losses are divided into rolling and sliding friction and calculated for every tooth engagement [9]. The hydrodynamic losses are divided into churning and squeezing losses. These losses cannot be calculated in AMESim using the underlying empiric equations by Terekhov [10]. Terekhov's calculation method is based on research on spur gears with a maximum module of 8 mm, which are evaluated at maximum circumferential speeds of 50 m/s [11]. However, the developed gearbox concepts use big teeth with modules of 10-24 mm, in the gear stages before the power split. Moreover, the circumferential speed in the PPPS gearbox concept is higher than 50 m/s in the fourth stage which means that Terekhov's methods lose their validity. According to Strasser, the load-independent losses (churning and squeezing losses) represent 1-13 % of the entire losses in the gearbox, depending on the operating point [11]. As long as there is an oil injection lubrication instead of a flood lubrication for every stage, no churning losses occur. The squeezing losses can be estimated at 0.37-10 % [11]. The relative comparability of the gearbox concepts based on their efficiency is still given, because the operating points of every concept are identical and due to the fact that the squeezing losses depend mainly on the circumferential speed and the lubricant viscosity [12]. For the seals, load independent losses are calculated using the approach according to [13].

The efficiency is defined as the relation of the generator output power and the rotor input power. First simulations are carried out at a lubricant temperature of 65 °C and for a start-up procedure of the WT up to rated power. No operating strategy regarding power split is implemented at this point, which means that all generators are symmetrically loaded at partial load. Figure 4 depicts the efficiencies of four different drive train configurations, where only the gearbox concept varies.

The variation during the entire operating range between the different concepts is less than 1 %, which is within the accuracy of the model. The drive train concept with power split in the third stage (PPSP) exhibits the best efficiency with 93.7 % at full load. The concepts with power split in the first (SPPP) and last stage (PPPS) basically display identical efficiency curves with a maximum efficiency of about 93.5 % at full load. The concept with power split in the second stage (PSPP) has 0.25 % lower efficiency.

The anticipated result, that the gearbox concept with the highest number of rotating parts (SPPP) would show the worst and the concept with the smallest number of parts (PPPS) the best efficiency, has not been confirmed. This can be traced back to the use of different roller bearings and the slightly different transmission ratio of the different concepts, due to their

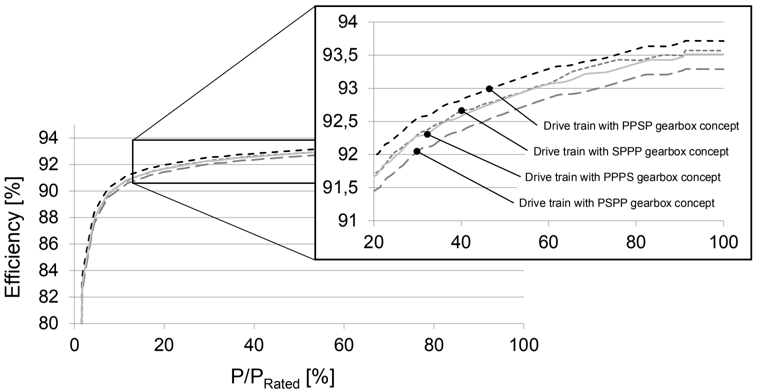

Figure 4: Results of the efficiency evaluation for different drive train configurations.

design and dimensioning. Particularly, the discrete steps between the used bearing sizes lead to different losses that influence the efficiency graphs. The simulation models for the different drive train configurations have been iteratively extended by adapting the gear and bearing parameters. Further adaptions regarding the simulation parameters are expected during the design process, which will lead to changes in the efficiency graphs.

Besides the advantages of modularity and weight, the SPPP gearbox concept also offers the greatest potential to improve the utilization capacity of the components and the increase in efficiency during partial load operation. This is due to the possible integration of switchable couplings in the gearbox, immediately after the first gear stage. In the next step of the design process, a housing including a cooling concept are developed for the SPPP concept.

6. Generator Topology

Three common electrical machine topologies are evaluated for their application in the proposed drive train. The evaluation is mainly based on the Esson power coefficient C, which is a parameter for the performance and utilization of an electrical machine. The Esson power coefficient directly relates the power that can be obtained from an electrical machine to its volume and speed. It can be calculated based on the tangential force σ, which acts on the surface of the machines rotor [14].

The tangential force depends on the design of the machine and can therefore be used to compare different machine types. σ is proportional to the current distribution A and the normal component of the magnetic field induction B. The magnetic field induction is limited by the nonlinear saturation of the soft magnetic electrical sheets in the stator and rotor of the machine. The current distribution depends on the electrical utilization and thus on the cooling of the machine [14].

Table 2 shows the tangential forces and the Esson power coefficients for the considered electrical machines. Typical values of other machine parameters needed for the calculation (power factor $cos\varphi$, winding factor ξ and efficiency η), are given as well.

The synchronous machine with permanent magnet excitation (PMSM) offers the highest power density, when compared to the other machine types. Synchronous machines are magnetically excited by a winding on the rotor (EESM) or by permanent magnets (PMSM). These types of magnetization lead to average values of the air gap flux density of B = 1.2 T. For the induction machine with squirrel cage rotor (SCIM) the magnetization is generated by the current in the stator winding. Air gap magnetic flux densities of B = 0.8 T can be reached. Higher air gap flux densities would lead to an increase in magnetization effort and reduce the power factor, due to the nonlinear behavior of the stator sheet material.

Electrical machine	Typical values		Tangential force σ [kN/m^2]	Esson power coefficient C [kW·min/m^3]
Squirrel cage induction machine SCIM	A = 40,000 A/m B = 0.8 T	$cos\varphi$ = 0.85 ξ = 0.95 η = 0.95	17.36	2.86
Electrically excited synchronous machine EESM	A = 40,000 A/m B = 1.2 T	$cos\varphi$ = 0.90 ξ = 0.95 η = 0.96	27.57	4.54
Permanent magnet synchronous machine PMSM	A = 40,000 A/m B = 1.2 T	$cos\varphi$ = 0.90 ξ = 0.95 η = 0.97	28.15	4.63

Table 2: Tangential force and Esson power coefficient for different electrical machines (compare [14]).

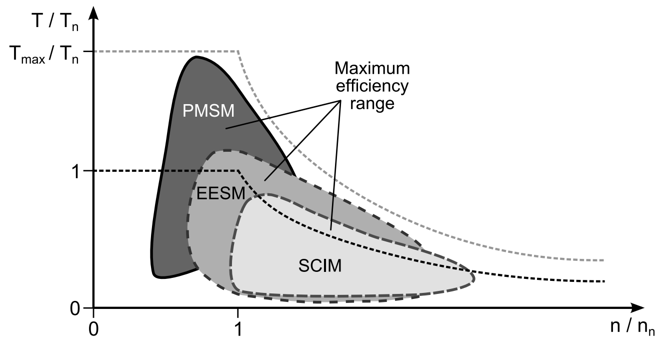

Figure 5: Exemplary efficiency ranges for different electrical machine topologies [15].

Both synchronous machines have higher efficiency in the base speed range, with the PMSM being most efficient, since no copper losses occur inside the rotor due to the permanent magnet excitation. This is most advantageous for the application as a WT generator, which generally operates in the base speed range. The induction machine has the highest efficiency in the field-weakening area, as illustrated in Figure 5.

For the high-speed application of the generator further requirements have to be regarded. Especially the mechanical stress on the rotor of the machines due to centrifugal forces has to be analyzed. For the proposed application, the circumferential speed should not exceed 100 m/s, which constraints the diameter of the rotor at D = 0.38 m (for a given speed of n = 5,000 rpm). The mechanical stress has local hot-spots, depending on the geometry. For the PMSM high stress occurs at the bridges around the permanent magnet slots. Another important aspect at higher speeds are the iron losses inside the electrical steel sheets, which become critical with increasing frequency and magnetic flux density [16].

A SCIM is designed for a rated power of P = 1 MW and a rated speed of n = 5,000 rpm based on analytical methods and considering the values in Table 2. The resulting machine has a total volume of 0.1116 m^3 (including end windings of stator winding) and a power density of 8.96 MW/m^3. With a specific price of 16 €/kg for copper and 5 €/kg for electrical sheet [1], [17], [18], the cost of the active magnetic material for one SCIM is 4,758 € (see Table 4).

The PMSM is designed with V-shaped buried magnets to minimize eddy current losses inside the magnets [16]. Table 3 lists the main parameters and Figure 6 depicts the cross section of the machine. An efficiency map is calculated for this design by means of the finite element method (FEM). A maximum efficiency of 98.6 % can be reached (see Figure 7). The resulting design has a total volume of 0.1104 m^3 and thus a power density of 9.06 MW/m^3 (see Table 4). To analyze the high mechanical stresses that occur in the electrical sheets of the rotor, especially in the bridges around the buried permanent magnets, a FEM calculation is performed. The geometry is too complex for an analytical consideration. The evaluation is based on the von Mises stress. The rotor geometry is optimized so that the resulting maximum value is 419.7 MPa, which is less than typical values of modern electrical sheets. Thus, the von Mises stress is below the yield strength of the material.

The cost of the total active magnetic material for one PMSM amounts to 5,727 €. A specific price for permanent magnets of 58 €/kg is assumed [1], [17], [18]. As shown in Table 4, the SCIM has a cost advantage of about 17 % over the PMSM. However, it must be considered that the power factor of the SCIM is lower compared to the PMSM (see Table 2), which means that the converter has to provide a higher apparent power. This leads to a larger size and cost of the converter.

Due to its high power density, the PMSM is chosen as generator and regarded in following simulations.

Machine parameters		
Rated power	P_N	1 MW
Rated voltage	U_N	690 V
Rated speed	n_N	5,000 rpm
Active length	l_i	480 mm
Stator		
Outer radius	$r_{S,out}$	240 mm
Rotor		
Outer radius	$r_{R,out}$	150 mm
Inner radius	$r_{R,in}$	70 mm
PM height	h_{PM}	10 mm
Pole pairs	p	3

Table 3: Parameters of the PMSM.

The vibration behavior of the developed drive train has to be evaluated, in order to make sure that no resonant frequencies are excited and to guarantee a safe and stable operation. For this purpose, a modal analysis of the PMSM with its mechanical structure (housing, shaft, bearings etc.) is performed by means of structural-dynamic simulations. Figure 8 shows that resonant frequencies of the PMSM occur above its maximum operating mechanical frequency of f_m = 83.33 Hz (at 5,000 rpm). This ensures that no resonant frequency is excited by the operating speed. To rule out additional resonant frequencies, that can have other excitation sources, further simulations are required. A vibration analysis of the entire drive train will be carried out in future works by means of multibody simulation (MBS).

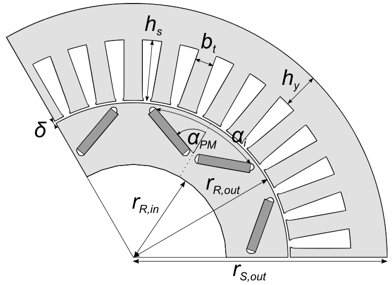

Figure 6: 120° cross section of the PMSM.

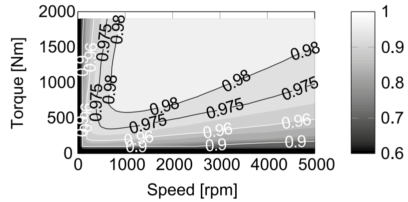

Figure 7: Efficiency map of the PMSM.

Electrical machine	SCIM	PMSM
Outer diameter	478.23 mm	480.00 mm
Total length (incl. end windings)	621.26 mm	610.00 mm
Volume	0.1116 m^3	0.1104 m^3
Power density	8.96 MW/m^3	9.06 MW/m^3
Efficiency	95 %	98 %
Active material costs	4,758 €	5,727 €

Table 4: Comparison of the SCIM and PMSM concepts.

Figure 8: First six modes of the PMSM including mechanical structure.

7. Operating Strategy

A drive train concept with multiple generators offers the possibility to switch off individual generators during partial load operation, so that the remaining generators can work at their rated operating point and in their optimum efficiency range. The decoupling of total gear trains by using switchable clutches in the gearbox can offer further potential for increasing the efficiency during partial load operation.

During start-up and full load operation the operating strategy is identical compared to conventional WTs. The strategy during partial load operation has to be extended. Using six generators, the partial load operation needs to be divided into six individual operating areas. Each of these areas must be provided with both a speed control and a pitch control strategy, in order to protect the WT during short-term changes of the wind speed. The possible ranges of operation during partial load operation are dependent on the torque characteristics of the electric generators and are limited by the rated torque.

In order to meet these requirements, a generic WT controller is developed, which in a first step uses a characteristic-curve based WT analogous model. Thereby, the inertia is reduced to a single mass and the aerodynamic rotor torque and the rotor speed are calculated depending on the rotors c_p-characteristic.

The WT analogous model is loaded with wind loads that are calculated via a wind file generated using the tool TurbSim from NREL. According to the wind conditions, the pitch angle and the necessary number, torque and speed of generators are simulated by the controller.

Figure 9 depicts a simulated start-up at an average wind-speed of 14 m/s and a turbulence of 16 %. In the beginning the rotor blades are turned away from the wind and the pitch angle is 90°. The main controller initiates the start-up sequence if the wind speed is high enough for a given period of time. Then, the blades are turned into the wind with a rate of 3°/s. First, at 15s a rise of the generator speed can be noticed. This late rise is due to the WT operating

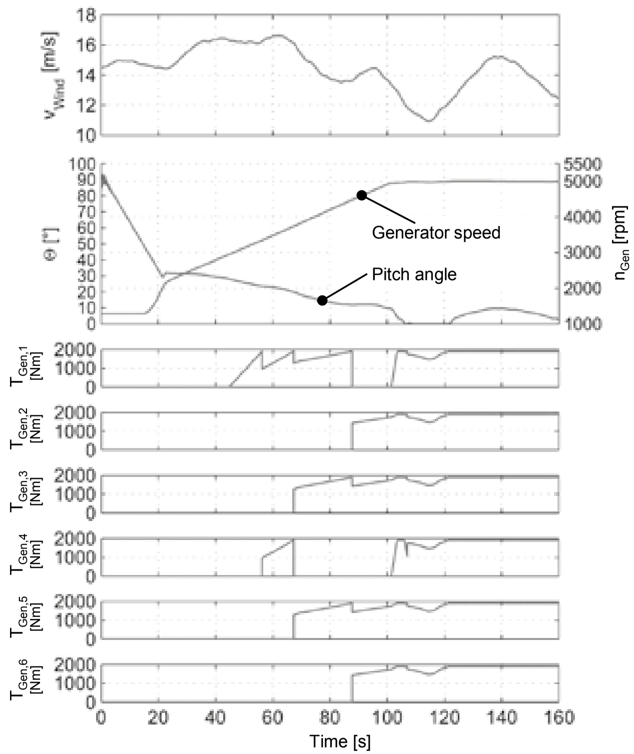

Figure 9: Simulation of the WT operating strategy during start-up with a generic controller.

point, which is still outside the c_p-characteristic of the analogous model. At 45s the switching on speed is reached and the first generator is switched on. While the rotor speed increases, the torque rises until the generator has reached rated torque. At this point the second generator is switched on and the torque is distributed symmetrically on both generators. Further generators are connected successively this way, as soon as the operating generators reach their rated torque of T_n = 1,900 Nm.

In the shown start-up process of the WT the switching procedure of individual generators takes place until four generators are activated. The state of operation with five operating generators will be skipped, because the generator speed increases rapidly and torque dynamics have to be avoided. The state between 106s and 107s shows this switching procedure. The torque on the fourth generator drops to switch on to the operation mode with five generators. Before the torque can drop to 0 Nm, the torque controller activates all six generators. With increasing wind speed, full load operating range is reached (from 120s).

An idealized switching procedure; comparable to the switching procedure presented above, has been added to the efficiency calculation model in section 5 to show the potential of increasing the efficiency during partial load operation. The moments of connection or disconnection of several generators are defined by reaching a multiple of their rated torque (T_n = 1,900 Nm). In the drive train model in section 5, the gear trains which are not required, can initially also be decoupled and switched on separately together with the generators. This behavior simulates the use of a coupling after the spur gear stage and therefore after the power split in the gearbox.

The results of this efficiency simulation for different drive train configurations are shown in Figure 10. The results show a significant efficiency increase in the lower range of the partial load operation, due to the connection of individual drive trains. As soon as all generators are switched on, the efficiency characteristic is the same as in the case where no switching procedure is used. Examining the efficiency trends for the operating strategy with individual switching of generators, efficiency drops can be seen at the switching points. These result from the additional losses at low torque operating points, after an individual gear train including generator has been connected.

The greatest efficiency increase (more than 7 %) is reached for the drive train configuration with power split in the first gear stage. For this concept, three planetary stages per gear train are decoupled and thus the highest number of parts is disconnected from the power flow, when compared to the other concepts.

This efficiency increase leads to a higher electrical output power of the WT and to a higher energy yield. In low-wind regions the WT operates up to 70 % of the total operating time at partial load. Therefore, the use of such a drive train concept with the illustrated switching procedure is particularly suitable for these locations. The WT energy output is calculated by multiplying the wind speed dependent electrical output power by the relative occurrence of the wind speed. For a low-wind site with a mean wind speed of 5.3 m/s an increase in energy yield during partial load operation of up to 1.15 % is achieved, only when using a switching procedure for individual gear trains and generators. The energy needed for the switching process is not regarded.

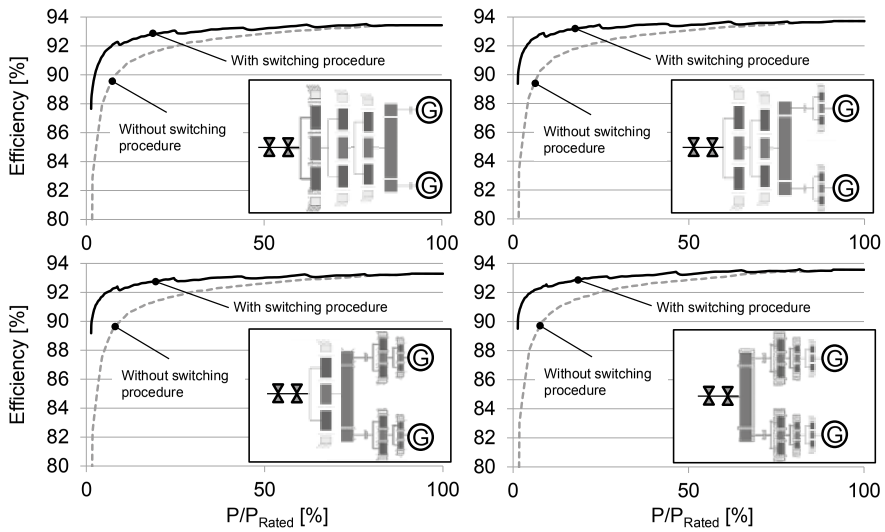

Figure 10: Efficiency characteristics without and with power split for different drive train configurations.

8. Conclusion

This paper describes the development of an alternative drive train configuration with six high-speed generators (rated at 1 MW and 5,000 rpm) for a 6 MW WT. Different gearbox concepts and electrical machines have been investigated, in order to determine the potential of a higher power density and an efficiency increase, as well as the advantage of a mechanical power split in the gearbox and an electrical power summation on the grid side. The SPPP gearbox configuration shows advantages regarding both weight and modularity. Efficiency simulation models for the entire drive train were created, considering a PMSM topology as a generator.

Simulation results display an efficiency increase of up to 7 % during partial load operation, provided that an operating strategy is considered, where gear trains and generators are individually connected and disconnected.

Acknowledgement

This work was funded by the German Federal Ministry for Economic Affairs and Energy under Grant 0325642.

References

[1]. H. Polinder, F. F. A. van der Pijl, G.-J. de Vilder and P. J. Tavner, "Comparison of Direct-Drive and Geared Generator Concepts for Wind Turbines," *IEEE Transactions on Energy Conversion*, vol. 21, no. 3, pp. 725-733, 2006.

[2]. S. Hoenderdaal, L. Tercero Espinoza, F. Marscheider-Weidemann and W. Graus, "Can a dysprosium shortage threaten green energy technologies?," *Energy*, vol. 49, pp. 344-355, 2013.

[3]. T. Barthel, K. van Gelder and R. Zeichfüßl, "HybridDrive 3.0 MW - Development and Testing of a New Drive Train Concept," in *Conference for Wind Power Drives*, Aachen, 2013.

[4]. Clipper Windpower Plc, *Liberty 2.5 MW Wind Turbine*, Product Brochure, 2009.

[5]. Winergy, "Multi Duored," 2015. [Online]. Available: https://www.winergy-group.com/cms/website.php?id=/en/products/gear-boxes/multi-duored-gearbox.htm. [Accessed 05 October 2015].

[6]. E. Hau, Wind Turbines: Fundamentals, Technologies, Applications, Economics, London: Springer, 2013.

[7]. G. Bywaters *et al.*, "Northern Power Systems WindPACT Drive Train Alternative Design Study Report," Technical Report, NREL, Colorado, 2005.

[8]. Schaeffler Gruppe Industrie (Schaeffler Group Industry), *Großlagerkatalog (Large Bearings Catalogue)*, Firmenschrift (Product Brochure), 2009.

[9]. N. E. Anderson and S. H. Loewenthal, „Spur-Gear-System Efficiency at Part and Full Load," NASA Technical Paper 1622, Technical Report 79-46, 1980.

[10]. A. S. Terekhov, „Hydraulic losses in gearboxes with oil immersion," *Russian Engineering Journal*, vol. 55, 1975.

[11]. D. Strasser, *Einfluss des Zahnflanken- und Zahnkopfspiels auf die Leerlaufverlustleistung von Zahnradgetrieben (Influence of Tooth Flank and Tooth Tip Backlash on the No-Load Losses of Gearboxes)*, Bochum: PhD Thesis, 2005.

[12]. G. Niemann und H. Winter, Maschinenelemente, Band II, Getriebe allgemein, Zahnradgetriebe - Grundlagen, Stirnradgetriebe (Machine Elements, Vol. II, Gearboxes, Gear Transmissions - Fundamentals, Spur Gears), Berlin: Springer, 1989.

[13]. H. Linke, Stirnradverzahnung, Berechnung - Werkstoffe - Fertigung (Spur Gears, Design - Materials - Manufacture), Munich: Hanser, 2010.

[14]. G. Müller, K. Vogt and B. Ponick, Berechnung elektrischer Maschinen (Design of Electrical Machines), Weinheim: Wiley-VCH, 2008.

[15]. T. Finken, *Fahrzyklusgerechte Auslegung von permanentmagneterregten Synchronmaschinen für Hybrid- und Elektrofahrzeuge (Driving Cycle Based Design of Permanent Magnet Synchronous Machines for Hybrid and Electric Vehicles)*, Aachen: PhD Thesis, 2011.

[16]. T. Finken, M. Hombitzer and K. Hameyer, "Study and Comparison of several Permanent-Magnet excited Rotor Types regarding their Applicability in Electric Vehicles," *Emobility - Electrical Power Train*, pp. 1-7, 2010.

[17]. Argus Media, "Metal-Pages," [Online]. Available: http://www.metal-pages.com/. [Accessed 5 October 2015].

[18]. London Metal Exchange (LME), "London Metal Exchange," Hong Kong Exchanges and Clearing (HKEx) Group, [Online]. Available: http://lme.com/. [Accessed 5 October 2015].

Numerical Analysis of Effects of Leading-Edge Protuberances at Low Reynolds Number

Ming Zhao , Mingming Zhang, and Jianzhong Xu

Institute of Engineering Thermophysics, Chinese Academy of Sciences,100190 Beijing, People's Republic of China

Abstract

This paper presents a numerical investigation of the aerodynamic performance of an airfoil with leading-edge protuberances within stall region at Reynolds number of 2×10^5. An IDDES (Improved Delayed Detached Eddy Simulation) method was developed based on a transition model through the modification of turbulence length and the limitation of intermittency factor and validated through quantitative comparison with experimental results. Utilizing the developed method, the vortex evolution and thus the physics of the dominant bi-periodic phenomenon were uncovered. In addition, the effects of bi-periodic flow patterns on aerodynamic forces were also investigated. It was found that bi-periodic phenomenon deteriorated the aerodynamic performance by the inducement of massive flow separation at leading edge. Moreover, the variations in the flow patterns led to little change in total lift coefficient around stall region.

keyword: DES method; flow control; bi-periodic phenomenon; CFD

1. Introduction

The controls of the airfoil flow separations at a low chord Reynolds number ($\mathrm{Re}_c = \frac{U_\infty c}{\nu}$ less than 5×10^5) are becoming increasingly important from both fundamental and industrial point of view. Recently, a new kind of passive flow control technique, i.e. "leading-edge protuberance", has received many interests, which was inspired by the work of marine biologists who studied the morphology of humpback whales' pectoral flippers [1]. It has already been applied in the aerodynamic shape optimization of wind turbine [2] (see Figure 1). The implementation of tubercles on foils has demonstrated significant benefits, with the stall becoming more gradual and typically delayed [3].

Fig. 1 Geometric model of the modified blade

Deploying this bionic means, many investigations have been conducted; however, the underlying mechanisms were still not clearly understood. In [3], Michael et al. summarized several hypotheses of the mechanisms, including "vortex generator", "wing fence" etc. For the VG case, Malipeddi et al. [4] observed that the streamwise vortices produced by the protuberances carried higher momentum flow into boundary layer, which kept the flow attached to airfoil surface. Furthermore, Zhang et al. [5] found that the ratio of effective height of leading-edge protuberance to boundary layer thickness δ should lie in the interval between 0.1 and 0.5 by means of experimental investigations, similar to micro vortex generators. For the "wing fence" case, Pedro [6] numerically described the tubercles to create physical barriers to the span-wise motion which prevented the separation growth from the tip to the root of the wing.

On the other hand, bi-periodic phenomenon, i.e. convergent and divergent flow patterns at neighboring trough sections along the spanwise direction of the leading-edge protuberance, has been drawn much research attention. In the aspect of experimental study, Custodio [7] performed tuft and dye visualizations and observed that the occurrence of bi-periodic phenomenon was related to airfoil configuration and angle of attack (AOA).

In the meantime, bi-periodic phenomenon has also been studied by numerical methods. First of all, RANS methods have been proved to have the capacity of capturing bi-periodic phenomenon [8]. However, the details of unsteady turbulent flows were missed due to the time-averaged property of RANS methods and the massive flow separations could not be accurately depicted [8, 9]. To overcome this, the detached-eddy simulation (DES) method, a combination of RANS and LES methods, has been implemented. For example, Malipeddi et al., [4] and Camara et al., [10] adopted DES method to simulate the flow field of modified airfoils, respectively. As a result, Malipeddi et al., [4] assumed that the interactions between vortices of neighboring valleys triggered bi-periodic phenomenon. In addition, Camara et al., [10] found that bi-periodic could only be observed at high angle of attack (18°) for specific configuration.

Although a lot of work has been conducted on the bi-periodic phenomenon, the specific mechanism and its influence on airfoil aerodynamic performance were still unknown.

In present study, an IDDES method (the latest version of DES method) based on a transition model was developed through the modification of turbulence length and the limitation of intermittency factor, which was utilized to simulate the flow field of NACA 63_4-021 airfoil with and without wavy leading edge around stall region. Moreover, the mechanism which triggered bi-periodic phenomenon was thus given under current circumstances. Eventually, the effect of bi-periodic phenomenon on aerodynamic performance and relative physics were discussed in detail.

2. Numerical schemes

2.1 Turbulence modeling

As mentioned in Section I, the inducement of bi-periodic phenomenon was associated with the development of unsteady turbulent flow and massive flow separation, RANS method was thus not applicable. Considering feasibility and accuracy, the DES method was adopted in present study, which has recently become much favored in the study of the unsteady and geometry-dependent separated flows [9]. In present study, IDDES method based on Fu-Wang transition model [11] was developed to capture the development of laminar flow and massive turbulent flow separation.

In general, Fu-Wang transition model was based on k-ω SST turbulence model. To capture flow transition, another transport equation of intermittency factor γ was introduced. The effective eddy viscosity (μ_{eff}), which is a combination of the non-turbulent and turbulent contributions, $\mu_{eff} = (1-\gamma)\mu_{nt} + \gamma\mu_t$, takes the place of viscous eddy viscosity (μ_t). The transport equation for intermittency factor (γ) is

$$\frac{\partial(\rho\gamma)}{\partial t} + \frac{\partial(\rho u_j \gamma)}{\partial x_j} = \frac{\partial}{\partial x_j}\left\{(\mu + \mu_{eff})\frac{\partial \gamma}{\partial x_j}\right\} + P_\gamma - \varepsilon_\gamma \quad (1)$$

where P_γ and ε_γ represent the production and dissipation, respectively. They are modeled as follows

$$P_\gamma = C_3 \rho F_{onset}\left[-\ln(1-\gamma)\right]^{0.5}\left(1 + C_4 \frac{k^{0.5}}{(2E_u)^{0.5}}\right)\frac{d}{\nu}\left|\nabla E_u\right| \quad (2)$$

$$\varepsilon_\gamma = \gamma P_\gamma$$

Subsequently, IDDES method based on Fu-Wang transition model can be constructed through modifying the dissipation term of the turbulent kinetic energy (TKE) equation. After introducing a length scale, L_{hybrid}, the TKE equation can be given in tensor form as

$$\frac{\partial(\rho k)}{\partial t} + \frac{\partial(\rho u_j k)}{\partial x_j} = \frac{\partial}{\partial x_j}\left[\left(\mu + \frac{1}{\sigma_k}\mu_t\right)\frac{\partial k}{\partial x_j}\right] + \tau_{ij} S_{ij} - \frac{\rho k^{3/2}}{L_{hybrid}} \quad (3)$$

The IDDES length-scale combining the DDES and WMLES scales can be implemented as

$$L_{hybrid} = \overline{f_d}(1+f_e)L_{RANS} + (1-\overline{f_d})L_{LES} \quad (4)$$

$\overline{f_d} = \max\left\{(1-f_{dt}), f_B\right\}$ with $f_{dt} = 1 - \tanh\left[(8r_{dt})^3\right]$.

It was worth to mention that γ should be 1 in LES mode.

2.2 Numerical Methods and Validations

The STVD scheme adopted can be shortened as S6WENO5. In addition, a LU-SGS method with Newton-like subiteration in pseudotime was taken as the time-marching method. Wall surfaces were regarded as no-slip and adiabatic for viscous simulation. The approach was in parallel algorithm using domain decomposition and MPI strategies for the platform on PC clusters, and the computations were all based on our in-house solver UNITs [12].

Using the developed numerical schemes, the flow fields over the smooth and wavy airfoil with mean chord length c = 100mm and span length s = 200mm were investigated, consistent with the ones in our previous experimental study [5]. The wavy leading edge had an amplitude of A=12mm and a wavelength of λ=25mm. Figure 2 demonstrates a slice of the computational mesh. Specifically, the structured grid system with $y^+ \approx 1$ and the growth ratio ≈ 1.12 was established, satisfying the minimum requirement recommended in [13]. The overall amounts of grids were 1.08×10^7 and 8.6×10^6 for airfoils with and without wavy leading edge, respectively.

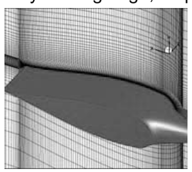

Fig. 2 Illustration of a slice of the computational mesh

The numerical work was validated using previous experimental results [5, 14]. To this end, four angles of attack (α) were selected, i.e., 6°, 12°, 18° and 21°, and the free-stream velocity U_∞ and Re_c were 30m/s and $Re_c=2\times10^5$, respectively. In addition, The time step was set to 1.667×10^{-5}s, and the solution proceeded until 0.1s. The variations of lift and drag coefficients with α are displayed in Figure 3. It could be observed that the computational results were in good agreements with experimental results within pre-stall regime and their difference was only within 5%.

Within the post-stall region, the wavy airfoils exhibited improved aerodynamic characteristics, resulting in the maximum 54.5% increase in C_l [5]. Nevertheless, C_l seemed to be around 0.88 around the stall region for modified airfoil, which was at most 15% lower compared with the baseline case. Furthermore, C_d was at most 50% higher within the same interval.

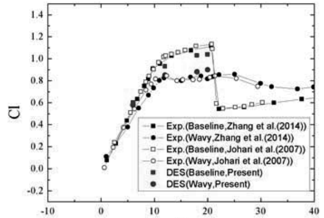

(a) Lift coefficient

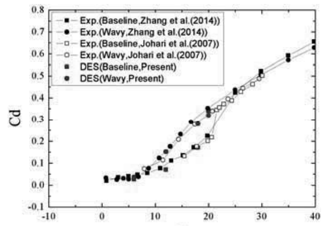

(b) Drag coefficient

Fig. 3 Variations of lift and drag coefficients with α

3. Results and Discussions

3.1 Mechanisms of Bi-periodic Phenomenon

For airfoil with wavy leading-edge, the processes of vortex evolution were rather complicated. Figure 4 gives the corresponding instantaneous flow structures after they became stable. At α =6°, the flow pattern was periodic from one trough to the next (Figure 4a). It could be observed that vortices migrate towards troughs, causing a coalescence of fluid between protuberance peaks near the airfoil leading edge and then dissipation towards the trailing edge.

Nevertheless, at α =12°, the flow pattern was no longer periodic and the bi-periodic phenomenon appeared, as shown in Figure 4b. The fact that vortices dispersed at one trough as soon as it left the leading edge indicated that there was flow interaction between neighboring troughs. At the neighboring trough, vortices were confined to the valley of current trough and this flow pattern repeatedly appeared in spanwise direction. The processes of vortex evolution were similar at α =18° and 21°, as shown in Figure 4c and Figure 4d, and the non-equilibrium between neighboring troughs became more obvious. Consequently, it could be inferred that the occurrence of bi-periodic phenomenon was highly related to α, consistent with the finding in [7]. For convenience, the trough where vortices dispersed was named trough-A, and the neighboring trough was named trough-B (Figure 4c).

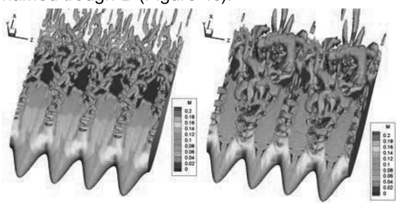

(a) α=6° (b) α=12°

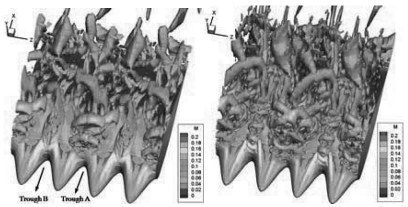

(c) α=18° (d) α=21°

Fig. 4 Sketches of instantaneous flow structures of airfoil with leading-edge protuberances

To further clarify the bi-periodic flow over the airfoil suction side, we took the case at α =18° for example. Correspondingly, four typical time instants were selected, i.e., T0, T1, T2 and T3, to depict the whole process of vortex evolution. At T0 (=0.0067s after the beginning of IDDES iterations), no difference on the flow patterns between neighboring troughs existed, and flow structures were almost the same at neighboring troughs (Figure 5). F, N and S represented focus, node and saddle here.

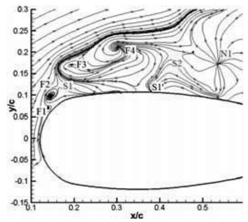

a) Distribution of streamlines at trough-A

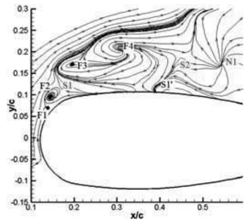

b) Distribution of streamlines at trough-B

Fig. 5 Distribution of streamlines and topological structures at T0

At T1 (=0.0071s), although the 3D vortex structures seemed to remain periodic, the difference between neighboring troughs emerged. Essentially, this was related with the variations in the boundary layer near the airfoil surface, indicated in Fig.6. Clearly, the topological structures of the separated flow around node N2 and saddle S1' (bounded by blue dashed lines) were different; moreover, the momentum convection at leading-edge was also affected. Actually, it could be observed that the 2D vortex structures corresponding to the vortex rings around leading-edge were different (bounded by red dashed lines). The development of follow-up vortices, especially the vortex rings above the suction surface, would be therefore affected.

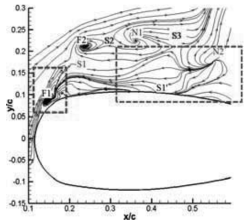

a) Distribution of streamlines at trough-A

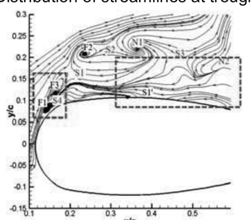

b) Distribution of streamlines at trough-B

Fig. 6 Distribution of streamlines and topological structures at T1

At T2, the condition deteriorated as shown in Figure 7a. The development of the vortex rings was severely affected and the single periodic pattern began to collapse. Along with the development of the vortex system, the difference between neighboring troughs enlarged. At T3 (=0.023s), the vortices from trough-A crossed the neighboring peak, and forced the fluid to squeeze into trough-B (Figure 7b), which led to an increase of velocity and a decrease of static pressure at trough-B.

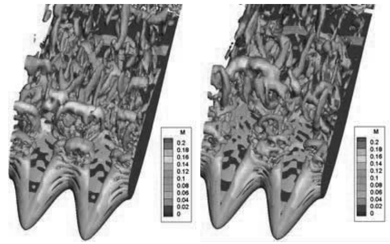

(a) t=T2 (b) t=T3

Fig. 7 Evolution of instantaneous flow structures of airfoil with leading-edge protuberances

To have an intuitive understanding, a slice in x-z plane (y/c=0.11) at T3 was demonstrated in Figure 8. Here static pressure was nondimensionalized by free-stream kinetic energy. Distinctions between trough-A and B could be recognized. In detail, the distribution of Mach number around mid-span was different, which indicated that flow with higher momentum got into the valley of trough-B (bounded by red dashed lines). In the meantime, the difference of pressure distribution emerged in the same area (bounded by blue dashed lines). Once the balance between neighboring troughs was broken, the non-equilibrium was gradually exacerbated. Eventually, bi-periodic pattern was reached as shown in Figure 4c.

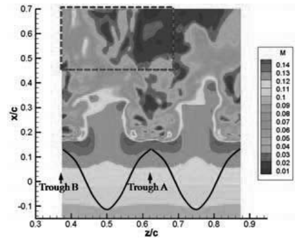

(a) Distribution of Mach number

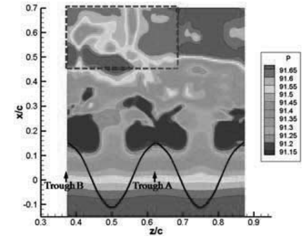

(b) Distribution of static pressure

Fig. 8 Distributions of Mach number and static pressure at y/c=0.11

3.2 Effects of Bi-periodic Phenomenon on Aerodynamic Performance

Although the aerodynamic performance of modified airfoil is better than the baseline one within post-stall region, lift degradation is inevitable around stall region. To further optimize the aerodynamic performance, it is necessary to clarify the mechanism of the lift degradation.

Figure 9 shows the typical profiles of the normalized mean streamwise velocity at α =18° for wavy airfoil; Note the velocity profiles for smooth and peak cases were coincident with the experimental results in [5], validating the accuracy of present simulation again.

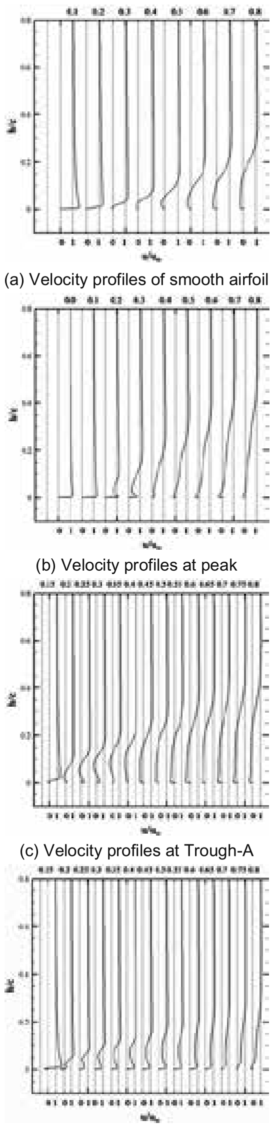

(a) Velocity profiles of smooth airfoil

(b) Velocity profiles at peak

(c) Velocity profiles at Trough-A

(d) Velocity profiles at Trough-B

Fig. 9 Velocity profiles of smooth and modified airfoils

For smooth airfoil, the flow separation evidently occurred at x/c=0.3. Although the instantaneous vortex structures at peak were rather complicated as shown in Figure 4, the velocity profiles were quite simple in time-averaged form. Compared with the results of smooth airfoil, the occurrence of reversed flow moved backward to a location between x/c=0.4 and x/c=0.5.

In addition, bi-periodic phenomenon was clearly reflected in the mean velocity profiles at troughs. The distinctions between trough-A and B were obvious (Figure 9c and 9d). At trough-A, flow separation occurred near the leading edge. To the contrary, flow separation occurred near x/c=0.15 at trough-B, and then reattachment took place at x/c=0.3. However, flow reattachment did not stick to the trailing edge and the reversed flow clearly appeared once more near x/c=0.75. Evidently, the massive flow separation at troughs probably imposed negative effects on aerodynamic lift and it tended to be more significant for trough-A case.

The flow field for the airfoil with leading-edge protuberances would lead to the corresponding variable aerodynamic characteristics of C_l and C_d within stall region in Fig. 3. To prove this, Figure 10 illustrates the distributions of pressure coefficients along x-direction. In general, compared with the results of smooth airfoil, aerodynamic suction decreased due to the massive flow separation at troughs. Furthermore, bi-periodic phenomenon aggravated the lift degradation, which removed the aerodynamic suction at the leading-edge of trough-A, especially at α = 18° and 21°. This conclusion was coincident with the analyses of velocity profiles. Meanwhile, above mechanisms also increased the static pressure at the leading edge, which consequently enlarged the pressure drag. The aerodynamic drag increment around stall region could thus be somehow interpreted [5].

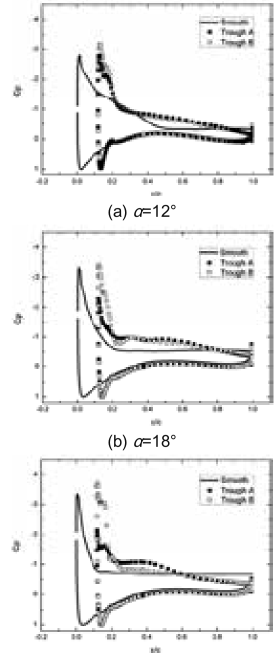

(a) α=12°

(b) α=18°

(c) α=21°

Fig. 10 Distributions of pressure coefficient along x-direction

Together with above results, the flow physics was analyzed using 3D time-averaged static pressure and streamline (α =18°), illustrated in Fig.11. Flow separations at leading edge were indicated by blue dashes; meanwhile, flow attachments around the centerlines of peaks were also indicated by red dashes. Bi-periodic phenomenon could be distinguished in an intuitive way. In detail, flow separation was more severe at the leading edge of trough-A than that of trough-B; consequently, aerodynamic suction almost vanished around trough-A, which was coincident with Fig.10b. Meanwhile, the flow attachment carried higher momentum flow into boundary layer, which delayed the flow separation around peaks as shown in Fig.9b. Consequently, it could be inferred that peaks provided a large portion of the aerodynamic lift.

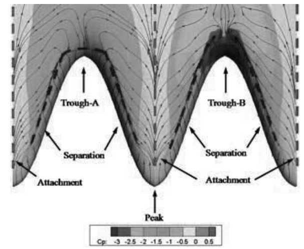

Fig. 11 Distribution of static pressure and streamlines (α=18°)

In addition, as shown in Fig.3, The variation range of C_l around stall region was within 6%, which was a favorite feature for wind turbine blade since the stall tended to be rather gentle. To understand this, Fig.12 gives C_l -distributions along z-direction, and it could be inferred that the lift coefficients of α = 18° and 21° were approximately equal to 0.88 in consideration of the contributions of those spanwise sections (i.e., Peak, Middle, Trough-A and Trough-B), and they were a little higher than that of α = 12°. Evidently, peaks contributed a large portion of the aerodynamic lift, which was consistent with the analyses of Fig.11.

Then the lift coefficients of those spanwise sections at α = 18° and 21° were analyzed in detail. The variation tendencies of local lift coefficients around peaks and troughs were opposite, which could be interpreted by local flow conditions around them. In detail, as flow was mostly attached at peaks, lift coefficients increased as angle of attack increased. To the contrary, flow separation dominated the flow field around troughs, therefore the degradation of lift coefficients deteriorated along with the increase of angle of attack. Meanwhile, the influence of bi-periodic phenomenon certainly extended to the middle sections, as the variation tendencies of the lift coefficients of the middle sections around peak were opposite. In general, these variations in the flow patterns led to little change in total C_l around stall region.

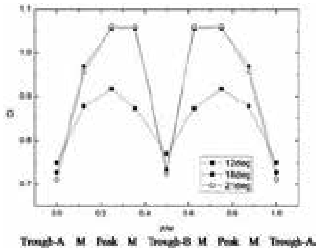

Fig. 12 Distributions of lift coefficient along z-direction

4. Conclusions

A numerical investigation of the aerodynamic performance of an NACA 63_4-021 airfoil with leading edge protuberances and its smooth counterpart was presented at a low Re_c of 2.0×10^5. The associated flow field and the inherent physics were analyzed in detail. These led to the following conclusions:

1) Within the stall region, C_l seems to be around 0.88 for modified airfoil, which was at most 15% lower compared with the baseline case. Furthermore, C_d was at most 50% higher within the same region.

2) The vortex evolution and thus the physics of the dominant bi-periodic phenomenon were uncovered. In addition, it was found that bi-periodic phenomenon imposed considerable influence on aerodynamic performance. Compared with the troughs where vortices converged, the negative effects of the flow separation at the troughs where vortices diverged were more remarkable.

3) The variation range of C_l around stall region was within 6%, which was a favorite feature for wind turbine blade since the stall tended to be rather gentle. In addition, the inherent physics were discussed through analyses of flow patterns.

5. Future works

1) Present study concentrated on the analyses of the control physics of bionic airfoil. Furthermore, The application of this technique on wind turbines will be attempted in the near future.

2) The study also suggested that the aerodynamic performance were probably affected by flow conditions (for example Re_c) and geometrical shape of the protuberances. A straightforward extension of present work is an evolution of the influences of above factors on the aerodynamic performance of a modified airfoil.

6. Acknowledgments

This work was supported by the National Natural Science Foundation of China (Grant No. 51222606 and 51506201) and National High-tech R&D Program of China (863 Program) (Grant No. 2012AA051303).

References

[1] Fish FE, Battle JM. "Hydrodynamic Design of the Humpback Whale Flipper". Journal of Morphology 1995; 225:51–60.

[2] Bellequant LLC, Howle LE. "Whalepower wenvor blade. A report on the efficiency of a whalepower corp. 5 meter prototype wind turbine blade". Canada Whalepower Co., 2009.

[3] Michael DB, Richard MK, Maziar, A. "A Review of Tubercles and Their Applications". Journal of Aerospace Engineering; in press.

[4] Malipeddi AK, Mahmoudnejad N, Hoffmann KA. "Numerical Analysis of Effects of Leading-Edge Protuberances on Aircraft Wing Performance," Journal of Aircraft 2012; 49(5):1336-1344.

[5] Zhang MM, Wang GF, Xu JZ. "Experimental Study of Flow Separation Control on a Low-Re Airfoil using Leading-Edge Protuberance Method". Experiments in Fluids 2014; 55:1710.

[6] Pedro HTC, Kobayashi MH. "Numerical Study of Stall Delay on Humpback Whale Flippers". 46th AIAA Aerospace Sciences Meeting and Exhibit 2008.

[7] Custodio D. "The Effect of Humpback Whale-Like Leading Edge Protuberances of Hydrofoil Performance". M.S. Thesis, Worcester Polytechnic Institute 2007.

[8] Dropkin A, Custodio D, Henoch CW, Johari H. "Computation of Flowfield Around an Airfoil with Leading-Edge Protuberances". Journal of Aircraft 2012; 49(5):1345-1355.

[9] Shur ML, Spalart PR, Strelets MK, Travin AK. "A hybrid RANS-LES Approach with Delayed-DES and Wall-Modeled LES Capabilities". International Journal of Heat and Fluid Flow 2008; 29:1638-1649.

[10] Camara JFD, Sousa JMM. "Numerical Study on the Use of a Sinusoidal Leading Edge for PassiveStall Control at Low Reynolds Number". 51st AIAA Aerospace Sciences Meeting and Exhibit 2013.

[11] Fu S, Wang L. "RANS Modeling of High-Speed Aerodynamic Flow Transition with Consideration of Stability Theory". Progress in Aerospace Sciences 2013; 58:36–59.

[12] Xiao Z, Jian L, Luo K, Huang J, Fu S. "Investigation of Flows Around a Rudimentary Landing Gear with Advanced Detached-Eddy-Simulation Approaches". AIAA Journal 2013; 51(1):107-125.

[13] Spalart PR. "Young-Person's Guide to Detached-Eddy Simulation Grids". NASA/CR-2001-211032.

[14] Johari H, Henoch C, Custodio D, Levshin A. "Effects of Leading-Edge Protuberances on Airfoil Performance". AIAA Journal 2007; 45(11):2634-2642.

Design and CFD-based Performance Verification of a Family of Low-Lift Airfoils

Panagiotis K. Chaviaropoulos[1], tchaviar@fluid.mech.ntua.gr
George Sieros[2], gsieros@cres.gr
John M. Prospathopoulos[1], jprosp@fluid.mech.ntua.gr
Konstantinos Diakakis[1], diak@fluid.mech.ntua.gr
Spyros G. Voutsinas[1], spyros@fluid.mech.ntua.gr

[1]National Technical University of Athens, 9 Heroon Polytechniou, 15780, Zografou, Athens, Greece
[2]Centre of Renewable Energy Sources and Saving, 19th km Marathonos Ave., 19009, Pikermi, Greece

Abstract:

The design methodology and performance verification of a family of low lift airfoils is presented in this paper. High performance low lift profiles are well suited to low power density rotor designs. Such designs are suitable for increasing the energy yield of mufti-MW offshore wind turbines using larger diameter rotors under moderate loading conditions. For the design of the profiles numerical optimization techniques are used for maximizing a suitable performance–based cost function which is evaluated using XFOIL. The resulting shapes are assessed by means of high fidelity CFD tools. The main uncertainty characterizing the performance of such profiles, at the relative low flow angles where the maximum performance occurs, comes from transition modelling. This uncertainty is even higher at the very large Reynolds numbers encountered in the 10+ MW rotors of our interest. To handle the uncertainty our design options are selected on the conservative side.

Keywords: Airfoil design, low lift profiles, airfoil performance verification.

1 Introduction

In the framework of INNWIND.EU FP7 Project CRES and NTUA investigate the potential of low-induction rotors (LIR) in improving the energy yield of large offshore turbines and reducing the cost of electricity produced. As discussed in [1] and [2] the best way to implement the LIR concept is by using low-lift airfoils, e.g. airfoils having their maximum $k = C_L/C_D$ at moderate $C_{L\text{-}DES}$ (design C_L) values. It is not straightforward, however, to get a high performance, thick enough, airfoil with k values 100+, which is a normal achievement for the high lift airfoil families. This difficulty is increasing as $C_{L\text{-}DES}$ gets smaller. The design and performance verification, with state of the art CFD, of such a family of low lift profiles aiming to operate in the range or Reynolds and Mach numbers corresponding to a 10MW LIR is the scope of the present work.

2 Design methodology

The airfoils are parameterized using Bezier curves with 9-12 control points for representing the complete shape in one piece. The trailing edge thickness is directly set, while the position of maximum thickness and the maximum thickness are controlled through the Bezier parameters. The number of control points was chosen so that the resulting representation could reproduce well-known families (NACA, FFA) with less than 0.5% RMS error.

The objective of the design is the maximization of the airfoil performance (lift over drag) within a desired range of lift coefficients. This can be expressed as

$$Maximize\left[\int_{C_{LDES1}}^{C_{LDES1}}\left\{W_l\left(\frac{C_L}{C_D}\right)_l + W_t\left(\frac{C_L}{C_D}\right)_t\right\}dC_L\right]$$

$$W_l + W_t = 1$$

where [C_{LDES1}, C_{LDES2}] is the range of the design lift coefficient, centred around the actual design point and Wl, Wt are the laminar and turbulent flow weights. The reason for performing the optimisation for more than a single C_L value is to avoid degenerate solutions that display a rapid drop in performance when this value is exceeded. In addition, with this general objective functions we can optimize the weighted airfoil performance at both transitional and fully turbulent flow conditions.

The constraints on the design are imposed through the available range of movement for the control points. The main parameters that are affected are

- Trailing edge thickness (which is fixed at the original value)
- Maximum thickness (specified for each design)
- Maximum thickness location (allowed to shift, but retaining a basic similarity between the airfoil shapes for different thicknesses)

The optimizer used employs a combination of evolutionary and gradient-free methods. The latter are used for the final convergence once the evolutionary method has reached a minimum The direct solver used for the calculation of the objective function is XFOIL, but the results are later assessed using higher fidelity flow solvers.

3 Application on the Design of Low Lift Profiles

3.1 Design specifications

Table 1 shows the operating conditions at different blade sections of a LIR version of the 10MW Reference Wind Turbine of INNWIND.EU. The relative thickness of the airfoils along the original blade span varies from 60% in the near-root section to 21% at the tip. Next to the relative thickness we present the Reynolds and Mach numbers at rated conditions as well as their minimum value within the turbine operating envelope. Since the same airfoil is used at different spanwise locations there are multiple rows in the table sharing the same thickness. From those we select the highlighted rows as the operating conditions.

Following our earlier conclusions of [1] and [2] the low lift airfoils shall be designed for C_{LDES} = 0.8, instead of C_{LDES} =1.2 to1.3 which is the normal range for high lift profiles. To avoid deep minima (a highly optimized objective function which rapidly deteriorates when the design variables are slightly perturbed) that characterize single point designs, we shall design the airfoils for a maximum mean performance within a range of design lift coefficients C_{LDES} =[0.7 to 0.9] instead of using the single C_{LDES} =0.8 value.

An important issue for the design specifications is the way one handles transition. We are referring to designs at very high Reynolds numbers and, therefore, a back-loaded laminar airfoil may perform significantly better than a front-loaded one which better suits fully turbulent flows. On the other hand it is known that the performance of laminar airfoils may become very poor when the flow is tripped to turbulent. But even if a good part of laminar flow exists over the airfoil it is quite uncertain how the high turbulence content of the atmospheric boundary layer will influence the transition location through the bypass mechanism. To introduce some conservatism in our designs we are optimizing the airfoil shapes for their weighted transitional / fully turbulent performance as described in section 3.2 below.

Section Thickness	Re (rated)	Ma (rated)	Re (Min)	Ma (Min)
60.00%	7.0×10^6	0.05	4.4×10^6	0.03
40.10%	11.0×10^6	0.07	7.0×10^6	0.05
35.00%	14.0×10^6	0.09	9.0×10^6	0.06
30.00%	17.0×10^6	0.12	10.0×10^6	0.07
24.00%	20.0×10^6	0.16	12.0×10^6	0.10
24.00%	16.0×10^6	0.25	11.0×10^6	0.15
24.00%	13.0×10^6	0.30	8.0×10^6	0.18
21.00%	20.0×10^6	0.16	12.0×10^6	0.10
21.00%	16.0×10^6	0.25	11.0×10^6	0.15
21.00%	13.0×10^6	0.30	8.0×10^6	0.18
18.00%	16.0×10^6	0.25	11.0×10^6	0.15
15.00%	16.0×10^6	0.25	11.0×10^6	0.15

Table 1: Intended thickness and operating conditions

The transition model used in our analysis is the XFOIL built-in e^N where N is the critical amplification factor. For conservatism we shall use in our transitional calculations N=4 corresponding to high ambient turbulence flow conditions (N=9 is the usual choice for natural transition).

3.2 Designed airfoils

Following the design specifications of Table 1 we produced low-lift profiles with relative thicknesses 15%, 18%, 21%, 24%, 30% and 40%. With the exception of the two ending family members (15% and 40%) where a single low-lift airfoil was designed, we generated for all other thicknesses two low-lift profiles of different laminar / turbulent flow weighting.

The laminar / turbulent weighting was set to 30%-70% (denoted as 30-70 from this point on) for the first low-lift and to 10-90 (or 20-80 for the thicker members) for the second family. Figure 1 shows the 30-70 low-lift family and Figure 2 the10-90/20-80 one.

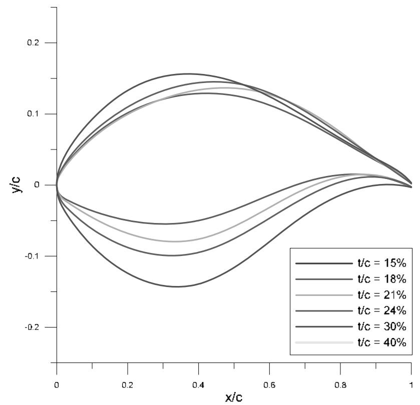

Figure 1: The 30-70 family of Low Lift profiles

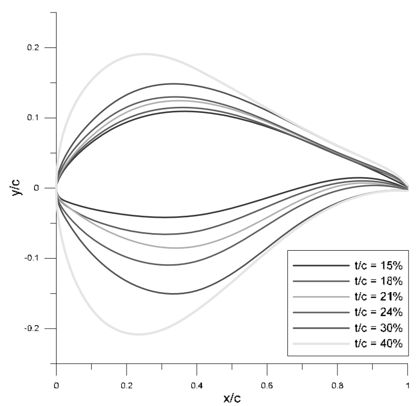

Figure 2: The 10-90/20-80 family of Low Lift profiles

Figure 3 shows the aerodynamic performance of the two families at fully turbulent flow conditions. Clearly the 30-70 is performing slightly worse than the "more conservative" 10-90/20-80 one at the design lift value of our interest. In all cases, with the exception of the 40% airfoil, L/D at the design lift coefficient exceeds 70 units even for the 30% thick profile.

On the contrary, the 30-70 family is performing better (some members like the 21% and 24% much better) that the 10-90 one when the flow is transitional. Figure 4 demonstrates the statement with calculation done for N-factor equal to 4. It is also seen that in all cases (with the exception of the 40% profile) the performance of the airfoils at design lift exceeds 120 units, even for 30% thickness.

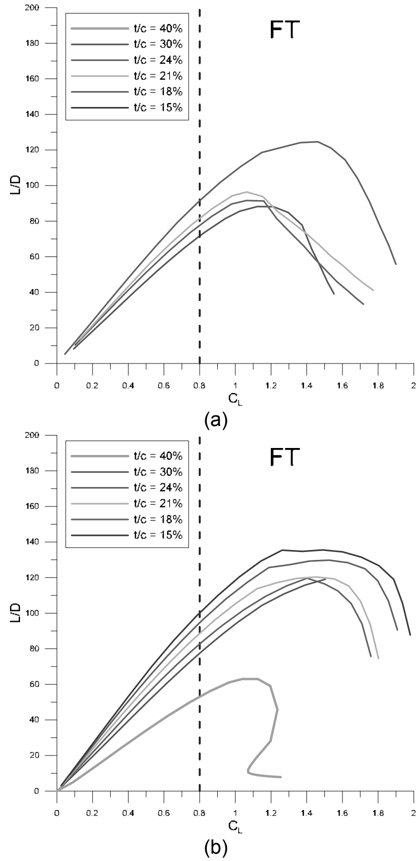

Figure 3: Performance (L/D) of the Low Lift family profiles at fully turbulent flow conditions. (a) the 30-70 and (b) the 1(2)0-9(8)0

Using a higher weight for the laminar part the maximum thickness of the profile is moving backwards and its performance around the design point is increasing but at the same time worsens when the profile operates at fully turbulent conditions.

The 10-90/20-80 family looks more consistent, both geometrically (location of maximum thickness) and performance wise (changing monotonically with the thickness), than the 30-70 one. For the above reasons and for introducing further conservatism to the potential energy capture gains we shall focus our further attention on the 10-90/20-80 family only.

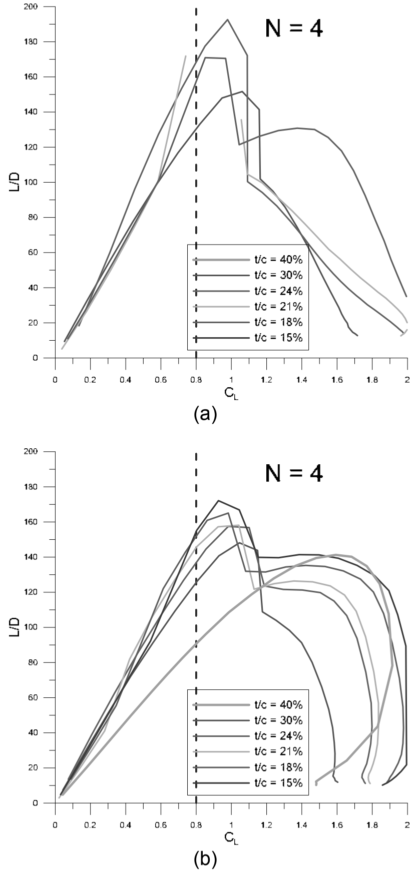

Figure 4: Performance (L/D) of the Low Lift family profiles for transitional (N=4) flow conditions (a) the 30-70 and (b) the 1(2)0-9(8)0

4 Numerical Simulation of the Designed Airfoils

4.1 Numerical Tools

In order to verify the performance of the low lift 10-90/20-80 profiles, simulations for fully turbulent and transitional flow conditions are performed using the MaPFlow [3] and Foil2w [4] in-house numerical solvers developed at NTUA. Both methods have been successfully applied to the simulation of FFA airfoils at high Reynolds numbers, in the context of the benchmarking of aerodynamic models, included in the Deliverable 2.2.1 of the INNWIND.EU project [5].

MaPFlow: MaPFlow is a multi-block MPI enabled compressible solver equipped with preconditioning at low Mach numbers. The discretization scheme is cell centred and makes use of the Roe approximate Riemann solver for the convective fluxes. The scheme is second order accurate in space and time and applies the Venkatakrishnan's limiter [6] defined for unstructured grids. Dual time stepping has been introduced for facilitating convergence. The solver is equipped with the Spalart-Allmaras (SA) and the k-ω SST eddy viscosity turbulence models.

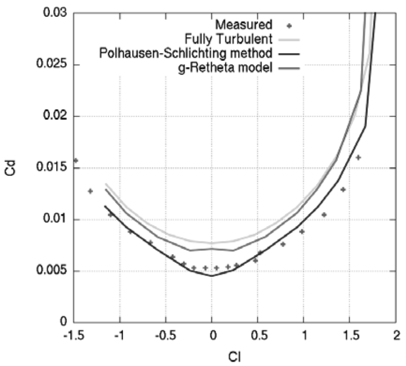

Figure 5: Predictions of the NACA 63-418 C_D polar by the Granville/Schlichting and the γ-Reθ models using the MaPFlow solver. Reynolds number is $20 \cdot 10^6$

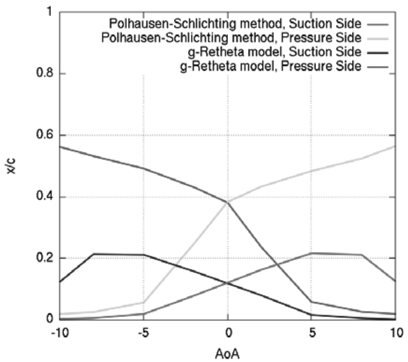

Figure 6: Predictions of the NACA63-418 transition locations by the Granville/ Schlichting and the γ-Reθ models using the MaPFlow solver. Reynolds number is $20 \cdot 10^6$

Two transition models have been implemented in MaPFlow, the correlation γ-Re_θ model of Menter [7] and the Granville/ Schlichting transition method described in [8]. The first is a two transport equation model for the intermittency and the momentum thickness Reynolds number. It utilizes local variables easily computed in each cell and does not need boundary layer definition and parameters. The second one is based on boundary layer characteristics expressed in terms of the Polhausen variables. In order to estimate these variables, the velocity on the edge of the boundary layer is computed using the pressure coefficient value on the viscous wall derived by the RANS solver. The instability and transition points are then defined using empirically calibrated diagrams proposed by Granville.

Simulations using MaPFlow have shown that the Granville/ Schlichting method gives better predictions of the drag coefficient compared to the γ-Re_θ model (Figure 5) for high Reynolds numbers ($Re > 3{\cdot}10^6$). This results from the fact that transition is predicted at different locations by the two models as shown in Figure 6. Therefore, the Granville/ Schlichting is adopted for the present simulations. Fully turbulent simulations are performed using the k-ω SST model.

The numerical mesh is an O-type grid of 104000 elements, 520 around the airfoil and 200 in the normal to the wall direction, generated using the ICEMCFD ANSYS software. The non-dimensional distance of the first node from the wall is less or equal to 10^{-5}, resulting in $y^+<1$. Steady state simulations are performed for the whole angles of attack AOA range.

Foil2w: Foil2w is a viscous-inviscid interaction code. The potential flow part is simulated by singularity distributions along the airfoil geometry and the wake. The wake is represented by vortex particles which are allowed to freely move with the local flow velocity. The viscous flow solution is obtained by solving the unsteady integral boundary layer equations. The coupling of the two sets of equations is achieved through a transpiration velocity distribution along the airfoil surface that represents the mass flow difference over the boundary layer height between the real viscous flow and the equivalent inviscid flow.

The boundary layer equations are discretized using finite differences and the final set of the non-linear equations are solved simultaneously using the Newton-Raphson algorithm. The boundary layer solution is supplemented by a transition prediction model based on the e^N spatial amplification theory and by a dissipation closure equation for the maximum shear stress coefficient over the turbulent part.

4.2 Performance Verification of the Designed Airfoils

Performance (L/D) results for the 18% airfoil are presented In Figure 7. At transitional flow conditions, all models predict considerably high values around the design point C_{LDES}=0.8, ranging between 135 and 150. MaPFlow predictions using the Sclichting-Polhausen transition model seem to be the most conservative ones, predicting the lowest performance. At fully turbulent flow conditions, a lower performance around the design point C_{LDES}=0.8 is expected. Indeed, performance reduces considerably ranging between 85 and 95, but still remains at high levels. It must be noted that there is a significant divergence among the predictions of the different models in the range $0.8<C_L<1.4$ which corresponds to the linear region (2^o<AOA<8^o). This suggests that a different slope of the C_L-AOA curve is predicted in that region.

The performance of the designed airfoil decreases with thickness as expected (Figure 8 to Figure 10). For the 30% 20-80 airfoil the performance predictions have dropped to 115-125 in transitional flow, and to 65-75 in fully turbulent flow (Figure 10). This implies a total performance reduction of 16%-21% and 23%-25% at the design point for transitional and fully turbulent conditions respectively. However, the fact that the performance levels remain greater than 100 for transitional conditions, demonstrates the high efficiency of the designed low lift airfoil family.

Figure 7 to Figure 10 also indicate that the predicted differences between fixed and free transitional flow at the design point C_{LDES}=0.8 reduce with thickness. For the 30% thickness no significant difference can be observed in the MaPFlow predictions.

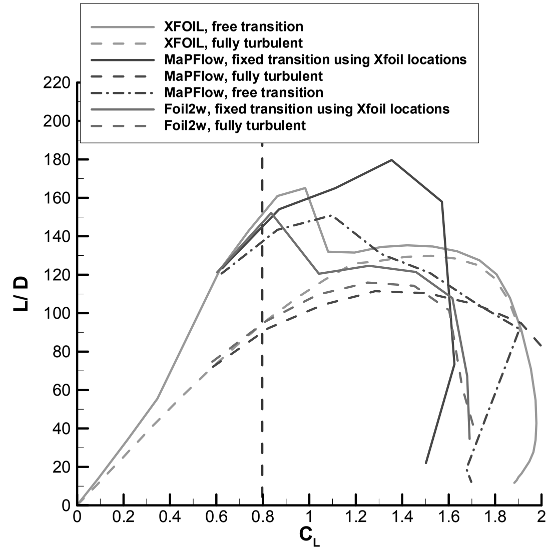

Figure 7: Performance (L/D) of the 18% Low Lift 10-90 airfoil for transitional and fully turbulent flow conditions. Comparison among MaPFlow (CFD solver), Foil2w (viscous-inviscid interaction solver) and XFOIL calculations. Fixed transition locations were taken from XFOIL using the e^N model with N=4

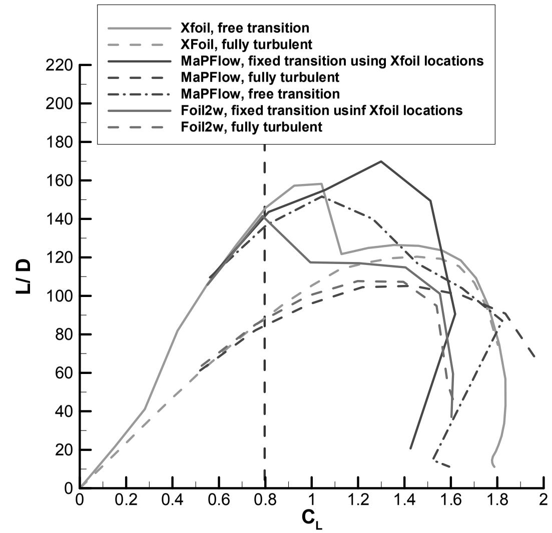

Figure 8: Performance (L/D) of the 21% Low Lift 10-90 airfoil for transitional and fully turbulent flow conditions. Comparison among MaPFlow (CFD solver), Foil2w (viscous-inviscid interaction solver) and XFOIL calculations. Fixed transition locations were taken from XFOIL using the e^N model with N=4

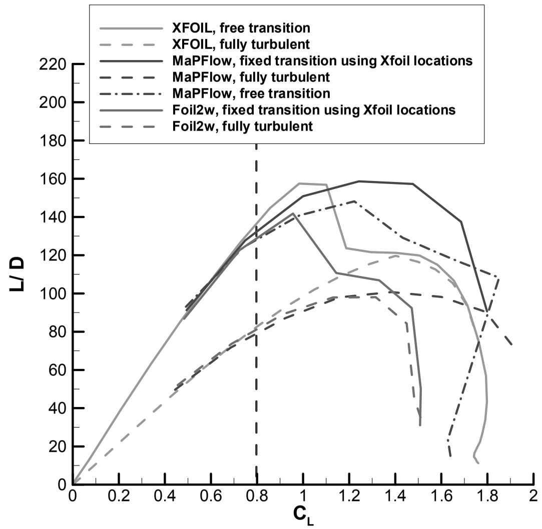

Figure 9: Performance (L/D) of the 24% Low Lift 10-90 airfoil for transitional and fully turbulent flow conditions. Comparison among MaPFlow (CFD solver), Foil2w (viscous-inviscid interaction solver) and XFOIL calculations. Fixed transition locations were taken from XFOIL using the e^N model with N=4

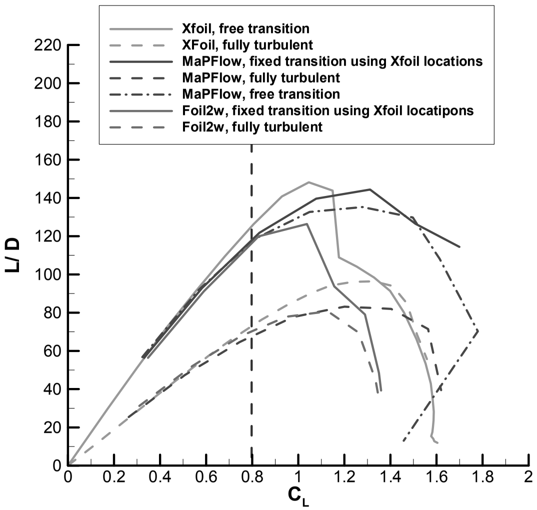

Figure 10: Performance (L/D) of the 30% Low Lift 10-90 airfoil for transitional and fully turbulent flow conditions. Comparison among MaPFlow (CFD solver), Foil2w (viscous-inviscid interaction solver) and XFOIL calculations. Fixed transition locations were taken from XFOIL using the e^N model with N=4

5 Conclusions

A design method for producing low lift airfoil profiles was developed and applied to the different blade sections of a LIR version of the INNWIND.EU Reference Wind Turbine, at specific operating conditions.

Two low-lift profile families were designed, with relative thicknesses ranging from 15% to 40%. The low-lift families differ in the laminar / turbulent weighting which is driving the design. Using a higher weight for the laminar part the maximum thickness of the profile is moving backwards and its performance around the design point increases but at the same time worsens when the profile operates at fully turbulent conditions. In the present work the weighting was set to 30%-70% for the first low lift family and to 10-90 (or 20-80) for the second.

The 10-90/20-80 family looks more consistent, both geometrically (location of maximum thickness) and performance wise (changing monotonically with the thickness). For these reasons and for introducing some conservatism to the possible energy capture gains of the low induction rotor this family has been selected for low induction INNWIND.EU 10 MW rotor design.

The performance of the selected low lift airfoils was verified using a CFD and a viscous-inviscid interaction solver. Both solvers predict high performance levels at the design point C_{LDES}=0.8. For the 18% airfoil the predicted performance is higher than 135 and 85 in transitional and turbulent flow conditions respectively. For the 30% airfoil the predicted performance decreases but still remains higher than 100 and 60 in transitional and fully turbulent conditions respectively.

Using the 10-90/20-80 polars calculated with CFD we proceeded to the aerodynamic design of a 10MW LIR in the framework of the INNWIND.EU project. Compared to the 10MW Reference Wind Turbine of the project [9] the LIR yield (capacity factor CF) was 7.5% higher. From that 4.5% is attributed to the LIR planform and the remaining 3% from the dedicated low lift profiles that replaced the high lift FFA-W3-xx (same thickness) profiles of the reference.

Acknowledgment

The research leading to these results has received funding from the European Community's Seventh Framework Program-me under grant agreement No. 2012-308974 (INNWIND.EU).

References

[1] New aerodynamics rotor concepts specifically for very large offshore wind turbines", Edited by H.A. Madsen, L. Bergami and F. Rasmussen. INNWIND.EU D2.11 Deliverable, Sept 2013.

[2] Chaviaropoulos PK, Sieros G, "Design of Low Induction Rotors for use in large offshore wind farms", Proc. Scientific Track, EWEA 2014, Barcelona"

[3] Papadakis G. and Voutsinas S.G, "In view of accelerating cfd simulations through coupling with vortex particle approximations" in: The Science of Making Torque from Wind *Journal of Physics: Conference Series*, IOP Publishing Copenhagen pp. 012126, 2014.

[4] Riziotis V.A. and Voutsinas S.G, "Dynamic stall modelling on airfoils based on strong viscous–inviscid interaction coupling", *International Journal for Numerical Methods in Fluids*, 56 2 185-208, 2008

[5] Zahle F, Riziotis V., Bergami L., Madsen H.A., "Benchmarking of aerodynamic and aeroelastic models", Part B of Deliverable 2.2.1 of INNWIND.EU project, Contract No. 308974.

[6] Venkatakrishnan V., "On the accuracy of limiters and convergence to steady state solutions", *AIAA* Paper 93-0880, 1993

[7] Langtry RB, Menter FR, "Correlation-Based Transition Modeling for Unstructured Parallelized Computational Fluid Dynamics Codes", *AIAA* Journal, Vol. 47, No. 12, December 2009

[8] Schlichting H: "*Boundary Layer Theory*", McGraw-Hill, 1968.

[9] Bak C., Zahle F., Bitsche R., Kim T., Yde A., Henriksen L.C., Andersen P.B., Natarajan A., Hansen M.H.: "Design and performance of a 10 MW wind turbine", J. Wind Energy, To appear.

Aerodynamic analysis of 10 MW-class wind turbine using CFD

Ryo Yamada*, Keiichi Murakami, Atsushi Hashimoto, Takashi Aoyama, Makoto Iida**, Yuichi Matsuo and Chuichi Arakawa

Ryo Yamada, Makoto Iida and Chuichi Arakawa
The University of Tokyo, 7-3-1 Hongo, Bunkyo-ku, Tokyo, 113-8656 Japan
Keiichi Murakami, Atsushi Hashimoto, Takashi Aoyama and Yuichi Matsuo
Japan Aerospace Exploration Agency, 7-44-1 Jindaijihigashimachi, Chofu-shi, Tokyo, 182-8522 Japan

Key Words: 10 MW-class wind turbine, Two-bladed rotor, CFD, BEM, Rotor aerodynamics

Abstract

To decrease blade mass for effectively reducing construction costs, the application of slender blades or two-bladed rotors to 10 MW-class wind turbines is proposed. Since few wind turbine designs have adopted this approach, it is important to investigate the effects of applying slender blades and two-bladed rotors. Considering this possibility and the relationship between the flow characteristics around the blade and the Reynolds number, it is useful to implement an aerodynamic analysis on actual-scale wind turbines using computational simulations such as blade element momentum (BEM) theory and computational fluid dynamics (CFD). In this study, we executed an aerodynamic analysis of two- and three-bladed 10 MW reference wind turbines proposed by the New Energy and Industrial Technology Development Organization. For the aerodynamic analysis, we used the fast CFD solver FaST Aerodynamic Routines (FaSTAR), which was developed by the Japan Aerospace Exploration Agency. First, we validated and confirmed rotor performance by comparing with the results obtained using BEM theory. The power and thrust coefficients (C_P and C_T) obtained by FaSTAR are generally in agreement with those obtained using BEM theory. These results suggest that rotor performance can be captured correctly by FaSTAR. Furthermore, the 3D effects caused by flow separation are seen only in FaSTAR. Regarding the difference in the number of blades, the values of C_P and C_T for the two-bladed rotor change more gradually than those for the three-bladed rotor. Moreover, the 3D effects around the root in two-bladed rotors are more significant than those in three-bladed rotors.

1. Introduction

Wind turbine rotor diameters have been upsized to increase power and utilize higher wind speeds for decreasing power costs[1]. Today, investigations on the realization of wind turbines with a rated power output of 10 MW are being undertaken[2][3]. When upsizing the diameter, blade mass and drive train mass increase, thereby increasing manufacturing costs. Some solutions to these problems are suggested as follows: use a slender blade and change its structure or material[2][4], increase the tip speed ratio (defined as the tip speed divided by the inflow speed) to decrease the load on the drive train, and reduce the number of blades by applying two-bladed rotors[3][5]. In particular, the application of two-bladed rotors is an effective solution because it can reduce both rotor mass and manufacturing costs. Furthermore, it can easily increase the tip speed ratio.

However, there are some problems with two-bladed rotors. For example, because they are inferior to three-bladed rotors in terms of their aerodynamic balance, they are more sensitive to yaw error and the atmospheric boundary layer (ABL). Furthermore, aerodynamic loads on the blades increase for two-bladed rotors. Thus, to apply a two-bladed rotor to a 10 MW-class wind turbine, investigating the effects that fewer blades would have on its aerodynamic characteristics is necessary. When considering the relationship between the flow characteristics and Reynolds number, investigations on full-scale wind turbines are desirable. However, implementing such experiments using actual wind turbines is difficult. Thus, the aerodynamic characteristics investigation using computational simulations such as blade element momentum (BEM) theory and computational fluid dynamics (CFD) is important.

BEM theory is widely used in the wind turbine industry because of its low computational costs and high accuracy. In BEM theory, the flow around the blade is considered 2D. However, the actual flow around the blade is 3D because of stall and flow separation. Moreover, the aerodynamic airfoil characteristics used in BEM theory are basically 2D. As a result, it is likely that rotor performance cannot be predicted precisely when a stall or flow separation occurs and the three-dimensionality of the flow becomes strong.

On the other hand, a CFD analysis can consider complex flow around the blade when it is governed by 3D governing equations. As a result, we can discuss the relations between rotor performance and flow around the blades using CFD. In addition, more detailed information about the flow around the blade can be obtained with CFD. Thus, it is worth evaluating the effects of applying a two-bladed rotor to a 10 MW-class wind turbine with CFD. Furthermore, few studies have focused on these problems so far.

This study contributes to the development of a 10 MW-class wind turbine by clarifying the aerodynamic characteristics of two- and three-bladed rotors in the ABL and with yaw error, which affects aerodynamic balance. As a first step of this study, we execute the CFD analysis under uniform inflow conditions for validating and confirming rotor performance by comparison with BEM theory results. Moreover, we discuss the merits of applying CFD to the aerodynamic analysis of 10 MW-class wind turbines. Besides, we examine the difference in aerodynamic characteristics between two- and three-bladed rotors.

*Presenting author. ** Corresponding author.
E-mail:
r.yamada@gg.cfdl.t.u-tokyo.ac.jp (Ryo Yamada)
iida@ilab.eco.rcast.u-tokyo.ac.jp (Makoto Iida)

2. Approach

2-1. Analysis object

As the analysis object in this research, we selected the New Energy and Industrial Technology Development Organization (NEDO) 10 MW reference wind turbine (RWT)[3], which was proposed as the reference for 10 MW-class offshore wind turbines by NEDO. The specifications for the NEDO 10 MW RWT are shown in Table 1. Two- and three-bladed rotor models are proposed. The rated tip speed and designed tip speed ratio of the two-bladed rotor model are greater than those of the three-bladed model. The blade shape for the two- and three-bladed rotor models are shown in Figure 1. As shown in the figure, the two-bladed rotor blade is more slender than the three-bladed rotor blade. Moreover, the distributions of airfoil profiles and twist angles along the blades are different in both rotor models. However, the Reynolds numbers based on the chord length in the blades are around 10^7 in both rotor models. Thus, it is assumed that the aerodynamic characteristics of the blade are quite similar. Also, at Reynolds numbers higher than about 10^6, there are few experimental results about the aerodynamic airfoil characteristics obtained in wind-tunnel tests. The three-bladed rotor model used in the CFD analysis is shown in Figure 2. In this analysis, we used rotor models without nacelles or spinners in order to generate computational grids more easily.

Table 1: Specifications for NEDO 10 MW RWT.

	Two-bladed	Three-bladed
Rotor position [-]	Upwind	
Rotor diameter [m]	200	
Number of blades [-]	2	3
Rated tip speed [m/s]	110	90
Designed tip speed ratio [-]	12.2	10
Airfoil profiles [-]	FFA-W3	

Figure 1: Blade shapes for NEDO 10 MW RWT[3] (Upper: three-bladed, Lower: two-bladed).

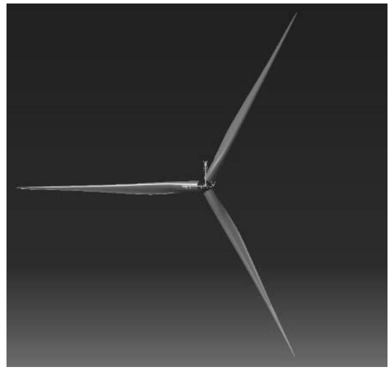

Figure 2: Three-bladed rotor model used in CFD.

2-2. BEM process

BEM can predict the rotor performance of wind turbines especially at the designed operational point. Hence, we used the BEM theory results to validate and confirm the CFD results. For BEM theory calculation, we used the FAST[6] code developed by the National Renewable Energy Laboratory. FAST is composed of many modules combining it to a full aeroelastic code. In FAST, the BEM calculation is carried out in the aerodynamic calculation (AeroDyn) module, which has been validated in many past studies. Thus, it is reliable to use the results obtained by FAST for validating and confirming rotor performance obtained by CFD. We mainly used the AeroDyn module as we focused on the aerodynamic analysis in this research.

When applying BEM theory to aerodynamic analysis, the relationship between the flow characteristics and Reynolds number must be considered for executing a highly accurate analysis.

The aerodynamic airfoil characteristics at a Reynolds number of about 10^7 are used, which is close to the Reynolds number for a rotating blade. Here, the Reynolds number is based on the chord length. In the aerodynamic analysis of ultra-large scale wind turbines, the aerodynamic airfoil characteristics obtained by 2D CFD analysis at a Reynolds number of about 10^7 are often used because there are few experimental results obtained in wind-tunnel tests at Reynolds numbers higher than about 10^6.

In this research, we used the aerodynamic airfoil characteristics cited on the DTU 10 MW RWT project site[7] for using with BEM theory. We used the 3D corrected data based on the 2D airfoil data, which are made by using the correction model[8]. The 2D CFD solver Ellipsys2D was used to create the 2D airfoil data. According to the DTU Wind Energy Report[9], the Reynolds numbers were chosen with representative values for each airfoil, ranging from 6×10^6 to 1.2×10^7. These values were chosen to correspond to the values for a rotating blade. The meshes were O-type meshes with 512 cells around the airfoil surface and 256 cells in the normal direction, and the resolutions are very fine. For this reason, it is assumed that mesh independence is ensured in this analysis. In addition, the 2D CFD analysis of FFA-W3 foils using C-type meshes with 256 cells around the airfoil at a Reynolds number of 1.6×10^6 shows good agreement with experimental results obtained at the same Reynolds number[10]. This results reinforces the assumption.

Two aerodynamic airfoil characteristics were available for each airfoil used on the NEDO 10 MW RWT. One was obtained with the $k-\omega$ SST model by assuming a fully developed turbulent boundary layer on the surface. Another was obtained using the $\gamma - Re_\theta$ correction-based model assuming a free transition from laminar to turbulent flow. There are fairly small differences between the fully turbulent and transition model. Moreover, it is natural to consider the flow as fully turbulent when the Reynolds number is about 10^7. Therefore, in this research, we used the results obtained for the fully turbulent model. More information about the 2D CFD analysis is available in the DTU Wind Energy Report.

2-3. CFD analysis code

When using CFD for the aerodynamic analysis of ultra-large scale wind turbines, it is desirable to use CFD solver, which has the ability to execute the analysis with a grid of about one billion cells. Moreover, it is important to use a parallel computation such as message passing interface (MPI) to lower computational costs.

In this research, we used the fast CFD solver FaST Aerodynamic Routines (FaSTAR)[11], which was developed by the Japan Aerospace eXploration Agency (JAXA). FaSTAR was developed for executing low-cost CFD analyses[12]. It can also use MPI for parallel computation. Moreover, when executing the computation on a supercomputer system, we can perform the analysis with a grid of around several billion cells.

The governing equations in FaSTAR are the compressible Navier–Stokes equations, which are discretized using a finite volume method (FVM). FaSTAR is an unstructured grid flow solver; hence, it can be used with HexaGrid[13][14], which was also developed by JAXA for generating unstructured grids automatically. Using HexaGrid with FaSTAR, fast preprocessing and CFD analysis can be accomplished. Consequently, we can shorten the total computation time effectively.

As an example of previous researches of wind turbines using FaSTAR, an aerodynamic analysis of the MexNext wind turbine rotor was executed[15]. This analysis was executed to clarify whether or not FaSTAR is applicable to aerodynamic analysis of wind turbines. In this analysis, the results including rotor performance and wake characteristics agreed closely with the experimental results. These results imply that we can predict the rotor performance and the flow characteristics around the blade precisely using FaSTAR. We basically used the same computational grid information and numerical analysis conditions used in the MexNext analysis.

2-4. Computational grid

Grid information from this research is shown in Table 2. The computational grids were generated by HexaGrid; the grid near the blade is prismatic, and the one for the far-field region is Cartesian. Denoting the rotor diameter as D, the analysis domain is $10D \times 10D \times 10D$, and the rotor is set at the center of the domain. We set the "refinement region" as 1D downstream from the rotor plane, where the grid is subdivided so that the resolution around the blade is sufficiently small. Denoting the chord length at $r/R = 0.8$ as c, the grid resolution on the blade is $0.022c$. Here, R is the rotor radius. We emphasize that the resolution along the span is the same as that along the chord. The height of the first cell on the blade is within $y^+ = 1$. The total number of cells is about 80 million in the three-bladed rotor case and 52 million in the two-bladed case. The computational grid around the three-bladed rotor is shown in Figure 3, and the grid around the airfoil at $r/R = 0.8$ is shown in Figure 4.

Table 2: Computational grid information.

Analysis domain	$10D \times 10D \times 10D$
Refinement region	$1.5D \times 1.5D \times 1.5D$
Resolution in the refinement region	$1.6c \times 1.6c \times 1.6c$
Resolution on the blade	$0.022c$
Height of the first cell on the blade	$y^+ \approx 1$
Total number of cells	52 M (two-bladed) 80 M (three-bladed)
Remarks	$D = 200$ m $c = 1.9$ m (at r/R=0.8)

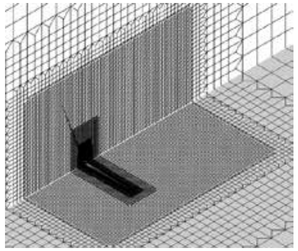

Figure 3: Computational grid around the three-bladed rotor.

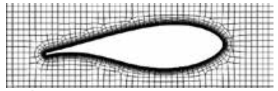

Figure 4: Computational grid around the airfoil at $r/R = 0.8$.

2-5. Numerical analysis conditions

The numerical analysis conditions in this research are shown in Table 3. We used the u-MUSCL scheme as the reconstruction method. Thus, the resolution in space is third-order for the uniform grid. The Spalart–Allmaras turbulence model with rotational correction is used as the turbulence model. The rotation of the rotor is represented by moving grids[16]. The analysis cases in this research are shown in Table 4. Here, λ is the tip speed ratio, which is defined by Eq. (1). U_∞ is the inflow velocity, R is the rotor radius, and Ω is the angular velocity of the blade rotation, respectively. The tip speed is constant, and the inflow speed is changed for changing λ. When decreasing λ, the angle of attack at the blade increases. The blade pitch angle is constant, whereas the power coefficient is maximum at the designed λ, shown in red in Table 4. The inflow velocity is about 9 m/s at the designed λ in both the two- and three-bladed rotor cases.

$$\lambda = \frac{R\Omega}{U_\infty} \tag{1}$$

Table 3: Numerical analysis conditions.

Governing equations	Reynolds-averaged Navier–Stokes equations
Space discretization	Cell-centered FVM
Inviscid flux	SLAU
Gradient	GLSQ
Limiter	Hishida's limiter
Reconstruction	u-MUSCL
Turbulence model	Spalart–Allmaras
Rotation of wind turbine	Moving grids
Time integration	LU-SGS
CFL number	1 (local time stepping)

Table 4: Analysis cases (designed λ is shown in red).

	Tip speed ratio λ [-]	Tip speed [m/s]
Two-bladed	5, 6, 7, 8, 9, 10.1, 11, 12.2, 13, 14, 15, 16	110
Three-bladed	4, 5, 6, 7, 8.3, 9, 10, 11, 12, 13, 14, 15	90

3. Analysis results

In this research, all computations were executed on JAXA Supercomputer Systems (JSS)[17] or JSS2 SORA (SORA: Supercomputer for earth Observation, Rockets and Aeronautics)[18]. The calculation time in each case was about 24 hours. The vorticity contour around the three-bladed rotor at $\lambda = 10$ is shown in Figure 5, as an example of the obtained results. The flow field around the rotor was captured in this image.

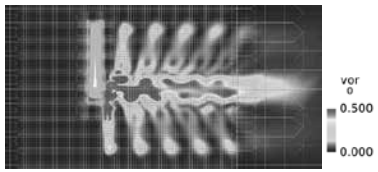

Figure 5: Vorticity contour of the three-bladed rotor at $\lambda = 10$.

3-1. Power/Thrust coefficients

The relationships between the power/thrust coefficients C_P/C_T obtained by FaSTAR or FAST and the tip speed ratio λ are shown in Figures 6 and 7, respectively. In these figures, the results obtained by FaSTAR are named "CFD", and those obtained by FAST are named "BEM." Also, "Two-bladed" and "Three-bladed" mean that the corresponding results were obtained in the two- and three-bladed rotor cases. The coefficients C_P and C_T are defined by Eqs. (2) and (3), respectively:

$$C_P = \frac{P}{\frac{1}{2}\rho U_\infty^3 \pi R^2} \quad (2)$$

$$C_T = \frac{T}{\frac{1}{2}\rho U_\infty^2 \pi R^2} \quad (3)$$

where P and T are the power and thrust of the rotor, respectively, and ρ is the density of the inflow.

As shown in Figure 6, the relationships between λ and C_P obtained by FaSTAR are similar to those obtained by FAST. In particular, the C_P values at the designed λ obtained by FaSTAR agree with those obtained by FAST. It is known that BEM theory has high rotor performance predictability near the designed λ. Thus, these results suggest that the rotor performance of 10 MW-class wind turbines can be predicted using FaSTAR.

As shown in Figure 7, the C_T values obtained by FaSTAR are larger than those obtained by FAST at the designed λ. However, the trends of varying C_T with changing λ obtained by FaSTAR agree with those obtained by FAST, and these results also suggest that the rotor performance of 10 MW-class wind turbines can be predicted using FaSTAR.

When focusing on the difference between the results obtained by FaSTAR and those obtained by FAST, both the C_P and C_T values obtained by FaSTAR are smaller than those obtained by FAST when λ is lower than the designed λ. In a 2D CFD analysis for FFA-W3 airfoils, Ellipsys2D overestimates the stall angle, and this tendency is more significant than in FaSTAR. Hence, it is assumed that the decrement of power and thrust in BEM theory occurs at the lower values of λ compared to the results obtained by FaSTAR.

Furthermore, the coefficients obtained by FaSTAR change more gradually than those obtained by FAST at lower values of λ. It is known that the flow around the blade is 3D, and this tendency becomes more significant after flow separation occurs. Moreover, 3D flow inhibits the performance decrement. Hence, it is inferred that 3D flow makes the performance declines obtained by FaSTAR less obvious than those obtained by FAST. The difference in rotor performance at $\lambda = 5$ and $\lambda = 6$ in the two-bladed rotor case also infers that the performance decline resulting from a stall is not as obvious when considering 3D flow on the blade. These results suggest that it is necessary to consider the effects induced by 3D flow when flow separation occurs. Considering that, it is assumed that using CFD is effective when considering the relationship between the rotor performance and the flow around the rotor.

When focusing on the difference in the number of blades, the C_P and C_T values of the two-bladed rotor change more gradually than those of the three-bladed rotor. Moreover, the C_P value of the three-bladed rotor at the designed λ is higher than that of the two-bladed rotor. These trends agree with general wind turbine characteristics. Also, at the same inflow speed ($\lambda = 10$ for the two-bladed rotor and $\lambda = 12.2$ for the three-bladed rotor), C_T is almost the same, which implies that the thrust per blade of the two-bladed rotor is larger than that of the three-bladed rotor.

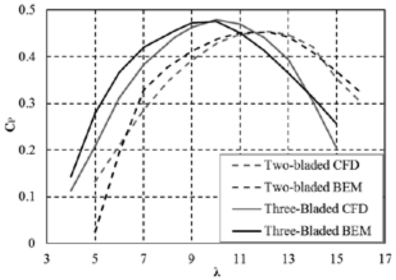

Figure 6: Power coefficient C_P.

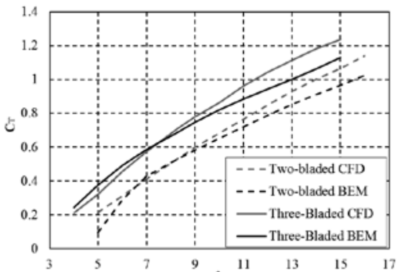

Figure 7: Thrust coefficient C_T.

3-2. Tangential/normal force coefficient distributions along the blade at the designed tip speed ratio

Next, we focus on the normal/tangential force coefficient distributions along the blade. The normal force coefficient C_x acting in the normal direction of the rotor plane is shown in Figure 9, and C_y acting in the tangential direction of the rotor plane is shown in Figure 10. The coefficients C_x and C_y are defined by Eqs. (4) and (5), respectively:

$$C_x = \frac{F_x}{\frac{1}{2}\rho U_{\mathrm{rel}}^2\, c} \quad (4)$$

$$C_x = \frac{F_x}{\frac{1}{2}\rho U_{\mathrm{rel}}^2\, c} \quad (5)$$

where F_x and F_y are the normal and tangential forces per unit length acting on the blade and are defined as shown in Figure 8. c is the chord length, and U_{rel} is the relative inflow speed at each radial position, respectively. We noted that the relative inflow speed in the two-bladed rotor case is faster than in the three-bladed case. However, the difference between them is quite small. Thus, it is implied that the flow characteristics around the blades are quite similar. For this reason, to address the aerodynamic characteristics of the blade, we non-dimensionalized the local forces using the relative inflow speed.

As shown in Figures 9 and 10, the local force coefficients obtained by FaSTAR are generally larger than those obtained by FAST. It is inferred that these differences arise depending on whether or not we are considering the 3D flow around the blade. However, the trends show good agreement in the values of both C_x and C_y. These results suggest that rotor performance can be captured correctly using FaSTAR.

When focusing in detail on the differences between FaSTAR and FAST, decreases are obtained at about $r/R = 0.15$ by FaSTAR only. At $r/R = 0.15$, the blade shape changes from cylinder to airfoil. At this transition, complex flows can occur, induced by the flow separation, which may result in a decrement of rotor performance. Furthermore, the declines which seem to result from blade tip losses are obvious only in the results obtained by FaSTAR. These results suggest that aerodynamic analysis using FaSTAR can capture the blade tip loss effect, which is difficult to capture using BEM theory.

When focusing on the differences related to the number of blades, the values of C_x from $r/R = 0.2$ to $r/R = 0.6$ in the two-bladed rotor case are greater than those in the three-bladed case as shown in Figure 9. The angles of attack are different in the two- and three-bladed rotor cases because the twist angle distributions and rotational speeds are different. This may result in a difference in rotor performance, as shown in Figures 9 and 10. However, the trend of varying C_x with changing r/R and the values from $r/R = 0.6$ onward are in good agreement.

Moreover, the trends of varying C_y with changing r/R are also in good agreement as shown in Figure 10. However, the values obtained in the two-bladed rotor case are generally smaller than those obtained in the three-bladed case. The twist angle along the blade in the two-bladed rotor case is generally smaller than in the three-bladed case, and, consequently the lift action in the y-direction declines. Furthermore, the C_y value at $r/R = 0.15$ in the two-bladed rotor is negative, unlike in the three-bladed rotor. These results suggest that the flow separation induced by the airfoil shape transition impacts the rotor performance more significantly in two-bladed rotor case.

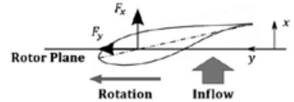

Figure 8: Definition of local forces F_x and F_y along the blade.

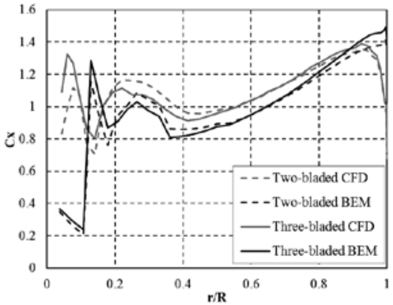

Figure 9: Normal force coefficient C_x distributions along the blade.

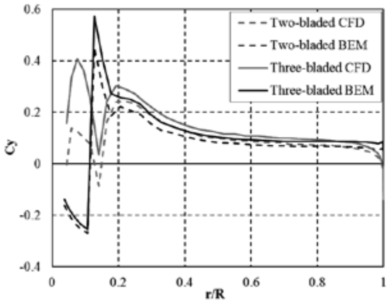

Figure 10: Tangential force coefficient C_y distributions along the blade.

4. Consideration of the separation-induced effect at the designed tip speed ratio

The decreases of C_x and C_y at about $r/R = 0.15$ are assumed to be caused by the 3D flows induced by the transition of blade shape from cylinder to airfoil. These phenomena are very interesting from the point of view of aerodynamics or fluid dynamics. Therefore, we focused on the flow separation and the separation-induced effect at around $r/R = 0.15$.

The dynamic pressure distributions on the blade acting in the tangential direction of the rotor plane at about $r/R = 0.15$, denoted as p'_y, are shown for the two- and three-bladed rotor cases in Figures 12 and 13, respectively. Streamlines on the blade are also plotted in black lines. Here, the relationships between F_y and p'_y and p'_y are defined by Eqs. (6) and (7):

$$F_y \sim \int_c p'_y \, \mathrm{d}s \tag{6}$$

$$p'_y = (p - p_0)(\mathbf{n} \cdot \mathbf{e}_y) \tag{7}$$

Here, p_0 is the pressure at the stagnation point, $\mathbf{n}$ is the normalized inward normal vector on the airfoil, defined as shown in Figure 11, and $\mathbf{e}_y$ is the unit vector in the y-direction.

As shown in Figures 12 and 13, a negative value is shown at the trailing edge at about $r/R = 0.15$. Moreover, a concentration of streamlines, apparently induced by the flow separation, is also seen. At $r/R = 0.15$, the blade shape changes, particularly at the trailing edge. This shape transition can cause flow separation, and, consequently, the value of C_y decreases.

When focusing on the difference related to the number of blades, the negative value of p'_y at about $r/R = 0.15$ is greater in the two-bladed rotor case than in the three-bladed case. The negative region is also larger in the two-bladed rotor case than in the three-bladed case. These phenomena suggest that the 3D effects around the root are more significant in the two-bladed rotor case than in the three-bladed case.

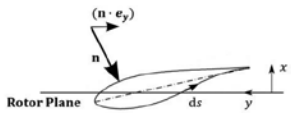

Figure 11: Definition of the normalized normal vector $\mathbf{n}$ on the airfoil.

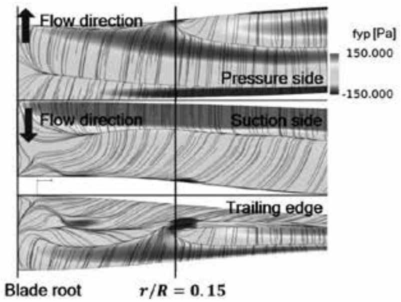

Figure 12: p'_y distribution on the blade at about $r/R = 0.15$ in the two-bladed rotor case (Upper: pressure side, Middle: suction side, Lower: trailing edge).

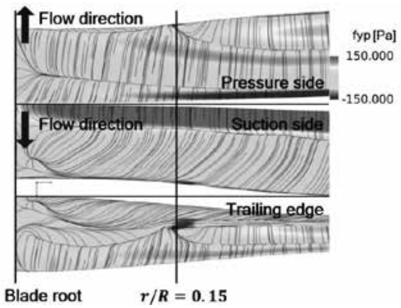

Figure 13: p'_y distribution on the blade around $r/R = 0.15$ in the three-bladed rotor case (Upper: pressure side, Middle: suction side, Lower: trailing edge).

5. Conclusion

We executed a CFD analysis of two- and three-bladed rotors using a 10 MW-class offshore wind turbine proposed by NEDO as a reference. First, we validated and confirmed rotor performance through a comparison with the BEM results. Moreover, we discuss the merits of applying CFD to the aerodynamic analysis of wind turbines. Besides, we investigated the differences in aerodynamic characteristics when the number of blades was changed. The obtained results are as follows:

- The results obtained by FaSTAR generally agree with the BEM results. Thus, wind turbine performance can be captured correctly by FaSTAR.
- It is believed that the CFD analysis in this research captured tip losses and 3D effects that are difficult to capture using BEM theory.
- It is important to consider the effects induced by the 3D flow around the blade when flow separation occurs. Thus, it is assumed that using CFD is effective when considering the relationship between the rotor performance and the flow around the rotor.
- The C_P and C_T values of a two-bladed rotor change more gradually than those of a three-bladed rotor.
- The C_P value of a three-bladed rotor at the designed λ is greater than that of a two-bladed rotor. However, the C_T value of a three-bladed rotor at the designed λ is not very different.
- The 3D effects and losses around the root are larger in two-bladed rotors than in three-bladed rotors.

6. Future work

In this research, we focused on the aerodynamic characteristics when the blade pitch is at the designed angle and investigated the local force distributions along the blade in detail at the designed tip speed ratio. In our future research, we will focus on the differences in local force distributions along the blade when the inflow speed changes. Then, we will execute CFD analyses with differing blade pitch angles to assess the differences in aerodynamic characteristics for two- and three-bladed rotors when the angle of attack changes.

Acknowledgments

This research was supported by the NEDO project. We used the computational resources of JAXA to conduct the CFD analysis. Also, The authors would like to thank Enago (www.enago.jp) for the English language review.

References

[1] Technology Roadmap: Wind Energy-2013 edition, IEA.
[2] Frederik Zahle, Robert Bitsche, Taeseong Kim, Anders Yde, Lars Christian Henriksen, Morten H. Hansen, José Blasques, Mac Gaunaa, and Anand Natarajan. "The DTU 10-MW reference wind turbine."*Danish wind power research* (2013).
[3] New Energy and Industrial Technology Development Organization, "Research Study about 10-MW class wind turbine (Japanese)", http://www.nedo.go.jp/content/100575922.pdf, Accessed: 2015/05/08
[4] Christian Bak, Robert Bitsche, Anders Yde, Taeseong Kim, Morten H. Hansen, Frederik Zahle, Mac Gaunaa, José Blasques, Mads Døssing Jens-Jakob Wedel Heinen, and Tim Behrens. "Light Rotor: The 10-MW reference wind turbine." *EWEA 2012-European Wind Energy Conference & Exhibition*. 2012.
[5] Bergami, Leonardo, Helge A. Madsen, and Flemming Rasmussen. "A Two-Bladed Teetering Hub configuration for the DTU 10 MW RWT: loads considerations." *European Wind Energy Conference & Exhibition 2014*.
[6] National Renewable Energy Laboratory, "FAST", https://nwtc.nrel.gov/FAST, Accessed: 2015/09/28
[7] Denmarks Tekniske Universitet, "The DTU 10MW Reference Wind Turbine Project Site", http://dtu-10mw-rwt.vindenergi.dtu.dk/login?back_url=http%3A%2F%2Fdtu-10mw-rwt.vindenergi.dtu.dk%2F, Accessed: 2015/10/05
[8] Christian Bak, and Jappe Johansen, "Three-dimensional corrections of airfoil characteristics for wind turbines based on pressure distributions." Proceedings of EWEC Conference. 2006.
[9] Christian Bak, Frederik Zahle, Robert Bitsche, Taeseong, Kim, Anders Yde, Lars Christian Henriksen, Anand Nata-rajan, Morten Hartvig Hansen, "Description of the DTU 10 MW Reference Wind Turbine", DTU Wind Energy Report-I-0092 (2013).
[10] Franck Bertagnolio, Niels Sorensen, Jeppe Johansen, and Peter Fuglsang, "Wind Turbine Airfoil Catalogue", Riso-R-1280, 2001.
[11] Atsushi Hashimoto, Keiichi Murakami, Takashi Aoyama, Keiichi Ishiko, Manabu Hishida, Masahide Sakashita, and, Paulus R. Lahur. "Toward the fastest unstructured CFD code 'FaSTAR'." *AIAA paper* 1075 (2012).
[12] Hashimoto, A., K. Murakami, and T. Aoyama. "JAXA Digital/Analog Hybrid Wind Tunnel: Decelopment of Digital Wind Tunnel." *Proceedings of the 2nd Workshop on Integration of EFD and CFD*. 2010.
[13] Atsushi Hashimoto, Keiichi Murakami, Takashi Aoyama, and Paulus R. Lahur. "Lift and Drag Prediction Using Automatic Hexahedra Grid Generation Method." *AIAA paper* 1365 (2009): 2009.
[14] Atsushi Hashimoto, Keiichi Murakami, Takashi Aoyama, and Paulus R. Lahur. "Drag Prediction on

NASA CRM Using Automatic Hexahedra Grid Generation Method." *AIAA paper* 1417 (2010): 2010.
[15] Makoto Iida, Takamasa Obata, Chuichi Arakawa. “Wake Numerical Analysis of Horizontal Axis Wind Turbine using Fast Flow Solver FaSTAR.”, Proceedings of the Conference on Computational Engineering and Science 18, 4p, 2013-06.
[16] J.Blazek, “Computational Fluid Dynamics: Principles and Applications, Second Edition,” Elservier, 2005.
[17] Inari, V. Takayuki Abe V. Tomohide, and V. Ken Seki. "JAXA Supercomputer Systems with Fujitsu FX1 as Core Computer." *Fujitsu Sci. Tech. J* 44.4 (2008): 426-434.
[18] Japan Aerospace eXploratrion Agency, “SORA/JSS2”,
https://www.jss.jaxa.jp/,
Accessed: 2015/10/05

Smart Fatigue Load Control on a Large-scale Wind Turbine Based on Different Sensing Strategies

Mingming ZHANG*, Bin TAN, Jianzhong XU

Institute of Engineering Thermophysics, Chinese Academy of Sciences,
P. O. Box 2706, Beijing 100190, P. R. China
*Presenting author: Tel.: +86 10 82543023.
Email-address: mmzhang@mail.etp.ac.cn

Abstract

This paper presented a numerical study on the smart fatigue load control of a large-scale wind turbine blade. Three typical control strategies, with sensing signals from flapwise acceleration, root moment and tip deflection of the blade, respectively, were mainly investigated on our newly developed aero-servo-elastic platform. It was observed that the smart control greatly modified in-phased flow-blade interaction into an anti-phased one at primary 1P mode, significantly enhancing the damping of the fluid-structure system and subsequently contributing to effectively attenuated fatigue loads on the blade, drive-chain components and tower. The aero-elastic physics behind the strategy based on the flapwise root moment, with stronger dominant load information and higher signal-to-noise ratio, was more drastic, and thus outperformed the other two strategies, leading to the maximum reduction percentages of the fatigue load within a range of 12.0 ~ 22.5%, in contrast to the collective pitch control method. The finding pointed to a crucial role the sensing signal played in the smart blade control. In addition, the performances within region III were much better than those within region II, exhibiting the benefit of the smart rotor control since most of the fatigue damage was believed to be accumulated beyond the rated wind speed.

Keywords

Smart rotor control; Offshore wind energy; Fatigue load; Sensing signal; Flow-blade interaction

I. Introduction

In recent years, with the rapid development of the global offshore wind power, the R&D on large turbines by a perceived potential to reduce cost of energy, has attracted wide attention. Nevertheless, the aerodynamic load status of the corresponding long flexible wind turbine blades becomes much worse due to the influences of wind shear, turbulence, tower shadow and wake from the upstream turbine, etc, forming serious threat to the safety and reliability of the operating turbine [1]. To improve this situation, it is very necessary to develop an available blade load control method, which may also be helpful to reduce the loads on other turbine components as well as to ensure the decreased maintenance requirements and an overall lower cost per kWh for a large-scale offshore wind turbine.

Considering the complicated and changeable aerodynamic load within the rotor plane, a new kind of control concept, i.e. „smart rotor control", a term used in the rotorcraft research [2], was recently proposed to exert the controllable action for each blade at any azimuthal position and any span-wise station. The essence of the control was to drive the local aerodynamic surfaces through a combination of sensors, actuators and controllers, and thus provide a good load control capacity. This would undoubtedly remedy the drawbacks of the traditional strategy utilizing the integral, low response and excessive wear pitch control method (e.g. collective, cycle or independent pitch control method), mostly applied in current wind turbines. Therefore, the aspect of the smart rotor control has become one of the hot research areas within the wind community for more than one decade.

A large amount of work has been focused on the development of the available actuator/aerodynamic surface in the past. By comparing the different schemes, e.g. micro tab [3], morphing [4], active twist [5], suction/blowing [6] and synthetic jet [7], etc, the "deformable trailing edge flap (DTEF)", a flap that deformed in a flexible shape to generate a substantial change in the lift coefficient of the airfoil by altering the pressure distribution along the chord, characterized by its positive performance, fast response, small size, wide bandwidth and low flow disturbance, had been found to be the most potential actuator candidate for the smart rotor means [8]. Furthermore, many investigations have also been conducted utilizing the DTEFs in terms of DTEF modeling [9-11], controller implementation [12-16], load control effectiveness and analysis [17-21], small-scale wind tunnel experiments [22-24] and full-scale field tests [25,26].

On the other hand, the investigations on the sensing signals, equally important to the control performance, of the DTEF based smart rotor system, have been very active lately. Generally speaking, researchers have deployed and collected information on many different sensing signals, including acceleration [27], strain [17,28], inflow velocity and attack angle [28], displacement [14] and surface pressure difference [29], etc, and studied the influences of the number and location of the sensors on the control effectiveness, as well summarized in [30]. However, the comparison and analysis among representative sensing methods were still little reported before. Moreover, the corresponding aero-elastic control physics behind has not been well understood. These unsolved issues might greatly block the optimal design of the smart rotor system on the large-scale offshore wind turbine in the future engineering applications.

To this end, three types of sensing strategies were mainly studied in this paper based on the flapwise acceleration on the blade surface (a), the blade flapwise root moment (M_y , relative to the strain at the blade root) and the blade flapwise tip deflection (D_x , or displacement), i.e. a -strategy, M_y -strategy and D_x -strategy, and their effects on the fatigue load control on the blades as well as other typical components of the wind turbine, were individually examined and compared. Note these sensing signals could be easily measured using accelerometer, strain gauge and displacement transducer in practice. Like many previous investigations [12-14, 16-21, 28, 33], the variable speed, pitch controlled NREL UpWind/5 MW offshore wind turbine [31], with a 126 m rotor diameter and a 90 m hub height, was selected as a control subject, and the hydrodynamic properties were not considered for simplicity. All this work had been conducted under the Normal Turbulence Mode (NTM) wind condition, followed by the International Electro-technical Commission (IEC) standard [32], using our newly developed aero-servo-elastic numerical platform [33], which was built by improving the FAST/Aerodyn codes with the integration of the internal DTEF controller into the Matlab/Simulink software. In addition, the corresponding modifications in the coupled aero-elastic interactions between flow and blade for the three strategies were discussed in detail.

II. Sensing and control schemes

The purpose of the present smart rotor control was to effectively suppress the fluctuating magnitude of the sensing signals (i.e. a , M_y and D_x) and thus the primary fatigue loading source, i.e. M_y , on the UpWind/5 MW wind turbine blade, using the controllable DTEF actuation by an internal controller. This was realized by an aero-servo-elastic numerical platform, consisting of aerodynamic, structural dynamic and control sub-models, and one might go through our recent published paper [33] for more information. Moreover, without loss of generality, the incoming wind was set to be the medium wind class (IIB) with the reference speed V_{ref} and the turbulence intensity I_{ref} of 42.5 m/s and 0.14, followed by the IEC NTM standard [32]. Wind data was generated using NREL Turbsim code [34], with 3D turbulent wind formed using a von Kármán spectrum and a wind shear power law exponent of 0.2.

The aerodynamic sub-model was mainly built on the NREL AeroDyn code [35], combining the Blade Element Momentum (BEM) and the Generalized Dynamic Wake (GDW) theories, to calculate the lift, drag and pitching moment forces at an attack angle α from the corresponding lookup tables. Specifically, the lift coefficient (C_l), drag coefficient (C_d) and moment coefficient (C_m) as a function of $\alpha = -20^\circ \sim 23^\circ$, were first computed by RFOIL code [36] for each DTEF deflection angle φ in 1° increments. After that, these coefficient tables were pre-processed using the Viterna method to expand to the α range of $-180^\circ \sim +180^\circ$. The camber curve of the DTEF was generated by fitting a cubic spline through the mean camber line of the baseline airfoil and the new trailing edge point, and a group of DTEF parameters, i.e. the spanwise length L_f , normalized by the rotor radius R , the central chordwise length c_f , normalized by the averaged chord length c at the DTEF location, and the deflection angle range $|\varphi|$, were set to be 0.20, 0.10 and $\pm 15^\circ$, respectively, where very good performance had been confirmed in our recent investigation [21]. Furthermore, four other built-in models, including the 3D rotational stall delay model, the Prandtl tip and hub loss model, and the tower shadow effect model, were also used in the AeroDyn code to further improve the accuracy.

In addition, as Lackner and Kuik [13] did, a quasi-steady assumption was presumed to neglect the influence of the unsteady dynamic stall. Correspondingly, the averaged magnitude of the major peak in the PSD of the DTEF angle (or the majority of energy) was computed to occur at a reduced frequency *k*, *i.e.*, *k* = *cω*/*U*, representing the degree of unsteadiness of an airfoil section subject to external disturbance, of about 0.02 (not shown), much less than 0.05, beyond which the aerodynamics of the airfoil section could be considered to be unsteady. Based on this, we had confirmed that even though the aerodynamics of DTEF sections, were not entirely quasi-steady, which might influence the smart rotor simulations to some degree, it was indeed a safe assumption to do so. Here *c*, *U* and *ω* stood for the mean chord length of the section with the installment of DTEFs, the sectional relative velocity and the frequency of the disturbance in units of radians per second, respectively.

The structural dynamic sub-model was based on the NREL FAST code [37], where a combined modal and multi-body representation of the turbine was built to determine its response to the applied force. By doing so, the structural dynamic might be aero-elastically coupled to its aerodynamic counterpart by means of the structural deformation velocities and the aerodynamic forces. As a result, the time histories of the fatigue load on the blades were generated with the input aerodynamic forces calculated by the Aerodyn code.

The control sub-model incorporated internal and external parts. Consuming no noise and time delay or lag interferences, the former mainly focused on how to reasonably manipulate the DTEFs for good control performance on the fatigue load, shown in Fig. 1. For each sensing

where *x*, *y*, *z* axes and origin was orthogonal with *y* and *z* axes, pointing towards the trailing edge of blade and parallel with the chord line at the zero-twist blade station, pointing along the pitch axis towards the tip of blade, and intersection of the blade‟s pitch axis and the blade root, respectively. The transformed variables were then assumed to be time-invariant and the typical linear time invariant control technique, e.g. proportional-integral-derivative (PID) control, could be used, which was based on the error input between the reference and the actual feedback input. Furthermore, since the goal of the flap controller was to minimize the fluctuating a_i , M_{yi} and D_{xi} , the corresponding referenced variations were set to be zero. The governing equations were:

$$\theta_s(t) = k_p(0 - Q_s(t)) + \frac{1}{T_I}\int_0^t (0 - Q_s(t))dt + \frac{T_D d(0 - Q_s(t))}{dt} \quad (1)$$

$$\theta_c(t) = k_p(0 - Q_c(t)) + \frac{1}{T_I}\int_0^t (0 - Q_c(t))dt + \frac{T_D d(0 - Q_c(t))}{dt} \quad (2)$$

Here $\theta_s(t)$ and $\theta_c(t)$ were the yaw-wise and tilt-wise DTEF deployment angle, respectively, defining how the individual DTEF angle varied from the collective one, and $Q_s(t)$ and $Q_c(t)$ stood for the instantaneous a, M_y and D_x in the fixed nacelle frame. Thus the control actions

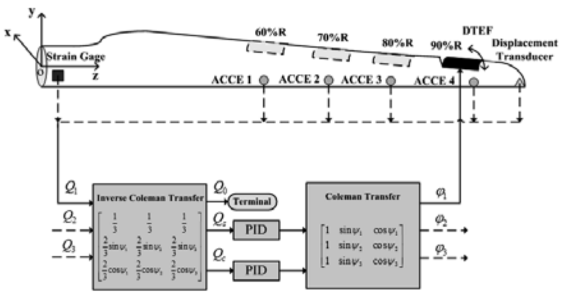

Figure 1: Schematic layout of the control sub-model using various sensing strategies.

strategy, the signals Q_i (*i* = 1, 2, 3), i.e. a_i , M_{yi} or D_{xi} , originated from three rotational turbine blades, was separately transformed into the fixed nacelle/yaw frame of reference using the inverse Coleman transformation to remove the periodic coefficients in the equations of motion. The coordinate system was defined in Fig. 1,

in the fixed frame were exerted through reasonably adjusting the proportional coefficient k_p , the integration time constant T_I , and the derivative time constant T_D to minimize the corresponding standard deviation of a_i , M_{yi} and D_{xi} as well as to prevent the saturation of the DTEF position limits. Finally, the resultant control was again transformed back into the rotating frame using the Coleman transformation to assign the proper DTEF angle φ_i to each blade for the effective control of a_i , M_{yi} and D_{xi} . Then the performances of each sensing strategy on M_y were compared.

The external controller originally built by NREL [31] was still utilized for power regulation through the generator torque control and the above rated full-span pitch control.

III. Control performances using various sensing signals

To compare the performances using various sensing signals, the smart blade control using the aforementioned aero-servo-elastic platform was first conducted based on the acceleration signal a , i.e. a -strategy. The typical results of blade1 were only displayed for simplifying the analysis. Figure 2 indicates the effect of the central

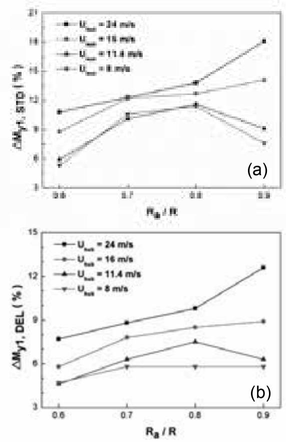

Figure 2: Effect of the central spanwise location of the accelerometer, i.e. R_a , on the reduction percentages in the standard deviation of the flapwise root moment $\Delta M_{y1,STD}$ (a) and the root damage equivalent load (DEL) $\Delta M_{y1,DEL}$ (b) of blade1 at various hub velocities U_{hub}.

spanwise location of the accelerometer, i.e. R_a , on the reduction percentages in the standard deviation of the flapwise root moment $\Delta M_{y1,STD}$ and the root damage equivalent load (DEL) $\Delta M_{y1,DEL}$ of blade1 under different hub velocity U_{hub} . Here the DEL magnitude was computed through the rain flow counting algorithm, followed by the Miner‟s rule, and the S-N curve of the material, to determine the number of the cycles in M_y signal at various amplitudes. A Woehler exponent of 10 was set for the blade, a typical value for the glass fiber composite material. To effectively reduce the standard deviation of all quantities, the present computations were separately carried out under four turbulence seeds with a time length of 620 s (the data within the first 20 s period was not considered since the computation was unstable) for each, generated using Turbsim code, and the final results were then averaged. Note one accelerometer and one DTEF, with the same central spanwise location, instead of multi sensors and actuators, were utilized for the sake of simplification. Even so, a good performance was still achieved later. Furthermore, for each location of the accelerometer, the control effectiveness was also calculated when the DTEF was placed at different spanwise stations. It was found that the best performance was obtained if the center location of the flap and the sensor was at the same spanwise place, which we thus choose to set our configuration.

Obviously, $\Delta M_{y1,STD}$ and $\Delta M_{y1,DEL}$ tend to increase with increasing R_a/R and then suddenly decrease near the tip of blade1 for U_{hub} = 8 m/s case (typical region II case [31], i.e. beyond the rated hub velocity (11.4 m/s)), implying the gradually impaired control performance towards the tip. According to our computation, the attack angle of the airfoil (α) close to the blade tip, where the NACA64618 airfoil was deployed, fluctuated around 4.8° for the uncontrolled condition. Moreover, the C_l - α relationship deviated from the linear zone as α > 3.0°, leading to flow separation from the airfoil trailing edge to some extent along the chordwise direction. Furthermore, the variation in the pressure gradient along the spanwise direction might also induce the flow detachment. The resultant complicated outboard flow field around the blade tip was thought to be responsible for the lower performance of the DTEF control than those at most of the blade inboard part. Interestingly, $\Delta M_{y1,STD}$ showed a similar trend at the rated wind velocity, i.e. U_{hub} = 11.4 m/s [31], as U_{hub} = 8.0 m/s case, suggesting that the effect of the flow separation phenomenon on smart control was still strong at the end of region II.

In contrast, as the turbine was operated into region III (U_{hub} > 11.4 m/s), the control performances on $\Delta M_{y1,STD}$ and $\Delta M_{y1,DEL}$ were greatly improved and both of them gradually augmented with R_a / R, especially for U_{hub} = 24 m/s case, under which the maximum $\Delta M_{y1,STD}$ and $\Delta M_{y1,DEL}$ reached 18.1% and 12.6% around the blade tip, respectively. The significantly reduced flapwise tip deflections were believed to be associated with much impaired blade vibration and thus the fluctuating M_{y1}, indicated by the results of the reduction percentages in the standard deviation of the flapwise tip deflection ($\Delta D_{x1,STD}$) at U_{hub} = 16 m/s and 24 m/s in Figs. 3(a) and 3(b). On the other

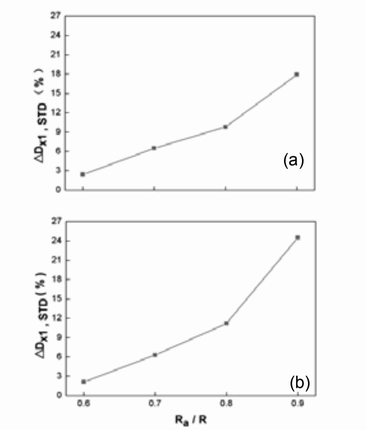

Figure 3: Effect of the central spanwise location of the accelerometer (R_a) on the reduction percentages in the standard deviation of the flapwise tip deflection ($\Delta D_{x1,STD}$) of blade1: (a) U_{hub} = 16 m/s case; (b) U_{hub} = 24 m/s case.

hand, the blade pitch within region III could function to reduce α and thereafter greatly suppress the uncontrolled flow separation phenomenon. In fact, the section attack angle α along the blade, computed using Aerodyn code, had made the corresponding flow pattern successively enter into the linear zone (attached flow zone) with enhancing U_{hub} (not shown). In this way, the DTEF control tended to exert a better effect on the well-organized fluid field and then $\Delta M_{y1,STD}$ and $\Delta M_{y1,DEL}$ for higher U_{hub} cases. This suggested that the pitching action had played an important role in the control of the rotor fatigue load. It was worth noticing that similar influences of smart control on M_y in regions II and III were also observed in our previous paper [21]. The interpretation on the flow phenomenon concerned in Fig. 2 will be further clarified by our numerical and experimental study in the near future. Additionally, as pointed out by Smit et al. [38] that most of the fatigue damage was accumulated within the range from the rated wind speed to the cut-out one, i.e. region III condition, the results in Fig. 2 justified the benefit of smart blade control in the fatigue load of the large-scale wind turbine blade.

In addition to a-strategy, the investigations using D_x- and M_y-strategies, where DTEFs

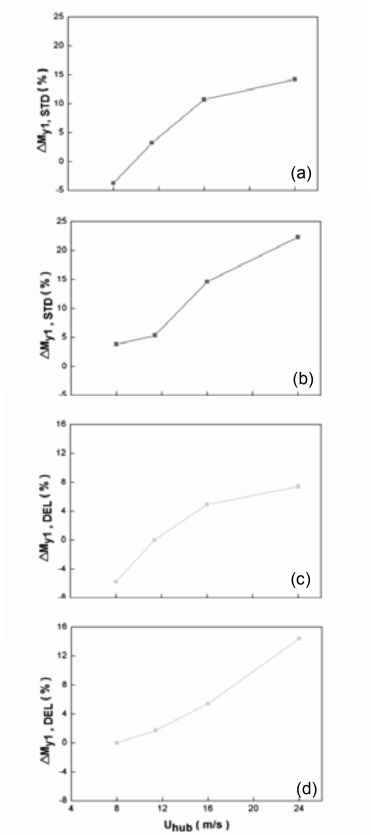

Figure 4: The reduction percentages in $\Delta M_{y1,STD}$ and $\Delta M_{y1,DEL}$ of blade1 for D_x -strategy and M_y -strategy: (a) D_x -strategy, $\Delta M_{y1,STD}$; (b) M_y -strategy, $\Delta M_{y1,STD}$; (c) D_x -strategy, $\Delta M_{y1,DEL}$; (d) M_y -strategy, $\Delta M_{y1,DEL}$.

were installed at the same spanwise location R_s near the blade tip as a-strategy, i.e. R_s / R = 0.9, were also examined, illustrated in Fig. 4. Evidently, irrespective of strategies, control became more effective when U_{hub} all the way increased in terms of $\Delta M_{y1,STD}$ and $\Delta M_{y1,DEL}$, exhibiting the same trend as a-strategy. At U_{hub} = 24 m/s, the best performances were acquired, with themaximum $\Delta M_{y1,STD}$ and $\Delta M_{y1,DEL}$ up to 14.0% and 7.3% for D_x-strategy and up to 22.5% and 14.7% for M_y-strategy, respectively.

To further compare the effectiveness of the smart rotor control among three sensing strategies, the typical results in time and frequency domains were proposed at U_{hub} = 24 m/s in Fig. 5. It was worth pointing out that U_{hub} =

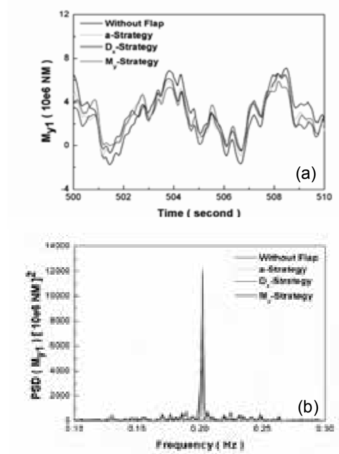

Figure 5: Typical time domain (a) and frequency domain (b) results of M_{y1} using different control strategies.

24 m/s case was chosen as a typical example to represent the high fatigue load and high damage contribution condition [38], and would be primarily investigated in the following sections besides where otherwise stated. In addition, the installment configuration of DTEF for a-strategy was the same as D_x-strategy and M_y-strategy. Clearly, after the introduction of DTEF, the fluctuating magnitude in M_{y1} effectively decreased, compared with the case without flap [Fig. 5(a)]. The control tended to be worse in the order of M_y-, a- and D_x-strategies, agreeing with the results in Figs. 2 and 4. Correspondingly, the dominant 1P spectral Hz, were significantly reduced up to 71.2%, 66.8% and 55.3% in the power spectral density (PSD) of M_{y1}, i.e. $E_{M_{y1}}$, seen in Fig. 5(b), showing the great impairment in the energies of M_{y1}.

In addition, interests were also aroused to study the DTEF control of the fatigue loads on other representative turbine components, i.e. the bending moments of the sectional low-speed shaft, i.e. M_{LSSya} and M_{LSSza}, the tower-top pitch moment and the tower-top yaw moment, i.e. M_{Yawyn} and M_{Yawzn}, and the tower base yaw moment, i.e. M_{TwrBzt}. Table 1 summarized their maximum reduction percentages in the standard deviation, compared with the traditional collective pitch control. Obviously, all quantities were subject to very effective impairment and the performances using M_y-strategy tended to perform much better than the other two strategies in every category, resulting in the maximum reduction percentages in M_{LSSya}, M_{LSSza}, M_{Yawyn}, M_{Yawzn} and M_{TwrBzt} of 12.0%, 16.0%, 13.0%, 16.1% and 17.0%, respectively.

To sum it up, the DTEF control was very effective to reduce the fatigue loads on blade and turbine components; compared with the other two strategies, the best control performances were acquired if the flapwise root moment M_y

Table 1: The reduction percentages in the standard deviation of the fatigue loads on typical drive-chain components and tower using different sensing strategies.

Fatigue load / Sensing Strategy	M_{LSSya}	M_{LSSza}	M_{Yawyn}	M_{Yawzn}	M_{TwrBzt}
D_x-Strategy	3.0%	7.0%	2.0%	7.0%	7.0%
a-Strategy	11.0%	14.0%	11.0%	14.0%	14.0%
M_y-Strategy	12.0%	16.0%	13.0%	16.1%	17.0%

was chosen to be the sensing signal. It lay in higher signal intensity and less interference noise of signal M_y than signals D_x and a (not shown).

This was reasonable since the blade tip was much more flexible than the root part and thus the signals acquired near the tip were more easily influenced by the complicated 3D turbulent flow. The resultant signals D_x and a decreased the strength of 1P mode influenced by other (turbulent) disturbances to some extent, leading to the lower performances of D_x - and a -strategies than M_y -strategy. Analogously, Anderson et al. [18] found that the decreased SNR would impair the control effectiveness of the smart blade system. This analysis will be further investigated in our future numerical and experimental work.

IV. Discussions

The effectively impaired fatigue loads on the wind turbine blades for the sensing cases mentioned above were discussed to uncover the involved aero-elastic physics behind. This was done by investigating the spectral phase $\phi_{m1m2} = \tan^{-1}(Q_{m1m2} / Co_{m1m2})$ and the spectral coherence $Coh_{m1m2} = (Co_{m1m2}^2 + Q_{m1m2}^2) / E_{m1}E_{m2}$ among three quantities, i.e. the DTEF deflection angle φ , the nearby normal force on the element along the local flapwise direction F_n , and the local flapwise acceleration a of the blade. The analogous methods had been verified in our previous publications on active flow control [20,21,39]. Here Co_{m1m2} and Q_{m1m2} stood for the co-spectrum and quadrature spectrum of the variables $m1$ and $m2$, respectively, while E_{m1} and E_{m1} meant the power spectrum density of $m1$ and $m2$, respectively.

Figure 6 proposed the typical spectral phase shifts $\phi_{\varphi_1 F_{n1}}$ between φ_1 and F_{n1} at U_{hub} = 24 m/s for different sensing strategies. Recall that the flap deflection angle φ_1 fluctuated within a rather small range ($|\varphi|$ = ±15°), the DTEF might be approximately thought to be activated in the local flapwise direction. Obviously, for D_x -strategy, $\phi_{\varphi_1 F_{n1}}$ at primary frequency f_{1P} (≈ 0.20 Hz) was close to π [Fig. 6(a)], suggesting that the controllable flap perturbation and the nearby aerodynamic sectional force on the blade was in anti-phase or opposing interactions at f_{1P} .

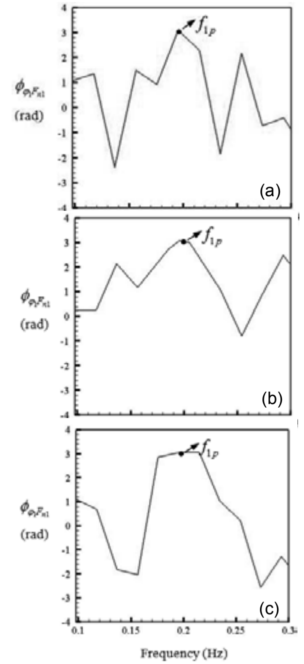

Figure 6: Typical spectral phase $\phi_{\varphi_1 F_{n1}}$ between the deflection angle of flap1 φ_1 and the normal force F_{n1} on blade1, corresponding to the central location of flap1, for different sensing strategies: (a) D_x -strategy; (b) a -strategy; (c) M_y -strategy.

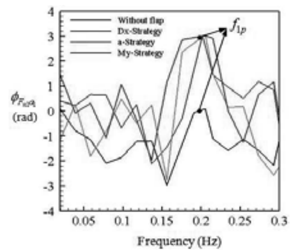

Figure 7: Typical spectral phase $\phi_{F_{n1}a_1}$ between F_{n1} and a_1 at R_s / R = 0.9, corresponding to the central location of flap1, for different sensing strategies.

This would induce the energy dissipation of the flow around the blade, leading to an effective impairment in F_{n1} . From another point of view, the reduced F_{n1} might impose an important impact on the aero-elastic relationship between flow and blade near the flap since F_{n1} provided the main aerodynamic force excitation on the blade. To further clarify this, the spectral phase of F_{n1} and a_1 at R_s / R = 0.9, representing the relationship between the sectional force and the resulting blade vibration, was calculated with and without DTEF control, indicated in Fig. 7. The frequency range near f_{1P} , corresponding to the strong synchronizing flow and structural vibration. Once controlled using D_x -strategy, $\phi_{F_{n1}a_1}$ at f_{1P} was changed from 0 to π , that is, the synchronizing F_{n1} and a_1 turned into collided interactions against each other. In contrast, for a - and M_y -strategies, the $\phi_{\varphi_1 F_{n1}}$ and $\phi_{F_{n1}a_1}$ at f_{1P} were also near π [Figs. 6(b) and 6(c) and Fig. 7]. Note the phenomena happened over a narrow and a wide range of frequencies around f_{1P} for a - and M_y -strategies, respectively, resulting in much more impaired fluid-structure interaction near 1P frequency using the two strategies than D_x -strategy.

On the other hand, at the location of R_s / R =0.9, the spectral coherence $Coh_{F_{n1}a_1}$ at f_{1P} in Fig. 8 decreased by 17.1%, 31.4% and 42.9% for D_x -, a - and M_y -strategies, respectively. In addition, similar observations were also found in Fig. 9 at another two representative spanwise locations of blade1, i.e. R_s / R = 0.60 and 0.98, where $Coh_{F_{n1}a_1}$ were still subject to significant reductions at f_{1P} and the trends in the corresponding reduction percentages were maintained in the same sequence for the three strategies. Based on these results, the decoupled aero-elastic correlation between flow and structural vibration on the whole blade was caused by the smart blade control. Hence, the flapwise root moment on the blade and subsequent aerodynamic load on other turbine components would be greatly suppressed. In addition, it was easily to note that the control using M_y -strategy performed the best, compared with its two counterparts. All these analyses agreed with the results in Figs. 2-6.

V. Conclusions

To investigate the effect of the sensing signals on the fatigue load control and understand the aero-elastic physics behind, three strategies, i.e. D_x -, a - and M_y -strategies, corresponding to the signals from the blade flapwise tip deflection,

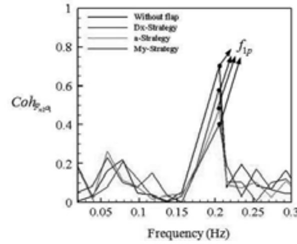

Figure 8: Typical spectral coherence between F_{n1} and a_1 at R_s / R = 0.90, corresponding to the central location of flap1, for different sensing strategies.

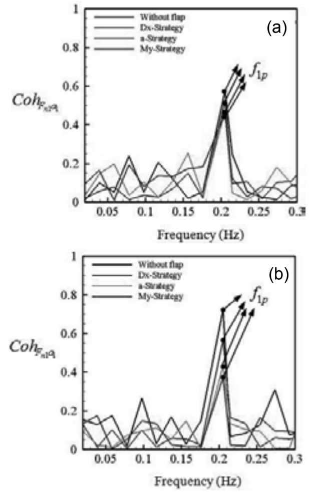

Figure 9: Typical spectral coherence between F_{n1} and a_1 for different sensing strategies at various spanwise locations: (a) R_s / R = 0.60; (b) R_s / R = 0.98.

acceleration and root moment, respectively, were numerically conducted on a Upwind/NREL 5 MW large-scale wind turbine, based on our newly developed aero-servo-elastic platform. The investigations led to three conclusions.

(1) The smart control using three sensing strategies greatly suppressed the fatigue loads on blades, drive-chain components and tower. The best performance was obtained for M_y -strategy case and the maximum reduction percentages in

the standard deviation lay in a range of 12.0 ~ 22.5%, compared with the original collective pitch control method.

(2) For a-strategy, the effectiveness became worse near the outboard part compared to the inboard one within region II, related with the complicated flow separation near the blade tip, while the reverse was the case within region III and the general outcomes tended to be much better, due to the effective flow attachment on the blade surface caused by the turbine pitching action.

(3) The presently proposed smart control effectively turned the in-phased flow and bladevibration at the dominant 1P mode into anti-phased through the controllable DTEF excitation against the nearby fluid field. In other words, the synchronized motion between fluid and structure along the whole blade span was modified to opposition between them, leading to the obviously increased damping ratios of the fluid-structure system. Finally, the fatigue loads on the blade and thus the other turbine components were significantly impaired. This control physics was more evident for M_y-strategy than D_x-, and a-strategies since the signal M_y at the blade root was stronger and contained less interference noise, and thus reflected more primary 1P fatigue load pattern in the flapwise direction, subsequently guaranteeing the best results.

Acknowledgement

This work was supported by the National Natural Science Foundation of China (Grant No. 51222606) and National High-tech R&D Program of China (863 Program) (Grant No. 2012AA051303).

References

[1] Burton T, Sharpe D, Jenkins N, Bossanyi E. *Wind Energy Handbook*; John Wiley & Sons, Ltd: England, 2001; 209-309.

[2] Chopra I. "Review of state of art of smart structures and integrated systems". *AIAA Journal* 2002; 40:145-187.

[3] van Dam CP, Chow R, Zayas JR, Berg DE. "Computational investigation of small deploying tabs and flaps for aerodynamic load control". *Journal of Physics* 2007; 75:012027.

[4] Stanewsky E. "Adaptive wind and flow control technology". *Progress in Aerospace Science* 2008; 37:583-667.

[5] Kota S. "Variable geometry airfoils and active flow control". In: Proceedings of the IEA topical expert meeting on the application of smart structures for large wind turbine rotor blades, Sandia National Labs, Alberquerque, NM, USA; 2008.

[6] Tongchitpakdee C, Benjanirat S, Sankar LN. "Numerical studies of the effects of active and passive circulation enhancement concepts on wind turbine performance". *Journal of Solar Energy Engineering-Transactions of the ASME* 2006; 128(4):432-44.

[7] Vadillo L, Agarwal R, Cary A, Bower W. "Numerical study of virtual aerodynamic shape modification of an airfoil using a synthetic jet actuator". In: 33rd AIAA fluid dynamics conference and exhibit, Orlando, FL, USA; 2003.

[8] Barlas TK, van Kuik GAM. "Review of state of the art in smart rotor control research for wind turbines". *Progress in Aerospace Science* 2010; 46:1–27.

[9] Buhl T, Gaunaa M, Bak C. "Potential load reduction using airfoils with variable trailing edge geometry". *Journal of Solar Energy Engineering-Transactions of the ASME* 2005; 127:503-16.

[10] Barlas TK, Madsen HA. "Influence of actuator dynamics on the load reduction potential of wind turbines with distributed controllable rubber trailing edge flaps (CRTEF)". In: 22nd International Conference on Adaptive Structures and Technologies, Corfu, Greece, October 10-12; 2011.

[11] Smit J, Bernhammer LO, Navalkar S, Bergami L, Gaunaa M. "Sizing and control of trailing edge flaps on a smart rotor for maximum power generation in low fatigue wind regimes". In: 32nd ASME Wind Energy Symposium, National Harbor, Maryland, USA, January 13-17; 2014.

[12] Wilson DG, Berg DE, Barone MF, Berg JC, Resor BR, Lobiz DW. "Active aerodynamic blade control design for load reduction on large wind turbines". In: European Wind Conference & Exhibition, Marseille, France, March 16-19; 2009.

[13] Lackner MA, van Kuik GAM. "A comparison of smart rotor control approaches using trailing edge flaps and individual pitch control". *Wind Energy* 2010; 13:117-34.

[14] Barlas TK, van der Veen GJ, van Kuik GAM. "Model predictive control for wind turbines with distributed active flaps: incorporating inflow signals and actuator constraints". *Wind Energy* 2012; 15:757-71.

[15] Houtzager I, van Wingerden JW, Verhaegen M. "Rejection of periodic wind disturbances on a smart rotor test section using lifted repetitive control". *IEEE Transactions on Control Systems Technology* 2013; 21:347-59.

[16] Plumley C, Leithead W, Jamieson P, Bossanyi E, Graham M. "Comparison of individual pitch and smart rotor control strategies for load reduction". *Journal of Physics* 2014; 524:012054.

[17] Andersen PB, Henriksen L, Gaunaa M, Bak C, Buhl T. "Deformable trailing edge flaps for modern megawatt wind turbine controllers using strain gauge sensors". *Wind Energy* 2010; 13:193-206.

[18] Lackner MA, van Kuik GAM. "The performance of wind turbine smart rotor control approaches during extreme loads". *Journal of Solar Energy Engineering-Transactions of the ASME* 2010; 132:011008-1-8.

[19] Bergami L. "Adaptive trailing edge flaps for active load alleviation in a smart rotor configuration". Ph.D. Thesis, Technical University of Denmark; 2013.

[20] Zhang MM, Yu W, Xu JZ. "Aerodynamic physics of smart load control for wind turbine due to extreme wind shear". *Renewable Energy* 2014; 70:204-10.

[21] Zhang MM, Tan B, Xu JZ. "Parametric study of sizing and placement of deformable trailing edge flap on the blade fatigue load reduction". *Renewable Energy* 2015; 77:217-26.

[22] van Wingerden JW, Hulskamp AW, Barlas T, Marrant B, van Kuik GAM, Molenaar DP et al. "On the proof of concept of a „smart" wind turbine rotor blade for load alleviation". *Wind Energy* 2008; 11:265-80.

[23] Madsen HA, Andersen PB, Andersen TL, Bak C, Buhl T. "The potentials of the controllable rubber trailing edge flap (CRTEF)". 2010 European Wind Energy Conference & Exhibition, Warsaw, Poland, April 20-23; 2010.

[24] Hulskamp AW, van Wingerden JW, Barlas T, Champliaud H, van Kuik GAM, Bersee HEN et al. "Design of a scaled wind turbine with a smart rotor for dynamic load control experiments". *Wind Energy* 2011; 14:339-54.

[25] Castaignet D, Couchman I, Poulsen NK, Buhl T, Wedel-Heinen JJ. "Frequency-weighted model predictive control of trailing edge flaps on a wind turbine blade". *IEEE Transactions on Control Systems Technology* 2013; 21:1105-16.

[26] Berg JC, Barone MF, Yoder NC. "SMART wind turbine rotor: data analysis and conclusions". SAND2014-0712. Sandia National Labs, Albuquerque, NW, USA; 2014.

[27] Abdallah I. "Advance load alleviation for wind turbines using adaptive trailing edge geometry: sensoring techniques". M.Sc Thesis, Technical University of Denmark; 2006.

[28] Andersen PB. "Advanced load alleviation for wind turbines using adaptive trailing edge flaps: sensing and control". Ph.D. thesis, Technical University of Denmark; 2010.

[29] Gaunaa M, Andersen PB. "Load reduction using pressure difference on airfoil for control of trailing edge flaps". In: European Wind Energy Conference & Exhibition, Marseille, France, March 16-19; 2009.

[30] Cooperman A, Martinez M. "Load monitoring for active control of wind turbines". *Renewable and Sustainable Energy Reviews* 2015; 41:189-201.

[31] Jonkman J, Butterfield S, Musial W, Scott G. "NREL Technical Report". NREL/TP-500-38060, Golden, CO, USA ; 2009.

[32] Wind turbines-Part 1: Design requirements. International Electro-technical Commission (IEC), IEC 61400-1 Ed. 3; 2005.

[33] Yu W, Zhang MM, Xu JZ. "Effect of smart rotor control using a deformable trailing edge flap on load reduction under Normal and Extreme Turbulence". *Energies* 2012; 5:3608-26.

[34] Jonkman BJ. "Turbsim User"s Guide, Version 1.50". NREL/TP-500-46198, Technical Report for NREL, Golden, CO, USA; 2009.

[35] NWTC Design Codes, NREL, Golden, CO, USA, http://wind.nrel.gov/designcodes/simulators/aerodyn/; 2005.

[36] van Rooij RPJO M. "Technical Report IW-96087R". Delft University of Technology; 1996.

[37] NWTC Design Codes, NREL, Golden, CO, USA, http://wind.nrel.gov/designcodes/simulators/fast/; 2005.

[38] Smit J, Bernhammer LO, Navalkar S, Bergami L, Gaunaa M. "Sizing and control of trailing edge flaps on a smart rotor for maximum power generation in low fatigue wind regimes". 32nd ASME Wind Energy Symposium, National Harbor, Maryland, USA, January 13-17; 2014.

[39] Zhang MM, Cheng L, Zhou Y. "Control of poststall airfoil aerodynamics based on surface perturbation". *AIAA Journal* 2008; 46:2510-2519.

Post-mortem study on structural failure of a wind farm impacted by super typhoon Usagi

Xiao Chen*, Chuanfeng Li, Jianzhong Xu
National Laboratory of Wind Turbine Blade Research and Development Center, Institute of Engineering Thermophysics, Chinese Academy of Sciences. 11 Beisihuanxi Road, Beijing, 100190, China.
*Corresponding author: drchenxiao@163.com

Abstract: Extreme wind conditions such as typhoons severely endanger structural integrity of wind turbines. This paper presented a post-mortem study on structural failure of a coastal wind farm impacted by super typhoon Usagi in 2013. A particular focus was placed on the effect of strong winds and the change of wind direction on tower collapse and blade fracture. Failure investigation was conducted at the field, and data of local winds, tubular steel towers and composite rotor blades were collected and analyzed. A systematic procedure was developed by integrating wind characterization using CFD method, wind load calculation through aeroelastic analysis and structural analysis by the classic beam theory to quantitatively examine structural failure response of wind turbines. It was found that strong winds and the change of wind direction during typhoon impact had significant effect on tower collapse and blade fracture. The fuse function of the rotor blade whose fracture would protect the tower from collapse was also addressed. The findings obtained from this study provide more understanding on structural failure of wind farms located in typhoon/hurricane-prone regions worldwide.

Keywords: wind profile; tower collapse; composite blade; local yielding; fuse function

1. Introduction

Super typhoon Usagi, which was on category 4 according to the Saffir-Simpson hurricane scale [1], impacted a wind farm near Shanwei city on the southeast coast of China in 2013, see Figure 1. During typhoon impact, the wind farm experienced strong winds with a maximum wind speed (3s average) of 57 m/s at 10m elevation and a large change of wind direction according to a nearby weather station, see Figure 2. As a result of this super typhoon, eight turbine towers collapsed, eleven rotor blades broke off and three turbines were burned, leading to approximately $16 million loss to the wind farm.

Authors of this paper carried out a post-mortem study on the wind farm focusing on the tower collapse and blade failure. Aerodynamic analysis was conducted to characterize local wind speeds of wind turbines. Aeroelastic analysis was used to determine the wind loads acting on the turbines. Structural analysis was performed to examine the failure response of turbine towers and rotor blades. During this process, data of wind records, terrain topography and turbine status were collected, analyzed and assessed together with field investigation and user inquiry. Through this study, essential factors affecting structural failure of the wind farm were addressed. This paper summarized the process of and the key findings from structural failure investigation on the wind farm. It is expected that insights gained from this study could assist structural failure mitigation of wind farms under extreme wind conditions.

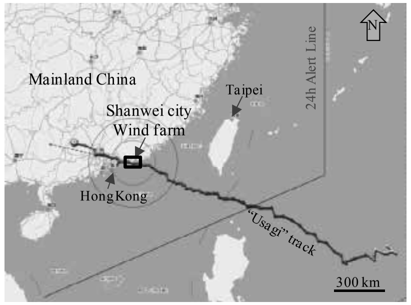

Figure 1 Typhoon Usagi and the wind farm location

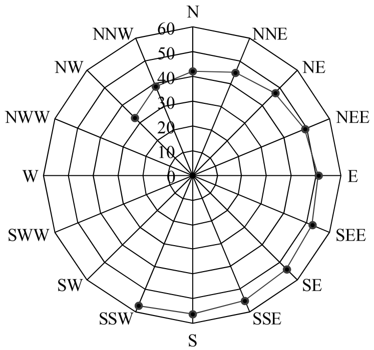

Figure 2 Maximum wind speeds (3s average) at 10m elevation for different wind directions

2. Approach

The proposed procedure for the post-mortem study on structural failure of the wind farm is shown in Figure 3. The wind profile along the turbine height was estimated based on wind data recorded at the weather station and the typhoon wind profile model. Wind loads acting on the wind turbines were then calculated considering turbine positions at an emergency stop state and the terrain effect of the wind farm, which was numerically reconstructed in a three dimensional model using Global Positioning System (GPS) data. Computational Fluid Dynamics (CFD) simulation was followed to capture wind characteristics of the concerned wind farm terrain under typhoon impact.

Wind loads acting on the turbines were calculated according to aeroelastic analysis and structural wind engineering approach. Structural models of tubular steel towers and composite rotor blades were reconstructed as cantilever beam models based on the information obtained from turbine specification, design documents, user inquiry as well as field investigation. Structural failure response of the towers and the blades was examined and further compared with post-mortem observation in terms of failure mode and failure location.

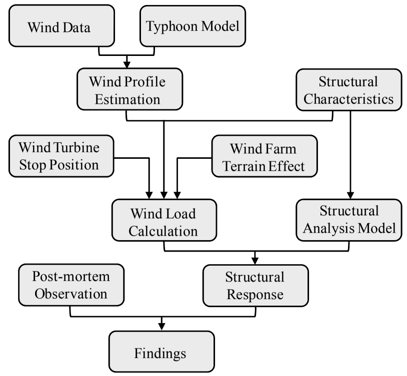

Figure 3 The proposed procedure for the post-mortem study

3. Post-mortem Observation

Field investigation on the wind farm was conducted after Usagi impact. Representatively, an overview of structural failure is shown in Figure 4. Failure statistics showed that eight out of twenty-five towers collapsed, three out of twenty-five turbines were burned and eleven out of seventy-five blades fractured. The number of the fractured blades would be thirty-five if the blades installed on the collapsed towers were taken into account, leading to 46.7% rotor blades failed in the wind farm.


Figure 4 Structural failure of the wind farm

It is found that all tubular steel towers were failed by local buckling and collapsed towards a direction of SW or SSW, suggesting the dominating wind loads coming from NE or NNE upon tower collapse. The composite blades were found to fracture at a location ranging from the inboard to the middle span, where the load-carrying box-beams inside the blades were totally fractured. Severe cracks were also found at sandwich shells of the blades which did not break off.

The distribution of structural failure over the wind farm appeared to be relevant to the terrain characteristics. Six out of eight collapsed towers were found on the flat valley floor while most towers located on ridges with higher elevations remained intact. On the contrary, most blade breakage occurred at the turbines located on ridges rather than on the valley floor.

4. Computational Fluid Dynamics (CFD) Model

4.1 Simulation Method

To obtain wind characteristics of the wind farm based on available wind records. CFD analysis was conducted on the wind farm. The atmospheric flow was predicted by solving the incompressible Reynolds averaged Navier-Stokes equations using the commercial FLUENT code [2]. The equations were discretized using finite volume method and the second order upwind algorithm was used for the spatial discretization. Pressure-velocity coupling was carried out using SIMPLE algorithm. The turbulence was modeled by the two equations standard k-ε model with model constants modified according to reference [3].

A user-defined wall function for the near-wall treatment was used taking into account the assumption that the atmospheric boundary layer friction velocity u^* is equal to the laminar bottom layer friction velocity u_{r0}.

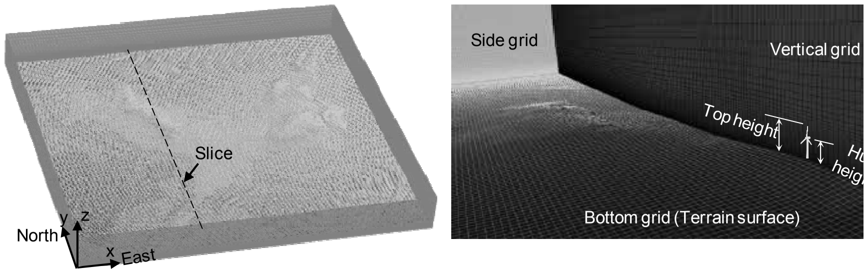

(a) CFD calculation domain (b) Local grids at Slice

Figure 5 CFD grid of the offshore wind farm

For a fully turbulent region [4]:

$$u^+ = \frac{1}{\kappa}\ln(\frac{z_p}{z_0}) = \frac{1}{\kappa}\ln(\frac{z^+}{Z_0^+}) \quad (1)$$

where u^+ is the dimensionless wall tangential velocity. The dimensionless height z^+ is defined as $z^+=u_{\tau0}z_p/v$, where v is the kinetic viscosity of the flow, and z_p is the distance from the center of the first grid cell to the wall surface, z_0 is the roughness length of the wall, $Z_0^+=u_{\tau0}z_0/v$ is the dimensionless roughness length, κ is the von-Karman constant and is 0.41 in this study.

4.2 CFD Grid

Using GPS data, the wind farm terrain was numerically reconstructed in a 3D model, which was further used as the computational domain of CFD analysis as shown in Figure 5(a). The size of the domain was 5790m×5580m×500m (x×y×z). The height of the domain was considerably larger than the peak elevation (z=56.4m) of the terrain so that the influence of the terrain on the top surface of the domain could be ignored.

Structured grid method was used to mesh the domain and the total number of grid cells were 500×500×55. The bottom surface of the domain characterizing the terrain were meshed with equidistant spacing grids in x and y direction. Representatively, the local grids are shown in Figure 5(b). The height of the first grid was determined based on the roughness length z_0, and the height of grid cells along z direction was changed incrementally from $2z_p$ to 3.0 m in the region between terrain surface and the top height of wind turbines. The value of z_p was determined to be $3.69z_0$ according to [4].

4.3 Boundary Condition

According to reference [5], the roughness length z_0 ranges between 0.03 and 0.1 m for an open terrain such as the nearshore water with a wind speed higher than 30 m/s and the countryside with low grasses. The value of 0.1 m was used for the island ground based on its vegetation condition and the upper bound value of 0.1 m was used for the nearshore water considering that the recorded wind speeds were much higher than 30 m/s during the typhoon event.

The bottom surface, or terrain surface, of the domain was defined as a non-slipped wall, and the top surface of the domain was defined as a symmetry boundary assuming that the atmospheric flow was fully developed at the altitude. For four vertical sides of the domain, velocity inlet or outflow boundary conditions are applied based on different wind directions.

According to D.A. Spera [6] and B.A. Harper et al. [7], neutral or near-neutral atmosphere conditions have been observed to prevail at high wind speeds, for which the logarithmical model was able to model the wind profile. M.D. Powell et al. [8] analyzed wind data measured from GPS sondes and proved that logarithmical model was able to describe wind profiles of tropical cyclones. Therefore, the logarithmical model is adopted in this study to describe the relationship between the mean wind speed u_z of strong winds like tropical cyclones and the height z and it can be described by equation (2).

$$u_z = \frac{u^*}{\kappa}\ln(\frac{z}{z_0}) \quad (2)$$

where u^* is the atmospheric boundary layer friction velocity which could be back-calculated using the recorded wind speed at 10m elevation, i.e., u_{10}.

For neutral atmosphere conditions, the turbulent kinetic energy, k, and turbulent dissipation rate, ε, as shown in equations (3) and (4) can be used to model the turbulence, where decreased shear stresses were introduced to modify the turbulent kinetic energy [4]. Therefore, for the velocity inlet boundary, the longitudinal log-law velocity distribution as shown in equation (2) was used and turbulence properties were modeled by equations (3) and (4).

$$k = \frac{u^{*2}}{\sqrt{C_\mu}}(1-\frac{z}{h_g})^2 \quad (3)$$

$$\varepsilon = \frac{u^{*3}}{\kappa z} \quad (4)$$

where C_μ is a modified constant in k-ε model and it is 0.03 in this study, h_g is Geostrophic plane elevation and it is defined as:

$$h_g = \frac{u^*}{6f} \quad (5)$$

f is Coriolis parameter and is defined as f=2Ωsin(|λ|), where Ω is angular velocity of the earth's rotation and it is 7.2722×10^{-5} rad/s, λ is the latitude of the wind farm and it is 22.75ºN. It is noted that instead of using a standard air density of 1.225 kg/m^3, this study used the value of 1.094 kg/m^3 for the moist air in typhoon event.

4.4 Model Assessment

To examine whether the model is able to obtain a sustainable wind profile with the model settings, the simulation method was applied to an empty fetch with a same size as the wind farm. Representatively, three wind profiles with u_{10} of 33, 47.2, and 57 m/s were applied to the domain inlet. The wind profiles calculated at the middle, or the center of the domain, and the outlet are shown in Figure 6.

It is found that wind speed profiles were maintained well along the empty fetch with minor differences within 4%, suggesting that the proposed method and the model settings are justifiable and can be applied to analyze the wind farm terrain.

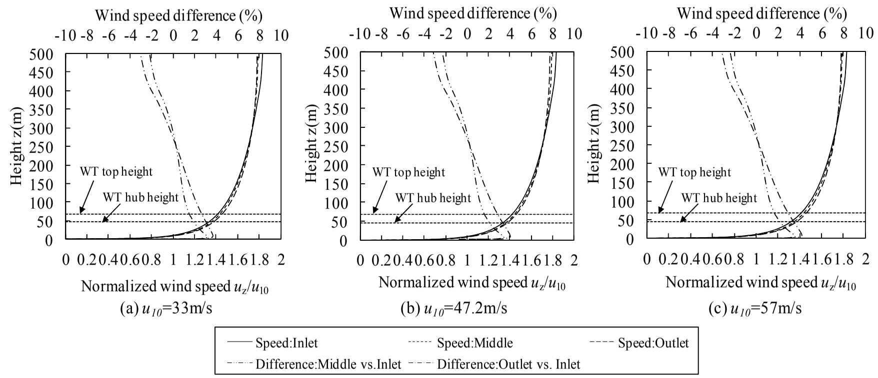

Figure 6 Wind profiles of an empty fetch with the same size as the offshore wind farm

5. Wind Load Calculation

5.1 Examined Cases

This study focuses on the wind turbine at an emergency stop state due to power loss during Usagi impact. The stop position of a wind turbine can be determined by the nacelle heading direction, or the yaw angle, the blade pitch angle and the azimuth angle. To facilitate discussion, typical stop positions were investigated according to the wind farm operator. The nacelle heading direction of NW was considered to represent the most possible stop positions of wind turbine upon power loss. The blade pitch angle was set to 90 degree for all three blades, i.e., 90-90-90, which is the pitch angle required by the turbine when pitch system works properly. Another pitch angle of 0-90-90 was also examined to represent the case with pitch malfunction in the turbine as observed in the field. The azimuth angle was considered to be zero as this would result in one blade pointing upwards and sustaining a maximum wind speed. Two wind directions are considered. The one is NNE the wind came from which resulted tower collapse towards SSW, and the other is SSW the wind came from which had a maximum speed during Usagi. The wind loading cases are shown in Table 1.

5.2 Methods for Load Calculation

Two methods were considered for wind load calculation. One was from a structural wind engineering perspective considering that only the emergency stop state is of concern in the current study. A well-established calculation procedure specified in the design standard [9] can be used for a stopped turbine. Geometrically, the tower was

Table 1 Examined wind loading cases

Case No.	Turbine stop position		Wind condition			
				Inlet without terrain elevation		With terrain elevation
	Nacelle direction	Blade pitch	Wind direction	Wind speed @ 10m(m/s)	Wind speed @ hub(m/s)	Wind speed @ hub(m/s)
#1	NW	90-90-90	NNE	45	59.8	63.3
#2		0-90-90				
#3			SSW	57	75.8	83.3

simplified as a cantilever cylinder with variable cross-sectional diameters; the blade was simplified as a cantilever beam with cylindrical inboard sections and flat outboard sections; and the nacelle was simplified as a rectangular parallelepiped. The other method was based on aeroelastic analysis using an open source code, FAST [10], developed by National Renewable Energy Laboratory (NREL).

It is noted that a power law model is used in FAST code to define wind profile. Curve fitting was applied to the wind profiles obtained from CFD simulation. Appropriate power law coefficients were then determined and used in FAST code. It is noted that little discrepancy was found between wind profiles and their power-law representation with regard to the wind speed within the height range from 10m elevation to the turbine top.

Blade bending moments due to wind loads calculated from FAST code and design standard were compared in Figure 7 for two representative wind speeds. It shows that two methods agree well in predicting wind loads of the blade. Because FAST does not include the capability to calculate wind loads acting on the tower and the nacelle, the method specified in the design standard was used instead. The wind loads acting on the blade were calculated from FAST code.

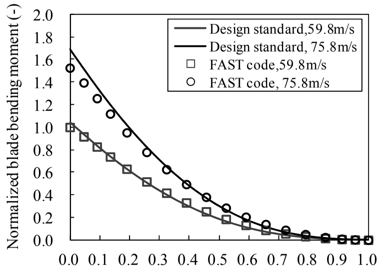

Figure 7 Comparison of wind loads calculated from different methods

In addition to wind loads, there are other external loads subjected by the tower as depicted in Figure 8, where P_{tower} is the wind loads of the tower; W_{top} and W_{tower} are the gravity forces from the tower top mass and the tower itself, respectively; W_{top} consists of nacelle weight $W_{nacelle}$ and rotor weigh W_{rotor}; $F_{nacelle}$ and F_{rotor} are the resultant wind loads from nacelle and rotor, respectively; M_{rotor} is the resultant wind moment from rotor. It is worth noting that among these load sources, $F_{nacelle}$, F_{rotor} and M_{rotor} are dependant on the stop position of the turbine.

It should be noted that when a blade fractures, the structural configuration of the blade changes and wind loads acting on wind turbine would change accordingly. To simulate this failure process, the structural configuration of wind turbine would be updated in the model. Before structural failure, the whole wind turbine was analyzed and structural response of blade and tower was obtained. Upon blade failure, the remaining blade and the tower were analyzed with updated wind loads, i.e., $F_{nacelle}$, F_{rotor}, M_{rotor}, and W_{rotor}, and used for the subsequent loading. This iterative loading process allows interaction between blade fracture and tower collapse in the failure scenario.

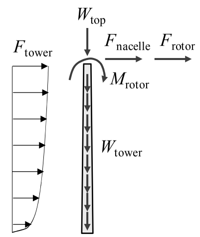

Figure 8 The external loads acting on the tower

6. Structural Failure Response

6.1 Structural Analysis Models

The rotor blades are made from glass fiber composites and they can be treated as a cantilever beam from a structural point of view. Two blade shells are light sandwich constructions and they are used to provide aerodynamic shapes of the blade. A box beam spar of unidirectional (UD) composites is bonded inside the blade shells as a supporting structure responsible for load-carrying. The bending stiffness of the composite blade was calculated according to design documents. The distributed wind loads calculated from FAST code were applied along the blade span and bending strains of the blade were then calculated using the classic beam theory. Compressive failure strain of UD composites was used as failure criterion to determine failure load and failure location of the blade. Upon the blade failure, the blade sections at the outboard of the failure location were removed from the structural model and only wind loads acting on inboard sections of the blade remained the same.

The turbine tower is a cantilever steel tube. The shell wall thickness of the tower changes with the tower height and butt welding is used to join steel shells with different thicknesses. As the local shell buckling has been found to be the failure mode of the tower, the elastic buckling strength of the tower has been first calculated and it was found to be not likely the cause of tower collapse. Subsequently, it was suspected that inelastic response may play a role in the tower collapse. In order to accurately obtain the local stress of the failure section, stress concentration factor (SCF) has to be taken into account in the stress analysis. For the tower section where two steel shell sections have different thicknesses and are butt welded together, SCF can be well predicted according to reference [11] and it is expressed by equations (6-1) to (6-3).

$$\mathrm{SCF}=1+\frac{6(\delta_t+\delta_m)}{t}\cdot\frac{1}{1+(T/t)^{\beta}}e^{-\alpha} \quad (6\text{-}1)$$

$$\alpha=\frac{1.82L}{\sqrt{Dt}}\cdot\frac{1}{1+(T/t)^{\beta}} \quad (6\text{-}2)$$

$$\beta=1.5-\frac{1.0}{\log(D/t)}+\frac{3.0}{(\log(D/t))^2} \quad (6\text{-}3)$$

Where, δ_t = shift in neutral axis at thickness transition =0.5(T-t), δ_m= fabrication tolerance which equals to a typical value of 0.15t in many steel fabrication standards, T and t are the thicknesses of the thicker and thinner steel shell at transition region, respectively, L= length of transition in thickness, and D=diameter of tubular shell. All parameters were readily available according to design documents and field measurements.

The nominal compressive stress of the tower was calculated using the classic beam theory. A multiplier of SCF was then applied to the nominal value to obtain the actual compressive stress at the tower section with shell wall thickness change. The yielding stress of the steel was used as failure criterion to determine the occurrence of local steel yielding and the associated inelastic buckling of the tubular tower.

6.2 Results and Discussion

(1) Failure location and tower collapse direction

Structural response of the tower and the blade at three cases are shown in Figure 9, where the tower height and the blade length are normalized by their respective total values, and compressive stress of the tower and compressive strain of the blade are normalized by yielding stress of the steel and failure strain of UD composite, respectively.

It can be seen that the locations with peak stress/strain agree reasonably with failure regions of tower/blade observed from post-mortem investigation. For the blade, the peak strain occurs at a normalized length of 0.32, which is within the range from 0.26 to 0.48 as observed in the field. For the tower, the peak stress occurs at a normalized height of 0.23, which is slightly larger than the range from 0.20 to 0.22 as observed in the field.

The results of Case#1 as shown in Figure 9(a) suggest that if the wind turbine stops with the nacelle heading towards NW and all blades being feathered, the wind from NNE with a hub wind speed of 63.3 m/s would cause the blade to sustain a strain level lower than the failure strain. However, the tower has to experience material yielding which further leads to the local inelastic buckling. Consequently, tower collapse towards SSW is inevitable due to the prevailing wind load coming from NNE. The results justified the massive tower collapse towards SSW as observed in the field.

It is worth noting that the turbines are designed to survive a maximum wind speed of 70 m/s regardless of their stop positions. In other words, any stop position should have been examined and verified in the turbine design. According to the investigation, however, it appears that the towers did not have sufficient strength at the section with a rapid reduction of shell wall thickness even when they were subjected to a wind speed lower than the design survival wind speed.

(2) Effect of blade pitch malfunction

Figure 9(b) shows the results of Case #2 when one blade has malfunction in the pitch system and is not able to pitch to 90 degree as intended. It is found that the blade strain is very small and the tower stress is reduced to a level significantly below the failure criterion. This suggests that the tower collapse which should have occurred when the blade pitch system works properly is prevented due to the pitch malfunction. The stop position once structurally unfavorable to the turbine becomes favorable when wind direction changes. The results show the vital importance of stop position to the failure of the turbine.

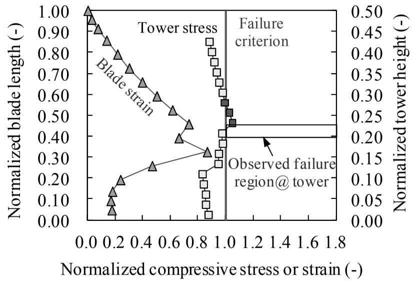

(a) Case #1

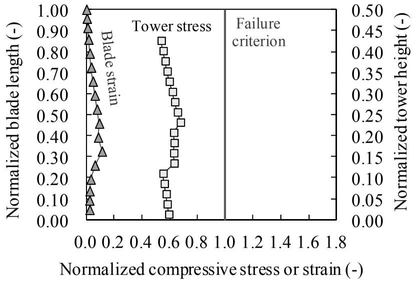

(b) Case #2

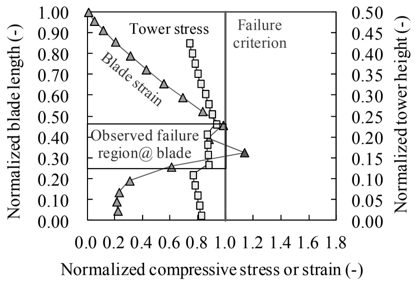

(c) Case #3

Figure 9 Tower stress and blade strain at different wind loading cases

(3) Fuse function of the blade

Interestingly, if not all blades are feathered as intended due to possible malfunction in the pitch system, failure scenario of the wind turbine would change dramatically as shown in Figure 9(c). The blade failure would occur when the wind comes from SSW with a hub wind speed of 83.3 m/s, which far exceeds the design survival wind speed of the turbine. Due to the blade failure, the bending stresses of tower caused by F_{rotor} and M_{rotor} are significantly reduced. As a result, the total tower stress becomes further away from meeting the failure criterion, meaning that the tower survives the typhoon impact taking advantage of the blade failure. In this case, the blade actually performs as a protective fuse component and its sacrifice prevents the tower from collapse.

According to the cost breakdown of a typical onshore wind turbine [12], one blade only shares about 8% of the total cost of the whole turbine while the majority of the turbine cost comes from the tower and mechanical components inside the nacelle, e.g., generator, transformer, gearbox, power convertor, etc. Therefore, it is not only structurally effective but also economically beneficial to sacrifice one blade during extreme wind conditions in order to protect the tower, whose collapse would be otherwise catastrophic and could lead to the total loss of the turbine.

7. Conclusion

Post-mortem study was conducted systematically on a coastal wind farm severely damaged by the super typhoon Usagi. It was found that strong wind speed was the main reason for the destructive structural failure of the wind farm. Nevertheless, the stop position of wind turbine also played a vital role for the tower collapse and blade breakage due to the change of wind direction during typhoon event. The study also suggested that the tower collapse might associate with a design defect in tower wall thickness as local inelastic buckling of the tower was predicted to occur at a wind speed lower than the design survival wind speed of the turbine. The blade not pitched as intended was found to be able to protect the tower from collapse taking advantage of its fracture. Upon blade fracture, the wind loads on the rotor considerably reduce and the stress sustained by the tower decreases consequently. Considering the small proportion of the blade cost in the total turbine cost, it may be advisable to design a blade as a fuse component in order for the rest of structural components of wind turbines to survive the extreme winds.

Acknowledgement

This study is financially supported by the National Natural Science Foundation of China (Grant No. 51405468), the Scientific Research Foundation for the Returned Overseas Chinese Scholars, State Education Ministry and National High-tech R&D Program of China (863 Program) (Grant No. 2012AA051303).

References

[1] National Hurricane Center, Saffir-Simpson Hurricane Wind Scale, www.nhc.noaa.gov/aboutsshws.php, accessed on September 16, 2015.

[2] ANSYS, Inc. ANSYS FLUENT 13.0 User's Guide, ANSYS, Inc., Canonsburg, PA, USA, 2010.

[3] Bechmann A, Sørensen N N, Johansen J, Vinther S, Nielsen B S and Botha P. Hybrid RANS/LES method for high Reynolds numbers, applied to atmospheric flow over complex terrain. Journal of Physics: Conference Series, 75, 012054, 2007.

[4] Zhang X D. CFD simulation of neutral ABL flows. Risø-R-1688(EN). Roskilde: Risø DTU National Laboratory for Sustainable Energy; 2009.

[5] Harper B A, Kepert J D and Ginger J D. Guidelines for converting between various wind averaging periods in tropical cyclone conditions. Geneva: World Meteorological Organization; 2008.

[6] D.A. Spera, Wind Turbine Technology-Fundamental Concepts of Wind Turbine Engineering, Second edition, ASME, New York, NY, USA, 2009.

[7] B.A. Harper, J.D. Kepert, J.D. Ginger, Guidelines for converting between various wind averaging periods in tropical cyclone conditions. World Meteorological Organization, Geneva, 2008.

[8] Powell M D, Vickery P J and Reinhold T A. Reduced drag coefficient for high wind speeds in tropical cyclones. Nature, 2003, 422: 279-83.

[9] National standards of the People's Republic of China, Code for design of high-rising structures GB 50135-2006, China Planning Press, Beijing, 2007.

[10] NWTC Information Portal (FAST). https://nwtc.nrel.gov/FAST, accessed on August 15, 2015.

[11] I. Lotsberg, Stress concentrations due to misalignment at butt welds in plated structures and at girth welds in tubulars, International Journal of Fatigue, 31, 1337-1345, 2009.

[12] International Renewable Energy Agency, Renewable energy technologies: cost analysis series, wind power, June, 2012.

Detailed Simulation of Offshore Wind Turbine

V. Leble, Y. Wang, G.N. Barakos*
School of Engineering, University of Liverpool, Harrison Hughes Building
Liverpool, L69 3GH, U.K.

Abstract

This paper presents results of numerical computations for floating off-shore wind turbines using, as an example, a machine of 10-MW rated power. The aerodynamic loads on the rotor are computed using the Helicopter Multi-Block flow solver developed at the University of Liverpool. The method solves the Navier-Stokes equations in integral form using the arbitrary Lagrangian-Eulerian formulation for time-dependent domains with moving boundaries. Hydrodynamic loads on the support platform are computed using the Smoothed Particle Hydrodynamics method, which is mesh-free and represents the water and floating structures by a set of discrete elements, referred to as particles. The motion of the floating offshore wind turbine is computed using a Multi-Body Dynamic Model of rigid bodies and frictionless joints. Mooring cables are modelled as a set of springs and dampers. All solvers were validated separately before coupling, and the results are presented in this paper. The importance of coupling is assessed and the loosely coupled algorithm used is described in detail alongside the obtained results.

Notation

	Latin
d	distance between the particles [m]
I	inertia tensor [$kg \cdot m^2$]
m	mass [kg]
w	relative weight between the fluid and body particles [-]
	Greek
α	artificial viscosity parameter [-]
γ	adiabatic index [-]
	Acronyms
BEM	Blade Element Momentum method
BILU	Block-Implicity Upper Lower factorisation
CD	Central Differences
CFL	Courant-Friedrichs-Lewy number
FOWT	Floating Off-shore Wind Turbine
FSI	Fluid Structure Interaction
GCG	Generalised Conjugate Gradient
GMRES	Generalised Minimal Residual method
HMB2	Helicopter Multi-Block CFD Solver
HPC	High Performance Computer
IBQN-LS	Interface Block Quasi-Newton with an approximation for the Jacobian from a Least-Squares model
IQN-ILS	Interface Quasi-Newton algorithm with an approximation for the inverse of the Jacobian from a Least-Squares model
MBDM	Multi-Body Dynamic Model
MPI	Message Passing Interface library
SPH	Smoothed Particle Hydrodynamics Method
WT	Wind Turbine

*Corresponding Author: g.barakos@liverpool.ac.uk

1 Motivation and objectives

Wind is a substantial renewable energy source, and historical trends show the large development of on-shore wind turbine size and power capacity over the last three decades. However, high potential sites on land are already occupied, and others are hard to utilise due to e.g. difficult access, high altitude, costly transportation and on-site assembly. Therefore, a recent trend is to exploit the off-shore wind potential and take advantage of the available space and steady winds. Shallow water regions suitable for constructing seabed-fixed, off-shore wind turbines are also limited, and for sea depths exceeding 30-60 m, floating structures become more economic. Hence, emphasis is placed on the development of floating offshore wind turbines (FOWTs). Unlike onshore machines, the FOWT is a highly dynamic system since it is simultaneously subjected to the wind and wave loads and only constrained by a mooring system. Further, the rotor frequency is low due to the large size of the blades, and wave frequencies may come close or coincide with the rotational frequency of the rotor. It is, therefore, important to develop a method for the analysis of this air-structure-water system.

The common approach is to combine simplified tools into one hybrid model to predict wind turbine responses under wind and wave loads. The Blade Element Momentum (BEM) method is frequently used to calculate aerodynamic loads on the blades and tower (*e.g.* Jonkman,[19] Skaare *et al.*,[35] Karimirad *et al.*[21]). Sometimes analytical models are used, that take the form of algebraic equations for the applied thrust that is proportional to the area of the rotor and the relative velocity between the wind and the hub as in Roddier *et al.*[33] and Karimirad *et al.*[20] Aero-elasticity is included in BEM methods, where the structure is described by a multi-body formulation in which wind turbine structures are subdivided into a number of bodies and each body consists of an assembly of Timoshenko beam elements.[23] Another approach is to characterise flexible bodies using linear modal representation, which usually implies the assumption of small deflections.

The hydrodynamic loads on the support structure are often modelled with a linear potential theory assuming inviscid, incompressible and irrotational flow, also known as Airy wave theory.[19,21,33] In this case, frequency dependent hydrodynamic-added-mass and hydrodynamic-damping matrices, and wave-excitation force vector are precomputed for a given problem, and serve as an input to the coupled model. At the beginning of the computation, the wave-radiation-retardation kernel is obtained by integrating user-supplied added-mass or damping coefficients. This way external computer routines can be linked to the aerodynamic solver as a function, that employs convolution integrals and returns hydrodynamic loads at given instances. Since the equations are linear, the non-linear hydrodynamic viscous drag is included from Morison's equation using strip theory. Linearisation of the hydrodynamic problem implies that the translational displacements of the support platform are small relative to the size of the body, and that amplitudes of the incident waves are much smaller than their wavelengths *i.e.* steep or breaking waves can not be modelled.

Some extentions to the second-order potential flow was performed *e.g.* by Marino *et al.*[26] and Roald *et al.*[32] Even with second-order hydrodynamic terms included, however, the potential hydrodynamic theory might not completely apply to floating wind turbine platforms due to the large displacements encountered.[27]

Mooring lines constraining the FOWT are represented by springs,[34] flexible beams[35] or multi-body chains of rigid bodies.[27] Sometimes, precomputed non-linear force-displacement relationships are employed as in Karimirad *et al.*[20] Some of the works in the field of FOWT modelling are summarised in Table 1.

The purpose of this paper is to present a coupling algorithm that brings together two Navier-Stokes solvers. For this, the Helicopter Multi-Block (HMB2) solver developed at Liverpool University[2] is used to solve for the aerodynamic forces acting on the wind turbine (WT) blades. Hydrodynamic forces on the support platform are solved using the Smoothed Particle Hydrodynamics (SPH) method.[13,39] Both solvers are coupled by exchanging information while the FOWT is represented by a lumped mass model.

The remainder of the paper is organised as follows. First, the numerical solvers are described, and this is followed by validation cases for each one of them. Then, the coupling algorithm is described. Finally, test cases for the coupled computations are put forward, and results are presented and discussed before drawing conclusions.

2 Numerical methods

The HMB2 code is a 3D multi-block structured solver for the Navier-Stokes equations in 3D. HMB2 solves the Navier-Stokes equations in integral form using the arbitrary Lagrangian-Eulerian formulation for time-dependent domains with moving boundaries. The solver uses a cell-centred finite volume approach combined with an implicit dual-time method. Osher's upwind scheme[30] is used to resolve the convective fluxes. Central differencing (CD) spatial discretisation is used for the viscous terms. The non-linear system of equations that is generated as a result of the linearisation is solved by integration in pseudo-time using a first-order backward difference method. A Generalised Conjugate Gradient (GCG) method[9] is then used in conjunction with a Block Incomplete Lower-Upper (BILU) factorisation as a pre-conditioner. The HMB2 solver has a library of turbulence closures including several one- and two- equation models. Turbulence simulation is also possible using either the Large-Eddy or the Detached-Eddy simulation approach.[36] The solver was designed with parallel execution in mind and the MPI library along with a load-balancing algorithm are used to this end. The flow solver can be used in serial or parallel fashion for large-scale problems. Depending on the purposes of the simulations, steady and unsteady wind turbine CFD simulations can be performed in HMB2 using single blade or full rotor meshes generated using the ICEM-Hexa tool. Rigid or elastic blades can be simulated using static or dynamic computations. HMB2 allows for sliding meshes to simulate rotor-tower interaction cases as described in Steijl *et al.*[37] Alternatively, overset grids can be used with the details presented in Jarkowski *et al.*[18] To account for low-speed flows, the Low-Mach Roe scheme (LM-Roe) developed by Rieper[31] is employed for wind turbine cases.[6]

The sea is modelled with the SPH method. Each SPH particle has individual material properties and moves according to the Navier-Stokes equations solved in the Lagrangian form. SPH offers a variety of advantages for fluid modelling, particularly those with a free surface and moving bodies. Due to the Lagrangian nature of the SPH method, the free surface requires no special treatment. Further, submerged bodies can be represented with particles. Therefore, it is natural for the method to include floating objects.

The motion of the FOWT components is computed with a multi-body model (MBDM) of rigid bodies and frictionless joints. Mooring cables are modelled as a set of springs and dampers, according to Savenije.[34] The coordinate partitioning method of Nikravesh[28] is used to solve the resulting system of mixed differential-

Table 1: Works relevant for the complete FOWT models.

Author(s)	Aerodynamic method	Hydrodynamic method
Jonkman[19]	BEM	Linear potential
Skaare *et al.*[35]	BEM	Linear potential
Roddier *et al.*[33]	Analytical	Linear potential
Karimirad *et al.*[21]	BEM/Analytical	Linear potential/Second-order potential/Morison's equation

algebraic equations. The time integration scheme is explicit and can be either the Runge-Kutta method of fourth order or Euler's method. The non-linear position equations are solved using the Newton-Raphson method with exact, an analytical, Jacobian.

Clearly, many disciplines converge in the coupled model of the FOWT. Current implementation is schematically presented in Figure 1. Anoter option would be to employ a multi-phase solver (e.g. Volume of Fluid). However, this approach does not tackle the problem of coupling, but shifts it to the structure-fluid side.

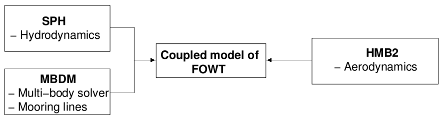

Figure 1: Schematic of the solvers employed in the floating off-shore wind turbine model.

2.1 Validation of the aerodynamic solver

The HMB2 CFD solver has so far been validated for several wind turbine cases, including the NREL Annex XX experiments,[14] where the effect of the blades passing in front of the tower was captured, as can be seen by the deficit of the thrust values presented in Figure 2a. The pressure and PIV data of the MEXICO project[5] have also been used for validation, where the wake was resolved on a fine mesh capable to capture and preserve the vortices downstream the rotor (Figure 2b), which enabled the prediction of the onset of wake instabilities.[7]

2.2 Validation of the hydrodynamic solver

The hydrodynamic loads are estimated using the SPH method validated against the experiments of Greenhow and Lin[15] for the high speed entry of a half-buoyant solid cylinder into calm water. Following the experimental setup shown in Figure 3a, a cylinder of density of

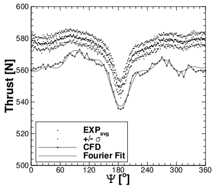

(a) Deficit in thrust of the NREL Annex XX blade when passing in front of the tower with corresponding Fourier series fit of five harmonics.

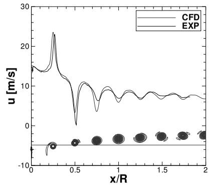

(b) Axial velocity profile passing through the first vortex generated by the MEXICO blade.

Figure 2: Validation cases for the HMB2 solver. (a) Thrust prediction over a full revolution of the NREL Annex XX wind turbine at 7m/s wind speed; (b) Prediction of MEXICO rotor wake, including axial velocity profile.

$500kg/m^3$ was allowed to fall freely from the height of $0.8m$ under gravity acceleration; the water depth was $0.3m$. The density of the cylinder was assigned by defining the relative weight between fluid and cylinder particles to be $w = 0.5$. Simulations were run with a cubic spline kernel, artificial viscosity with viscosity parameter $\alpha = 0.1$, adiabatic index $\gamma = 7$, and Courant-Friedrichs-Lewy number $CFL = 0.2$. The viscosity between the cylinder SPH particles and fluid particles was neglected. Five cases were compared with different distances d between the particles. The penetration depth of the cylinder for all cases along with experimental results are shown in Figure 3b, whereas Figure 4 shows the water surface deformation. The results were used for estimating the particle density and viscosity necessary for computations of floating bodies. Note, that the best agreement with the experiment was obtained with distances between the particles $d = 0.23cm$, what corresponds to 25 particles per radius of the cylinder.

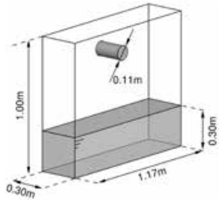

(a) Schematic of the SPH validation setup.

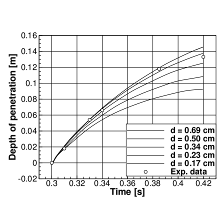

(b) Depth of penetration of a cylinder.

Figure 3: Validation case for the SPH solver. (a) Schematic of the SPH validation setup; (b) Depth of penetration of a cylinder of density 500 kg/m^3: SPH results for different distances between particles (d); and (c) experimental results of Greenhow and Lin.[15]

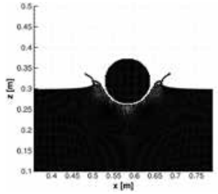

(a) Cross section view.

(b) Experiment.

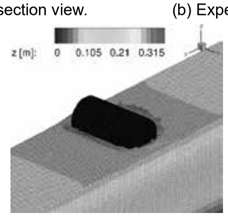

(c) Isometric view.

Figure 4: Surface deformation during water entry of a cylinder for time $t = 0.32s$ from the beginning of the fall. Comparison between CFD results with distance $d = 0.23m$ between particles and experimental results by Greenhow and Lin.[15]

2.3 Validation of multi-body dynamics solver

The MBDM was validated using simple mechanical systems of known solution as presented in Haug[16] like 2D and 3D slider-crank mechanisms. A 2D slider crank mechanism consists of a ground, crank, arm and slider bodies with properties summarised in Table 2. Although the configuration of the mechanism is planar, the employed bodies are three dimensional. The slider moves in the compression chamber, as shown in Figure 5b. As the slider moves to the inside of the chamber, a resisting force due to compression of the gas acts on the slider. This force increases until the exhaust valve opens. Equation 1 defines the gas force F_C on the slider during the compression, that is, when $\dot{x}_3 > 0$. At $x_3 = 5m$, the valve opens. During the intake stroke, no gas force acts on the slider.

$$F_C = \begin{cases} -\frac{282857}{6-x_3} + 62857, & 1.5 \leq x_3 \leq 5 \\ -11 \cdot 10^4[1 - \sin(2\pi(x_3 - 5.25))], & 5 < x_3 \leq 5.5 \end{cases} \quad (1)$$

Figure 5(c) shows the gas force as a function of the position and velocity of the slider.

Table 2: Properties of the bodies employed to represent the 2D slider-crank mechanism for dynamic analysis.

Name	Mass $[kg]$	Inertia tensor $[kg \cdot m^2]$
Crank	200	$\begin{bmatrix} 450 & 0 & 0 \\ 0 & 450 & 0 \\ 0 & 0 & 450 \end{bmatrix}$
Rod	35	$\begin{bmatrix} 35 & 0 & 0 \\ 0 & 35 & 0 \\ 0 & 0 & 35 \end{bmatrix}$
Slider	25	$\begin{bmatrix} 0.02 & 0 & 0 \\ 0 & 0.02 & 0 \\ 0 & 0 & 0.02 \end{bmatrix}$
Ground	1	$\begin{bmatrix} 1 & 0 & 0 \\ 0 & 1 & 0 \\ 0 & 0 & 1 \end{bmatrix}$

To match the conditions used by Haug,[16] the gravitational force was acting in the positive x direction. The initial orientation of the crank was set to $\phi(0) = \pi$ and the initial angular velocity of the crank was set to $\dot{\phi}(0) = 30rad/s$. The followed notation is as shown in Figure 5a. A constant torque of $41,450Nm$ was applied to the crank, and results are presented in Figure 6. The integration scheme employed for this computation is the Runge-Kutta method of fourth order, with time step chosen as $\Delta t = 0.001s$.

2.4 Coupling algorithms

Coupling algorithms were studied extensively for the past three decades. Coupling problems arise in many multi-physic phenomena, like fluid-structure interaction (FSI), but can also result from domain decomposition, where each sub-domain employs different discretisation or is solved with different method.[40] The multi-physics problem with adjacent domains can be simulated in a monolithic or in partitioned way. The former refers to the flow equations and structural equations being solved simultaneously, while the latter means that they are solved separately. The monolithic approach

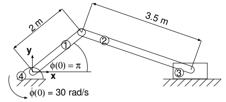

(a) Schematic representation of slider-crank mechanism.

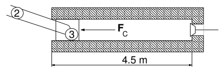

(b) Slider in a compression chamber.

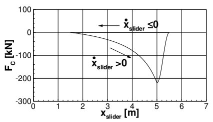

(c) Gas force versus slider position.

Figure 5: Validation case for the MBDM solver - dynamic analysis of the 2D slider-crank compressor mechanism.

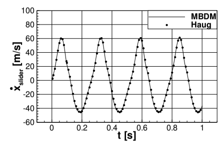

(a) Velocity of the slider.

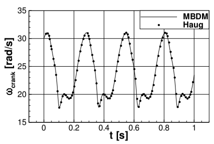

(b) Rotational velocity of the crank.

Figure 6: Comparison between velocity in x direction of the slider, and rotational velocity of the crank for the MBDM code and results obtained by Haug.[16]

requires a specific solver for the particular combination of physical problems, whereas the partitioned approach allows for solver modularity. Moreover, the partitioned approach allows to solve the fluid equations with different techniques developed specifically for the air and water. Further, this approach reduces the computational complexity per time-step, simplifies explicit/implicit treatment, facilitates sub-cycling, and eases replacements when better mathematical models and methods emerge in the fluid sub-disciplines. On the other hand, the partitioned simulation requires a special treatment to account for the interaction between the involved domains. Hence, computational efficiency over a monolithic approach is not necessarily guaranteed.[11] The monolithic solution - which is the ultimate form of strong coupling, does not recognise the differences between the mathematical properties of the subsystems. Furthermore, it tends to ignore the issues of software modularity, availability, and integration, even though each of these issues can be in practice a major obstacle.[10] Considering that two available and validated solvers (HMB2 and SPH) can be used in this work, the emphasis is placed on partitioned algorithms.

Partitioned coupling can be weak or strong. Explicit algorithms are weak (or loose) as the solvers exchange information once per time step, and the coupled equations are not exactly satisfied due to explicit treatment. Depending on the formulation, one side of the coupling boundary conditions is usually lagging behind another. This can be improved with staggering or extrapolation techniques, but the scheme remains weak, and coupling errors may be introduced. However, loosely coupled algorithms are attractive, since among all solution methods, they are the simplest to implement for realistic applications, and the most computationally inexpensive per time step.

Implicit algorithms are strong (or tight), and enforce exactly the coupling conditions at each time level. This is obtained by conducting iterations until boundary equations are satisfied to certain, prescribed accuracy. The coupling problem can be formulated either as fixed-point or root-finding problem. For the former, fixed-point Jacobi or Gauss-Seidel methods can be employed. Although easy to implement, those methods converge slowly if at all. Under-relaxation techniques can be used to improve convergence of the fixed-point iterations. Methods like fixed under-relaxation, adaptive Aitken's under-relaxation or steepest descent relaxation are some of the possible choices.[8,22] Newton's method can also be used. This method requires Jacobians relating the solutions of both solvers, that are usually not known. This can be circumvented by employing approximation of Jacobian or Jacobian-vector product. Those type of coupling methods are called Quasi-Newton. Recently, new strongly coupled algorithms have been proposed.

Vierendeels *et al.*[38] proposed an Interface Quasi-Newton algorithm with an approximation for the inverse of the Jacobian from a Least-Squares model (IQN-ILS). This approach was further investigated by Degroote *et al.*,[8] where they compared its performance with the Interface Block Quasi-Newton with an approximation for the Jacobian from a Least-Squares model (IBQN-LS), Aitken relaxation, and the Interface Generalised Minimal Residual method (Interface-GMRES(R)) algorithms. Demonstrated results showed that IQN-ILS and IBQN-LS performed similarly, using 3 times less evaluations and converging 4 times faster than the Aitken's relaxation method. IQN-ILS and IIBQN-LS were also found to use 2 times less evaluations and be almost 3 times faster than the Interface-GMRES algorithm.

Fernandez *et al.*[12] reformulated fluid-structure interaction as a non-linear problem in the state of the structure, with the flow states considered as internal variables of the problem. This system was subsequently solved with the Newton-Raphson method using an exact Jacobian. The performance of this algorithm was compared with the performance of the Aitken relaxation and Quasi-Newton GMRES methods, for the inviscid flow in an elastic tube. Results showed that Aitken's relaxation was twice as slow as the Quasi-Newton and the exact Jacobian methods, and required almost 40 times more iterations. Further, for time steps of $\Delta t = 10^{-4}s$, both latter algorithms showed similar behaviour in convergence. However, for time steps of $\Delta t = 10^{-3}s$, the fixed-point and Quasi-Newton algorithms failed to converge. This implies sensitivity of the methods to the employed Jacobian.

The strong coupling may be important if the phenomena occurring in both fluids have similar time scales. Due to frequency similarities, resonances may occur and the exact response of a system will deviate from what is predicted by a loosely coupled algorithm. On the other hand, if time scales are largely different, loosely coupled algorithm may be sufficient. The exact bounds when the strong coupling is required for particular FOWT must be carefully assessed. Some indication comes from the waves and rotor frequency analysis. The sea state, wave height, wave frequency, and wind speed are empirically related in terms of range and most probable values *e.g.* in Lee.[24] On the other hand, every wind turbine is designed to operate at a particular rotational frequency for a given wind speed. This allows to construct a "Campbell" diagram for the FOWT investigated in this work (Figure 7). It is clear, that for sea states between 3 and 4 (or wind speed about $9m/s$) resonances may occur. The rated power production for this 10-MW FOWT corresponds to the wind speed of $11.4m/s$, or sea state 4. This indicates, that for rated conditions, the weakly coupled algorithm may be sufficient.

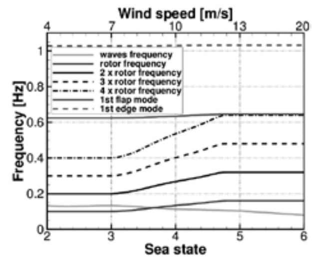

Figure 7: Campbell diagram for the investigated FOWT showing frequencies of the rotor and the waves as function of sea state and wind speed.

2.5 Coupling scheme and its implementation

In general, the exchange of information without stopping the computations can be implemented in three ways: through files, shared memory or the Message Passing Interface (MPI). Writing a file is the simplest solution. Both solvers can be launched separately and write files whenever exchange of information is required. This approach calls for very minor changes to both codes. The drawback is that writing and reading from hard drive creates a bottleneck, and slows down the computation especially if information is exchanged often, and large amount of data is to be exchanged.

In the shared memory approach multiple processes have access to the same memory, allowing them to change it and read changes made by other processes. If the random access memory (RAM) is to be used, it requires a shared memory machine, which may not be available on a general High Performance Computer (HPC). The file system can be used instead by mapping the memory on the hard drive. This approach suffers from the same drawback as the case of writing files.

Both employed CFD solvers are parallelised using MPI and the Single Program, Multiple Data (SPMD) paradigm, where each instance of the solver is assigned to perform the same task on different sets of data. Therefore, the easiest way to combine solvers is to employ MPI, but in Multiple Program, Multiple Data (MPMD) approach, where different programs operate on different sets of data. However, direct MPMD implementation of SPMD solvers requires additional effort to split the global communicator, such that each of the solvers is in a separate communicator (*MPI_COMM_WORLD*) with a separate ordering of precesses, as detailed in.[29] This can be avoided by dedicating one process to be in charge of executing both solvers with *MPI_Comm_spawn* routine. The dedicated code is referred to as master program or parent, and spawned processes are referred to as children. This approach has number of advantages briefly summarised as:

1. Spawned program has its own *MPI_COMM_WORLD*, therefore no modifications are required to original code with respect to processes that are going to communicate inside the child group.

2. Ordering of the processes is separate for parent and children. This way no modifications are required to original code with respect to process that is going to be in charge of the computation inside the child group.

3. Child process can easily identify if it was spawned or launched directly with MPI command. This maintains the original code functionality.

In the present work, the communication between the solvers was established through the Message Passing Interface (MPI), where the MBDM is executed as a single process and is dedicated to start SPH and HMB2 parallel solvers. The data flow diagram of the implementation is presented in Figure 8. The communication

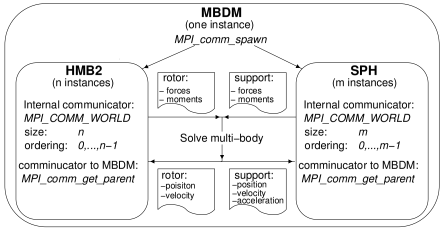

Figure 8: Flow chart of the MPI implementation and data exchange for coupled model.

was validated by executing separately SPH or HMB2, and comparing with the results were the body motion was introduced by MBDM. Due to the Lagrangian nature of the SPH method, the submerged bodies can be represented with particles and do not require specific coupling. Therefore, by utilising MPI, the MBDM substituted the body motion routines of the SPH solver and reduced the number of coupled codes to two - SPH and HMB2. This implies that MBDM is advancing in time with the same integration scheme as SPH using a symplectic method in this case.[25]

In the present paper, a weakly coupled approach is employed, namely the parallel conventional staggered method shown in Figure 9. Both solvers are advancing with different but constant time steps. SPH employs a time step of $\Delta t_{SPH} = 2 \cdot 10^{-4}s$ with $CFL = 0.2$, whereas HMB2 employs a time step of $\Delta t_{HMB2} = 2 \cdot 10^{-2}s = 100\Delta t_{SPH}$ with implicit $CFL = 5.0$. The small time step for the SPH method is required by the explicit integration scheme. The HMB2 solver employs an implicit dual-time method by Jameson[17] that is superior for larger time steps. Synchronisation of the solvers is performed at the end of each HMB2 step.

At the beginning of each synchronisation time step, the position and velocities of the rotor are transferred to the HMB2 aerodynamic solver, and forces and moments on the rotor are passed to the SPH. The two solvers are then advancing to a new time level with different methods and different number of steps. SPH performs 100 symplectic steps, while HMB2 performs 350 implicit pseudo-time steps. During the symplectic steps of the SPH code, the aerodynamic loads are kept constant (frozen). In return, the position and velocities of the rotor are kept constant during the implicit steps of HMB2. Once the synchronisation point is reached, the new position and velocities of all bodies, and rotor loads are obtained. Then, the algorithm proceeds to the new time level and information between the solvers is exchanged.

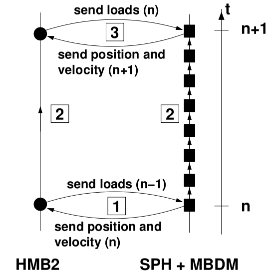

Figure 9: The parallel conventional staggered method employed in present work.

3 Test case description

A 10-MW wind turbine design by Bak *et al.*[1] is used in this work. The rotor diameter is $178.3m$, and the wind turbine operates at a wind speed of $11m/s$ with a rotational speed of $8.8rpm$. The blades have a pre-coning of $2.5°$ and nonlinear pre-bending with $3.3m$ displacement at the blade tip.

The wind turbine is attached to the floating support which consists of three cylindrical floats that increase the buoyancy and stability of the structure. A similar concept of the support platform was investigated by Roddier *et al.*[33] Unlike that design, the present support is simplified to be symmetric with respect to the location of the tower and the floats are connected to the base of the tower with a solid frame. The size of the tower is taken from,[1] and the dimensions of the support were calculated to provide sufficient buoyancy. A schematic of the studied FOWT is shown in Figure 10.

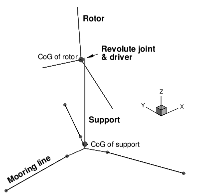

(a) Schematic of the MBDM model of FOWT.

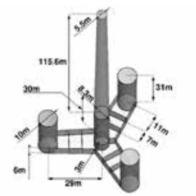

(b) Dimensions of the support and tower.

Figure 10: Schematic of the employed model of FOWT (a), and dimensions of the semi-submersible support and tower (b). FOWT model consists of three mooring lines and two rigid bodies: the rotor (blue) and combined body representing nacelle, tower and support (red).

In the present model, the FOWT is represented by three mooring lines and two bodies, as shown in Figure 10a. The first body represents the rotor (three blades with the spinner), and the second body represents the combined nacelle, tower and floating support rigidly linked to each other. The two bodies are connected by a revolute joint and a constraint of constant rotational speed is applied to the rotor. The resulting system has 6 unconstrained degrees of freedom. The mechanical properties of the bodies and mooring lines are presented in Table 3.

Table 3: Mechanical properties of the employed bodies and mooring lines.

Rotor	
m $[kg]$	$227,962$
I $[kg \cdot m^2]$	$\begin{bmatrix} 1.56 \cdot 10^8 & 0 & 0 \\ 0 & 7.84 \cdot 10^7 & 0 \\ 0 & 0 & 7.84 \cdot 10^7 \end{bmatrix}$
Nacelle, support and tower	
m $[kg]$	$4,223,938$
I $[kg \cdot m^2]$	$\begin{bmatrix} 2.03 \cdot 10^{10} & 0 & 0 \\ 0 & 2.03 \cdot 10^{10} & 0 \\ 0 & 0 & 2.81 \cdot 10^9 \end{bmatrix}$
Mooring lines	
120.0	Angle between adjacent lines [°]
20.6	Depth of anchors below SWL $[m]$
7.0	Depth of fairleads below SWL $[m]$
116.73	Length of the relaxed line $[m]$
$400 \cdot 10^6$	Mooring line extensional stiffness $[N/m]$
$40,000$	Mooring line damping coefficient $[Ns/m]$

The FOWT is placed in a shallow tank of length $500m$, width $150m$ and height $30m$. The tank is filled with water to a depth of $20.6m$. The waves are generated using a paddle on one side, and dissipated using a beach-like slope on the other side of the tank. The tank is presented in Figure 11. Waves are generated to represent the specific sea state corresponding to a given wind speed. Based on the measurements of annual sea state occurrences in the North Atlantic and North Pacific,[24] the wind speed of $11m/s$ corresponds to a sea state 4 with a mean wave height of $1.88m$ and a period of $8.8s$.

4 Results and Discussion

4.1 CFD mesh

The aerodynamic grid consists of the rotor and nacelle *i.e.* the tower is not included (for economies in CPU time) and the effect of the blade passing on the tower is not investigated. The grid consists of $8M$ cells, where 24 cells are used in the boundary layer, and 166 cells are distributed around the aerofoil section as presented in

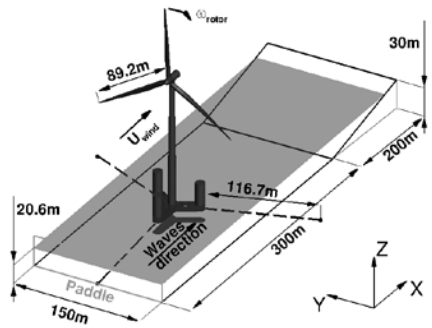

Figure 11: The FOWT model placed in a shallow tank. Mooring lines are shown with dashed lines.

Figure 12b. The surface of the blade is resolved with 90 cells along the span, as shown in Figure 12a.

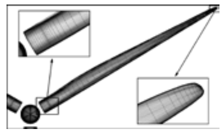

(a) Surface mesh.

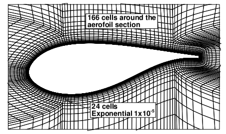

(b) Slice close to the blade surface.

Figure 12: $8M$ mesh used to solve for aerodynamic loads. Surface mesh (a), and slice through the volume close to the blade surface (b).

4.2 SPH setup and resolution

The hydrodynamic domain is resolved using $5M$ particles with initial uniform spacing of $d = 0.625m$. Note, that the best agreement with experimental data was obtained for 25 particles per radius of the cylinder, as shown in Section 2.2. Here, the employed spacing corresponds to 9 particles per radius of the cylindrical leg, or to spacing $d = 0.69cm$ in Figure 3b. The coarse particle distribution was chosen for economies in CPU time, where coarse domain is obviously solved faster, but tends to under-predict the slamming loads on the structure. Three test were performed to investigate the influence of the domain width and particle spacing on the force acting on the support structure, as presented in Table 4. The average hydrodynamic forces acting on the support during $1s$ of simulation were used for comparison. Percentage difference is computed relative to the size and spacing employed for the coupled computation. As can be seen, the size of the hydordynamic domain has little effect on the average hydrodynamic force. On the other hand, improving the spatial resolution results in about 18% different hydrodynamic force. This agrees with observations made in Section 2.2. We would have liked to use spacing $d = 0.3125m$, but to improve computational performance we had to employ spacing of $d = 0.625m$.

4.3 Initial conditions

Each of the solvers was executed separately before coupling to obtain a periodic solution of the loads. During this phase of computation the floating support was fixed, and the waves were generated for approximately $30s$. The rotor was computed until the loads converged, and was spinning about the axis aligned with the direction of the incoming wind. Once the initial conditions were obtained, the coupled computations were initiated.

4.4 Test cases

The first test case consists of the FOWT at the described configuration. Calm sea is considered, and the constant thrust of $1500kN$ is applied at the location of the rotor. A second test case considered time varying rotor thrust as shown in Figure 13. The thrust variation was estimated from a separate CFD computation of the rotor with the tower included. Five Fourier harmonics were used to fit the CFD data. The average thrust over the full revolution was $1500kN$. Both test cases were solved for 150 seconds. Note, that both cases are not coupled simulations, since the thrust force is prescribed and independent of the platform motion. Further, rotor inertia and the associated gyroscopic effects were not taken into account for those cases.

The last test case is a coupled computation, as described in Section 2.5. This case was solved for 60 seconds.

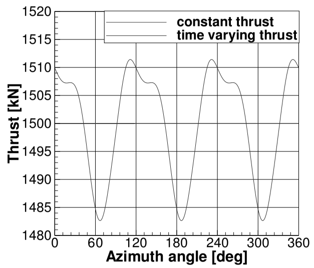

Figure 13: Thrust as function of azimuth angle of the rotor. Two test cases are shown: with constant thrust and estimated time varying thrust.

4.5 Decoupled cases - constant and time-varying thrust

The results of two first cases are presented in Figure 14. As can be seen, the FOWT moves in the direction of the thrust by about $0.215m$ (displacement in x). The FOWT also sinks in the water for about $0.603m$ (displacement in z), and tends to settle at a pitch angle of around $0.09rad$ or 5.2 degrees (rotation about y axis). The SPH particles are settling for the first 15 seconds as is visible in the acceleration plot. This can not be avoided even if the floating body is fixed and particles are let to settle. This is because releasing the floating structure is equivalent to a drop, and therefore does not represent equilibrium.

Also, the overall response is dominated by the initial imbalance of the forces, and the differences are barely visible in Figure 14.

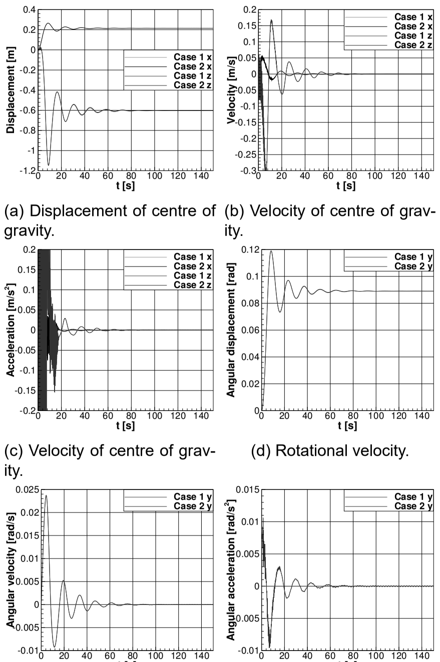

(a) Displacement of centre of gravity. (b) Velocity of centre of gravity.

(c) Velocity of centre of gravity. (d) Rotational velocity.

(e) Acceleration of centre of gravity. (f) Rotational acceleration.

Figure 14: Comparison of lateral and rotational dynamics of the support for two test cases: constant thrust (Case 1) and time varying thrust (Case 2).

Table 4: Test cases investigating the influence of the domain width and particle spacing on the forces acting on the support structure.

Domain size $x \times y[m]$	Spacing $d[m]$	1s averaged hydrodynamic force $[N]$	Difference $[\%]$
500×150	0.6250	$1.070 \cdot 10^7$	–
500×300	0.6250	$1.068 \cdot 10^7$	0.2%
500×150	0.3125	$1.267 \cdot 10^7$	18.4%

The last $20s$ of lateral and rotational accelerations are presented in Figure 15. The differences for both cases are now clearly visible. The effect of time varying thrust on the angular acceleration in pitch (about y axis) can be seen in Figure 15c, where the variation for the second test case is overlaid on the response for the first case. The variation in the shape and frequency, corresponds to the applied time dependent thrust.

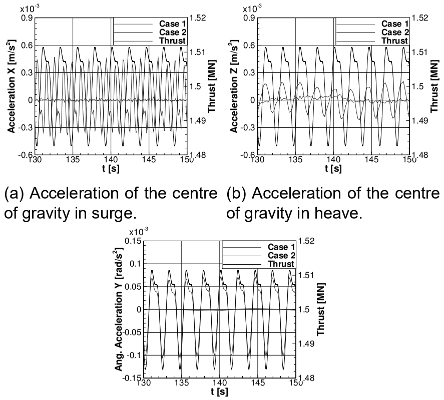

(a) Acceleration of the centre of gravity in surge. (b) Acceleration of the centre of gravity in heave.

(c) Pitching acceleration about the centre of gravity.

Figure 15: Comparison of last 20 seconds of lateral and rotational accelerations of the support for two test cases: constant thrust (solid line) and time varying thrust (dashed line). Solid line represents time varying thrust, as applied in the second test case.

The effect of time varying thrust on the lateral accelerations can be seen in Figure 15. Again, the acceleration in heave (in z direction) for the second test case (constant thrust) is overlaid on the response for the first case (time varying thrust). Here, the frequency of acceleration corresponds to the frequency of the thrust, but some phase shift is present and the shape of the response does not follow the shape of the thrust. This is because the motion in heave is linked to the applied thrust only through the rotational motion of the support i.e. through the second time integral of the angular acceleration, that does follow the shape of the thrust as shown in Figure 15c. The acceleration in the x direction is directly linked to the applied thrust, and the frequency dependence on thrust without the phase shift is clearly visible. However, the shape of the acceleration is not following the shape of applied thrust. This is a result of high stiffness of the mooring lines in this direction, where high frequency response of the mooring system augments the overall response of the support platform.

There are three sources of momentum for the decoupled computations: hydrodynamics, prescribed aerodynamics and mooring lines. Time histories of forces and moments for the test case with constant thrust are presented in Figure 16. Note, that for clarity, the time starts at $20s$. Also, note the differences in magnitude of the computed moments, where moments about y axis are three order of magnitude bigger, as compared to the other moment components.

First, it should be noted, that mooring lines are in general opposing the hydrodynamic forces introduced by the SPH solver. This is not true for the pitching moment, where hydrodynamics and mooring lines are acting together to counter the imbalance of the moment due to the thrust. For the mooring lines, moment is created by the displacements of the fairleads, whereas for the hydrodynamics, moment is created by the change of the buoyancy introduced by the rotation of the support. One would expect similar, cooperative behaviour for the forces in surge (in x direction). The obtained results suggest otherwise, as shown in Figure 16a. As can be seen, only the mooring lines are responsible for balancing the thrust force. Since the water is considered calm for the decoupled cases, the only source of hydrodynamic force acting in x direction is the hydrodynamic damping. Therefore, it is acting in the opposite direction of the motion, and as a result in opposite direction to the mooring force, which is a main source of motion in this direction. Lastly, small spurious moments and forces are noted, e.g. force in sway (y direction), which is normal to the plane of symmetry of the support. This is due to the SPH, where motion of the particles is never indeed symmetric. However, these discrepancies diminish with the number of particles, as was seen when test cases from Table 4 were computed. Further, the SPH method is known for its pressure instabilities, where the pressure field of the particles exhibits large pressure oscillations due to

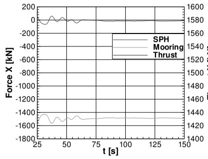

(a) Forces in surge

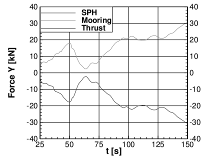

(b) Forces in sway

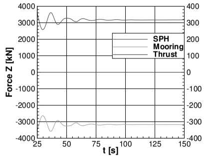

(c) Forces in heave

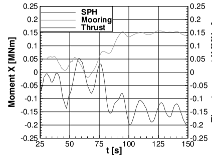

(d) Moments in roll

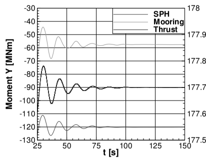

(e) Moments in pitch

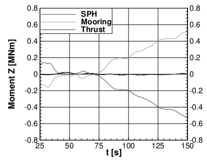

(f) Moments in yaw

Figure 16: Forces and moments acting at CoG of the support for constant thrust case.

acoustic waves present in compressible fluids. This is commonly tackled with solution smoothing techniques, also termed particles smoothing. Schemes up to the second order were proposed in the literature.[3,4] In the present work, no particles smoothing was applied, including validation test cases. In fact, stability issues were encountered when a zero-order Shepard density filter was applied to the decoupled test case every 50 and 100 SPH steps.

The time histories of forces and moments for the second test case with time varying thrust are presented in Figure 17. Visible trends and relations are analogous to the case with constant thrust, and support the observations made in the previous paragraph. The main difference is the expected variation of the forces in surge and moments in pitch, due to the unsteady aerodynamic forcing. Also, hydrodynamic and mooring forces in the y direction changed sign, although the mooring line forces are still opposing the forces of the SPH solver. The same is observed for the moments about z axis. Those quantities are dependent, and opposite rotation creates opposite mooring line forces.

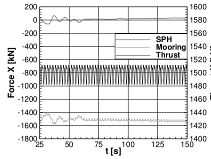

(a) Forces in surge

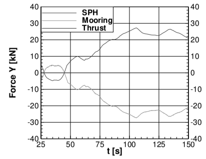

(b) Forces in sway

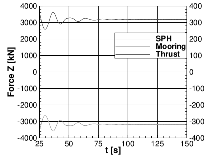

(c) Forces in heave

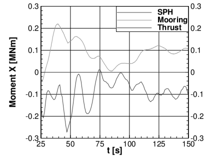

(d) Moments in roll

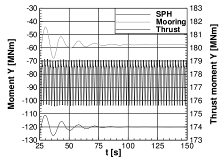

(e) Moments in pitch

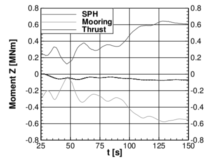

(f) Moments in yaw

Figure 17: Forces and moments acting at CoG of the support for time varying thrust case.

4.6 Coupled case

Coupled computations were also performed, and results are presented in Figure 18. The aerodynamic forces acting on the rotor as functions of time are shown in Figure 19a. The platform motion shows similar trend as for the previous, decoupled test cases. However, the rotor thrust is now dependent on the position and velocity of the rotor. As the wind turbine pitches under the the thrust force, the rotor moves in the direction of the wind (velocity in x direction in Figure 19b). In return, the thrust force decreases due to the smaller inflow speed and the orientation of the rotor disk. As the applied force is reduced, the rotor velocity decreases. The inverse relation between the aerodynamic force and velocity of the hub in x direction is clear in Figure 19. Further, due to the pitch angle, a component of the thrust is acting along the z axis. As a result, the FOWT experiences higher displacement in heave - $0.8m$ as compared to $0.6m$ for decoupled solutions.

The initial motion of the FOWT is dominated by the imbalance of the forces due to the applied thrust, and the effect of the first wave passage is not visible. However, the effect of every consecutive wave is clearly visible in periodic variation of the moment about the y axis, as shown in Figure 18f.

To facilitate the analysis of forces and moments acting on the system, the aerodynamic moments were transferred to the centre of gravity of the support platform. The resulting time histories of forces and moments for the coupled test case are presented in Figure 20. First, we observe lasting for about $10s$ high frequency hydrodynamic forces and moments due to initial particles settling. Similar was observed for decoupled test cases. After an initial phase, the hydrodynamic forces show periodic variation related to the frequency of the passing waves. Next, the mooring line forces are opposing the SPH forces in all directions. Finally, periodic variation of the aerodynamic forces with frequency of the waves is noted. A phase shift is present, since the aerodynamic forces are dependent on velocity and position, rather than on forces, as was discussed in previous paragraphs.

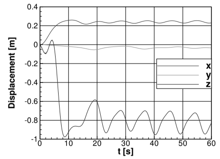

(a) Displacement of centre of gravity.

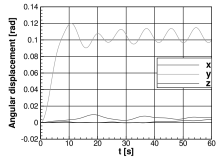

(b) Angular displacement.

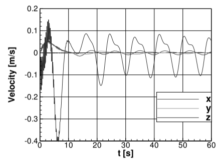

(c) Velocity of centre of gravity.

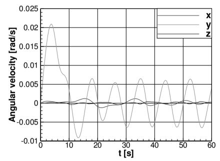

(d) Rotational velocity.

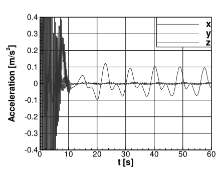

(e) Acceleration of centre of gravity.

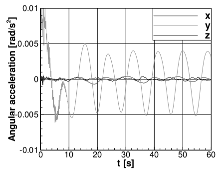

(f) Rotational acceleration.

Figure 18: Lateral and rotational dynamics of the support platform for coupled test case.

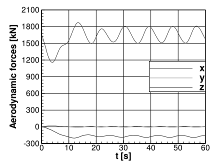

(a) Aerodynamic forces acting on the rotor.

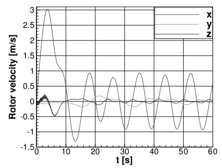

(b) Velocity of centre of gravity of the rotor.

Figure 19: Forces acting on the rotor and velocity of centre of gravity of the rotor as function of time for coupled computation.

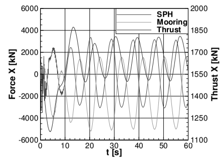

(a)

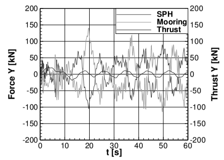

(b)

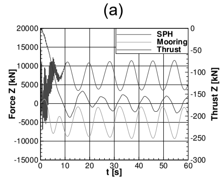

(c)

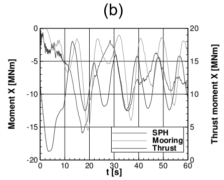

(d)

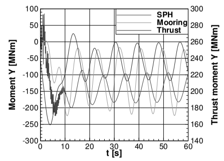

(e)

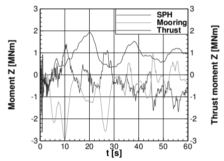

(f)

Figure 20: Forces and moments acting at CoG of the support for the coupled test case.

For the moments, pitching moment (about y) is dominating and after the initial phase the solvers tend to a periodic solution. The aerodynamic moment follows the inverse relation to the the hydordynamic pitching moment. The phase shift for the mooring lines moment is present, as it depends on the orientation of the support. The aerodynamic moment about x axis applied at the rotor is a result of a driving force created by the lift. Clearly,the driving force follows the same trend as the thrust force i.e. inverse relation with the velocity of the hub. Part of this moment is transferred to the structure, and hydrodynamic and mooring lines moments are trying to compensate for this moment. Finally, the mooring lines are opposing the hydrodynamic moments for the moment about z axis (yawing).

Figure 21 presents different positions of the FOWT during the computation.

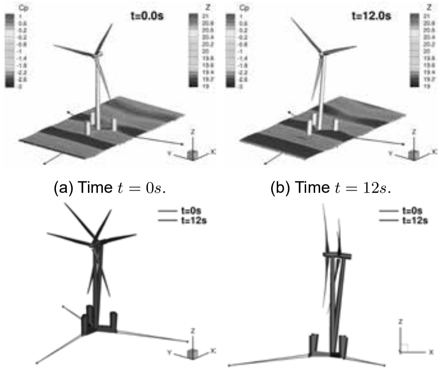

(a) Time $t = 0s$. (b) Time $t = 12s$.

(c) Isometric view of position at times $t = 0s$ and $t = 12s$. (d) Side view of position at times $t = 0s$ and $t = 12s$.

Figure 21: Position and orientation of the FOWT at times $t = 0s$ and $t = 12s$ during coupled computation. Contours on the rotor correspond to pressure coefficient Cp, contours on the water surface correspond to surface elevation z in meters.

4.7 Computational performance

For all cases, the SPH solver with MBDM were executed on a single 8 cores Intel®Xeon®CPU machine with 16 threads. Each of the CPU cores had a clock rate of $2GHz$, and $6.6GB$ of dedicated memory. As no interconnect switch was involved, the message passing delay between SPH and MBDM solvers was reduced to minimum. For the coupled case, HMB2 was executed on 29 dual-core AMD Opteron™processors with 4 threads, giving in total 116 parallel instances of the solver. Each of the CPU cores had a clock rate of $2.4GHz$, and $4GB$ of random access memory. It should be noted, that the SPH method requires only local (limited by the kernel function) weighted average in the vicinity of the given particle, whereas HMB2 solves the complete set of equations involving all the cells in the domain. Hence, more processing units were assigned to the aerodynamic side of the coupled problem.

The average time required to compute a second of the solution for the coupled case is 27.26 hours, where about 27.25 hours were spent to solve aerodynamics, 21.3 hours to solve hydrodynamics, and 0.24 hours to solve multi-body equations. The average time spent to exchange information for a second of the solution is 0.53 seconds, and was mostly dictated by the communication between the SPH and the MBDM solvers.

It should be noted, that time accuracy can be improved, if the coupling step is reduced. In the presented coupled case, the information is exchanged every 100 SPH steps ($\Delta t = 2 \cdot 10^{-2}$). When information between the solvers is exchanged every 50 SPH steps ($\Delta t = 1 \cdot 10^{-2}$), the average time required to compute a second of the solution becomes 45.0 hours. If information is exchanged every single SPH step ($\Delta t = 2 \cdot 10^{-4}$), the average time per one second extends to about 438.9 hours. In the former case, HMB2 requires on average 237 pseudo-time steps to achieve the level of convergence below 10^{-2}, and 45 pseudo-time steps for the later case. The convergence is defined as L2-norm of the residual vector. This suggests, that computational cost can be further reduced by employing explicit schemes for both solvers and performing less evaluations (four for Runge-Kutta scheme of 4th order). However, the biggest possible explicit step for HMB2, that would satisfy explicit CFL condition of 0.4 for the smallest cell in the domain is about $3.6 \cdot 10^{-9}$ seconds. Therefore, the aerodynamic time-step becomes limiting and prohibits this approach. More information about the computational performance is presented in Table 5. Stability issues were encountered for a time step $\Delta t = 2 \cdot 10^{-2}$ and HMB2 implicit CFL number 10.0, where the residual vector does not converge as fast as for CFL number 5.0. This indicates that CFL number of about 8.0 would be an optimal choice for this time step.

5 Conclusions

The paper presented a coupling method for the analysis of off-shore wind turbines. The HMB2 CFD solver was used for the analysis of blade aerodynamics and via a multi-body dynamics method it was coupled to a smoothed particle hydrodynamics tool to model the floating part of the turbine. The results showed that the weak coupling method put forward in this paper is adequate for the solution of the problem at hand. The work suffers from the lack of experimental data for a coupled system and for this reason validation was only possible for the components of the model. Data from the MEXICO project were used for aerodynamics; good overall agreement has been seen between CFD and test data. For the hydrodynamics solver, experiments related to drops of solid objects in water were used. Again, with a refined set of particles, the SPH method delivered good results. The third component of the method was the multi-body dynamics and this was validated using simple slider-crank problems.

Presented results showed that FOWT is a highly dynamic system. To obtain a deeper understanding of how rotor thrust and torque vary under dynamic conditions, efforts should be put forward to study aerodynamic flow and loads when wind turbine undergoes prescribed motion in pitch and yaw. Likewise, the comparison of the results of high-fidelity coupled models with those obtained with the simplified engineering tools like BEM, could potentially lead to improvements of later. Also, in the future, the work will continue with the validation of the method and comparisons with a strong coupling technique. Another aspect that should be addressed is the experimental measurements. Clearly, each of the components can be validated separately, but the set of comprehensive data for the complete FOWT system is crucial for the model validation. The following measurements would be an asset: forces and moments due to the mooring system, water basin tests with small- or full-scale wind turbine including pressure distributions on support and rotor, and the overall FOWT time responce including transient and periodic states.

Table 5: Computational performance of the coupling algorithm for various coupling time steps.

Coupling Δt [s]	HMB2 CFL number	HMB2 Newton steps	SPH steps	Time per coupling step [s]	Time per 1s of solution [s]
$2 \cdot 10^{-2}$	5.0	315	100	$1.95 \cdot 10^{3}$	$9.81 \cdot 10^{4}$
$2 \cdot 10^{-2}$	10.0	350	100	$2.29 \cdot 10^{3}$	$1.15 \cdot 10^{5}$
$1 \cdot 10^{-2}$	5.0	237	50	$1.61 \cdot 10^{3}$	$1.62 \cdot 10^{5}$
$1 \cdot 10^{-2}$	10.0	105	50	$1.04 \cdot 10^{3}$	$1.06 \cdot 10^{5}$
$2 \cdot 10^{-4}$	5.0	45	1	$3.13 \cdot 10^{2}$	$1.58 \cdot 10^{6}$
$2 \cdot 10^{-4}$	10.0	23	1	$1.59 \cdot 10^{2}$	$7.97 \cdot 10^{5}$

Author contact:
Vladimir Leble, vleble@liverpool.ac.uk;
George Barakos, g.barakos@liverpool.ac.uk (Corresponding Author);

Acknowledgments

The financial support of the Marie Curie Host Fellowships Program: FP7-PEOPLE-2012-ITN-309395 - New Materials And Reliability In Offshore Wind Turbines Technology "MARE-WINT" is gratefully acknowledged.

References

[1] C. Bak, F. Zhale, R. Bitsche, T. Kim, A. Yde, L. C. Henriksen, P. B. Andersen, A. Natarajan, and H. M.H. Description of the dtu 10 mw reference wind turbin. Technical Report I-0092, DTU Wind Energy, 2013.

[2] G. Barakos, R. Steijl, K. Badcock, and A. Brocklehurst. Development of cfd capability for full helicopter engineering analysis. In *31st European Rotorcraft Forum*, 2005. Paper No. 91.

[3] T. Belytschko, Y. Guo, W. Kam Liu, and S. Ping Xiao. A unified stability analysis of meshless particle methods. *International Journal for Numerical Methods in Engineering*, 48(9):1359–1400, 2000.

[4] G. Bilotta, G. Russo, A. Herault, and C. D. Negro. Moving least-squares corrections for smoothed particle hydrodynamics. *Annals of Geophysics*, 54(5), 2011.

[5] M. Carrión, R. Steijl, M. Woodgate, G. Barakos, X. Munduate, and S. Gomez-Iradi. Computational fluid dynamics analysis of the wake behind the mexico rotor in axial flow conditions. *Wind Energy*, 2014.

[6] M. Carrión, M. Woodgate, R. Steijl, and G. Barakos. Implementation of all-mach roe-type schemes in fully implicit cfd solvers – demonstration for wind turbine flows. *International Journal for Numerical Methods in Fluids*, 73(8):693–728, 2013.

[7] M. Carrión, M. Woodgate, R. Steijl, G. N. Barakos, S. Gomez-Iradi, and X. Munduate. Understanding wind-turbine wake breakdown using computational fluid dynamics. *AIAA Journal*, 53(3):588 – 602, 2015.

[8] J. Degroote, R. Haelterman, S. Annerel, P. Bruggeman, and J. Vierendeels. Performance of partitioned procedures in fluid-structure interaction. *Computers & Structure*, 88(7-8):446–457, Apr. 2010.

[9] S. C. Eisenstat, H. C. Elman, and M. H. Schultz. Variational iterative methods for nonsymmetric systems of linear equations. *SIAM Journal on Numerical Analysis*, 20(2):345–357, 1983.

[10] C. Farhat, K. G. van der Zee, and P. Geuzaine. Provably second-order time-accurate loosely-coupled solution algorithms for transient nonlinear computational aeroelasticity. *Computer Methods in Applied Mechanics and Engineering*, 195(17–18):1973 – 2001, 2006. Fluid-Structure Interaction.

[11] C. A. Fellipa, K. C. Park, and C. Farhat. Partitioned analysis of coupled mechanical systems. Technical Report CU-CAS-99-06, University of Colorado, Boulder, Colorado, USA, March 1999.

[12] M. A. Fernández and M. Moubachir. A newton method using exact jacobians for solving fluid-structure coupling. *Computers & Structure*, 83(2-3):127–142, Jan. 2005.

[13] M. Gomez-Gesteira, B. D. Rogers, A. J. C. Crespo, R. A. Dalrymple, M. Narayanaswamy, and J. M. Dominguez. Sphysics - development of a free-surface fluid solver - part 1: Theory and formulations. *Computers & Geosciences*, 48:289–299, Nov. 2012.

[14] S. Gómez-Iradi, R. Steijl, and G. N. Barakos. Development and validation of a cfd technique for the aerodynamic analysis of hawt. *Journal of Solar Energy Engineering*, 131(3):031009, 2009.

[15] M. Greenhow and W. M. Lin. Nonlinear-free surface effects: Experiments and theory. Technical Report 83-19, MIT, Dept. of Ocean Engineering, Sept. 1983.

[16] E. J. Haug. *Computer Aided Kinematics and Dynamics of Mechanical Systems. Vol. 1: Basic Methods*. Allyn & Bacon, Inc., Needham Heights, MA, USA, 1989.

[17] A. Jameson. Time dependent calculations using multigrid, with applications to unsteady flows past airfoils and wings. In *10th Computational Fluid Dynamics Conference*. American Institute of Aeronautics and Astronautics, 1991.

[18] M. Jarkowski, M. A. Woodgate, G. N. Barakos, and J. Rokicki. Towards consistent hybrid overset mesh methods for rotorcraft cfd. *International Journal for Numerical Methods in Fluids*, 74(8):543–576, 2013.

[19] J. Jonkman. Dynamics modeling and loads analysis of an offshore floating wind turbine. Technical Report NREL/TP-500-41958, NREL, November 2007.

[20] M. Karimirad and T. Moan. A simplified method for coupled analysis of floating offshore wind turbines. *Marine Structures*, 27(1):45 – 63, 2012.

[21] M. Karimirad and T. Moan. Modeling aspects of a floating wind turbine for coupled wave–wind-induced dynamic analyses. *Renewable Energy*, 53:299–305, 2013.

[22] U. Küttler and W. A. Wall. Fixed-point fluid–structure interaction solvers with dynamic relaxation. *Computational Mechanics*, 43(1):61–72, 2008.

[23] T. J. Larsen and T. D. Hanson. A method to avoid negative damped low frequent tower vibrations for a floating, pitch controlled wind turbine. *Journal of Physics: Conference Series*, 75(1):012073, 2007.

[24] W. T. Lee, S. L. Bales, and S. E. Sowby. *Standardized Wind and Wave Environments for North Pacific Ocean Areas*. David W. Taylor Naval Ship Research and Development Center, 1985.

[25] B. J. Leimkuhler, S. Reich, and R. D. Skeel. Integration methods for molecular dynamics. In *In Mathematical Approaches To Biomolecular Structure And Dynamics, IMA Volumes In Mathematics And Its Applications*, pages 161–185. Springer, 1996.

[26] E. Marino, C. Borri, and U. Peil. A fully nonlinear wave model to account for breaking wave impact loads on offshore wind turbines. *Journal of Wind Engineering and Industrial Aerodynamics*, 99(4):483 – 490, 2011. The Fifth International Symposium on Computational Wind Engineering.

[27] D. Matha, M. Schlipf, A. Cordle, R. Pereira, and J. Jonkman. Challenges in simulation of aerodynamics, hydrodynamics, and mooring-line dynamics of floating offshore wind turbines. In *21st Offshore and Polar Engineering Conference*, June 2011.

[28] P. E. Nikravesh. *Computer-aided Analysis of Mechanical Systems*. Prentice-Hall, Inc., Upper Saddle River, NJ, USA, 1988.

[29] Open MPI. Open MPI documentation, 2015.

[30] S. Osher and S. Chakravarthy. Upwind schemes and boundary conditions with applications to euler equations in general geometries. *Journal of Computational Physics*, 50(3):447–481, June 1983.

[31] F. Rieper. A low-mach number fix for roe's approximate riemann solver. *J. Comput. Phys.*, 230(13):5263–5287, June 2011.

[32] L. Roald, J. Jonkman, A. Robertson, and N. Chokani. The effect of second-order hydrodynamics on floating offshore wind turbines. *Energy Procedia*, 35:253 – 264, 2013. DeepWind'2013 – Selected papers from 10th Deep Sea Offshore Wind R&D Conference, Trondheim, Norway, 24 – 25 January 2013.

[33] D. Roddier, C. Cermelli, and A. Weinstein. WindFloat: A Floating Foundation for Offshore Wind Turbines–Part I: Design Basis and Qualification Process. In *ASME 2009 28th International Conference on Ocean, Offshore and Arctic Engineering*, pages 845–853. ASME, 2009.

[34] L. B. Savenije, T. Ashuri, G. J. W. Bussel, and J. W. Staerdahl. Dynamic modeling of a spar-type floating offshore wind turbine. In *Scientific Proceedings European Wind Energy Conference & Exhibition*, 2010.

[35] B. Skaare, T. Hanson, F. Nielsen, R. Yttervik, and A. Hansen. Integrated dynamic analysis of floating offshore wind turbines. In *Proceedings of 2007 European Wind Energy Conference and Exhibition*, 2007.

[36] P. R. Spalart, W. Jou, M. Strelets, and S. R. Allmaras. Comments on the Feasibility of LES for Wings, and on a Hybrid RANS/LES Approach. In *Proceedings of the First AFOSR International Conference on DNS/LES*, 1997.

[37] R. Steijl and G. Barakos. Sliding mesh algorithm for cfd analysis of helicopter rotor–fuselage aerodynamics. *International Journal for Numerical Methods in Fluids*, 58(5):527–549, 2008.

[38] J. Vierendeels, L. Lanoye, J. Degroote, and P. Verdonck. Implicit coupling of partitioned fluid-structure interaction problems with reduced order models. *Computers & Structures*, 85(11-14):970–976, June 2007.

[39] M. A. Woodgate, G. N. Barakos, N. Scrase, and T. Neville. Simulation of helicopter ditching using smoothed particle hydrodynamics. In *39th European Rotorcraft Forum*, September 2013.

[40] O. C. Zienkiewicz, R. L. Taylor, and J. Z. Zhu. *The Finite Element Method Set (Sixth Edition)*. Butterworth-Heinemann, Oxford, 2005.

Wake effects above rated wind speed. An overlooked contributor to high loads in wind farms.

Torben J. Larsen[1)], Gunner Larsen[1)], Helge A. Madsen[1)] and Søren M. Petersen[2)]

[1)] Department of Wind Energy, Technical University of Denmark (DTU)

[2)] Siemens Wind Power A/S

tjul@dtu.dk

Abstract

In this paper a new validation of the Dynamic Wake Meandering method for calculating wake effects on power and load levels on a turbine is presented based on load and power measurements on a turbine located in the Lillgrund wind farm. What is unique is the large set of measurements available, where the wake effects from multiple neighboring turbines in high wind speed conditions could be included. It appears that the DWM method gives accurate results in single wake situations as well as for multiwake situations below rated wind speed. However, the so far used method for superposition of multiple wakes above rated wind speed has led to non-conservative load predictions for high wind speeds. Therefore a new approach is presented and compared to both measurements and present practice in the IEC61400-1 standard.

1. Introduction

The Dynamic Wake Meander (DWM) model [l1,2] has previously been validated both directly against full-scale flow field data [7,8,12] and indirectly by comparing simulated wind turbine loads resulting from wake affected inflow fields with full-scale load measurements [2,3,6,10,11].

Concerning validation in terms of derived structural wind turbine loads, the most comprehensive comparisons were performed in the Egmond aan Zee study [3], where a very satisfactory agreement between model predictions and measurements was concluded for the ambient mean wind speed regime between 3m/s and 14m/s. This study was based on full-scale measurements from a Vestas V90 turbine located in the Dutch Egmond aan Zee wind farm (WF) [3] for the specific wind direction, where the turbine in focus was located as the 6'th turbine in a row with uniform turbine interspacings equal to 7 rotor diameters (D).

In general only very limited load validation material from multiwake wind farm exist, and for wind situations above rated wind speed practically nothing has so far been published. So far the main interest in wake effects has been on the power consequences, which is mainly important for wind speed below rated.

This paper describes a load validation study based on simulated and measured fatigue loads from the Swedish Lillgrund off-shore wind farm, which has a layout characterized by exceptionally small wind turbine (WT) inter-spacings. Full-scale measurements from this wind farm have previously been presented with focus on power production [5,11] as well as on wind turbine fatigue loading [4] effects in the below rated mean wind regime. In the load study predicted flapwise fatigue loads for a full polar were shown to agree very satisfactorily both for single turbine wake situations and for deep array wake operation up to about rated (ambient) mean wind speed. However, for higher than rated (ambient) mean wind speeds, significant deviations between predictions and full-scale measurements were observed for deep array wake cases; i.e. for wake situations characterized by multiple upstream turbines.

In the present paper a simple update to the DWM model is proposed for multiple wake operation in the high ambient wind speed regime, and the performance of the updated model under such conditions is investigated in terms of both flapwise fatigue loads and tower fatigue loads with particular emphasis on deep array cases. Simulations and full-scale measurement are compared, and as the DWM model is about to be included in the new edition of the IEC61400-1 ed. 4 standard, these results are expected to be of major importance for future wind farm projects. For completeness, the measured results are further compared to load predictions as based on the existing recommended practice in the IEC61400-1 ed. 4 standard [9].

2. DWM model update

The DWM model basically simulates the non-stationary wind farm flow field, which is required for wind farm load predictions, as a linear superposition of an ambient turbulent atmospheric boundary layer (ABL) flow and a non-stationary wake flow contribution. The wake contribution is obtained by treating WT wakes as passive tracers transported downstream by the mean ABL flow field superimposed by a stochastic meandering process driven by the large scale cross wind turbulence components [1]. The method for deriving the deficit and the magnitude of the added wake turbulence can be found in [2]. The result is an intermittent type of flow field with the intermittence resulting from the wake meandering. This wake flow model has been integrated with the DTU aeroelastic code HAWC2 in order to facilitate load and production predictions of wind turbines located in wind farms.

Compared to the DWM version applied in the former Lillgrund study [4], the DWM sub-model, used to determine the aggregated wake deficit from upstream turbines at a given WF location, has been revised in the present study. Two different wake superposition approaches are applied for the wind regimes corresponding to respectively below and above rated wind speed:

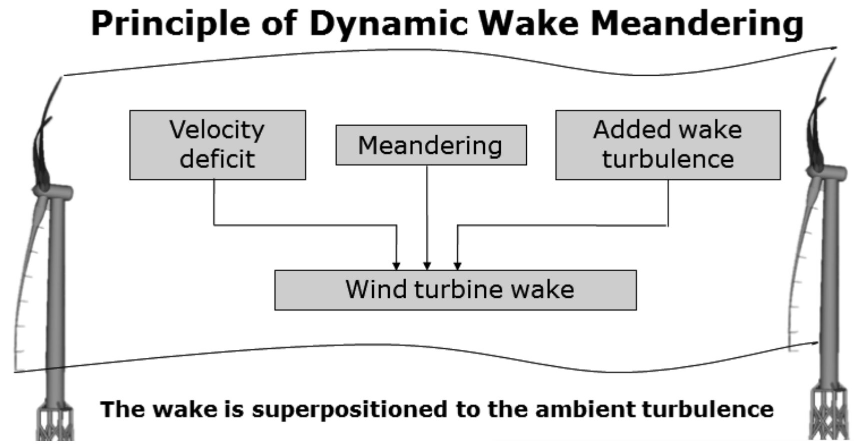

Figure 1: Illustration of the main components of the DWM method. A cascade of deficits are transported downstream in a process governed by the large scale turbulent flow field.

Below rated wind speed: For a WT with the rotor centre located at the spatial position, **x**, within the WF, the temporally varying wake flow contribution at the rotor polar coordinate (r,Θ) is determined by the *dominating wake among wake contributions from all upstream turbines at any time*.

$$\boldsymbol{U}_w(r,\theta,t|\boldsymbol{x}) = \underset{i}{\mathrm{MIN}}\left(\boldsymbol{U}_{w,i}(r,\theta,t|\boldsymbol{x})\right) \qquad (1)$$

where $(r,\Theta,t|\boldsymbol{x})$ denotes a temporal coordinate (t) combined with a spatial coordinate in a polar frame of reference centered at the spatial position $\boldsymbol{x}$, and where each individual upstream emitted wake flow field is given by $\boldsymbol{U}_{w,i} = (U_{w,i}+u_{w,i})\boldsymbol{e}_1 + v_{w,i}\boldsymbol{e}_2 + w_{w,i}\boldsymbol{e}_3$, *with* $\boldsymbol{e}_j$, j = 1,2,3, being unit normal vectors in respectively the longitudinal, transversal and vertical mean flow directions. The parameter i includes all upstream turbines relative to the spatial position $\boldsymbol{x}$ for a given mean wind direction.

The wake self-induced small scale turbulence is denoted by $(u_{w,i}, v_{w,i}, w_{w,i})$, and as the wake deficit flow field component in the longitudinal flow direction is by far the dominating component and further the most load critical, only this deficit component is included.

Above rated wind speed: Using the nomenclature introduced above, (1) is replaced by a linear summation of wake contributions from all upstream turbines, i.e.

$$\boldsymbol{U}_w(r,\theta,t|\boldsymbol{x}) = \sum_i \boldsymbol{U}_{w,i}(r,\theta,t|\boldsymbol{x}) \qquad (2)$$

This linear perturbation approach is consistent with WT's being more "flow transparent" for higher wind speeds, which in turn results in relatively smaller wake deficit magnitudes and thereby improving the accuracy of a linear flow field approximation.

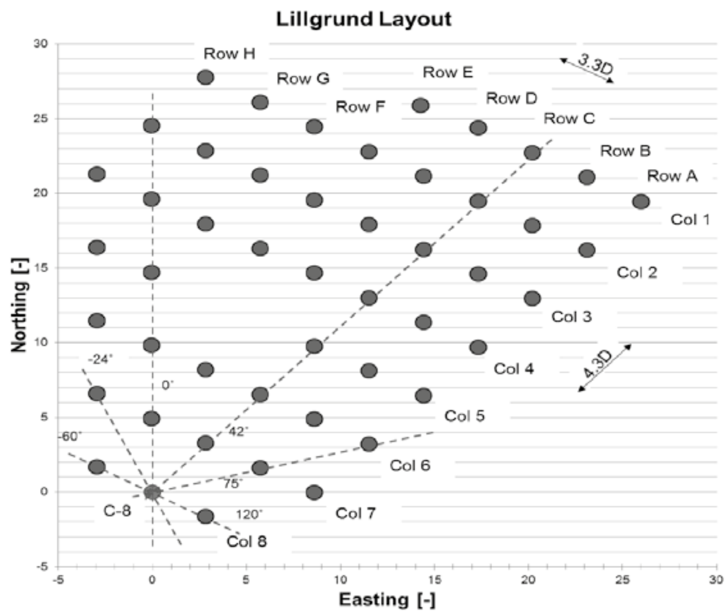

Figure 2: The Layout of the Lillgrund wind farm and location of WT C-8. Distances are non-dimensioned with the rotor diameter

Note, that before the model update superposition of wakes emitted by upstream turbines was treated according to the algorithm described by equation (1) for the entire the wind regime.

3. Validation Case

The Lillgrund wind farm consists of 48 Siemens SWT-2.3-93 turbines, and one of these (C-8) is instrumented with strain gauges resolving blade, main shaft and tower loads, see Figure 2. The present DWM model validation is based on recordings from this turbine.

Whereas the Egmond aan Zee wind farm is characterized by a "conventional" turbine inter spacing, the layout of the Lillgrund wind farm is, as mentioned, characterized by very small turbine inter spacing's; i.e. down to 3.3 D. This makes the present Lillgrund load validation case a unique supplement to the former validation based on the Egmond ann Zee wind farm.

Measured and predicted fatigue loads are quantified as fatigue equivalent moments using the Palmgren-Miner approach; and Wöhler exponents of 5 and 10 were assumed for the tower and blade composite structures, respectively.

The validation scenarios include load cases associated with normal turbine operation with mean wind speeds ranging from 8m/s to 16m/s. Measured wind speed dependent turbulence intensities (TI's) are used, reflecting the offshore wind speed dependent "surface" roughness. However, no attempt is done to resolve TI as function of upstream fetch (i.e. direction). Thus, in the mean wind speed regime 6m/s-14m/s a TI of 5.8% is used - gradually increasing to 6.2% at 16m/s.

4. Results

For a complete direction rose simulated and measured fatigue equivalent moments are compared (mean wind speed) bin wise for two WT main components – i.e. blade and tower. With the complete direction rose being represented, a multitude of load cases – ranging from ambient inflow conditions over single wake cases to various types of multiple wake inflow cases – are thus covered. Further, as a supplement to the DWM validation, the investigation includes also comparative load simulations as based on the existing recommended practice in the IEC61400-1 ed. 4 standard [9]. This consist of a set of loads obtained using the IEC class 1A, as most offshore turbine are approved for such conditions, as well as the wake simulation method suggested by Frandsen [13], where the thrust coefficient C_T is approximated with $7/U_{amb}$ for the sectors where increased background turbulence from the entire farm is expected, U_{amb} represents the ambient mean wind speed.

All presented fatigue loads have been normalized with the fatigue load representing the respective sensors at 9m/s in the free sector.

The results for the blade load comparison can be seen in Figure 3. Results are presented as function of the wind direction for each wind speed bin covered. In the left column of the figure is shown the results from comparing the measurements, IEC class 1A and the Frandsen method to results obtained with the DWM approach using the maximum deficit operator (1). In the right column a similar comparison to the DWM approach using a linear superposition for multiple wake situations (2) is shown. A similar comparison for the tower bottom bending moment is shown in Figure 4.

An excellent agreement between measurements and the DWM approach with the maximum deficit operator is seen for the flapwise bending moment at low wind speeds, where the turbine thrust is high. The Frandsen method results in blade loads in the slightly conservative region of measured load levels. The highest loads are seen in the sector with the closest located upstream wind turbine. In this case the single wake situation with 3.3D spacing.

At 10-12 m/s, the agreement between measurements and the DWM approach using the maximum deficit operator still shows an excellent agreement for the 3.3D single wake situation. A slight increased load level can be seen in the measurements for the multi-wake sector, which is however still in fine agreement with the simulation results.

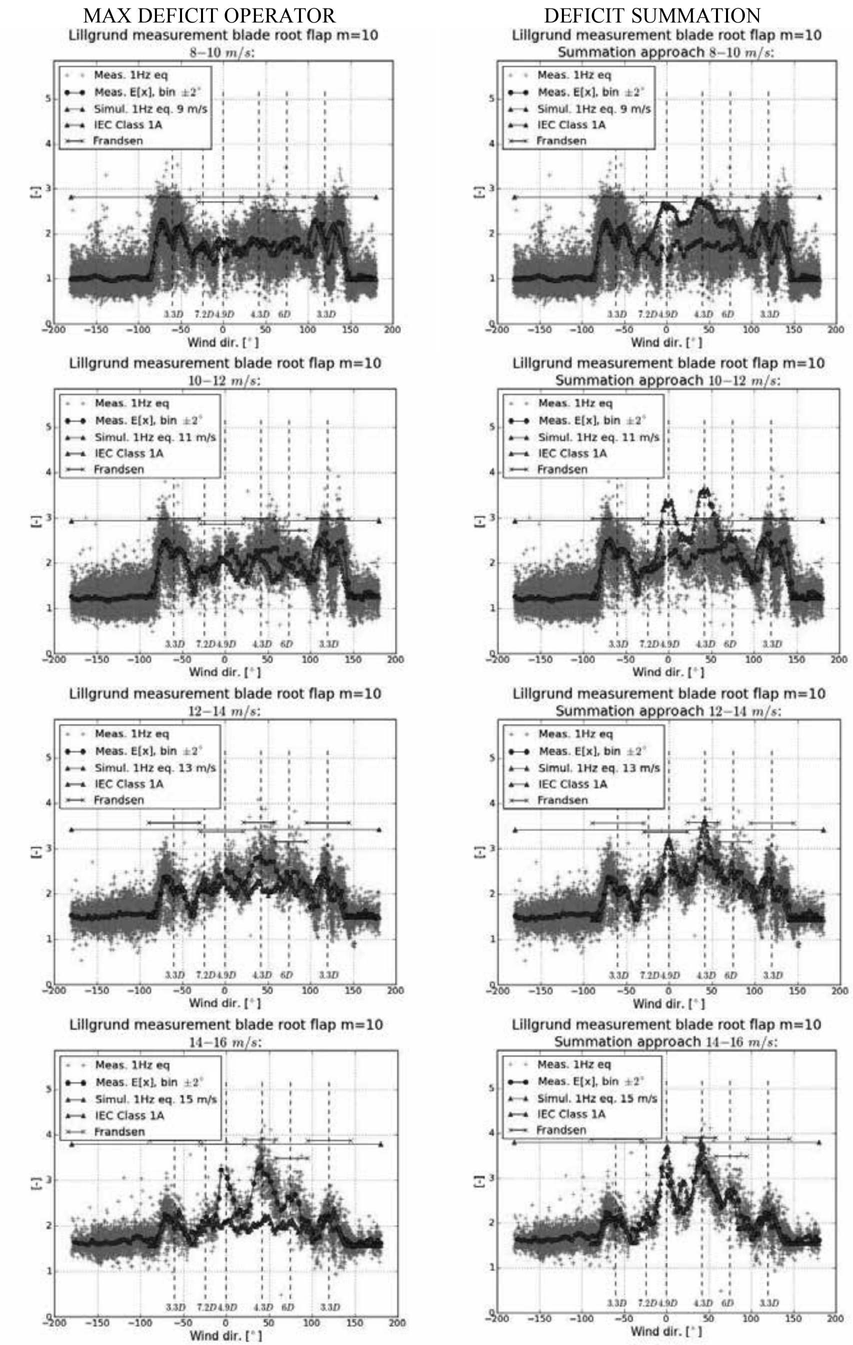

Figure 3: Comparison of blade root bending 1 Hz fatigue loads at wind speed from 8 to 16m/s. Left: DWM using max operator. Right: DWM using linear superposition.

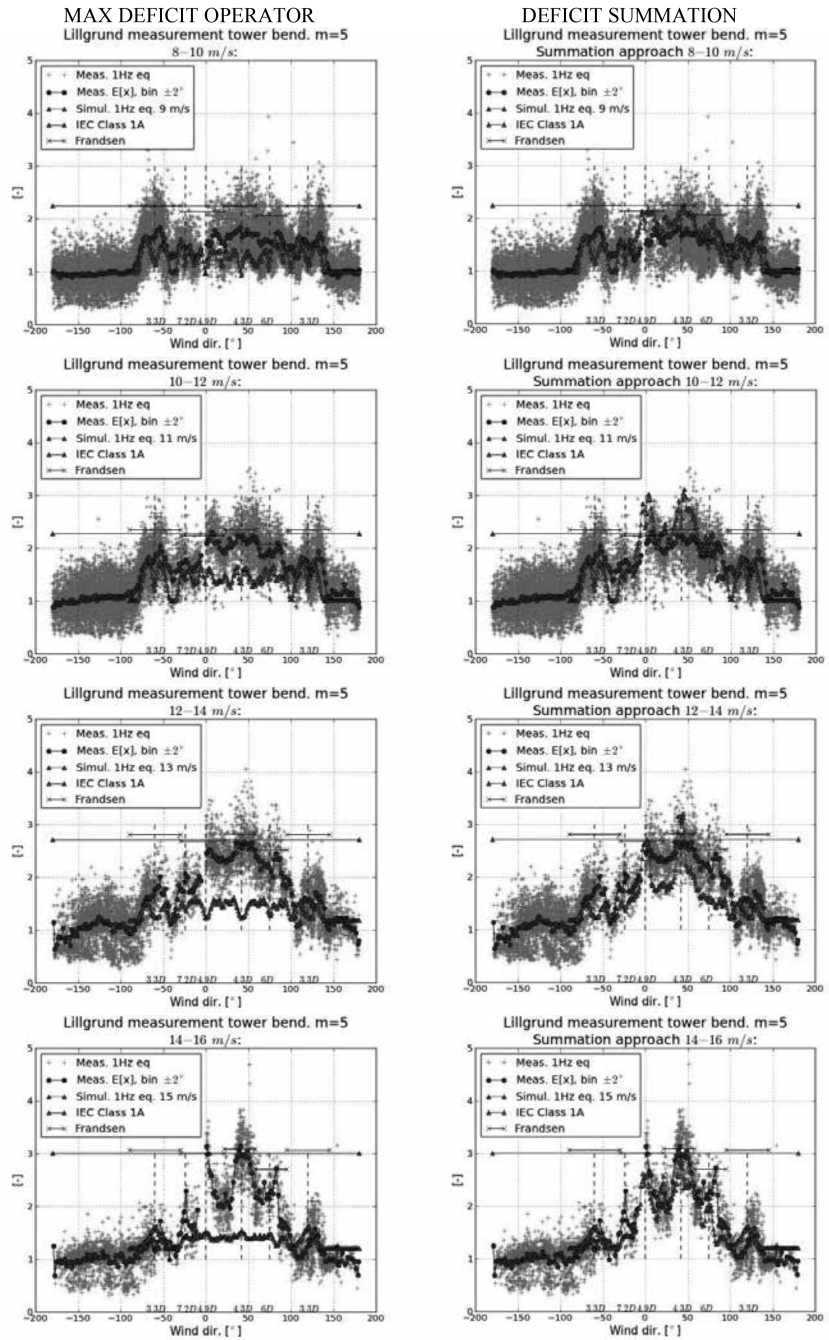

Figure 4: Comparison of tower bottom bending 1 Hz fatigue loads at wind speed from 8 to 16m/s. Left: DWM using max operator. Right: DWM using linear superposition.

At 12-14 m/s it becomes clear that the blade load for multiwake operation is not sufficiently captured by the DWM approach using the maximum deficit operator, and at 14-16 m/s the measurements show a significantly larger load level then the model predictions. It is consequently clear that *the maximum deficit approach cannot be used for high wind speeds*!

In the right hand column of the figure, the simulations results using the simple deficit superposition method is shown. This method seems slightly conservative regarding the blade loads for low wind speeds, but at high wind speeds the match is excellent.

A similar conclusion can be drawn when observing the tower bottom bending moments. The maximum deficit approach seems to result in a fine agreement for low wind speeds, but near rated and above only the superposition approach catches the load levels measured in the multi-wake sector.

Regarding the fatigue load levels obtained using the Frandsen method, it appears that this method is highly conservative for the low wind turbine spacings investigated in this study. Especially at wind speeds above rated in single wake situations, the method leads to a load levels 2-3 times higher than measured. As the measured loads increase significantly in multi-wake situations at high wind speeds, the load levels predicted by the Frandsen method actually fits quite well, but this is not caused by the modeled added ambient turbulence level, as this only has marginal influence of the modeled wake turbulence level.

The fatigue load level obtained from the class 1A site conditions appears to result in a conservative and safe design of the turbine compared to the measured load conditions.

5. Discussion

In general a very fine agreement between the DWM simulations and measurements is seen below rated wind speed. Excellent agreement between DWM fatigue load predictions and full-scale measurements has previously been demonstrated for the ambient mean wind speed regime below rated wind speed, whereas significant differences between model predictions and measurement were observed above rated wind speed. A revision of the DWM sub-model for wake aggregation has improved the model/measurement agreement significantly, and excellent agreement between DWM fatigue load predictions and full-scale measurements is now shown also for the ambient mean wind speed regime above rated wind speed.

For a complete direction rose simulated and measured fatigue equivalent moments are compared (mean wind speed) bin wise for two WT main components – i.e. blade and tower. With the complete direction rose being represented, a multitude of load cases – ranging from ambient inflow conditions over single wake cases to various types of multiple wake inflow cases – are thus covered.

Even though a fine agreement between the DWM approach and measurements can be achieved by using the maximum deficit operator below rated wind speed and the linear superposition above rated, it is also clear that multiple wake situations is a highly complex load situation. Especially the findings regarding the significantly increased load levels above rated wind speed, may (hopefully) cause increased attention for future studies. Especially large eddy CFD simulations could increase the insight in how to properly handle merging wakes.

6. Conclusion

A key finding in this study is that even though a wind turbine is more “aerodynamic transparent” above rated wind speed and therefore has a reduced wind speed deficit compared to below rated, the wake induced load levels increased significantly in multi-wake situations.

With this study it is also concluded that the DWM method can with great accuracy be used to predict the load level of wind turbines in wind farm conditions. However, when handling multiple wake situations above rated wind speed, the previous recommendation based on the Egmond aan Zee study [3] is <u>NOT</u> sufficient. An alternative, still simple, approach using linear wake deficit superposition was demonstrated to result in load levels in agreement with the measured levels and is thus recommended.

Further, as a supplement to the DWM validation, the investigation includes also comparative load simulations as based on the existing recommended practice in the IEC61400-1 ed. 4 standard [9]. Here it can be concluded that the Frandsen approach is highly conservative for single wake situations, especially above rated wind speed. This in turn means that adopting the DWM approach, with site specific conditions allow for quantification of the build-in safety reserve in the existing IEC61400-1 recommended practice or, alternatively, use the DWM approach to reduce this safety reserve if appropriate. Even for a wind farm as the Lillgrund, with turbine spacings between 3 and 4D, a class 1A turbulence level still results in a conservative load level.

7. Acknowledgements

Siemens Wind Power has provided the unique measurements, which is gratefully acknowledged. The EUDP project “Impact of atmospheric stability conditions on wind farm loading and production” under contract 64010-0462 and the Danish PSO project ‘Wake affected offshore tower and foundation loads’ under contract 2010-1-10546 are acknowledged for financial support and thus for making this study possible.

References

[1] Larsen, G.C.; Madsen, H.Aa.; Thomsen, K. and Larsen, T.J. (2008). Wake meandering - a pragmatic approach. Wind Energy, 11, pp. 377–395.

[2] Madsen, H.Aa.; Larsen, G.C.; Larsen, T.J.; and Troldborg, N. (2010). Calibration and Validation of the Dynamic Wake Meandering Model for Implementation in an Aeroelastic Code. J. Sol. Energy Eng., 132(4).

[3] Larsen, T.J.; Madsen, H.Aa.; Larsen, G.C. and Hansen, K.S. (2013). Validation of the Dynamic Wake Meander Model for Loads and Power Production in the Egmond aan Zee Wind Farm. Wind Energy, Volume 16, Issue 4, pp. 605–624.

[4] Larsen, T.J.; Larsen, G.C.; Madsen, H.Aa.; Thomsen, K. and Petersen, S.M. (2015). Comparison of measured and simulated loads for the Siemens SWT 2.3 operating in wake conditions at the Lillgrund wind farm using HAWC2 and the Dynamic Wake Meander model. EWEA offshore 2015, Copenhagen 10 – 12 March 2015.

[5] Nilsson, K.; Ivanell S.; Hansen K.S.; Mikkelsen R.; Sørensen J.N., Breton S.-P. and Henningson D. (2015). Large-eddy simulations of the Lillgrund wind farm, Wind Energy. 18, pages 449–467. doi: 10.1002/we.1707.

[6] Madsen, H.A.; Larsen G.C. and Thomsen. K. (2005). Wake flow characteristics in low ambient turbulence conditions, Proceedings of the Copenhagen Offshore Wind, Copenhagen, 2005. On CD-rom. www.ewea.org.

[7] Bingöl, F.; Mann, J. and Larsen, G.C. (2010). Light detection and ranging measurements of wake dynamics. Part I: one-dimensional scanning. Wind Energy; 13(1): 51–61.

[8] Trujillo, J.; Bingöl, F.; Larsen, G.C. and Mann, J. (2011). Light detection and ranging measurements on wake dynamics. Wind Energy; 14: 61–75.

[9] Frandsen, S. (2005). Turbulence and turbulence-generated structural loading in wind turbine clusters. Technical Report Risø-R-1188(EN), Risø-DTU.

[10] Keck, R.-E.*;* de Maré, M.*;* Churchfield, M.J.*;* Lee, S.*;* Larsen, G.C. *and* Madsen, H.Aa. *(*2015*).* Two improvements to the dynamic wake meandering model: including the effects of atmospheric shear on wake turbulence and incorporating turbulence build-up in a row of wind turbines, Wind Energy*,* 18*, pages* 111–132. *doi:* 10.1002/we.1686.

[11] Keck, R.-E. (2014). Validation of the standalone implementation of the dynamic wake meandering model for power production. Wind Energy. doi: 10.1002/we.1777.

[12] Machefaux, E.; Larsen, G.C.; Troldborg, N.; Gaunaa, M. and Rettenmeier A. (2014). Empirical modeling of single-wake advection and expansion using full-scale pulsed lidar-based measurements, Wind Energy, doi: 10.1002/we.1805.

[13] Frandsen, Sten Tronæs (2007). Turbulence and turbulence-generated structural loading in wind turbine clusters. 130 p. (Denmark. Forskningscenter Risoe. Risoe-R; No. 1188(EN)).

People vs. Windfarms? - To what extent are strategies for public participation used to foster social acceptance in the European wind energy sector?

EWEA Annual Event 2015

Wesche J.P.; Dütschke E.; Schneider U. (presenting author),

Fraunhofer Institute for Systems and Innovation Research ISI

Fon +49 721 6809-459 | Fax +49 721 680977-459

Julius.wesche@isi.fraunhofer.de

Breslauer Straße 48 | D-76139 Karlsruhe

Abstract

Wind is the most mature of the existing Renewable Energy Technologies and it is expected to play a fundamental role towards the transition to a sustainable energy system. European citizens are generally in favour of wind energy; however, on a local level wind farm developers often have to deal with opposition. Thus, finding strategies to support constructive discussions around wind farms is crucial for the further diffusion of wind energy. To contribute to this process this paper maps the status quo of public participation strategies in the European wind sector. More specifically, it summarizes the findings from an expert survey: 207 questionnaires from 13 European countries were collected filled in by representatives from relevant administrative bodies, project developers, cooperatives active in wind farm development, environmental organisations, financial institutions and others active in the field of wind farm development.

We find a high prevalence of social acceptance issues in the sample as the majority of study participants has experienced stops or at least delays of projects due to a lack of social acceptance. Concerning public participation we see that it is very often common in wind energy project development to engage in public participation and that these activities often exceed legal requirements. Although public participation is frequent in wind energy projects, many organisations involved do not have a standard procedure to deal with it and guidelines and other advice giving documents are often not known nor used. The main barrier to apply this knowledge seems to be the difficulty to transfer it to the specific conditions of a project.

Keywords

Wind energy, social acceptance, public participation, strategies, European perspective,

1 Introduction

For the EU to meet its 2020 climate and energy targets, increased renewable energy generation and extensions of the electricity infrastructure are necessary. Wind is the most mature of the existing renewable energy technologies. It is expected to play a fundamental role in achieving the EU 2020 climate and energy targets. Moreover, beyond 2020, wind energy is the key technology in all EU energy scenarios [1].

Generally speaking, European citizens are in favour of wind energy [2], [3]. They also support the EU goal of moving away from conventional electricity generation towards renewable power. However, on a local level, project developers are repeatedly confronted with criticism and opposition by the public [4]. This lack of public support contributes to the fact that over 20 % of wind energy projects are delayed and nearly 20 % are seriously threatened due to appeals [4]. Therefore, dealing with social acceptance[1] of wind energy infrastructure is a necessity for all stakeholders involved in wind energy projects. Implementing public participation and engagement strategies into project management for onshore wind energy farms is often seen as a promising strategy to avoid and solve these aforementioned challenges. However, to the best of our knowledge, there has not been a specific analysis (1) on the extent to which strategies are utilised and (2) what they usually consist of. These two topics are therefore addressed in this paper.

This paper was generated as part of the WISE Power project, a project funded by the European Union to further develop the social acceptance of wind energy, aiming at significantly improving local engagement and support for wind turbines while enhancing local community participation in the planning and implementation of wind energy projects (http://wisepower-project.eu/). More detailed info about the study presented here is published in Dütschke & Wesche [6].

[1] Acceptance is a general evaluation, that is, the extent to which people (dis)favour a particular energy alternative [5].

2 Data and methods

In order to answer the outlined research questions (see above) an expert survey was conducted in 13 European countries. It entailed both closed and open questions and explored the experience and evaluation of activities in the respondent's country regarding public participation and social acceptance.

For the survey countries were selected that cover different stages of development of wind energy (from emerging to developed wind markets). 466 potential respondents were contacted within the 13 target countries. This resulted in 207 completed questionnaires from six different stakeholder groups (Figure 1). On average, 15 questionnaires per country were obtained.

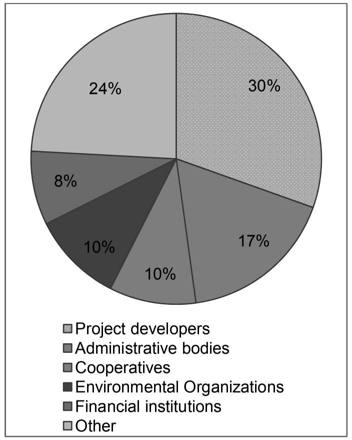

Figure 1. Organisational affiliation of the respondents (n=207)

The sample includes respondents from administrative bodies, project developers, environmental organisations, financial institutions, cooperatives and others active in the field of wind farm development (Figure 1). These groups were chosen in order to provide a comprehensive picture of the issues under study for each country by combining different perspectives of wind energy project development. As the questionnaire covered a variety of topics, it was created in a modular way so that it could be individually adapted to the field of expertise of the respective respondents.

3 Results

Before addressing the topics laid out in the introduction (cf. Section 3.2-3.3), the data will be analysed aiming to ascertain that social acceptance indeed challenges the timely development of wind farms across Europe as suggested by the results of the Wind Barriers project [4].

3.1 Social acceptance as a challenge in wind farm development

In order to pin down the relevance of negative impact of the lack of social acceptance on project development those respondents who claimed to have experience with public participation activities (n=121) were asked about their experiences. It turns out that the majority of the survey participants have experienced stops or at least delays of projects due to a lack of social acceptance, which supports the findings of the Wind Barriers project [4].

Focusing on the 70 project developers and representatives from cooperatives in this subsample, a share of 57 % has experienced delays and stops of wind farms due to a lack of social acceptance while less than a third has not; 14 % indicate they do not know (Figure 3).

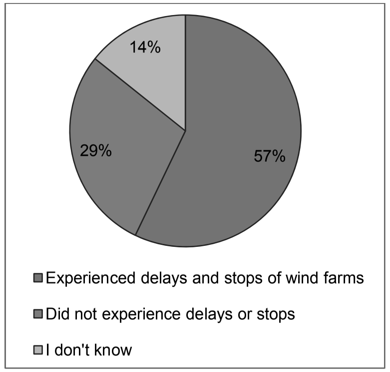

Figure 3. Experience of delays and stops of wind farms due to lack of social acceptance (project developers and cooperatives – n=70)

From the remaining 51 respondents of the subsample, i.e. respondents from administrative bodies, financial institutions, environmental organisations and other relevant actors around half reported that they have experienced delays and/or blockages of wind farm development due to a lack of social acceptance of the proposed wind farms (Figure 2). Conversely 16 % of the respondents have not experienced such impacts and 33 % do not know.

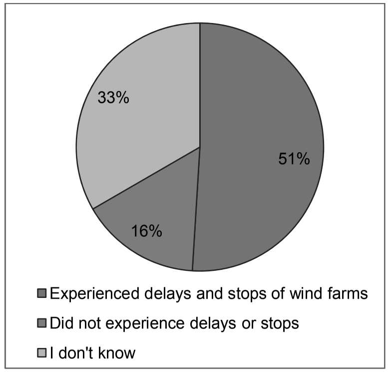

Figure 2. Experience of delays and stops of wind farms due to lack of social acceptance (administrative bodies, financial institutions, environmental orgs. and other relevant actors – n=51)

Respondents were also surveyed about which reactions their company or organisation has experienced in relation to wind power projects in the past three years (2012-2014). While the majority reported one or more reactions, 17 % of the respondents stated that they have not experienced any public reaction to the wind farms they have been involved in. Overall, negative experiences are reported much more often: 861 negative reactions were indicated compared to 478 positive ones. However, it has to be taken into account that the overwhelming number of negative reactions may in part be due to the fact that positive reactions are usually not officially filed.

Looking more specifically at the positive issues raised in relation to wind power, local economic benefits and CO_2-emissions reductions are stated most frequently (multiple responses possible; Figure 4).

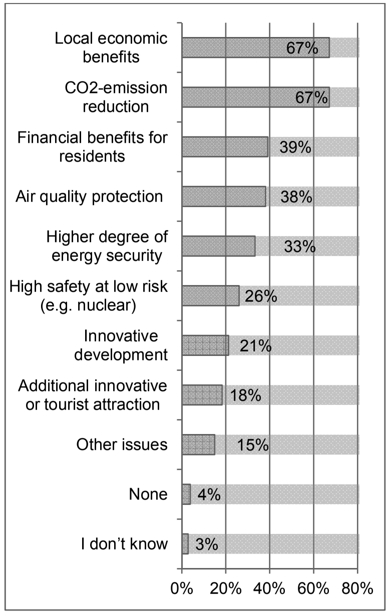

Figure 4. Main positive issues raised in relation to wind power - past three years (n=207; multiple responses possible)

Financial benefits for residents, air quality protection and high degree of energy security are also repeatedly discussed. Wind farms as tourist attractions and wind energy as a low risk and innovative technology are given the least relevance in current discussions.

The main negative issues raised in relation to wind power projects are the visual impact on landscapes followed by noise and the impact on the local ecosystem and wildlife (Figure 5). Other topics, which were named only a few times are light emissions at night, lack of or late provision of information and unfair division of benefits and impacts.

Besides local economic benefits, arguments used to promote wind energy mainly refer to a national or global level.

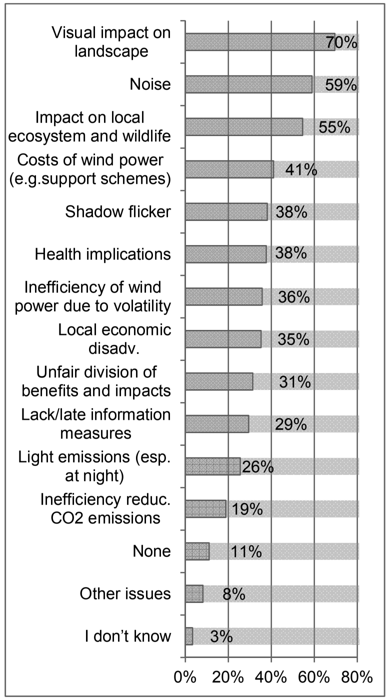

Figure 5. Main negative issues raised in relation to wind power in the past three years (n=207: multiple responses possible)

3.2 Utilisation and design of strategies for public participation

In this step, only respondents who work in organisations that have been directly involved in activities for public participation (n=121) are included in the analyses presented. 48% of the respondents state that there are binding policies in place for public participation during wind farm development (Figure 6). A further third of the respondents state that there are obligatory measures where installations fulfil certain criteria.

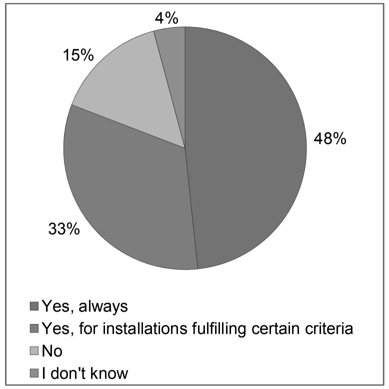

Figure 6. Are elements of public participation obligatory during any phase of wind farm development? (Only respondents who have been directly involved in activities for public participation; n=121)

Thus, it seems to be widely acknowledged that interacting with the local community is relevant in wind farm development.

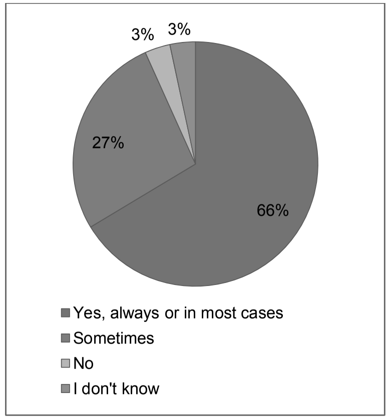

Figure 7. Independent of the fact whether public participation is obligatory, are elements of public participation part of the usual procedure? (Only respondents who have been directly involved in activities for public participation; n=121)

This is also supported by the fact that we found that two thirds of the respondents claim that elements of public participation and engagement are part of the usual procedure during planning, building and operating wind farms – therefore exceeding national or local legislative requirements (Figure 7). Despite the fact that public participation is frequent in wind energy projects, only about 34% percent of the respondents (Figure 8) state that there are standard procedures in place.

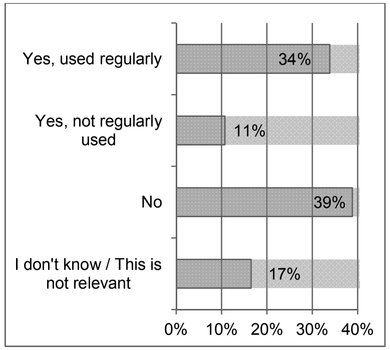

Figure 8. Does your company or organisation have a standard procedure or guideline on how to conduct public participation activities for wind power projects? (Only respondents who have been directly involved in activities for public participation; n=121)

If there are standard procedures used they seem to have been developed internally, often drawing on information generated from discussions with interest groups.

Published resources from others are hardly applied. The questionnaire listed six such advice giving documents that were identified within deliverable 2.1 of the WISE Power project and asked respondents whether they are aware of them. The most common document among them has only been used by 12 % of the respondents.

In order to explore the reasons for the meagre utilisation of standard procedures or published guidelines, potential barriers to using them were surveyed (Figure 9). The reason stated most often is a lack of resources. Furthermore, they are considered as not helpful for actual project development processes. Some respondents do not see the need to use them.

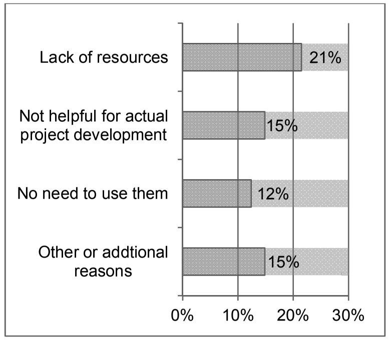

Figure 9. If you know of one or more such guidelines/toolkits, but do not use any of them – what are the reasons for it? (Only respondents who have been directly involved in activities for public participation, n=121; multiple responses possible)

The following additional barriers were furthermore mentioned repeatedly by respondents:

- standard guidelines, toolkits and best practices often do not fit the local realities,
- material is perceived as abstract and difficult to transfer to the concrete project,
- approaches are needed which can be individually adjusted.

Furthermore, the respondents were asked to what degree resources (time, money, expertise) are systematically allocated to participation and communication activities during project development. 39 % of the respondents who are directly involved in public participation activities state that allocating resources is always part of the standard project planning procedure (Figure 10).18 % quote that specific resources are only allocated under certain conditions and 15 % state that resources are hardly or never allocated towards participation and communication activities. 28 % state not to have any knowledge how their organisation deals with resource allocation on this issue.

Further analysis show that those respondents who report that their organisation usually allocates resources for participation are also more likely to have a standard procedure for this, i.e. pointing to a higher level of professionalism in this regard in these organisations.

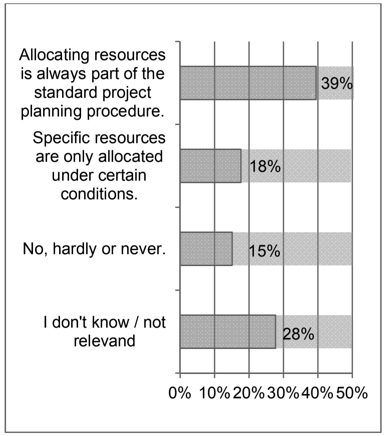

Figure 10. To what extent are resources allocated systematically to participation and communication activities during project development? (Only respondents who have been directly involved in activities for public participation, n=121)

3.3 Methods and content of social acceptance strategies

In order to assess the respondents' experience with regard to different levels of public involvement three different approaches were presented:

Informational measures refers to activities such as distributing brochures/leaflets or provide possibilities where citizens may ask questions.

Consultation and dialogue with the public includes giving the possibility to the public to give feedback on the project and its specifications and that this feedback is then considered by the project team and / or relevant administration.

Empowerment of the public means sharing the decision making process, i.e. the public is involved e.g. via a citizen vote.

Assessing the experience with these three levels of public involvement measures with regard to social acceptance, firstly it can be stated that experiences are on average positive. Overall, the involvement level of consultation and dialogue is rated most positively, followed by solely informational measures and empowerment of the public scoring lower which is mainly due to lower ratings by project developers.

Further comments by the respondents include the following:

The comments on the utilisation of *informational measures* mainly suggest that they are only considered a fundamental requirement, but they are not sufficient as such to create public support.

Consultation and dialogue with the public is considered the next step and by many respondents of the survey also considered a basic requirement. On the other hand negative experiences within dialogues with the public or poor levels of interest are reported. This shows that consultation and dialogue does not necessarily lead to success.

The comments on the issue of *empowering the public* suggest that this approach has not been implemented very often and thus it has not been possible to gather a lot of experience with it yet. The comments indicate that it might be challenging at times to find the right point in time, the right format and to make sure that all representatives of the community including the opponents of wind power take part in such processes.

Beyond the general levels of public involvement there are further methods that are deemed to improve local acceptance. The participants were introduced to three generic components: shared ownership of the wind farm, involvement of the community in the designing process and community benefits (e.g. set up of a fund which invests in the wellbeing of the local community). When analysing the data it can be seen that respondents perceive all of these measures as promising in potentially enhancing social acceptance (Figure 11). Respondents also had the possibility to comment on the different options.

Most of these comments towards *shared ownership* are positive, stating that it has the potential to increase social acceptance. However, it is acknowledged by the respondents that shared ownership also means shared risk and thus does not guarantee the absence of opposition, e.g. if a municipality invests funds into wind projects that could otherwise be invested with more direct benefits to community members. Another negative aspect of shared ownership which requires individual investment lies in – according to respondents' comments – potentially splitting the community into two groups: one group that is affluent enough to purchase shares of the proposed wind farm and one group that cannot afford to do so.

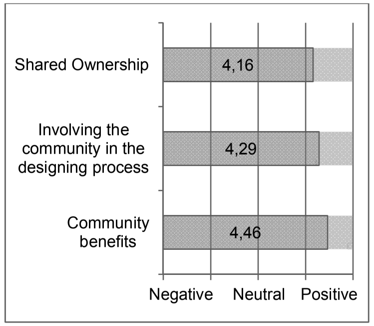

Figure 11. What measures are perceived to contribute to social acceptance for wind power projects? (n=202-203)

Involving the community is seen very positively amongst the respondents that commented on this issue. It minimises the potential for misunderstandings and gives the local population a feeling of being respected and not overlooked. However, the participants also acknowledge the limitations of involving the community as for instance it is not possible to determine the appropriate siting of wind turbines with all members of all stakeholder groups (due to organisational and technical reasons).

Community benefits are perceived similarly positive though it was also mentioned that it does not necessarily ensure local community support. On the contrary, some respondents warn that it might turn the initial acceptance into opposition where community benefits are considered as bribery. It is therefore suggested by the respondents that community benefits will have a positive impact on acceptance if they are implemented along with other participation measures; a combination of shared ownership with a benefit package for those without the resources to invest is seen as an ideal solution by the respondents.

On top of that, some respondents are convinced that there are a number of individuals in most communities that cannot be convinced regardless of the level of consultation and information delivered. In addition, it is suggested by the interviewed experts that actions involving the community should be steered by the municipalities seen as neutral institutions rather than by project developers.

4 Summary and Discussion

This study looked into the status quo of social acceptance of wind farms and social acceptance measures around them based on expert survey across Europe. The data shows quite clearly that a lack of local social acceptance for onshore wind farms indeed presents a challenge to the Europe-wide development of onshore wind. This is proved by the fact that the majority of study participants has experienced stops or at least delays of projects due to a lack of social acceptance. Furthermore, much more negative than positive reactions to wind farms are reported by the respondents. These findings underline, as expected and already shown by the Wind Barriers project [4], the relevance of social acceptance issues and the need for the development and implementation of social acceptance strategies.

The data shows furthermore that this is to some extent already common knowledge in wind farm project development as two thirds of the respondents claim that elements of public participation are part of the usual procedure during planning, building and operating wind farms. While many respondents report that integrating elements of public perception are obligatory in their country, the percentage of those stating that they are also part of usual procedure is even higher. This indicates that it is the usual case to go beyond what is mandatory.

However, these public engagement strategies are usually not informed by published resources nor based on a standard procedure. Only about a third of the respondents state that they utilise standard procedures or guidelines when planning to conduct public participation activities. The reason stated most often why this is not done is a lack of resources. Likewise, allocating resources for these activities is not part of the usual procedure for many organisations. This leads to the supposition that public engagement is mainly conducted hands on and spontaneously. This does not necessarily mean that it is not done well, however, could make it difficult to react to unexpected arguments or dynamics. Furthermore it might become challenging if further resources are needed unexpectedly during project development. Overall, social acceptance management around wind farms could probably increase in professionalism, i.e. by applying standardisation and knowledge management.

With regard to different levels of public participation respondents are more in favour of consultation and dialogue as well as informational measures. Empowerment of the public where the public has the possibility get involved in the decision itself is evaluated less positively. This finding is due to the fact that the surveyed project developers are less enthusiastic about this issue. To leave the decision to the local public can certainly be time-consuming and also risky as it may lead to refusal. However, if the refusal follows in a later stage through juridical decisions this may even be more costly. Furthermore, a public vote could also help to find out whether opposition is a majority opinion or maybe only a (loudly voiced) minority standpoint.

It is also noteworthy that only about 25 % of the respondents mention a lack or late information measures as an issue (cf. Figure 5). Thus, this does not seem to be frequent in discussions around wind farms; nonetheless, providing information is very often seen as a prerequisite but may not be sufficient to gain acceptance. Shared ownership, community benefits and involvement of the community in the design process are all perceived as helping to foster social acceptance across all respondents. Though, also the problems of these approaches were mentioned. These include in case of shared ownership for instance the risk to split the community between those who are affluent enough to purchase shares and others who are not. The main challenge related to community benefits was that they need careful implementation in order to avoid the impression of bribery.

5 Conclusion

If these findings are taken together, they point out that although the awareness for social acceptance and public participation is high there may be a lack of professionalism, i.e. standardisation and knowledge management. This is maybe due to the fact that social acceptance is still not high enough on the priority ladder of many developers and other organisations dealing with wind power.

However, opposition to wind farms seems mostly specific, i.e. restricted to a specific installation: the survey shows that the main negative issues mentioned in relation to wind power projects are the visual impact on landscapes followed by noise and the impact on the local ecosystem and wildlife (cp. [7] for similar results). Arguments that question wind energy on a more general level, e.g. whether it contributes to mitigating climate change, are less frequently reported to play a role. This is further confirmed by the finding that on the positive side respondents report that the reduction of CO_2 emissions or enhanced air quality are often addressed in discussions around wind farms. Therefore it seems to be advisable to highlighting more arguments which make projects more appealing from a local or regional point of view beyond economic issues. Thus, it seems important to further highlight broader lines of arguments why a wind farm is necessary and useful in a specific area and how it contributes to the widely accepted goal of a transition of the energy system.

Against this background, it seems worthwhile to further engage into knowledge generation and implementation of social acceptance strategies as they are likely to facilitate the discussion process around wind farms, which is the base for positive wind farm development decisions.

Acknowledgements

The research leading to these results has received funding from the European Union's Intelligent Energy - Europe Programme (WISE Power Project) (IEE/13/528/SI2.674872).

Disclaimer

The sole responsibility for the content of this publication lies with the authors. It does not necessarily reflect the opinion of the European Union. Neither the EASME nor the European Commission are responsible for any use that may be made of the information contained therein.

References

[1]. European Commission (2011): Energy Roadmap 2050, available on the European Commission's website http://eur-lex.europa.eu/legal-content/EN/TXT/PDF/?uri=CELEX:52011DC0885&from=EN, last accessed 03/15/2015.

[2]. European Commission (2007): Eurobarometer on Energy Technologies: Knowledge, Perception, Measures, available on the European Commission's website, http://ec.europa.eu/public_opinion/index_en.htm, last accessed 03/15/2015.

[3]. European Commission (2011): Special Eurobarometer 364 - Public Awareness and Acceptance of CO2-capture and storage, available on the European Commission's website, http://ec.europa.eu/public_opinion/archives/ebs/ebs_364_en.pdf, last accessed 03/15/2015.

[4]. Wind Barriers (2010): Administrative and grid access barriers to wind power, available on Wind Barriers website, www.windbarriers.eu

[5]. Perlaviciute, G.; Steg, L. (2014): Contextual and psychological factors shaping evaluations and acceptability of energy alternatives_ Integrated review and research agenda. In Renewable Energy (77), pp. 259–267.

[6]. Dütschke E. & Wesche J.P. (Fraunhofer ISI;2014): Wind-Acceptance a user guide for developers and municipalities review of best practices, guidelines and toolkits on social acceptance in the wind energy sector, compiled within the WISE Power project, funded under the intelligent Europe program, available on www.wisepower-project.eu

[7]. Hübner. G. & Pohl, J. (2012). Offshore-Windenergienutzung – Erwartungen und Erfahrungen von Anwohnern und Touristen. Broschüre, Martin - Luther-Universität Halle-Wittenberg.

Evaluation of Bird Detection using Time-lapse Images around a Wind Farm

Ryota Yoshihashi, Rei Kawakami, Makoto Iida and Takeshi Naemura

The University of Tokyo, Hongo 7-3-1, Bunkyo-ku, Tokyo, 113-8656, Japan

Fig. 1. Appearance of birds in images around a wind farm (left) is significantly different from those in a generic image-recognition dataset (right).

ABSTRACT

One of the primary environmental concerns of wind farms is the increase in bird mortality. To assess environmental risks around wind farms, the demand for automatic bird monitoring increases rapidly. Considering recent advancements in object detection methods in computer vision, automated monitoring based on images is promising. However, the accuracy of state-of-the-art methods in a practical environment remains uncertain due to the significant difference between the images taken in a practical environment and those used in generic object detection competitions. This study evaluates these image-based bird detection and classification methods. We also introduce a bird monitoring system with a whole image processing pipeline. For evaluation in a practical environment, we utilize an open-access time-lapse image dataset around a wind farm. As a state-of-the-art method, we include convolutional neural networks, a rising method of deep learning for image recognition, which shows performance improvement.

Index Terms— Image recognition, bird detection, ecological conservation, social acceptance

1. INTRODUCTION

Environmental concerns in developing wind farms have been highlighted by both the wind-energy community and ecological experts [1, 2, 3] as the demand for wind power energy grows rapidly around the world to meet public policies for renewable energy. One of the primary concerns is the increase in bird mortality caused by collision with blades, loss of nesting and feeding grounds, and interception on migratory routes [3, 4, 5, 6]. Hundreds of annual bird fatalities, including those of charismatic species, have been reported at several sites [6]. To assess such risks during the establishment and operation of wind farms, investigation of bird ecology and assessment of potential risks are necessary. Conventional bird monitoring has been carried out by manual observation, which is expensive and laborious [7]. Automation in this task can lower the cost, enable long-term monitoring, and lead to higher accuracy and reproducibility. However, an automatic system is required to perform bird detection as well as classification of bird species, both of which have been non-trivial for machines to achieve.

Image-based detection using cameras is one of the promising approaches [8, 9, 7, 10], while radar-based [11, 12, 13] and acoustic-based [14] detections have been commonplace in the literature. Rich visual information with a higher resolution can be utilized, and the recognition performance has improved dramatically in the last decade, owing to the availability of big data, high performance computers, and algorithm improvement in machine learning and computer vision research fields. Reviewing recent milestones in computer vision, robust features have been invented [15, 16, 17], good classifiers have been found [18, 19], good image structures have been proposed [20, 21], huge image datasets have been established [22, 23, 24], and object detection competitions using them have been held [22, 25]. Deep neural networks [26] have likewise resulted in further improvement in detection and classification during these competitions [27, 25]. Their strength is in their adaptive learning of features and classifiers during training.

However, despite the excitement over these improvements, the advancement, accuracy, precision, and recall of such state-of-the-art methods in practical environments for wild bird monitoring remain uncertain. An exception is May *et al.*'s work reporting that DTBird detected 76% to 96% of total birds in an experimental setting in Smøla [9]. In practical environments around wind farms, birds tend to appear in low resolution even in a high resolution image since the monitoring system has to cover a wide field of view to assess the distribution of birds and to notice the approach of birds well ahead of time. Figure 1 shows such images. As shown in the figure, the actual appearance of birds is significantly different from those used in generic object detection competitions [27, 25], in which most of the methods are designed and experimented. It is not clear whether these methods are suitable for low-resolution images.

To reveal the actual precision and recall of state-of-the-art methods for low-resolution bird detection and classification, this study utilizes a wild bird image dataset around a wind farm as a benchmark [28] and evaluates the performance of several state-of-the-art methods, including one utilizing deep neural networks. In addition, we present a whole image processing pipeline of an automated bird monitoring system for wind farms, about which very few scientific papers discuss. Our system utilizes background subtraction [29] and convolutional neural networks (CNN) [30] for accurate and robust detection and classification.

The rest of the paper is organized as follows. Section 2 describes our bird detection and classification pipeline. Section 3 experimentally [Inst1]evaluates the performance of state-of-the-art detection and classification methods. Section 4 concludes this paper.

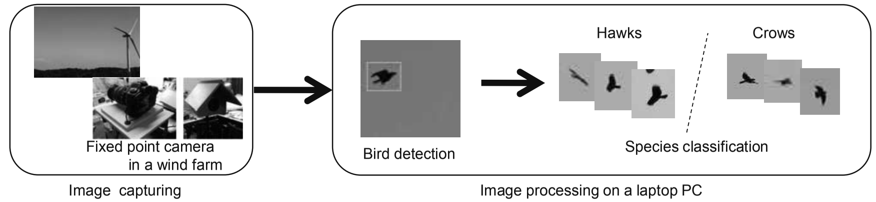

Fig. 2. Overview of our image processing pipeline for bird detection and classification.

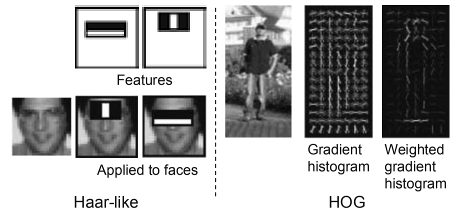

Fig. 3. Image features used in the system, Haar-like [17] (left) and HOG [16] (right).

2. BIRD DETECTION AND CLASSIFICATION PIPELINE

Our bird monitoring system consists of a fixed camera, a laptop computer for control, and recognition software. It captures images automatically and processes them to detect and classify birds as shown in Fig. 2. The core algorithm is based on machine learning for robustness, and the details are evaluated below. The system is able to discriminate birds from others or a species of birds from others after the training phase. During training, the classifier is optimized in accordance with training images including birds and others.

2.1. Setup

We use a still camera with a telephoto setup to capture a bird with a one-meter wing span 580 meters away that would cover an area of 20 pixels in the image, considering the distance between the camerafs location and the wind turbine. This setup enables us to monitor a wide area suitable for bird investigation, including the wind turbine. The resolution of the sensor is 5616 times 3744 pixels, and the field of view is 27 times 19 degrees. The interval of image capture is two seconds because of the transfer rate between the camera and the laptop.

2.2. Algorithm

Our algorithm is a combination of background subtraction [29] and object classification. Background subtraction is a method for extracting moving objects from fixed backgrounds and works well with our scenes that are mostly static. However, regions extracted still include some background objects, such as parts of the turbine, trees, or clouds; thus, we utilize machine learning-based classifiers to filter birds from others.

Specifically, we will compare the following two classifiers in the next section: First is AdaBoost [18], a widely used learning algorithm in computer vision. This algorithm is often combined with image features such as Haar-like [17] or Histogram of Orientated Gradients (HOG) [16] for further robustness. The performance of these methods is known to depend highly on both the types of targets (faces, people, birds, etc.) and scene properties (indoor, street, wind farm, etc.).

Second is convolutional neural networks (CNN) [30], the most successful deep networks for object recognition to date. The strength of CNN is that it learns features by itself; *i.e.*, it does not need manually designed image features that are not guaranteed to be optimal. Yet, it is important to reveal whether CNN outperforms others on low-resolution detection and classification tasks. Since CNN is unexplored, it is therefore unclear what types of data and tasks it prefers.

Below, we briefly explain the details of each method.

AdaBoost AdaBoost [18] is a two-class classifier based on feature selection and weighted majority voting. A strong classifier is made as a weighted sum of many weak classifiers, and the resulting classifier is shallow but robust. The algorithm overview is as follows.[Inst2] First, we uniformly initialize the weights of the training samples. Second, we select one weak classifier with the lowest error rate using the weighted training samples. Third, the weight of the selected weak classifier is set on the basis of the error it produces. A larger weight is set for a smaller error rate, since weak classifiers with smaller error rates are more reliable. Fourth, we update the weights of training samples based on the error rate of the reweighted classifier. Then, we iterate from the second to the fourth step a fixed number of times.

Haar-like Haar-like [17] is an image feature that utilizes contrasts in images. It extracts the light and the shade of objects by using black-and-white patterns as shown in the left figure in Fig. 3. Haar-like first succeeded in face detection [17] and is used as a fast and robust feature.

HOG HOG [16] is a feature used for grasping the approximated shape of objects. A visualized HOG is shown in the right figure in Fig. 3. First it computes the spatial gradient of the image and makes a histogram of the quantized direction of the gradient in each local region, called a cell in the image. Next it concatenates the histograms of the cells in the neighboring groups of the cells, the blocks, and normalizes them by dividing by their Euclidean norms in each block. HOG was first used for pedestrian detection and afterwards applied to various tasks including generic object detection.

CNN CNN [30] is a type of neural network characterized by convolutional layers. Convolution is an operation which associates an image with a feature map by using the inner product between each patch in the input image and another fixed patch, called a kernel. In CNN, each convolutional layer has multiple kernels and outputs multi-channel feature maps. These kernels in the convolutional layers are interpreted as connection weights between neurons and are optimized in training. Other components of CNN are pooling layers and fully-connected layers. Pooling layers are placed after convolutional layers to downsample feature maps. These layers output lower-resolution feature maps by taking the maximum in each local region, *e.g.*, a two-by-two patch, in input feature maps. Fully-connected layers are placed at the end of the network. These layers perform as a classifier, which receives the features from convolutional and pooling layers and outputs the class of the input image.

Among the variations of CNN architectures, ours is based on one of the handwriting recognition methods [30] and refined by utilizing two recent discoveries for improving performance: Rectified linear units (ReLU) and dropout from [26]. ReLU is a type of activation function, that is, the relationship between input and output in a single neuron. It requires a low computing cost and is easy to optimize due to its simple derivative. Among the variety of functions, the effectiveness of ReLU was discovered recently. ReLU is formulated as follows.

$$y(\mathbf{x}) = \max\{0, \mathbf{w}\mathbf{x} + b\}$$

Here w is weight parameters and b is a bias parameter. Dropout is a training heuristic for removing neurons selected randomly in each iteration of parameter updates. Removed neurons are regarded to output zero independently from their inputs. The whole network is shown in Fig. 4.

The training of CNN is to compute the weights and biases which minimize the classification error rate. For this purpose, gradient methods are widely used. We use stochastic gradient descent [31]. This method allows us to approximately acquire the minimum with a relatively low computational cost.

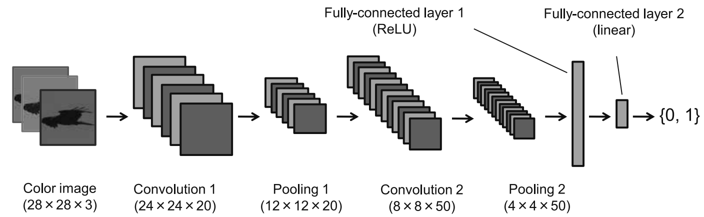

Fig. 4. CNN architecture we used. This is based on a handwriting recognition method [30].

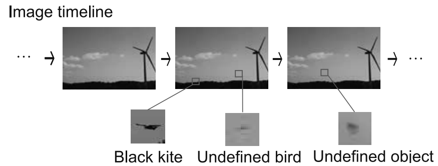

Fig. 5. Structure of dataset [28]. It includes time-lapse images, bounding boxes of birds and other flying objects, and their class labels.

3. EVALUATION EXPERIMENTS

3.1. Bird Image Dataset for Training and Evaluation

For the performance evaluation of bird detection and classification methods, we utilize a dataset of birds at a wind farm [28]. This dataset offers open access and has preferable attributes; it contains a large amount of data and presents a detailed specification of birds. The dataset [28] is a sequence of images of a scene at a wind farm, and it provides annotations of bird information appearing in the images as shown in Fig. 5. Annotations were added to the images by bird experts who are members of a bird association and have experience in field surveys. They checked the image timelines, found birds, and annotated bounding boxes with class labels for each bird. 32,442 images were processed and 32,973 birds were found.

3.2. Experimental Procedure

Using the dataset, we conducted two recognition experiments: bird detection and two-class species classification. Below, *detection* is defined as a classification of birds and non-birds, given the candidate regions suggested from motion information. *Classification* is defined as a classification between hawks and crows, which is a fundamental task in a bird-monitoring system. They are the most frequent classes of birds in the area, and we have a sufficient amount of data for accurate evaluation. This two-class classification is also practical because many endangered species are included in hawks.

For any machine learning methods, we need positive and negative samples for training. In the detection experiment, positive samples (birds) were collected from bird regions labeled in the dataset. Negative samples (non-birds) are background regions clipped by background subtraction. Examples of the birds and non-birds are shown in Fig. 6. We used five-fold cross-validation to efficiently conduct the experiment on this dataset.

In the classification experiment, hawks labeled in the dataset are positive samples, and crows are negative samples. Classification is a more difficult task than detection in this dataset; thus, in order to analyze each method's behaviors in detail, we investigated the effect of image resolution by dividing the positive and negative images into groups on the basis of resolution. Specifically, images of hawks and crows are divided into the groups of 15–20, 21–30, and 31–50 pixels, as shown in Fig. 6. On each group, we conducted holdout validation using 800 hawks and 150 crows for training data and others for test data.

In these experiments, we evaluated CNN [30], as well as AdaBoost [18] combined with three types of features, Haar-like [17], Histogram of Orientated Gradients (HOG) [16] features, and RGB (image pixel values without transformation). For reproducibility, we list the parameters of each algorithm in the following. As for CNN, we used the architecture of [30] with the exception of inputting color images and using more effective nonlinearity from [26]. For the training of CNN, we used stochastic gradient descent [31], and we set the learning rate at iteration i to $0.001(1 + 0.0001i)^{-0.75}$, momentum to 0.9, and weight decay to 0.0005 as optimization parameters. In AdaBoost, we set the number of weak

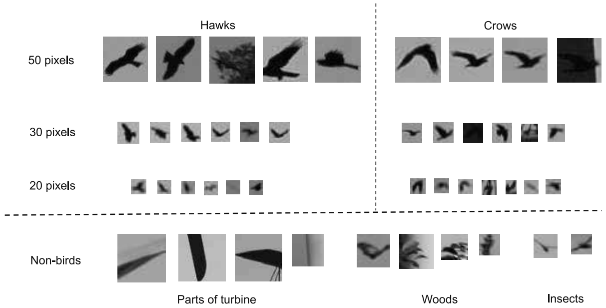

Fig. 6. Bird and non-bird image examples. Bird images are grouped by resolutions.

classifiers to 400. The feature patterns for Haar-like were the same as [17], and the pattern sizes were 2, 6, and 10 pixels square. The cell size of HOG was 4 pixels square, and the block size was 3 by 3 cells.

3.3. Results

We evaluated the detection and classification performances using two measures, true positive rate (TPR) and false positive rate (FPR). TPR is given as the number of true positives divided by the number of all positives in the test data. FPR is the number of false positives divided by the number of all negatives in the test data. Because there is a trade-off between TPR and FPR, the total performance of an algorithm is represented by the receiver operating characteristic curve (ROC), a curve drawn by FPR and TPR of each point on the trade-off. A curve near the upper-left corner means better performance.

The result of detection is shown in Fig. 7. In the figure, FPR means the rate of misrecognizing backgrounds as birds, and TPR means the rate of correctly recognizing birds. The best performance is achieved by Haar-like. At the false positive rate of 0.01, over 0.98 of birds are still detected with Haar-like, which is a successful performance. The other methods including CNN showed worse performances.

The result of classification is shown in Fig. 8. Here, FPR is the rate of misrecognizing crows as hawks, and TPR is the rate of correctly recognizing hawks. Because of visual similarity, species classification is more difficult than birds-versus-others classification; thus, lower performance is apparent. The trend of well-performing methods is also different from detection. CNN performed the best and Haar-like the worst in all resolutions. In addition, the dependency of features' performance on resolution was observed. RGB features performed better in the 15–20 pixels group and HOG in the 30–50 pixels group.

4. DISCUSSION

In the detection experiment, Haar-like outperformed others, and the performance difference among those except Haar-like is subtle. This may be due to the low quality of the images. Haar-like is a simple feature for grasping only the contrast in images. More complex features like HOG can represent details of images and are preferred in tasks like pedestrian detection and generic object detection. However, it can be less robust for low-resolution bird detection.

Similarly, CNN may have failed to learn effective features from the data. The performance of CNN depends on the parameters of the network and optimization. Although we used the parameters established in handwriting recognition [30], there may exist better parameters for our images. More efforts for parameter search may improve the performance.

Fig. 9 shows example images that are misrecognized as birds by Haar-like. They are moving backgrounds such as parts of the turbine, trees blown by the wind, and flying objects such as airplanes and insects. Flying objects are more difficult negatives due to their visual similarity to birds. Note that the number of false detections depends on the number of negative samples in the data. More negative samples mean more false detections with the same false positive rate. Thus, the actual number of false detections can change depending on the test environments.

In the experiment of classification, CNN outperformed the other methods in all groups with different resolution. In contrast, Haar-like, which performed the best in detection, resulted in the worst performance.

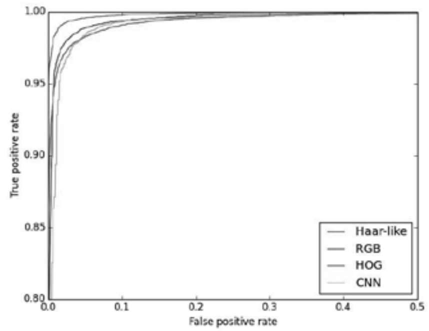

Fig. 7. Results of detection (bird-versus-others).

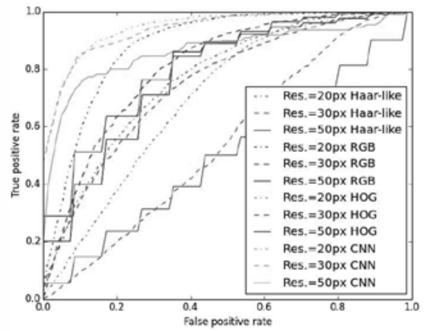

Fig. 8. Results of classification (hawk-versus-crow).

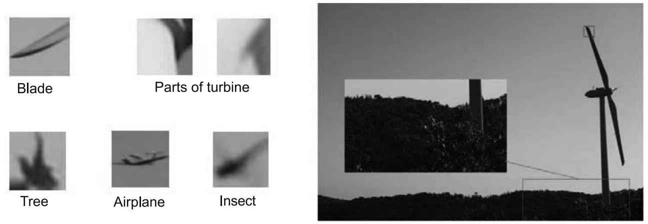

Fig. 9. Example images that are misdetected as birds.

The hand-crafted features may be less effective in classification because of the subtle difference between the classes. Conversely, the learned features of CNN succeeded in adapting to the classification task through training.

Fig. 10 shows examples of correct and wrong classification with CNN in each resolution group. Visually similar images are sometimes correctly classified but sometimes not. Instead of high performance, CNN does not have explicit trends in its misclassification because of the black-box process of training.

5. CONCLUSION

To evaluate a bird monitoring system on the basis of time-lapse images, we have conducted experiments of bird detection and classification. By using a dataset from a realistic environment and representative methods in computer vision, we provided practical results of recognition performance. We showed successful results for detection and the possibility of species classification using image recognition. The effectiveness of rising CNN in classification is also observed. However, there is room for performance improvement, especially in species classification. Improvement of the software for more accurate bird monitoring is necessary. Our system is a hopeful solution to bird strikes and can contribute to the social acceptance of wind energy.

ACKNOWLEDGEMENTS

A part of this work is entrusted by the Ministry of the Environment, JAPAN (MOEJ), the project of which is to examine effective measures for preventing birds, especially sea-eagles, from colliding with wind turbines.

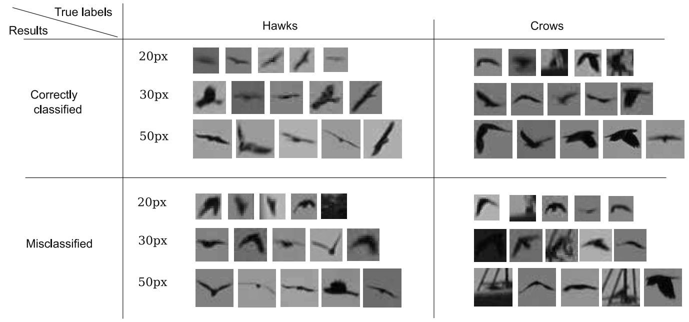

Fig. 10. Example images of correct and wrong classification in each resolution group.

6. REFERENCES

[1] B. Snyder and M. J. Kaiser, "Ecological and economic cost-benefit analysis of offshore wind energy," *Renewable Energy*, vol. 34, no. 6, pp. 1567–1578, 2009.

[2] W. P. Kuvlesky, L. A. Brennan, M. L. Morrison, B. M. Ballard K. K. Boydston, and F. C. Bryant, "Wind energy development and wildlife conservation: Challenges and opportunities," *The Journal of Wildlife Management*, vol. 71, no. 8, pp. 2487–2498, 2007.

[3] K. S. Smallwood, L. Rugge, and M. L. Morrison, "Influence of behavior on bird mortality in wind energy developments," *The Journal of Wildlife Management*, vol. 73, no. 7, pp. 1082–1098, 2009.

[4] A. L. Drewitt and R. H. W. Langston, "Assessing the impacts of wind farms on birds," *Ibis - the International Journal of Avian Science*, vol. 148, pp. 29–42, 2006.

[5] A. L. Drewitt and R. H. W. Langston, "Collision effects of wind-power generators and other obstacles on birds," *Annals of the New York Academy of Sciences*, 2008.

[6] A. L. Drewitt and R. H. W. Langston, "Risk evaluation for federally listed (roseate tern, piping plover) or candidate (red knot) bird species in offshore waters: A first step for managing the potential impacts of wind facility development on the atlantic outer continental shelf," *Renewable Energy*, 2011.

[7] S. C. Clough, S. McGovern, D. Campbell, and M. M. Rehfisch, "Aerial survey techniques for assessing offshore wind farms," *International Council for the Exploration of the Sea (ICES), Conference and Meeting (CM) Documents*, 2012.

[8] A. Rioperez and M. de la Puente, "Dtbird: A self-working system to reduce bird mortality in wind farms," *EWEA Conference*, 2010.

[9] R. May, O. Hamre, and T. Nygard R. Vang, "Evaluation of the dtbird videosystem at the smola wind-power plant: Detection capabilities for capturing near-turbine avian behaviour," *NINA Report 910*, 2012.

[10] S. C. Clough and A. N. Banks, "A 21st century approach to aerial bird and mammal surveys at offshore wind farm sites," *EWEA Conference*, 2011.

[11] D. Lack and G. C. Varley, "Detection of birds by radar," *Nature*, vol. 156, pp. 446, 1945.

[12] W. L. Flock, "Monitoring bird movements by radar," *IEEE spectrum*, pp. 62–66, 1968.

[13] N. Huansheng, C. Weishi, M. Xia, and L. Jing, "Bird-aircraft avoidance radar," *IEEE A&E systems magazine*, 2010.

[14] E. Wiggelinkhuizen, S. Barhorst, L. Rademakers, H. den Boon, and S. Dirksen, "Wt-bird: Bird collision monitoring system for multi-megawatt wind turbines," *EWEC*, 2007.

[15] David Lowe, "Distinctive image features from scaleinvariant keypoints," *International Journal of Computer Vision (IJCV)*, vol. 60, no. 2, pp. 91–110, 2004.

[16] N. Dalal and B. Triggs, "Histograms of oriented gradients for human detection," *Proc. CVPR*, vol. 1, pp. 886–893, 2005.

[17] P. Viola and M. Jones, "Rapid object detection using a boosted cascade of simple features," *Proc. CVPR*, vol. 1, pp. I–511–I–518, 2001.

[18] Y. Freund and R. Schapire, "A decision-theoretic generalization of on-line learing and an application to boosting," *Computational Learning Theory*, vol. 904, pp. 23–37, 1995.

[19] C. Corinna. and V. Vapnik, "Support-vector networks," *Machine Learning*, vol. 20, no. 3, pp. 421–436, 1995.

[20] G. Csurka, C. Dance, L. Fan, J. Willamowski, and C. Bray, "Visual categorization with bags of keypoints," *Workshop on statistical learning in computer vision, European Conference on Computer Vision*, 2004.

[21] P. Felzenszwalb, R. Girshick, D. McAllester, and D. Ramanan, "Object detection with discriminatively trained part-based models," *IEEE TPAMI*, 2010.

[22] M. Everingham, L. Van Gool, C. Williams, J. Winn, and A. Zisserman, "The PASCAL Visual Object Classes Challenge 2012 (VOC2012) Results," *url: http://www.pascal-network.org/challenges/VOC/voc2012/workshop/*.

[23] J. Xiao, J. Hays, K. Ehinger, A. Oliva, , and A. Torralba, "Sun database: Large-scale scene recognition from abbey to zoo," *Proc. CVPR*, 2010.

[24] J. Deng, W. Dong, R. Socher, L. J. Li, K. Li, and L. Fei-Fei, "Imagenet: A large-scale hierarchical image database," *Proc. CVPR*, pp. 248–255, 2009.

[25] O. Russakovsky, J. Deng, H. Su, J. Krause, S. Satheesh, S. Ma, Z. Huang, A. Karpathy, A. Khosla, M. Bernstein, A. C. Berg, and L. Fei-Fei, "Imagenet large scale visual recognition challenge,," *arXiv:1409.0575*, 2014.

[26] A. Krizhevsky, I. Sutskever, and G. Hinton, "Imagenet classification with deep convolutional neural networks," *Anual Conference on Neural Information Processing Systems*, 2012.

[27] Q. Chen, Z. Song, J. Dong, Z. Huang, Y. Hua, and S. Yan, "Contextualizing object detection and classification," *IEEE TPAMI*, 2015.

[28] R. Yoshihashi, R. Kawakami, M. Iida, and T. Naemura, "Construction of a bird image dataset for ecological investigation, ieee international conference on image processing," *IEEE International Conference on Image Processing*, 2015.

[29] P. Massimo, "Background subtraction techniques: a a review," *IEEE International Conference on Systems, Man and Cybernetics*, 2004.

[30] Y. LeCun, L. Bottou, Y. Bengio, and P. Haffner, "Gradient-based learning applied to document recognition," *Proceedings of the IEEE*, 1998.

[31] L. Bottou, "Stochastic gradient descent tricks," *Neural Networks: Tricks of the Trade*, pp. 421–436, 2012.

Reducing LCOE in offshore wind farms through project procurement – The joint challenge of project lifetime - thinking

Salla Lutz (Corresponding author), University of Southern Denmark, Niels Bohrs Vej 9, 6700 Esbjerg, Denmark. E-mail: salla@sam.sdu.dk

Tove Brink, University of Southern Denmark, Niels Bohrs Vej 9, 6700 Esbjerg, Denmark . E-mail: tbr@sam.sdu.dk

Svend Ole Madsen, University of Southern Denmark, Niels Bohrs Vej 9, 6700 Esbjerg, Denmark. E-mail: som@sam.sdu.dk

Abstract

This study focuses on project procurement practices in offshore wind farm projects, and to which extent they can contribute to reduction of LCOE. In general terms, project procurement is a relevant area to consider in an attempt to make offshore energy more competitive due to the vast amount of procurements undertaken in projects. The study is carried out by conducting 39 qualitative inquires in the installation and operation and maintenance phases among 23 different offshore wind industry actors.

The findings pinpoint three major areas of challenges. First, each offshore wind farm is unique in nature and therefore using standard and verified solutions can be challenging. Moreover, in seek for reducing LCOE new technological solutions are imperative resulting in procurement of the solutions that in the given time do not exist yet. Second, project procurement is characterized by practices that to a large extent focus on procurement in the installation rather than stretching the procurement mind set to encompass the whole project lifetime of 20 to 25 years. Third, the companies involved in the project procurement may have different goals.

By focusing on project procurement practises it is possible to reduce LCOE in offshore wind farm. It is necessary for the participating companies to obtain a more holistic overview of the procurement, i.e., adopt a new project paradigm, as the effects on it stretch over the whole lifetime of a wind farm. In relation to this, a better collaboration within the various project procurement teams and with the suppliers becomes pertinent.

Keywords: Project procurement, project lifetime, offshore wind farm, sustainable project, LCOE.

1. Introduction

The motivation for this study arises from the Offshore Wind Denmark –project that focuses on, how development in business practices in offshore wind farms can contribute to the reduction of levelized cost of energy (LCOE). The definition of LCOE varies and is subject to continuous debate. Briefly, LCOE can be seen as the lifetime cost of the wind farm per unit of energy generated. Remarkable cost reductions are needed in order to make electricity produced through this renewable source competitive. In relation to this, it is relevant to look into project procurement practices, as procurement in this specific project-context entails a vast amount of purchases with high technical demands and financial risk. Moreover, the harsh weather combined with the fact that it can be difficult to access the wind farms call for both durable and affordable solutions.

However, procurement as an acknowledged area in relation to projects has only recently been recognized [1,2]. Even though the project management literature deals extensively with such issues as selecting appropriate suppliers for the project task [3,4,5] and managing relationships with project suppliers [6,7,8,9], the more comprehensive insight into project procurement practices in specific project contexts e.g., [10,11] needs to be further unveiled.

Therefore, the aim of this study is to shed light on procurement undertaken in a specific project context by posing the following research question: *What procurement challenges can be identified in the offshore wind farm projects?* To answer this research question, a project network of companies employed in the installation and operation and maintenance phases of offshore wind farms are investigated through a qualitative inquiry. This article aims at contributing to the emerging literature within project procurement management and making companies within offshore wind farm projects more aware of the manifold nature of the project procurement management.

The rest of the article is structured as follows. The next section reviews the literature by combining the streams from the project procurement management and economically sustainable projects. Thereafter, the methodology is presented followed by the research findings and discussion. A conclusion finalises the article.

2. Literature review

Producing energy from renewable sources is a cornerstone for meeting the growing global energy consumption. In this context offshore wind farms provide a possibility to meet the increasing need for energy from a sustainable source. However, offshore wind energy is typically 2-3 times more costly than e.g., onshore wind energy [12]. In the period from 2010 to 2014 LCOE has decreased with 11% primarily due to 'industries early adoption of larger turbines [13].

The industry actors have been aware of the need for renewable offshore wind energy to become more competitive compared with other energy sources for several years. Lately, in the European Wind Energy Association (EWEA) Offshore Conference 2015 in Copenhagen, the requirement was highlighted by emphasizing the urge for collaboration when aiming for reducing LCOE. In this context project procurement practices provide an eminent platform to investigate possibilities to reduce LCOE through a practical, yet relatively important area in relation to the projects. Offshore wind farms are large procurement projects, where demanding technological solutions are procured to a high value.

When studying procurement in the project context, it is relevant to look at it from the project management literature point of view. Project Management Institute acknowledges project procurement as one of the relevant project knowledge areas and defines it as follows: *'Project Procurement Management includes the processes to purchase or acquire the products, services or results needed from outside the project team to perform the work'* [14] *(PMBOK® Guide, 2013)*. The processes are identified as follows:

1. Planning Procurement Management
2. Conducting Procurements
3. Controlling Procurements
4. Closing Procurements

Planning procurements is concerned with, which products or services a project will need to procure from an external source. Conducting procurement the process of obtaining supplier responses, selecting a supplier, and awarding a contract. In relation to this both the selection of the appropriate suppliers ([3,4,5]) and managing relationships with project suppliers ([6,7,8,9]) play a crucial role.

Moreover, the project procurement management's distinctive focus is to control that the supplier delivers what is stated in the contract within the project's time limit. This is emphasized by the following statement: "*This (controlling procurements) is the most time consuming of the procurement processes as far as the project management team is concerned as it covers monitoring the seller's performance against the terms specified in the contract*" [14, p. 29].

In the context of offshore wind farms an interesting issues arises when considering project procurement management. Namely, when does the project end? Obviously, in the specific context there can be identified several project starts and ends, e.g. in terms of development, construction, maintenance and operation and dismantling/repowering phases. However, even though there can be identified different project starts and ends, in this very context it is appropriate to look at the offshore wind farms over the lifetime of 20-25 years. Therefore, it is relevant to look at the project procurement practices by considering the lifetime of wind farms. This is also in line with the concern of reducing the LCOE that takes into account the whole lifetime of an offshore wind farm.

This aspect of lifetime can be further detected in the project management literature in terms of sustainable project management [15, p. 79] that can be defined as follows: *Sustainable Project Management is the planning, monitoring and controlling of project delivery and support processes, with consideration of the environmental, economical and social aspects of the life-cycle of the project's resources, processes, deliverables and effects, aimed at realising benefits for stakeholders, and performed in a transparent, fair and ethical way that includes proactive stakeholder participation.*

The definition above embraces sustainability by employing the environmental, economical and social aspects of it [16] that can be considered as 'three pillars' of sustainability. When considering this from the LCOE point of view, the economical sustainability gains increased relevance and the article will focus on it as the main area of sustainability.

When considering economic sustainability, life cycle costing (LCC) [17] can be adopted. LCC is defined as an economic evaluation process that can assist in deciding between alternative investments by comparing all of the significant differential costs of ownership over a given time period [18]. In the project context it is recognized as a relevant area and is also winning terrain (e.g., [19, 6]). At the same time it seems to be a complex issue to deal with, as stated by Ruparathna and Hewage [10, p. 1]: "*Ad hoc statistics show that modern initiatives such as sustainability, life cycle costing, and standardization are getting integrated with procurement. However, there is no unified view in the construction industry on procurement as a project process*".

In relation to the generic project procurement management that emphasizes the importance of ensuring the supply of the requested items and services within the agreed project timetable and at the same time acknowledging the necessity to consider the project lifetime to ensure the economic sustainability the following proposition can be defined:

Considering project procurement practices over the whole project lifetime will contribute to reduction of LCOE in offshore wind farms.

3. Methodology

For this study, a qualitative research design was applied. The overall unit of analysis was an offshore wind farm network, including also the organizational levels.

Data collection for this study was carried out in two different areas and in two phases. In the first phase the unit of analysis was related to the installation phase of a wind farm project. At this stage six different companies dealing with the development and the installation phase of offshore wind farms were interviewed. In total 19 interviews were conducted during the period of January 2013 – July 2014. Based on these interviews the companies' project procurement activities were identified based on the theoretical pre-understanding based on organizational buying behaviour and project procurement management [20, 21, 22, 23,24, 25, 26, 14].

In the second phase of the data collection, the area of operations and maintenance (O&M) was chosen in order to obtain a more comprehensive understanding of project procurement activities in the offshore wind farm context. This part of the research was based on qualitative semi-structured interviews during the period of June 2014 – March 2015. 20 semi-structured and open-ended interviews were conducted with actors carrying out O&M activities in offshore wind farms, including wind farm owners, wind turbine producers and small and medium sized enterprises (SMEs) operating as suppliers and service providers to O&M. These interviews were in-depth interviews related to the challenges and lessons learned for reduction of LCOE from activities related to different offshore farms. In total, 39 interviews with actors in 23 different companies (see Table 1) were conducted during the period of January 2013 - March 2015. By interviewing actors from the main companies in the offshore wind farm project context, high validity of the results was achieved.

	Company	Number of companies	Number of interviews	Interviewees
Phase I (January 2013 – July 2014)	Project Owner	1	3	Senior Project Manager
	1st Tier Supplier	1	2	Project Manager
	2nd Tier Supplier	2	11	Sales Director, Senior Project Manager, Senior Purchasing Manager, QHSE Manager
	3rd Tier Supplier	2	3	Key Account Manager, Technical Specialist
Phase II (October 2014 – March 2015)	Wind Farm Owner	4	7	Site Manager, Logistics Manager, Development Manager
	Wind Turbine Producer (OEM)	3	3	O&M Manager
	Independent Service Provider	3	3	O&M Manager
	Logistics Supplier	3	3	CEO, Logistics Manager
	Capital Partner	2	2	Partner
	Industry Association	2	2	CEO, Manager
	Total	23	39	

Table 1: The interviews conducted with the companies involved in the offshore wind farm projects.

4. Findings and discussion

This section presents the empirical findings of the research. The proposition suggested was supported, but the conducted interviews revealed three main areas of procurement challenges. These areas were related to the general context of offshore wind farm projects, the scope of project procurement and the actor commitment in the projects. The topics are presented and discussed in turns below.

4.1 The general context of offshore wind farms

'Everything that can break down offshore will break down'. This citation by one of the interviewed companies illustrates that the context of offshore wind farm projects is very challenging. Even though there has been erected a remarkable number of offshore wind farms since 1991, the interviewed companies stressed the complex nature of the projects by focusing on two major areas.

First, every new offshore wind farm is to a large extent considered as unique as also stated by one of the companies in the following way:

'It is difficult to transfer knowledge from one wind farm to another. They are simply too different'.

Moreover, the new projects are placed further away from the coast resulting in wind farms in deeper waters and with harsher weather conditions. These somewhat unknown locations make it difficult to define a suitable specification for the solutions needed. This is likely to create costly challenges, when e.g., components need to be replaced. In relation to this, all the interviewed persons in the O&M phase identified the access to the wind turbines as one of the major challenges.

Second, the necessity to reduce LCOE has a great impact on the technological development of the wind turbines. In the recent years there has been a growing focus on producing turbines with up to 8-10 MwH, but at the same time the actors are aware of that these turbines are solutions under development at the time when they are procured. One of the companies referred to this by saying *'we are selling green bananas'*, while another company stressed the time lag of several years between designing the wind farm and the actual execution of it. In these terms companies are procuring solutions that do not necessarily even exist at the time when the orders are placed.

This challenge is not unknown among the industry actors and there has been a growing interest in creating industry standards and working more intensively with modularized solutions. The fact that the circumstances for erecting offshore wind farms are so challenging makes it difficult to carry out sustainable project procurement, because of many unknown factors and difficult circumstances. However, in relation to this learning from previous projects becomes pertinent, despite the unique nature of the single wind farm. The experiences gained over the years need to be collected and managed in a more systematic way. It seems that this is under development, as also highlighted by one of the companies in the following way:

'We will soon introduce our first wind turbine that has been constructed on the basis of our experiences in operation and maintenance in offshore wind farms'.

All in all, when carrying out project procurement in these unique and difficult circumstances, it is important to aim at balancing between the needed, but also unknown specifications and the learning from the previous projects, including the O&M phase.

4.2 The scope of project procurement

When interviewing the companies in the first phase, it became evident that there was a high focus on finishing the installation phase in time. All in all, the informants labelled offshore wind as *'a bad business case'*, and compared it often with offshore oil and gas industry that was considered as *'a good business case'*. By this impression they emphasized the necessity to finish the installation phase according to the time plan agreed upon, so that the electricity production could start as soon as possible.

Apart from the time factor, the interviewed companies in the first phase were also concerned with selecting suppliers with sufficient experience from offshore and ability to meet the strict quality and time requirements. Moreover, the economical part played also an important role. In relation to this, the typical negotiations prior to the final supplier selection were finalised by a negotiation round termed as *'BAFO – best and final offer'*.

The interviews in the installation phase indicated also clearly that learning from previous projects was mainly concerned with *'lessons learnt'* from the previous installation projects. Not only was this activity relatively new in the studied context, but it was also used to evaluate a project organization's efficiency in carrying out the project. Therefore, it became clear that the project procurement activities undertaken were determined by a strict project timetable. In this context the time factor was understood in terms of finishing the installation phase so that the wind farm was ready to produce electricity. The aspect of the entire lifetime of the wind farms did not seem to occupy the respondents that were involved in the installation phase.

This relatively narrow project scope was confirmed in the second phase of the interviews with actors involved in the O&M practices. One of the interviewees elaborated on the lacking knowledge sharing between installation and O&M phases by expressing the following:

'Previously, suppliers visited me on a regular basis and told about new products and solutions. But they don't do it anymore. Any do you know why? It's because many purchasers have just one main aim: to reduce the price and to get a good deal. This means we get product in worse quality and might have difficulties in finding suppliers willing to deliver'.

To sum up, the findings above indicate that reducing LCOE is challenging and the need for cost reductions is often translated as procuring solutions to meet the project triangle requirements in the installation phase.

4.3 Actor commitment in the projects

The third research finding confirmed the different roles that the companies represent in the offshore wind farm projects. Large wind turbine producers and energy providers have traditionally dominated the different project phases. This is also stated in in in Andersen et al. [27, p. 56] in the following way:

'O&M today is to a great extent an exclusive market, where wind turbine producers and energy providers so far define the regime of the collaboration'.

The different company roles had a crucial impact on the project procurement activities carried out. It seemed that depending on the company type, their goal with the solutions provided were different. For example, there could be identified a large number of subcontractors and independent service providers (ISP) that were keen on developing this business area by providing solutions that took the long lifetime and the diversity of the wind farms into account. For example, an ISP stressed this by stating the following:

'New crew transfer solutions are under development, which will require different approaches on different offshore wind farms'.

On the other hand, there could be also identified companies that had a different view regarding, how durable the solutions in offshore wind farms should be. One of the interviewed companies expressed this by saying the following:

'We make money on that things break down. O&M is an attractive business area for us'.

Obviously, the project context under scrutiny provides many possibilities for the participating companies to consider it as lucrative. However, the industry's challenge to make offshore wind energy more competitive is a joint challenge.

This urge for collaboration to achieve competitiveness in wind energy was also stressed at the European Wind Energy Association (EWEA) Offshore Conference 2015 in Copenhagen; the need to reduce the levelized cost of energy (LCOE) was emphasized. The following headline from EWEA 2015 illustrates the goal:

'The offshore wind power industry has tremendous potential, but to achieve that potential, the industry must collaborate. MHI Vestas Offshore Wind, DONG Energy and Siemens Wind Power—three of the industry's biggest players and our event partners for EWEA OFFSHORE 2015—have initiated a joint declaration outlining the concept of a "United Industry." The goal of the declaration is to inspire the industry to come together around the promise of reducing its cost of energy'.

Along these lines, all the interviewed companies acknowledged the need for collaboration, and one of the interviewee's stated this by saying the following.

'The big actors are in the process of looking into the whole cost structure of the wind farms… They have been in the business for 10-15 years now, and it is necessary to start considering the overall costs. We should not compromise on quality, because it makes it far too expensive to run the parks'.

This need for collaboration is interesting from the procurement point of view. The project procurement management introduced in the literature review focuses to a large extent on a single company's management of procurement in the project. The research findings introduced in this article have also pinpointed the companies' own concerns both regarding the project timetables and the business opportunities available.

These findings can be aligned with the three shifts of sustainable project management [28]. First, mind shift takes responsibility for sustainable development, and second, paradigm shift embraces a holistic perspective on managing change. Finally, scope shift is concerned with managing social, environmental and economic impact. As offshore wind farm projects are complex construction projects with many actors and processes involved, it is difficult to manage all the shifts at once. Therefore, by focusing on the different operational activities, like e.g., project procurement small steps can be taken towards a more sustainable approach.

By focusing on the project procurement challenges disclosed above, the industry has an opportunity to benefit from more sustainable approach to reducing LCOE. Enlarging the project scope from present relatively narrow project management approach, to cover the entire lifetime of the offshore wind farms, can do this. In this context reaping learning form the previous projects gains enhanced importance and the implementing industry standards where ever it is possible becomes of interest. Finally, the industry actors have for a long time acknowledged the importance of increased level of collaboration. However, the finding indicated that this is done in a limited manner and mostly with those actors that mutually know one another.

The findings can be further illustrated by combining the level of collaboration with the scope of project lifetime, as shown in Figure 1. In the narrow scope the focus is on a more traditional project triangle, which in the offshore context can be translated into installation phase. The long-term scope entails the sustainable project management in terms of considering the whole project lifetime. In the present stage a relatively low level of collaboration characterizes the project procurement in the offshore wind farms and the narrow scope contributes to the sub-optimization of the practices in an organizational level. By focusing on enhanced collaborative procurement over the entire lifetime of the wind farms the LCOE can be reduced.

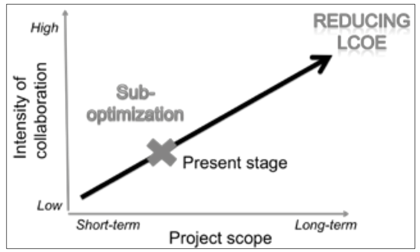

Figure 1: The present stage of project procurement in offshore wind farms

5. Conclusion

This article has shed light on the project procurement practices in the offshore wind farms context. This was done by conducting 39 qualitative inquires in the installation and operation and maintenance phases among 23 different offshore wind industry actors. The conducted interviews revealed three main areas of procurement challenges. These areas were related to the general context of offshore wind farm projects, the scope of project procurement and the actor commitment in the projects.

Project procurement in offshore wind farms is characterized by difficult and unique project circumstances. The findings also disclosed a relatively short-term focus on reducing LCOE when conducting project procurement. The urge for reducing the costs was often translated as the necessity for the suppliers to reduce prices. This may affect the quality of the supplied products negatively and increase the ultimate costs in the operation and maintenance phase.

Moreover, even though offshore wind farms have an expected lifetime of 20-25 years, the procurement practices focus to a great extend on meeting the project requirements in the installation phase. Therefore, an enhanced understanding of the whole project lifetime is needed.

The study reveals the necessity of focusing on project procurement practises as one of the means to reduce LCOE in offshore wind farms. It is necessary for the participating companies to obtain a more holistic overview of the procurement, i.e., adopt a new project paradigm, as the effects on it stretch over the whole lifetime of a wind farm. In relation to this, a better collaboration within the project procurement teams and with the suppliers becomes pertinent.

Acknowledgement: This research article has been financed through Offshore Wind Denmark (OWD) – project. It is a joint initiative between the Danish Wind Industry Association and Offshoreenergy.dk funded by Growth Forum of Southern Denmark and EU Regional Fund. OWD is a four-year project that started in December 2012 and it runs until the end of 2016.

References

[1]Lindstrom, D. L. "*Procurement Project Management Success*". J.Ross Publishing, 2014.

[2] Macbeth, D. K., Williams, T., Humby, S., & James, K. *"Procurement and supply in projects: misunderstood and under-researched"*. 2012.

[3] Martinsuo, M., & Ahola, T. Supplier integration in complex delivery projects: Comparison between different buyer–supplier relationships. *International Journal of Project Management, 2010, 28*(2), 107-116.

[4] Ruuska, I., Ahola, T., Martinsuo, M., & Westerholm, T. "Supplier capabilities in large shipbuilding projects". *International Journal of Project Management,* 2013, *31*(4), 542-553.

[5] Rwelamila, P. D., & Edries, R. "Project Procurement Competence and Knowledge Base of Civil Engineering Consultants: An Empirical Study". [Article]. *Journal of Management in Engineering,* 2007, *23*(4), 182-192.

[6] Eriksson, P. E., & Westerberg, M. "Effects of cooperative procurement procedures on construction project performance: A conceptual framework". *International Journal of Project Management,* 2011, *29*(2), 197-208.

[7] Ojansivu, I., Alajoutsijärvi, K., & Salo, J. "The development of post-project buyer–seller interaction in service-intensive projects". *Industrial Marketing Management,* 2013, *42*(8), 1318-1327.

[8] Olsen, B. E., Haugland, S. A., Karlsen, E., & Johan Husøy, G. "Governance of complex procurements in the oil and gas industry". *Journal of Purchasing and Supply Management,* 2005 *11*(1), 1- 13.

[9] Söderlund, J. "Pluralism in project management: navigating the crossroads of specialization and fragmentation". *International Journal of Management Reviews,* 2011, *13*(2), 153-176.

[10] Ruparathna, R., & Hewage, K. "Review of Contemporary Construction Procurement Practices". *Journal of Management in Engineering,* 2013.

[11] Lutz, S and Ellegaard C. "The Mobilization of Supplier Resources for Complex Projects – a Case Study of Routines in the Offshore Wind Turbine Industry". *Australasian Marketing Journal,* 2015, *23(2), 107-116.*

[12] Open EI, - accessed on September 29, 2015 http://en.openei.org/apps/TCDB/index.php?pMin=2009&pMax=2012&dMin=2009&dMax=2012&gf=h&dol=0&l=n&t=lcoe&ct=bDOE%20–%20US%20Department%20of%20Energy

[13] Offshore Renewable Energy Catapult. "Cost reduction Monitoring Framework". *Summary report to the Offshore Wind Programme Board*. - accessed on September 29, 2015 https://ore.catapult.org.uk/documents/10619/110659/ORE%20Catapult%20report%20to%20the%20OWPB/a8c73f4e-ba84-493c-8562-acc87b0c2d76

[14] Institute, P. M. *A Guide to the Project Management Body of Knowledge (PMBOK® Guide)*: Project Management Institute, Incorporated. 2013.

[15] Silvius, A. J., & Schipper, R. P. "Sustainability in Project Management: A literature review and impact analysis". *Social Business*, *4*(1), 2014, 63-96.

[16] Elkington, J. *Cannibals with Forks: the Triple Bottom Line of 21st Century Business*. 1997.

[17] Woodward, D. G. "Life cycle costing—theory, information acquisition and application". *International Journal of Project Management,* 1997, *15*(6), 335-344.

[18] Johnson, V. S. "Minimizing life cycle cost for subsonic commercial aircraft". *Journal of Aircraft,* 1990, *27*(2), 139-145.

[19] Tysseland, B. E. "Life cycle cost based procurement decisions: a case study of Norwegian defence procurement projects". *International Journal of Project Management,* 2008, *26*(4), 366-375.

[20] Johnston, W. J., & Lewin, J. E. "Organizational buying behavior: toward an integrative framework". *Journal of Business research,* 1996, *35*(1), 1-15.

[21] Johnston, W. J., & Bonoma, T. V. "The Buying Center: Structure and Interaction Patterns". *Journal of Marketing,* 1981, *45*(3), 143-156.

[22] Sheth, J. N. "Organizational buying behavior: past performance and future expectations". *Journal of Business & Industrial Marketing,* 1996, *11*(3/4), 7-24.

[23] Sheth, J. N. "A model of industrial buyer behaviour". *The Journal of Marketing*, *1973,* 50-56.

[24] Webster, F. E., Jr., & Wind, Y. "A General Model for Understanding Organizational Buying Behavior". *Journal of Marketing,* 1972, *36*(2), 12-19.

[25] Bunn, M. D. "Taxonomy of buying decision approaches". *The Journal of Marketing,* 1993, *57*(1), 38-56.

[26] Robinson, P. J., Faris, C. W., & Wind, Y. *Industrial buying and creative marketing*: Allyn & Bacon Boston. 1967

[27] Andersen, P.H, Drejer, I and Gjerding A. N. "Offshore Wind Industry in Denmark".2014, *Report Offshore wind Denmark,* viewed 28. September 2015,http://www.windpower.org/da/fakta_og_analyser/publikationer___rapporter.html

[28] Silvius, A.J.G., Schipper, R., Planko, J., van den Brink, J., & Köhler, A. *Sustainability in Project Management*, Farnham: Gower Publishing, 2012.

Offshore Wind Turbine Sub-Assembly Failure Rates Through Time

James Carroll
University of Strathclyde
j.carroll@strath.ac.uk

Alasdair McDonald
University of Strathclyde
alasdair.mcdonald@strath.ac.uk

Oswaldo Barrera Martin
University of Strathclyde
seb12185@uni.strath.ac.uk

David McMillan
University of Strathclyde
d.mcmillan@strath.ac.uk

Roozbeh Bakhshi
University of Maryland
roozbeh@calce.umd.edu

Abstract

O&M costs can make up to 30% of the lifetime CoE of an offshore wind farm [1]. As a means of reducing this cost operators and O&M providers need a greater understanding of what is driving that O&M cost. Failure rates of wind turbines and their components are a key driver of O&M costs. Past papers have modelled O&M costs assuming a fixed average failure rate for wind turbine subsystems [2]. This work aims to determine if it is accurate to assume a fixed failure rate or if a failure rate distribution through time can be provided to allow for more accurate O&M cost modelling and in turn CoE modelling.

This paper shows the results of an analysis of offshore wind turbine annual failure rates over an 8 year period. The analysis is based on around 350 modern multi MW offshore turbines located in 5-10 offshore wind farms throughout Europe. The literature review for this paper indicated that a constant average failure rate should only be used if the shape parameter of the failure distribution is around 1. However results from the failure rate analysis in this paper have shown that in many cases a constant failure rate is not correct for O&M Modelling.

Keyword

Failure rate, failure rate distribution, wind turbine subassembly, offshore wind turbine

1. Introduction

a. General

Traditional wind farm O&M modelling may be resulting in inaccurate O&M cost forecasts due to the use of incorrect failure rates as model inputs. Past papers have shown that when failure rates are not at a steady state average failure rates should not be used in modelling [3]. This paper aims to answer the question "Can a failure rate time characteristic be identified for offshore wind turbine components based on an offshore wind turbine population of approximately 350 wind turbines?"

The analysis detailed in this paper builds on earlier work from [4] in which average failure rates are provided for the population mentioned above. This paper builds on that work by providing failure rates for each subsystem each year allowing conclusions to be drawn on the failure behaviour of the different wind turbine subsystems with time. The paper gives an overview of all subsystems before focusing on the following sub-systems or groups:

- Gearbox
- Generator
- Converter
- Rest of Turbine

These four are the focus of this analysis because this was the grouping used in past failure rate analyses and O&M modelling [2].

Failure rate analyses have been carried out in the past [5-11]. While [5] and [9] detail failure rates vs. time some of the past papers do not. A literature review has shown that this paper is novel due to the fact that such an analysis has never before been published for a population of modern multi MW offshore wind turbines. References [5-11] are based on a population of smaller older onshore wind turbines. This work contributes to the wind turbine O&M knowledge by providing operators and maintenance providers with an overview of how wind turbines and their sub-assemblies fail in relation to time. This can be used in O&M modelling or to assist with O&M decision making.

b. Reliability Theory

Wind turbine and wind turbine component failure rates are a key input to any O&M modelling. Past O&M modelling carried out by the authors of this paper and O&M modelling encountered in the literature review has used constant failure rates. However, reference [3] has stated that

1. "The assumption of constant failures and the adoption of average failure intensity is only valid in the case of no reliability growth (positive or negative) (Shape parameter equal to 1)"

2. "When positive reliability growth occurs the final failure intensity must be chosen as the expected value. (Shape parameter less than 1)"

3. "On the other hand when negative growth occurs the initial failure intensity should be used" (Shape parameter greater than 1)

Figure 1 shows the failure distributions with the shape parameters mentioned above.

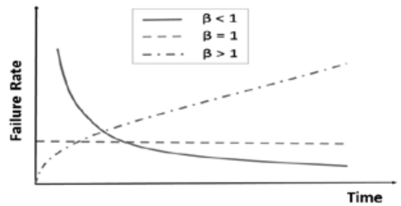

Figure 1: Shape Parameters

It is clear from the graph that any shape parameter below 1 demonstrates a reliability improvement with time, above 1 shows a decline in reliability with time and a shape parameter of 1 shows a steady failure rate. These shape parameters are evident in the bathtub curve. The bathtub curve is shown in Figure 2. The first section of the bathtub curve shows rapid reliability improvements with a shape parameter of less than 1, this represents early failures in a component. The 2nd section has a constant failure rate with a shape parameter of 1 and represents intrinsic failures. The third section shows reliability decline with an increase in failure rate and a shape parameter of greater than 1. This is the component deterioration stage. The "early failures" and "deterioration" section are a special case non-homogenous Poisson process and can be represented by the power law process (PLP) [12] shown by the following equation:

$$\lambda(t) = \rho\,\beta t^{\beta-1} \quad (1)$$

where:

$\lambda(t)$ = Failure rate as a function of time

ρ = Scale Parameter

β = Shape Parameter

t = time

As mentioned, it is β that determines which stage of the bathtub curve the failure trend follows. If beta is one in this equation the process becomes a Homogenous Poisson Process (HPP) meaning that the failures are random and can be represented with an average failure rate [12].

A number of steps for determining if a set of failure data are a HPP or PLP have been outlined in [3]. These steps can be seen in Section 3b. This paper will follow that process to determine whether the failure rates for the gearbox, generator, converter and "rest of turbine" are PLP with improving reliability, PLP with deteriorating reliability or HPP.

The bathtub curve in Figure 2 is for a repairable system such as a wind turbine. A repairable system can usually be returned to operation after a failure by some repair process other than complete system replacement.

Reference [3] states that in a repairable system repairs can be defined as:

- Minimal Repair (The failed unit is brought back to the condition it was in immediately before failure)
- Perfect Repair (The failed unit is brought back to the condition it was in as new and TBF are identically distributed)
- Renewal model (acts like a non-repairable system statistically).

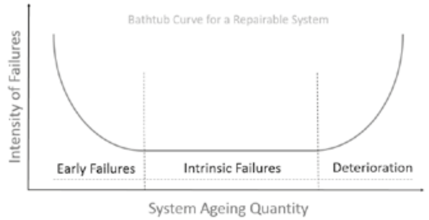

Figure 2: Bathtub curve for a repairable system

Minimal repair is often assumed with wind turbines, returning the wind turbine back to the condition it was in before failure [3]. The bathtub curve in Figure 2 should not be confused with the bathtub curve of a non-repairable component. For a non-repairable system the curve shape is the same but the y-axis displays the hazard function instead of the intensity of failures and the 3 stages are called burn in, useful life and wear out rather than early failures, intrinsic failures and deterioration.

c. Average failure rates and O&M Modelling

Figure 3 from [4] shows the average failure rates which were obtained from the same population analysed in this paper. Figure 4 from [2] then shows modelled O&M costs for different drive train types based on these results. The O&M results shown in Figure 4 are based on the assumption that the failure rates in figure 3 are constant, i.e. $\beta = 1$ and are considered to be a HPP. Figure 1 shows a curve of failure rates with time where $\beta = 1$.

The majority of wind turbine components are designed to last the 20 year design life of the wind turbine. As the oldest turbines in the population analysed for this paper are no more than half way through their design life the authors would not expect to be observing wear out failures at this stage. However early life failures from the first section of the bathtub curve may be observed. If this is the case the assumption that all failure rates are random used in the modelling in [2] may prove to be incorrect. It is with this possibility in mind that the failure rate vs time for the four components/groups mentioned in section 1 were analysed to determine if their shape parameters demonstrate a trend.

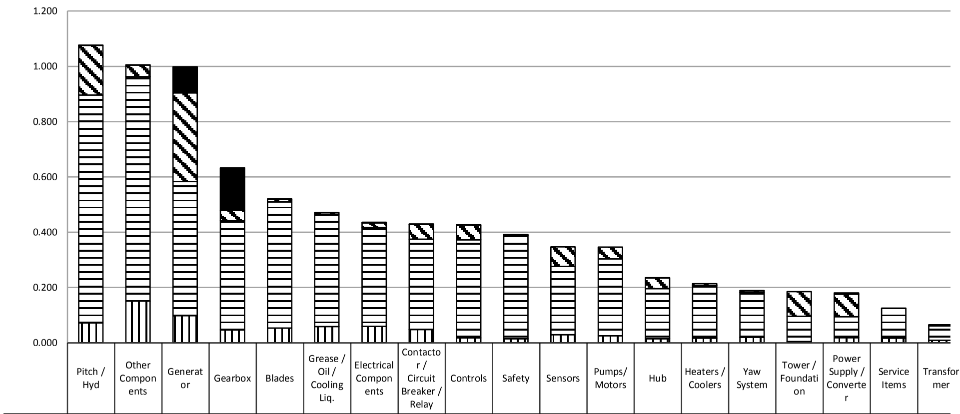

	Pitch / Hyd	Other Components	Generator	Gearbox	Blades	Grease / Oil / Cooling Liq.	Electrical Components	Contactor / Circuit Breaker / Relay	Controls	Safety	Sensors	Pumps/ Motors	Hub	Heaters / Coolers	Yaw System	Tower / Foundation	Power Supply / Converter	Service Items	Transformer
Replacement	0.001	0.001	0.095	0.154	0.001	0.000	0.002	0.002	0.001	0.000	0.000	0.000	0.001	0.000	0.001	0.000	0.005	0.000	0.001
Repair	0.179	0.042	0.321	0.038	0.010	0.006	0.016	0.054	0.054	0.004	0.070	0.043	0.038	0.007	0.006	0.089	0.081	0.001	0.003
Repair	0.824	0.812	0.485	0.395	0.456	0.407	0.358	0.326	0.355	0.373	0.247	0.278	0.182	0.190	0.162	0.092	0.076	0.108	0.052
st Data	0.072	0.150	0.098	0.046	0.053	0.058	0.059	0.048	0.018	0.015	0.029	0.025	0.014	0.016	0.020	0.004	0.018	0.016	0.009

Figure 3: Average failure rates for population [4]

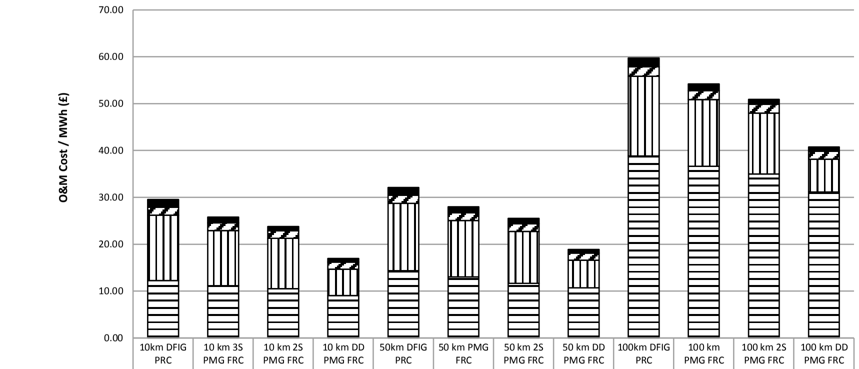

	10km DFIG PRC	10 km 3S PMG FRC	10 km 2S PMG FRC	10 km DD PMG FRC	50km DFIG PRC	50 km PMG FRC	50 km 2S PMG FRC	50 km DD PMG FRC	100km DFIG PRC	100 km PMG FRC	100 km 2S PMG FRC	100 km DD PMG FRC
Repair Costs (£)	1.61	1.26	0.94	0.79	1.65	1.26	1.15	0.80	1.88	1.46	1.08	0.89
Staff Costs (£)	1.71	1.63	1.6	1.49	1.74	1.65	1.65	1.5	2.01	1.9	1.85	1.71
Transport Costs (£)	13.95	11.75	10.73	5.66	14.37	12.05	11.06	5.88	17.03	14.24	13	7.02
Lost Production Costs (£)	12.26	11.16	10.53	9.04	14.37	13.03	11.68	10.72	38.81	36.63	35	31.13

Figure 4: Modelled O&M costs based on Average failure rates [2]

2. Methodology

1. Offshore reliability data was obtained from industrial partners for the 5-10 wind farms throughout Europe

2. Data was processed (cleaned and organised) to ensure all failures from the list of work orders were captured and no scheduled operations were wrongly captured as failures.

3. Data was analysed to determine overall failure rates and modes for each turbine.

4. Data was analysed to determine overall failure rates per cost category for each subassembly of the turbine.

5. Data was analysed to determine overall failure rates for each turbine and subassembly vs. Time.

6. Failure intensity functions were created and tested for goodness of fit and HPP or PLP properties.

7. Conclusions were drawn on correct failure rates to be used in O&M modelling.

The population obtained from step 1 is outlined in the following paragraphs.

The population analysed in this paper builds up to around 350 turbines over an eight year period. These turbines come from between 5-10 wind farms throughout Europe. The years of installation for the population are shown in Figure 5. It can be seen that 68% of the population analysed is between three and five years old and 32% is greater than 5 years old. In total this population provides 1768 turbine years or around 15.5 million hours of turbine operation.

All turbines in this population have the same rated power and rotor size. The rated power is between two and four MWs and the rotor diameter is between 80 and 120 metres. Exact population details cannot be provided for confidentiality reasons.

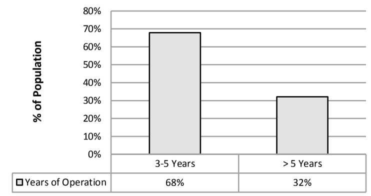

Figure 5: Population Operational Years

3. Results

As a means of determining whether the failures observed in the population described in Section 2 occurred randomly or displayed some form of early failure or reliability deterioration trend the annual failure rate was plotted against the operational year for the gearbox, generator, converter and for a grouping called rest of turbine. This section also shows a similar graph to Figure 3, except instead of showing overall average failure rates for each sub-system a failure rate was provided for each of the 8 operational years for each subsystem.

a. Average failure rate vs. time

Figure 6 shows each of the failure sub-systems before the “rest of turbine grouping” is carried out. The rest of turbine grouping combines all failure components in Figure 6 except for the generator, gearbox and converter. Closer examination of Figure 6 shows that the average failure rate across all years of a component is often different to the average failure rate for each sub-system shown in Figure 3. There are two reasons for this: (i) The population size in each year is different and (ii) there is a small sub-population of turbines that have failures where the year of operation is not known. These turbines and failures are excluded from the analysis in Figure 6 but not from the analysis in Figure 3.

b. Failure Trends

To determine whether failure trends for the gearbox, generator, converter and rest of turbine group follow a PLP or HPP a number of steps had to be taken. Firstly the average failure rate for each operational year was plotted and a trend line was fitted. The shape parameter was estimated using the least squares estimation method. The trend line and shape parameter then had to be tested for a 95% goodness of fit and a final test on whether the trend was following the PLP or HPP was carried out.

The same process as the one carried out in [3] was used to test the goodness of fit of the trend line in which the following equation, equation (2), was used to calculate a chi square value which could then be tested off standard probability tables to determine if the null Hypothesis that “the data was governed by the assumed distribution” could be accepted or rejected.

$$\boldsymbol{X}^2 = \sum \frac{(observed - expected)^2}{expected} \quad (2)$$

A similar test based on equation (3) is carried out to determine whether the null hypothesis that “The failure trend follows the HPP” can be accepted or rejected.

$$\boldsymbol{X}^2 = \sum_{i=0}^{8} \frac{(O_i - E_i)^2}{E_i} \quad (3)$$

where:

O_i =Observed failures in time period *i*
E_i = Expected failures in time period *i*

Expected failure rates in time period *i* is given by the number of turbines in time period *i* × mean failure rate.

When the results of equations (2) and (3) are compared to the standard tables it can be determined if the goodness of fit is acceptable. As detailed in [3] once the goodness of fit is accepted, Table 1 [3] can be used to determine if the failure trend is deteriorating, improving or remaining steady.

H_0 = HPP	Shape Parameter	Result
Rejected	$\beta < 1$	Early Failures
Rejected	$\beta > 1$	Deterioration
Accepted	0.79 < β < 1.2	Constant Failure

Table 1: Interpretation of HPP and PLP [3]

c. Gearbox

The failure distribution for the gearbox can be seen in Figure 7. The gearbox passes the goodness of fit analysis. The trend line has a shape parameter of 0.869. The HPP hypothesis is rejected. Based on Table 1, all of the above means the gearbox displays slight early failure characteristics. This is not the case with the gearbox data examined in [3] in which early failures are not observed. A reason for the difference may be the learnings from the move from onshore to offshore.

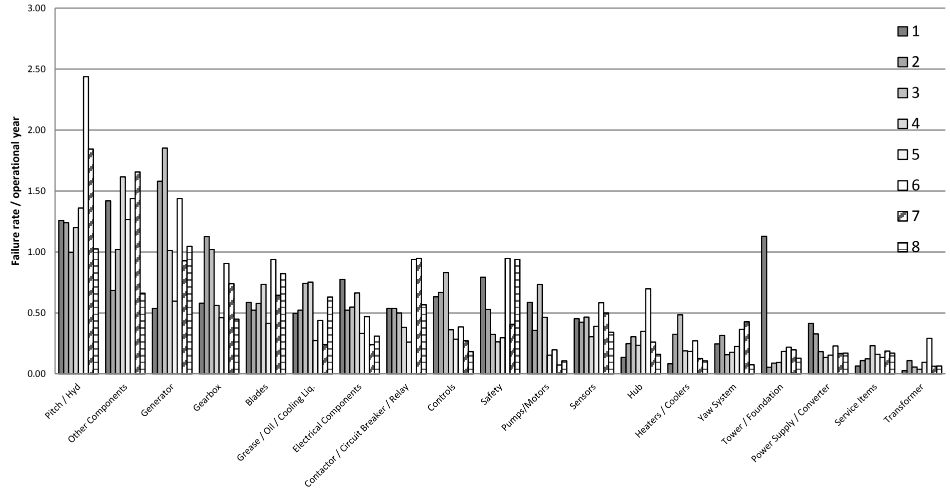

Figure 6: Failure rate per turbine per year of operation for each subassembly

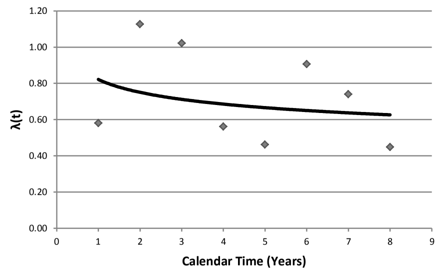

Figure 7: Gearbox failure rate with time . R^2 = 0.066

Figure 8 shows what the failure rate per operational year consists of. It can be seen that the gearbox shows mostly minor repair but a high percentage of major issues in comparison to the rest of turbine group seen in Figure 14. These major issues are seen in the earlier years of operation and reduce in the later years.

For the purpose of this study a minor repair is any repair that the cost of materials for repair was less than €1000, a major repair was between €1,000 and €10,000 and a major replacement was over €10,000.

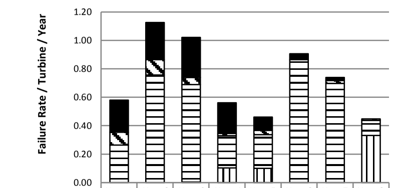

	Year 1	Year 2	Year 3	Year 4	Year 5	Year 6	Year 7	Year 8
Major Replacement	0.23	0.26	0.28	0.21	0.09	0.04	0.02	0.00
Major Repair	0.09	0.11	0.05	0.02	0.03	0.00	0.02	0.01
Minor Repair	0.26	0.76	0.69	0.23	0.24	0.86	0.70	0.11
No Cost Data	0.00	0.00	0.00	0.10	0.10	0.00	0.00	0.33

Figure 8: Gearbox failure categories

c. Generator

The failure distribution for the generator can be seen in Figure 9. The generator passes the goodness of fit analysis. The trend line has a shape parameter of 1.118. The HPP hypothesis is rejected. Based on Table 1 all of the above mean the generator displays slight failure deterioration characteristics. This is not the case with the onshore generators data examined in [3] where the trend can often be represented by a HPP. A reason for the difference may be the harsher environment offshore leading to a slightly increasing failure rate with time. Early failures from the move to offshore may not have been seen because the type of generator used in this analysed population is a very mature and understood generator for the manufacturer.

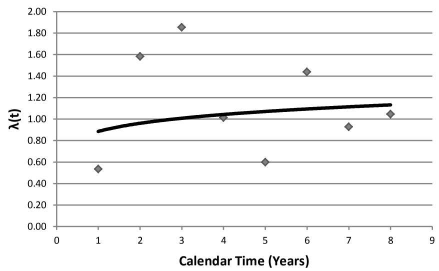

Figure 9: Generator failure rate with time. R^2 = 0.035

Figure 10 shows what the failure rate per operational year consists of. It can be seen that the generator experiences less minor issues than the rest of turbine group and a higher percentage of major repairs than the gearbox.

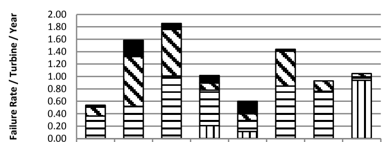

	Year 1	Year 2	Year 3	Year 4	Year 5	Year 6	Year 7	Year 8
Major Replacement	0.03	0.26	0.10	0.12	0.20	0.03	0.00	0.00
Major Repair	0.14	0.80	0.75	0.12	0.11	0.56	0.17	0.05
Minor Repair	0.36	0.52	1.00	0.57	0.18	0.84	0.76	0.05
No Cost Data	0.00	0.00	0.00	0.21	0.11	0.00	0.00	0.94

Figure 10: Generator failure categories

d. Converter

The failure distribution for the converter can be seen in Figure 11. The converter passes the goodness of fit analysis. The trend line has a shape parameter of 0.561. The HPP hypothesis is rejected. Based on Table 1 all of the above means the converter displays early failure characteristics. This is also the case in [3] and [13] with onshore power converters.

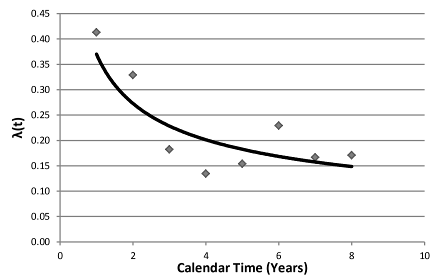

Figure 11: Converter failure rate with time. R^2 = 0.622

Figure 12 shows what the failure rate per operational year consists of. It can be seen that the converter shows a high percentage of major repair in the earlier years of operation. As mentioned these major repairs cost between €1,000 and €10,000 for material repairs. This is consistent with the cost of replacement IGBT modules. Similar converter repair costs for IGBT modules can be seen in [13] for onshore turbines.

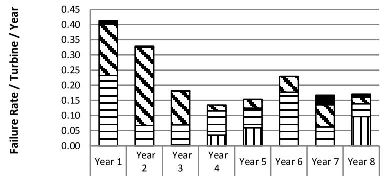

	Year 1	Year 2	Year 3	Year 4	Year 5	Year 6	Year 7	Year 8
Major Replacement	0.01	0.00	0.00	0.00	0.00	0.00	0.03	0.01
Major Repair	0.17	0.26	0.11	0.02	0.03	0.05	0.07	0.02
Minor Repair	0.23	0.07	0.07	0.08	0.07	0.18	0.06	0.04
No Cost Data	0.00	0.00	0.00	0.04	0.06	0.00	0.00	0.10

Figure 12: Converter failure categories

d. Rest of Turbine

The failure distribution for the "Rest of Turbine" group can be seen in Figure 13. The "Rest of Turbine" group passes the goodness of fit analysis. The trend line has a shape parameter of 0.944. This suggests that the trend line is close to being represented by HPP. However, the HPP hypothesis is rejected even though the shape parameter is close to 1. As the HPP hypothesis is rejected and based on table 1 the "Rest of Turbine" group displays very slight early failure characteristics. Previous work [3] has shown that when turbine components and sub systems are grouped the combination of different component types produce a random failure rate over time. Even if it is the case that one of the components in the overall group shows a certain trend this trend becomes random when grouped with a number of different components. However the slight early failure trend observed in this data may be explained by the move offshore.

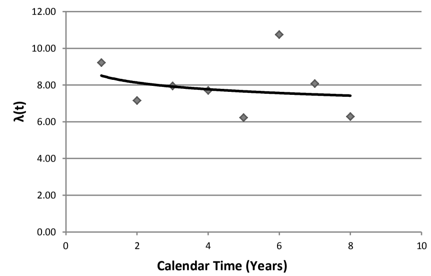

Figure 13: "Rest of Turbine" failure rate with time. R^2 = 0.063

Figure 14 shows what the failure rate per operational year consists of. It can be seen that the "Rest of turbine" group consists mostly of minor repairs. These are similar findings to [4], which would be expected as both analyses were carried out on the same population for offshore wind turbines.

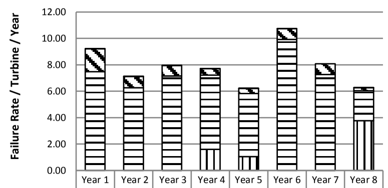

	Year 1	Year 2	Year 3	Year 4	Year 5	Year 6	Year 7	Year 8
Major Replacement	0.01	0.03	0.00	0.01	0.01	0.02	0.00	0.02
Major Repair	1.73	0.85	0.79	0.47	0.39	0.81	0.81	0.23
Minor Repair	7.48	6.26	7.13	5.62	4.76	9.92	7.24	2.25
No Cost Data	0.00	0.00	0.03	1.61	1.06	0.00	0.03	3.78

Figure 14: "Rest of Turbine" failure categories

Discussion and Conclusion

The results from this paper have shown that all four sub-system/groups analysed display either early failure or reliability deterioration trends. Even though shape parameters were sometimes between 0.79 and 1.2, none of the four subsystem/groups could be represented by the HPP, which past O&M modelling has assumed. Based on these results and findings from other papers that suggest average failure rates should not be used when failure trends are observed it can be concluded that past O&M cost modelling may be improved by observing failure rate trends prior to selecting the failure rate to represent the turbine subsystem.

The gearbox displayed a slight early failure trend suggesting that rather than taking the average failure rate over the 8 year period the failure rate from year 8 should be taken as an input for O&M modelling. The same can be said for the converter and "Rest of turbine failure rates". The generator displayed failure deterioration suggesting the failure rates from the first year of operation should be used as an input for O&M modelling.

In the case of this population, even though all 4 subsystems/groups passed the hypothesis test for goodness of fit, a low R^2 value and a large amount of variance from the trend lines can be seen in most graphs. The shape parameters were also in the range that can represent HPP. It is for these reasons that it is hard to have confidence that values taken from the failure trends would be significantly more representative than average failures. An investigation into this is an area of further work for the authors.

Even though the turbine population presented in this paper is produced by a single manufacturer and is essentially the same turbine type (rating, rotor size), there remains some variance in sub-populations and these have not been analysed. For example, manufacturers often introduce upgrades from one turbine version to the next and this may influence failure rates and trends. This analysis has been carried out based on the year of operation of each turbine and not the calendar year. Consequently, factors tied to a calendar year are hidden. This data is obtained from several different wind farms, each of which experiences different site conditions and maintenance regimes.

The analysis in this paper ignores these variations in the population and so the conclusions should be interpreted with this in mind.

Acknowledgements

The authors would like to acknowledge their industrial partners that provided the data to make this paper possible.

References

[1] Dinwoodie I, McMillan D, Revie M, Lazakis I, Dalgic Y. Development of a Combined Operational and Strategic Decision Support Model for Offshore Wind. in Proc. DeepWind Conf., Trondheim, Norway, Jan. 24–25, 2013

[2] Carroll J, McDonald A, Dinwoodie I, McMillan D, Revie M, Lazakis I. A Comparison of the Availability and Operation & Maintenance Costs of Offshore Wind Turbines with Different Drive Train Configurations. Submitted to Wiley Wind Energy Journal September 2015

[3] Spinato F. The Reliability of Wind Turbines. PhD Thesis. Durham University. December 2008.

[4] Carroll J. McDonald A. McMillan D. Failure Rate, Repair Time and Unscheduled O&M Cost Analysis of Offshore Wind Turbines. Wiley Wind Energy Journal, July 2015.

[5] Spinato F, Tavner P, van Bussel GJW, Koutoulakos E. Reliability of wind turbine subassemblies. IET Renew Power Generation, Vol 3, Iss 4, 2009.

[6] Ribrant J, Bertling L. Survey of failures in wind power systems with focus on Swedish wind power plants during 1997-2005. IEEE Trans. on Energy Conversion, vol. 22, pp. 167 – 173, March 2007.

[7] Wilkinson M, Harman K, Spinato F, Hendriks B, Van Delft T. Measuring Wind Turbine Reliability - Results of the Reliawind Project. in Proc. Eur. Wind Energy Conf. Brussels 2011.

[8] Hahn B, Durstewitz M, Rohrig K. Reliability of Wind Turbines. Experiences of 15 years with 1,500 WTs. ISET, Available: file:///D:/Users/fdb12199/Downloads/0deec517c00%20(1).pdf

[9] Echavarria E, Hahn B, van Bussel G,. Tomiyama T. Reliability of Wind Turbine Technology Through Time. Journal of Solar Energy Engineering, vol. 130, pp. 1-8, August 2008.

[10] Tavner P, Xiang J,Spinato F, Reliability Analysis for Wind Turbines. Wind Energy, vol 10, pp. 1-18, December 1998.

[11] K Alewine. Wind Turbine Generator Failure modes analysis and occurance. NREL, 2011.

[12] Ansell J. Phillips M. Pratical Methods for Reliability Data Analysis. Oxford Science Publication 1994

[13] Carroll J, McDonald A, McMillan D. Reliability Comparison of Wind Turbines with DFIG and PMG Drive Trains. IEEE Trans. on Energy Conversion. 2015

Towards reliable power converters for wind turbines: Field-data based identification of weak points and cost drivers

Katharina Fischer

Fraunhofer Institute for Wind Energy and Energy System Technology IWES,
Appelstr. 9a, 30167 Hannover, Germany
Katharina.Fischer@iwes.fraunhofer.de

Jan Wenske

Fraunhofer Institute for Wind Energy and Energy System Technology IWES,
Am Seedeich 45, 27572 Bremerhaven, Germany
Jan.Wenske@iwes.fraunhofer.de

Abstract

The power-converter system in variable-speed wind turbines is a frequent source of failure, which causes considerable maintenance cost and downtime. As a basis for the development of effective measures for enhancing the converter reliability, it is crucial to understand the prevailing causes and mechanisms leading to these failures within the wind-power application. This is the subject of a research project carried out in a large consortium including wind-turbine and component manufacturers, operators and maintenance service providers, Fraunhofer institutes and academia. This paper presents first results of the statistical analysis of field-failure and cost data collected during 2003-2014, which covers 1269 operating years of onshore wind turbines with doubly-fed induction generator (DFIG) and electrically-excited synchronous generators (EESG). Stepping from subsystem to component-level reliability analysis, the investigation aims at identifying the weak points and main cost drivers within the converter system. For both DFIG- and EESG-based wind turbines, the phase-module category, which includes the power-electronic components, their driver boards as well as DC-link capacitors and busbars, stands out with respect to failure rates, related downtime and repair cost. A comparison of repair cost and revenue losses resulting from downtime shows that the economic impact of converter failure is dominated by the repair cost. Based on the analysed dataset, the reliability of the fully-rated power converters in the turbines with EESG is found to be higher than that of the partially-rated converters in the turbines with DFIG.

Keywords

wind turbine, power electronics, converter, reliability, failure, root-cause analysis

1. Introduction

Numerous studies have identified the power converter as a frequent source of failure in variable-speed wind turbines (cf. [1-5]). This is in line with the experiences made by wind-turbine operators worldwide, who state the limited converter reliability to be a considerable driver of maintenance cost and downtime. However, the development of remedial measures is hindered by the fact that little is known about the causes and mechanisms underlying the converter failures.

Comprehensive research has been carried out on the thermal- and power-cycling induced failure mechanisms known to be life-limiting in IGBT-based converters in other applications (see e.g.[6-13]): the lift-off or fatigue-damage of the bond wires, and the fatigue of die-attach or baseplate solder joints. However, the results of a first study on the root causes of converter failure [14][15] suggest that those mechanisms play a minor role in wind turbines and emphasise the importance of a field-experience based approach to the problem.

On this background, a research cluster for enhancing power-converter reliability in wind turbines has been established in Germany [16]. In this cluster, numerous companies join forces with Fraunhofer institutes and academia in order to move from suspected failure causes to clear evidence and, in the next step, to effective countermeasures. The project consortium includes a wind-turbine OEM and converter manufacturers, converter-component suppliers, wind-turbine operators, maintenance service providers, an insurer and companies specialised in measuring and monitoring technology. Among the key tasks of the project is an extensive root-cause analysis, which is based on comprehensive field-data analysis, directed measurement campaigns, post-mortem analysis of failed converter components as well as a detailed modelling of the dynamic interaction of mechanical and electrical drivetrain components. In addition, the research subjects of the cluster include condition-monitoring approaches for the power converter and fault-tolerant generator-converter systems, with the overall objective to enhance the reliability and maximise the availability of power converters in wind turbines.

This paper presents first results of the statistical field-data analysis carried out within the research cluster described above. The objective of this analysis is to identify the predominantly failing components within the power-converter system as well as the main cost drivers, including both the repair cost and the revenue losses resulting from converter unavailability. In this way, the work aims to provide a basis for directing subsequent research to the most critical components of the converter system.

The paper is structured in the following way: Section 2 describes the dataset and the wind-turbine fleets from which the data was collected. The procedure of analysis and the key equations are provided in Section 3. The results obtained for the wind-turbine fleets with doubly-fed induction generators (DFIG) and electrically-excited synchronous generator (EESG), respectively, are presented in Section 4. Finally, the key conclusions and an outlook to future work are provided in Section 5.

2. Data basis

The analysis is based on a dataset of maintenance and operating data that includes repair-cost and downtime information for each failure event. The results presented in the following are based on two different fleets: The first one consists of 103 wind turbines equipped with DFIG, which are located in 11 onshore wind parks in Germany. This dataset spans in total 925 years of wind-turbine operation during 2003-2014. The partially-rated converters in the turbines with DFIG are IGBT-based low-voltage converters (two-level back-to-back voltage source converters). The fleet consists of turbines of three manufacturers, with the commissioning dates of the turbines ranging from 1999 to 2007 and turbine rated capacities in the range of 1500 kW to 2300 kW. The second fleet consists of 41 turbines with rated capacities of 500 kW to 1800 kW located in 4 onshore wind parks in Germany, with turbine commissioning dates in the period 1997-2002. The EESG dataset covers 344 years of operation during the years 2003-2014.

3. Method of analysis

In contrast to the preceding study described in [14][15], the present work takes the complete converter system into consideration. Based on failure descriptions and information on used spare parts contained in the maintenance records, the failures of the converter are classified according to the following categories:

- phase module (including IGBT modules and corresponding driver boards, DC-link capacitors, busbars)
- converter control board
- crowbar (DFIG only)
- cooling system
- semiconductor fuse
- main circuit breaker
- grid-coupling contactor
- other converter failures

Note that within the scope of this analysis, only faults requiring on-site repair and the consumption of material or spare parts are considered as failures (i.e. faults remedied e.g. by a remote reset or by cleaning components are not included). Because phase modules are typically replaced as complete units, the data does not allow a further localisation of the defect inside the phase modules.

The average failure rate of each converter-component category is calculated according to

$$f = \frac{\sum_{i=1}^{I} N_i}{\sum_{i=1}^{I} X_i \cdot T_i} \tag{1}$$

with N_i denoting the number of failures of the component in the time interval i, X_i describing the number of wind turbines reporting to the database in time interval i, and T_i being the duration of the time interval i. All failure rates are given in failures per wind turbine and year. Note that calendar time is used for the calculation, i.e. turbine downtime is not excluded.

Correspondingly, the average repair cost c_{rep} and average downtime t_{down} arising from each component category per turbine and year are calculated using

$$c_{rep} = \frac{\sum_{i=1}^{I} C_{rep,i}}{\sum_{i=1}^{I} X_i \cdot T_i} \tag{2}$$

and

$$t_{down} = \frac{\sum_{i=1}^{I} t_{down,i}}{\sum_{i=1}^{I} X_i \cdot T_i}. \tag{3}$$

4. Results and discussion

Figure 1 shows the average failure rates in the different converter-component categories as well as the overall rate of converter failure events. With an average number of 0.21 failures per turbine and year in DFIG and 0.08 in EESG turbines, the phase modules have the highest failure rate among the considered component categories. On average, there were 0.53 converter failure events per year on the DFIG turbines and 0.15 in the EESG fleet, respectively. Due to the fact that in case of approximately a fifth of the failure events, components from two or three categories were replaced to restore the functionality, the sum of the component failure rates is higher than the overall converter failure rate.

Figure 2 illustrates the percentage distribution of failed components over the different categories. Besides the phase modules, the semiconductor fuses connected to these, the main circuit breaker and the converter control board constitute the largest portions in the DFIG fleet. In case of the EESG turbines, the converter control board, the semiconductor fuse and the cooling system are the components being most often affected by failures besides the power-module category.

Figure 3 shows the distribution of repair cost over the component categories. It reveals that the converter repair cost is clearly dominated by the phase-module category in both DFIG and EESG turbines. Note that some uncertainty arises from the abovementioned failure of several components in one incident, as in those cases the repair cost is a bulk sum and the exact shares for repair of the different defect components are unknown. In these cases, the repair cost corresponding to the respective failure events is estimated based on the following assumptions:

If multiple component categories are affected in the failure event but the phase module remained intact, the repair cost is equally distributed over the concerned categories. In case there are multiple affected categories and these include a phase module, the cost is divided at the ratio of 90:10 (or 80:10:10 in case of three affected categories), as the cost for replacing a phase module by far exceeds the cost of replacing other components.

A similar procedure is used to estimate the downtime caused by failures in each category (see the downtime distribution in Figure 4). However, due to the fact that no systematic difference in the downtimes related to phase-

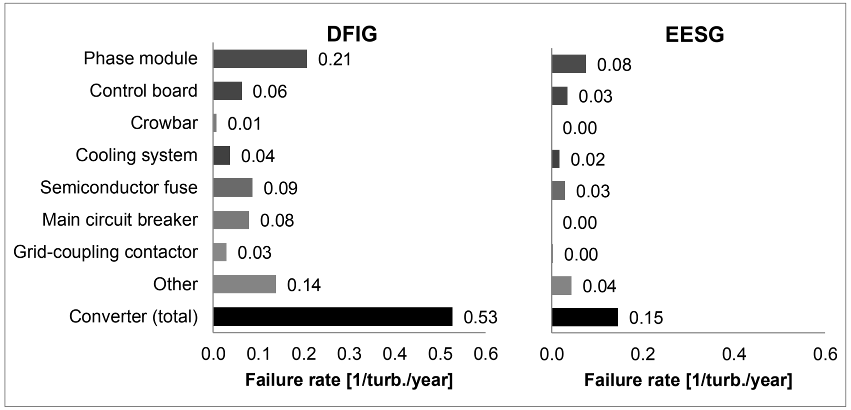

Fig. 1: Average failure rates of the converter components

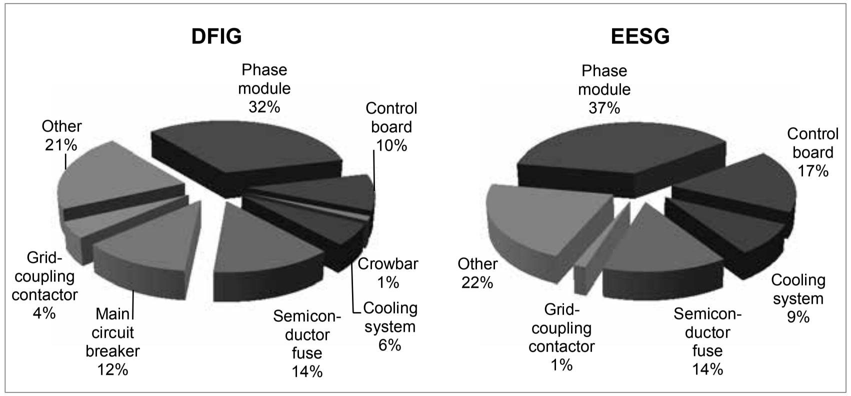

Fig.2: Distribution of failed converter components over categories

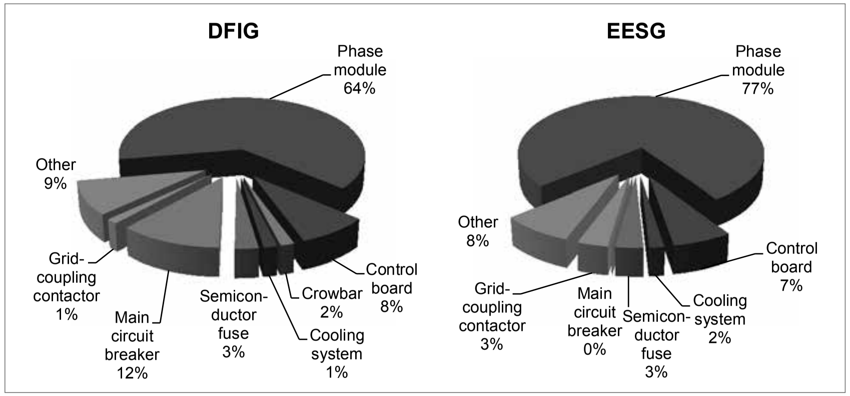

Fig.3: Distribution of converter repair cost over component categories

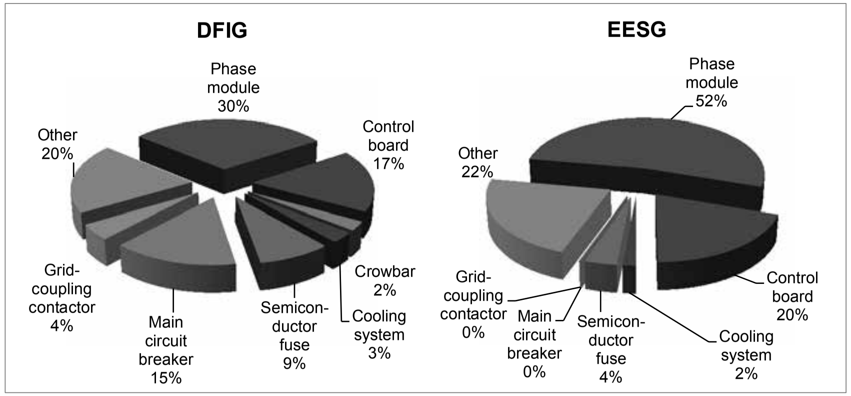

Fig.4: Distribution of converter-related downtime over component categories

module and other converter failures is observed in the data, the downtime is assigned to the affected component categories in equal portions for all multiple-category failures.

In order to assess the economic impact of the downtime, the average revenue loss resulting from converter unavailability is estimated. With an average rated capacity of $P_{rated,mean}$ = 1.67 MW per DFIG-based turbine and assuming a sales price of electricity of C_{el} = 85 €/MWh as well as a capacity factor of cf = 0.18, the mean converter-related downtime of 24h in the DFIG fleet translates into an annual revenue loss of approximately 600 € per wind turbine and year according to:

$$c_{rev.loss} = P_r \cdot cf \cdot t_{down} \cdot C_{el} \qquad (4)$$

This can be compared with the average repair cost due to converter failure per turbine and year of approximately 3600 € calculated using Eq.(2) , see Table 1. As a consequence of the lower converter failure rates found in the EESG fleet, both the resulting average repair cost and the revenue losses due to lost production are significantly lower for these turbines. The repair costs exceed the downtime-related losses by a factor of 3 to 6.

Table 1: Economic impact of converter failure through downtime and repair cost

	DFIG fleet ($P_{rated,mean}$ = 1.67 MW)	EESG fleet ($P_{rated,mean}$ =1.25 MW)
Average downtime (t_{down})	24 h/turb./a	8 h/turb./a
Associated revenue loss ($c_{rev.loss}$)	600 €/turb./a	160 €/turb./a
Repair cost (c_{rep})	3600 €/turb./a	530 €/turb./a

5. Conclusions and outlook

Within the main converter systems of the analysed fleet of wind turbines with DFIG and partially-rated converter, the phase-module category stands out with the highest failure rates. The number of 0.21 failures per turbine and year obtained for the fleet of DFIG turbines is in a similar order of magnitude as the value of 0.12-0.15 failures per turbine and year obtained for IGBT-module failures in the converters of DFIG turbines in [14][15]. Comparing the failure rates of the DFIG and EESG fleets analysed in this paper, both the average overall converter failure rate and the phase-module failure rate of the EESG turbines are found to be significantly lower than those of the DFIG fleet.

The economic impact of phase-module failures dominates over the other categories due to their high repair cost: Approximately 64% of the annual cost for converter repair in DFIG and 77% in EESG turbines is caused by failures of the phase modules. The economic impact of the repair cost is found to be considerably higher than that resulting from converter-related turbine downtime.

In summary, the phase modules can be concluded to be both the weak point in terms of reliability and the main cost driver in the considered converter systems. This suggests that future research should focus particularly on clarifying the root causes and developing reliability-enhancing solutions for this component.

The analysis presented in this paper is based on a subset of data that contains not only failure data but also the related repair-cost and downtime information. This data subset covers 1269 years of wind-turbine operation. As a result of the present work, the subsequent field-data analysis and root-cause investigations within the Innovation Cluster on Power Electronics for Renewables [16], for which a data basis with more than 5000 wind-turbine operating years is presently being collected and evaluated, will give particular attention to the phase-module components.

Abbreviations

DFIG Doubly-fed induction generator
EESG Electrically excited synchronous generator
IGBT Insulated gate bipolar transistor

Acknowledgments

The present work was carried out within the Fraunhofer-Innovationscluster "Leistungselek-tronik für regenerative Energieversorgung". The project funding by the Federal State of Lower Saxony and by Fraunhofer-Gesellschaft is gratefully acknowledged. The data analysed and presented in this paper was provided by wpd windmanager technik GmbH. We thank Fritz Brinkmann and Quang Minh Phan for their contributions to the field-data analysis within the scope of their thesis work.

References

[1] F. Spinato, P.J. Tavner, G.J.W. van Bussel, and E. Koutoulakos, "Reliability of wind turbine subassemblies," IET Renewable Power Generation, vol. 3, no. 4, pp.387-401, 2009, DOI: 10.1049/iet-rpg.2008.0060

[2] J. Bueno Gayo, "Final Publishable Summary of Results of Project ReliaWind", Project number 212966, 2011, online: http://cordis.europa.eu/publication/rcn/14854_en.html

[3] K. Fischer, F. Besnard, L. Bertling, "Reliability-Centered Maintenance for Wind Turbines Based on Statistical Analysis and Practical Experience," IEEE Transactions on Energy Conversion, vol.27, no.1, pp.184-195, 2012, DOI: 10.1109/TEC.2011.2176129

[4] J. Carroll, A. McDonald, D. McMillan, "Reliability Comparison of Wind Turbines With DFIG and PMG Drive Trains", IEEE Transactions on Energy Conversion vol. 30, no. 2, pp. 663-670, 2015, DOI 10.1109/TEC.2014.2367243

[5] C. Kaidis, B. Uzunoglu, F. Amoiralis, "Wind turbine reliability estimation for different assemblies and failure severity categories", IET Renewable Power Generation, 2015, doi: 10.1049/iet-rpg.2015.0020

[6] M. Bartram, I. von Bloh, R.W. De Doncker, "Doubly-fed machines in wind-turbine systems: Is this application limiting the lifetime of IGBT frequency-converters?," Proc. of the 35th Annual IEEE Power Electronics Specialists Conference, pp. 2583-2587, Aachen, Germany, June 20-25, 2004

[7] F. Fuchs, A. Mertens, "Steady state lifetime estimation of the power semiconductors in the rotor side converter of a 2 MW DFIG wind turbine via power cycling capability analysis," Proc. of the EPE 2011 - 14th Europ. Conf. on Power Electronics and Applications, Birmingham, UK, Aug. 30 - Sept. 1, 2011

[8] M. Musallam and C.M. Johnson, "Impact of different control schemes on the life consumption of power electronic modules for variable speed wind turbines," in Proc. of the EPE 2011 - 14th Europ. Conf. on Power Electronics and Applications, Birmingham, UK, Aug. 30 - Sept. 1, 2011

[9] L. Wei, R.J. Kerkman, R.A. Lukaszewski, H. Lu, and Z. Yuan, "Analysis of IGBT power cycling capabilities used in doubly fed induction generator wind power system," IEEE Transactions on Industry Applications, vol. 47, no. 4, 2011, DOI: 10.1109/TIA.2011.2153172

[10] H. Wang, K. Ma, and F. Blaabjerg, "Design for reliability of power electronic systems," in Proc. of the IECON 2012 - 38th Annual Conference on IEEE Industrial Electronics Society, IEEE, pp. 33-44, Montreal, Canada, Oct. 25-28, 2012, DOI: 10.1109/IECON.2012.6388833

[11] E.E. Kostandyan and K. Ma, "Reliability estimation with uncertainties consideration for high power IGBTs in 2.3MW wind turbine converter system," Microelectronics Reliability, vol. 52, no. 9–10, pp. 2403-2408, Sep. 2012, DOI: 10.1016/j.microrel.2012.06.152

[12] S. D'Arco, T.M. Undeland, M. Bohlländer, J. Lutz (2012): A Simplified Algorithm for Predicting Power Cycling Lifetime in Direct Drive Wind Power Systems, 2012 - 9th International Multi-Conference on Systems, Signals and Devices (SSD), Chemnitz, Germany, 20-23 March 2012, DOI: 10.1109/SSD.2012.6197971

[13] Ke Ma; M. Liserre, F. Blaabjerg, T. Kerekes (2015): "Thermal Loading and Lifetime Estimation for Power Device Considering Mission Profiles in Wind Power Converter," IEEE Transactions on Power Electronics, vol.30, no.2, pp.590-602, Feb. 2015, DOI: 10.1109/TPEL.2014.2312335

[14] K. Fischer, T. Stalin, H. Ramberg, T. Thiringer, J. Wenske, R. Karlsson, "Investigation of converter failure in wind turbines", Final report of the project CONFAIL, Elforsk report 12:58, Stockholm, 2012, online: www.elforsk.se/Global/Vindforsk/Rapporter%20VFIII/12_58_report_ConFail.pdf

[15] K. Fischer, T. Stalin, H. Ramberg, J. Wenske, G. Wetter, R. Karlsson, T. Thiringer, "Field-experience based root-cause analysis of power-converter failure in wind turbines", IEEE Transactions on Power Electronics, vol. 30, no.5, pp. 2481-2492, 2015, DOI: 10.1109/TPEL.2014.2361733

[16] Website of the Fraunhofer Innovationscluster „Leistungselektronik für regenerative Energieversorgung" (Innovation cluster on power electronics for renewables), www.power4re.de

Fatigue Failure Accident of Wind Turbine Tower in Taikoyama Wind Farm

Yin LIU[1], Takeshi ISHIHARA[2]

[1,2]Department of Civil Engineering, School of Engineering, the University of Tokyo, Tokyo, Japan

Abstract

One of the wind turbine nacelles at Taikoyama wind farm collapsed due to the fatigue failure of high tension bolts. Strain gauges and accelerometers were installed on the wind turbine to verify the aerodynamic model. Furthermore a FEM model was built in order to find out the relationship between tower tube and high tension bolts at the position of flange joint, where the fracture occurred. When the bolt's pre-tension force decreases, its stress range increases. Less the pretension force left, the larger the stress range will be. Hence when pre-tension force is 0%, the fatigue life is left for only a few days. On the other hand when 17 bolts are damaged, the turbine tube stress is three times larger than the stress when all the bolts are in good condition. Hence the fatigue evaluation shows that the life time rapidly decreases to less than two months compared with that of the normal life time which is 20 years.

Key Words: Fatigue failure, pre-tension force, high tension bolt, nacelle collapse.

1. Introduction

The Taikoyama wind farm is located at the top of Taikoyama Mountain, Kyoto Prefecture, Japan, which is surrounded by the Tango peninsular and faces north to the Sea of Japan. The construction cost is approximately 12.5 million dollars and it reduces nearly 5900 tons of carbon dioxide every year. The wind farm information is summarized in Table 1.

Table 1 Summary of Taikoyama wind farm

Name Operating time Manufacturer Unit Max power output	Taikoyama Wind Farm 15th, November, 2001 Lagerwey 6×750kW 4500kW	
Performance	Cut-in wind speed Rated wind speed Cut-out wind speed Resistant wind speed	3m/s 12m/s 25m/s 60m/s
Rotor	Diameter Generation rotor speed Number of blades Hub height	50.5m 13~33rpm 3 50m
Tower	Height Material	46m SM400 (steel)
Flange connection high-tension bolts	F10T	M24
Nacelle	Dimensions Material	W5.6×L3.3×H6.5m SS400, GFRE
Wind direction control	Control method	Active yaw control
Rated power output control	Control method	Pitch control

In March 2013 the nacelle of No.3 wind turbine collapsed[1] and the accident scene and schematic diagram of the wind turbine is shown in Fig. 1.

(a) Collapsed nacelle

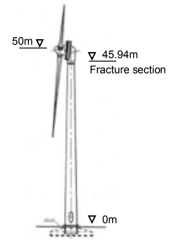

(b) Fracture section (c) Vertical cross section

Fig. 1 Accident scene and schematic diagram

The detailed structure is shown in Fig. 2.

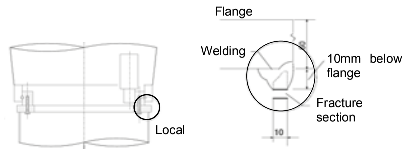

(a) Flange joint (b) Fracture section in detail

Fig. 2 Detail drawing of fracture section

The field investigation indicates that the wind condition satisfied the construction requirement based on the IEC 61400-1[2] including annual wind speed, turbulence intensity and flow inclination angle. By observing the fracture section of the tower tube, we found that the material strength was strong enough, but evidence of fatigue crack propagation was detected at the inner surface of the tube. Furthermore, 17 broken bolts were found during the field investigation and fatigue cracks were also detected. By comparing the two aspects, fracture is considered to be preceded by a certain degree of fatigue damage caused by the reduction of bolts pre-tension force up to 30%~100%.

The wind turbine collapsed very early in 12 years, where the expected life period was 20 years. Moreover, the accident happened only three months after the periodical inspection was carried out. Additionally, there are more than 120 wind turbines in service of the same type across Japan. Therefore, it is necessary and urgent to understand the cause of this accident, so that this kind of accident can be prevented in the future.

This paper proceeds as follows: 1) Field measurement; 2) Aerodynamic modelling and verification; 3) Clarify the fracture section's aerodynamic characteristics; 4) Explain the relationship between nominal stress, local stress and bolt stress using FEM model; 5) Evaluate the fatigue life of both high-tension bolt and tower tube, and reveal the reason for the failure.

2. Field measurement

2.1 Wind condition investigation

All the data were measured from Feb. 2nd 2015 to Feb. 28th 2015.

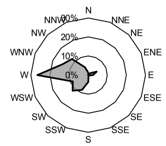

Fig. 3 Occurrence frequency

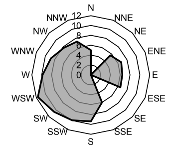

Fig. 4 Average wind speed

Fig. 3 and Fig.4 indicate the occurrence frequency and average wind speed respectively. The occurrence frequency of dominate wind direction WSW, W and WNW is 9%, 27% and 15% respectively.

Since the SCADA data contains only maximum wind speed and average wind speed in a time scale of 1 minute, we calculated the turbulence intensity according to reference [3] in equation (1).

$$I_p = \frac{U_{max}/U_{mean}-1}{P}, \quad P = \frac{1}{2} ln \frac{T}{t} \qquad (1)$$

The maximum wind speed U_{max} and average wind speed U_{mean} are derived from the 10min SCADA data, the peak factor P is evaluated by a time scale T of 600 seconds and average time t of 1 second. Consequently 1m/s bin average is calculated. Fig. 5 shows the field turbulence intensity.

Because of the insufficient high wind speed data

1 Presenting and corresponding author, PhD candidate, E-mail: liuyin@bridge.t.u-tokyo.ac.jp

(>17m/s) during the measurement period, the high wind speed turbulence intensity is extrapolated assuming the normal turbulence intensity in reference[2], and it is described as equation (2)

$$\sigma_1 = I_{ref}(0.75V_{hub} + b), \quad b = 3.8 \tag{2}$$

I_{ref} is the expected value of hub-height turbulence intensity at a 10 min average wind speed of 15m/s, V_{hub} is the wind speed at hub height and σ_1 is hub-height longitudinal wind velocity standard deviation.

As a result for aerodynamic simulation, a combined turbulence intensity is used: measurement value for low wind speed ($\ll 17\mathrm{m/s}$) and the extrapolated value for high wind speed respectively (>17m/s).

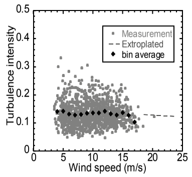

Fig. 5 Turbulence intensity in the direction of WSW+W+WNW

For the turbulence spectrum, the Kaimal model is used. The lateral and vertical turbulence intensity component are considered as 0.8 σ_1 and 0.5 σ_1 according to reference [2].

2.2 Moment measurement

Strain gauges with sampling frequency of 20Hz were installed in eight directions in order to get the moment at the height of 12.6m above tower base. Fig. 6 shows the strain gauges installment.

The nacelle was forced to rotate one circle without operating for the estimation of the strain gauges' installment error, and the compensation value can be calculated by the amplitude of the sin curve.

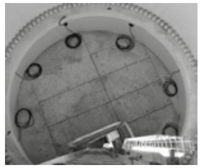

Fig. 6 Strain gauges installment

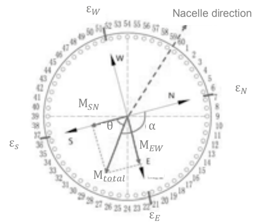

Fig. 7 Moment calculation schematic diagram

The measurement moment was calculated following the method by Ishihara and Phuc[4]. According to Fig. 7, the East-West moment and South-North moment were given in equation (3) and (4) respectively. Where M and ε is the moment and strain at corresponding direction, EI is the stiffness of tower tube and D is the inner diameter.

$$M_{EW} = EI\frac{\varepsilon}{D} = EI\frac{\varepsilon_E - \varepsilon_W}{D} \tag{3}$$

$$M_{SN} = EI\frac{\varepsilon}{D} = EI\frac{\varepsilon_S - \varepsilon_N}{D} \tag{4}$$

The total moment is given in equation (5). If the direction of total moment is opposite to the nacelle direction, then the total moment will be positive, otherwise it is negative.

$$M_{total} = \sqrt{M_{EW}^2 + M_{SN}^2} \tag{5}$$

The average bending moment, maximum bending moment and standard deviation of bending moment are plotted in Fig. 8.

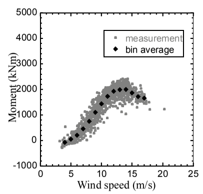

(a) Average moment

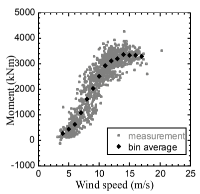

(b) Maximum moment

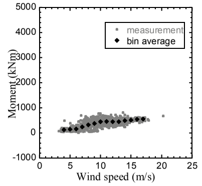

(c) Standard deviation of moment

Fig. 8 Comparison of measurement and bins average moment

3. Aerodynamic analysis and fatigue life investigation

3.1 Aerodynamic modelling

Aerodynamic model is built to simulate the dynamic performance by GL's Bladed wind turbine modelling tool[5]. The tower section refers to the real engineering drawings. For commercial confidentiality, the blade profile is not available from manufacturer. As a result we selected airfoils from NREL's airfoil family, which are S818 for root section, S830 for primary section and S831 for tip section[6], and thickness/chord ratio, Reynolds number, lift coefficient C_l and draft coefficient C_d were determined.

For control method, some adjustment had been applied. In case of the high turbulence intensity in the mountainous area, the wind turbine encounter over speed at times. Once it exceeds the maximum rotor speed of 33 rpm, it stops suddenly and starts to operate again when the rotor speed drops below the maximum value which causes frequent downtime. Hence the manufacturer modified the maximum rotor speed and power output to decrease the downtime.

Since the details were commercial confidentiality, we adjust rated power output and maximum rotor speed according to the measurement data. Moreover a five degrees pitch angle error is considered to eliminate the error in pitch control. With the adjustment above the power output, rotor speed and pitch angle are now close to the measurement data as shown in Fig. 9.

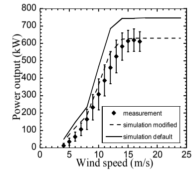

(a) Power output

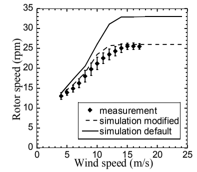

(b) Rotor speed

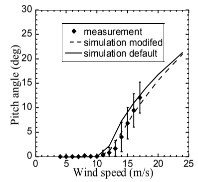

(c) Pitch angle

Fig. 9 Comparison of power output, rotor speed and pitch angle

The proportional gain K_{QP} and integral gain K_{QI} for torque control, and proportional gain K_{SP} and integral gain K_{SI} for pitch control were calculated based on *Guidelines for Design of Wind Turbine Support Structures and Foundations, JSCE*[7],and optimal mode gain K_{opt} was modified to validate the dynamic simulation results with measurement results.

Some key parameters for Bladed modelling are summarized in Table 2.

Table 2 Key parameters for Bladed modelling

	Optimal mode gain K_{opt}	Demanded generator toque (Nm)	Rated Power generation (kW)	Rotor speed (rpm)	Error in Pitch angle (degree)	Torque control	Pitch control
Default	22583.5	216450	750	33rpm	0	K_{QP}=789139 K_{QI}=516780	K_{SP}=0.458180 K_{SI}=0.847957
Modified	23340.2	231387	630	26rpm	5	K_{QP}=461249 K_{QI}=176551	K_{SP}=0.492799 K_{SI}=0.771005

A field test was carried out to measure the natural frequency of the tower. The damping ratio of the 1st order frequency was applied as 0.5% based on the field inspection [1]. The natural frequency is shown in Table 3, which is consistent with the aerodynamic simulation result.

Table 3 Comparison of tower natural frequencies

Tower natural frequencies	Measurement	Simulation
1st order (fore-art)	0.515Hz	0.533
1st order (side-side)	0.518Hz	0.533
2nd order (fore-art)	3.838Hz	3.685
2nd order (side-side)	3.832Hz	3.578

Finally, Fig. 10 shows the measurement and simulation results for moment at 12.6m above tower base were in good agreement, and the aerodynamic model is verified to be correct.

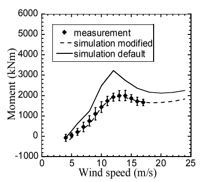

(a) Average moment (12.6m)

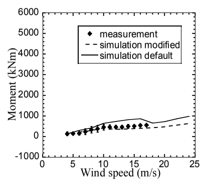

(b) Std of moment (12.6m)

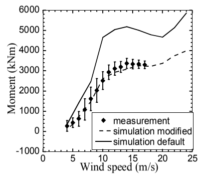

(c) Maximum moment (12.6m)

Fig. 10 Comparison of moment

3.2 Characteristics of fracture section

Fig. 11 (a) and Fig. 11 (b) show simulated axial force N and bending moment M at the tower fracture section (45.94m) at different wind steps respectively according to simulation result.

Hence the nominal stress can be calculated from equation (6), where A is the sectional area and Z is the sectional resistance moment.

$$\sigma_n = \frac{N}{A} - \frac{M}{Z} \qquad (6)$$

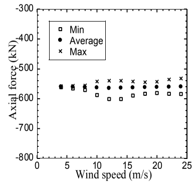

(a) Axial force N (45.94m)

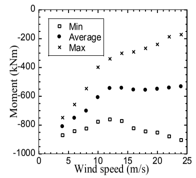

(b) Bending moment M (45.94m)

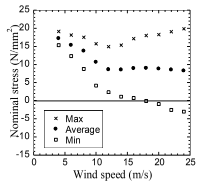

c) Nominal stress (45.94m)

Fig. 11 Aerodynamic characteristics at the fracture section

As shown in Fig. 11 (c), the nominal stress σ_n changes and varies with the increase of the wind speed. The minimum stress turns into negative value when the wind speed is above 18 m/s.

3.3 FEM modelling

The fracture section is very close to the top flange welding position, and according to the field investigation the fatigue failure propagated at the inner surface of the tower tube, so the stress concentration and spatial effect may influence the local stress σ_{local} significantly. A 3D FEM model is built to clarify the relationship between nominal stress σ_n , local stress σ_{local} and bolt get pre-tension force before and after the bolts damaged.

The relationship of nacelle weight, thrust force and top flange is illustrated in Fig. 12. The nacelle weighs 53.3t and it is rigidly connected to the yaw bearing.

The stress concentration factor of welding geometric profile was proposed by Caccese[8]. The case for Taikomaya wind turbine is as shown in Fig. 13. Solid element is used for the modelling of yaw bearing, top flange and bolts, and shell element is used for tower tube modelling. Furthermore, contact element is considered for the contact surface of yaw bearing and top flange and the friction factor is 0.2. The bolts are rigidly connected to the yaw bearing.

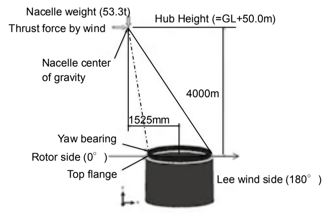

Fig. 12 Force applying position relationship

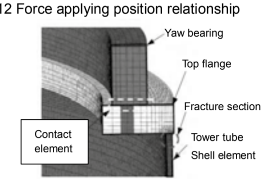

Fig. 13 FEM detail at top flange position

3.4 Investigation of the tower tube fatigue life

As for the tower tube, Fig. 14 shows the cases when 17 bolts broken.

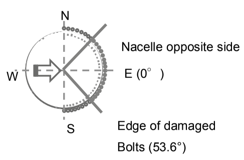

Fig. 14 Diagram of the damage area

Thrust force is considered in seven cases from 0kN to 250kN to simulate different wind loading. Fig. 15 shows an example of the local stress σ_{local} before and after 17 bolts are damaged at wind speed of 16m/s.

Fig. 15 (a) implies that the cause of maximum tensile stress happens at the inner tube because of the law of lever, which is consistent with the observation of fracture face. According to Fig. 15 (b), the local stress is much larger when 17 bolts are broken.

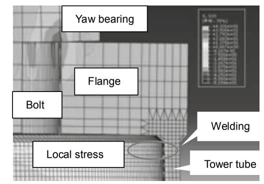

(a) Bolts normal

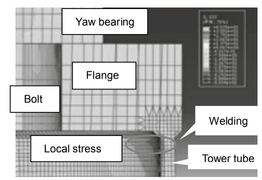

(b) 17 Bolts broken

Fig. 15 Comparison of the local stress (16m/s)

The relationship between nominal stress and local stress considering the welding stress concentration [7] is now given as following respectively:

Bolts normal

$$\sigma_{local} = -3.05 + 2.65\sigma_n \qquad (7)$$

17 bolts broken

$$\sigma_{local} = -10.6 + 6.35\sigma_n + 0.16\sigma_n^2 \qquad (8)$$

Equation (7) and (8) are plotted in Fig. 16. When 17 bolts are broken, the local stress is more than three times larger than bolts at normal condition.

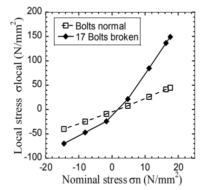

Fig. 16 Local stress vs. nominal stress

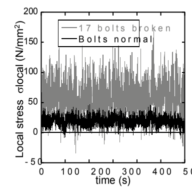

Fig. 17 Time history of local stress (22m/s)

With a time period of 10 minutes, the time series simulation result is available for each wind speed combining aerodynamic model with equation (7) and (8). When the wind speed is low, the tensile stress predominates. However with increase in wind speed, compressive stress occurs and the stress amplitude increases. The case of wind speed at 22m/s is shown in Fig.17.

With the time history of bolt pre-tension stress, we can investigate its fatigue life. Rain flow counting algorithm is used for fatigue analysis in order to reduce the spectrum of varying stress into a set of simple stress reversals. Goodman relation as shown in equation (9) is used to quantify the interaction of mean and alternating stresses.

$$\sigma_a = \sigma_w(1 - \sigma_m/\sigma_B) \quad (9)$$

σ_a is the alternating stress from rain flow counting result, σ_m is the mean stress, σ_w is the fatigue limit for comple`tely reversed loading and σ_B is the ultimate tensile strength of the material, which is 493Mpa for SM400 steel.

By using the fatigue limit for completely reversed loading σ_w, S-N curve based on *GL wind 2005* with a detail category of 71[9], and Miner's rule, the accumulative fatigue damage *D* in 10 minutes is given in Equation (10), and failure is reached when *D* equals to 1.

$$\sum_{i=1}^{k} \frac{n_i}{N_i} = D \quad (10)$$

Frequency distribution of the wind speed is based on Rayleigh distribution with a mean annual wind speed of 8.5m/s.

The fatigue life of tower tube is shown in Fig. 18. When the bolts are in normal condition the fatigue life is 27.5 years, which is in agreement with the design requirement. However, if 17 bolts are broken, the fatigue life decreases dramatically to 0.09 years, approximately one months. It is in accordance with the time interval between the last periodical inspection and the accident.

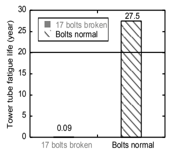

Fig. 18 Tower tube fatigue life

3.5 Investigation of the high tension bolts fatigue life

Based on the field investigation [1], six bolts at nacelle's opposite side were found to have reduction pre-tension force reduced as shown in Fig. 19.

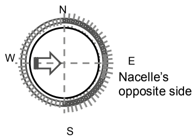

Fig. 19 Bolts pre-tension force decreasing

In order to recreate the real situation, blots pre-tension force is set in six different cases which were 100%, 80%, 60%, 40%, 20% and 0% of the design pre-tension force corresponding to 850kNm torque. The relationship between the nominal stress and bolt pre-tension stress is given as shown in Fig. 20. With the nominal stress increasing, the gradient increases as pre-tension decreases, and it is much more obvious when the pre-tension force decreases. The larger the gradient the larger the bolt stress range will be, and the bolt's fatigue load. Since the nominal stress ranges mainly between -5N/mm² to 25 N/mm2 according to Fig. 11(c), the stress range may vary a lot especially when the bolts pre-tension stress drops to 0% as illustrated in Fig. 20.

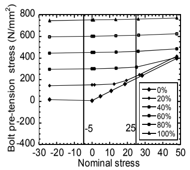

Fig. 20 Nominal stress Vs. bolt pre-tension stress

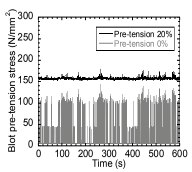

Fig. 21 Time history of bolt pre-tension stress (14m/s)

Fig.21 shows one example of the time history of the bolt pre-tension stress at the wind speed of 14m/s. It is clear that when the pre-tension force drops the stress range increases significantly.

The fatigue life investigation follows the rules mentioned in Section 3.4. The ultimate tensile strength of FT10 bolts is1000Mpa and the detail category is 36.

The bolts fatigue life is shown in Fig. 22.

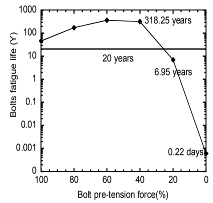

Fig. 22 Bolts fatigue life vs. bolt pre-tension percentage

As we can see that when the pre-tension force is over 40%, the life time does not decrease. However when the pre-tension force is below 40% the fatigue life time drops dramatically as only a few days left, when the pre-tension force is 0%.

4. Conclusions

This research is based on the collapse accident of Taikoyama wind farm No.3 turbine. The field measurement of tower model frequency, SCADA data and strain gauge data were measured. At the same time the aerodynamic model was built. In addition, the tower top FEM model was built to evaluate the high-tension bolts and tower tube fatigue life.

The cause of the collapse of the wind turbine is discussed and the following conclusions were drawn:

1) Due to high turbulence intensity at site, the control of the wind turbine was modified by manufacturer. Power output and maximum rotor speed were adjusted according to measurement data, and a five degree of pitch error was applied. With this control method the simulation results show good agreement with measurement results;

2) For the high tension bolts, by considering the nonlinear phenomenon and stress concentration closed to welding zone, when the pre-tension force decreases, the stress range increases, especially when pre-tension force is 0% it is 30 times larger. The less the pre-tension force left, the larger its range is. As a result, when the pre-tension force is below 40% the fatigue life time drops drastically and it is only a few days when the pre-tension force is 0%;

3) Similarly, the FEM model shows that with 17 bolts broken the local stress at fracture section increases more than three times compared with the case of bolts at normal condition. This phenomenon accelerated the fatigue initiation and propagation and the fatigue life of the fracture section decreases dramatically to 1/200 of its life time.

4) The reason for the Taikoyama wind farm accident is now clearly understood in a detailed manner. It is not the matter of design or material, but was due to the fatigue failure caused by the reduction of high tension bolts' pre-tension force.

For the Taikoyama wind turbines' high tension bolts, according to the service manual the temporary torqueing and final torqueing was applied. And at the time of 500 hours after bolt changing, the re-torqueing must be applied. However at the time of periodical bolt changing operation, the re-torqueing was not applied. The wind turbine is a rotating machine system, in which the contact surface and the bolt itself plasticity deforms accompany with the wind turbine operation, and therefore the pre-tension force reduces.

Moreover, according to the service manual, 5% of the bolts should be inspected per year, which means only three bolts were inspected. We should check at least 16 bolts per year in order to cover the bolts in all wind direction.

Besides, during the year from 2005 to2008, the workers only conducted the method of counter mark inspection to make sure the torque was enough.

It is a serious problem between manufacturer and operator that expertise technique is not transferred accurately and efficiently. Clear rules must be made even after guarantee periods, or it may lead to devastating accident.

Reference

[1] Kyoto fu, Report of the accident in Taikoyama wind farm No.3 wind turbine, Kyoto, 2013.

[2] International Electrotechnical Commission, (2005). IEC 61400-1, 3rd edition, Part 1: Design requirements. Geneva.

[3] Ishizaki, H.(1983) Wind profiles, turbulence intensities and gust factors for design in typhoon-prone regions. Journal of Wind engineering & Industrial Aerodynamics, 13: 55-66.

[4] T. Ishihara, P.V. phuc, Yozo Fujino. A Field Test and Full Dynamic Simulation on a Stall Regulated Wind Turbine. *The sixth Asia-Pacific Conference on Wind Engineering*, Seoul, September 2005: 599-612.

[5] Garrad Hassan Bladed, version 4.4, DNV-GL, 2013.

[6] Tony Burton, David Sharpe, Nick Jenkins. Wind Energy Handbook. John Wiley & Sons Ltd, Chichester, 2001.

[7] Japan Society of Civil Engineers, (2010). Guidelines for Design of Wind Turbine Support Structures and Foundations. Task Committee on Dynamic Analysis and Structural Design of Wind Turbine Committee of Structural Engineering, Tokyo.

[8] V. Caccese, P.A. Blomquist, K.A. Berube. Effect of weld geometric profile on fatigue life of cruciform welds mad by laser/GMAW processes. Marine Structures, 2006, 19: 1-22.

[9] Germanischer Lloyd WindEnergie GmbH (2005), Guideline for the Certification of Offshore Wind Turbines. Germanischer Lloyd WindEnergie, Hamburg.

Wind Turbine Non-Intrusive Torque Monitoring

Michael Secker, Christopher J. Crabtree, Donatella Zappalá
School of Engineering and Computing Sciences
Durham University, UK
m.p.secker@durham.ac.uk, c.j.crabtree@durham.ac.uk, donatella.zappala@durham.ac.uk

Abstract

Wind Turbine (WT) global installed capacity is expected to increase from 318GW to 596GW between 2013 and 2019, with an increasing proportion being from offshore wind farms. With up to 70% of Operations and Maintenance (O&M) costs coming from unplanned maintenance, the adoption of cost effective condition monitoring (CM) techniques is crucial for competitive development of offshore wind.

Monitoring the torque of a WT can provide much information about the WT's health and it has been shown to be successful in the detection of faults in the main drive train components. Although WT torsional effects are important, torque measurement on such a large, low speed, inaccessible machine is practically and logistically difficult, although it is possible using costly specialised intrusive in-line equipment.

This paper presents the development of a non-intrusive method for monitoring the drive train torque using timing differences between optical probe measurements along a shaft. An algorithm has been developed and initially verified using a simulated WT for speed and torque data. The algorithm torque was accurate to within ±3% of the input.

The initial performance of the proposed technique has been successfully tested experimentally under both steady and transient torque conditions. Experimental results show good agreement between the algorithm predictions and the measurements. The proposed algorithm successfully detects changes in shaft speed and torque, with the torque mean percentage error within 16-25%. Once implemented on a WT drive train, the proposed non-intrusive method can overcome the majority of problems limiting the industrial application of CM systems (CMSs) based on shaft torque measurements.

Keywords: Wind turbine, torque, non-intrusive measurement, condition monitoring.

1. Introduction

Wind energy is seeing huge increases in production with the Global Wind Energy Council reporting that global installed wind capacity has increased from 6.1 GW in 1996 to 318 GW in 2013, and is predicted to rise to 596 GW by the end of 2018 [1]. Offshore wind has significant generation potential, in particular in Europe, with increasingly large-scale sites identified as suitable for offshore development and benefiting from a favourable wind resource. Offshore wind is therefore expected to play a significant role in meeting this target, with projections of an increase in the proportion of offshore turbines from 2% to 10% of global wind capacity between 2015 and 2020 [2]. There any many advantages for going offshore including higher quality wind resources, less turbulence, larger WT ratings and less problematic visual intrusion. However, the harsher conditions offshore produce more significant variable loading along with difficult site accessibility for maintenance as favourable weather conditions and special service vessels are required for transportation of the maintenance team [3]. As large-scale wind farms (WF) move further offshore, achieving a high availability and capacity factor and ensuring that loss of energy and turbine downtime is minimised, are essential for a competitive cost of energy. The costs of offshore O&M have been quantified as three to five times higher than those onshore [4], with a considerable part, typically up to 65-70%, associated with unscheduled maintenance [5, 6], resulting in unexpected WT downtime, reduced availability and lost revenue. Repair costs are not the only consequence of maintenance as the time that is lost in which the turbine could have been generating energy and revenue must also be considered. These issues highlight the importance of O&M strategy within economic viability evaluation of large offshore WFs [7]. The adoption of cost effective condition monitoring (CM) techniques is crucial in reducing O&M costs, avoiding catastrophic failures and minimizing costly corrective maintenance. As the loading on the WT drive train components is highly variable the study of transient conditions is fundamental to the development of reliable CM techniques.

The potential of monitoring different WT drive train components using the shaft torque signal is significant as it contains information on the mechanical response to wind before any generator effects. Recent studies have shown the potential benefits of adopting condition monitoring systems (CMSs) based on the measurement of WT drive train shaft torque for the detection of rotor electrical asymmetry and machine winding faults [8-10], mass imbalance [11], gearbox failures [12], blade mass imbalance and aerodynamic asymmetry [13]. However, the measurement of shaft torque is largely limited to the laboratory environment. The major obstacle to industrial application is the costly and intrusive nature of the required measurement equipment, which is impractical for long-term use on operating WTs [14, 15].

This paper details research conducted on a low-cost, non-intrusive WT torque measurement method based on timing differences between optical probe signals along the shaft with a focus on tracking transient conditions for use in a CMS.

2. Theoretical Background

The torque applied to a rotating shaft is proportional to the twist angle between two points on the shaft [16]:

$$T = I\ddot{\theta} + C\dot{\theta} + K\theta \qquad (1)$$

where T is the applied torque (Nm), I is the shaft moment of inertia (kgm^2), C is the shaft damping coefficient (kgm^{2}s^{-1}rad^{-1}), K is the shaft torsional stiffness $(\mathrm{Nm/rad})$ and θ is the relative twist angle (rad) given by:

$$\theta = \theta_a - \theta_0 \qquad (2)$$

where θ_a is the absolute twist angle and θ_0 is the no-load twist. θ_a can be calculated by measuring the timing difference and rotational speed between two points on the shaft [17]:

$$\theta_a = \frac{2\pi}{60}\omega\Delta t \qquad (3)$$

where ω is the shaft rotational speed (rpm) and Δt is the timing difference or phase shift (s). The no-load twist θ_0 is the absolute twist angle before torque has been applied to the system.

3. Non-Intrusive Torque Measurement Algorithm

The proposed non-intrusive torque measurement approach employs equation (1) to calculate the torque from the phase shift between the pulses generated by two bar codes and optical probes, one at each end of the shaft. The optical probes identify a black or white segment and produce a fixed voltage when reading white and zero volts when reading black, resulting in two pulse trains as the shaft rotates (Figure 1).

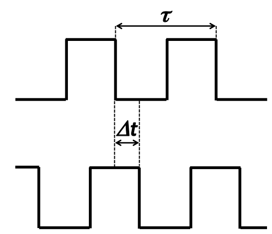

Figure 1: Typical pulse trains from the two shaft ends, where τ is the period and Δt is the phase shift.

The shaft rotational speed is calculated as:

$$\omega = \frac{60}{\tau p} \qquad (4)$$

where p is the number of pulses per shaft revolution and τ is the pulse train period (s).

For a given shaft stiffness, damping coefficient and moment of inertia, the measurement of the phase shift between two pulse trains Δt and the calculation of ω, allow the calculation of the shaft torque from equations (1)-(3).

4. Simulation Results

To validate the proposed approach, simulated WT drive train data were created using DNV GL's Bladed 4.6 software. The aim of using the Bladed simulations was to prove the effectiveness of the process of reconstructing the shaft speed and torque signals by using discrete pulse trains. The twist angle has been reconstructed from the simulation speed and torque data and used to generate an example pulse train. By analysing this pulse train, the ability of the algorithm to reverse the process could be tested. The main features of the reference example WT used in the simulations are shown in Table 1.

Table 1: WT parameters used in the simulations.

Blade Length (m)	38.75
Cut-In Speed (m/s)	4
Cut-Out Speed (m/s)	25
Gearbox Ratio	83.33

High speed shaft speed and torque data were collected at 20 Hz under a mean wind speed of 12m/s with 16% longitudinal turbulence intensity. The data were resampled to 50 kHz and interpolated to create pulse trains for the calculation of shaft speed and torque by using the shaft parameters of the example WT in Bladed. The resulting algorithm response compared to input data is shown in Figure 2.

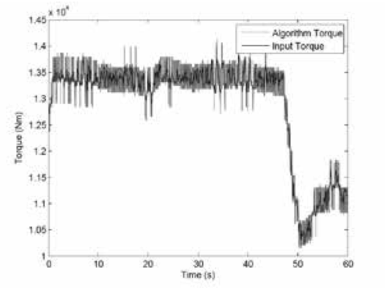

Figure 2: Algorithm response to WT simulation.

The trend of the input data simulated by Bladed is followed well by the algorithm output with a maximum percentage error noise associated of ±3%. The non-perfect reversibility between the original simulated signal and the one reconstructed by the algorithm introduces a slight reduction in the signal accuracy and the introduction of a certain level of noise.

An increase in the re-sampling frequency of the input data up to 100 kHz has shown a reduction of the noise levels to ±1.5%, suggesting that the sampling frequency and subsequent noise were issues requiring further investigation. The analysis of the pulse trains proved this to be correct as extra time steps at a higher sampling rate meant that the pulses were generated to a higher accuracy. The effect of resampling at a higher frequency is to produce signals which allow a smoother and continuous monitoring of the phase shift and period changes in the pulse trains. Consequently the algorithm measured the phase shift and period to a higher precision which produced a more accurate measurement.

5. Test Rig

Physical testing was performed to verify the proposed algorithm. Figure 3 provides a schematic of the torque test rig developed at Durham University and Figure 4 is a photo of the test stand which shows its main components and instrumentation system.

The test rig features a 4-pole 5 kW grid-connected induction generator driven by a 4-pole 5 kW induction motor. The motor shaft speed is varied via an inverter drive. The generator is connected to a VARIAC in order to vary the stator voltage and hence the shaft torque. An in-line Magtrol TM 212 torque transducer, measuring the shaft torque and speed, acts as a reference for comparison with the algorithm output. On either side of the transducer are the bar codes and OPTEK optical probes used to generate input data for the algorithm. Each bar code features 8 pulses per revolution and has been designed such that it divides into equal black and white segments, in both number and size, and that its total length fits exactly around the shaft. This design was selected so that the resulting pulses have a 50% duty cycle which makes phase shift measurement processing easier. The optical sensors consist of an Infrared (890nm) Light Emitting Diode (LED) and a NPN silicon Phototransistor, mounted side-by-side on converging optical axes. Couplings and bearings along the shaft ensure minimal radial shaft displacement helping to minimise a source of error when reading the bar codes.

Signals recorded from the optical probes are transmitted to a National Instruments data acquisition pad (USB-6009 DAQ pad) which is in turn connected by USB connection to the LabVIEW data acquisition environment. The probe sampling frequency was set at 24 kHz as this was the maximum possible for the NI USB-6009 data acquisition hardware. The torque transducer output is connected to a computer interface through the Magtrol Torque 1.0 data acquisition software and compared to the algorithm torque as verification.

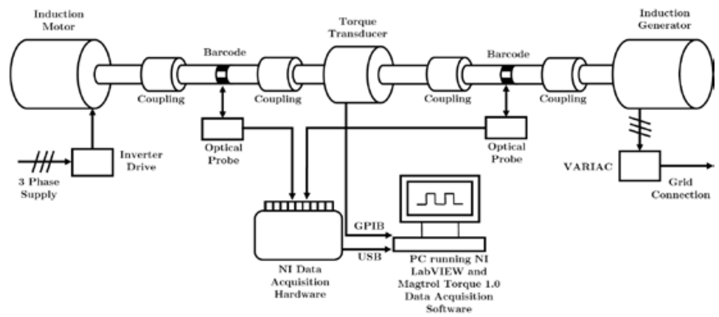

Figure 3: Schematic diagram of the torque test rig.

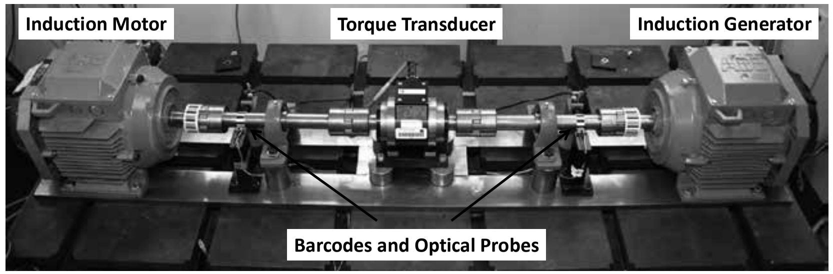

Figure 4 Torque test rig: main components and instrumentation.

6. Data Filtering

Data filtering has been performed on the signals recorded during the experiments in order to reduce the inherent systematic noise associated to the laboratory environment and to guarantee accuracy in the algorithm output.

Firstly a digital conversion was required to covert the optical probe voltage signals. A MATLAB code was implemented to convert any high voltage signal to a 1 and any low voltage signal to a 0. This conversion to a digital signal was performed in order to improve the algorithm train pulse edge detection and therefore the period and phase shift measurements.

Further filtering was carried out to ensure that any spikes in the middle of pulses were smoothed out. This was accomplished by comparing each data point with the previous 400μs of data as well along with following 400μs. If all of these data points matched except the one being examined, a noise spike was detected and converted to match the other 800μs of data points. Examination of these spikes showed they had a less than 40μs duration, therefore analysing each data point using a range ten times larger than this assures that checks are made on the digital state of the pulse rather than on noise spikes. A larger analysis period than 400μs risked analysing beyond a transition stage which means errors would not be detected through this method.

Preliminary experimental results showed that the physical optical probes did not display the transition in the pulse trains as a sharp edge but oscillated from previous to final state for up to 200μs before settling. A filter was then designed to detect any change in digital state between consecutive time steps. It inspected the state of the pulse in the previous 400μs and the state of the pulse for the next 400-800μs. A 400μs period was chosen for the same reason as mentioned above whilst analysing from 400μs after each state change was to ensure that the state of the pulse after a transition was checked rather than the state during a transition. At a transition, these two sets should give the exact opposite of each other (i.e. a set of 1's and a set 0's) and if this was detected, the entire oscillating transition period was converted into the final state of the transition. The importance of removing all the high frequency spikes was to avoid the algorithm using them to calculate extremely high erroneous speeds.

Finally, a low pass filter with cut-off frequency of 1 kHz was implemented to filter out periodic noise due to high frequency components in the signal.

7. Experimental Results

The algorithm has been fully developed by experimentally defining the relationship between torque and twist. Tests were performed according to the procedure below:

1) Run the motor up to 1600rpm;
2) Take a no-load measurement (0V applied to the generator stator using the VARIAC);
3) Record pulse and transducer data for 60s;
4) Use the VARIAC to apply a torque of -0.5Nm;
5) Record pulse and transducer data for 60s;
6) Repeat steps 4-5 for increasing magnitude of torque;
7) Repeat 1-6 for different super-synchronous speeds.

Pulse data were analysed using part of the algorithm to calculate the twist. For each 60s experiment, the means of the measured twist and torque were calculated and plotted to find the experimental relationship between torque and relative twist (Figure 5). The trend of the experimental data was then fitted by the following quadratic curve:

$$\mathrm{T} = -8025\theta^2 - 76\theta - 0.5453 \qquad (5)$$

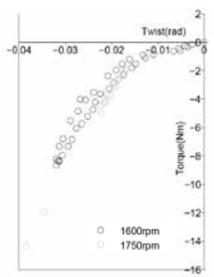

Figure 5: Test rig relationship between torque and twist.

The non-linear relationship between torque and twist described by equation (5) suggests that steady conditions during the experiments were not exactly obtained, especially at low magnitude torque values, and that dynamic conditions played a crucial role according to that predicted by the theoretical relationship (1).

Tests were then performed to validate the proposed algorithm under both steady state and transient conditions. The shaft speed and torque responses were calculated by implementing the proposed algorithm in MATLAB and compared with the transducer measurements. Figure 6 shows results for a steady state test at 1600 rpm and -3 Nm torque. The algorithm mean speed predictions show good agreement with transducer measurements with a percentage error of 0.06% and noise of ±0.3%. The algorithm mean torque predictions overestimate the transducer measurements by 44% with 200% noise. It is believed that the reason for the overestimation is due to the large amount of noise which occurred when calculating the twist, linked to the sampling frequency.

The proposed algorithm was then tested under transient conditions with the purpose of producing signals comparable to those encountered on an operational WT. Figure 7 shows results for transient conditions obtained by running the shaft up to 1600 rpm and smoothly varying the torque from 0 Nm to -10 Nm and back to 0 Nm. Both algorithm speed and torque track the transducer measurements well, particularly speed showing a percentage error of below 0.1%.

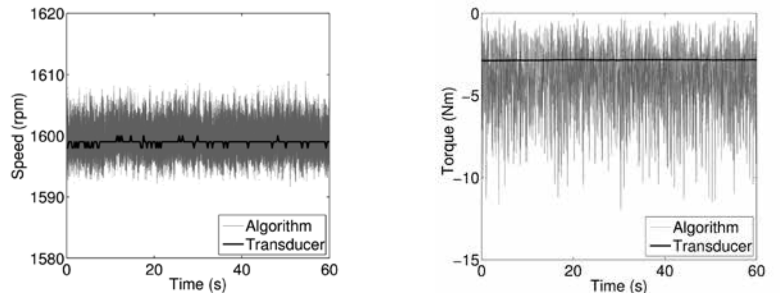

(a) (b)

Figure 6: Algorithm speed (a) and torque (b) response to steady state conditions of 1600 rpm and -3 Nm.

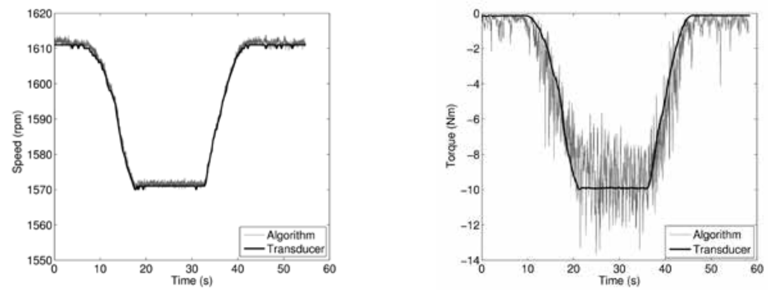

(a) (b)

Figure 7: Algorithm speed (a) and torque (b) response to shaft torque variations.

Figure 8 shows results for transient conditions obtained by keeping the generator stator voltage constant at 50% of the maximum whilst ramping the motor speed from 1525 rpm to 1750 rpm, holding for 30 s and then ramping back to 1500 rpm. The algorithm speed shows again good agreement with measurements with percentage errors less than 0.1%. For torque above 2 Nm, the average error was consistently around 25%, suggesting a systematic error was present. Figure 9 shows the effects of a step change in torque. The shaft speed was initially set at 1590 rpm and, starting from an initial torque of -3 Nm, four torque step changes were applied. The algorithm speed and torque follow the step changes well and without any timing delay. The algorithm predictions show good agreement with the measurements, with systematic errors lower than 0.1% for the speed and a torque mean percentage error of 16-25%. It is believed that the torque error is due to limitations in the signal sampling frequency. By increasing the sampling frequency during data acquisition it is expected that the systematic error associated with the measure of the phase shift between the two pulse trains would be reduced. This would result in improved predictions by the algorithm of the shaft twist angle, calculated by using equation (3), and of the relative torque values, calculated by using equation (5).

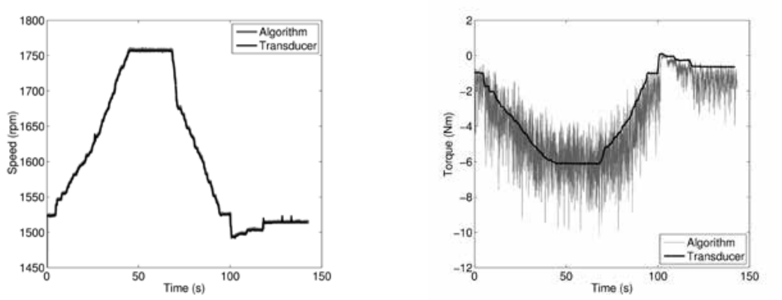

(a) (b)

Figure 8: Algorithm speed (a) and torque (b) response to motor speed variation at fixed generator voltage.

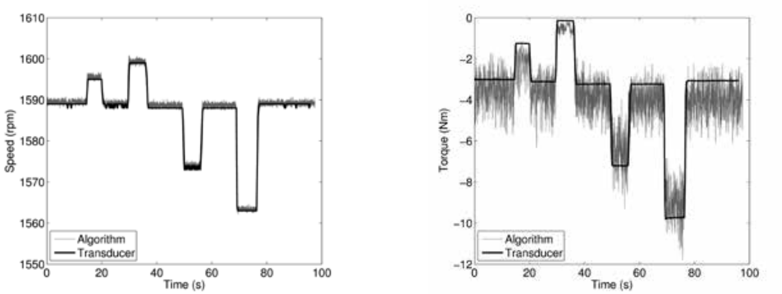

(a) (b)

Figure 9: Algorithm speed (a) and torque (b) response to step torque inputs.

8. Discussion

Although further investigation is required to reduce noise and tune the algorithm, the experimental results show that the proposed technique is successful in predicting changes in shaft speed and torque similar to those typically encountered by operating WTs.

Previous work has shown the strong potential of using the WT torque signal for CM purposes [8-13]. The major obstacle to its industrial application is the costly and intrusive nature of the required measurement equipment, which is impractical for long-term use on operating WTs. For this reason, in some cases, operators are only able to run short measurement campaigns by using specially installed torque transducers. Given the increasing awareness about the importance of long-term torque measurements for fully understanding the WT dynamics and for CM purposes, the wind industry is showing increasing interest in measuring the torque with cheap and non-intrusive techniques.

This work presents a novel approach to measure the drive train shaft torque by using a non-intrusive technique and could be a viable tool for WT CM. The proposed methodology is relatively simple and cheap to implement into a commercial WT CMSs for non-intrusive torque monitoring.

Although still at the small-scale stage implementation the economic benefits of the proposed technique, based on the use of two barcodes and two optical probe sensors, over the conventional in-line torque transducer are evident. While the non-intrusive equipment costs overall less than €100, the in-line sensor cost for a small shaft of 470 mm goes well beyond €5000. This difference in costs will be even larger in a commercial WT application due to the bigger WT drive train shaft diameter, which would increase the fitting cost of an in-line torque transducer.

The torque imposed on a rotating shaft has been measured in the past using strain gauges through a wireless telemetry or a slip ring system. However, the accuracy of the torque measurements provided by strain gauges often does not meet engineering requirements because the uncertainty of such measurements is rather large due to electromagnetic interference [17]. The results of the proposed non-intrusive technique correlate closely with the transducer measurements and it is believed that, once the sampling frequency of the data acquisition system will be increased and the main sources of signal noise and systematic errors removed, the algorithm should show a higher accuracy, compared to other methods, in predicting the speed and torque values during the WT operation.

Despite the promising results obtained in this study, the reliability of the proposed approach for CM purposes is currently under further investigation. In particular, drive train seeded-fault testing and analysis will be performed on the torque test rig with the aim of developing reliable torque signal processing algorithms for fault detection.

9. Conclusions

This paper presents a non-intrusive technique for torque measurement on a WT drive train. It can be concluded that:

- Torque measurement is achieved by measuring the angle of twist from the timing between pulse trains produced by two sets of bar codes and optical probes.
- The proposed algorithm was validated, computationally and through physical testing, under steady state and transient conditions. In both cases the derived algorithm torque correlated closely with the torque transducer measurements, with ±3% and 16-25% torque mean percentage errors, respectively.
- Higher sampling frequency of the data acquisition system is expected to reduce the noise and the systematic error associated with the algorithm output.
- Unlike conventional torque transducers, the proposed approach does not require any embedded sensors on the rotating shaft, overcoming the majority of problems limiting the industrial application of CMSs based on shaft torque measurements.
- Experimental investigation is currently carried out at Durham University with the aim to address the role played by the shaft moment of inertia, damping coefficient and torsional stiffness in controlling the torque predicted by the theoretical relationship given by equation (1), for both steady and transient conditions.
- Future work will focus on further validating the method using experimental data and developing suitable and reliable signal processing algorithms for fault detection.

Acknowledgements

This work was funded as part of the UK EPSRC Supergen Wind Energy Technologies programme, EP/H018662/1.

References

[1] Fried, L., Sawyer, S., Shukla, S., Qiao, L. (2014). 'Global Wind Report Annual Market Update 2013'. GWEC, available at http://www.gwec.net/wp-content/uploads/2014/04/GWEC-Global-Wind-Report_9-April-2014.pdf, last accessed 24th January 2015.

[2] GWEC. 'Global offshore': http://www.gwec.net/global-figures/global-offshore/. Last accessed on 16/03/15.

[3] Shafiee, M., Patriksson, M., Stromberg, A.-B., Bertling, L. (2013). A redundancy optimization model applied to offshore wind turbine power converters. In 2013 IEEE Grenoble PowerTech (POWERTECH), pages 1–6.

[4] McMillan, D., Ault, G.W. (2007). Quantification of Condition Monitoring Benefit for Offshore Wind Turbines. Wind Engineering. 31(4): 267-285.

[5] Walford, C.A. (2006). 'Wind Turbine Reliability: Understanding and Minimizing Wind Turbine Operation and Maintenance Costs'. Sandia National Laboratories SAND2006-1100, available at http://prod.sandia.gov/techlib/access-control.cgi/2006/061100.pdf, last accessed 21st February 2015.

[6] BVG Associates (2012). 'Pathways to Cost Reduction in Offshore Wind Technology: Technology workstream', available at http://www.bvgassociates.co.uk/Publications/BVGAssociatespublica%ADtions.aspx, last accessed 16th October 2015.

[7] Sheng, S., Veers, P. (2011). Wind Turbine Drivetrain Condition Monitoring - An Overview. Proceedings of Machinery Failure Prevention Technology (MFPT) Society 2011 Conference. Virginia Beach, Virginia.

[8] Yang, W., Tavner, P.J., Crabtree, C.J., Wilkinson, M. (2010). Cost-Effective Condition Monitoring for Wind Turbines. IEEE Transactions on Industrial Electronics. 57(1): 263-271.

[9] Abdusamad, K.B., Gao, D.W., Li, Y. (2014). Condition monitoring system based on effects of electrical torque pulsations of wind turbine generators. In PES General Meeting Conference Exposition, 2014 IEEE.

[10] Djurović, S., Vilchis-Rodriguez, D.S., Smith, A.C. (2012). Vibration Monitoring for Wound Rotor Induction Machine Winding Fault Detection. Proceedings of XXth International Conference on Electrical Machines, ICEM, Marseille, France.

[11] Wilkinson, M.R., Spinato, F., Tavner, P.J. (2007). Condition Monitoring of Generators & Other Subassemblies in Wind Turbine Drive Trains. Proceedings of 2007 IEEE International Symposium on Diagnostics for Electric Machines, Power Electronics and Drives (SDEMPED 2007). Cracow, Poland.

[12] Soker, H., Kieselhorst, S., Royo, R. (2004). Load monitoring on a mainshaft. A case study. German Wind Energy Conference DEWEK, Wilhelmshaven.

[13] Perišić, N., Kirkegaard, P.H., Pedersen, B.J. (2015). Cost-effective shaft torque observer for condition monitoring of wind turbines. Wind Energy. 18: 1-19.

[14] Lu, B., Li, Y., Wu, X., Yang, Z. (2009). A Review of Recent Advances in Wind Turbine Condition Monitoring and Fault Diagnosis. Proceedings of 2009 IEEE Symposium on Power Electronics and Machines in Wind Applications. PEMWA 2009. Lincoln, Nebraska.

[15] Yang, W., Tavner, P. J., Crabtree, C. J., Feng, Y., Qiu, Y. (2014). Wind Turbine Condition Monitoring: Technical and Commercial Challenges. Wind Energy. 17(5): 673-693.

[16] Friswell, M.I., Penny, J.E.T., Garvey, S.D., Lees, A.W. (2010). *Dynamics of Rotating Machines*. Cambridge University Press.

[17] Sue, P., Wilson, D., Farr, L., Kretschmar, A. (2012). High precision torque measurement on a rotating load coupling for power generation operations. In Instrumentation and Measurement Technology Conference (I2MTC), IEEE International.

Efficient load and power monitoring by stochastic methods

M. Wächter[1], P.G. Lind[1], Iván Herraez Hernandez[1], P. Rinn[1], P. Milan[1], B. Stoevesandt[2], J. Peinke[1,2]

[1]ForWind Center for Wind Energy Research, University of Oldenburg, Germany,
[2]Fraunhofer IWES, Oldenburg, Germany

Science & research paper submitted for EWEA 2015

Subject area *"O&M & logistics: Reliability, condition monitoring"*

Abstract

Monitoring of performance and loads of wind energy systems supports reliable and efficient operation. This is emphasized by the typically harsh and non-stationary operating conditions especially at offshore but also onshore sites. These external conditions also form substantial challenges to both the sensor equipment and the data analysis methods. Due to strong fluctuations and site specific situations, currently such monitoring is dependent on long term data.

Here we present results obtained by stochastic methods which reliably extract the deterministic machine characteristics even under strongly fluctuating and non-stationary conditions. Moreover, we achieve an efficient load monitoring from standard operational data, without the need for additional measurement hardware.

1 Introduction

Wind energy systems operate under harsh and strongly changing conditions. Reliably monitoring the power performance of wind farms under such conditions is of great importance to all wind farm operators. Due to the strong fluctuations and site specific situations, currently such monitoring is dependant on long term data.

Stochastic methods have proven to be efficient tools in this field. Here we present latest results which confirm and considerably extend the fields of application for stochastic methods in wind energy. After shortly introducing the approach in section 2, in section 3.1, we present examples of performance monitoring results, namely for inhomogeneous inflow conditions as well as several effects in special situations. Section 3.2 presents results on wind farm performance monitoring, and in section 3.3 we show new results of stochastic load modeling and a connected monitoring approach.

2 Approach

A conditional Langevin approach was shown to be successful for systems with strong and non-stationary variability [1], among others for the dynamic power characteristics of wind energy converters (WEC), the so-called Langevin Power Curve [2, 3].

The conditional Langevin equation models an observed time series (such as power, force, or torque) in terms of a first-order stochastic differential equation

$$\dot{X}(t) = D^{(1)}(X, y) + \sqrt{D^{(2)}(X, y)} \cdot \Gamma(t) . \qquad (1)$$

Here, X is the observable (e.g., power, force, or torque), y represents an external operating condition (typically the wind speed), and $\Gamma(t)$ denotes an uncorrelated, Gaussian noise of variance two [1]. Thus, for each value of y we obtain a stochastic differential equation defined by the functions $D^{(1,2)}(X, y)$. These functions are estimated directly from measurement data in a mathematically rigorous way, cf. [1–3].

3 Results

3.1 Wind turbine performance monitoring

From the stochastic model (1) the dynamic power characteristics of a wind turbine, the Langevin Power curve (LPC), is derived as the fixed points of its dynamics [2, 3]. In most cases operational data of the SCADA system can be used, given that a 1 Hz resolution is available. The LPC constitutes a fingerprint of the wind turbine's performance characteristics, and is widely independent of external conditions such as turbulence, stability, wake condition, etc. Because it is derived from high-frequency measurements, typically only very few days of measurement are needed, given that the wind speeds of interest are covered.

3.1.1 Icing of nacelle anemometer

During winter, unrealistically high power values occurred in the LPC of a 5 MW Senvion 5M offshore wind turbine in the German offshore wind farm "alpha ventus" for very low wind speeds, see Fig. 1(a). It turned out later that the reason was icing on the nacelle anemometer, leading to reduced wind speed measurements [4]. The power curve similar to IEC 61400 is almost unaffected by this effect.

3.1.2 Power reduction

At the same turbine a short disturbance in operation lead to an automatic reduction in power output for less than 8 h in a month. Even for this short period of anomalous behavior, the LPC clearly points out the deviation, see Fig. 1(b) [4]. Also here the IEC-like power curve does not show conclusive results.

3.1.3 Control strategy effects

For a different multi-MW offshore wind turbine an interesting effect of the control system on the performance characteristics was observed, see Fig. 2. Around $u/u_{max} \approx 0.4$ we observe a characteristic step in the LPC (Fig. 2(a)) [5].

In the power histogram (Fig. 2(b)) we observe that around the respective power value the probability for lower power output is significantly higher than for higher power values. In other words, a certain amount of energy production is lost due to this effect. In contrast to the LPC, the IEC power curve added to Fig. 2(a) does not give any hint of this situation.

3.1.4 Free stream vs. wake

A recent measurement campaign using a scanning nacelle-based wind lidar [6] demonstrated that the LPC is indeed turbine-specific and not sensitive to site characteristics, such as different turbulence levels. In Fig. 3 two LPC measurements at the same turbine are compared, where only wake or free stream inflow conditions have been used, respectively [7]. Also here, the measurements were performed on a 5 MW Senvion 5M offshore wind turbine in the German offshore wind farm "alpha ventus".

Traditional power curve measurement following IEC 61400-12 is known to depend on site chracteristics such as shear and turbulence conditions, which leads to a necessity of elaborate data filtering and long measurement times.[1] Given a high quality wind inflow measurement, the Langevin Power curve provides turbine-specific performance characteristics independent of site-specific influence or, in this case, possible wake situations.

3.2 Wind farm performance monitoring

Also for performance monitoring of wind farms the Langevin Power Curve turns out to provide sensitive and helpful information. In an onshore wind farm of 12 turbines of the 2 MW class the cumulative electrical power output was recorded, and both ten minute averaged (denoted as IEC power curve) and LPC power characteristics of the wind farm were derived. The case of a downtime of one turbine was simulated in the power data in several variants. The LPC showed higher sensitivity to detect the downtimes in all cases [8]. In this case, turbine type and location are confidential.

Fig. 4 shows results for the case of 12 h downtime of one turbine. While the IEC power curve of the wind farm (left) is not affected at all, whereas the drift coefficient $D^{(1)}$ (cf. eq. (1)) shows significant variation (middle). Because the affected wind speed regime is narrow, in the LPC (right) only one additional fixed point is obtained for the respective wind speed. It nevertheless clearly and quantitatively points out the temporal performance reduction.

[1] Power characteristics similar to IEC 61400 are shown for comparison in Figs. 1, 2, and 4.

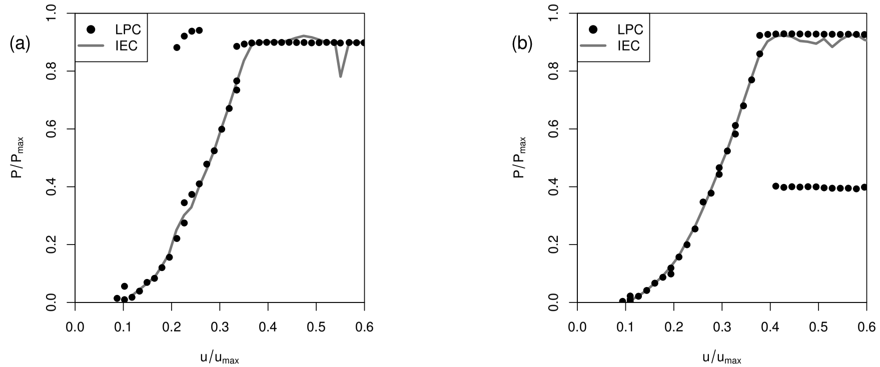

Figure 1: Langevin Power Curve (LPC) of a multi-MW offshore wind turbine. (a) Icing of the nacelle anemometer caused unrealistically high power values for low wind speeds around $u/u_{max} \approx 0.3$. (b) Due to a short disturbance in operation the power output was reduced by the control system for less than 8 h in a month. Despite the short duration of anomalous behavior it is clearly detected by the LPC. A power characteristic similar to IEC 61400 is shown as gray line for comparison in both cases. The turbine in both cases is a 5 MW Senvion 5M in the German offshore wind farm “alpha ventus”.

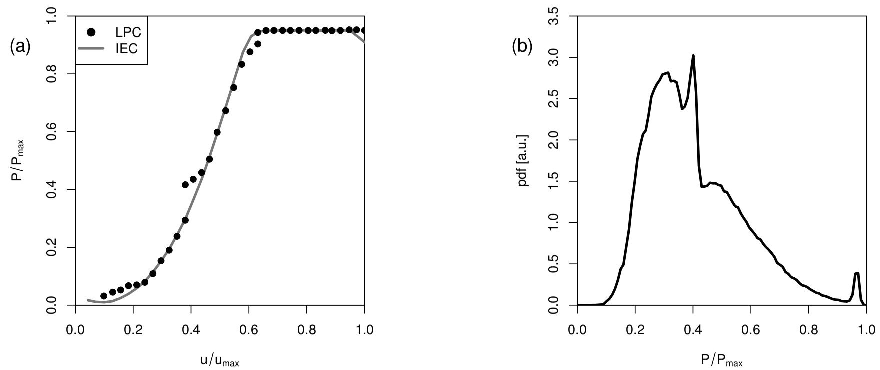

Figure 2: Langevin Power Curve (LPC) of a multi-MW offshore wind turbine. (a) A step in the LPC appears at wind speeds around $u/u_{max} \approx 0.4$, which appears to be connected to the transition from variable-speed to variable-torque operation. A power characteristic similar to IEC 61400 is shown as gray line for comparison. (b) In the power histogram it is visible that this step leads to a certain loss of higher energy production times in favour of lower energy ones.

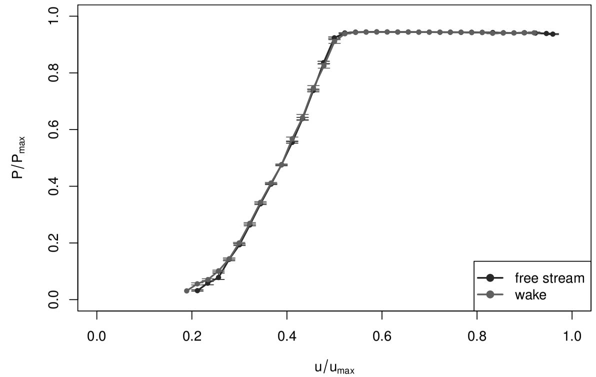

Figure 3: Langevin Power Curves (LPC) of a multi-MW offshore wind turbine. Wind speed was measured by a nacelle-based scanning lidar system [6]. Power performance is shown for free stream (blue line) and wake conditions (red line). Same turbine as in Fig. 1.

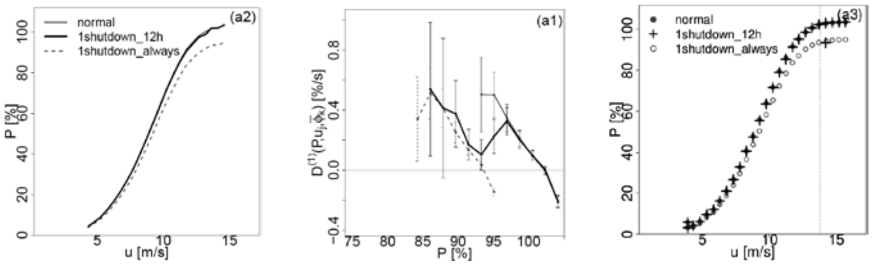

Figure 4: Wind farm performance monitoring by 10 minute averages as in IEC 61400 (left), by the drift coefficient $D^{(1)}$ of eq. (1) (middle), and using the LPC (right). Line styles of the left graphic apply to the middle one as well, here showing clearly a transition between two power performance states. The measured cumulative power output of twelve turbines was used, where the contribution of one turbine was artificially set to zero for 12 h and for the complete time, respectively.

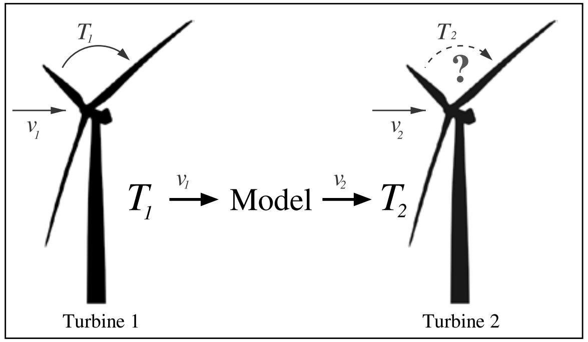

Figure 5: Sketch of the procedure for efficient estimation of fatigue loads on multiple machines. A stochastic model is derived from measurements of wind speed and torque at Turbine 1. Using this model and the wind speed measured at Turbine 2, we are able to model the torque at Turbine 2 in a statistically correct way. From this estimated torque time series we estimate the fatigue loads (see text).

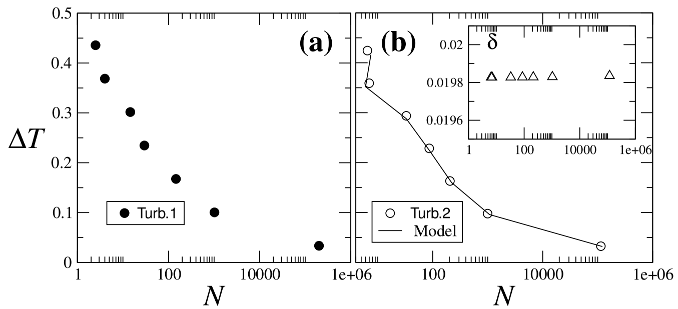

Figure 6: Torque statistics (rainflow counts) at the main shaft of two neighboring multi-MW turbines in the same offshore wind farm. Torque cycle amplitudes ΔT are normalized by the maximum value of the load. Most of the cycles have an amplitude smaller than 0.5, leading to insufficient statistics for higher values. (a) measured torque statistics at turbine 1, (b) torque statistics at turbine 2, both measured (symbols) and reconstructed (solid line) by the stochastic model (1). From turbine 2 only the wind speed time series of the nacelle anemometer was used. The inset shows the relative deviation δ of the estimate with respect to the experimental results. Both turbines are 5 MW Senvion 5M offshore models in the German offshore wind farm "alpha ventus".

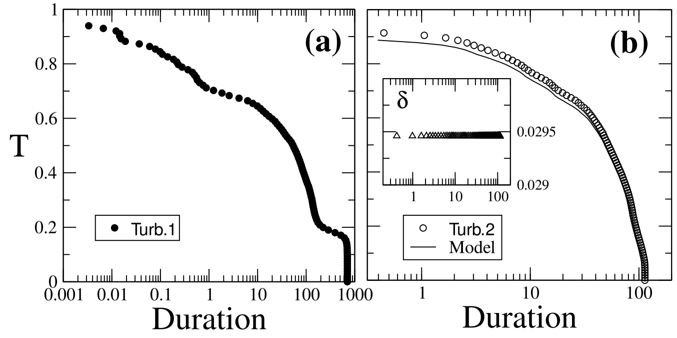

Figure 7: Load duration distribution (LDD) observed for the load time series at (a) Turbine 1 and (b) Turbine 2. While for Turbine 1, the empirical data were used for deriving the model, for Turbine 2 we use the derived model for reconstructing the data and comparing the estimated loads with the observed ones. In the inset, we show the relative deviation δ of the estimate with respect to the results for the measurements.

3.3 Load monitoring in wind farms

A stochastic model following Eq. (1) has been set up for the torque on the main shaft of a multi-MW offshore wind turbine. Here we analyzed again operational data of the 5 MW Senvion 5M offshore wind turbine in the German offshore wind farm "alpha ventus". The torque on the main shaft T is computed from the measurements of the power output and the rotor rotational speed. The model was shown to accurately estimate the load time series from a given, respective wind speed signal. In a next step the model was generalized in order to reproduce the load time series measured at another turbine of the same type within the same wind farm, see Fig. 5. While the stochastic model had been estimated at turbine 1, for the reproduction of the loads at turbine 2 only the wind speed time series of its nacelle anemometer was used. The load statistics as presented in Fig. 6 show very good correspondence [9]. In Fig. 7 we additionally present the respective load duration distributions (LDD) for the same case. Also here, a good correspondence is achieved. The method therefore offers a quick way to obtain load collectives of a turbine in arbitrary wind conditions, once it has been calibrated on a specific turbine type.

The method thus allows to monitor loads in wind farms without any additional measurement equipment. Once the stochastic model has been derived for a certain turbine type, loads are obtained using only available nacelle anemometry. The benefits are apparent for offshore and remote windfarms.

4 Conclusion

New results presented demonstrate an extension of the range of applications for stochastic methods with respect to wind energy systems. The Langevin Power curve turns out to provide accurate turbine-specific information independent of site or inflow-specific conditions.

A considerable extension of the method was achieved by modeling specific load signals in wind turbines. The stochastic model turned out to be transferable between turbines of the same type and still deliver accurate results. This approach allows for an extremely efficient load monitoring from standard measurement signals without the need to install additional monitoring equipment, which is especially important for offshore locations.

For the power performance of a wind farm we showed that even by monitoring only the cumulative power output, the stochastic model can sensitively detect performance anomalies.

Using properly estimated stochastic models, power output and loads can this way be estimated and sensitively monitored both for single turbines and wind farms. The methods presented thus enable the development of extremely efficient, sensitive and reliable monitoring systems.

Acknowledgements

Significant parts of this work have been performed as part of the German offshore research initiative "Research at Alpha Ventus" (RAVE) within the projects "OWEA", "OWEA Loads" and "LIDAR II", as well as in the project "BALTIC I". We thank all of our project partners for the fruitful collaboration, as well as the German Federal Ministry for Economic Affairs and Energy for funding of the initiative.

References

[1] Friedrich, R., Peinke, J., Sahimi, M., and Reza Rahimi Tabar, M., "Approaching complexity by stochastic methods: From biological systems to turbulence," *Physics Reports*, Vol. 506, No. 5, Sept. 2011, pp. 87–162.

[2] Anahua, E., Barth, S., and Peinke, J., "Markovian power curves for wind turbines," *Wind Energy*, Vol. 11, No. 3, 2008, pp. 219–232.

[3] Gottschall, J. and Peinke, J., "How to improve the estimation of power curves for wind turbines," *Environmental Research Letters*, Vol. 3, No. 1, 2008, pp. 015005 (7pp).

[4] Kühn, M., Steinfeld, G., Cheng, P.-W., Schaumann, P., and Neumann, T., "Abschlussbericht des RAVE-Forschungsprojektes Verifikation von Offshore-Windenergieanlagen (OWEA)," Tech. rep., Carl von Ossietzky Universität Oldenburg, Universität Stuttgart, Leibniz Universität Hannover, Deutsches Windenergie-Institut GmbH, 2013.

[5] Kühn, M., "Regelung von Offshore-Windparks durch lokale Leistungsprognose sowie Monitoring der Leistungs- und Belastungscharakteristik (Baltic I)," Tech. rep., ForWind - Carl von Ossietzky Universität Oldenburg, 2014.

[6] Rettenmeier, A., Bischoff, O., Hofsäß, M., Schlipf, D., and Trujillo, J., "Wind Field Analysis Using A Nacelle-Based LiDAR System," *Proceedings of EWEC, Warsaw, 20.-23. April 2010*, Warsaw, 2010.

[7] Kühn, M., Reuter, R., and Cheng, P.-W., "Abschlussbericht des Forschungsprojekts Entwicklung gondelbasierter Lidar-Technologien für die Messung des Leistungsverhaltens und die Regelung von Windenergieanlagen (LIDAR II)," Tech. rep., Carl von Ossietzky Universität Oldenburg, Universität Stuttgart, 2015.

[8] Milan, P., Wächter, M., and Peinke, J., "Stochastic modeling and performance monitoring of wind farm power production," *Journal of Renewable and Sustainable Energy*, Vol. 6, No. 3, 2014, pp. 033119 (29 p.).

[9] Lind, P. G., Herráez, I., Wächter, M., and Peinke, J., "Fatigue Load Estimation through a Simple Stochastic Model," *Energies*, Vol. 7, No. 12, 2014, pp. 8279–8293.

DETECTING CRITICAL SCOUR DEVELOPMENTS AT MONOPILE FOUNDATIONS UNDER OPERATING CONDITIONS

Jannis Weinert
Ramboll Wind[a] and Stuttgart Wind Energy[b],
now Loughborough University
J.Weinert@lboro.ac.uk

Ursula Smolka
Ramboll Wind[a]
Ursula.Smolka@ramboll.com

Björn Schümann
Ramboll Wind[a]

Po Wen Cheng
Stuttgart Wind Energy[b]

[a]: Ramboll Wind, Stadtdeich 7, 20097 Hamburg, Germany
[b]: Stuttgart Wind Energy, University of Stuttgart, Allmandring 5b, 70569 Stuttgart, Germany

Abstract

Early warning systems for critical conditions at offshore wind turbines are needed to reduce maintenance costs and avoid catastrophic failures. Monitoring of the critical scour development at monopile foundations is commonly done with cost-intensive scour depth measurements. The scour condition is regarded critical when the depth exceeds the maximum allowed design scour depth during normal operation or due to a severe storm. This practice can lead to high maintenance costs and potentially unnecessary maintenance activities such as refilling of the scour hole or reconstruction of the scour protection. Instead, the exploitation of the structural reserves of fatigue driven monopile foundation designs stemming from design assumption versus real site conditions is suggested. Damage accumulation is highly influenced by the time behaviour of the transient scouring and real soil properties. This paper elaborates on novel low cost monitoring methods to detect when a scour development is truly critical when taking site conditions into account. A combination of fatigue monitoring and natural frequency supervision is proposed for critical scour identification in the framework of an early warning system.

Keywords

Offshore Wind Turbine, Operation and Maintenance, Monopile, Scour, Structural Health Monitoring, Early Warning System, Natural Frequency

1 Introduction

Unscheduled maintenance activities due to unexpected failures are a key driver of Operation and Maintenance (O&M) costs for offshore wind turbines. Increased turbine sizes and the move farther offshore, increase the risk of potentially significant losses of production. Wind farm operators seek to optimize their maintenance strategy by balancing preventive measures, costly scheduled inspections and remote wind farm surveillance. It is well accepted that continuous condition and health monitoring of the wind turbine could greatly contribute to the mitigation of operational and financial risks related to O&M. In practice, such an early warning system has to fulfil a number of requirements: be failure mode specific, assess the level of degradation or severity of failure, produce reliable alarms that are easy to understand and ideally operate in an automated mode.

This paper addresses unexpected scour development at monopile foundations as a consequence of extreme events, strong currents as well as failures of scour protection as documented in [1] and [2]. Monopiles are the most commonly used support structures used for current European offshore wind projects [3]. Scour is a serious hazard for monopiles, as it can cause a loss of stability. Furthermore the flexibility of the structure increases with this effect. Recent scour research has focused on the prediction of scour development and design of scour protection measures. The remaining uncertainties in predictions for scouring within tidal environments [2] and the substantial costs and susceptibility to failure of scour protection [1] call for continuous monitoring.

In section 2 the suitability of different scour indicators are assessed analytically. Section 3 describes the detailed analysis conducted with structural response calculations for different scenarios. As a result, the suitability of natural frequency monitoring as a critical scour depth indicator is discussed in section 4. Section 5 includes the motivation of monitoring fatigue for scour detection and refers to recently developed load monitoring approaches. The final conclusions are given in section 6.

2 Analytical assessment of scour indicators

From a design perspective, a condition is regarded critical where the structure is prone to loading that exceeds the design resistance, defined by limit states: ultimate (ULS), fatigue (FLS) and serviceability (SLS). Hence, the critical scour depth is a state where due to scouring one of these three limit states is violated. Violation of limit states leads to yielding, fracturing and the loss of the global stability.

Ideally, an indicator value for critical scouring directly reflects the closeness to the limit state that the support structure was designed for. An alarm is raised when the chosen threshold is exceeded. Due to the complexity of the damage mechanisms linked to scour and the consequently changed static and dynamic behaviour of the structure as well as financial and technical limitations of measurement principles, indicators for critical scour depth are indirect. For example, measuring the sour depth (indicator), allows detection of when the design scour depth (threshold) is exceeded. But only in the absence of structural reserves will this lead to a critical condition of the support structure, as defined by the limit state formulations. For optimal maintenance decisions, further information is required to truly asses the criticality.

These considerations lead to desired properties for a critical scour indicator that can be summarized in three categories:

- Criticality
- Measurability
- Uniqueness

Criticality means that the indicator value for critical scouring relates to all affected limit states as directly as possible. For example, the tilt of the pile as SLS can be directly monitored with low cost inclinometers but is not sufficient as an indicator for critical scour depth.

Measurability means that cost-effective and reliable measurement techniques for the indicator exist, delivering acceptable data quality in a robust and maintenance free manner. For example, the FLS of one spot can be directly monitored with strain gauges but the technology lacks robustness in the offshore environment.

Uniqueness of the indicator to describe scour is crucial to allow for root cause detection and enable target-orientated maintenance. For example, a change in the global natural frequency does not necessarily relate to a changed scour depth.

Below, the suitability of the scour depth, the global natural frequency as well as tilting and fatigue variables as indicator values are discussed in view of the above defined criteria. Table 1 gives an overview of the indicators, their ability to identify a critical state, known thresholds, possible detection methods and their uniqueness in detecting scour.

The scour depth S, which is the deviation of the standard mudline level around the monopile, is not directly linked with any failure or serviceability limit state. A common criterion for the allowed scour depth relates to the pile diameter at mudline *D* and can be estimated according to design guidelines ($S < 1.3\,D$ [4]). There are several approaches to measure the scour depth directly via optical methods or float-out devices. No other effect besides scouring or seabed movement is known to affect the scour depth.

The first global natural frequency f_0 will decrease due to increased scouring, leading to changed fatigue life consumption (linked to FLS) and unfavourable resonance effects. There are no universal upper or lower bounds defined for f_0, but the frequency should not coincide with excitation frequencies. Germanischer Lloyd recommends in its guideline [5] that the ratio of a rotor-induced excitation to one of the natural frequencies of the tower shall not be between 0.95 and 1.05. Natural frequencies can be assessed by measuring accelerations and performing modal analysis [6]. f_0 is affected by any stiffness or mass change of the system, e.g. more mass due to marine growth, less mass and stiffness due to corrosion, more or less oscillating added water mass due to changing water levels or a stiffness reduction as result of soil degradation. Furthermore, stiffness changes may occur in a grouted connection, as result of cracks or other structural effects.

The pile head rotation at mudline φ_{head} increases with increasing scour and is directly linked with the SLS. The criterion $\varphi_{\text{head}} < 0.25°$ for the permanent accumulated rotation is listed as an example in the DNV guideline [4] as a serviceability criterion and is usually defined by the turbine manufacturer. Measurement of the non-permanent rotation can provide an indication for the loss of equilibrium and violation of the ultimate limit state. The pile rotation may be measured by an inclinometer at mudline. Similar criteria for the overturning risk as the loss of vertical tangent, zero-toe-kick and maximal displacement at mudline [5] are harder to measure. Soil degradation and the load intensity can affect the pile tilt besides scouring.

Fatigue damage as a result of accumulated cyclic loading changes as the scour hole affects the global natural frequency. The stress cycles adding up to a Damage Equivalent Load (DEL) at selected hot spots can be directly measured with strain gauges and subsequent rainflow counting. The DEL relate to the fatigue limit state via the material S-N curve. The DEL is insufficient for the detection of critical scouring as a number of environmental and operational parameters have an impact on the cyclic loading.

To sum up, none of the presented values is solely capable of satisfying all requirements set out for a critical scour indicator.

3 Simulation study

The effects of scouring on the limit states are manifold. As argued above, a scour indicator cannot be based on a single measurement but requires a combination of different favourable monitoring approaches that relate directly to the limit state formulations of the design. To assess the structural response under scouring quantitatively, detailed load and natural frequency calculations are performed as described below.

Indicator	Criticality	Threshold	Measurability	Uniqueness
S	None	1.3 *D* (design)	Sonar, radar, float-out devices	Yes
f_0	Resonance (fatigue)	±5% of 1P, 3P	Accelerometers and modal analysis	Marine growth, corrosion, water level, soil degradation, grout…
φ_{head}	Overturning	0.25° (design)	Inclinometer at mudline	Load intensity, soil degradation
DEL	Fatigue	S-N curve	Strain gauges, accelerometers	Load composition, various

Table 1: Possible scour indicators

The software used for the simulation study is Ramboll Offshore Structure Analysis Programs (ROSAP), a tool package of programs to design and optimize offshore structures. The core of ROSAP is a finite-element-based program for static and dynamic analysis of spatial frames, truss structures and piping systems. The support structure and the rotor-nacelle assembly are modelled in ROSAP as masses, moments of inertia and eccentricities. Elements are defined as Timoshenko beams considering shear deformations. The soil resistance and stiffness are implemented as a non-linear spring model according to American Petroleum Institute's standard for designing of offshore structures [7]. Natural frequency calculations consider added water masses for all structural parts. Marine growth and corrosion can be implemented and evaluated.

A sensitivity study of the natural frequency is conducted with the Natural Frequency Analysis (NFA) tool of ROSAP, in order to evaluate the impact of other environmental parameters on global natural frequency then the scour. A baseline scenario is defined for scour depth, marine growth, corrosion and water level. These parameters are individually varied up to extreme values.

The impact of scour is evaluated with ULS, FLS, SLS and NFA checks with concept study detail according to current guidelines. In the scope of this research work, distributed hydrodynamic loads are combined with concentrated loads from the wind turbine for ultimate and fatigue loading calculations. Different scour depths are investigated.

The design fatigue uncertainty is evaluated by reruns of FLS simulations with varied settings.

A monopile design of an up-to-date project with a large turbine with >5 MW power and a deep water site is used for this research (Design I). Additionally, validations have been done for ULS, FLS, SLS and NFA calculations for a second realistic monopile design (Design II) with a different specific water depth and mounted turbine type.

4 Natural frequency as scour indicator

The NFA calculations confirm the correlation between natural frequency and developing scour. In Figure 1 the normalized values of the first global natural frequency against normalized scour depth are visualized for designs I and II. Selected results of other natural frequency calculations for scour at monopiles from [8], [9] and [10] are added. The frequency reduction by scouring is of distinctly different sizes for different designs.

The impact of different environmental effects on the natural frequency is investigated and the according results are given in Table 2. The natural frequency reduction by scour is distinctly stronger than for corrosion, water level changes or marine growth. All minor effects together reduce the natural frequency in the order of only one eighth of the scour impact. In addition, a second limited sensitivity study for a design variant confirms the order of the impacts, although the specific values differ.

The correlation of scour and the natural frequency can be used to define a look-up table for identifying scour. Measured natural frequencies can be easily transformed to scour depths, if the function is known for the specific design.

Coinciding scour, corrosion and water level variations are investigated. Lifetime corrosion allowances (0.3 mm/a external, internal 1 mm) and 50 year extreme water levels are combined with scour states from 0 to $1.3\,D$ in a factorial investigation. A linear interpolation between the natural frequency look-up values is assumed for the determination of scour depths. The resulting look-up error due to unknown corrosion and water level states is visualized in Figure 2. The determination of scour depth from frequency measurements can deviate by more than 0.2 *D* in the flat part of the frequency curve near the reference. However, the error is smaller for the more critical larger scour depths where the frequency curve is steeper. The look-up table monitoring approach is mostly conservative with scour depths greater than the real scour depth if other effects interfere.

The results of ULS, FLS, SLS, and NFA calculations with different scour depths give information about the criticality of the natural frequency. In Table 3 the limits of tolerable scour depths are given for the two investigated designs. The support structure designs are fatigue driven and any scour results in an unacceptable fatigue lifetime reduction. The natural frequency change is not the most critical consequence for these designs, but fatigue is dependent on the natural frequency. The specific scour depth limits according to NFA, ULS and SLS checks vary up to 0.4 *D* for the two designs.

All in all, the measurability and uniqueness of the natural frequency are seen as appropriate, but the direct links to the limit state formulations are missing.

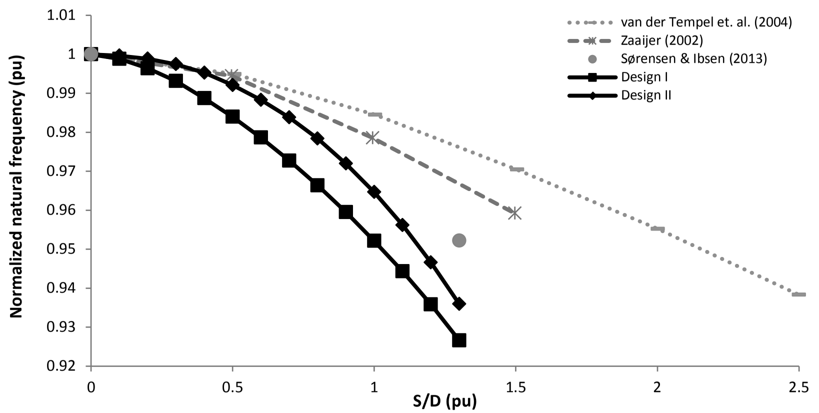

Figure 1: Natural frequency dependency on scour for different designs. Frequency normalized to the reference frequency, scour depth *S* normalized to the monopile diameter *D* and given per unit (pu)

Effect	Parameter limit	Frequency change
Scour	$S/D = 1.3$	$-5.04\,\%$
Corrosion	Lifetime (0.3 mm/a extern and 0.15mm/a intern)	$-0.49\,\%$
Corrosion (intern restricted)	As above, intern ≤1 mm	$-0.37\,\%$
Positive water level change	Upper splash zone border	$-0.18\,\%$
Marine growth	Basic GL [5] recommendation	$-0.03\,\%$
Negative water level change	Lower splash zone border	$+0.14\,\%$

Table 2: Global natural frequency changes for extreme variations of environmental parameters

5 Fatigue monitoring

5.1 Motivation

If amongst the limit state formulations during design, fatigue is the limit state with the least reserves under scouring, a monitoring of the cyclic loading is required to continuously determine the level of criticality. Several assumptions or simplifications in the site specific fatigue load calculation may even lead to a compensation of fatigue damage caused by scouring.

The main parameters that influence the fatigue loads and damage calculation are listed in Table 4 and grouped in five categories. *Systematic* assumptions are in accordance with the procedures described in the design guidelines. Parameters like the Design Fatigue Factor of 3

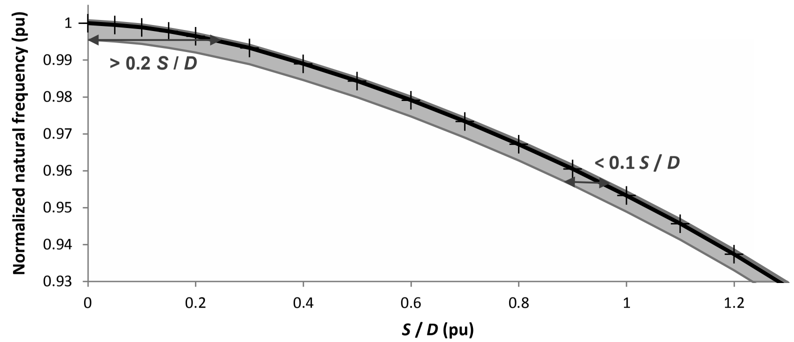

Figure 2: Uncertainty in scour depth look-up from natural frequencies due to unknown corrosion state and water levels, marked as grey area. Natural frequencies normalized to reference, scour depth *S* normalized to pile diameter *D* and given per unit (pu).

Limit state calculation		Scour limit, design I	Scour limit, design II
Fatigue Limit State		$S = 0$	$S = 0$
Natural Frequency Analysis		$S \le 0.5D$	$S < 0.9D$
Ultimate Limit State	Pile displacement	$S < 0.6D$	$S \le 0.6D$
	Steel utilization	$S \le 1.0D$	$S \le 0.7D$
	Soil stability	$S \le 1.1D$	$S \le 0.8D$
Serviceability Limit State		$S \le 1.2D$	$S \le 1.6D$

Table 3: Tolerable scour depths according to different limit states for two investigated modern monopile designs. Scour depth *S* normalized to the pile diameter *D*.

Category	Parameter
Systematic	Turbine and soil model
	Sea state simulation by spectrum
	Rainflow counting
	Palmgren-Miner rule (linear damage accumulation)
	Design Fatigue Factor (DFF) / material factor
	Stress Concentration Factors (SCF)
Design	S-N curves
	Damping
	Pile driving damage
Loads	Mean wind speed and directional distribution
	Wave characteristics
	Misalignment of wind and waves
	Turbine non-availability time
Environment	Scour
	Water level
	Corrosion
	Marine growth

Table 4: Parameters influencing the design Fatigue Limit State (FLS) calculation

are commonly used to introduce desired conservatism in design, but could be omitted when determining the site specific loading with measurements. The *design* category collects specific material characteristics or design choices for the calculation as e.g. the specific S-N curve. The categories *loads* and *environment* include the used wind or wave characteristics and the environmental boundaries as e.g. scour.

To assess the impact of selected parameters on the fatigue damage accumulation, a selection of the listed parameters is varied in a FLS sensitivity study. The parameters are changed in small steps, using realistic value ranges where possible. Figure 3 shows the resulting fatigue damage of the studied variations.

A reduced water level is investigated by an implementation of a less conservative global water level rise. The marginal water level reduction of 0.3 m could already compensate a slight scour with a depth of $S = 0.15D$. Load equivalent turbulence intensities are provided by the turbine manufacturer for a park configuration, which is used in the reference, or for IEC class B turbulence intensity. The damage per year due to wind loads at approx. 0.025 higher turbulence intensity is nearly as high as the one with an extreme scour depth ($S = 0.5\ D$). The equivalent wind loads are defined for a site-specific average mean speed. A variation of this assumed mean speed by approx. $\pm 0.5\ \mathrm{m/s}$ results in a damage change larger than in the case of slight scour. An increase of structural damping by 0.1 percentage points results in a damage reduction of a similar magnitude.

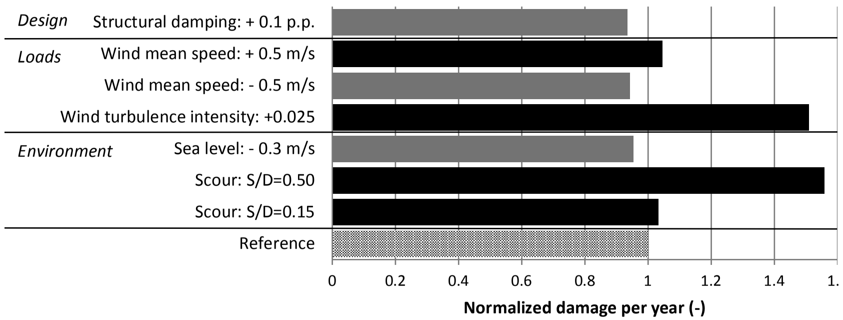

Figure 3: Yearly fatigue damage for selected parameter variations

The sensitivity assessment of design parameters on FLS is idealised and highly dependent on the final structural design and site specific conditions. The study highlights qualitative changes in the resulting fatigue damage, nevertheless. The impact of the stochastic variables on fatigue damage is sufficiently high to justify the fatigue monitoring technique as a method to monitor FLS thresholds in cases of fatigue driven designs.

5.2 Realisation

Application of strain or acceleration sensors below sea level or even below mudline may provide sufficient loading data for a monitoring of fatigue. Continuous and long-term operation of these sensors could be very costly with respect to the maintenance effort. However, more cost-efficient load monitoring approaches have been developed recently by [11], [12] and [13].

If continuous load measurements or estimations are available, stress cycles can be counted to generate a parameter similar to the design process. With the Palmgren-Miner rule damage can be estimated and compared with the corresponding design damage.

Fatigue monitoring can additionally contribute to the opportunity of lifetime extension. This may be reasonable in the opposite case, if the real damage is smaller than the assumed damage calculated in the design.

Fatigue monitoring is linked with the dynamic failure caused by scour for fatigue driven designs. Dynamic load measurement and estimation have been investigated in research projects recently and an adequate measurability with low costs is presumed. Uniqueness for detecting critical scour is not given at all for fatigue monitoring.

6 Conclusions

The suitability of different methods for critical scour monitoring is assessed at two example fatigue driven support structure designs. A global natural frequency look-up approach is found reasonable to monitor critical conditions due to scouring with respect to ULS and SLS. The accuracy of scour depth prediction is good despite the presence of other frequency changing effects. The check on the defined criteria – criticality, measurability, uniqueness – on a scour indicator reveals a lack of a direct link to FLS.

The FLS calculation is based on a number of parameters that lead to conservatism. Different over- or underestimated effects may compensate each other when monitoring fatigue loads at the site. A sensitivity study revealed that fatigue monitoring is suitable to detect structural reserves and allow for temporarily deeper scour depth than the design scour depth without the need for maintenance activities.

A combination of fatigue monitoring and natural frequency supervision is suggested for the detection of critical scour conditions in the sense of ULS, FLS and SLS. However, in order to establish an early warning system using effective thresholds for natural frequency changes and yearly damage accumulation the design conditions of the support structure have to be known.

Future research may focus on the implementation of the suggested combined measurement strategy to check the measurability criterion in more detail. According to in-house experience, fatigue or natural frequency limits are most likely to be driving for upcoming designs of monopile substructures. If extreme loads are decisive, the supposed method will not succeed and other approaches will have to be investigated.

Acknowledgments

This paper is part of student research at Rambøll in the scope of a master's thesis in cooperation with Stuttgart Wind Energy, University of Stuttgart. The authors thank Kolja Müller, Stuttgart Wind Energy, for his contribution as co-adviser of the thesis.

References

[1] M. B. Zaaijer and J. van der Tempel, "Scour protection: a necessity or a waste of money?," *Proceedings of the 43 IEA Topixal Expert Meeting,* 2004.

[2] R. J. S. Whitehouse, J. M. Harris, J. Sutherland and J. Rees, "The nature of scour development and scour protection at offshore windfarm foundations," *Marine Pollution Bulletin,* vol. 62, no. 1, pp. 73-88, 2011.

[3] EWEA, "The European offshore wind industry - key trends and statistics 2014," European Wind Energy Association, Brussels (Belgium), 2015.

[4] DNV GL AS, "Design of Offshore Wind Turbine Structures. Offshore Standard DNV-OS-J101," DNV GL AS, Høvik (Norway), 2014.

[5] GL, "Guideline for the Certification of Offshore Wind Turbines IV-2," GL Renewables Certification, Hamburg (Germany), 2012.

[6] M. El-Kafafy, C. Devriendt, W. Weijtjens, G. De Sitter and P. Guillaume, "Evaluating Different Automated Operational Modal Analysis Techniques for the Continuous Monitoring of Offshore Wind Turbines," *Dynamics of Civil Structures,* vol. 4, pp. 313 - 329, 2014.

[7] API, Recommended Practice for Planning, Designing and Constructing Fixed Offshore Platforms - Working Stress Design, Washington (USA): API Publishing Services, 2007.

[8] J. van der Tempel, M. B. Zaaijer and H. Subroto, "The effects of Scour on the design of Offshore Wind Turbines," *Proceedings of the 3rd International conference on marine renewable energy Marec,* 2004.

[9] M. B. Zaaijer, "Tripod support structure. Pre-design and natural frequency assessment for the 6 MW DOWEC," DOWEC, Delft (Netherlands), 2002.

[10] S. P. H. Sørensen and L. B. Ibsen, "Assessment of foundation design for offshore monopiles unprotected against scour," *Ocean Engineering 63,* 2013.

[11] U. Smolka and P. W. Cheng, "On the Design of Measurement Campaigns for Fatigue Life Monitoring of Offshore Wind Turbines," *Proceedings of the Twenty-third International Offshore and Polar Engineering,* 2013.

[12] H. Braam, T. S. Obdam and T. W. Verbruggen, “Low cost load monitoring for offshore wind farms,” in *International Conference on Noise and Vibration Engineering 2012, ISMA 2012, including USD 2012: International Conference on Uncertainty in Structure Dynamics*, 2012.

[13] N. Perišić and P. H. Kirkegaard, “Low-Cost Tower Root Fatigue Load Estimation for Structural Health Monitoring of Grouted Connections in Offshore Wind Turbines,” *Key Engineering Materials,* Vols. 569-570, pp. 676-683, 2013.

Towards Whole Life-Cycle Costing of Large-Scale Offshore Wind Farms

Mahmood Shafiee, Feargal Brennan, Inés Armada Espinosa

Centre for Offshore Renewable Energy Engineering
Cranfield University, Bedfordshire MK43 0AL, UK
Corresponding author. Email: m.shafiee@cranfield.ac.uk

Abstract This paper presents a whole life cost (WLC) analysis framework for offshore wind farms throughout their lifespan (~25 years). A mathematical tool is developed to evaluate all the costs associated with five phases of offshore wind projects, namely, pre-development and consenting (P&C), production and acquisition (P&A), installation and commissioning (I&C), operation and maintenance (O&M), and decommissioning and disposal (D&D). Several critical factors such as geographical location and meteorological conditions, power rating and capacity factor of wind turbines, reliability of subassemblies, and availability and accessibility of transportation means are taken into account in cost analyses. A net present value (NPV) approach is used to quantify the current value of future cash flows and a bottom-up estimate of the overall cost is obtained. Finally, the model is tested on an offshore 500 MW baseline wind farm project. Our results indicate that the capital cost of wind turbines and their sub-assemblies as well as the installation cost account for the largest proportion of LCC, followed by the O&M costs.

Key Words Whole life cost (WLC); Offshore wind farm; Levelized cost of energy (LCOE), Operation and Maintenance (O&M).

1. Introduction

Along with the growth of the market for offshore wind energy, the investors and developers need to accurately evaluate the feasibility of future offshore wind projects. Presently, the cost per kilowatt hour of electricity generated by onshore wind turbines is approximately 8.66 cents, while offshore wind is estimated to cost 22.15 ¢/kwh (i.e., 2.55 times more expensive than onshore wind) [1]. In order to reduce this extra cost, the impact of some critical factors (e.g. failure rate of wind turbines, water depth, spare parts lead times, weather conditions) on offshore wind project costs needs to be properly quantified. For this purpose, the capital expenditure (CAPEX), operating expenditure (OPEX) and the levelized cost of energy (LCOE) must be calculated by considering all the costs over the project's life cycle, from the pre-development to the decommissioning phase [2].

The life cycle cost (LCC) modelling and analysis of wind power systems has received a significant attention during the last few years due to the growing investment in new wind projects. Several organizations such as European Wind Energy Association (EWEA) and the National Energy Renewables Laboratory (NREL) publish annual statistical reports on wind power generation costs. Kaiser and Snyder [3] addressed all aspects concerning the installation and decommissioning phases of offshore wind projects and then developed a model to calculate the associated costs. The LCC analysis of wind power systems has also been addressed in Nilsson and Bertling [4] and Nordahl [5], however, these works mainly focus on evaluating the operation and maintenance (O&M) costs. A comprehensive methodology for the economic evaluation of the floating offshore wind turbines was recently presented in Castro-Santos and Diaz-Casas [6]. Myhr *et al.* [7] presented an analysis model to compare the cost of electricity produced by various offshore floating wind turbine concepts. Madariaga *et al.* [8] point out that the development of a realistic and accurate method for LCC analysis of offshore wind farms with taking into account all important aspects of project is a very complex task. To the best of authors' knowledge, there is no universal and integrated framework for LCC analysis of offshore wind farms enabling to compare different projects on a same basis. Therefore, it is crucial to develop an enterprise cost analysis model not only to assist stakeholders in evaluating the performance of ongoing projects, but also to help the decision makers undertake long-term profitable investments and make the offshore wind power generation price-competitive with onshore.

This paper aims to present a whole life cost (WLC) analysis framework for offshore wind farms considering all the costs that will be incurred throughout the project life cycle. The key cost drivers of offshore wind projects are identified and a mathematical tool is proposed to evaluate the associated costs. Several critical factors, e.g. geographical location and meteorological conditions, power rating and capacity factor of wind turbines and reliability of subassemblies are taken into consideration in cost analyses. A net present value (NPV) approach is also used to calculate the current value of future cash flows, and then, a bottom-up estimate of the overall cost is obtained.

The rest of this paper is organized as follows. In Section II, the whole life cost analysis framework is presented. In Section III, the model is applied to an offshore baseline wind farm project. In Section IV, the results are presented. Section V concludes our study.

2. Proposed framework

In this Section a "parametric" whole life cost analysis framework for offshore wind farms is presented. The developed model is based on a combined multivariate regression/neural network approach in which the cost experience of completed projects provides a baseline for estimating the costs of future offshore wind projects. The cost drivers of offshore wind projects mainly fall into five categories: pre-development and consenting (P&C), production and acquisition (P&A), installation and commissioning (I&C), operation and maintenance (O&M), and decommissioning and disposal (D&D). These cost categories are then broken down into their constituent elements and a database/spreadsheet is built for each cost element. All costs are estimated based on the current prices data and using a NPV method. In this method, cash flows arising at different points in time are converted to a common reference point (i.e., present time) by using the following formula [9]:

$$\mathrm{NPV}(d,N)=\sum_{t=0}^{N} C_t/(1+d)^t , \quad (1)$$

where C_t , d and N represent, respectively, the cash flow at time t, annual interest rate, and the number of years in which the investment takes place. In what follows, the cost categories are described in details:

2.1. Predevelopment and consenting (P&C)

These costs are related to project management (C_{projM}), legal authorisation (C_{legal}), the surveys conducted ($C_{surveys}$), engineering activities (C_{eng}) and contingencies ($C_{contingency}$). Thus,

$$C_{P\&C} = C_{projM} + C_{legal} + C_{surveys} + C_{eng} + C_{contingency}. \quad (2)$$

2.1.1. Project management

The total cost for project management is usually expressed as a percentage of CAPEX. According to [10], it is estimated to be around 3%, i.e.,

$$C_{projM} = 0.03 \times \mathrm{CAPEX}. \quad (3)$$

2.1.2. Legal authorisation

During the legal authorization process, appropriate documents are provided and some local authorities are contacted and asked for approval. The cost of legal authorization is estimated to be approximately 0.13 percent of CAPEX [11, 12]. Then,

$$C_{legal} = 0.0013 \times \mathrm{CAPEX}. \quad (4)$$

2.1.3. Surveys

Currently, four types of surveys are used for offshore wind farm developments: environmental, coastal processes, sea-bed and metocean conditions. So,

$$C_{surveys} = C_{surv\text{-}EN} + C_{surv\text{-}CP} + C_{surv\text{-}SB} + C_{surv\text{-}MO}, \quad (5)$$

where $C_{surv\text{-}EN}$, $C_{surv\text{-}CP}$, $C_{surv\text{-}SB}$ and $C_{surv\text{-}MO}$ represent the cost of carrying out, respectively, environmental, coastal, sea-bed, and metocean surveys.

2.1.4. Engineering

The engineering cost comprises of the costs associated with main engineering activities ($C_{eng\text{-}main}$) and design verification process ($C_{eng\text{-}verif}$) [10], i.e.,

$$C_{eng} = C_{eng\text{-}main} + C_{eng\text{-}verif}. \quad (6)$$

In this paper, we assume that $C_{eng\text{-}main}$ is the sum of a fixed-base cost (C_{base}) and the term described by an increasing linear function of the installed capacity as follow:

$$C_{eng\text{-}main} = C_{base} + C_{eng\text{-}unit} \times \mathrm{IC}. \quad (7)$$

2.1.5. Contingencies

The contingency cost is considered around 10% of CAPEX [12], i.e.,

$$C_{contingency} = 0.1 \times \mathrm{CAPEX}. \quad (8)$$

2.2. Production and acquisition (P&A)

The P&A cost includes all costs associated with the procurement of wind turbines (C_{WT}), support structures (C_{SS}), power transmission system (C_{PTS}), and the monitoring system ($C_{monitoring}$). Then,

$$C_{P\&A} = C_{WT} + C_{SS} + C_{PTS} + C_{monitoring}. \quad (9)$$

2.2.1. Wind turbines

The total cost of procurement of wind turbines is described as a function of the number of wind turbines being installed (N_{WT}) as follows:

$$C_{WT} = (C_{wt\text{-}mat} + C_{wt\text{-}trans}) \times N_{WT}, \quad (10)$$

where $C_{wt\text{-}mat}$ represents the material costs of a wind turbine with all its constituent sub-systems, and $C_{wt\text{-}trans}$ is the transportation cost of a wind turbine from manufacturing location to installation site. The cost of materials depends on the nominal wind turbine power rating (PR) and is modelled by:

$$C_{wt\text{-}mat} = 3{,}000{,}000 \times Ln(\mathrm{PR}) - 662{,}400. \quad (11)$$

The transportation cost of a wind turbine is calculated by multiplying the average vessel-day required ($N_{v\text{-}d}$) by the daily rate of hiring a vessel (Vr), i.e.,

$$C_{wt\text{-}trans} = N_{v\text{-}d} \times \mathrm{Vr}. \quad (12)$$

2.2.2. Support structures

The cost of a support structure is divided into two parts, one for material costs ($C_{ss\text{-}mat}$) and another one for transport and installation ($C_{ss\text{-}trans}$). Thus,

$$C_{SS} = (C_{ss\text{-}mat} + C_{ss\text{-}trans}) \times N_{WT}. \quad (13)$$

Dicorato *et al.* [13] modelled the cost of materials used for a support structure by:

$$C_{ss\text{-}mat} = 339{,}200 \times \mathrm{PR} \times (1 + 0.02 \times (\mathrm{WD} - 8)) \times \left[1 + 0.8 \times 10^{-6}\left(h\left(\frac{d}{2}\right)^2 - 10^5\right)\right], \quad (14)$$

where h and d represent the hub height and the rotor diameter of a wind turbine in meter, respectively.

2.2.3. Power transmission system

The power transmission system is composed of a number of cables that connect wind turbines to the grid and onshore/offshore substations. So,

$$C_{PTS} = C_{cables} + C_{of\text{-}subs} + C_{on\text{-}subs}. \quad (15)$$

The cables used for power transmission from offshore wind farms are divided into three parts: inter-array (i=1), export (i=2) and onshore (i=3). The cable cost for each part can be calculated by product of the price of unit length of cable ($C_{cable\text{-}unit}$), number of lines (N_{lines}) and the average length of each line (L). So,

$$C_{cables} = \sum_{i=1}^{3} C_{cable\text{-}unit\,i} \times L_i \times N_{lines\,i} + C_{protection}, \quad (16)$$

where $C_{protection}$ represents the cable protection cost which varies depending on the number of wind turbines installed. In this study, a linear regression model is applied on our dataset and the cost of offshore substation is estimated as follow:

$$C_{of\text{-}subs} = 583{,}300 + 107{,}900 \times \mathrm{IC}; \quad \text{for } \mathrm{IC} \geq 100\ \mathrm{MW}. \quad (17)$$

Finally, the cost of onshore substation is considered to be half of the $C_{of\text{-}subs}$ [6, 11], i.e.,

$$C_{on\text{-}subs} \cong C_{of\text{-}subs}/2. \quad (18)$$

2.2.4. Monitoring system

The cost of SCADA and condition monitoring systems (CMSs) for an offshore wind farm depends on the number of wind turbines installed [14]. Then,

$$C_{monitoring} = (C_{SCADA} + C_{CMS}) \times N_{WT}. \quad (19)$$

where C_{SCADA} and C_{CMS} represent the cost of, respectively, SCADA and CMS for a wind turbine.

2.3. Installation and commissioning (I&C)

The I&C phase involves all activities related to the construction of offshore wind farms. The costs incurred at this stage include those related to port ($C_{I\&C\text{-}port}$), installation of the components ($C_{I\&C\text{-}comp}$), commissioning of the wind turbines and electrical system (C_{comm}), and the construction insurance ($C_{I\&C\text{-}ins}$). Hence,

$$C_{I\&C} = C_{I\&C\text{-}port} + C_{I\&C\text{-}comp} + C_{comm} + C_{I\&C\text{-}ins}. \quad (20)$$

2.3.1. Port

Annual fees must be paid to local authorities for the use of port infrastructure, quayside docking, and the permission for crane use [15], which all are assumed to be fixed in this paper ($C_{port\text{-}use}$). In addition, the annual payments to wind farm labourers who carry out project activities must be taken into account ($C_{port\text{-}labour}$). Then,

$$C_{I\&C\text{-}port} = C_{port\text{-}use} + C_{port\text{-}labour}. \quad (21)$$

The port labour cost is calculated by multiplying the average labour-day required ($N_{l\text{-}d}$) by the fixed daily labour rate (Lr), i.e., [16]

$$C_{port\text{-}labour} = N_{l\text{-}d} \times \mathrm{Lr}. \quad (22)$$

2.3.2. Installation of the components

Several operations need to be performed during the installation process of an offshore wind farm project. The cost of installation, according to the type of components installed, is divided into four parts: foundation, wind turbine, offshore and onshore electrical system. Then,

$$C_{I\&C\text{-comp}} = C_{I\&C\text{-f}} + C_{I\&C\text{-wt}} + C_{I\&C\text{-ofsubs}} + C_{I\&C\text{-onsubs}}. \quad (23)$$

2.3.3. Commissioning

Before starting up an offshore wind farm, the wind turbines, electrical systems, SCADA and CMSs are tested to detect early failures as well as improving the reliability [14]. The cost of commissioning (C_{comm}) mainly consists of the costs associated with hiring vessels and crew members which can be calculated similarly as given in Eqs. (12) and (22).

2.3.4. Insurance

The cost of insurance packages during the installation and commissioning phase often varies in accordance with the capacity of offshore wind farm:

$$C_{I\&C\text{-ins}} = C_{ins\text{-unit}} \times IC, \quad (24)$$

where $C_{ins\text{-unit}}$ represents the insurance cost per unit installed capacity (MW).

2.4. Operation and maintenance (O&M)

The O&M cost of an offshore wind farm is divided into two parts, one for the operational expenses (C_O) and the other one for the maintenance expenses (C_M). Thus,

$$C_{O\&M} = C_O + C_M. \quad (25)$$

2.4.1. Operation

The operational expenses of an offshore wind project include the rental/lease payments (C_{rent}), insurance costs ($C_{O\&M\text{-ins}}$) and the transmission charges ($C_{transmission}$). Thus,

$$C_O = C_{rent} + C_{O\&M\text{-ins}} + C_{transmission}. \quad (26)$$

2.4.1.1. Rental (lease)

The amount of rental fees is generally expressed as a fraction of the wind farm's revenue. We assume that rental charges are calculated using:

$$C_{rent} = \ell \times E \times P_E, \quad (27)$$

where $0 < \ell < 1$ is the rental percentage, and E and P_E respectively represent the amount of energy and the average price of unit energy produced by wind farm.

2.4.1.2. Insurance

The operational insurance packages are contracted in order to secure the offshore wind infrastructures against design faults, collision damages or substation outages. The cost of insurance packages can be calculated similarly as given in Eq. (24).

2.4.1.3. Transmission charges

The transmission charges are generally determined according to the capacity of wind farm. Thus,

$$C_{transmission} = C_{transmission\text{-unit}} \times IC. \quad (28)$$

where $C_{transmission\text{-unit}}$ represents the transmission charges per unit installed capacity (MW).

2.4.2. Maintenance

The maintenance costs can be categorized into two types of direct ($C_{M\text{-direct}}$) and indirect ($C_{M\text{-indirect}}$). Then,

$$C_M = C_{M\text{-direct}} + C_{M\text{-indirect}}. \quad (29)$$

2.4.2.1. Direct maintenance cost

Direct maintenance cost consists of the costs related to transport of failed components, maintenance technicians who carry out the repair/replacement actions, and all consumables and spare parts required for wind farm maintenance. In general, the maintenance strategies for offshore wind farms are categorized into two classes: corrective maintenance (CM) and proactive maintenance (ProM). The main difference between these two classes is that the former is carried out after the system failure whilst the latter takes place prior to any failure (i.e., before a failure occurs) [2]. The cost of a CM action varies depending on the type of component being failed. Let *n* represent the number of components in a wind turbine system and denote by $C_{CM\,j}$ the cost of performing a CM action for component *j* (=1, 2, …,*n*). Then,

$$C_{CM\,j} = C_{trans\,j} + C_{labour\,j} + C_{consum\,j}, \quad (30)$$

where $C_{trans\,j}$, $C_{labour\,j}$ and $C_{consum\,j}$ represent respectively the transportation cost, maintenance labour cost and consumables cost. In order to reduce the costs of CM, two proactive strategies, namely scheduled maintenance (SM) and condition-based maintenance (CBM) are employed by wind farm managers. Under SM, the repair tasks are undertaken at predetermined regular intervals, but CBM activities are initiated in response to a specific system condition (e.g. temperature, vibration, noise) [17].

Let λ_j represent the annual failure rate of component *j* and $0 < P_d < 1$ be the probability that an event can be detected at a reasonably long time ahead of failure occurrence. Thus, the annual direct maintenance cost for a wind turbine can be expressed by:

$$C_{M\text{-direct}} = (1-P_d) \times \sum_{j=1}^{n} \lambda_j C_{CM_j} + P_d \times \sum_{j=1}^{n} \lambda_j C_{SM}, \quad (31)$$

where C_{SM} represents the direct cost corresponding to a scheduled maintenance action.

2.4.2.2. Indirect maintenance cost

Indirect maintenance cost consists of the cost of activities that are undertaken to maintain the direct effort involved in providing repair services. The indirect maintenance cost is expressed by the following Equation:

$$C_{M\text{-indirect}} = C_{ind\text{-port}} + C_{ind\text{-ves}} + C_{ind\text{-labour}}, \quad (32)$$

where $C_{ind\text{-port}}$, $C_{ind\text{-ves}}$ and $C_{ind\text{-labour}}$ represent, respectively, the port fees, vessel-hiring costs and maintenance labour costs.

2.5. Decommissioning and disposal (D&C)

The wind turbines at the end of their anticipated operational life are decommissioned, the wind farm equipment are either removed or recycled, the offshore site is cleared and some post-decommissioning monitoring activities are performed. Then,

$$C_{D\&C} = C_{decom} + C_{WM} + C_{SC} + C_{postM}, \quad (33)$$

where C_{decom}, C_{WM}, C_{SC} and C_{postM} represent the costs associated with, respectively, decommissioning, waste management, site clearing and post monitoring.

2.5.1. Decommissioning

The decommissioning cost consists of the costs associated with port preparation ($C_{D\&C\text{-port}}$) and removal operations (C_{remov}). Then,

$$C_{decom} = C_{D\&C\text{-port}} + C_{remov}. \quad (34)$$

2.5.2. Waste management

The main disposal options available for wind farm elements are: reuse, recycle, incineration with energy recovery, and disposal in a landfill site [19]. The materials must be first processed into smaller pieces and then transported to predetermined locations which incur the costs $C_{W\text{-proc}}$ and $C_{W\text{-trans}}$, respectively. A fixed fee has also to be paid when the materials are taken to a landfill ($C_{landfill}$). Then,

$$C_{WM} = C_{W\text{-proc}} + C_{W\text{-trans}} + C_{landfill} - SV, \quad (35)$$

where SV represents the salvage (residual) value of the decommissioned assets.

2.5.2.1. Waste processing

The cost of waste processing varies in accordance with the complexity and size of components. In this paper, $C_{W\text{-proc}}$ is modelled as a function of the total weight of waste material being treated. Hence,

$$C_{W\text{-}proc} = \sum_{j=1}^{n} W_j \times C_{proc\text{-}unit}, \quad (36)$$

where $C_{proc\text{-}unit}$ is the fixed cost of waste processing per ton and W_j is the weight of waste material from component j in tons.

2.5.2.2. Waste transport

The transportation cost is calculated by multiplying the expected number of trucks required to transfer the waste materials by the fixed charge per truck shipment (C_{truck}), i.e.,

$$C_{W\text{-}trans} = \left\lceil \left(\sum_{j=1}^{n} W_j \right) / W_{truck} \right\rceil \times C_{truck}, \quad (37)$$

where W_{truck} represents the capacity of a truck in tons and $\lceil x \rceil$ rounds x to the nearest larger integer.

2.5.2.3. Landfill

We denote by W_j^{R} and W_j^{NR} the weight of, respectively, recyclable and non-recyclable materials for component j, where $W_j^{R} + W_j^{NR} = W_j$. The non-recyclable materials are disposed in a landfill whose associated cost is calculated by multiplying the fixed landfill cost per ton ($C_{landfill\text{-}unit}$) by the total weight of non-recyclable materials disposed, i.e.,

$$C_{landfill} = \sum_{j=1}^{n} W_j^{NR} \times C_{landfill\text{-}unit}. \quad (38)$$

2.5.2.4. Salvage value

The salvage value of the items removed from an offshore wind farm depends on the type, quantity and the quality of their materials and is expressed by following formula:

$$SV = \sum_{j=1}^{n} W_j^{R} \times V_{unit}. \quad (39)$$

where V_{unit} is the salvage value per ton of material.

2.5.3. Site clearance

The cost associated with site clearance is calculated by multiplying the site area in km^2 (A) by the clearance cost per unit area ($C_{SC\text{-}unit}$), i.e.,

$$C_{SC} = A \times C_{SC\text{-}unit}. \quad (40)$$

2.5.4. Post-decommissioning monitoring

The cost of a post-decommissioning monitoring program (C_{postM}) is determined according to several factors such as scale, nature and the conditions of remains [20].

3. Application

In this Section, the proposed whole life cost methodology is applied to an offshore wind farm consisting of 100 5MW wind turbines. This baseline case has so far been studied in several articles (see [6, 7, 12]) and therefore, it enables us to compare our results and validate the model. In order to implement the model, some further aspects of the offshore wind project were identified and are presented briefly below:

- The offshore wind farm is planned to be built at 40km far from shore and 45m water depth. The distance to the onshore grid connection point is 10km. The seabed rental charges equal 2% of the farm's gross revenue. The transmission charges are also paid to National Grid [12].
- The electrical system is composed of 33kV array cables, a 500 MW HVAC transmission system and 220kV export cables. The length of the export cables equals the distance between the installations and the shoreline, whereas the length of the onshore cables is the distance from land to the grid connection point.
- The installation of foundations and wind turbines is performed by multi-purpose self-propelled jack-up vessels. A heavy-lift crane is required for the installation of substation. Some specialized cable-laying vessels are used to lay the power transmission cables underwater.
- The O&M activities are coordinated onshore, but two service vessels are always available to carry out offshore operations. Wind turbines undergo a preventive maintenance (PM) program once a year, whereas the scheduled inspections of foundations and array cables are carried out every five years [20]. CMS detectability level is set at 90%. The costs associated with corrective maintenance are calculated according to the system's failure rate.
- During the five year warranty period from the date of operation, all maintenance and insurance costs are paid by the service contract provider.
- The offshore wind farm is decommissioned at the end of its service life. The waste materials are processed and transported to a scrapyard. Wind turbine tower, jacket and the met-tower are sold to be recycled by industry. About 60% of the nacelle and hub's materials can be reused while recyclability is 40% for other items.

4. Results and discussion

In this Section, the results obtained from our whole life-cycle cost model are presented and discussed. The LCC analysis is carried out in terms of three elements, namely, CAPEX, OPEX and LCOE. The CAPEX consists of the P&C, P&A and I&C costs, whereas the OPEX only includes the O&M costs. Fig. 1 shows the relative contribution of each cost driver to CAPEX and OPEX of the baseline wind farm project. As can be seen, wind turbine costs account for the largest proportion of the CAPEX (29%), followed by foundation costs (25%) and installation costs (19%). On the other side, transmission charges account for the largest proportion of the OPEX (44%), followed by PM costs (22%) and CM costs (16%). The I&C insurance packages cost 2% of the CAPEX, whereas the operational insurance charges represent 9% of the OPEX.

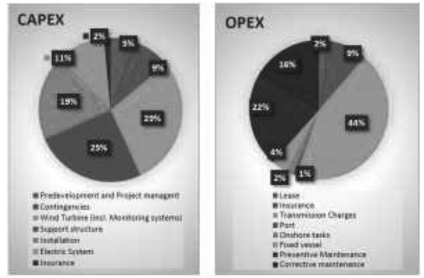

Figure 1. Contribution of each cost driver to CAPEX/OPEX.

The LCOE is determined using the following equation:

$$\mathrm{LCOE} = \sum_{t=1}^{N} \mathrm{C}_t / (1+d)^t \Big/ \sum_{t=0}^{N} \mathrm{E}_t / (1+d)^t, \quad (41)$$

where C_t and E_t represent the cash flow and the yield output at time t, respectively. Our results indicate that the costs incurred over the P&A phase have the greatest impact on LCOE (47%), followed by O&M costs (26%). Among five phases of the project life cycle, the D&D phase contributes the least percentage (~1%) to the LCOE. When comparing the results obtained from our LCC analysis model with other research, very minor differences are found which shows that the model has captured the general trend in the data quite well.

5. Conclusions and topics for future research

The development of a realistic and accurate method for life cycle cost (LCC) analysis of offshore wind farms is a very complex task. In this paper, a parametric whole life cost (WLC) analysis model was developed to identify the key cost drivers of offshore wind projects. The proposed model is based on a combined multivariate regression/neural network approach in which the cost experience of completed/ongoing projects provides a baseline for estimating the costs of future projects. A cost breakdown structure (CBS) was presented to identify various cost elements involved in five phases of offshore wind projects, namely, pre-development and consenting (P&C), production and acquisition (P&A), installation and commissioning (I&C), operation and maintenance (O&M), and decommissioning and disposal (D&D). A database/spreadsheet was also built for each unit cost and several mathematical tools were used to evaluate all costs incurred during the life of the project.

Our results indicated that the capital cost of wind turbines and support structures as well as the costs associated with installation account for the largest portion of overall cost, followed by the O&M costs. The installed capacity of wind farm, distance from shore, and fault detection capability of condition monitoring system were identified as factors having the greatest impact on levelized cost of energy (LCOE). Since the service lifetime of a wind farm is relatively long, the variation of interest rates could also significantly affect the whole project cost. The results of this study not only assist stakeholders in evaluating the performance of ongoing projects, but also help the decision makers to undertake long-term profitable investments and make the electricity generated more price-competitive.

The proposed model will be extended in the nearest future by taking into account more of the factors which are known to affect the cost of electricity generation from offshore wind.

Acknowledgements

The authors gratefully acknowledge the support provided by the owners of several European offshore wind farms during field visits and data collection. The authors would also like to thank James Ingram, Technical Director of Low Carbon at Xodus Group for his valuable advice.

References

[1] U.S. Energy Information Administration, 2014. Levelized cost and levelized avoided cost of new generation resources in the annual energy outlook. Available online: http://www.eia.gov.

[2] Shafiee, M., 2015. Maintenance logistics organization for offshore wind energy: current progress and future perspectives. Renewable Energy 77, 182–193.

[3] Kaiser, M.J. and Snyder, B., 2012. Offshore wind energy cost modelling: installation and decommissioning. Springer, London, UK.

[4] Nilsson, J. and Bertling, L., 2007. Maintenance management of wind power systems using condition monitoring systems—life cycle cost analysis for two case studies. IEEE Transactions on Energy Conversion 22(1), 223–229.

[5] Nordahl, M., 2011. The development of a life cycle cost model for an offshore wind farm. Chalmers University of Technology, Gothenburg, Sweden.

[6] Castro-Santos, L. and Diaz-Casas, V., 2014. Life-cycle cost analysis of floating offshore wind farms. Renewable Energy 66, 41–48.

[7] Myhr, A., Bjerkseter, C., Ågotnes, A. and Nygaard, T.A., 2014. Levelised cost of energy for offshore floating wind turbines in a life cycle perspective. Renewable Energy 66, 714–728.

[8] Madariaga, A., de Alegría, I.M., Martín, J.L., Eguía, P. and Ceballos, S., 2012. Current facts about offshore wind farms. Renewable and Sustainable Energy Reviews 16(5), 3105–3116.

[9] Levitt, A.C., Kempton, W., Smith, A. P., Musial, W. and Firestone, J., 2011. Pricing offshore wind power. Energy Policy 39(10), 6408–6421.

[10] Offshore Design Engineering Ltd., 2007. Study of the costs of offshore wind generation. Renewables Advisory Board and Department of Trade and Industry, UK.

[11] The Crown Estate, 2010. A guide to an offshore wind farm. London, United Kingdom.

[12] Howard, R., 2012. Offshore wind cost reduction pathways project – simple levelised cost of energy model. The Crown Estate, London, United Kingdom.

[13] Dicorato, M., Forte, G., Pisani, M. and Trovato, M., 2011. Guidelines for assessment of investment cost for offshore wind generation. Renewable Energy 36(8), 2043–2051.

[14] Tavner, P., 2013. Offshore wind turbines: Reliability, availability and maintenance. The Institution of Engineering and Technology, London, United Kingdom.

[15] Maples, B., Saur, G. and Hand, M., 2013. Installation, operation, and maintenance strategies to reduce the cost of offshore wind energy. NREL/TP-5000-57403, National Renewable Energy Laboratory, Colorado, USA.

[16] Shafiee, M. and Dinmohammadi, F., 2014. An FMEA-based risk assessment approach for wind turbine systems: a comparative study of onshore and offshore. Energies 7(2), 619–642.

[17] Shafiee, M. and Finkelstein, M., 2015. An optimal age-based group maintenance policy for multi-unit degrading systems. Reliability Engineering and System Safety 134:230–238.

[18] GL Garrad Hassan, 2013. A guide to UK offshore wind operations and maintenance. Scottish Enterprise and The Crown Estate, UK.

[19] Department of Energy & Climate Change (DECC), 2011. Decommissioning of offshore renewable energy installations under the Energy Act 2004, URN 10D/1025, DECC, London, United Kingdom.

[20] Det Norske Veritas (DNV), 2010, Design of offshore wind turbine structures, DNV-OS-J101, Norway.

Variations of the wake height over the Bolund escarpment

presenting author: Julia Lange
co-authors: Jakob Mann, Nikolas Angelou, Jacob Berg, Mikael Sjöholm, Torben Mikkelsen

DTU Wind Energy
Technical University of Denmark
Risø Campus

October 11, 2015

1 Abstract

The here presented results are part of a paper that is submitted and accepted with minor revisions by the Boundary-Layer Meteorology journal.

The wake zone behind the escarpment of the Bolund peninsula in the Roskilde Fjord, Denmark, has been investigated with the help of a continuous-wave Doppler lidar. The instrument measures the line-of-sight wind speed 390 times per second in highly resolved 7-m tall profiles by rapidly changing the focus distance and beam direction. The profiles reveal the detailed and rapidly changing structure of the wake induced by the Bolund escarpment. The wake grows with distance from the escarpment, with the wake height depending strongly on the wind direction, such that the minimum height appears when the flow is perpendicular to the escarpment. The wake increases by 10% to 70% when the wind direction deviates $\pm$ 15° from perpendicular depending on the distance to the edge and to a lesser degree on the method by which the wake height is determined.

Keywords: Bolund, Wake height, Complex flow, WindScanner

2 Introduction

To obtain high quality results in numerical and physical modelling for wind energy purposes, is it important to verify these models with reliable real world measurements [1, 2, 3, 4, 5, 6]. Bolund, an isolated flat-topped hill with steep sides in the Roskilde Fjord, Denmark, (Fig. 1) serves as such a baseline reference for various studies with respect to numerical and physical modelling since a mast based atmospheric experiment was conducted by DTU Wind Energy during winter 2007-2008 [7, 8]. To obtain a more comprehensive understanding of the flow pattern over the Bolund peninsula, especially close to the surface, a complementary field experiment on the Bolund peninsula was conducted. In October 2011 a laser anemometer, in the following called WindScanner [9, 10], was placed on the peninsula 20 m inland from the westward facing escarpment.

3 Approach

The WindScanner, aligned on the 270° axis, was operated during westerly wind conditions to scan the area downstream of the Bolund edge. The atmospheric flow was measured in seven, 7-m high vertical profiles with distances between 8 m and 31 m from the scanning lidar (Fig. 2). In addition to the seven vertical profiles a horizontal arc extending $\pm$ 60° was scanned 120 m away from the instrument. The line-of-sight wind speeds of the eighth profile were used to determine the undisturbed inflow wind speed and wind direction.

While westerly wind directions prevailed, lidar measurements were recorded continuously during an almost 24 hour long measurement period.

Figure 1: Photo of Bolund, taken south of the peninsula.

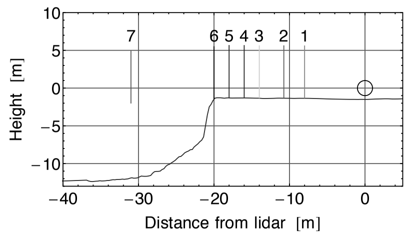

Figure 2: The position and height of the 7 vertical profiles scanned by the lidar relative to the Bolund escarpment. The position of the WindScanner itself is indicated by the circle.

4 Method

The characteristic of the escarpment-induced wake height is further investigated by identifying the boundary between the turbulent wake layer and the freestream flow above. Due to the high measurement-sampling rate a precise determination of the interface between the two distinctly different layers is possible. We determine the wake height δ using three different methods.

1. The first approach determines the displacement thickness, δ_1, that is defined as the distance that the boundary layer is displaced to compensate for the reduction in flow rate on account of the wake formation, where $u(z)$ is the line-of-sight wind speed at height z and u_0 is the freestream velocity [11]

$$\delta_1 = \int_0^\infty \left(1 - \frac{u(z)}{u_0}\right) dz. \qquad (1)$$

2. The second approach identifies the height of the maximum gradient of the line-of-sight wind speed, δ_2, of each vertical scan [12, Sect. 2.2.2]

$$\delta_2 = \arg\max_z \left[\frac{du(z)}{dz}\right]. \qquad (2)$$

3. The third approach identifies the height at which the average between the integral of the two atmospheric layers is the greatest, δ_3, which resembles [13] and [12, Sect. 2.2.3]. Here, z_{top} is the top of the profile,

$$\delta_3 = \arg\max_z \left[\frac{1}{z_{top} - z}\int_z^{z_{top}} u(z)dz - \frac{1}{z}\int_0^z u(z)dz\right]. \qquad (3)$$

The results of the wake height identifications of all three methods are presented in Fig. 3. All three methods manage to identify a wake height, although the actual height differs between the methods. Method 1 gives the highest value of the wake heights.

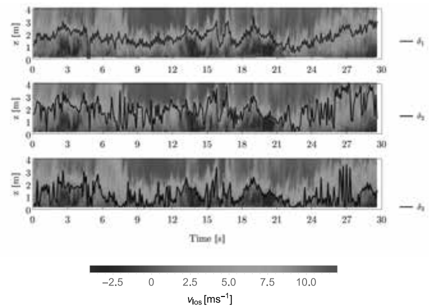

Figure 3: The line-of-sight projected wind speed of profile 3, 12 m away from the WindScanner lasting for 30 s with the defined wake heights using three different methods.

The calculated wake height for each profile location can be placed in relation to the undisturbed wind direction and speed (Fig. 4). With increasing distance from the escarpment, the wake heights show a stronger dependence on the wind direction. The lowest wake heights of every profile is located at a wind direction of 270°. Depending on the distance from the escarpment the wake height increases between 10% and 80% when the wind direction deviates from west, either to the north or the south ± 15°. At larger direction deviations the height seems constant.

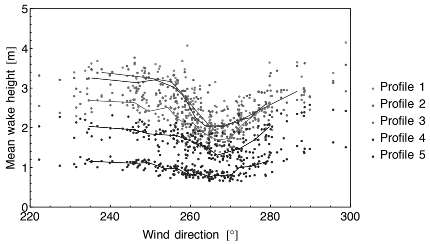

Figure 4: Dependence of the determined wake height and the wind direction. The solid lines depict the average wake height. The profile number increases with increasing distance from the WindScanner. The wake height is calculated through the definition of the displacement thickness.

5 Conclusion

The new remote sensing based wind profile measurements provide a unique data set for validation of unsteady flow modelling over complex terrain for wind energy. Based on the analysis of the high frequency atmospheric measurements with a rapidly scanning continuous-wave Doppler lidar a relationship between the escarpment induced wake height and the wind direction could be shown.

References

[1] P.S. Jackson and J.C.R Hunt. Turbulent flow over a low hill. *Quarterly Journal of the Royal Meteorological Society*, 101:929–955, 1975.

[2] J.C.R. Hunt, S. Leibovich, and K.J. Richards. Turbulent shear flows over low hills. *Quarterly Journal of the Royal Meteorological Society*, 114:1435–1470, 1988.

[3] Fotini Katopodes Chow and Robert L. Street. Evaluation of Turbulence Closure Models for Large-Eddy Simulation over Complex Terrain: Flow over Askervein Hill. *Journal of Applied Meteorology and Climatology*, 48(5):1050–1065, May 2009.

[4] F. A. Castro, J. M. L. M. Palma, and A. Silva Lopes. Simulation of the Askervein Flow. Part 1: Reynolds Averaged Navier–Stokes Equations (ke Turbulence Model). *Boundary-Layer Meteorology*, 107(3):501–530, 2003.

[5] A. Silva Lopes, J. M. L. M. Palma, and F. A. Castro. Simulation of the Askervein flow. Part 2: Large-eddy simulations. *Boundary-Layer Meteorology*, 125(1):85–108, July 2007.

[6] B. Conan. *WindResource Assessment in Complex Terrain by Wind Tunnel Modelling*. PhD thesis, 2012.

[7] A. Bechmann, J. Berg, M.S. Courtney, H.E. Jørgensen, J. Mann, and N.N. Sørensen. The Bolund Experiment : Overview and Background Risø-R-Report. Technical Report July, 2009.

[8] J. Berg, J. Mann, A. Bechmann, M.S. Courtney, and H.E. Jørgensen. The Bolund Experiment, Part I: Flow Over a Steep, Three-Dimensional Hill. *Boundary-Layer Meteorology*, 141(2):219–243, July 2011.

[9] M. Sjöholm, N. Angelou, P. Hansen, K. H. Hansen, T. Mikkelsen, S. Haga, J.A. Silgjerd, and N. Starsmore. Two-Dimensional Rotorcraft Downwash Flow Field Measurements by Lidar-Based Wind Scanners with Agile Beam Steering. *Journal of Atmospheric and Oceanic Technology*, 31(4):930–937, April 2014.

[10] N. Angelou, J. Mann, M. Sjöholm, and M. Courtney. Direct measurement of the spectral transfer function of a laser based anemometer. *Review of Scientific Instruments*, 83(3):33111, 2012.

[11] J.O. Hinze. *Turbulence*. McGraw-Hill series in mechanical engineering, 1975. ISBN: 0070290377.

[12] S. Emeis, H.P. Frank, and F. Fiedler. Modification of air flow over an escarpment. Results from the Hjardemål experiment. *Boundary-Layer Meteorology*, 74(1-2):131–161, April 1995.

[13] K. J. Davis, N. Gamage, C. R. Hagelberg, C. Kiemle, D. H. Lenschow, and P. P. Sullivan. An Objective Method for Deriving Atmospheric Structure from Airborne Lidar Observations. *J Atmos Ocean.*, 17(11):1455–1468, November 2000.

Comparison of full scale and wind tunnel measurements of the spatial distribution of turbulence components over the Bolund Island

Cuerva, A.
DAVE
alvaro.cuerva@upm.es

Gallego-Castillo, C.
DAVE
cristobaljose.gallego@upm.es

Lopez-Garcia, O.
DAVE
oscar.lopez.garcia@upm.es

Pérez, J.
IDR
javier.perez@upm.es

Yeow, T. S.
IDR
teeseong.yeow@upm.es

Universidad Politécnica de Madrid, ETSI Aeronáutica y del Espacio, E-28040 Madrid, Spain

Abstract:

We present experimental spatial distributions of turbulence intensity components over a 1:115 scale model of the Bolund hill. Our measurements are determined in a boundary layer wind tunnel (WT) without stratification. Our results are compared with full scale (FS) ones. The FS results are obtained from the analysis of the database provided by RISØ-DTU after the Bolund experiment. This experiment was conducted by them during a 3-month period in the winter of 2007-2008. Three component time resolved hotwire anemometry (3CHW) and two component particle image velocimetry (PIV) are used in our experiment in order to explore the dependence of the results on the experimental technique.

Keyword

Bolund experiment, atmospheric boundary layer, wind tunnel, particle image velocimetry, hotwire anemometry.

1 Introduction

Bolund is a hill of about 130 m$\times$75 m$\times$12 m, surrounded by water with a long uniform fetch for most of the upstream directions of interest. Due to the number and quality of sensors deployed during the Bolund experiment campaing and the ammount of numerical flow modellers involved, the Bolund experiment is probably the most relevant test case of flow models oriented to wind energy analysis, in this case, over highly complex terrains, in neutral conditions and non-affected by Coriolis forces. The mentioned FS conditions make the Bolund test an ideal case for wind tunnel modeling. Several numerical and physical models have been applied during the Bolund experiment and also after it, Bechmann et al. [2, 3], Berg et al. [4], Prospathopoulos et al. [10], Yeow et al. [15], Conan et al. [6].

One of the main geometric characteristics of Bolund is the escarpment facing westerly winds (see figure 5.1). For westerly winds, the geometry of Bolund guarantees that flow detaches at the edge of the escarpment, provided a sufficiently large Reynolds number. The long (in the mean flow direction) flat top ensures reattachment of the flow on the island. For this direction, the lee side of the hill presents a slope with a maximum inclination around -40°, leading as well to intermittent recirculation patterns. The existence of detachment at the escarpment has been verified by full-scale measurements of intermittent recirculation patterns downstream of the escarpment edge (see Mann et al. [9] and figure 13 in Berg et al. [4]). Intermittent recirculation patterns have been also visualized by means of PIV in wind tunnel, for the 270° wind direction,Yeow et al. [14], [15].

Most of the published results are focused on the values of mean speed and turbulent kinetic energy at the locations where the met mast were installed in the FS experiment (indicated by Mn, $n = 1,..,8$ in figure 5.1). Our interest is now in how the turbulent kinetic energy is distributed among the velocity components (what is relevant for wind turbine response), and to which extent our wind tunnel experiment can reproduce these distributions. Aimed to put some light on these questions, we have calculated metrics of the bias of the WT results respect to the FS ones. We have calculated the bias related to full sacle values in the determination of different statistical flow parameters, from measuments taken with the two velocimetry techniques and for two test Reynolds numbers.

2 Approach

Since we are specially concerned in how the turbulent kinetic energy (TKE) is distributed among the velocity components, the accuracy in the determination of the different components of the instantaneous flow velocity is a must for us. This is why we have extremely cared about the positioning and orientation of the sensors (3CHW probe, PIV camera and laser head) and the calibration process, see figure 5.2. (left). With this regard, we have developed a new directional calibration algorithm for 3CHW probes which leads to a higher directional accuracy. In figure 5.2. (right), we present results for the inclination flow angle, Γ_P, versus the direction flow angle, Θ_P, determined by the 3CHW probe during one of our directional calibration tests.

The results obtained after applying the new calibration method (Measured Directional) compare better with the true values (Geometric) than the results determined by means of the standard calibration algorithm (Measured RMS, root mean squared) in the mentioned figure.

The surface finishing of the mock-up is smooth. The front area of the mock-up is estimated to be less than 2% of the test section area, so blockage effects were expected to be minimized. No additional boundary layer (BL hereafter) generators were used. The floor along the fetch was made out of plywood without any added roughness elements. During the wind tunnel test, the 3CHW probe was sampled at 8 kHz during 130 s. 3 kHz low-pass hardware filtering was used when required. During the PIV test, 1000 image pairs were sampled during approximately 6 minutes. The characteristic size of the sensing part of the 3CHW was about 1 mm, whereas the size of the PIV interrogation window was well below this value.

3 Main results

The flow field in the empty test section of our WT has been measured using three techniques (PIV, 2CHW and 3CHW) to have redundancy measurements in order to cross check the quality of the results. The velocity profiles from the empty WT were used as reference inflow conditions. Reference measurements were taken at the two test Reynolds numbers based in the maximum height of the island, h, and the upstream speed at this height, U_h, $\mathrm{Re}_{h1} = 4.15\times10^4$ and $\mathrm{Re}_{h2} = 8.21\times10^4$. The main characteristics of the inflow boundary layer are presented in table 1 and in figure 5.3. From the z_0 values reported in table 1, a roughness Reynolds number $u_* z_0 \nu^{-1} \approx 0.21$ was adopted. Thus, the inflow in our wind tunnel should be considered transitionally rough, taking into account the lower limit of the fully rough regime, $u_* z_0 \nu^{-1} = 5$, and the upper limit of the fully smooth one, $u_* z_0 \nu^{-1} = 0.2$, as indicated in Bowen [5], although in Snyder and Castro [12] the lower limit for the fully rough regime is reduced down to $u_* z_0 \nu^{-1} = 1$ and even down to $u_* z_0 \nu^{-1} = 0.5$, for certain roughness geometries. Similar conditions were described for the wind tunnel simulations of Askervein in Teunissen et al. [13] where values $u_* z_0 \nu^{-1} = 0.16, 0.54$ and 1.7, respectively, were declared; or in Røkenes and Krogstad [11], where a value $u_* z_0 \nu^{-1} = 0.13$, well within the smooth regime, was reported. As in the mentioned experiments, the present case should be understood as the simplest possible reference case. One of the weak points of our experimental set-up, related to this low roughness value, is that the boundary layer height of our wind tunnel is only two times the height of the island (see value $h^{-1}\delta \approx 2$ in table 1) whereas in the FS case is much larger. One consequence is that in the full-scale BL, the upstream reference point, $z = 5$ m, is well immersed in the constant flux layer and the inflow TKE is homogeneous in z direction, whereas in our wind tunnel it is not (at the equivalent scaled $z = 5/115$ m height, as can been seen in figure 5.3). Some possible effects of the reported low value for $u_* z_0 \nu^{-1}$ are discussed in Yeow et al. [15]of.

We analyze the flow field for a 270° wind direction and we present results along transects at two heights ($z = 2$ m and $z = 5$ m a.g.l) along line B in the Bolund community jargon, see figure 5.1.

In figures 5.4, 5.5 and 5.6 we present the values of the longitudinal, lateral and vertical turbulence intensities, respectively. The results are normalized with the corresponding value at the reference upstream location ($z = 5$ m). The results are presented for transects at $z = 2$ m and $z = 5$ m height a.g.l, the two mentioned test Reynolds numbers and for the 3CHW and PIV techniques. The full scale results are also indicated for comparison purposes. The velocity components are expressed in the Bolund reference system to allow the comparison between the two component PIV measurement, 3CHW and full-scale results.

The evolution of the normalized increment of TKE for line B and westerly winds presented in previous works (see Yeow et al. [15] and Bechmann [1]) showed a large increment of TKE in M6 location, mainly at $z = 2$ m height, moderated values in M3 locations, and larger values again in the lee side, in M8, in this case at $z = 5$ m height. These patters are also reproduced by the parameters $I_{u_i} I_{u_i05}^{-1}$ in figures 5.4, 5.5 and 5.6. Our PIV results reproduce the high values of the three parameters $I_{u_i} I_{u_i05}^{-1}$ around M7. These high values are due to very reduced speed values (in front of the escarpment at low heights) rather than to high values of the standard deviations of the velocity components.

In figures 5.7 and 5.8 we present the value of the ratios of the standard deviations of the velocity component fluctuations. In the case of the normalized turbulence intensity, I_v/I_{v05}, and the ratio, σ_v/σ_u, no-results for PIV are presented since our PIV technique is not stereo PIV, and the v component of the flow velocity is not resolved. As in the cases of the normalized turbulence intensities, the velocity components are expressed in the Bolund reference system to allow the comparison between the two component PIV measurement, 3CHW and full-scale results.

In tables 2 and 3 we present the bias of our WT results related to the FS results at the met mast locations, according to the expression

$$\epsilon_{I_{u_i}} = 100\frac{I_{u_i}I_{u_i05}^{-1}\big|_{WT} - I_{u_i}I_{u_i05}^{-1}\big|_{FS}}{\big|I_{u_i}I_{u_i05}^{-1}\big|_{FS}}, \tag{3.1}$$

for the normalized turbulence intensities, and

$$\epsilon_{\sigma_{u_i}\sigma_u^{-1}} = 100\frac{\sigma_{u_i}\sigma_u^{-1}\big|_{WT} - \sigma_{u_i}\sigma_u^{-1}\big|_{FS}}{\big|\sigma_{u_i}\sigma_u^{-1}\big|_{FS}}, \tag{3.2}$$

for the ratios of the standard deviations of flow velocity fluctuations.

After observing the figures 5.4, 5.5 and 5.6, and the table 2, it is evident than the worst predicted location at $z = 2$ m is M6 for almost all the analyzed parameter. This was also a general conclusions for most of the models compared in the Bolund blind experiment, see Bechmann [1]. One possible reason for this mismatch is that the mock-up does not reproduce the sharpness of the real escarpment edge. More information can be found in Yeow et al. [15]. The values in M8 are also poorly predicted in general. Both locations, M6 and M8 are affected by flow detachment processes from the escarpment edge and the lee side, respectively.

The influence of the test Reynolds number and the used experimental technique on the results has been analyzed by comparing the mean of the absolute bias values for met mast M6, M3 and M8, for both heights, $z = 2$ m and $z = 5$ m, for each experimental case. The results for the three normalized turbulence intensities, $I_{u_i}I_{u_i05}^{-1}$, the ratio of sigmas, $\sigma_w\sigma_u^{-1}$, speed-up, ΔS, and normalized increase of TKE, $\Delta\bar{k}$, are presented in table 4.

The results in table 4 indicate that some differences exist between PIV and 3CHW techniques. The PIV technique produces lower values of the mean value of the absolute bias for some parameters such as I_w/I_{w05} and $\Delta\bar{k}$. The differences between the two Reynolds number cases are neither so evident nor so systematic, but in the case of $\Delta\bar{k}$, where the test at higher Reynolds number leads to a mean value of the absolute value of the bias in the determination of $\Delta\bar{k}$ about 5 to 7 percentage points lower (see Lim et al. [8] for effects of Reynolds number in the determination of second order statistics of flow velocities around sharp edged bodies). Table 4 indicates that typical absolute values of the bias in our wind tunnel for the three normalized turbulence intensities (longitudinal, lateral and vertical) are 35%, 42% and 42% respectively. These values are close to two times the typical absolute bias value for the speed-up (20%). This is an expected result since turbulence intensities involve the calculation of second order statistics of velocity component fluctuations. We put the focus on the low value of the ratio $\sigma_w\sigma_u^{-1}$ (14%) which indicates that the relative value of velocity fluctuation components that form the TKE is better predicted than the value of the components themselves.

4 Conclusions

We have measured the flow field over a 1:115 scale model of the Bolund hill in our boundary layer wind tunnel. Two experimental techniques: three components hotwire anemometry and two components particle image velocimetry, have been used in order to detect any dependence of the measurements on the technique. Additionally the tests have been run at two Reynolds numbers. Different statistical flow parameters have been compared with full scale values and the corresponding biases have been determined.

The bias results show that, for the normalized turbulence intensities, the bias values are higher (as expected) for $z = 2$ m than for $z = 5$ m, ranging from the largest bias (-66.9%) for I_w/I_{w05} in M6 at $z = 2$ m to the lowest bias (6.8%) for I_w/I_{w05} in M6 at $z = 5$ m. The predictions of the ratios $\sigma_{u_i}\sigma_u^{-1}$ are rather good, meaning that the energy of the fluctuation of one flow velocity component relative to another is well captured. The PIV predictions are better for some parameters such as I_w/I_{w05} and $\Delta\bar{k}$. Systematic differences in the bias for the two analyzed Reynolds numbers are only detected for $\Delta\bar{k}$.

5 Acknowledgments

This work was carried out as a part of the activities supported by the Spanish Ministerio de Economía y Competitividad, within the framework of the ENE2012-36473, TURCO project (Determination of the Spatial Distribution of Statistic Parameters of Flow Turbulence over Complex Topographies in Wind Tunnel) belonging to the Spanish National Program of Research (Subprograma de investigación fundamental no orientada 2012). The authors wish to thank the technical staff in IDR-UPM for their contribution. The authors also wish to thank VKI for the valuable collaboration and RISØ-DTU for the full-scale data from the Bolund experiment.

References

[1] A. Bechmann. Presentations from "The Bolund Experiment: Workshop" 3-4$^{\rm th}$ December 2009. Technical Report Risø-R-1745(EN), Risø, 2010.

[2] A. Bechmann, J. Berg, M. S. Courtney, J. Jørgensen, H.E. Mann, and N. N. Sørensen. The Bolund Experiment: Overview and Background. Technical Report Risø-R-1658(EN), Risø, 2009.

[3] A. Bechmann, N. N. Sørensen, J. Berg, J. Mann, and P. E. Rethore. The Bolund Experiment, Part II: Blind Comparison of Microscale Flow Models. *Boundary-Layer Meteorology*, 141(2):219–243, 2011. doi: 10.1007/s10546-011-9637-x.

[4] J. Berg, J. Mann, A. Bechmann, M. S. Courtney, and H. E. Jørgensen. The Bolund Experiment, Part I: Flow Over a Steep, Three-Dimensional Hill. *Boundary-Layer Meteorology*, 141(2):219–243, 2011. doi: 10.1007/s10546-011-9636-y.

[5] A. J. Bowen. Modelling of Strong Wind Flows over Complex Terrain at Small Geometric Scales. *Journal of Wind Engineering and Industrial Aerodynamics*, 91:1859–1871, 2003. doi: 10.1016/S0167-6105(00)00046-5.

[6] B. Conan, Ch. Ashvinkumar, S. Aubrun, J. van Beeck, J. Hämäläinen, and A. Hellsten. Experimental and Numerical Modelling of Flow over Complex Terrain: The Bolund Hill. *Boundary-Layer Meteorology*, 2015. doi: 10.1007/s10546-015-0082-0.

[7] F. E. Jørgensen. How to measure turbulence with hot-wire anemometers-a practical guide. Technical report, DANTEC Dynamics, 2002.

[8] H. C. Lim, I. P. Castro, and R. P. Hoxey. Bluff Bodies in Deep Turbulent Boundary Layers: Reynolds-Number Issues. *Journal of Fluid Mechanics*, 571:97–118, 2007. doi: 10.1017/S0022112006003223.

[9] J. Mann, N. Angelou, T. Mikkelsen, K. H. Hansen, D. Cavar, and J. Berg. Laser Scanning of a Recirculation Zone on the Bolund Escarpment. In *The Science of Making Torque from Wind, October, 9-11, Oldenburg*, 2012.

[10] J. M. Prospathopoulos, E. S. Politis, and P. K. Chaviaropoulos. Application of a 3D RANS Solver on the Complex Hill of Bolund and Assessment of the Wind Flow Predictions. *Journal of Wind Engineering and Industrial Aerodynamics*, 107:149–159, 2012. doi: 10.1016/j.jweia.2012.04.011.

[11] K. Røkenes and P. A. Krogstad. Wind Tunnel Simulation of Terrain Effects on Wind Farm Siting. *Wind Energy*, 12:391–410, 2008. doi: 10.1002/we.310.

[12] W. H. Snyder and I. P. Castro. The Critical Reynolds Number for Rough-Wall Boundary Layers. *Journal of Wind Engineering and Industrial Aerodynamics*, 90:41–54, 2002. doi: 10.1016/S0167-6105(01)00114-3.

[13] H. W. Teunissen, M. E. Shokr, A. J. Bowen, C. J. Wood, and D. W. R. Green. The Askervein Hill Project - Wind-Tunnel Simulations at 3 Length Scales. *Boundary-Layer Meteorology*, 40(1-2):1–29, 1987. doi: 10.1007/BF00140067.

[14] T. S. Yeow, A. Cuerva, B. Conan, and J. Pérez. Wind Tunnel Analysis of the Detachment Bubble on Bolund Island. In *The Science of Making Torque from Wind, October, 9-11, Oldenburg*, 2012.

[15] T. S. Yeow, A. Cuerva, and J. Pérez-Alvarez. Reproducing the Bolund experiment in wind tunnel. *Wind Energy*, 18(1):153–169, 2015. doi: 10.1002/we.1688.

Appendix. Figures and tables

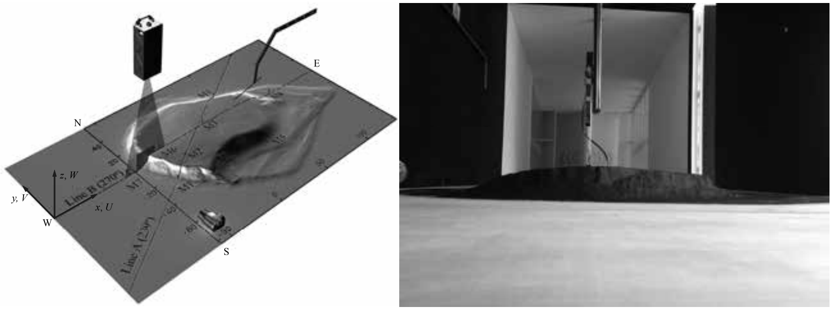

Figure 5.1: Left: Mounting of the 3CHW probe 55P91 and its support, see [7]. $[x, y, z]$ is the Bolund reference system. Right: View of the Bolund mock-up in the ACLA16 wind tunnel, seen from west.

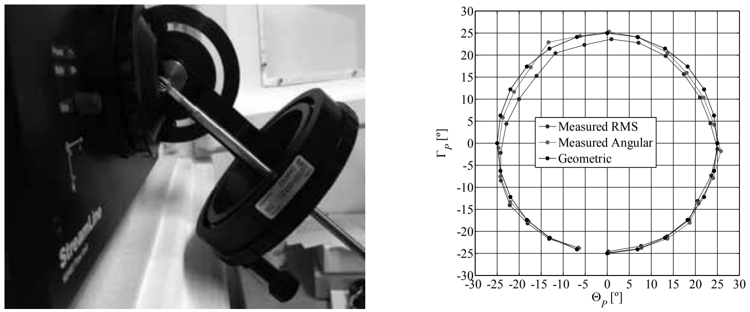

Figure 5.2: Left: The used 3CHW probe DANTEC 55P91 during a directional calibration test in our ACLA16 WT. Right: Inclination angle Γ_P versus direction angle Θ_P reproduced during a directional calibration test.

		Re_{h1}		Re_{h2}	
	Full-scale	3CHW	PIV	3CHW	PIV
δ [m]	-	0.220	-	0.210	-
u_* [m/s]	-	0.293	0.306	0.572	0.565
u_{*05} [m/s]	0.47	0.267	0.247	0.520	0.484
$z_0 \times 10^5$ [m]	60	1.08	1.02	0.54	0.59
$\hat{\theta} \times 10^3$ [m]	-	20.3	-	18.1	-
$h^{-1}\delta$	-	2.148	-	2.050	-
$I_u\|_{h_0} \times 10^2$	12.0	10.0	9.5	9.2	9.4
$I_v\|_{h_0} \times 10^2$	8.0	7.1	-	6.6	-
$I_w\|_{h_0} \times 10^2$	5.0	5.5	4.9	5.1	4.7
$I_u\|_{h} \times 10^2$	-	0.075	0.073	0.068	0.074
$I_v\|_{h} \times 10^2$	-	5.4	-	5.0	-
$I_w\|_{h} \times 10^2$	-	4.3	4.3	4.0	3.9
$\sigma_v/\sigma_u\|_{h_0}$	0.76	0.70	-	0.71	-
$\sigma_w/\sigma_u\|_{h_0}$	0.46	0.54	0.52	0.55	0.51
$h^{-1}L_u^x$	-	3	-	3.5	-
$U_\delta\hat{\theta}\nu^{-1} \times 10^{-4}$	-	1.00	-	1.80	-
$u_* z_0 \nu^{-1}$	18	0.212	0.208	0.205	0.226
$\mathrm{Je} = h\, z_0^{-1} \times 10^{-4}$	1.96	0.94	1.00	1.90	1.70

Table 1: Main characteristics of the undisturbed inflow boundary layer for $\mathrm{Re}_{h1} = 4.15 \times 10^4$ and $\mathrm{Re}_{h2} = 8.21 \times 10^4$. The lengths δ and z_0 for the wind tunnel simulations are shown in WT scale. The declared interval for the FS Reynolds number is $4.25 \times 10^6 \leqslant \mathrm{Re}_h \leqslant 10.2 \times 10^6$. A reference value for the boundary layer height $\delta = 0.22$ m is selected hereafter. $\hat{\theta}$ is the momentum thickness.

%	M7	M6	M3	M8	MAE	MAE*
ϵ_{I_u}	40.8	-67.3 (W)	-17.6 (B)	-54.4	45.1	46.5
ϵ_{I_v}		-66.1 (W)	-23.4 (B)	-62.4	-	50.6
ϵ_{I_w}	21.8 (B)	-66.9 (W)	-29.7	-64.7	45.8	53.7
$\epsilon_{\sigma_w\sigma_u^{-1}}$	-8.1	8.4	-6.2 (B)	-16.1 (W)	9.7	10.3
$\epsilon_{\sigma_v\sigma_u^{-1}}$	-	9.2 (B)	-9.7	-12.6 (W)	-	10.5
$\epsilon_{\Delta S}$	-1.5 (B)	52.9 (W)	14.0	18.1	21.6	28.3
$\epsilon_{\Delta\bar{k}}$	12.2 (B)	-190.1 (W)	-34.6	-39.3	69.0	88.0

Table 2: Bias in the determination of turbulence intensities, ratios of standard deviations, speed-up and normalized increase of TKE. $z = 2$ m. MAE indicates the absolute mean bias from M7, M6, M3 and M8, and MAE* from M6, M3 and M8. $\epsilon_{\Delta S}$ and $\epsilon_{\Delta\bar{k}}$ have been reproduced from [15]. (W) worst predicted, (B) best predicted. Mean values of PIV, 3CHW, Re_{h_1} and Re_{h_1}.

%	M7	M6	M3	M8	MAE	MAE*
ϵ_{I_u}	23.3	-13.2 (B)	-25.1 (W)	-23.8	21.4	20.7
ϵ_{I_v}		-28.6 (B)	-34.2	-36.1 (W)	-	33.0
ϵ_{I_w}	12.9	6.8 (B)	-37.4 (W)	-36.5	23.4	26.9
$\epsilon_{\sigma_w\sigma_u^{-1}}$	-2.7 (B)	35.2(W)	-8.4	-9.1	13.8	17.6
$\epsilon_{\sigma_v\sigma_u^{-1}}$		-23.2(W)	-14.1	-12.0 (B)	-	16.4
$\epsilon_{\Delta S}$	1.7 (B)	-6.1	11.3	16.0 (W)	8.8	11.1
$\epsilon_{\Delta\bar{k}}$	11.7 (B)	-29.8	-43.3 (W)	-34.6	29.8	35.9

Table 3: Bias in the determination of turbulence intensities, ratios of standard deviations, speed-up and normalized increase of TKE. $z = 5$ m. MAE indicates the absolute mean bias from M7, M6, M3 and M8, and MAE* from M6, M3 and M8. $\epsilon_{\Delta S}$ and $\epsilon_{\Delta\bar{k}}$ have been reproduced from [15]. (W) worst predicted, (B) best predicted. Mean values of PIV, 3CHW, Re_{h_1} and Re_{h_1}.

Fig. 1.1.a. **OK. FORMATO**

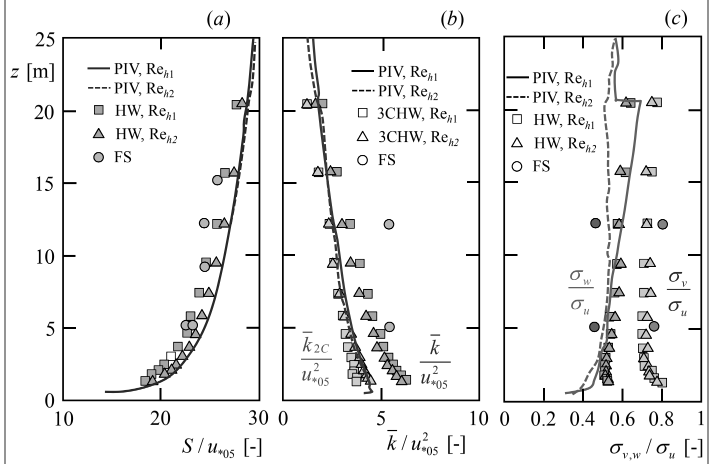

Figure 5.3: Vertical inflow profiles of a) Normalised flow speed S/u_{*05} (u_{*05} is an estimation of the friction velocity), b) Normalized TKE, $\overline{k}/u_{*05}^2$ and c) ratios of STDs of velocity components, σ_v/σ_u and σ_w/σ_u. Continuous lines: PIV for Re_{h1}, dashed lines: PIV for Re_{h2}, squares: 3CHW for Re_{h1} and triangles: 3CHW for Re_{h2}. In b) the green symbols represent the "two-components" TKE, $\overline{k}_{2C}$ calculated from the 3CHW measurements. Circles correspond to full-scale values.

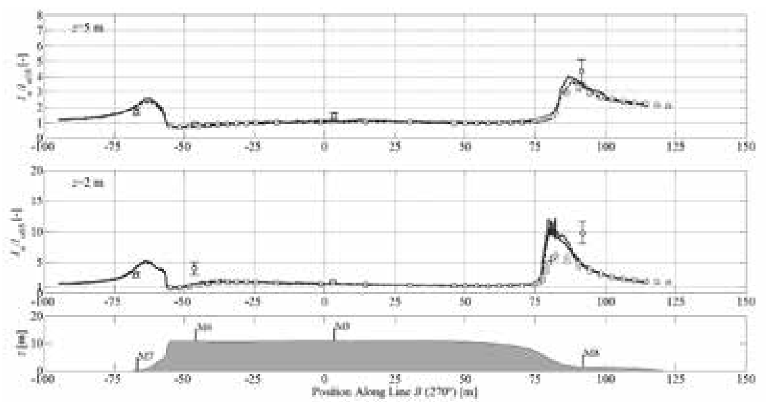

Figure 5.4: Normalized longitudinal turbulence intensity I_u/I_{u05} at $z = 2$ m a.g.l. and $z = 5$ m a.g.l.: Continuous lines, PIV for Re$_{h1}$; dashed lines, PIV for Re$_{h2}$; squares, 3CHW for Re$_{h1}$; triangles, 3CHW for Re$_{h2}$. Full-scale results (yellow dots with uncertainty bars). Velocity components expressed in the Bolund reference system. Line B. Wind direction $270°$.

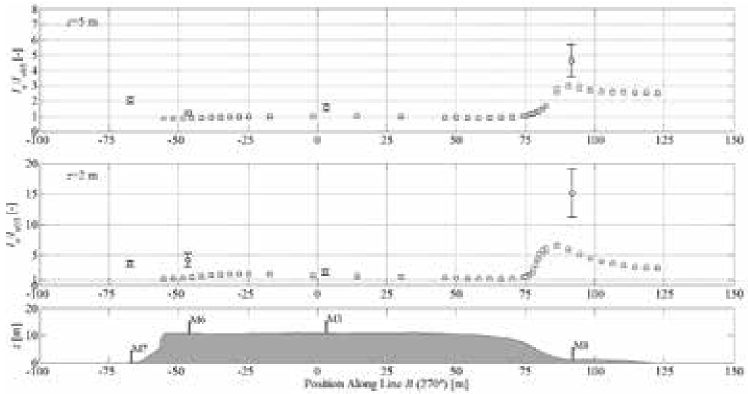

Figure 5.5: Normalized lateral turbulence intensity I_v/I_{v05} at $z = 2$ m a.g.l. and $z = 5$ m a.g.l.: Squares, 3CHW for Re$_{h1}$; triangles, 3CHW for Re$_{h2}$. Full-scale results (yellow dots with uncertainty bars). Velocity components expressed in Bolund reference system. Line B. Wind direction $270°$.

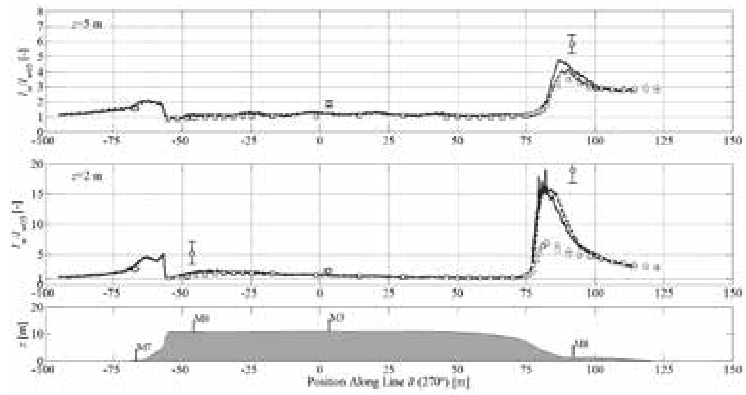

Figure 5.6: Normalized vertical turbulence intensity I_w/I_{w05} at $z = 2$ m a.g.l. and $z = 5$ m a.g.l.: Continuous lines, PIV for Re$_{h1}$; dashed lines, PIV for Re$_{h2}$; squares, 3CHW for Re$_{h1}$; triangles, 3CHW for Re$_{h2}$. Full-scale results (yellow dots with uncertainty bars). Velocity components expressed in Bolund reference system. Line B. Wind direction $270°$.

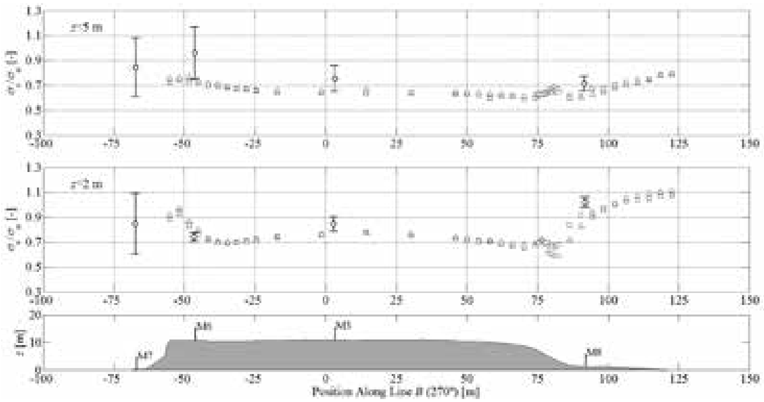

Figure 5.7: Ratio of standard deviations σ_v/σ_u on a isoheight line at $z = 2$ m a.g.l. and $z = 5$ m a.g.l.. Squares: 3CHW for Re_{h1} and triangles: 3CHW for Re_{h2}. Full-scale results (yellow dots with uncertainty bars). Velocity components expressed in Bolund reference system. Line B. Wind direction $270°$.

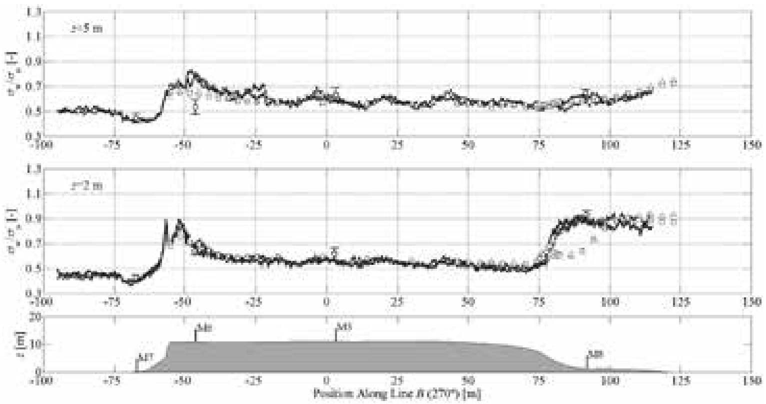

Figure 5.8: Ratio of standard deviations σ_w/σ_u on a isoheight line at $z = 2$ m a.g.l. and $z = 5$ m a.g.l.. Continuous lines: PIV for Re_{h1}, dashed lines: PIV for Re_{h2}, squares: 3CHW for Re_{h1} and triangles: 3CHW for Re_{h2}. Velocity components expressed in Bolund reference system. Full-scale results (yellow dots with uncertainty bars). Line B. Wind direction $270°$.

%	ϵ_{I_u}		ϵ_{I_v}		ϵ_{I_w}	
	Re_{h1}	Re_{h2}	Re_{h1}	Re_{h2}	Re_{h1}	Re_{h2}
3CHW	36.2	34.0	41.85	41.8	44.15	43.15
PIV	31.05	35.6	-	-	38.8	38.85

%	$\epsilon_{\sigma_w\sigma_u^{-1}}$		$\epsilon_{\Delta S}$		$\epsilon_{\Delta\bar{k}}$	
	Re_{h1}	Re_{h2}	Re_{h1}	Re_{h2}	Re_{h1}	Re_{h2}
3CHW	12.9	14.5	20.67	19.40	69.38	64.34
PIV	13.5	14.75	17.96	21.05	60.53	53.69

Table 4: Mean of the absolute bias values for the three normalized turbulence intensities, $I_{u_i}I_{u_i05}^{-1}$, the ratio of sigmas, $\sigma_w\sigma_u^{-1}$, speed-up, ΔS, and normalized increase of TKE, $\Delta\bar{k}$, for met mast M6, M3 and M8 and for both heights, $z = 2$ m and $z = 5$ m, obtained for each experimental case (3CHW, PIV, Re_{h1} and Re_{h2}).

MIND THE ENERGY GAP: HOW COASTAL TRANSITION AND STABLE ATMOSPHERIC CONDITIONS AFFECT VELOCITY PROFILES.

Christiane Montavon[1], Måns Håkansson[2], Niklas Sondell[2], Ian Jones[1]

[1] ANSYS UK Ltd, 97 Jubilee Avenue, Milton Park, Abingdon, Oxfordshire, OX14 4RW, UK.
[2] Statkraft Sverige AB, Sveavägen 9, 11157 Stockholm, Sweden.
christiane.montavon@ansys.com, Tel: +44 1235 432 333

ABSTRACT: For many wind farms close to a shoreline, the atmospheric conditions at the site can be markedly affected by the transition between sea and land, and vice versa. This can significantly affect the performance of the wind farm and the associated turbulence levels. A numerical investigation is carried out into the effect of a coastal transition, with roughness and thermal discontinuity across the sea/land interface, using a transient RANS approach which includes atmospheric stability. After validating the model's ability to accurately capture the growth rate of the developing internal boundary layer downstream of the transition, the model is applied to a wind farm on the Smøla island. We show that when stable conditions prevail downstream of the transition, the Internal Boundary Layer (IBL) grows very slowly. For fetches of the order of 5-10 km, the resulting IBL height tends to be smaller than a typical hub height of 70m, for sea/land temperature contrasts in excess of 5K. If such conditions are frequent, using mast data from within the surface layer can lead to significant overestimation of the hub-height wind speed when extrapolating with the measured shear. The change in the shape of the velocity profile also negatively impacts the rotor equivalent wind speed (i.e. the available energy) when stable surface conditions prevail. Both these effects combine and help to explain the gap between the actual P50 and the P50 predicted using a constant shear assumption, which in the case of Smøla is about 20%.

1. INTRODUCTION

In this paper we consider the effect of a coastal transition, with a change in roughness and thermal conditions across a sea-land interface. An Internal Boundary Layer (IBL) develops downstream of the transition, in which the flow and turbulence evolve to come into equilibrium with the changed surface conditions. This is very relevant for many offshore and onshore wind farms close to large water bodies. We discuss the issues associated with the developing IBL, especially those encountered when working with data recorded at masts located within the IBL, and vertically extrapolating the measurement to hub heights and above.

2. APPROACH

For a site with relatively flat terrain, with discontinuities in both aerodynamic roughness and surface stability conditions, we model the development of the wind speed profiles downstream of the transition with Computational Fluid Dynamics (CFD). The results are then compared with data from the literature, for idealised cases, and with wind speed data gathered at masts on a real site.

The CFD simulations are solved with a transient RANS approach, carried out with ANSYS WindModeller [1], using the CFX solver. Turbulence is modelled with a two-equation model (k-ε and SST tested for 2D cases, SST only for the real site), with a standard set of constants, as described in [2]. Atmospheric stability effects are modelled via a transport equation for the dry potential temperature, and buoyancy effects are accounted for, both in the vertical momentum equations and in the turbulence model. See [3] for details on the model implementation.

3. VALIDATION

The first part of the analysis focuses on simplified 2D cases over flat terrain and compares the predicted growth rate of the IBL, downstream of the transition, with expressions from the literature derived from measured data. Two cases are presented: a roughness discontinuity with purely neutral stability conditions, and a land-to-sea transition, with stable conditions over the sea. In the second part of the study, we model a real site, an island off the Norwegian coast, and compare the simulation results with data gathered at masts on site.

3.1 2D case: roughness transition only

For the purely neutral case, we model a roughness change with z_0 changing from 0.00002 [m] to 0.0025 [m], comparing the resulting velocity profiles with those measured by Bradley [4], for a relatively short fetch (distance downstream from the roughness transition). The roughness values listed may sound unrealistically low, but were chosen as to match the roughness values derived in the original paper [4]. The IBL height h_{IBL} can be derived from various methods, based either on velocity profiles, stress profiles or temperature profiles, all of which can lead to a variation in the resulting height [5]. In this case, we derived h_{IBL} from the velocity profiles, defining h_{IBL} as the height at which the wind speed in developing profile reaches 99% of the wind speed at the same height at the transition location. When investigating the IBL growth downstream of the roughness transition, we find that the IBL height from the CFD is well fitted by the expression

$$h_{IBL} = 0.09x^{0.8} \tag{1}$$

where x is the fetch. For neutral flows, with a smooth to rough transition, the dependency with $x^{0.8}$ is in good agreement with the literature (see e.g. reviews by Garratt [5] and Barthelmie and Palutikof [6]).

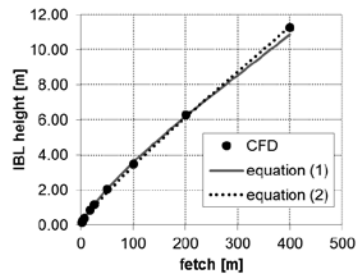

Figure 1. IBL height vs fetch for a smooth to rough transition in neutral stability conditions. Isolated symbols: CFD results, red continuous line: fit from equation (1), black dotted line: fit from equation (2) with $A = 1.25\kappa^2$.

Panofsky [7] proposed another relationship, from a diffusion analogue, leading to the implicit relationship

$$(h_{IBL}/z_{0r})[ln(h_{IBL}/z_{0r}) - 1] + 1 = Ax/z_{0r} \tag{2}$$

with $A \approx 1$. Pasquill and Smith [8] obtained a similar expression with $A = \kappa^2$, κ being the von Karman constant. The CFD results also agree well with equation (2) with a modified value of $A = 1.25\kappa^2$ as shown in Figure 1.

3.2 2D case: roughness and thermal transition

Another 2D case looks at the evolution of the IBL height downstream of a rough to smooth transition, with a thermal discontinuity. Upstream of the transition, we have a well-mixed boundary layer, with a potential temperature profile with neutral conditions throughout the boundary layer, and ISO stable conditions above (i.e. potential temperature gradient of 3.3 K/km). The surface conditions upstream of the transition are adiabatic, with a roughness of 0.03m. Downstream of the transition, the surface roughness is reduced to 0.0002m and a negative temperature offset $\Delta\theta$ is applied at the ground. The temperature offset is defined as the difference between the sea surface temperature and the potential temperature in the boundary layer upstream of the transition. These conditions attempt to reproduce those analysed by Mulhearn [9], who investigated the development of the IBL when a warm, well-mixed air-mass flows from the land over a cooler sea over the waters of Massachusetts Bay, for long fetches of up to ~ 100km. Mulhearn's expression for the IBL height is,

$$h_{IBL} = \alpha x \left(\frac{g' x}{U^2}\right)^{-\beta} \tag{3}$$

with $\alpha = 0.0146$, and $\beta = 0.47 \pm 0.047$, where

$$g' = g\frac{\Delta\rho}{\rho} \approx \frac{\theta_{land} - \theta_{sea}}{\theta_{land}} \tag{4}$$

is the reduced gravity associated with the sea/land temperature contrast. In his analysis, Mulhearn derived h_{IBL} from the height at which the developing potential temperature profile coincides with the constant potential temperature profile at the transition location. This metric was therefore also used to derive h_{IBL} from the simulations reported in this section.
As shown in Figure 2, the CFD results agree reasonably well with Mulhearn's expression with a value of 0.43 for β, well within the range estimated by Mulhearn. It is worth pointing out the slow growth of the IBL in stable conditions: for a temperature contrast

between the land and the sea in excess of 5K. In this case, the IBL height 10km downstream of the transition is typically less than 70m, a typical hub height for turbines.

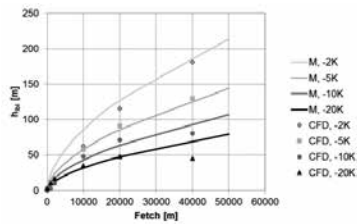

Figure 2. IBL height vs fetch for a land to sea transition with stable surface conditions over the sea. Isolated symbols: CFD results. Continuous lines: Mulhearn correlation with a slightly modified β of 0.43. From light grey to black: Sea/Land temperature contrasts of -2K, -5K, -10K and -20 K.

3.3 Real site: Smøla island

This approach has also been applied to the coastal transition with roughness and thermal discontinuity for the site of the Smøla wind farm, located on an island off the coast of Norway. Before the wind farm was built, the site was equipped with 4 masts, M102, M121, M122 and M123, as shown in Figure 3, all of them with instruments at 10, 30 and 50m. A taller, more recent mast, Mnew, was installed to collect data once the wind farm was operational. This mast measures the wind conditions at 10, 29, 65 and 68m, and is unaffected by turbine wakes for directions from the south-east to the north-west. The wind resource assessment at the wind farm was carried from the earlier data set, gathered at the shorter masts. A comparison between the actual and predicted net P50 for this wind farm shows that the predicted P50 was over-estimated by about 20%. Additional background information about the Smøla wind farm can be found in [10].

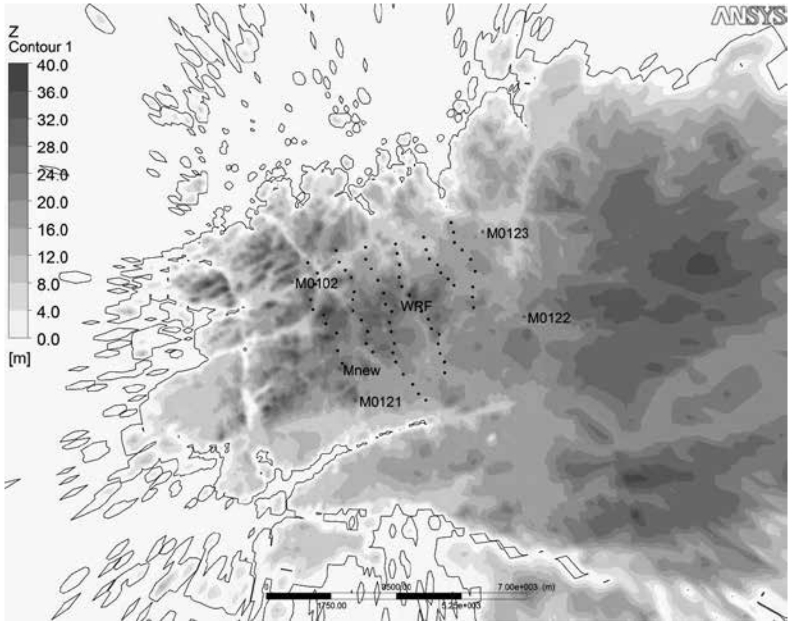

Figure 3. Smøla site terrain elevation. Turbine layout is shown with the black dots. The mast locations are shown with red symbols: M0102, M0121, M0122, M0123 are masts installed before the site was operational, Mnew is the mast recording during operation. WRF is the location where the WRF re-analysis data set is extracted.

The terrain on the island is of moderate complexity, with elevations from sea-level to a maximum of about 40m (Figure 3). Locally, the complexity results more from the jagged definition of the coastline than from changes in elevation. Note that because of the many little islands, upstream of the main island, the exact distance to the coast is not very well defined. For mast Mnew for example, for a direction from the southwest, the fetch can vary between ~ 6 to ~ 10km depending on how many of the small islands are accounted for as land. Further out (at distances of the order of 20km) the site wind conditions are influenced by abrupt terrain changes located to the south/south east of the island.

In this analysis, we focus on wind directions from the south west/west for which the flow upstream of the island travels over long fetches of the Norwegian Sea. The conditions modelled for the coastal transition assume a well-mixed boundary layer over the sea (roughness of 0.0002m) with adiabatic surface conditions and impose a temperature contrast $\Delta\theta$ between the sea and the land (increased roughness of 0.03m, and $\Delta\theta$ imposed to elevations above 1 m). While stationary boundary conditions are maintained, the flow field is solved via transient simulations, and solutions are analysed after having reached a stationary state. A range of temperature offsets was used, with values of -2K, -5K and -10K for stable surface conditions, and +2K, +5K, and +10K for unstable conditions.

The implications of the slow IBL growth in stable conditions are best illustrated by looking at the developing velocity profiles, examples of which are shown in Figure 4, for the mast location Mnew and for the wind direction 225˚. As clearly seen from these profiles, the resulting IBL height in stable conditions is strongly reduced as the temperature contrast increases. For temperature contrasts between the sea surface and the land that are larger than 5K, the thickness of the IBL is typically 50m or even less at 6-10 km downstream of the discontinuity. The wind shear in the internal layer is significantly stronger than in the layer above. A comparison between the profile at Mnew obtained with adiabatic conditions, and the upstream profile, demonstrates that the roughness increase on its own is reducing the wind speed in the lower levels. Because the turbulent mixing is not hindered downstream of the transition in the adiabatic case, the resulting profile shows a relatively constant shear exponent throughout the boundary layer (i.e. a more or less constant slope for the profile when plotted vs ln(z)). When stable conditions are combined with an increased roughness, however, the reduced turbulent mixing hinders the vertical momentum flux near the ground, which leads to an increased velocity deficit and the development of an inner layer with strongly increased shear.

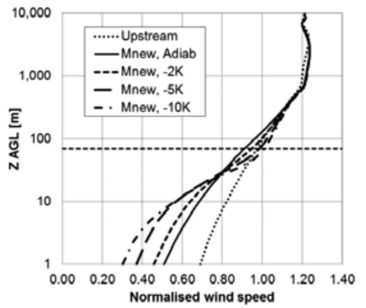

Figure 4. Velocity profiles for the sector 225° at location Mnew on the real site, located approx. 6km from the coast. The upstream profile over the sea is shown with a dashed line. The profiles at Mnew from neutral (adiabatic) to increasingly stable conditions are shown, labelled with the applied sea/land temperature contrast. The horizontal dashed line marks a typical hub height of 70m.

Equivalent profiles obtained from unstable cases are shown in Figure 5. When using adiabatic conditions or moderate temperature offsets (+2K) over the land, the dominating effect on the wind profile downstream of the transition is the effect of the increased roughness, which reduces the wind speed in the lower levels compared to the profile upstream. When stronger temperature offsets are applied, the increased turbulent mixing near the ground promotes downward momentum flux, which essentially negates the increased momentum sink at the ground associated with increased roughness. As a consequence, the wind speed at the low levels is quite similar or even exceeds that seen in the upstream profile. This is at the expense of the momentum flow at higher levels, for which we see a wind speed reduction. This results in wind speed profiles with a local maximum at a height of ~100 m, with negative wind shear above.

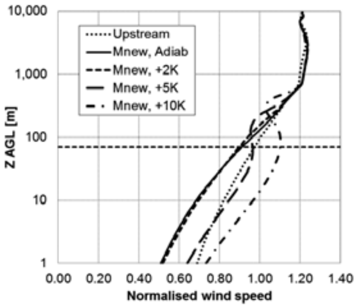

Figure 5. Velocity profiles for the sector 225° at location Mnew on the real site, located approx. 6km from the coast. The upstream profile over the sea is shown with a dashed line. The profiles at Mnew from neutral (adiabatic) to increasingly stable conditions are shown, labelled with the applied sea/land temperature contrast. The horizontal dashed line marks a typical hub height of 70m.

An attempt was made to compare the wind speed ratios obtained between pairs of anemometers at mast Mnew, with those simulated under various stability conditions. Without relevant temperature measurements on the site, surface stability conditions were instead derived and classified by the gradient Richardson number (between 2 and 60m) from a WRF reanalysis data set concurrent with the mast data set. The WRF reanalysis was carried out with a 6 km resolution for a period from 1979 to 2012 with ERA interim as boundary conditions. The planetary boundary layer scheme was the 1.5 order scheme of Mellor-Yamada-Janjic (MYJ). In order to filter out poorly correlated records between the mast data set and the WRF data set, both data sets were synchronised and records were discarded when the direction modelled by WRF was more than 30˚ away from the measured direction. From the filtered data set, wind speed ratios between 10 and 65m, and between 29 and 65m, were binned by Richardson numbers and averaged. The average ratios from the data derived this way were compared with the simulation results and with ratios expected from Monin-Obukhov (M-O) theory. Figure 6 shows the comparison between these for the wind direction 225. This reveals that for the unstable cases ($Ri < 0$), and mildly stable cases, the range of wind speed ratios at the mast from the model are reasonably close to the M-O theory and essentially within the range of measured data. For strongly stable cases however, the model appears to lead to wind speed ratios between 10 and 65m which strongly underestimates the measurements.

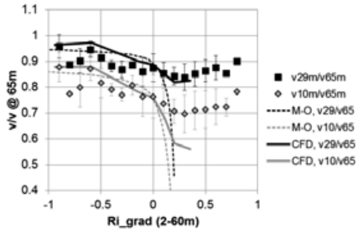

Figure 6. Wind speed ratios between 10 and 65m (grey) and 29 and 65m (black) for the wind direction 225˚. Continuous line: CFD results, dashed line: Monin-Obukhov theory, symbols and error bars: data at the mast binned by gradient Ri from WRF simulation.

To investigate this apparent deficiency of the CFD model, we carried out some comparisons between the simulated and measured velocity profiles at the location Mnew. In order to reduce potential issues associated with fast transient, we identified events with good persistence of the wind direction 225˚ (i.e. wind direction within 10˚ of the specified direction for a period of 4 hours). Figure 7 shows two such events. In the top chart, 4 consecutive measured profiles (labelled t, t+1h, t+2h, t+3h) were classified from the WRF Ri to evolve from adiabatic to strongly stable conditions. Comparing the measured profiles with the CFD simulation results (lines) suggests that for this stability classification, the wind data and the CFD are all in good agreement. The chart at the bottom of Figure 7 shows measured profiles which were all classified as being strongly unstable from the Ri derived from the WRF analysis. For this event again, we have good agreement between the WRF classification, the wind data and the CFD results.

Other events however show that the agreement between the wind data, CFD and WRF classification is not so good. Such an event is shown in Figure 8. In this case, based on the Ri from WRF, the conditions at the site are classified as strongly stable, yet the comparison between the measured profiles and the CFD suggest that the conditions are rather unstable. Turbulence intensity measurements at the mast for this event show high values, also suggesting that the conditions at the time were unstable. We conclude from this that the WRF classification of the stability conditions can be unreliable. A consequence of this is that events, which are wrongly classified as stable when in fact they are unstable, will lead to large values of the ratio v(10m)/v(65m) attributed to stable cases. This will introduce an upwards bias to the values of the averaged v(10m)/v(65m) at high Ri shown in Figure 6. We would therefore argue that what may have looked like a deficiency in the CFD model, with the ratio v(10m)/v(65m) from the CFD under-predicting the measured ratio, is in fact an issue with the stability classification. We expect that the true measured v(10m)/v(65m) would be lower than shown with a more robust stability classification.

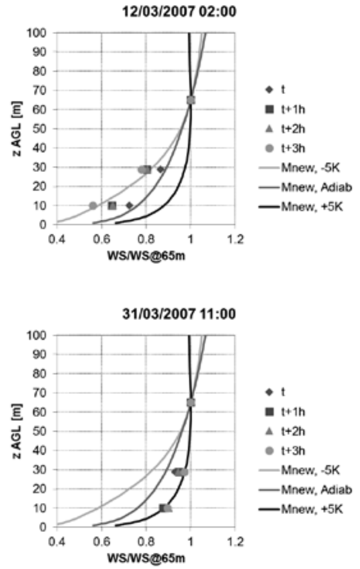

Figure 7. Symbols: measured velocity profiles at location Mnew, normalised by wind speed at 65m. The symbols blue to yellow correspond to 4 consecutive hours, with the label on the symbol showing the wind speed at 65m. Lines: simulation results for varying sea/land temperature contrasts. According to WRF data set: Top: Measured profiles evolving from mildly stable to strongly stable conditions, Bottom: Measured profiles all corresponding to strongly unstable conditions.

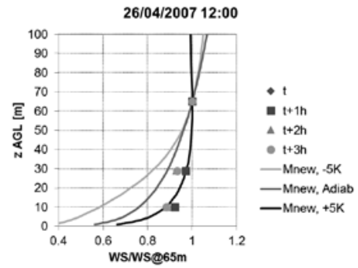

Figure 8. Event classified as strongly stable based on the Ri from WRF. Comparison between measured profile (symbols) and CFD (lines) suggests the conditions at the mast were unstable at the time.

4. IMPACT OF COASTAL TRANSITION ON RESOURCE ASSESSMENT

Should data from a mast shorter than the IBL height be used and extrapolated upwards to hub height for a resource assessment, then the extrapolated wind speed can significantly overestimate the actual wind speed at the hub (and in the upper part of the rotor). This is illustrated with Figure 9, plotting the normalised velocity profile vs the logarithm of the height above the ground. In the case of Smøla, the masts used for the resource assessment had measurement heights of 10, 30 and 50m. Extrapolating the data from the 30 and 50m levels to hub height (70m), assuming a constant shear exponent factor (i.e. along a straight line in the logarithm plot), leads to an overestimation of the wind speed if the prevailing conditions are stable (as shown with the continuous line).

Table 1 quantifies the wind speed overestimation that can occur when extrapolating to hub height in the presence of a sea/land coastal transition with well-mixed conditions over the sea, and stable conditions on land. These values are obtained for the location Mnew (6-10km inland depending on whether or not we account for transition upstream of the small islands or at the shore of the main island) for an upstream profile with 10m/s at 50m. As the conditions become increasingly stable, the over-prediction can reach values as high as ~4%.

In addition to the error associated with the vertical extrapolation, a compounding effect results from the fact that because of the changes in the shape of the velocity profiles, the rotor equivalent wind speed (REWS)

$$REWS = \left(\frac{1}{A}\int V^3 \, da\right)^{1/3} \tag{5}$$

is also affected by the stability conditions. We have attempted to quantify this by calculating the ratio between the REWS and the hub height wind speed for all 68 turbines on site. Table 2 gives the average of this ratio across the wind farm for adiabatic and stable surface conditions. With increasingly stable conditions, this ratio decreases. The implications is that, for a given hub height wind speed, the available power, proportional to the cube of the REWS, will decrease too as the conditions become increasingly stable. The errors associated with the extrapolation and reduction in REWS are of similar magnitude. In strongly stable conditions (thermal discontinuity of -5K or more), the superposition of both errors can lead to and overestimation of ~7-8% for the wind speed. In the cubic part of the power curve, this can translate to errors in the P50 of ~21-24%. Since the surface conditions on Smøla appear to be predominantly stable (in about ¾ of the time according to the distribution of gradient Ri for this site), this will seriously impact the resources for this site and goes a long way in explaining the gap between the predicted and actual P50.

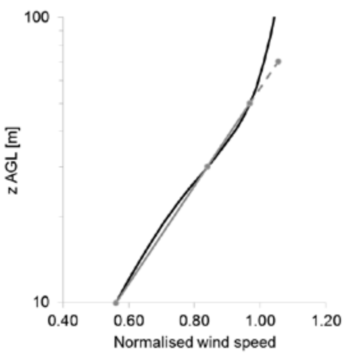

Figure 9. Dashed line: extrapolating data from 30 and 50m to hub height, assuming constant shear. Continuous black line: actual normalised wind speed profile for a temperature contrast of -10K.

Table 1. Overestimation of wind speed at 70m, when extrapolating data from 30 and 50m, assuming a constant shear. Location Mnew, conditions: 10 m/s @ 50m

Surface stability	Δ (wind speed)
Adiabatic	-0.4%
-2K	0.6%
-5K	2.6%
-10K	4.2 %

Table 2. Ratio of Rotor Equivalent Wind Speed to hub height wind speed in adiabatic and stable conditions.

Surface stability	REWS/Vhub
Adiabatic	98.5%
-2K	96.9%
-5K	95.7%
-10K	95.8 %

5. CONCLUSIONS

This investigation demonstrates that the CFD model is able to capture IBL growth downstream of a discontinuity, across which both roughness and surface stability conditions change. The resulting IBL growth agrees well with correlations from the literature, for both neutral and stable conditions downstream of the discontinuity.
This has significant implications for wind farms sited close to the coast. We show that when stable conditions prevail downstream of the coastal transition, the IBL grows very slowly. For fetches of the order of 5-10 km, the resulting IBL height tends to be smaller than a typical hub height of 70m, when the sea/land temperature contrast is in excess of 5K. If such conditions are frequent on site, then using mast data from within the surface layer can lead to significant overestimation of the resource at hub height when extrapolating with the measured shear. In addition to the vertical extrapolation error, the change in the shape of the velocity profile also negatively impact the rotor equivalent wind speed (i.e. the available energy) when stable surface conditions prevail. Both these effects go a long way in explaining the gap between the actual P50 and the P50 predicted without accounting for the presence of the coastal transition with predominantly stable conditions. In the case of the Smøla wind farm the shortfall was approximately 20%.

ACKNOWLEDGEMENTS

The authors wish to thank Statkraft for funding this analysis, and providing access to the information about the Smøla site.

REFERENCES

[1] C. Montavon, I. Jones, C. Staples, C. Strachan, I. Gutierrez, 2009, Practical issues in the use of CFD for modelling wind farms, EWEC Proceedings, Marseille.
[2] ANSYS CFX – Solver Theory Guide, Release 16.2, July 2015, ANSYS Inc.
[3] ANSYS WindModeller documentation – LS05c Atmospheric stability, July 2013, ANSYS UK Ltd.
[4] Bradley, E.F., 'A micrometeorological study of velocity profiles and surface drag in the region modified by a change in surface roughness', *Quart. J Roy. Met. Soc.*, 1968, 94,361-379.
[5] Garratt, J.R., 'The Internal Boundary Layer – A Review', *Boundary Layer Meteorol*, 1990, 50,171-203.
[6] Barthelmie, R.J. , Palutikof, J.P. , 'Coastal wind speed modelling for wind energy application', *J.Wind Eng. Ind Aerodyn*, 1996, 62,213-236.
[7] Panofsky, H.A., 'Tower Micrometeorology, Chapter 4 in Workshop on Micro-meteorology', ed. D.A. Haugen, pp 151-176., 1973, American Meteorological Society, Boston, MA.
[8] Pasquill F., Smith F.B., 'Atmospheric Diffusion', 3rd edition, Wiley and Sons, New York, 1983, 437 pp.
[9] P.J. Mulhearn, 'On the formation of a stably stratified internal boundary-layer by advection of warm air over a cooler sea', *Bound. Layer Met*, 1981, 21, 247-254.
[10] M. Håkansson, N. Sondell, 'Measurements and Power Production', PowerPoint presentation, 2012, NORCOWE Conference. http://www.norcowe.no/doc//konferanser/2012/NORCOWE%20Days%20sept%2019/S1%20Hakansson%20Measurements%20and%20Power%20Production%20(for%20handout).pdf (accessed 9/10/15).

Added value of high resolution forecast models in the assessment of UK offshore wind resource

Jessica Standen (1), Clive Wilson (1) and Alasdair Skea (1)
(1) Met Office, Exeter, United Kingdom

Abstract
In 2014 the Met Office were awarded a contract by The Crown Estate to produce a new UK wide offshore wind dataset at a height of 110m. This has been created using two forecast datasets produced using the Met Office's numerical weather prediction (NWP) model, the Unified Model. One of the datasets is a 4 year archive of high resolution (1.5km) operational forecast data; the other is 30 years of a 4.4km resolution hindcast dataset, produced specifically to be a long-term, high resolution and consistent dataset. The matching 4 years of data between the two datasets were used to calculate linear regression coefficients based on twelve 30° wind direction sectors. These were then applied to the full 30 years of 4.4km data to produce a dataset which utilised the high resolution, optimal configuration and data assimilation of the operational 1.5km archive as well as benefitting from the long term variability of the 30 year hindcast dataset.

The approach has been verified against met mast measurements and an improvement is seen above just using the 30 year dataset, especially in the absolute biases. The increased resolution in the 1.5km model archive results in a better resolved coastline which enables the new UK wide offshore wind dataset to have more detail over these coastal areas. Using two pre-existing datasets in this way was a computationally efficient method and shows the advantages that are possible to gain through combining different forecast datasets, including operational models.

Keywords
Offshore wind; wind atlas; numerical weather prediction; high resolution modelling

1. Introduction
The offshore wind resource of the UK is amongst the best in the world and The Crown Estate works with industry and government to bring investable opportunities to market. In December 2014 the Met Office were awarded a contract by The Crown Estate following a competitive tender process to produce a new UK wide offshore wind dataset.

Measurement campaigns to get an accurate representation of the winds offshore are a very costly process both financially and in time. For the initial screening process of potential wind farm sites, modelled data can be useful to give an indication of the potential wind resource without the financial outlay of costly measurement campaigns at multiple sites.

Wind atlases and gridded datasets, such as that produced in this project, can be used to identify possible areas with wind energy potential, to assist all parties in the planning process, and also for estimating the resource of a country or region as a whole. There are clearly a large number of other considerations, including environmental factors and existing infrastructure, that can limit the location of wind turbines; nevertheless wind atlases are a useful first look for the meteorological aspects. Wind atlases are not sufficient as the only resource siting tool as they do not contain detailed enough information for example on wind speed fluctuations or wind shear at sites. Neither do they take the place of in situ measurements.

The purpose of the project was to provide an updated wind resource layer for use within GIS systems by improving on the methodology used in the currently available Atlas of UK Marine Energy Resources, henceforth referred to as *Atlas 2008* [1]. The offshore wind data in the atlas was based on operational numerical weather prediction (NWP) model data from the Met Office mesoscale model which had a horizontal resolution of approximately 11km. The winds at a height of 10m were used and were taken up to a height of 100m using a neutral stability profile correction. Since the time the Atlas 2008 was produced, there have been huge advances in supercomputers and hence NWP models and so higher resolution model data are now available.

The new UK wide offshore wind dataset is also based on NWP model data, combining a 30 year hindcast at 4.4km resolution with an operational archive of 4 years of 1.5km resolution data. Further details on the models are provided in Section 2. By taking this method it utilises the long term variability from the hindcast and the very high resolution and data assimilation of the operational archive.

The new UK wide offshore wind dataset is a gridded dataset including average wind speeds, Weibull parameters and frequency distributions used to generate TAB files at a height of 110m. It is based on 30-years (December 1984 to November 2014) and was produced at two resolutions 4.4km and 1.5km over UK offshore areas (Figure 1).

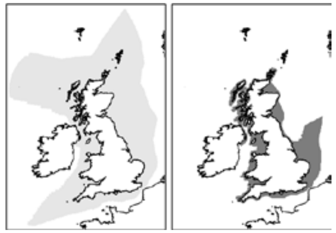

Figure 1: Renewable Energy Zone (REZ) Waters (green – produced at 4.4km resolution) and areas of water depth less than 40m (blue – produced at 1.5km resolution)

The remainder of this paper is set out as follows. A summary of the model data used is provided in Section 2. The post-processing techniques used to combine the two datasets are outlined in Section 3. Section 4 discusses the results. Conclusions are drawn in Section 5.

2. NWP model data used
The data used to produce the new UK wide offshore wind dataset was produced using the Met Office's NWP model, the Unified Model (MetUM). The MetUM is used operationally for both global and limited area NWP as well as climate and coupled atmosphere-ocean Earth-system modelling. The MetUM is a recognised state-of-the-art forecast and climate seamless modelling system [2]. The new offshore wind dataset uses two data sources, a 30 year hindcast produced at approximately 4.4km resolution over Europe (Section 2.2) and a 4 year archive of the operational high resolution (1.5km) forecast model over the UK, the UKV (Section 2.1).

2.1 UK high resolution 1.5km data
Since December 2010 the Met Office has been running a configuration of the MetUM called the UKV [3], resulting in a 4+ year archive of these forecasts. The UKV is a variable resolution model, where the central domain and area of focus is run at a resolution of 1.5km (purple area in Figure 2), but with a variable resolution area that blends from 4km to 1.5km.

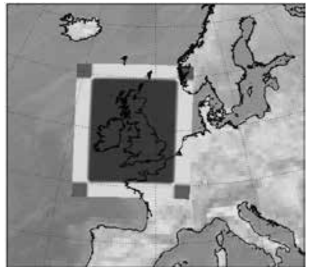

Figure 2: UKV Domain - purple shows 1.5km resolution area, red shows 4km resolution area, light green shows area where the grid boxes are 1.5km × 4km (or 4km × 1.5km), dark blue shows area of variable resolution

The UKV has 70 terrain-following vertical levels with a model top of 40km. The UKV uses incremental 3D variational data assimilation (3D-Var), on a grid half the model resolution, at approximately 3km.

The UKV is run and archived 4 times a day (03, 09, 15 and 21 UTC), which means it is possible for the data used in this project to be close to the analysis time by utilising all 4 forecasts per day. Three hours were allowed to account for the model spin-up, and hence the data used were 3-8 hours after the start of the forecast. This means that the final product is more closely influenced by real world observational data from a single model run of a day or more.

2.2 Euro4 hindcast
Mesoscale models are now widely used to downscale from global atmospheric reanalyses to produce hindcast datasets which can be used to provide site-specific guidance on wind resources and to produce wind maps. It has been shown that

this inclusion of mesoscale models either forced by reanalyses or operational forecast models reduce the biases substantially compared to modern reanalyses alone [4].

The Met Office has produced a hindcast dataset covering 1979-present at 4.4km resolution over Europe, created to provide a long-term, high resolution and consistent dataset. This is something that could not be achieved using the operational system as this 4.4km domain over Europe (Euro4) has only been running since 2013 and so there is only a short archive of operational data available.

The MetUM is used to downscale the complete period of ERA-Interim [5] since 1979 to provide a hindcast for this period, allowing there to be a consistent long-term hourly dataset. Operationally the Euro4 downscales directly the Met Office's operational global model, however this has a much higher resolution (~17km) than ERA-Interim (~80km); as a result for the hindcast another model was nested in between ERA-Interim and the Euro4 domain at a resolution of 12km to address this step change, as well as the change in model formulation. The domains of the 12km model and the Euro4 can be seen in Figure 3.

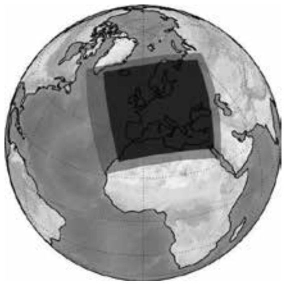

Figure 3: Euro4 domain - Euro4 domain (blue) nested inside 12km model domain (green)

The 12km model was reinitialised from ERA-Interim every 24 hours and used the 6-hourly ERA-Interim analyses at the boundaries. The 12km model in turn provided the initial and boundary conditions (hourly) for the Euro4 domain. The Euro4 started 6 hours in to the 12km forecast, and the first 6 hours of the Euro4 forecast were discarded to account for model spin up, the next 24 hours of forecast data were stored as the hindcast. This set-up resulted in the hindcast dataset comprising of 10,957 forecasts to span December 1984 to November 2014 inclusive (the period used for this work).

2.3 Benefits of UKV over Euro4 hindcast

The UKV is the primary forecast model used at the Met Office for UK forecasts and as a result there has been significant investment in the configuration, which means through using the archive of this forecast system the new offshore wind dataset is benefitting from many years of work to produce an optimised weather forecast model. It is considered to be a state-of-the-art forecasting model and is extensively verified daily over a variety of weather regimes and circulations. As an operational model it uses the optimal configuration and is driven by the operational global model, which until July 2014 was at ~25km horizontal resolution at mid-latitudes; July 2014 it was upgraded to ~17km resolution.

The UKV contains data assimilation and as such the results should be much closer to observations. The Euro4 hindcast does not contain data assimilation, though ERA-Interim does.

The increase in resolution of the UKV over the Euro4 (1.5km vs. 4.4km) means that there is an improved land sea mask, which is important when looking at winds in coastal regions. In addition the better resolved orography will also make an impact on the winds in coastal regions.

3. Processing

To produce the 1.5km resolution dataset, both the 4.4km and 1.5km datasets were combined to utilise the benefits of the very high resolution and data assimilation of the UKV, retaining the climatological information from the long Euro4 hindcast. A direction dependent linear regression was used to do this.

Four forecasts per day were used from the UKV archive, where the data were taken from T+3. Only one forecast per day is available in the Euro4 hindcast, which takes the data from T+6. A schematic of which forecast runs were used for each of the models can be seen in Table 1.

All of the matching forecast pairs (i.e. same validity time) between the UKV forecasts and the Euro4 hindcast were found over 4 calendar years December 2010 to November 2014. These matched pairs of data were binned dependent on the Euro4 wind direction into twelve 30° wind direction bins (-15°≤d<15°, 15°≤d<45°, …, 315°≤d<345°). For each of these bins linear regression coefficients were found. These were then applied to the 30 years of Euro4 hindcast data to produce the dataset which is representative of the 30 year climatology, but corrected using the directional dependent linear regression.

	UKV		Euro4	
00Z	21Z D-1	T+3	18Z D-1	T+6
01Z		T+4		T+7
02Z		T+5		T+8
03Z		T+6		T+9
04Z		T+7		T+10
05Z		T+8		T+11
06Z	03Z D+0	T+3		T+12
07Z		T+4		T+13
08Z		T+5		T+14
09Z		T+6		T+15
10Z		T+7		T+16
11Z		T+8		T+17
12Z	09ZD+0	T+3		T+18
13Z		T+4		T+19
14Z		T+5		T+20
15Z		T+6		T+21
16Z		T+7		T+22
17Z		T+8		T+23
18Z	15Z D+0	T+3		T+24
19Z		T+4		T+25
20Z		T+5		T+26
21Z		T+6		T+27
22Z		T+7		T+28
23Z		T+8		T+29

Table 1: Schematic showing forecast runs for UKV and Euro4 for each hour of the day

Both the calculation of the linear regression coefficients and the application to the Euro4 winds were done on the model level heights. Hence the results shown and discussed in this section are at 93.33m, the closest model level height to the final dataset height of 110m.

For each bin the correlation coefficient, R^2, was calculated. As expected due to the regression being between two modelled datasets both produced using the MetUM, there is a good level of correlation. Depending on the wind direction bin, between 48% and 96% of the points have a value of R^2≥0.70, with an average of 80% across all the bins. The areas with the lowest values of R^2 are mostly either downwind of land or very near coast, i.e. an inlet. For some very near coast points the values of R^2 are very low, however this tends to be for the bins where the wind direction is less frequent.

When looking at the values of R^2 for just the prevailing wind direction the lowest value is 0.29, with a maximum of 0.88 and an average of 0.80, Figure 4. Although the lowest value is still low, 98% of the domain has a value of R^2>0.70. Most of the areas which still have low values of R^2 are the inlets and areas around small islands, at these points this is where there will be the biggest differences between the land sea masks of the Euro4 and UKV models as this is very resolution dependent.

Once the regression has been applied the model level data was interpolated to the dataset output height, 110m, assuming a neutral logarithmic profile between the nearest two model levels, 93.3 and 133.3m.

4. Results

As both 4.4km and 1.5km resolution data are available in the new UK wide offshore wind dataset, it is possible to compare them and make some comparisons to show what the inclusion of 4 years of the high resolution forecast data adds to the dataset.

4.1 Validation

In this paper, 7 offshore and 4 near-shore met mast observations, some with multiple heights, were used to verify the dataset. The met mast data does not span the full 30-years, nor is much of it at the 110m height of the dataset; as a result time series at the met mast locations have been produced using the same method but at the height of the observation, so that the hourly data can be compared and also at the correct heights without any additional interpolation. It should be noted that all the near-shore and 2 of the offshore met mast observation periods are less than 1 year in length.

The observed and model wind speeds, at hourly frequency, show good agreement with R^2 values in the range 0.75-0.84 for both the 4.4km and 1.5km resolution data offshore and 0.63-0.75 for both the 4.4km and 1.5km near-shore. The inclusion of the 1.5km data at these 11 sites only made a small, but mainly positive impact on the R^2 values.

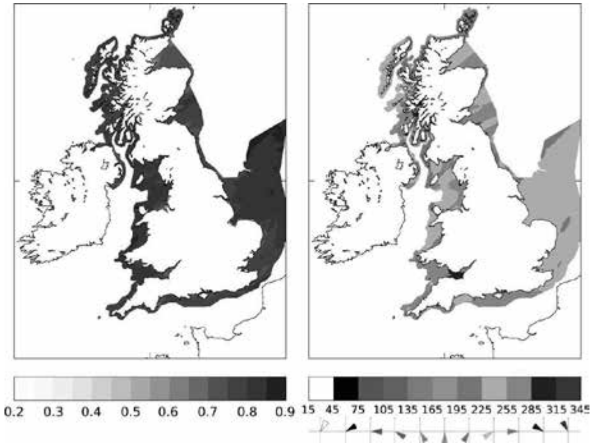

Figure 4: R^2 for the prevailing wind direction (left) and the prevailing wind direction (right)

Table 3 shows a summary of the verification of the 4.4km raw model data and the 1.5km regression corrected data. Table 3 (and also later Table 4) have had a weighting applied so that short observational periods do not dominate the results, a linear weighting is applied to any site with less than 360 days of observations. Where more than one height is available for a site a mean across all the heights is taken as the value for that site.

By using the 1.5km data, generally the bias and absolute bias are reduced except for the near-shore mean bias. The best values of the standard deviations of the biases are evenly split between the 4.4km and the 1.5km data.

When looking at the sites individually (Table 2), for offshore 47% of the site-height pairs (7 out of 15) have an improved bias through the application of the 1.5km regression, but 100% have an improved absolute bias. For near-shore 78% of the site-height pairs (7 out of 9) have both an improved bias and absolute bias by applying the 1.5km regression, however 22% (2 out of 9) are degraded by the application.

	Percentage of site-height pairs with improved bias	Percentage of site-height pairs with improved absolute bias
Offshore	47%	100%
Near-shore	78%	78%

Table 2: Percentage of site-height pairs improved using the 1.5km data over the raw 4.4km data

As part of this project The Crown Estate kindly provided high quality cleaned met mast data at 8 offshore sites for use in validation. Four of these were the same sites as in the 7 used in Table 3, however those provided by The Crown Estate were for longer periods and often at different heights and so they have been included. Table 4 shows a summary of this verification. This shows there is a reduction in the biases when using the 1.5km data compared to the raw 4.4km data. The standard deviations are very close for the 1.5km and the raw 4.4km resolution data.

		Mean bias	Standard deviation of bias	Mean absolute bias	Standard deviation of absolute bias
Offshore	4.4km raw data	0.097	0.112	1.360	0.531
	1.5km regression corrected	-0.049	0.122	1.288	0.780
Near-shore	4.4 raw data	-0.193	0.492	1.575	0.118
	1.5km regression corrected	-0.433	0.358	1.572	0.066

Table 3: Summary of wind speed verification – calculated for 7 offshore (15 site-height pairs) and 4 near-shore (9 site-height pairs) sites

		Mean bias	Standard deviation of bias	Mean absolute bias	Standard deviation of absolute bias
Offshore	4.4km raw data	0.133	0.111	1.360	0.391
	1.5km regression corrected	0.056	0.110	1.300	0.397

Table 4: Summary of wind speed verification – calculated for 8 offshore (24 site-height pairs) sites

When looking at the sites individually (Table 5), for offshore 71% of the site-height pairs (17 out of 24) have an improved bias through the application of the 1.5km regression, and 100% have an improved absolute bias by applying the regression.

	Percentage of site-height pairs with improved bias	Percentage of site-height pairs with improved absolute bias
Offshore	71%	100%

Table 5: Percentage of site-height pairs improved using the 1.5km data over the raw 4.4km data

The dataset has been verified against as many observations as were available to us (11 offshore and 4 near-shore combined across both verification data sets) giving 45 site-height pairs, spanning over 41 site-years of hourly data (108 site-height-years). However, 15 sites for a dataset comprising of 37,828 points (4.4km data) and 74,474 points (1.5km data) is still a very small sample.

4.2 Resolution comparison

As shown in Section 4.1, depending on the statistics used to assess the data the magnitude of the benefits of the inclusion of the 1.5km regression over using the raw 4.4km resolution data varies. However, especially when considering absolute bias, there is a clear benefit.

The other feature, which is not possible to verify without an extensive network of observations is the increased resolution of the data itself, giving more spatial variability to the winds and increased coastal detail. The difference between the two datasets is shown in Figure 5.

This shows that in general the application of the regression using the 1.5km data in general decreases the wind speeds slightly.

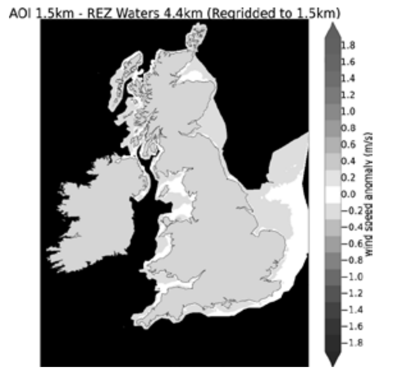

Figure 5: Difference in average wind speed over 30 years at 110m between 1.5km and 4.4km datasets – areas marked in black are outside of the 1.5km region and so there is no data, areas marked in pale green are those points considered to be land in the models.

Figure 6 shows a zoomed in section of this over the south-west of Scotland.

Firstly, this shows that due to the improved land sea mask in the 1.5km resolution model, winds are represented over sea points, and hence able to be used in the dataset, much closer inshore than in the 4.4km model, where many on the inlets and passages between islands are not fully represented. It is obviously not possible to show the differences in the wind speeds in these areas as they are only included in one of the datasets. Secondly, it can be seen, as in Figure 5, that in general the application of the regression using the 1.5km data decreases the wind speeds slightly, however there are some localised areas with larger increases or decreases in wind speed. Similar results are seen all around the UK coast; however this area is one of the most complex in the UK due to many small islands and inlets. Many of these more extreme increases and decreases will be as a result of new channels being opened up to funnel winds around islands in the 1.5km land sea mask which are not there in the 4.4km land sea mask.

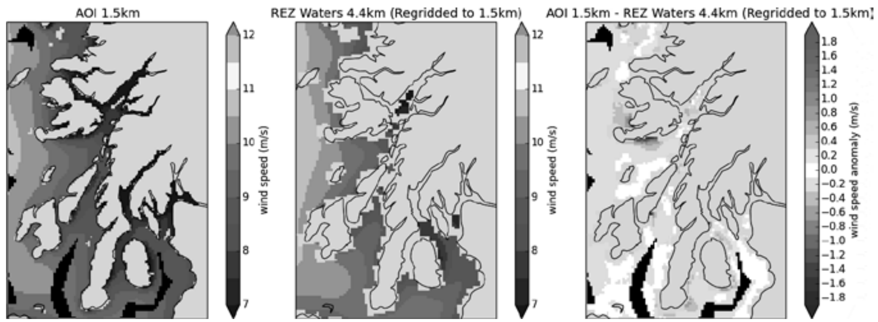

Figure 6: Average wind speed over 30 years at 110m for 1.5km dataset (left), 4.4km dataset (centre) and the difference between them (right) – areas marked in black are outside of the 1.5km region and so there is no data, areas marked in pale green are those points considered to be land in the models.

4.3 Dataset length

In addition to producing all of the fields based on 30 years of data, they were also produced based on the last 15 years of the period (December 1999 to November 2014). Figure 7 (taken from a paper by Bett et al. [6]) shows the inter-annual variability in the mean wind speed over England and Wales as calculated from the 20th Century reanalysis [7]. Whether the 1990s, which were windier on average, are included will make a large difference on the long term average wind speeds.

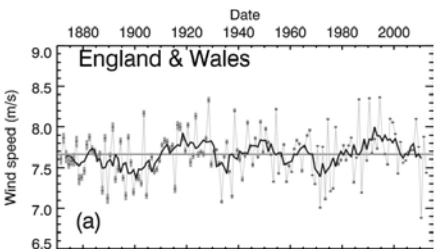

Figure 7: "Time series of the wind speed distribution for a region covering 5°W-1°E and 51°N-55°N. […] annual statistics are shown in *light colours/shading*, wind *darker lines* showing the data smoothed with a 5-year boxcar window. […] Ensemble-mean annual mean wind speed." Figure from [6]

Figure 8 shows the difference in long term mean wind speed between the 30 and 15 year period. As expected the average wind speeds over the whole area for the 15 year period are lower than those from the 30 year period as they do not include the windier 90s period. However, when looking in more detail at subsets, for example into seasonal averages, the differences are not so consistent (Figure 9), with autumn showing weaker winds in the 30 year period than the 15 over all but the far south-west of the region.

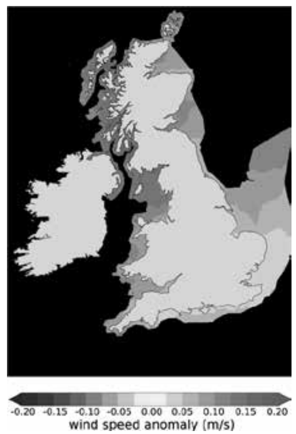

Figure 8: Average wind speed anomaly, 30 year period minus 15 year period at 110m from the regression corrected data

This shows the importance in the length of the data used in order to capture the inter-annual variability. When just looking at long term average wind speeds the effects may be smaller and more consistent and hence something that can be allowed for, but when looking at other factors, such as seasonality or Weibull parameters, the importance of fully sampling the wind speed distribution is very important. Due to the computational time and cost to produce multi decadal datasets the full sampling of a multi decadal period is often over looked.

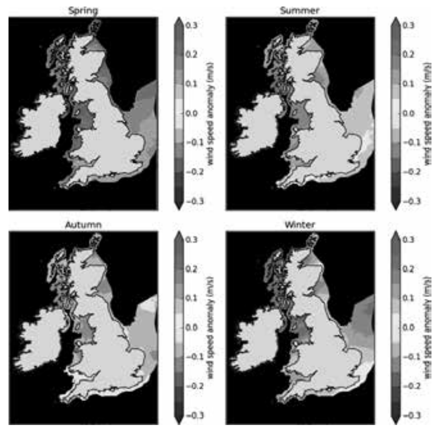

Figure 9: Average wind speed anomaly for each meteorological season, 30 year period minus 15 year period at 110m from the regression corrected data

5. Conclusions

A 30 year UK wide offshore wind dataset has been produced at a height of 110m above sea level, based on numerical modelling of the meteorological conditions over a 30 year period (December 1984 to November 2014). The dataset was produced at two resolutions, 4.4km over the renewable energy zone (REZ) Waters and at 1.5km over areas with a water depth of less than 40m. The 1.5km dataset used a directional dependent linear regression to combine 4 years of 1.5km resolution operational wind data with 30 years of a 4.4km hindcast dataset.

Using this operational high resolution model data means that the dataset benefits not only from increased resolution, which is particularly important over the coastal regions where a better resolved land sea mask will have a large impact on the winds, but also from the inclusion of high resolution data assimilation and four forecasts available per day. Then by combining this with the 30 years of hindcast data the UK wide offshore wind dataset benefits from the variability of the multi decadal period and hence is more representative of the long term wind speed distribution.

Both the 4.4km and 1.5km datasets are at a significantly higher resolution than the wind component of the Atlas 2008 that was previously being used.

The approach has been verified against a number of met masts both offshore and near-shore and at varying heights. It has been shown that in general there is an improvement by applying the directional dependent regression based on the 1.5km data, especially in the absolute biases.

In addition to the positive impact on the absolute biases by applying the direction dependent regression based on the 1.5km resolution, there is a better represented coastline in the model, resulting in increased coastal detail in the final dataset.

The 4.4km dataset is available on the Marine Data Exchange at: http://www.marinedataexchange.co.uk/search?q=%22wind%20strength%20and%20direction%22#fq=fq%3DProject%253AMDE1TCEEA7642

6. Acknowledgments

We would like to thank The Crown Estate for their useful input into this project throughout as well as for providing the high quality cleaned met mast data for use in the validation of this dataset.

References

[1]. ABPMer. "Atlas of UK Marine Renewable Energy Resources". 2008. [Online] Accessed 11 May 2015. Available: www.renewables-atlas.info.

[2]. Brown A, Milton S, Cullen M, Golding B, Mitchell J , Shelly A. "Unified Modeling and Prediction of Weather and Climate a 25-Year Journey". *B Am Meteorol Soc* 2012; **93**(12):1865-1877, doi:10.1175/Bams-D-12-00018.1.

[3]. Tang Y, Lean HW , Bornemann J. "The benefits of the Met Office variable resolution NWP model for forecasting convection". *Meteorological Applications* 2013; **20**(4):417-426, doi:10.1002/met.1300.

[4]. Wilson C , Standen J. "The added value and validation of mesoscale models compared to atmospheric reanalyses for resource assessment". In *EWEA 2013 Annual Event*, Vienna, Austria, 2013.

[5]. Dee DP, Uppala SM, Simmons AJ, Berrisford P, Poli P, Kobayashi S, Andrae U, Balmaseda MA, Balsamo G, Bauer P, *et al.* "The ERA-Interim reanalysis: configuration and performance of the data assimilation system". *Quarterly Journal of the Royal Meteorological Society* 2011; **137**(656):553-597, doi:10.1002/qj.828.

[6]. Bett P, Thornton H , Clark R. "Using the Twentieth Century Reanalysis to assess climate variability for the European wind industry". *Theor Appl Climatol* 2015:1-20, doi:10.1007/s00704-015-1591-y.

[7]. Compo GP, Whitaker JS, Sardeshmukh PD, Matsui N, Allan RJ, Yin X, Gleason BE, Vose RS, Rutledge G, Bessemoulin P, *et al.* "The Twentieth Century Reanalysis Project". *Quarterly Journal of the Royal Meteorological Society* 2011; **137**(654):1-28, doi:10.1002/qj.776.

A new method to estimate the uncertainty of AEP of offshore wind power plants applied to Horns Rev 1

Juan P. Murcia
PhD. Student, Dept. of Wind Energy, Technical University of Denmark
Pierre E. Réthoré
Senior Researcher, Dept. of Wind Energy, Technical University of Denmark
Kurt S. Hansen
Professor, Dept. of Wind Energy, Technical University of Denmark
Anand Natarajan
Senior Scientist, Dept. of Wind Energy, Technical University of Denmark
John D. Sørensen
Professor, Department of Civil Engineering, Aalborg University

Abstract: The present article proposes a framework for validation of stationary wake models that wind developers can use to predict the energy production of a wind power plant more accurately. The application of this framework provides a new way to quantify the uncertainty of annual energy production predictions. Additionally this methodology enables the fair comparison of different wake models. Furthermore the methodology enables the estimation of how much information can be obtain from a measurement dataset to quantify model inadequacy. In the present work the proposed framework is applied to the Horns Rev 1 offshore wind power plant. The model uncertainty of a modified N. O. Jensen wake model under uncertain undisturbed flow conditions was studied. Evidence of model inadequacy is found in terms of a bias in the predicted AEP distribution. It was found that the use of the official power curve compensates the errors in the wake model, as a consequence a larger uncertainty of the overall model is predicted. Furthermore a study of wake model benchmarking based on filtered flow cases indicates that measurement uncertainty in the wind speed and wind direction is large enough to obtain any evidence of model inaccuracy even for the simplest wake models.

Keywords: Uncertainty quantification, offshore wind power plant, power predictions, wake model, SCADA data reanalysis

1. Introduction

There is a need in the wind energy industry for better predictions of wind farm power production. In particular investors and financial institutions are interested in understanding the uncertainty of production predictions in order to help them take better decisions about investing in a particular wind energy project. Previous efforts for wake model benchmarking and validation using offshore wind plant supervisory control and data acquisition (SCADA) data have been performed in the past, some examples are the work of Barthelmie et. al. [1], Hansen et. al. [5], Gaumond et. al. [4], Peña et. al. [12], Réthoré et. al. [13] and Moriarty et. al. [10] . These studies were based on the filtering of the measurements database into wind speed and wind direction bins, also called flow cases. All the publications pointed out that due to the large uncertainties in the inflow conditions it has not been possible to obtain statistical evidence about model inaccuracy. Furthermore the large number of wake models that have been evaluated produce a wide spread of power production predictions for apparently simple flow cases.

In general filtering of SCADA databases is still a common practice and uncertainties in the inflow conditions are usually disregarded. The limitations of filtering the flow cases in terms of wind direction uncertainty has been studied in Gaumond et. al. [4]. It was concluded that for large enough wind direction bins (around 30 [deg]) an accurate prediction of the mean power production can be done even with the most simple models. In contrast for narrow wind direction bins, the power production can not be accurately predicted if the wind direction uncertainty is neglected. Additionally the flow cases that have been used in the literature reduce the observed data to only the very few cases in which all the wind turbines (studied) are available and under normal operation. Réthoré et. al. [14] reported that for a wind power plant with 80 turbines only between 9 to 20% of the observations can be used. This limited number of observations has made it challenging to conclude about the uncertainty in annual energy production (AEP) predictions due to the low representation of the flow cases observed in which all turbines are under normal operation.

1.1. Objectives of the present study

The present study has the following objectives:

(1) To map the wake model prediction error for a given wind power plant energy production as a function of the uncertain undisturbed flow conditions.

(2) To estimate the wake model uncertainty to predict the mean power production of a given wind power plant when there is measurement uncertainties in each variable.

(3) To estimate the uncertainty of AEP of a given wind power plant. It is important to remark that in the present work uncertainty in AEP refers to the probability density function or distribution of possible annual energy production and not just the standard deviation around its expected value.

1.2. Model validation under uncertainty

The present work follows the framework for verification, validation and uncertainty quantification of computer codes presented by Roy and Oberkampf [15]. This framework is very relevant for wind energy since it proposed a division between epistemic uncertainty (uncertainties that are due to lack of knowledge but that could be reduced e.g. individual measurement uncertainties, statistical uncertainty due to limited sample size and model uncertainty) from the aleatory uncertainty (uncertainties that can not be reduced e.g. real wind speed and real wind direction distribution during a time period). In this framework multiple realizations of the epistemic uncertainty of the inputs are sampled for each individual realization of the aleatory uncertainty of the inputs. By evaluating the model in each of this cases one can predict a set of distributions of the output. A similar approach is done for the possible realizations of the observed output: multiple realizations of the epistemic uncertainty are sampled for each realization of the aleatory uncertainty of the output. Roy and Oberkampf [15] and Ferson et. al. [3] have proposed the use of the area validation metric to compare the distributions of model predictions and measured outputs under measurement uncertainty. These articles argue that the area validation metric is a good estimator of the model uncertainty. In order to study the impact of measurement uncertainty and model uncertainty in the prediction of AEP it is important to be able to separate the natural (aleatory) variability of the flow resources from the measurement (epistemic) uncertainty of each individual 10-minutes measurement.

2. Methodology

2.1. Inputs/output measurements

The SCADA data was processed following the methodology for data reinforcement that has been described by Réthoré et. al. [14] in order to remove calibration shifts through time. In particular nacelle position sensors tend to have calibration shifts due to the inability to use magnetic north tracking close to large generators. Turbines are forced to perform a full 360 [deg.] turn to recalibrate the nacelle position signal. It is important to recognize that an individual turbine yaw angle signal is not an accurate estimator of the undisturbed wind direction. The settings of the yaw controllers are not known and therefore the yaw signal contains yaw errors and time dependency (filtering) due to the controller reaction time. The present work assumes that a large scale averaged undisturbed wind direction can be estimated from multiple yaw sensors, because the individual yaw errors of each turbine compensate each other.

Wind speed

The undisturbed wind speed (WS) was estimated using the average of the nacelle anemometers on the free flow operating turbines at each 10-minutes period. This average represents a spatially averaged undisturbed wind speed. Individual signals were checked for measurement quality before the averaging process was applied, which means that the number of available wind speed signals varied for each 10-minutes. The quality check consisted in comparing each individual upstream nacelle anemometer with the raw spatially averaged undisturbed wind speed. Periods that showed uncommon behavior (time increasing standard deviation) were removed.

Two additional corrections were applied to the undisturbed wind speed based on multiple nacelle anemometers. The nearby met masts hub height anemometers were used to fit a non-linear nacelle transfer function (NTF). This transfer function was used to correct the estimated wind speed for flow distortion due to the nacelle geometry and due to blade shadowing. The procedure followed is inspired in the procedure described in the IEC standard 64100-12-2 (2013) [7]. The difference with respect the standard lies in the fact that the spatial average undisturbed wind speed was used instead of a single nacelle located anemometer.

Finally an air density correction was applied following the IEC standard 64100-12-1 (2005) [6]. This correction scales the wind speed by the ratio of the current air density (10-min. mean) and the standard atmosphere air density to the one third power. This correction is recommended for normalization of power/wind speed measurements for pitch controlled wind turbines [6]. The 10-minutes mean density was estimated following the IEC standard and used the 10 min. mean barometer, air temperature, and water temperature signals.

The elicitation of the uncertainty of the undisturbed wind speed was done following the IEC standard [7]. The sources of uncertainty considered are shown in table 1. The air density correction uncertainty is the result of propagation of barometer, temperature and humidity measurement uncertainties trough the air density correction equation [7]. The large scale structures uncertainty was predicted using the trend inside the 10-minutes [11] by computing the difference between the two consecutive undisturbed wind speeds. All sources of uncertainty were assumed to be independent and normally distributed. It is important to remark that the uncertainty is estimated for each individual 10-minutes period.

Source	Type	Ref.
Calibration	B	[7]
Operation	B	[7]
Mounting	B	[7]
Data acquisition resolution	B	[7]
NTF correction	B	[7]
Air density correction	B	[7]
Large scales structures	B	[11]
Statistical	A	[7]

Table 1: Sources of uncertainty in spatially averaged undisturbed wind speed.

Note that type B uncertainties need to be normalized by applying a coverage factor of $1/\sqrt{3}$. The total uncertainty was evaluated using eq. 1 (this equation uses a general notation for any measured variable x). In this equation the left term contains the type A uncertainty estimated using N sensors and the term on the right is the combination of multiple type B uncertainties. Finally the real value of the wind speed is assumed distributed normal around the average of the multiple sensors, eq. 2 (this equation uses a general notation for any measured variable x).

$$U_x^2 = \left(\frac{std(x)}{\sqrt{N}}\right)^2 + \sum\left(\frac{U_{Bi}}{\sqrt{3}}\right)^2 \quad (1)$$

$$x_{real} \sim Normal\left(\bar{x}, U_x\right) \quad (2)$$

Wind direction

The undisturbed wind direction was estimated using the average of the nacelle positions signals of the free wind operating wind turbines. Individual signals were checked for calibration shifts [14] and for quality of the measurement. Each individual upstream nacelle position signal was re-calibrated based on the wind power plant layout and the power deficit of the first wake operating turbine. This procedure has been introduced by Réthoré et. al. [14].

The spatially averaged undisturbed wind direction (WD) obtained from the average of the multiple available nacelle positions showed a dependency on the wind speed. A correction based on the bias between WD and the wind vane at hub height at the nearby meteorological masts was fitted through a non-linear transfer function following the recommendations presented in the standard 64100-12-2 (2013) [7]. The correction for the wind direction consisted in removing the bias as a function of wind speed.

The elicitation of the uncertainty of the undisturbed wind direction followed the IEC standard [7] and is estimated for each individual 10-minutes period. The sources of uncertainty considered are shown in table 2. The total uncertainty was calculated using eq. 1, while the real value of the wind direction is assumed normally distributed, eq. 2.

Source	Type	Ref.
In-situ re-calibration	B	[7]
Yaw signal resolution	B	[7]
Data acquisition resolution	B	[7]
Sensor alignment	B	[7]
NTF correction	B	[7]
Large scales structures	B	[11]
Statistical	A	[7]

Table 2: Sources of uncertainty in spatially averaged undisturbed wind direction.

Power

The total power production was computed by assuming that the turbines not available under normal operation produce null power. Furthermore it was assumed that a considerable reduction of the thrust coefficient occurs under down-regulation and that the wake deficits can be neglected. The power measurement uncertainty is estimated for each 10-minutes observation following the standard [6]. The sources of uncertainty considered are shown in table 3. The total uncertainty was calculated using eq. 1, while the real value of the power is assumed normally distributed, eq. 2.

Source	Type	Ref.
Calibration	B	[7]
Current transducer	B	[7]
Voltage transducer	B	[7]
Data acquisition resolution	B	[7]

Table 3: Sources of uncertainty in power measurements.

Power curve

The present study used two different power curves: the official power curve and the experimental power curve. The experimental power curve was obtained following the recommendations of the IEC standard [7]. Since SCADA databases include a large number of turbines the experimental power curved was obtained by aggregating multiple upstream wind turbines power measurements as a function of the undisturbed wind speed (for a valid wind direction sector).

Availability

The prediction of normal operation was performed individually to each turbine following the outlier detection methodology presented in [14]. This procedure used the pitch angle and normalized power curve in order to detect when a turbine is not under normal operation conditions. The obtained wind turbine availability is a combination of the actual availability, down regulation conditions and measurement sensor errors.

2.2. Modeling

Wake model

The present work could be applied to any wake model. The wake model used in the present study is a modified N. O. Jensen (NOJ) model [8]. The modified NOJ model was selected for its simplicity and because it is a model still used in the industry. The model assumes a linear wake expansion coefficient (k_j) of 0.05 for offshore conditions. In contrast to the original NOJ model, the modified model includes a near wake expansion from 1-D momentum theory occurring at the rotor disc; further more the wake deficits are scaled by the local hub height wind speed at the wake generating wind turbine instead of the undisturbed wind speed. Finally the wake deficits are aggregated with linear superposition. The model used in the present study is open source and is available at https://github.com/DTUWindEnergy/FUSED-Wake along other wake models such as the original NOJ [8] and G. C. Larsen semi-empirical wake model [9].

The model used in this study has as inputs the undisturbed wind speed, the undisturbed wind direction, the power and thrust coefficients curves, the wind power plant layout, the linear wake expansion coefficient and the availability for each turbine. As a result the model predicts the power produced by each turbine.

It is important to note that the model was executed for each of the 10-minutes inputs. The wake model was run assuming that the unavailable turbines are not running (for which the idle thrust coefficient was used) during the 10-minutes period.

Propagation of input uncertainties

A Monte Carlo simulation based on LHS sampling was used to study the effect of input uncertainty in the power distribution prediction. Each 10-minute distribution of the real wind direction and wind speed are considered independent due to their epistemic nature [15]. 100 different possible realizations of the real undisturbed flow conditions during the 3 years of analysis were calculated. This enabled to separate the aleatory component of the wind resources from the epistemic uncertainty of the measurement/estimation of undisturbed flow conditions. The present approach can be summarized as a full time series reanalysis with detailed availability and uncertainty for each 10-minutes period.

Power measurement uncertainty sampling

A Monte Carlo simulation based on a 100 LHS sample was used to study the effect of the measurement uncertainty in the observed power distribution. This approached produced 100 possible realization of the real active power through the three years of analysis.

2.3. Model validation

Area validation metric

A validation metric describes a methodology to compare an experimental distribution of a variable (with measurement uncertainty) with the result of the propagation of input measurement uncertainties through a model. In the current work the area validation metric was used to characterized the error in the prediction of the expected power of the wind power plant (U_{model}). The area validation metric quantifies the model uncertainty by comparing the median rank based cumulative density function (CDF) of the measured and predicted powers, and not only their mean values [3].

Due to the (epistemic) measurement uncertainty, the CDF of the total power measurements is defined as the region between the worst and best realization of the real power. Similarly when the uncertainty in the inputs is propagated through the model then the predicted CDF of total power becomes the region between the worst and best realizations of the model. The area validation metric is the absolute area between the two regions. If there is no are between the two regions there is no evidence of model uncertainty. This could mean that the model is very accurate or that there is too much uncertainty in the inputs. In the present work several comparisons of flow cases were done that illustrate how to use this validation metric in power production and annual energy production predictions.

The area validation metric is used to predict the confidence interval of any quantile of the output [15]. Therefore it can be used to estimate the expected model error in the prediction of the annual energy production. It is important to understand model uncertainty as an epistemic uncertainty, this means that it produces uncertainty around the predicted distribution of power. This means that it captures an additional uncertainty in the prediction of power that is independent of the input uncertainties. Figure 1 shows an example of area validation metric applied to two models that use the mean wind speed to predict the mean power. It can be observed that there is measurement uncertainty that causes the distributions to be regions. It can be seen that the model on the left gives a better estimation of the mean power (at CDF(P)$= 0.5$), but both models are equally bad at modeling the power distribution. It is expected that such models will deviate significantly from case to case depending on the actual wind resources. Therefore the model uncertainty should be similar for both models. The area validation metric in both cases is around 45 [MW]. Finally the confidence interval that includes the mean power can be estimated as the distribution obtained by the input uncertainty propagation (blue region at CDF(P)$= 0.5$) and an additional bias (uniformly distributed) given by the validation metric:

$$\mathbb{E}(P_{WF\,real}) \in \overbrace{PDF(\mathbb{E}(P_{WF\,model}))}^{\text{Input Unc.}} \pm \overbrace{U_{model}}^{\text{Model Unc.}} \qquad (3)$$

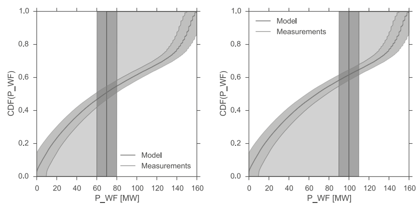

Figure 1: Example of area validation metric for CDF(P) for two models that use the mean wind speed to predict the mean power. First model prediction: $\mathbb{E}(P_{WF\,real}) \in [60,80] \pm 45 = [15,125]$ [MW]. Second model prediction: $\mathbb{E}(P_{WF\,real}) \in [90,100] \pm 45 = [45,145]$ [MW].

Boot-strapping AEP

In the present work the classical bootstrap technique [2] was used to predict the probability distribution of AEP. This technique consists in building a sample of artificial but probable years of climate, therefore it is sampling the variation (aleatory uncertainty) of the undisturbed wind. A single realization of a year was built by randomly picking a year out of the three available in the database for each of the 10-minutes periods in a given year. This was done keeping the date and time for the observation. The wind speed, wind direction, measured power, predicted power, and its respective uncertainties were chosen together. The statistical uncertainty due to a limited number of bootstrap sample was studied by following the convergence in the standard deviation of the AEP.

The bootstrapped sample is representative of the actual climate as it contains all the long term correlations such as the daily, the synoptic (high and low pressure driven patterns) and seasonal variations. The bootstrapped sample was used to evaluate the distribution of possible AEP. Finally the area validation metric based on CDF(P) was used to predict the confidence interval for the AEP. Note that this validation metric considered the area validation metric for $\mathbb{E}(P_{WF})$ (section 2.3) and the propagation of uncertainties in the undisturbed wind speed and direction through the model (section 2.2).

3. Results

3.1. Test case: Horns Rev 1

Horns Rev 1 is a Danish offshore wind power plant co-owned by Vattenfall AB (60%) and DONG Energy AS (40%). It is located 14 [km] from the Danish west coast (fig. 2). The total rated power is 160 [MW]. The power plant consists of 80 Vestas V80-2.0 [MW] wind turbines, see figure 3. The power plant started operation in 2002 and is still operating in 2015.

The present work has been done using 3 years (2005-2007) of measurements from the SCADA database of the power plant. The database contains 10-minutes mean, max., min. and standard deviation for power, nacelle anemometer, nacelle position (orientation), pitch angle and rotational speed for each individual wind turbine. The present study also uses signals from the nearby meteorological mast (M2, M6, M7). Anemometers at 70 [m] height, wind vane at 68 [m]

Figure 2: Location of the Horns Rev 1 offshore wind power plant. Image taken the 6th of October 2015 at http://maps.google.com.

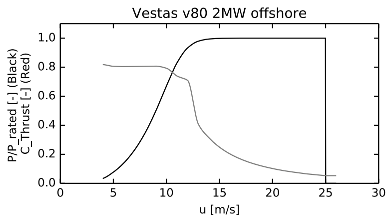

Figure 3: Vestas V80-2.0 [MW] official power curve (black line) and thrust coefficient curve (red line). April 2007 reported curves taken from the WAsP power curve database at http://wasp.dk

height, barometer sensor, air and water temperatures measurements. In the present work the available nacelle position and anemometer sensors of the free flow operating turbines were used to predict the undisturbed wind conditions. The estimation of the undisturbed wind conditions was done independently in four different undisturbed wind direction sectors, see figure 4.

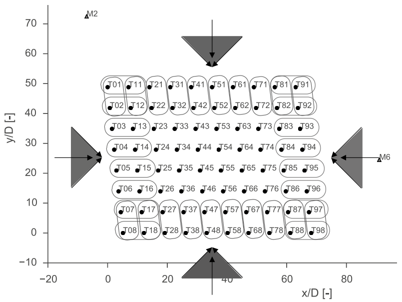

Figure 4: Selected benchmark case in Horns Rev 1. The colored area represents undisturbed wind directions. The sensors used for predicting the undisturbed flow conditions are circled and color coded.

Wind speed

Figure 5 presents an example of the transfer function correction based on the anemometer located at the top of the met mast M6 (height of 70 [m]). Note that the distance between meteorological mast and each nacelle anemometer is larger than the limit recommended in the IEC standard 64100-12-1 (2013) [7]: $4D$. Nacelle transfer functions were independently produced using M2, M6, M7 top anemometers and individual nacelle anemometers in order to asset the effect of the assumptions, similar transfer functions were obtained (not shown).

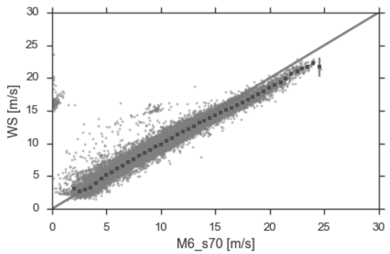

Figure 5: Nacelle transfer function between top anemometer at M6 and the large scale averaged undisturbed wind speed for the Eastern sector.

It is important to remark that the authors had not access to any information about the calibration, mounting, quality, maintenance of any of the anemometers in the wind farm. To compensate for this the uncertainty estimation is conservatively estimated. The elicitation of the uncertainty of the undisturbed wind speed is shown in table 4. This table does not present the type A uncertainty or the large scale uncertainty, since they are computed independently for each 10-min period.

Source	Type	Value
Calibration	B	0.25 [m/s]
Operation	B	class: 1.7A
Mounting	B	0.2%
Data acquisition resolution	B	0.05 [m/s]
NTF correction	B	2 %

Table 4: Estimated uncertainty in spatially averaged undisturbed wind speed.

Wind direction

An example of the nacelle position signal re-calibration based on the layout and the power deficit procedure is shown in fig. 6 for the turbines 04 and 14. In this figure the difference between the two blue lines represents the bias in the wind direction for the nacelle position senor of turbine 04.

The NTF correction for the wind direction consisted in removing the bias as a function of wind speed. Figure 7 shows the bias between the large scale averaged wind direction and the wind vane located at M6 at 68 [m] height. Similar results were obtained for M2 and M7.

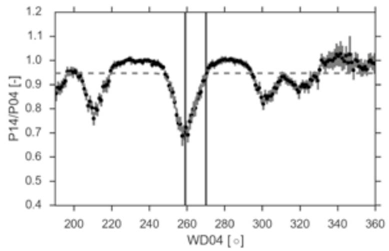

Figure 6: Nacelle position sensor for turbine 04 re-calibration based on the power ratio of turbines 14 and 04.

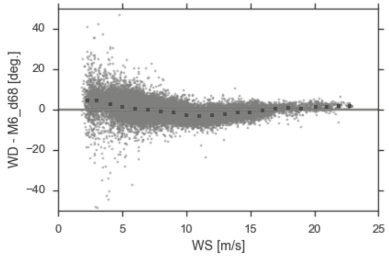

Figure 7: Undisturbed wind direction bias with respect to the wind vane at M6 at 68 [m] height as a function of the undisturbed wind speed for the Eastern sector.

A conservative elicitation of the uncertainty in the undisturbed wind direction was done following the standard for single nacelle anemometer uncertainty [7], table 5. This table does not present the type A uncertainty or the large scale uncertainty, since they are computed independently for each 10-min period.

Source	Type	Value
In-situ calibration	B	3 [deg]
Yaw signal resolution	B	2.5 [deg]
Data acquisition resolution	B	0.05 [deg]
Sensor alignment	B	1 [deg]
NTF correction	B	1 [deg]

Table 5: Estimated uncertainty in spatially averaged undisturbed wind direction.

Power

The estimated power measurement uncertainty for each 10-minutes observation is presented in table 6. Note that the power transducers have not been calibrated since installation, and it is observed that the zero power values changes between 1-2 % with reference to rated power.

Source	Type	Value
Calibration	B	2 %
Current transducer	B	2 %
Voltage transducer	B	0.9 %
Data acquisition resolution	B	2 [kW]

Table 6: Estimated uncertainty in power measurements.

Power curve

The official power curve and the multiple turbine averaged experimental power curve are presented in figure 8. Note that a simple site correction for the power curve based on the annual average turbulence intensity captures the obtained experimental power curve.

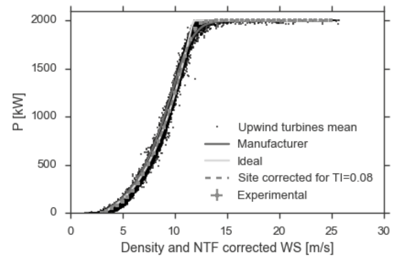

Figure 8: Official power curve and experimental power curve.

3.2. Time series of the main variables

An example of the time series of the undisturbed wind speed, wind direction, total availability, measured total power and model predicted power are presented in Figure 9. In this figure the colored areas represent the 99% confidence intervals for each of the variables. These confidence intervals include all sources of uncertainties and they should be understood as the region in which the real value lies. It is important to remark that the predicted power confidence interval is the result of the input uncertainty propagation process. This figure superficially reveals a good agreement between measurements and predictions.

Furthermore, figure 9 suggest that the confidence intervals predicted by the propagation of input uncertainty are larger than the ones caused by the measured power uncertainty. Note that the confidence intervals in the measured variables reveal that the uncertainty analysis is done for each time period. Some periods of non-available data can also be identified from this figure. Moreover the expected model prediction is build by averaging the 100 realizations of power for each 10-minutes (black line in the lower frame in figure 9).

3.3. Wind farm power rose: experimental and modeled

An example of the wind farm power rose is presented in figure 10 for a single realization of the input uncertainty during the 3 years and for a single realization of the output uncertainty during the 3 years. This figure demonstrates that

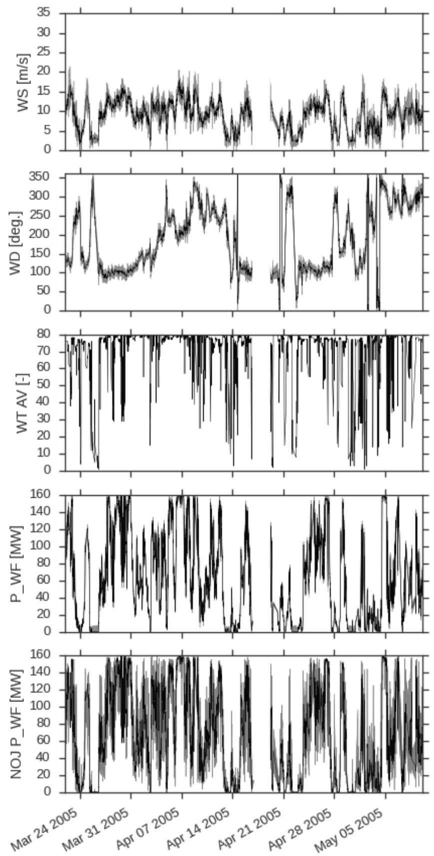

Figure 9: Example of time series of WS, WD, total availability and P_{WF} time series with 99% confidence intervals (colored areas).

the use of the actual available turbines improves the amount of data available to compare the performance of wind farm flow models.

In order to compare the level of agreement the first step is to analyze the distribution of the prediction error, see figure 11. This figure contrast the power prediction error as a function of the input variables for two cases. Using the official power curve (left frame in figure 11) produces an over-prediction of power at wind directions with less coherent wind turbine alignment; on the contrary, an under-prediction of power occurs at the wind directions of main turbine alignment. The prediction errors of the model that used the experimental power curve show a consistent under-prediction of power through the whole wind rose.

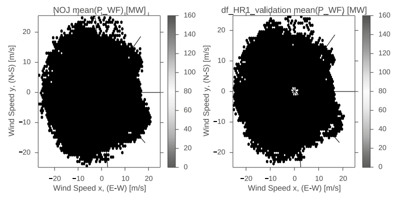

Figure 10: Wind farm power rose for (left) the model predictions based on a single realization of the inputs (right) a single realization of power measurements.

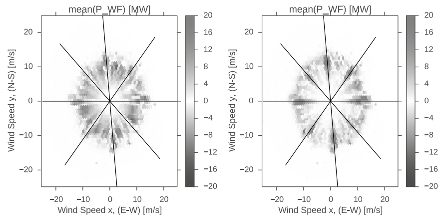

Figure 11: Power prediction error rose for a single realization of input uncertainty (left) official power curve (right) experimental power curve. Positive errors means power under-prediction (red areas) while negative errors represent power over-predictions (blue areas).

3.4. Model uncertainty for total plant expected power

The area validation metric was applied to the cumulative density function of the power, this validation metric gives an uncertainty estimation for the prediction of mean power production ($\mathbb{E}(P_{WF})$). The CDF of both measured and predicted power are shown in figure 12. Note that the CDFs presented in this figure are the areas between all the possible realization of both predicted power and measured power. It can be observed that the measurement uncertainty has negligible influence in the area validation metric. Figure 13 presents the comparison using the experimental power curve.

From figures 12 and 13, it can be observed that using the official power curve produces an over-prediction of powers below 90 [MW]. The opposite effect is observed when the experimental power curve is used: the power is under-predicted of powers below 90 [MW]. The obtained validation metrics normalized by the experimental mean power were 3% for the official power curve case, and 2% for the model that uses the experimental power curve. This suggests that the model uncertainty is lower if the experimental curve is used. The resulting model uncertainty estimations imply that using the NOJ model with the experimental power curve will predict the actual mean power with an error of $\pm 2\%$. It is important to highlight that the area validation metric is given in absolute value, which means that it does not hold the sign of the bias. The reason for this is that due to the epistemic nature of model uncertainty, the modeler does not know before hand whether the model over-predicts the power or under-predicts it. Furthermore, the area validation metric penalizes a model that might predict the mean by compensating under-predicitons with over-predictions [3].

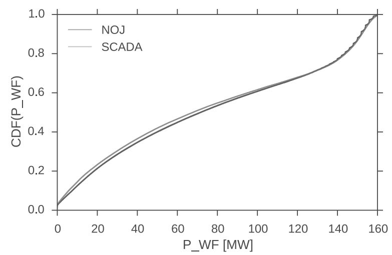

Figure 12: Area metric for CDF(P): $U_{model} = 3\% \, \mathbb{E}(P_{WF\,SCADA})$.

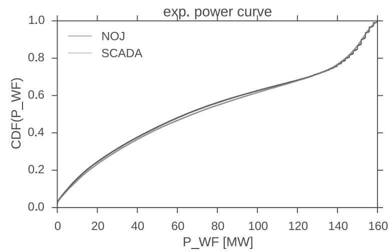

Figure 13: Area metric for CDF(P) using the experimental power curve: $U_{model} = 2\% \, \mathbb{E}(P_{WF\,SCADA})$

3.5. Model validation for AEP

The probability density function (PDF) of the AEP of 1000 possible years of inflow climate is presented in figure 14. This figure shows the distribution of a single realization of measurement uncertainty in the inputs (for the model), of a single realization of output uncertainty (for the SCADA database) and the aggregated distributions of AEP that include all possible realization of the measurement uncertainties. The single realization cases show peaks in the distribution which create variation in the prediction of the mean AEP (expected AEP, or P_{50}). It can also be observed that there is a bias in the model prediction of the expected AEP. This bias is due in part to the over-prediction of power caused by the official power curve. Finally it can be observed that the overall shape of the PDF of the AEP is well captured by the model. It can be concluded that the shape of the PDF of AEP only depends on the realization of the climate in the given year (bootstrapped sample).

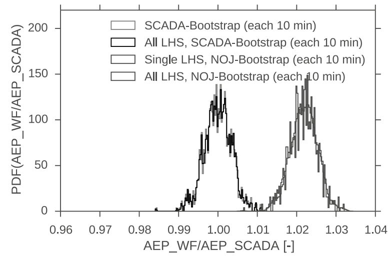

Figure 14: AEP distribution of 1000 possible years (bootstrap) with measurement uncertainties.

The final step is to combine the CDF of model AEP with the model uncertainty that was computed in section 3.4. This process is shown in figure 15. The combination of input uncertainty propagation through the model with the expected model uncertainty gives an expected range of AEP distributions. In this figure the blue are represents the range of possible CDF predicted by propagating of input uncertainties, while the green area includes the 3% model uncertainty. It can be observed that the actual distribution of AEP based on the SCADA data (red area) lies inside the predicted range (green area).

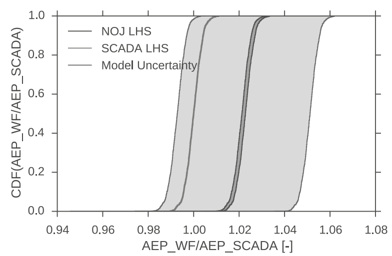

Figure 15: AEP cumulative probability distribution of 1000 possible years (bootstrap) with measurement uncertainties and wake model uncertainty.

The same procedure was repeated for the NOJ model using the experimental power curve. The probability density function of the AEP of 1000 possible years of inflow climate is presented in figure 16. This figure shows an under-prediction of the AEP. The confidence interval presented in figure 16 is a more accurate estimation of the actual bias of the NOJ model. The reason for this is the fact that the use of the experimental power curve minimizes the compensation caused by the over-prediction of the official power curve.

The combination of the CDF of model AEP with the model uncertainty is shown in figure 17 for the NOJ model with

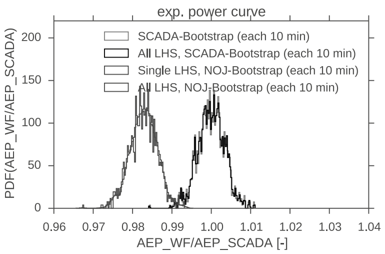

Figure 16: AEP distribution of 1000 possible years (bootstrap) with measurement uncertainties. NOJ model with experimental power curve.

the experimental power curve. The combination of input uncertainty propagation through the model with the expected model uncertainty gives an expected range of AEP distributions. It can be observed that the actual distribution of AEP based on the SCADA data lies inside the predicted region.

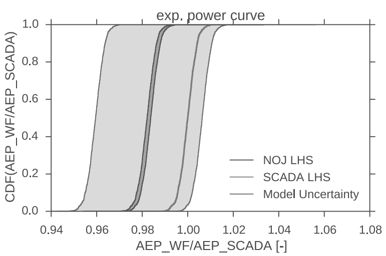

Figure 17: AEP cumulative probability distribution of 1000 possible years (bootstrap) with measurement uncertainties and wake model uncertainty. NOJ model with experimental power curve.

4. Discussion

The present framework can explain the difficulties seen in the previous wake model benchmarking campaigns. The main issue is the effect of input uncertainty in wind speed and direction in the binning process. As a consequence several of the observations obtained when filtering very narrow flow cases have actual values of wind speed and wind directions outside the bin. To show an example of the consequences of this miss-placement, the SCADA and modeled databases were filtered for an undisturbed wind direction inside [270, 272.5] [deg.] and a wind speed inside [10, 10.5] [m/s]. Figure 18 show the resulting regions of power distribution. These results reveal that due to the propagation of input uncertainty there is a null area validation metric when the model uses the official power curve. This can be interpreted as a lack of evidence of a model inadequacy in this flow case. This lack of evidence is not because of a perfect model but due to the large uncertainty in the inputs of the model.

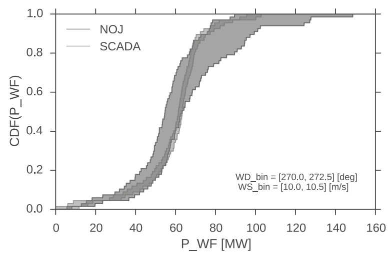

Figure 18: Area validation metric for CDF(P) for an individual flow case is null.

Figure 19 shows a similar analysis using the experimental power curve. In this case there is a relative model uncertainty of 3%. This evaluation of model inadequacy as a function of wind speed and wind direction requires to consider the measurement uncertainty in undisturbed flow conditions and in power.

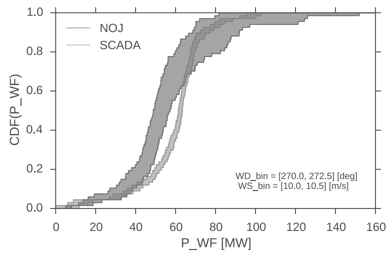

Figure 19: Area validation metric for CDF(P) for an individual flow case experimental power curve. 3%.

4.1. Further work for a full wind power plant AEP uncertainty prediction

The use of area validation metrics for power prediction distributions with uncertainty for each individual turbine inside the wind farm is planed. This study will conclude with the construction of a response surface that captures the dependency of the model uncertainty as a function of the wind speed and wind direction for each individual turbine (wake model validation region). From this results a predictive tool can be generalized such that the SCADA data from Horns Rev 1 could be use to predict the uncertainty on AEP prediction for an offshore wind power plant with an arbitrary layout. The proposed framework could be used to benchmark different wake models and to obtain individual validation regions for each model. This two aspects are the focus of the IEA-task 31.

The added uncertainty that come from modeling the power plant at full availability and by applying a percentage of operating turbines for each 10-minutes period will be studied using the area validation metric methodology. Finally the model discretization uncertainty will be quantified. This means to understand the effect of creating a wake model response database using a limited number of model evaluations.

5. Conclusions

A bias in the modified NOJ wake model prediction of annual energy production has been identified. The size and sign of this bias depends on whether the official or experimental power curve is used. The use of the official power curve makes it hard to identify the errors in the wake model, due to the errors in the turbine model. The use of the official power curve gives a larger uncertainty of the overall model based on the area validation metric of total power cumulative density function. The use of an experimental power curve or a site corrected turbulence intensity power curve indicate a lower level of superposition of turbine and wake model errors.

The standard deviation of the AEP distribution was found to be well captured by the NOJ model. It can concluded that it mainly depends on the realizations of the possible one-year wind climates and it can be more accurately predicted if the measurement uncertainty is taken into account.

Furthermore an explanation to the problem of wake model benchmarking based on filtered flow cases indicates that the measurement uncertainty in the wind speed and wind direction is large enough that there is no statistical evidence about the accuracy of the wake model if the official power curve is used. On the contrary there is statistical evidence of model inadequacy for a narrow flow case if the experimental power curve is used. Further work is planed in which the distribution of model prediction error (model uncertainty) as a function of both wind speed and wind direction for individual wind turbine power is studied.

Acknowledgments

This work was supported by the International Collaborative Energy Technology R&D Program of the Korea Institute of Energy Technology Evaluation and Planning (KETEP), granted financial resource from the Ministry of Trade, Industry & Energy, Republic of Korea. (No. 20138520021140). The authors thank DONG Energy AS and Vattenfall AB for the access to the SCADA data of Horns Rev 1.

Nomenclature

AEP	Annual energy production
CDF	Cumulative probability density function
$\mathbb{E}(x)$	Expected value of a random variable x
LHS	Latin hyper-cube sampling
PDF	Probability density function
SCADA	Supervisory control and data acquisition

References

[1] Barthelmie, R. J., Pryor, S., Frandsen, S. T., Hansen, K. S., Schepers, J., Rados, K., Schlez, W., Neubert, A., Jensen, L., and Neckelmann, S. (2010). "Quantifying the impact of wind turbine wakes on power output at offshore wind farms." *Journal of Atmospheric and Oceanic Technology*, 27(8), 1302–1317.

[2] Efron, B. (1979). "Bootstrap methods: another look at the jackknife." *The annals of Statistics*, 7(1), 1–26.

[3] Ferson, S., Oberkampf, W. L., and Ginzburg, L. (2008). "Model validation and predictive capability for the thermal challenge problem." *Computer Methods in Applied Mechanics and Engineering*, 197(29), 2408–2430.

[4] Gaumond, M., Réthoré, P.-E., Ott, S., Peña, A., Bechmann, A., and Hansen, K. S. (2014). "Evaluation of the wind direction uncertainty and its impact on wake modeling at the horns rev offshore wind farm." *Wind Energy*, 17(8), 1169–1178.

[5] Hansen, K. S., Barthelmie, R. J., Jensen, L. E., and Sommer, A. (2012). "The impact of turbulence intensity and atmospheric stability on power deficits due to wind turbine wakes at Horns Rev wind farm." *Power*, (November 2011), 183–196.

[6] IEC et al. (2005). "Iec 61400-12-1-2005 wind turbines-part 12-1: Power performance measurements of electricity producing wind turbine." *Switzerland: International Electrotechnical Commission.*

[7] IEC et al. (2013). "Iec 61400–12-2, wind turbines: part 12–2: Power performance of electricity producing wind turbines based on nacelle anemometry." *Switzerland: International Electrotechnical Commission.*

[8] Katic, I., Højstrup, J., and Jensen, N. O. (1986). "A simple model for cluster efficiency." *EWEC*, number October, 407–410.

[9] Larsen, G. C. (2009). "A simple stationary semi-analytical wake model." *Technical Report, Risø-R-1713(EN) August 2009*, Risø-DTU.

[10] Moriarty, P., Rodrigo, J. S., Gancarski, P., Chuchfield, M., Naughton, J. W., Hansen, K. S., Machefaux, E., Maguire, E., Castellani, F., Terzi, L., et al. (2014). "Iea-task 31 wakebench: Towards a protocol for wind farm flow model evaluation. part 2: Wind farm wake models." *Journal of Physics: Conference Series*, Vol. 524, IOP Publishing, 012185.

[11] Ott, S., Berg, J., and Nielsen, M. (2014). "Developments of the offshore wind turbine wake model Fuga." *Report No. DTU Wind Energy E-0046*, Risø-DTU, Roskilde, Denmark.

[12] Peña, A., Réthoré, P.-E., and Rathmann, O. (2014). "Modeling large offshore wind farms under different atmospheric stability regimes with the Park wake model." *Renewable Energy*, 70(June), 164–171.

[13] Réthoré, P.-E., Hansen, K. S., Larsen, G. C., Larsen, T. J., Ott, S., Rathmann, O., Peña, A., and Hasager, C. B. (2013). "Benchmarking of wind farm scale wake models in the eera - dtoc project." *Proceedings of the 2013 International Conference on Aerodynamics of Offshore Wind Energy Systems and Wakes (ICOWES2013).*

[14] Réthoré, P. E., Johansen, N. A., Frandsen, S. T., Hansen, B. K. S., Jensen, L. E., and Kristoffersen, R. (2009). "Systematic wind farm measurement data reinforcement tool for wake model calibration .." *EOW Conference 2009*, 1–10.

[15] Roy, C. J. and Oberkampf, W. L. (2011). "A comprehensive framework for verification, validation, and uncertainty quantification in scientific computing." *Computer Methods in Applied Mechanics and Engineering*, 200(25-28), 2131–2144.

WIND FARM LAYOUT OPTIMIZATION IN COMPLEX TERRAIN WITH CFD WAKES

Jonas Schmidt
Fraunhofer IWES, Oldenburg, Germany
jonas.schmidt@iwes.fraunhofer.de

Bernhard Stoevesandt
Fraunhofer IWES, Oldenburg, Germany
bernhard.stoevesandt@iwes.fraunhofer.de

Abstract:

For a complex terrain site in Bahia, Brazil, 28 CFD-RANS simulations were carried out, representing the relevant states of a wind rose with three degrees resolution. The resulting wind fields provide the background wind for the layout optimization of a wind farm with 64 wind turbines based on the AEP. The underlying wake model was deduced from CFD-RANS simulation results of an isolated actuator disk. We find that a hybrid optimization algorithm that combines genetic and gradient-based optimizers and subsequently increases the size of the wind farm yields good optimization results.

Keywords: Wind farms, wake models, complex terrain, layout optimization, CFD

1 Introduction

Wind farm layout optimization is crucial for advancing wind energy, since the successful minimization of wake losses both increases the annual energy production (AEP) of a wind farm and also reduces turbine loads. While in densely populated regions, like Germany, layout optimization for on-shore sites may not always be essential due to the strong constraints and the relatively small wind farm sizes, this may be different for other regions of the world. One example is Brazil, where the wind farms are typically large, the terrain is complex and wide regions are sparsely populated. Currently many wind farms in Brazil have line-dominated layouts, since easterly winds strongly dominate the wind rose. However, this may not be the most effective land usage of a given area, and eventually one may have to face the issue of wind farm optimization in complex terrain.

For a recent review on the topic of wind farm optimization and more than 20 years of related research see [1], also [2,3]. A summary on the related topic of optimised wind farm control can be found in [4]. Examples for state-of-the-art software on the industry level are *WindFarmer* [5], *WindPRO* [6] and *OpenWind* [7], a recent comparison of *WindPRO* and *OpenWind* can be found in [8]. Examples from the scientific community are TOPFARM by the Technical University of Denmark [9] and *flapFOAM* by Fraunhofer IWES [10–12].

Most approaches in the literature that describe wind farm layout optimization focus on off-shore or flat terrain scenarios. Also details from full computational fluid simulations (CFD) are usually not included in the calculation process. However, due to non-linear and non-local flow phenomena in the presence of terrain features, the latter may be the key ingredient in situations where the flow physics are complex and all other modelling fails. This paper gives the proof-of-principle that AEP optimization of a wind farm of reasonable size in complex terrain including wind potential fields from CFD calculations for a realistic wind rose and wakes from CFD simulations is possible.

All wake and wind farm modelling for this work has been achieved within the framework of the software *flapFOAM*, which has been developed at Fraunhofer IWES since 2011. For the optimization the software has been coupled to the powerful optimization tool box Dakota [13] by Sandia National Laboratories, USA, on a c++ library level [12]. *flapFOAM* was inspired by the software *FLaP*, which had been developed earlier at the University of Oldenburg (cf. [14]), without including code of the latter. The software is based on the idea of single-wake superposition, fully written in c++, and can read OpenFOAM [15] simulation results. Its strictly modular structure allows the developer to extend and improve models independently of the core functionality of the code, and the user to select between a broad range of models and settings. The proof-of-principle of the numerical wake model based on CFD solutions of the Reynolds-averaged Navier-Stokes equations (RANS) in presence of an actuator disc (AD) was presented in [10], and progress on the inclusion of complex terrain effects was reported in [11]. The order of magnitude of the uncertainty due to the choice of wake model during layout optimization was estimated in [12], which also includes a brief summary of the basic calculation algorithms of *flapFOAM*. A detailed description of the software will be given elsewhere.

The paper is organized as follows. In Section 2 the site of interest is briefly introduced, for which wind field simulations have been performed as described in Section 3. Section 4 summarises the numerical wake model that is applied to these background wind fields during layout optimization in Section 5. The method and results are discussed in Section 6 before we conclude in Section 7.

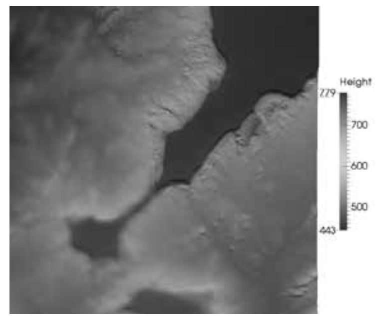

Figure 1: *The altitude of the terrain at the site.*

2 Site description

We study a fictional wind farm in complex terrain at a site in Bahia, Brazil, that features steep slopes and plateau regions. The altitude varies over a range of 336 m, cf. Fig. 1.


Figure 2: *The ground patch of the cylindrical fine mesh, and the wind farm boundary of size* 6×6 *km*^{2} *(black square).*

The model wind farm consists of 64 wind turbines of identical rotor type, and is initially arranged in a regular 8×8 pattern of size 5.8×5.8 km^2. The available area for the layout optimization is a square of 6×6 km^2, with orography as shown in Fig. 2. The numerical wind turbine model that is considered in this work has $D = 120$ m rotor diameter, $H = 120$ m hub height and 2.5 MW nominal power. In what follows the effective wind speed at the rotor is obtained directly from the centre point of the disk.

3 Background wind fields

The wind rose from Fig. 3 contains 120 sectors and up to eight wind speed bins with 2 m/s width per sector. Since winds from east-south-east (ESE) are very dominant, as it is typical for north-eastern Brazil, only a subset of the sectors is relevant. By ignoring states with frequency below 1% we reduce the number of considered wind rose states to 28. For each of these states, consisting of the wind direction of the sector and the centre of the wind speed bin, a CFD-RANS simulation of the flow over the terrain in neutral stratification is performed. The simulation results provide the background wind fields for the relevant inflow conditions; they represent the input flow states for the AEP optimization of the wind farm.

All simulations were carried out for the same

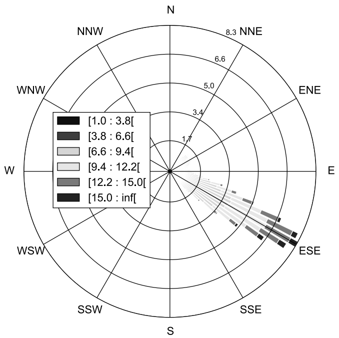

Figure 3: *The wind rose in 100 m height.*

structured cylindrical mesh with 2.8 mio. cells, a radius of 10 km and 1 km height, called the fine mesh in the following. The terrain is resolved within a square of 10×10 km^2, cf. Fig. 2. The horizontal resolution in the central region is 50 m. The fine mesh has 50 levels in upward direction, with first cell height of 1 m and at least 10 m resolution within 200 m above ground. All meshes used for this work were created using the IWES in-house tool *terrainMesher*, which is a follow-up of the open-source *terrainBlockMesher* [16].

The OpenFOAM solver *simpleFoam* (version 2.3.1) was used to solve the RANS equations with standard k-ϵ turbulence model, with parameters adjusted for ABL simulations [17]. Wall functions were used at the ground, the roughness length was chosen uniformly as 5 cm.

The inflow profiles for the wind velocity field U and the turbulence fields k and ϵ were obtained by consistently solving a single column of cells with cyclic boundary conditions, given the mass flow according to a standard log-profile. The desired profile and the inflow wind speed at 120 m above ground were well matched by the results of this precursor simulation. For the different wind directions the inflowing velocity profiles were rotated accordingly. At the cylindrical boundary of the domain either the profiles or vanishing gradients were imposed, depending on the relation of the flow vector and the face normal. The whole procedure is fully automatized and parallelized, here 16 cores were used for each of the states. All simulations converged with

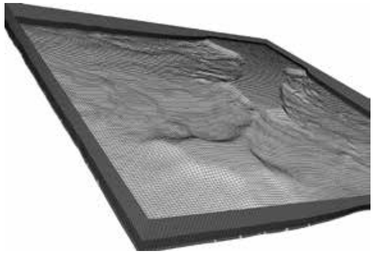

Figure 4: *The coarse mesh, not used for CFD simulations.*

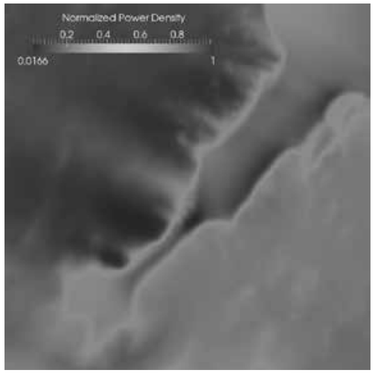

Figure 5: *The normalized mean wind power density in 120 m height above terrain.*

residuals below 10^{-4} for pressure and below 10^{-5} for all other fields.

To speed up the interpolation of the background wind field results during optimization a second mesh with with 0.4 mio. cells was created afterwards, called the coarse mesh in the following. As shown in Fig. 4 it only covers 8×8 km^2 of the central region of interest. In the range of 50–190 m height over terrain the vertical resolution is 10 m, horizontally it is 50 m.

The 28 resulting fields are associated with frequencies, according to the wind rose. The mean wind power density can then be calculated by an integration, the result at 120 m height over terrain is shown in Fig. 5. Clearly the speed-up at the plateau and also its wake are visible. It can be expected that the optimal layout prefers the south-easterly borders of the elevation and tries to avoid the west-northern part of the domain. Note that the field shown in Fig. 5 is not used during optimization, instead the individual CFD results as stored in the coarse mesh enter the calculation.

Figure 6: *Cut through the mesh and the actuator disk (red).*

4 Numerical wake model

Basically the 3D-RANS equations applied to an isolated actuator disk define a (4+x)-equation wake model, where x represents the turbulence model equations. Due to the complexity of CFD simulations they are obtained before run time of *flapFOAM* and span the range of inflow wind speeds of interest. Details of the implementation of a numerical wake model based on pre-calculated CFD-RANS results are given in [10]. Here we apply the wake model from our previous work [12], which is briefly summarised below.

Eight CFD-RANS simulations of a single uniform actuator disk in neutral stratification were run with OpenFOAM's *simpleFoam* solver (version 2.3.1), at inflow wind speeds 3, 5, 8, 10, 12, 15, 18 and 20 m/s at hub height 120 m. For intermediate inflow wind speeds, local second order interpolation is applied.

The mesh has dimensions $8.8 \times 1.5 \times 1.0$ km^3. It consists of 2.05 million cells, including the actuator disk with 1892 cells, cf. Fig. 6. The first cell height at the ground is 1 m and standard wall functions with roughness length 5 cm were used. Both grading and refinement were applied to improve the resolution of the wake and the near-disk region.

We applied the k–ϵ–f_P turbulence model [18] with parameters as recommended there. Compared to the standard k–ϵ model this version includes a correction of turbulent viscosity that depends on the change of velocity gradients due to the presence of the actuator disk, enhancing the wake

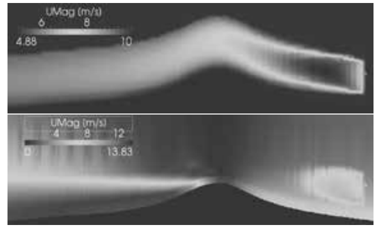

Figure 7: *Detail of a single CFD wake, in uniform background (top) and a CFD background solution (bottom), visualised in the coarse mesh. Notice that the flow direction is from right to left.*

deficit. All boundary conditions at the inlet were obtained by a one-dimensional cyclic precursor run, as described before. All variables converged to residuals below 10^{-5} in all simulations.

The addition of wake deficits is preformed quadratically under the square root, and no partial wake or meandering models are applied. The total wake deficit is then added to the pre-calculated CFD background wind field in terrain following manner, cf. Fig. 7. An additional deformation of the wake due to the presence of complex terrain as discussed in [11] is not included in the current study and left for future work, we refer to Section 6 for further discussion.

5 Layout optimization

The objective function that is used in throughout this work is the total wind farm AEP, normalized by the product of the number of turbines and the maximal AEP of the turbine model. Note that this quantity never exceeds the value one. The optimization variables are the horizontal positions of the wind turbines. The optimization constraints are defined by the rectangular boundary and the requirement of a minimal distance of 2 D between any two turbines.

We apply a hybrid of the genetic algorithm *soga*, which is part of the JEGA library [19], and the gradient based optimizer *conmin* [20], both as available trough Dakota [13] (version 6.0.0). Our algorithm is sketched in Fig. 8 and described in the following. The idea of subsequent turbine optimization has been applied before, for example in *WindPRO* [6] and *OpenWind* [7] (for a summary see [8]). We re-

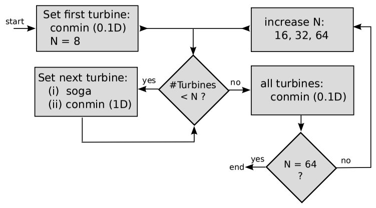

Figure 8: *Sketch of the optimization algorithm.*

Parameter	Value
Population size	10
Initialization type	unique random
Mutation type	replace uniform
Mutation rate	0.05
Replacement type	elitist
Constraint penalty	50
Max. function eval.	500
Convergence type	best fitness (20 gen., 1%)

Table 1: *Parameters of the* soga *algorithm, for details see [13].*

fer to Section 6 for a further discussion of the algorithm.

The first turbine is initially located near the south-eastern boundary of the domain, as shown in grey colour in Fig. 9. Starting from this position, a straight forward *conmin* search with step size 0.1 D finds the ideal position with maximal wind potential, compare Fig. 5 (red disk) and Fig. 9. The normalized AEP increases from 79.1% to 97.7%. However, for general initial positions a local optimization algorithm is not sufficient, due to many local maxima of the objective function and flat regions in the domain. Hence the need for a global optimizer, in our case a genetic algorithm, which is combined with subsequent local optimization for best results.

We subdivide the task of optimizing the layout or 64 turbines into sub tasks consisting of $N = 8, 16, 32$ and finally $N = 64$ turbines. Note that these numbers are coincidentally chosen as powers of 2, but that is no requirement for the algorithm. Until the total turbine number of wind turbines has reached the current N, turbines are subsequently added to the wind farm. The position of the new wind turbine is determined by the genetic *soga* algorithm with parameters as listed in Table 1, followed by the gradient-based *conmin* algorithm with step size 1 D.

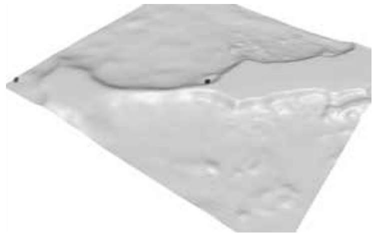

Figure 9: *The initial (grey) and optimized (red) first turbine position. Notice that the flow direction is from bottom to top of the image.*

If the new wind farm size equals N the complete layout is optimized again with the local optimizer and step size 0.1 D. Finally N is increased, or the algorithm stops if the maximal number of turbines has been reached.

The resulting layouts are shown in Fig. 10. For $N = 1, 8, 16, 32$ all wind turbines are placed on top of the plateau, as expected from the wind potential in Fig. 5. Also the narrow transition region between the two plateaus in the south-west and the north-east has been populated. The restriction of a minimal distance of 2 D between the turbines is apparent from the solution. Wakes effects are minimized according to the choice of representing the disk only by its centre point. The downstream area behind the elevation is avoided, upstream only hill tops are chosen for some of the turbines of the last optimization step $N = 64$.

Table 2 lists the normalized AEP values of the different steps after optimization. Clearly the single turbine case has the highest normalized AEP, since it can occupy the global maximum of the objective function. Up to limits of the genetic algorithm the turbines one after the other fill up the preferred regions of the wind potential in Fig. 5, yielding subsequently smaller AEP contributions. Finally, at large wind farm sizes, the wake effect further reduces the energy output of the wind farm.

6 Discussion

Flow over complex terrain in general is a complex phenomenon. It affects both the background wind and the wakes, in fact it remains to be shown that the superposition approach is even applicable in all cases. In this work we fully represent the effect on the background wind field by CFD-RANS simulations, which model the involved physics within the limits of the mesh and the turbulence model. Despite the fact that for realistic cases these simulations have to be validated before starting the optimization, the method is potentially more accurate for complex orography than other engineering methods.

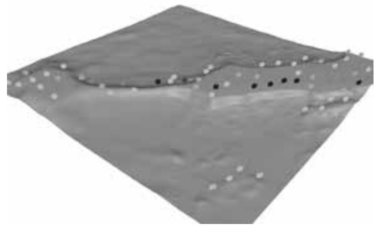

Figure 10: *The final optimized wind farm layout, with new turbines in red ($N = 1$), blue ($N = 8$), green ($N = 16$), yellow ($N = 32$) and grey ($N = 64$). Notice that the flow direction is from bottom to top of the image.*

N	1	8	16	32	64
AEP [%]	97.7	96.7	96.1	94.4	89.2

Table 2: *Optimization results in terms of the normalized AEP.*

As indicated in Fig. 7, the background wind solution captures the wake region behind hills and phenomena like flow separation. However, the wake transformation that has been applied in this work may be a very simple model to represent the real flow. A promising and more advanced CFD based approach has been studied in earlier work [11], and its generalization from isolated idealised hills to realistic orography is work in progress.

In principle the flow behaviour and especially the detachment of the wake at hill tops depends on stratification, and the strictly terrain following model that is applied here may only be relevant for modelling highly stable conditions. However, more research is needed to test this hypothesis, and generally to validate wake transformation functions in complex geometry. This is beyond the scope of the work presented here. Nevertheless, the flow accuracy in the wake of the plateau is not crucial for the studied layout optimization, since the wind rose clearly prefers south-easterly winds. Hence for the presented virtual wind farm one may argue that simple terrain following wakes may be sufficient, assuming that upstream and on top of the plateau the influence of model details is less significant, but again, this remains to be shown by comparing to measurement data.

Our optimization algorithm is a combination of a genetic and a gradient-based local optimizer, cf. Fig. 8. The turbines are added subsequently, and adding turbine number n comprises 2 optimization variables and $n-1+b$ constraints, where $b = 4$ is the number of constraints due to the wind farm boundary. As stated in Table 1 the population size of the evolutionary algorithm for the two variables is 10, and the maximally allowed number of objective function evaluations is 500, hence each optimization problem is relatively small and fast. We also evaluated both the genetic and the local optimizers also individually for the complete wind farm with 64 wind turbines. Both algorithms did not find satisfying solutions, in the latter case this is due to the complexity of the objective function. For the genetic algorithm a very large number of required function evaluations is needed for good results, in the studied case 10000 evaluations at population size 100 were not sufficient. Note that in that case the number of variables is 128 and the number of constraints is 2272. On a single core of a work station computer this required less than 48 hours, the algorithm from Fig. 8 less than 24.

As described in Section 5 and sketched in Fig. 8, our algorithm optimizes the complete layout with a local optimizer only when specific wind farm sizes N have been reached. This is a trade-off that has been made in order to speed-up the optimization as a whole, but in principle one may perform this step also after each turbine insertion. Furthermore it is straight forward to generalise the algorithm such that it ends after reaching the optimal number of wind turbines that complies with the optimization constraints.

The final layout from Fig. 10 reflects pure AEP optimization. For a realistic application more constraints need to be included, for example representations of the soil conditions and their suitability for realising the turbine foundation. Such constraints would possibly significantly influence some of the turbine positions, especially in the narrow transition region between the two plateaus at the site.

7 Conclusion

We demonstrated how CFD simulations of wind flow over complex terrain and CFD simulations of the flow through isolated rotors can be combined to realise wind farm layout optimization in complex orography based on CFD results. We found that a combination of a genetic algorithm for subsequently placing new turbines and gradient-based local optimization yields satisfying results.

All calculations were performed within the *flapFOAM* software framework. Once the precalculated CFD simulations were available, the computational time of the complete optimization on a single core of a workstation computer for a wind farm with 64 wind turbines was less than 24 hours.

One open issues is the validation of wake transformation functions in complex terrain. Also stratification and its impact on wakes at complex sites has to be included in the calculation. Furthermore the objective function and the optimization constraints need to be extended, for example to represent cable costs and other economic considerations. This is work in progress, as is the inclusion of turbulence intensity and wind turbine loads into the wind farm optimization.

Acknowledgements

The work is conducted in the scope of the project Smart Wind Farms funded by the German Federal Ministry for Economic Affairs and Energy (FKZ 0325851B). We would like to thank Casa dos Ventos Energias Renovaveis S.A. for providing the orography and typical wind rose data. We also thank Jerome Feldhaus for help with hybrid optimization solvers, and the computer time provided by the Facility for Large-scale Computations in Wind Energy Research (FLOW) at the University of Oldenburg, Germany.

References

[1] J. F. Herbert-Acero, O. Probst, P.-E. Rethore, G. C. Larsen, and K. K. Castillo-Villar. A review of methodological approaches for the design and optimization of wind farms. *Energies*, 7(11):6930–7016, 2014.

[2] M. Samorani. The wind farm layout optimization problem. Technical report, PowerLeeds School of Buisness, 2010.

[3] A. Tesauro, P.-E. Rethore, and G. C. Larsen. State of the art of wind farm optimization. In *EWEA*, Copenhagen, Denmark, 2012.

[4] Torben Knudsen, Thomas Bak, and Mikael Svenstrup. Survey of wind farm control-power and fatigue optimization. *Wind Energy*, 18(8):1333–1351, 2015.

[5] DNV GL. `http://www.gl-garradhassan.com/en/software/GHWindFarmer.php`, 2014. [Online; acc. 05-May-2014].

[6] EMD. `http://help.emd.dk/knowledgebase`, 2015. [Online; acc. 08-Oct-2015].

[7] AWS Truepower. `http://software.awstruepower.com/openwind`, 2015. [Online; acc. 06-Oct-2015].

[8] Eftun Yilmaz. *Benchmarking of Optimization Modules for Two Wind Farm Design Software Tools*. PhD thesis, Gotland University, 2012.

[9] P.-E. Rethore, P. Fuglsang, G. C. Larsen, T. Buhl, T. J. Larsen, and H. A. Madsen. Topfarm: Multi-fidelity optimization of wind farms. *Wind Energy*, 17(12):1797–1816, 2014.

[10] J. Schmidt and B. Stoevesandt. Wind farm layout optimisation using wakes from computational fluid dynamics simulations. In *EWEA conference proceedings*, Barcelona, Spain, 10–13 March 2014.

[11] Jonas Schmidt and Bernhard Stoevesandt. Modelling complex terrain effects for wind farm layout optimization. *Journal of Physics: Conference Series*, 524(1):012136, 2014. The Science of Making Torque from Wind, Copenhagen, Denmark.

[12] Jonas Schmidt and Bernhard Stoevesandt. The impact of wake models on wind farm layout optimization. *Journal of Physics: Conference Series*, 625(1):012040, 2015. Wake Conference, Visby, Sweden.

[13] B.M. Adams, L.E. Bauman, W.J. Bohnhoff, K.R. Dalbey, M.S. Ebeida, J.P. Eddy, M.S. Eldred, P.D. Hough, K.T. Hu, J.D. Jakeman, L.P. Swiler, and D.M. Vigil. Dakota, a multilevel parallel object-oriented framework for design optimization, parameter estimation, uncertainty quantification, and sensitivity analysis: Version 5.4 user's manual. Technical Report SAND2010-2183, Sandia Technical Report, 2009.

[14] B. Lange, H. P. Waldl, A. G. Guerrero, D. Heinemann, and R. J. Barthelmie. Modelling of offshore wind turbine wakes with the wind farm program flap. *Wind Energy*, 6(1):87–104, 2003.

[15] OpenFOAM. http://www.openfoam.org, 2013. [Online; accessed 05-November-2013].

[16] Jonas Schmidt. `https://github.com/jonasIWES/terrainBlockMesher.git`, 2013. [Online; acc. 13-March-2013].

[17] A Crespo et al. Numerical analysis of wind turbine wakes. In *Delphi Workshop on Wind Energy Applications, Delphi, Greece*, 1985.

[18] M. Paul van der Laan, Niels N. Sorensen, Pierre-Elouan Rethore, Jakob Mann, Mark C. Kelly, Niels Troldborg, J. Gerard Schepers, and Ewan Machefaux. An improved k-epsilon model applied to a wind turbine wake in atmospheric turbulence. *Wind Energy*, 18(5):889–907, 2015.

[19] John Eddy and Kemper Lewis. Effective generation of pareto sets using genetic programming. In *ASME Design Engineering Technical Conference*, 2001.

[20] G. N. Vanderplaats. Conmin - a fortran program for constrained function minimization user's manual. Technical Report NASA TM X-62,282, NASA Technical Memorandum, 1973.

Provision of primary frequency support and inertia emulation by offshore wind farms connected through multi-terminal VSC-HVDC links

S. Nanou A. Spetsiotis S. Papathanassiou
National Technical University of Athens (NTUA),
School of Electrical and Computer Engineering, Electric Power Division
sotnanou@central.ntua.gr argispets@gmail.com st@power.ece.ntua.gr

Abstract:

In this paper, the contribution of offshore wind farms connected through multi-terminal DC (MTDC) grids to onshore frequency regulation is investigated, employing a communication-based approach to emulate onshore frequency fluctuations at each offshore AC grid. A dynamic model of the MTDC grid and the interconnected offshore wind farms is developed in Matlab/Simulink, where time-domain simulations are performed applying different frequency control implementations to the individual wind turbines. The main goal is to provide insight to the possibilities offered by MTDC grids to provide primary frequency response and synthetic inertia emulation, exploiting the frequency response characteristics of the state-of-the-art offshore wind turbines.

Keywords: multi-terminal DC, frequency response, inertia emulation, offshore wind turbines.

1 Introduction

Technical requirements imposed to wind farms and other power stations are gradually extending to high-voltage DC (HVDC) connections, including offshore wind power plants (OWPPs) [1]. Among these, particularly important is the provision of over- and under-frequency response, combined with synthetic inertia emulation.

Fig. 1 depicts a typical frequency response characteristic, from the draft ENTSO-E network code for DC-connected power park modules [1], where two operating modes are identified:

- “Frequency sensitive mode – Over-frequency (FSM-O)”: The HVDC system is expected to curtail active power proportionally to the frequency increase $\Delta f/f_n$, where f_n is the nominal system frequency. This operating mode is limited by the minimum regulating level that the station is allowed to operate.
- “Frequency sensitive mode – Under-frequency (FSM-U)”: If under-frequency events occur, the HVDC system is expected to release additional active power up to its maximum capacity P_{max}. The resulted under-frequency response depends on the operating reserve policy applied to the DC-connected primary source (e.g. de-loaded operation of OWPPs).

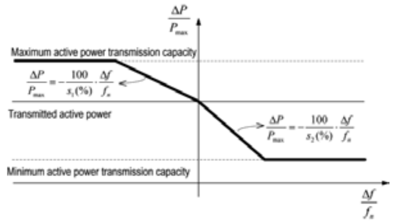

Figure 1: Active power regulation in FSM [1].

In the case of OWPPs connected through MTDC grids, a coordinated control approach is required between the onshore and offshore converter stations, in order for the onshore converters to provide a frequency-dependent active power modulation and meet the aforementioned requirements.

So far, relevant publications on frequency support by MTDC grids rely on DC voltage modulation techniques, performed by the onshore voltage source converters (VSCs), upon detection of onshore frequency deviations [2], [3], in order to evoke the desired frequency response characteristics by the MTDC grid. Further, the attention is often focused on obtaining the desired frequency response solely by the onshore VSCs of an MTDC grid which interconnects asynchronous AC networks [4], neglecting the potential offered by OWPPs to contribute to frequency control through the inherent frequency controllers of the individual WTs. In this paper, an alternative frequency control architecture is proposed for OWPPs connected through MTDC grids, relying on the existing communication infrastructure of the VSC-HVDC links in order to transmit onshore frequency deviation signals to the offshore VSCs. Following this approach, the provision of frequency response is achieved by activating the frequency response capabilities of the individual WTs. The modulated active power is delivered to the onshore grid via the DC voltage droop controllers of the onshore VSCs, which compensate the induced DC voltage variations. The communication delay introduced by the aforementioned approach has also been taken into account, including a brief parametric analysis showing its effect on the expected frequency response.

The paper is organized as follows. The generic layout of the MTDC grid is presented in Section 2. The control philosophy applied to each subsystem is briefly discussed in Section 3. Time-domain simulations are presented and discussed in Section 4, whereas the main conclusions are summarized in Section 5.

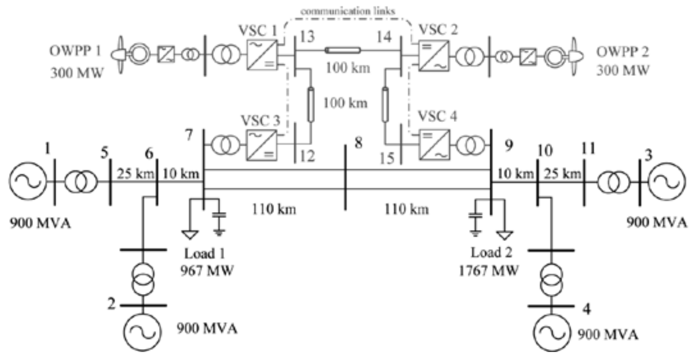

Figure 2: Study-case system comprising a 4-terminal MTDC grid connected to a two-area four generator power system.

2 System description

The single-line diagram of the conceptual MTDC grid under study is depicted in Fig. 2, where two 300 MW OWPPs are connected to a two-area four-generator power system, introduced in [5], which consists of four 900-MVA conventional generators, split into two areas. Each generator incorporates an automatic voltage regulator and a generic power system stabilizer, available in Matlab/Simulink library. For the purposes of this study, power plants 1-4 are modeled as steam turbine generators, using the IEEEG1 speed governor model [6].

The MTDC grid comprises the onshore and offshore VSCs and submarine HVDC cables. The length of each cable line is depicted in Fig. 2; electrical characteristics are provided in the Appendix.

To simplify converter modeling and reduce computational burden, an aggregate 300-MW WT based on full-power converters (FCWTs) is used to represent each OWPP, as further explained in Section 3.3. Since the main focus is on the frequency response of the MTDC grid, all high-frequency components related to the switching of power converters are neglected and the WT and HVDC converters are described by the fundamental frequency model of [7].

3 Controllers

3.1 Onshore VSC controller

The overall control scheme employed for the onshore VSCs is depicted in Fig. 3. VSCs

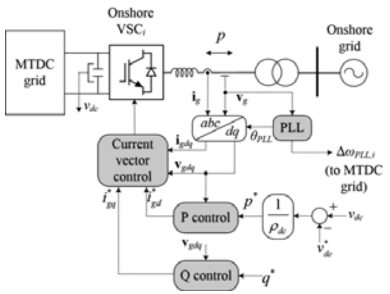

Figure 3: Onshore VSC and controller structure.

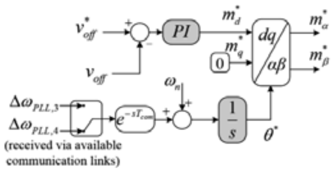

Figure 4: Offshore VSC controller with integrated frequency modulation technique.

#3 and #4 export DC power to the onshore grid by regulating the HVDC voltage v_{dc} via a DC voltage-power droop control concept [8]. The droop constant ρ_{dc} is assumed 4% for both VSCs. A conventional current vector controller operating in the synchronous reference frame (SRF) is considered for the inner control loop. The onshore frequency deviations are estimated by the phase-locked loop (PLL) of each onshore VSC (signal $\Delta\omega_{PLL,i}$ in Fig. 3, i=3,4), which are then transmitted to VSCs #1 and #2 via suitable communication links, i.e. fiber optic cables installed with the HVDC submarine cables. This communication network (Fig. 2) provides increased redundancy since an estimate of the onshore frequency is always available in case of a single communication link failure. The reactive output power can be controlled to support the grid voltage during faults and also to provide a certain amount of reactive power in steady-state, in accordance with grid code provisions.

3.2 Offshore VSC controller

The offshore VSCs (#1 and #2) operate as grid-forming power converters [9], where a

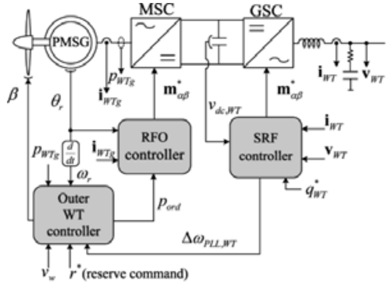

Figure 5: FCWT and controller structure.

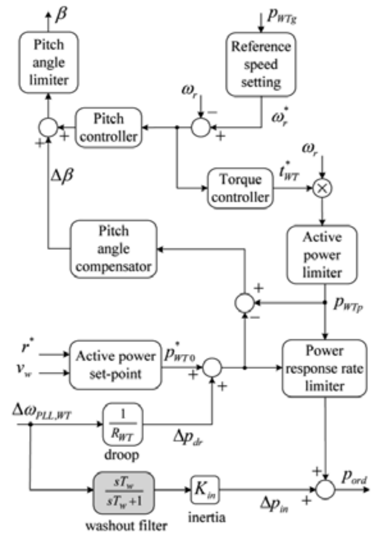

Figure 6: Outer WT controller of Fig. 5 in block diagram form, with integrated droop and inertia frequency controller.

Proportional-Integral (PI) AC voltage controller (Fig. 4) controls the magnitude of the grid voltage v_{off}, whereas a frequency controller emulates onshore grid conditions, by superimposing the frequency deviation signal $\Delta\omega_{PLL,i}$ (i=3 or 4), on the default value ω_n. For the purposes of this study, a communication delay T_{com} of 20 ms is first assumed, whereas a brief parametric analysis is also performed in Section 4 in order to illustrate its effect on the expected frequency response.

3.3 WT controller

The typical configuration of a FCWT based on a multi-pole permanent magnet synchronous generator (PMSG) is illustrated in Fig. 5 [10]. It is connected to the MV grid through an output LC filter and a step-up transformer. The PMSG is controlled by the machine side converter (MSC), which employs a rotor field oriented (RFO) control scheme, controlling the PMSG active power to the power order p_{ord} provided by the outer WT controller depicted in detail in Fig. 6. The grid side converter (GSC) operates in the SRF and regulates the dc link voltage $v_{dc,WT}$ to its nominal value. Further details can be found in [10].

The outer WT controller structure adopted, illustrated in Fig. 6, is based on the control philosophy presented in [11]. It performs the following tasks:

- *Torque control*. A torque controller regulates the WT rotor speed ω_r to the reference value provided by the maximum power point tracking characteristic. Based on the torque reference t^*_{WT} and the active power set-point p^*_{WT0}, the final active power order p_{ord} is then determined after applying rate and level limit functions. Controller settings are those recommended in [11] for the FCWT configuration.
- *Pitch angle control*. The pitch controller prevents over-speeding of the WT, whereas an additional pitch compensator is also utilized to reconfigure the WT operating point during de-loaded operation of the WT, by pitching of the blades. This controller is adopted in this work, using again the control settings recommended in [11] for the FCWT configuration.
- *Frequency control*. The desired frequency response is provided by modulating the power order p_{ord}, utilizing the droop and inertia frequency controllers illustrated in Fig. 6. The frequency controller utilizes the estimate of the offshore grid frequency $\Delta\omega_{PLL,WT}$, provided by the PLL unit of the GSC controller.

4 Time – domain simulations

4.1 Frequency response capability

The objective of this section is to assess the under-frequency response capability of the MTDC grid, applying different frequency control implementations to the offshore WTs. The study-case system of Fig. 2 is simulated in SimPowerSystems Toolbox of Matlab/Simulink using the phasor simulation method [12].

The overall system response is presented in Fig. 7, following a 200 MW step increase of the load connected at bus 7, at t=10 s. Each OWPP initially generates approximately 250 MW, while the reserve command r^* dispatched to the offshore WTs (see Fig. 5) is set to 10%. The droop constant and the virtual inertia gains shown in Fig. 6 are R_{WT}=5% and K_{in}=20 respectively.

The response of the system frequency in Fig. 7(a) is obtained using the different frequency control approaches presented in Fig. 6. If operation in FSM is suspended, a maximum frequency dip of approximately 0.38 Hz occurs, following the load increase (blue curve). Droop control alone (green curve) achieves a reduction of post-disturbance frequency deviation by approximately 8%, while a slight increase of the damping ratio of the dominant electromechanical mode is observed. When inertia control is applied (red curve), both the maximum frequency dip and the rate of change of frequency (ROCOF) are notably reduced. The combined droop and inertia (PD type) control (black curve) expectedly provides best results, as the maximum frequency excursion is reduced by 18%. In all cases, the DC voltage-power droop controllers of VSCs #3 and #4 successfully compensate DC voltage fluctuations (Fig. 7(b)); thus the frequency-dependent active power modulation of the WTs is reflected at the MTDC network output by the onshore VSCs (Fig. 7(c)). As for the WT rotor dynamics, the rotor speed deviations (Fig. 7(d)), assisted by the action of the pitch regulator, are acceptable in all cases.

4.2 Operation with adjustable power reserves

In this section, the ability of the MTDC grid to provide adjustable power reserves during normal operation, exploiting the de-loaded operation of the offshore WTs, is

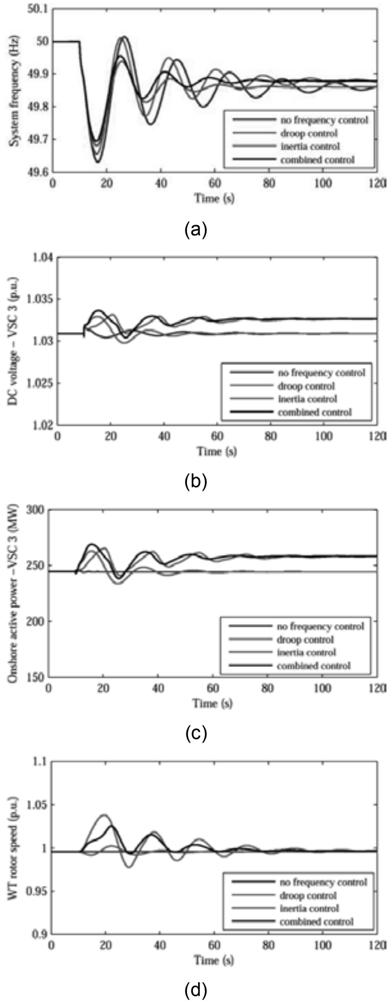

Figure 7: (a) System frequency, (b) HVDC voltage at VSC #3 station, (c) onshore active power (VSC #3), (d) WT rotor speed of OWPP #1, following a 200 MW step increase of bus 7 load at t=10 s, for alternative frequency control approaches (R_{WT}=5%, K_{in} =20).

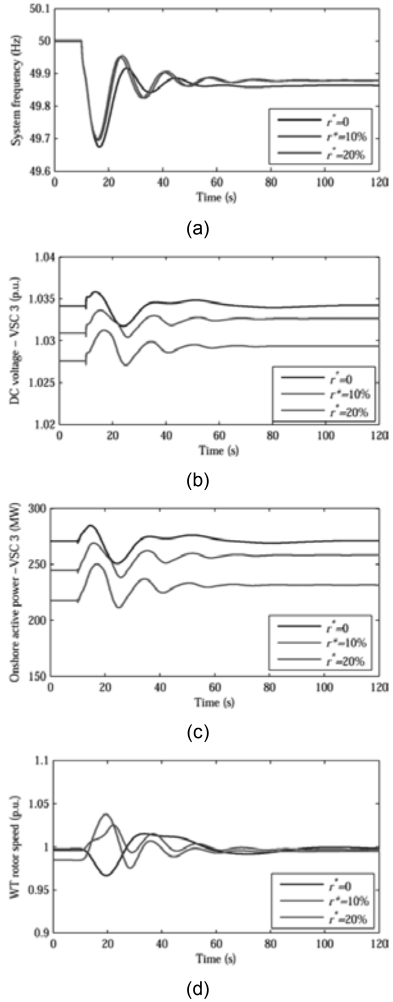

Figure 8: (a) System frequency, (b) HVDC voltage at VSC #3 station, (c) onshore active power (VSC #3), (d) WT rotor speed of OWPP #1, for the same disturbance as in Fig. 7, assuming operation at different reserve levels with combined (droop & inertia) control.

demonstrated in Fig. 8, for different levels of the power reserve command r^* (0, 10% and 20%), applying the combined frequency controller. Comparing Figs. 7(a) and 8(a), it is evident that the MTDC grid is still able to filter-out fast frequency excursions even in

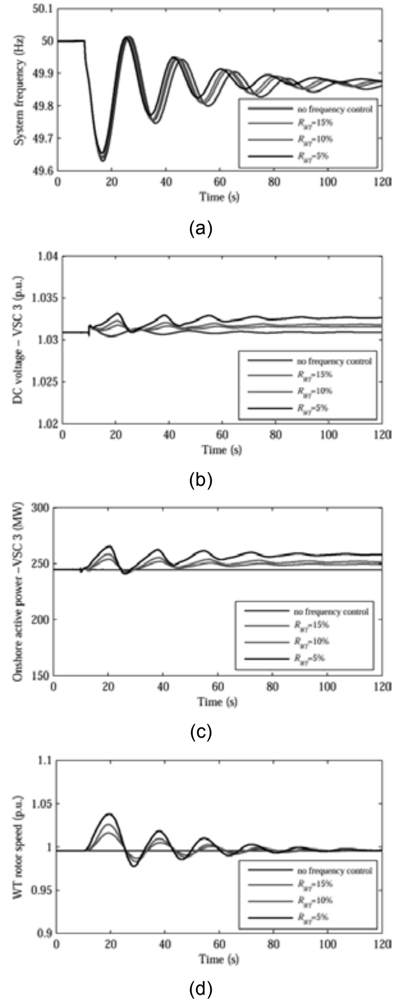

Figure 9: (a) System frequency, (b) HVDC voltage at VSC #3 station, (c) onshore active power (VSC #3), (d) WT rotor speed of OWPP #1, for the same disturbance as in Fig. 7. Droop-type WT frequency controller, with different droop parameter values.

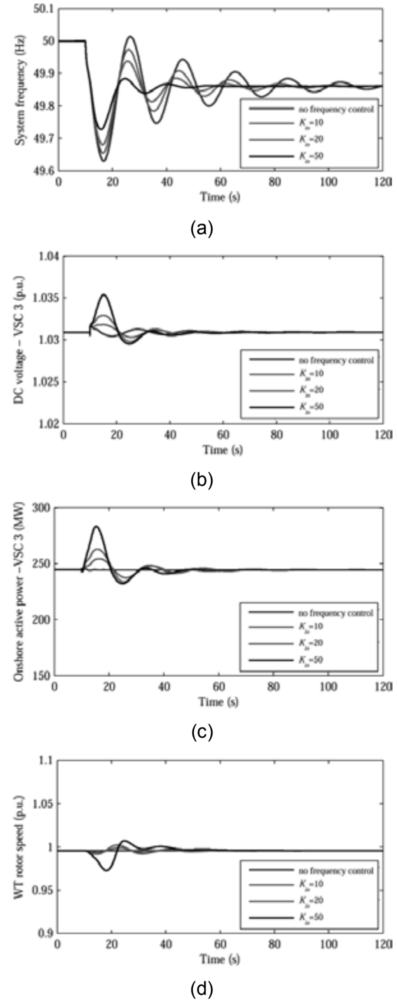

Figure 10: (a) System frequency, (b) HVDC voltage at VSC #3 station, (c) onshore active power (VSC #3), (d) WT rotor speed of OWPP #1, for the same disturbance as in Fig. 7. Inertia WT frequency controller, with different virtual inertia values.

the case where no power reserve is maintained, however the provision of sustained under-frequency response is not possible, since the WTs are unable to release additional active power permanently.

4.3 Effect of droop and virtual inertia values

To examine the response of the droop-type frequency controller in more detail, additional time-domain simulations are presented in Fig. 9, assuming different values of the droop constant R_{WT}. From Fig. 9, it is evident that low droops lead to improved response characteristics during under-frequency events, however larger WT rotor speed deviations are excited.

The system response using solely the inertia frequency controller (without droop) is demonstrated in Fig. 10, for different values of the synthetic inertia gain K_{in}. Increased K_{in} values are more effective in reducing both ROCOF and frequency excursions of the onshore AC grid, resulting in a notable damping of the system.

Nevertheless, such observations may depend on the particular characteristics of the study-case system, including the characteristics of the speed governor and the power system stabilizer of the individual generators operating in the onshore AC grid.

4.4 Impact of communication system latency

The robustness of the communication-based approach in the presence of different communication delays T_{com} is demonstrated in Fig. 11, assuming the application of the combined WT frequency controller, where it is evident that even large delays in the range of 100-500 ms do not alter the expected frequency response characteristics.

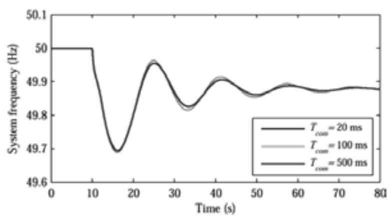

Figure 11: Impact of communication delay T_{com} on the frequency response, for the same disturbance as in Fig. 7, with combined droop and inertia control.

5 Conclusions

In this paper, the contribution of OWPPs connected through MTDC grids to onshore frequency regulation has been investigated, utilizing the existing communication infrastructure of the VSC-HVDC links in order to emulate onshore frequency fluctuations in each offshore AC grid and thus excite the frequency response capabilities of the WTs.

Results obtained from time-domain simulations demonstrate an important potential for the contribution of the MTDC grid to frequency control. The droop-type controller of the offshore WTs contributes to the reduction of post-disturbance frequency deviations, while the inertia controller increases the apparent system inertia and provides substantial damping to the dominant electromechanical modes of the power system. It is noteworthy that even if no power reserve is maintained by the offshore WTs, the OWPPs are still able to contribute to frequency regulation, utilizing the stored kinetic energy of the individual WTs as an energy buffer during frequency transients.

The communication-based frequency modulation approach is entirely feasible in practice, while the impact of communication system latency on the frequency response is insignificant, due to the slow nature of frequency variations in large onshore systems. For the study-case system examined in this work, the provision of frequency response by the MTDC grid becomes feasible without the need to implement additional droop-type or inertia frequency controllers in the control units of the onshore converter stations.

Acknowledgements

The work of Sotirios Nanou is supported by the IKY Fellowships of Excellence for Postgraduate Studies in Greece - Siemens Program.

Appendix: System parameters

HVDC cable	Value
Resistance	0.022 Ω/km
Inductance	0.191 mH/km
Shunt Capacitance	0.295 μF/km

HVDC VSC	Value
Nominal power	300 MW
Pole-to-pole DC voltage	300 kV
DC capacitance	290 μF
Phase reactor	33 mH

References

[1] ENTSO-E Draft Network Code on High Voltage Direct Current Connections and DC-connected Power Park Modules. *ENTSO-E*, Belgium, 2014.

[2] Chaudhuri NR, Majumder R, Chaudhuri B. "System Frequency Support Through Multi-Terminal DC (MTDC) Grids". *IEEE Trans. Power Systems*, 2013; 28:347-356.

[3] Zhu J, Guerrero JM, Hung W, Booth CD, Adam GP. "Generic inertia emulation controller for multi-terminal voltage-source-converter high voltage direct current systems". *IET Renew. Power Gener.*, 2014; 8:740-748.

[4] Akkari S, Petit M, Dai J, Guillaud X. "Interaction between the Voltage-Droop and the Frequency-Droop Control for Multi-Terminal HVDC Systems". Proceedings of the 11th IET Intern. Conf. on AC and DC Power Transmission (ACDC); 2015 Feb 10-12; Birmingham, pp. 1-7.

[5] Klein M, Rogers GJ, Kundur P. "A Fundamental Study of Inter-Area Oscillations in Power Systems", *IEEE Trans. Power Systems*, 1991; 6:914-921.

[6] "Dynamic Modes for Turbine-Governors in Power System Studies". *IEEE Power & Energy Society*, Tech. Report PES-TR1, 2013.

[7] Saad H, Peralta J, Dennetiere S, Mahseredjian J, Jatskevich J, Martinez JA, Davoudi A, Saeedifard M, Sood V, Wang X, Cano J, Mehrizi-Sani A. "Dynamic Averaged and Simplified Models for MMC-Based HVDC Transmission Systems". *IEEE Trans. Power Del.*, 2013; 28:1723-1730.

[8] Wang W, Barnes M. "Power Flow Algorithms for Multi-Terminal VSC-HVDC with Droop Control". *IEEE Trans. Power Systems*, 2014; 29:1721-1730.

[9] Rocabert J, Luna A, Blaabjerg F, Rodriguez P. "Control of Power Converters in AC Microgrids". *IEEE Trans. Power Electron.*, 2012; 27:4734-4749.

[10] Conroy JF, Watson R. "Frequency Response Capability of Full Converter Wind Turbine Generators in Comparison to Conventional Generation". *IEEE Trans. Power Syst.*, 2008; 23:649-656.

[11] Clark K, Miller NW, Sanchez-Gasca JJ. "Modeling of GE Wind Turbine-Generators for Grid Studies". *GE Energy*, New York, 2010.

[12] "SimPowerSystemsTM User's Guide". Hydro Québec and The MathWorks, Inc., Massachusetts, 2010.

Control of HVDC Diode Rectifier connected off-shore wind farm during cable faults in multi-terminal HVDC grids

S. Añó-Villalba, S. Bernal-Perez, R. Blasco-Gimenez
Universitat Politècnica de València
Valencia, Spain
Email: sanyo@die.upv.es, sbernal@die.upv.es, r.blasco@ieee.org

Abstract – The presented work shows the proof-of-concept operation of a HVDC diode rectifier (DR) station connected a multi-terminal HVDC grid. Previous work by the authors and others has shown that a wind power plant WPP can adequately control the off-shore ac-grid frequency and current and also deliver optimum power to the HVDC grid mainly in point-to-point configuration. This work aims to show the operation of the HVDC-DR in a multi-terminal HVDC grid and to study up to which extent the WPP control can be used to minimise the currents flowing through the HVDC-DR station during cable (pole-to-ground) faults. It has been found that reasonably fast DR station current reduction can be achieved and hence an active control of the WPP can help on simplifying the protections of the DR station in a muti-terminal environment.

***Index Terms*—Fault analysis, HVDC diode rectifier, HVDC grid, off-shore wind power plant.**

I. Introduction

HVDC diode rectifier (HVDC-DR) stations offer substantial benefits in terms of installation and operational costs for the connection of distant off-shore wind power plants [1]–[6]. Morevoer, they have been put forward as one of the most promising solutions for off-shore WPP connection. HVDC-DR converters use relatively simple, robust and low cost devices and do not require complex control installations. Moreover, a substantial reduction on off-shore platform footprint can be achieved if reduced filter banks are used [7], together with integrated oil-immersed diode rectifier units and compact SF_6 switchgear [6].

Moreover, the HVDC-DR solution also exhibits very good efficiency figures. These low losses, together with the inherent robustness of a diode rectifier will contribute to overall low operational costs.

The authors would like to thank the support of the Spanish Ministry of Economy and EU FEDER funds under grant DPI2014-53245-R. The support of CONICYT/FONDAP/15110019 is also kindly acknowledged.

Previous work by the authors and others has shown that the WPP can adequately control the off-shore ac-grid frequency and current and also deliver optimum power to the HVDC grid [1]–[3], [5], [6]

However, there are little previous literature con the connection of DR stations to multiterminal HVDC grids. This paper shows a proof-of-concept study for such kind of connection and how the WPP control deals with cable (pole-to-ground) faults in different scenarions. It has been proposed that adequate action on the wind turbines can help reducing the fault currents during cable faults [?].

Cable faults will cause a voltage dip on the off-shore ac-grid. At the same time, there will be a sharp increase on the reactive power demand of the HVDC-DR station. These two effects can be used by the wind turbines to detect the fault and act accordingly.

The proposed distributed protection mechanism includes the use of a Voltage Dependent Current Order Limit (VDCOL) in each wind turbine. The overall wind turbine current limit is shared between active and reactive current components. It will be shown that giving priority to the reactive current component leads to a faster reduction of fault currents.

The combined action of the VDCOL and the reactive current priority limit lead to the wind turbine currents to go to zero very rapidly, based only on local measurements.

When the currents through the HVDC-DR station are close to zero, the no-load switch of the corresponding pole is opened. Once the no-load switch is opened, then power injection is resumed in the healthy pole.

The proposed approach has been verified by means of detailed simulations using PSCAD, including a clustered model of the wind farm (5 clusters of different power) and a wide frequency model of the cables.

II. System Description

The proposed system consists of a HVDC grid with four terminals, Figure 1.

One of the terminals is an off-shore WPP represented by five aggregated wind turbines of different ratings: 5, 40, 80, 120 and 155 MW. Figure 2 shows the considered type-4 wind turbines i $(i = 1, 2, .., 5)$. The wind turbines are connected to the bus PPC_F through a full scale back-to-back converter and a transformer T_{Wi}. Z_{FR} represents the harmonic filters and C_F the reactive power compensation of both the diodes and the rectifier transformers. T_{R1} and T_{R2} are the rectifier transformers. These transformers connect to a bipolar 12-pulse diode-based rectifier. L_R is the rectifier smoothing reactor. Details about the distributed WPP description and modelling can be found in [1].

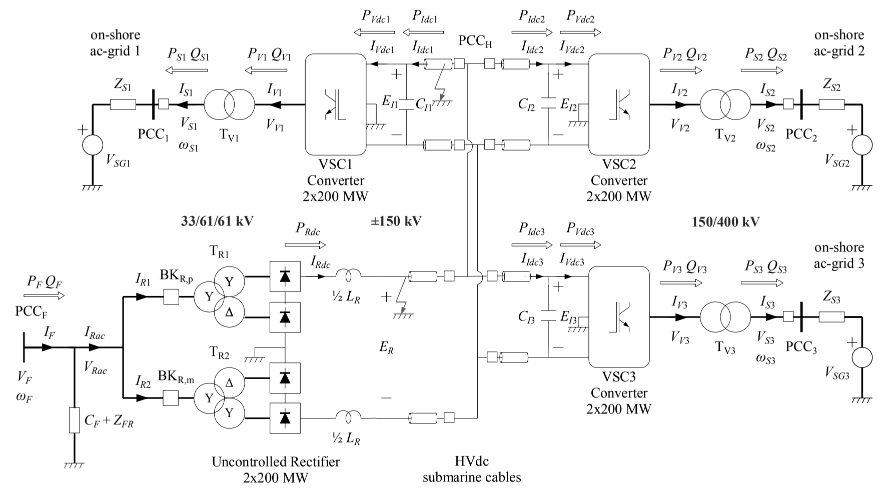

Fig. 1: Considered multi-terminal HVDC system

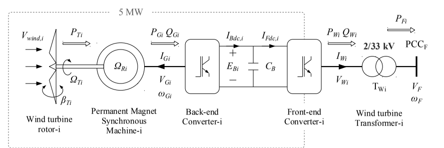

Fig. 2: Wind turbine cluster i $(i = 1, 2, ..5)$ connected to the off-shore PCC_F.

The other three terminals of the HVDC system consist of three $(j = 1, 2, 3)$ identical bipolar Voltage Source Converters (VSCs) connected to the on-shore ac-grid at PCC_j, Figure 3. Each converter has two step-up transformers T_{Vj}. The on-shore ac-grid is modelled by its Thevenin's equivalent parameters (Z_{Sj} and V_{SGj}).

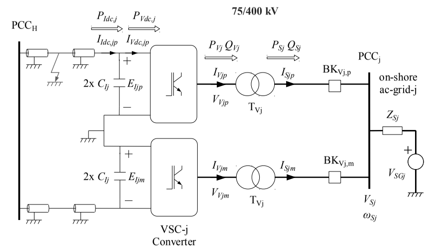

Fig. 3: HVDC-VSC terminal VSC_j $(j = 1, 2, 3)$ connected to the on-shore PCC_j.

The HVDC grid consists of submarine cables. As dc-faults represent very fast electromagnetic transients, a distributed frequency dependent parameter model is used, [8]. Description and parameters can be found in [9].

The table in the Appendix includes the parameters for the different elements of the proposed system.

A. WPP and HVDC-VSC Station Control

During normal operation the on-shore ac-voltages V_{Sj} are set by the on-shore ac-grids represented by V_{SGj} and

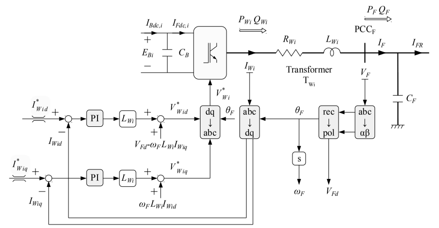

Fig. 4: Wind turbine grid-side converter current control loops

Z_{SGj}. The HVDC link voltages E_{Ij} and E_R are set by VSC1 and VSC3 using a voltage droop control. Finally, the off-shore ac-voltage magnitude V_F is clamped to the HVDC link voltage through the diode rectifier.

The wind turbines limit their front-end active currents $I_{Wd,i}$ in order to operate at optimum power, Figure 4. When the wind turbine active currents are not saturated, e.g. during WPP sudden disconnection, they control the off-shore ac-grid voltage V_{Fd} (islanding mode), Figure 5.

The off-shore ac-grid frequency is controlled by the wind turbine grid-side converter reactive currents $I_{Wq,i}$. A detailed description of these controls and current sharing between wind turbines can be found in [1].

The on-shore VSC1 and VSC3 control the HVDC link voltages $E_{I1,3}$ and the reactive power $Q_{S1,3}$.Therefore they will evacuate the active power injected to the HVDC grid by the WPP and by converter station 2 (VSC2), which operates at constant power reference.

Converter station 2 active and reactive power control is achieved by using standard inner current ($I_{Vjd,q}$) control loops. A detailed description of the control loops can be found in [5].

B. Protection devices

The considered protection devices include ac and dc circuit breakers to isolate parts of the circuit during faults. $BK_{R,p}$ and $BK_{R,m}$ are the ac-breakers connecting the WPP to the positive and negative poles of the diode rectifier, respectively. Figure 3 shows the ac-breakers of the VSCs, also connected to both poles, $BK_{Vj,p}$ and $BK_{Vj,m}$.

Regarding the HVDC grid, dc-breakers have been considered on each one of the cables reaching the bus PCC_H, as shown in Figure 1.

Clearly, each one of the cable sections can be isolated by a combination of ac and dc-breakers.

C. Fault-ride-through strategy during DC grid faults

During short-circuit faults it is imperative to protect the components of the WPP and the multi-terminal

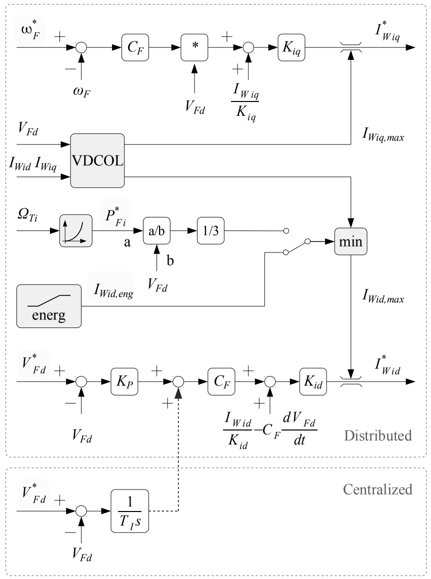

Fig. 5: Off-shore ac-grid frequency (ω_F) and voltage (V_{Fd}) control loops with optimum power tracking

HVDC system. A Voltage Dependent Current Order Limit (VDCOL) has been introduced in the wind turbines in order to limit their ac-currents during faults, as shown in Figure 5.

The VDCOL operation is relatively straight forward. The off-shore voltage V_{Fd} will drop during cable faults, leading to the reduction of the current limits $|I_{Wi}|_{max}$ to their corresponding VDCOL characteristic, Figure 6. The overall current limit is distributed between active and reactive current components prioritizing frequency control:

$$I_{Wiq,max} = |I_{Wi}|_{max} \tag{1}$$

$$I_{Wid,max} = \sqrt{|I_{Wi}|^2_{max} - I^2_{Wiq,max}} \tag{2}$$

A rate limiter is applied to the V_{Fd} measurement, before using it to calculate the current limit ($|I_{Wi}|_{max}$) using the characteristic in Figure 6. The downwards rate limit on the V_{Fd} measurement is almost non existent to allow for fast response at the fault onset. On the other hand, the upwards rate limit can be tailored to avoid large current di/dt during fault recovery.

This strategy allows for fast wind turbine response

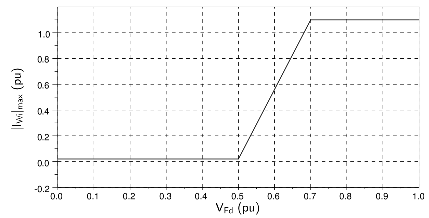

Fig. 6: VDCOL characteristic of WT grid-side converters

during faults, without the need for communication.

III. Case Studies

The proposed fault ride through procedure will be validated by considering positive pole to ground short circuits at two different locations, namely the midpoint of the cable connecting converter station 1 (VSC1) to the bus PCC_H and the junction of the positive pole cable with the DR station. The locations of these faults are clearly shown in Figure 1

A. Case 1: Pole-to-ground fault at the midpoint of VSC1-PCC_H cable

This case aims at verifying the co-ordination of the HVDC-DR station proposed fault-ride-through strategy with the complete HVDC grid protection mechanism.

To this avail, a pole-to-ground short-circuit is considered at the midpoint of the cable connecting VSC1 to PCC_H. It is assumed that the fault is cleared by the dc-breaker in about 20 ms (including processing delay and breaker operating time).

Figure 7 shows the relevant voltages and currents of both diode rectifier station and wind power plant during the cable short circuit occurring at $t = 0.1$ s.

The step-by-step evolution from fault onset to recovery is as follows:

1) At $t = 0.1$ s the short-circuit reduces both the dc-voltage E_{Hp} and the ac-voltage V_{Fd}.
2) Then the front-end VDCOL of the wind turbines reduces de current limits $|I_{Wi}|_{max}$, saturating the current control loops and driving both active and reactive currents to zero. Active and reactive currents go to zero in about 11 ms. At this stage, neither the off-shore grid ac-voltage V_{Fd}, nor its frequency ω_F follow their references.
3) At $t = 0.12$ ms the dc-breaker isolates the VSC1 cable and the fault currents are removed from the rectifier, VSC2 and VSC3.
4) Wind Power Plant remains blocked for 100 ms to allow for dc-fault clearance (a relatively large delay has been introduced for illustration purposes, but can easily be shortened). At $t = 0.2$ s, the wind turbine grid control is resumed, albeit with limited active power references P^*_{Fi}. At this stage both ac-grid voltage V_{Fd} and frequency ω_F are restored, see Figure 7.
5) Once the off-shore grid is stabilised, the wind turbine active power limits are increased and full power generation in both poles is restored from $t = 0.6$ s.

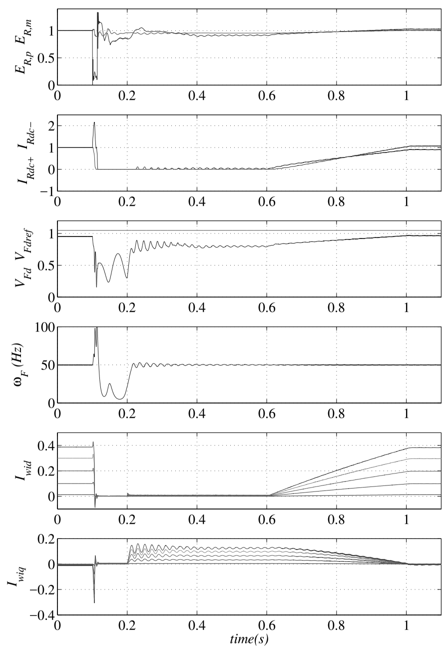

Fig. 7: Rectifier and off-shore grid behaviour during the VSC1 cable fault (case 1)

Figure 8 shows the ac-grid voltage V_F, rectifier transformer and Wind Power Plant currents (I_F and I_{Rac} respectively). Clearly, the proposed strategy leads to the absence of large voltage or current peaks during the fault and recovery. The aforementioned recovery steps can also be clearly appreciated, where the wind farm starts delivering reactive power to control the ac-grid voltage from $t = 0.2$ s onwards. Also at t=0.6s the rectifier transformer current ramps up, as the WPP ramps up its power production.

Figure 9 shows the total active power delivered by the rectifier station and by each one of the HVDC-VSC

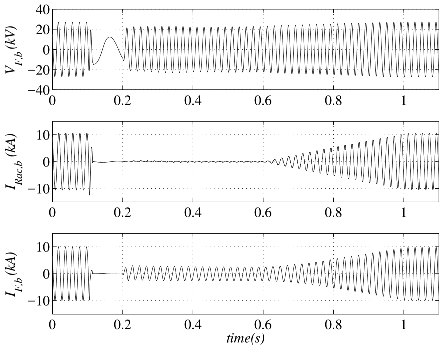

Fig. 8: Wind Farm and rectifier transformer ac currents (case 1)

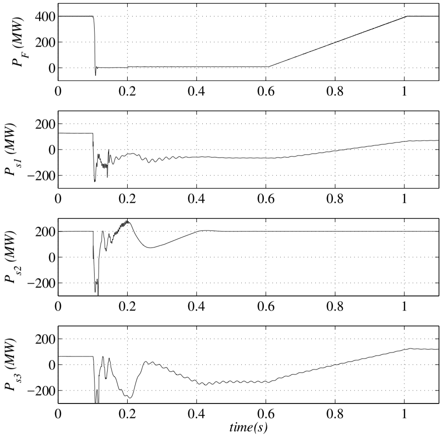

Fig. 9: Power delivered by each terminal during VSC1 cable fault (case 1)

stations. Initially the WPP is delivering its rated power (400 MW), and VSC2 is delivering its 200 MW power set point to the ac-grid 2.

VSC stations 1 and 3 participate in the overall droop control and both deliver 100 MW to complete the power injected by the WPP.

After the fault, the WPP resumes full power operation, and VSC2 also reaches its 200 MW set-point. However, now VSC1 is operating only with a single pole, so now the power delivered by VSC1 is below 100 MW, and the

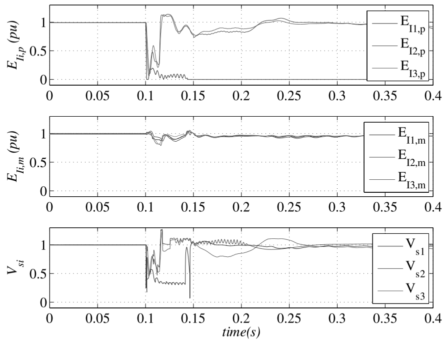

Fig. 10: AC-side, positive and negative pole voltages at the converter stations (case 1)

additional power is injected into the on-shore grid 3 by VSC3.

Figure 10 shows the details of the positive pole, negative pole and ac-side voltages for each one of the VSC stations ($E_{Ii,p}$, $E_{Ii,m}$ and V_{si} respectively).

The positive pole voltage traces $E_{Ii,p}$ clearly show that the fault propagates almost instantaneously through the HVDC grid. They also show that the dc-breaker clears the fault in about 20 ms. Clearly, the positive pole voltage of the faulted line remains at a very low or zero voltage from $t = 0.1$ s onwards.

Negative pole voltages are affected by the fault and their traces ($E_{Ii,m}$) show small oscillations, due to the positive and negative coupling via the corresponding ac-grids.

This coupling can be easily seen by looking at the ac-side voltage traces (V_{si}). Clearly, the cable fault causes a voltage dip in all the ac-grids. The depth of the ac-side voltage dip is smaller than that of the dc-side, helped by the transformer and ac-side line impedances.

Once the dc-fault is cleared, the ac-side voltages of VSC stations 2 and 3 quickly recover. However, the ac-side voltage of VSC1 only recovers when the positive pole ac-breaker finally isolates the faulted pole and cable.

B. Case 2: Pole-to-ground fault at the junction of the positive pole cable with the HVDC-DR station

This case assumes that a fault occurs at the junction of the positive pole cable with the HVDC-DR station, see Figure 1). This case aims to show up to which extent the proposed strategy can isolate a fault close to the HVDC-DR station switching the ac-side breaker at zero current.

Figure 11 shows the behaviour of the DR station and the off-shore ac-grid during the diode rectifier cable fault.

The step-by-step evolution from fault onset to recovery is as follows:

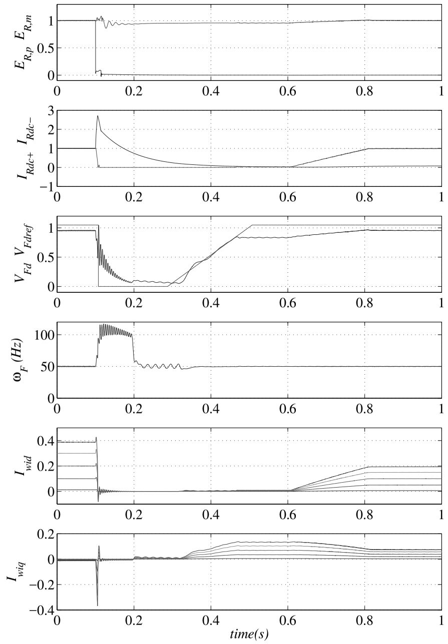

Fig. 11: Rectifier and off-shore grid behaviour during the DR cable fault (case 2)

1) A positive pole-to-ground short-circuit reduces both the dc-voltage E_{Rp} and the ac-voltage V_{Fd}.
2) At the same time, the reactive current demand of the rectifier station increases (this happens even before the voltage dip in V_{Fd} is large enough to generate zero current references). Therefore, the wind turbine reactive current components increase while the active components decrease, as reactive current injection has been prioritised, see Eq. (2).
3) When V_{Fd} goes below 0.7 pu, the front-end VDCOL reduces de current limits $|I_{Wi}|_{max}$ and the current control loops are saturated. The wind turbine currents go to zero in about 10 ms.
4) The dc-side breaker disconnects the faulted cable in about 20 ms (processing delay plus breaker operating time).
5) Once the rectifier station ac current I_{R1} goes to zero (or to a very small value), the DR ac-side breaker is tripped. Up to this stage both wind turbine grid-side converter active and reactive current references are

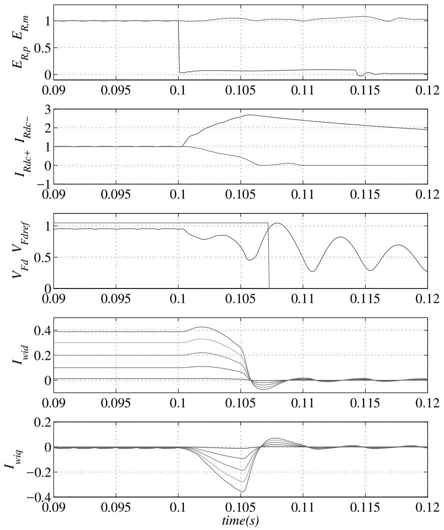

Fig. 12: Rectifier and off-shore grid behaviour during the DR cable fault (case 2) (detail)

set to zero, therefore the off-shore ac-grid voltage (V_F) and frequency (ω_F) cannot follow their references.
6) Once the fault is cleared, the wind turbines start the energisation procedure with relatively small limits on the delivered power. The ac-grid voltage is restored to its rated value in about 200 ms, allowing for controlled energisation of transformers, cables and filter banks.
7) When the negative pole rectifier starts conducting, the power limits are ramped up to 0.5 pu and the WPP power is delivered through the healthy negative pole.

As shown in Figure 11, the complete process takes less than 700 ms, although some waiting times can be reduced, and some delays are system specific.

Figure 12 shows the detailed behaviour of the WPP at the onset of the fault. At the beginning of the fault, the voltage drop in V_{Fd} is relatively small, so the wind turbines tend to keep constant power delivery and hence I_{wid} increase slightly.

As the DR station positive pole current increases due to the fault, the rectifier draws a relatively large amount of reactive power, which limits the amount of active current available for power delivery. At $t = 0.105$ s, V_{Fd} goes below 0.7 pu and the VDCOL reduces both

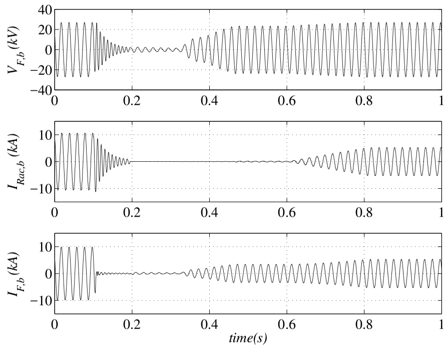

Fig. 13: Wind Farm and rectifier transformer ac currents (case 2)

active and reactive current references to zero. With the current system parameters, wind power plant currents are reduced to zero in about 11 ms.

It is also worth stressing that the positive pole current reaches it maximum 2.5 pu value 6 ms after the fault onset. Therefore, its initial reduction is not due to the dc-breaker action.

Note also V_{Fdref} is reduced to zero, in preparation to ramp up the off-shore ac-grid voltage once the breaker BK$_{R,p}$ clears the fault. In any case, the change of V_{Fdref} does not take any part in wind power plant current reduction.

Figure 13 shows the ac-grid voltage V_F, rectifier transformer and Wind Power Plant current (I_F and I_{Rac} respectively). These graphs show that BKR, p is operated at nearly zero current ($t = 0.2$ s). Clearly, the proposed strategy leads to the absence of large voltage or current peaks during the fault and recovery. The aforementioned recovery steps can also be clearly appreciated, where the wind farm starts delivering reactive power to control the ac-grid voltage from $t = 0.3$ s onwards ($I_{F,b}$ increase while $I_{Rabc,b}$ is still zero). Finally, at $t = 0.6$ s the rectifier transformer current ramps up, as the WPP ramps up its power production.

Figure 14 shows the total active power delivered by the rectifier station and by each one of the HVDC-VSC stations. Initially the WPP is delivering its rated power (400 MW), and VSC2 is delivering its 200 MW power set point to the ac-grid 2.

VSC stations 1 and 3 participate in the overall droop control and together deliver the remaining 200 MW to complete the power injected by the WPP.

After the fault, VSC2 starts delivering its 200 MW power set point. However, during fault recovery ($t = 0.5$ s to $t = 0.6$ s), the WPP is still not delivering any active

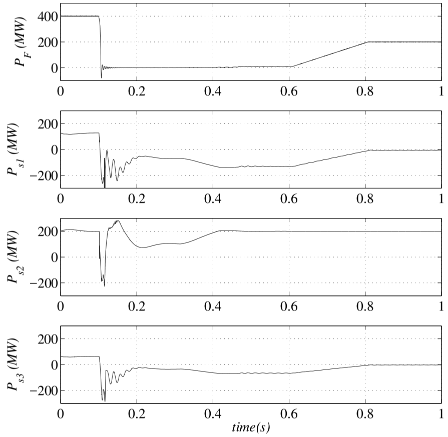

Fig. 14: Power delivered by each terminal during DR cable fault (case 2)

power, so the 200 MW delivered by VSC2 are injected into the HVDC grid by VSC1 and VSC3, by virtue of their aforementioned droop control.

After the fault, the WPP can only operate at half power, as only the healthy negative pole is available for operation. VSC2 is still operating at a constant 200 MW set-point. Therefore, both VSC1 and VSC3 will not draw or inject any power to the HVDC grid.

It is worth stating that if it is desired that both VSC2 poles deliver the same power (100 MW each), additional losses are incurred in the system. Clearly, the WPP 200 MW are only injected to the negative pole. Therefore part of the power has to circulate between positive and negative poles of VSC1 and VSC3. This issue can easily be solved by using different positive and negative pole power references for VSC2.

Figure 15 shows the details of the positive pole, negative pole and ac-side voltages for each one of the VSC stations ($E_{Ii,p}$, $E_{Ii,m}$ and V_{si} respectively).

The positive pole voltage traces $E_{Ii,p}$ clearly show that the fault propagates almost instantaneously through the HVDC grid and that the dc-breaker clears the fault in about 20 ms.

Negative pole voltages are affected by the fault and their traces ($E_{Ii,m}$) show small oscillations, due to the positive and negative coupling via the corresponding ac-grids.

This coupling can be easily seen by looking at the ac-side voltage traces (V_{si}). Clearly, the cable fault causes a voltage dip in all the ac-grids. The depth of the ac-

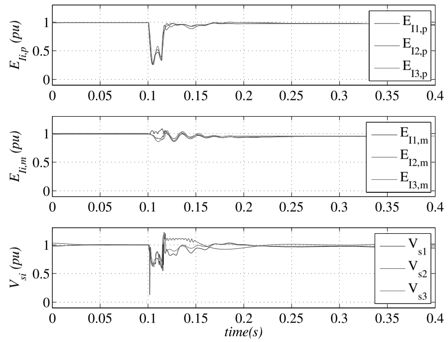

Fig. 15: AC-side, positive and negative pole voltages at the converter stations (case 2)

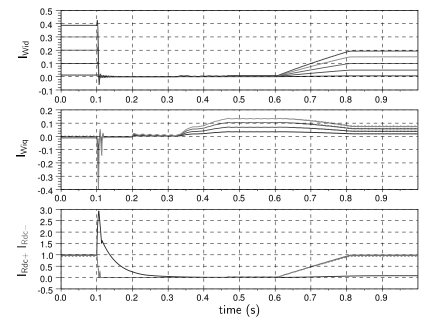

Fig. 16: Pole-to-ground short circuit at the Diode Rectifier station terminals with 50% L_R.

side voltage dip is smaller than that of the positive pole, helped by the transformer and ac-side line impedances.

C. Effect of the smoothing reactance

Clearly, the presented results depend on the particular installation, therefore, extensive sensitivity studies would be advisable. One of the main components affecting the behaviour of the diode rectifier station behaviour is the smoothing reactance L_R.

Therefore, case 2 (i.e. pole-to-ground short circuit at the diode rectifier terminals) has been studied with different values of the smoothing reactance (50% and 200% of the original values).

Figures 16 and 17 show the behaviour of the wind power plant and the diode rectifier station for 50% and 200% of L_R. Clearly, the system recovers with dynamics

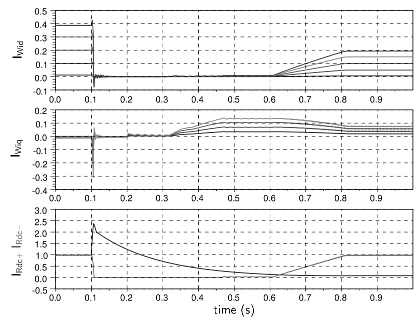

Fig. 17: Pole-to-ground short circuit at the Diode Rectifier station terminals with 200% L_R.

which are very almost the same as the nominal case (Figure 11).

The key difference between high and low L_R is clearly shown in the detailed traces shown in figures 18 and 19. Figure 18 shows that the peak value of the positive pole current (I_{Rdc}) increases to 3pu, while the current decreases much faster due to the smaller energy stored in the smoothing reactor.

On the other hand, figure 18 shows that the peak I_{Rdc} fault current is now 2.4 pu. However the fault current decreases with slower dynamics.

The following conclusions can be drawn from the sensitivity studies:

- It is possible to select a value of L_R in order to find an acceptable trade-off between peak diode current and $\int I_{Rdc}^2 dt$.
- Diode rectifier station fault current peak time depends on the wind power plant dynamics and is largely unaffected by changes in L_R.

IV. Discussion and conclusions

This work shows the technical feasibility of the connection of a large wind power plant to a multi-terminal HVDC grid by means of a HVDC Diode Rectifier station.

Particularly, this work has studied the possibility of using fast current control on the off-shore wind turbines to reduce short circuit currents through the HVDC-DR during cable faults in multi-terminal HVDC grids.

For the considered 400 MW wind farm, it has been found that the proposed approach leads to over-currents through the HVDC-DR of about 2.5 pu, which is generally considered within the short-time over-current capability of diode rectifiers. Afterwards, both ac-side and dc-side currents reduce to zero reasonably fast.

Two case studies have been carried out, namely response to cable faults not directly connected to the

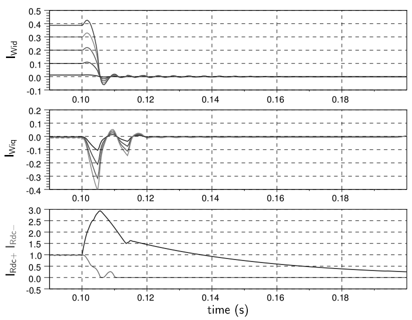

Fig. 18: Pole-to-ground short circuit at the Diode Rectifier station terminals with 50% L_R (detail).

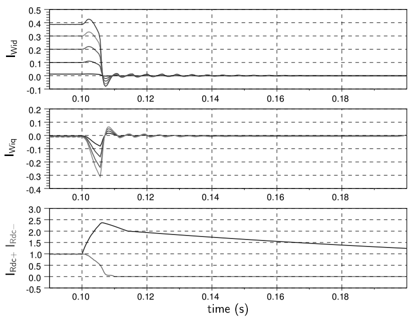

Fig. 19: Pole-to-ground short circuit at the Diode Rectifier station terminals with 200% L_R (detail).

HVDC-DR station and response to faults on cables connected to the HVDC-DR station.

In the former case, it has been shown that the proposed strategy operates adequately to reduce diode rectifier fault currents until the distant fault has been cleared by the corresponding dc-breaker.

For the latter case, the proposed fault-ride-through strategy can be used, in conjunction with the corresponding dc-breaker, to isolate the faulty cable and converter. The faulty pole DR converter is isolated by means of zero-current opening of its ac-side breaker.

The obtained results suggest that, provided the wind turbine current control is reasonably fast, it might be feasible to substitute the HVDC ac-side breakers by no-load switches.

The presented study considered type-4 wind turbines. Clearly, type-3 wind turbines current control during faults is not sufficiently fast. Moreover, a metallic ground return is considered. Although it is envisaged that configurations without a metallic ground return would also benefit of the presented strategy, detailed studies are required at this point.

This work shows that fast wind turbine current control can be used to reduce over-currents during cable pole-to-ground short circuits. Moreover, it shows that it is possible to reduce the peak value and clear diode rectifier station fault current in reasonable time by means of wind power plant control.

A sensitivity study shows that it is possible to select the value of the smoothing reactance to obtain a reasonable trade-off between peak diode station fault current and $\int I_{Rdc}^2 dt$.

APPENDIX

Aggregated Wind Turbines		
Front-end: 6 kVcc, 2 kVac, 50 Hz		
T$_{Wi}$: $2/33$ kV	$R_{Wi} = 0.005$ pu	$L_{Wi} = 0.06$ pu
Rated powers: $5, 40, 80, 120, 155$ MW		
HVDC Rectifier (based on Cigre benchmark model [10])		
Capacitor Bank: $C_F = 93,53$ μF		
ZF-low frequency filter		
$C_{a1} = 187.1$ μF	$C_{a2} = 2,079$ μF	$L_a = 4.874$ mH
$R_{a1} = 1.063$ Ω	$R_{a2} = 9.357$ Ω	
ZF-high frequency filter		
$C_b = 187.1$ μF	$R_b = 2.977$ Ω	$L_b = 0.4859$ mH
Transformer T$_{R1}$ and T$_{R2}$		
$33/61/61$ kV, 240 MVA	$L_{R,lk} = 0.18$ pu	$L_{R,m} = 0.01$ pu
dc-smoothing reactor: $L_R = 200$ mH		
HVDC VSCs (one pole) and ac-grids		
VSC: 150 kVcc, 200 MW, 75 kVac, 50 Hz, $C_I = 35.5$ μF		
T$_V$: $75/400$ kV, 250 MVA, $R_V = 0.01$ pu, $L_V = 0.17$ pu		
ac-grid: 400 kV, 500 MVA, Scc=2 pu, 80^o		
PI Controller Parameters		
Front-end voltage V_{Fd}:	$K_P = 203$	$T_I = 68.97 \times 10^{-6}$
Front-end dq-currents:	$K_P = 1488$	$T_I = 0.8065 \times 10^{-6}$
VSC dq-currents:	$K_P = 310.4$	$K_I = 29.32 \times 10^{-6}$
VSCs Voltage Droop Parameters		
$E_{Ilow1} = 146.25$ kV	$k_{droop1} =$	0.17778 kA/kV
$E_{Ilow3} = 146.25$ kV	$k_{droop3} =$	0.08889 kA/kV

REFERENCES

[1] R. Blasco-Gimenez, S. Añó-Villalba, J. Rodríguez-D'Derlée, F. Morant, and S. Bernal-Pérez, "Distributed voltage and frequency control of offshore wind farms connected with a Diode-Based HVdc link," *Power Electronics, IEEE Transactions on*, vol. 25, no. 12, pp. 3095–3105, 2010.

[2] S. Bernal-Pérez, S. Añó-Villalba, R. Blasco-Gimenez, and J. Rodriguez-D'Derlée, "Off-shore wind farm grid connection using a novel diode-rectifier and VSC-inverter based HVDC transmission link," in *IECON 2011 - 37th Annual Conference on IEEE Industrial Electronics Society*. IEEE, Nov. 2011, pp. 3186–3191.

[3] R. Blasco-Gimenez, S. Añó-Villalba, J. Rodriguez-D'Derlée, S. Bernal-Pérez, and F. Morant, "Diode-Based HVdc Link for the Connection of Large Offshore Wind Farms," *Energy Conversion, IEEE Transactions on*, vol. 26, no. 2, pp. 615 –626, Jun. 2011.

[4] R. Blasco-Gimenez, S. Añó-Villalba, J. Rodriguez-D'Derlée, S. Bernal-Pérez, and F. Morant, "Connection of large off-shore wind farms using diode based HVDC links," in *Wind Energy Conversion Systems. Technology and trends*. London: Springer-Verlag, 2012.

[5] S. Bernal-Pérez, S. Añó-Villalba, R. Blasco-Gimenez, and N. Aparicio, "Connection of off-shore wind power plants to VSC-MTdc networks using HVdc diode-rectifiers," in *2013 IEEE International Symposium on Industrial Electronics (ISIE)*, May 2013, pp. 1–6.

[6] P. Menke, "New grid access solutions for offshore wind farms," in *EWEA Offshore 2015*, Copenhagen, Mar. 2015, pO 208. [Online]. Available: http://www.energy.siemens.com/hq/en/energy-topics/tradeshows/ewea-2015/new-grid-access-solutions.htm

[7] R. Blasco-Gimenez, N. Aparicio, S. Añó-Villalba, and S. Bernal-Perez, "LCC-HVDC connection of offshore wind farms with reduced filter banks," *IEEE Transactions on Industrial Electronics*, vol. 60, no. 6, pp. 2372 –2380, Jun. 2013.

[8] L. Marti, "Simulation of electromagnetic transients in underground cables using the emtp," in *Advances in Power System Control, Operation and Management, 1993. APSCOM-93., 2nd International Conference on*, Dec 1993, pp. 147–152 vol.1.

[9] S. Ano-Villalba, R. Blasco-Gimenez, S. Bernal-Perez, and E. Belenguer, "Wind power plant integration in hvdc grids with voltage droop control," in *ELECTRIMACS 2014 - 11th International Conference on Modeling and Simulation of Electric Machines, Converters and Systems*, May 2014, pp. 573–578.

[10] M. Szechtman, T. Wess, and C. V. Thio, "First benchmark model for HVDC control studies," *Electra*, vol. 135, no. 4, pp. 54–67, 1991.

Site evaluation of harmonics distortions from modern wind turbines based on voltage source and harmonic impedances models

O.Caubet [1], S.Ratés[1]
oriol.cauber@power.alstom.com, sergi.rates-palau@power.alstom.com

[1]ALSTOM Energías Renovables España S.L. Roc Boronat, 78 08005 Barcelona (Spain)

Abstract

The modern wind turbines (WT), equipped with power converters (full or partial power converters) connected to the grid, have increased rapidly in recent years. Harmonic assessment of the power quality is a necessary study for interconnection of future wind farms to the grid. Normally, the power quality assessment in wind farm is done considering the power converter as an ideal harmonic current source, then, the injected harmonic currents are considered constant in any grid. This approach is not always valid since it neglects any grid harmonic impedance impact as well as the converter reaction to background harmonic voltages.

In this study it has been modelled the Alstom Haliade 150 6MW wind turbine converter as a harmonic voltage source, including its filter and transformer harmonic model; with the theoretical harmonic impedance model and the background harmonic voltages of Le Carnet Wind farm (France) . The predicted voltage and current harmonics have been compared with real data measurement. The accuracy of this evaluation is much closer to reality than considering converters as ideal current sources as usual.

Keywords

Grid Integration, wind turbine, power quality, harmonic distortions, full power converters, DFIG converters

1 Introduction

A standard approach about a theoretical wind farm power quality assessments are done considering each WT as an ideal harmonic current source [1]. In this case, the different harmonics currents are often taken during the WT prototype power quality certification [2] and these are measured in a particular site with a particular grid. This grid could be completely different than the future grids where this sort of WT will be installed; even this specific grid harmonic impedance could have some serial or parallel resonances in some particular frequencies [3]. Thereby, the Power Quality assessment of a particular site only shows the injected harmonic currents of this specific site. If the ideal injected harmonic currents are used in other sites, it is neglected their dependency with the harmonic grid impedance and the converter reaction to background harmonic voltages. Hence, the estimation of harmonic distortions obtained with this approach might deviate of the real harmonic distortion.

The intention on this proposal is using the real voltage source of harmonics and the grid characteristics (harmonic impedance and background voltage harmonics). So, from one side the converter inner harmonic voltages, the ones generated by the IGBT bridge which are almost constant and quasi-independent of the grid, and secondly face them against the grid model taken from the DSO (Distribution Systems Operators) data.

It is shown the results of a site evaluation example in Alstom Haliade150 WT prototype site (Le Carnet, France), where is demonstrated a good accuracy of this methodology to make a power quality assessment using the converter voltage harmonics and the grid model (harmonic impedance and background voltage harmonics).

Despite the current study only deals with WTs with full power converter, so all the harmonics face to the grid are generated by the line side of the power converter. In any case, this methodology might be easily extended to DFIG topology, where voltage harmonics generated by the machine side of the power converter which are transferred to the grid also by the rotor/stator winding generator.

2 Evaluation process

The converter and grid harmonic currents are calculated separately in this methodology. A first model includes the harmonic impedances of the wind turbine and the grid; with the voltage harmonic source belongs to power converter side in order to get the current harmonics really caused by the converter. A second model includes the harmonic impedances of the wind turbine and the grid as well, but with the background voltage harmonics in order to get the current harmonics caused by the converter reaction to background voltage harmonics.

2.1 Voltage harmonics.

As the case analysed deals with a full power converter, the only sources of harmonics at the wind turbine level are coming from the Line Side Converter on the IGBT output and the voltage harmonics coming from the grid as background harmonics before connecting any WF.

The voltage harmonics from the converter have been measured directly on the IGBT side of the line side converter (Fig. 1) switching at fs=4kHz, and the background voltage harmonics coming from the grid have been measured on the MV of the transformer having the WT disconnected (Fig. 2).

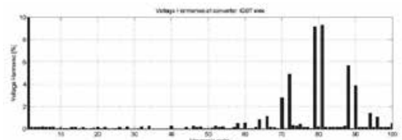

Figure 1. Voltage harmonics at converter IGBT side (WT source)

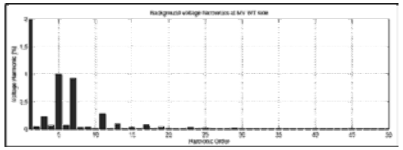

Figure 2. Background voltage harmonics at MV WT side (Grid source)

2.2 *System model.*

The system has modelled using the wind turbine data (filters + transformer) and the grid data from the DSO [4] to calculate the different sections (each section modelled in "PI" models) as it is depicted in figure 3.

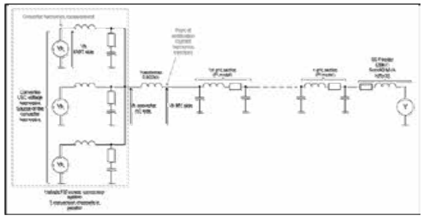

Figure 3.Converter, cables and grid model

The grid model MV impedance has been collated with the Z_h obtained by a direct V_h/I_h measurements and both $Z_h(f)$ are so similar, so the theoretical grid model provided by DSO (Fig. 4) is quite valid for being used for the voltage distortion assessment.

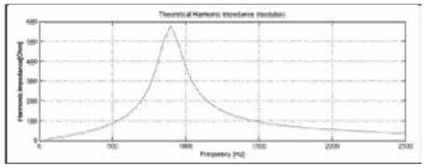

Figure 4.Theoretical harmonic impedance

2.3 *Voltage and current harmonics calculation.*

The voltage and current harmonics have been obtained with the method of Modified Nodal Analysis (MNA) [5] which is an extension of classical Nodal Analysis [6], per each harmonic. The procedure is depicted in Figure 5

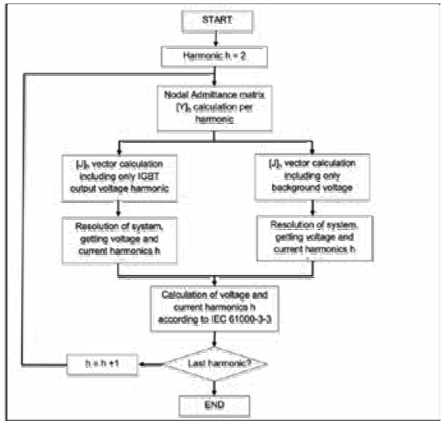

Figure 5.Voltage and current harmonics calculation procedure

Converter and grid harmonic currents are calculated separately: the 1st simulation for calculating only the impact of the power converter harmonics (Fig. 6), having then the background grid harmonics off, i.e. voltage source short-circuited; and the 2nd simulation for getting only the converter reaction to the background voltage harmonics coming from the grid (Fig. 7) and having then the power converter source short-circuited.

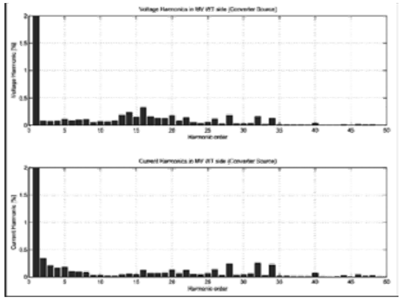

Figure 6. Voltage and current harmonics in the MV WT side (converter source)

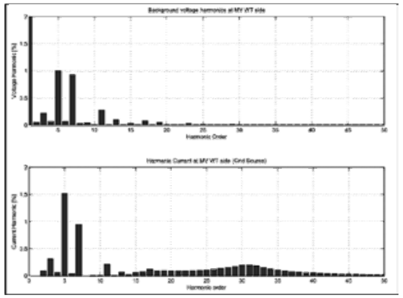

Figure 7. Voltage and current harmonics in the MV WT side (Grid source)

The two terms (current and voltage harmonics) have been summed using the summation rule proposed in the IEC 61000-3-3 [7]. From simulations results we can obtain the current harmonics on the MV, the harmonic impedance (impedance vs freq.), and the voltage distortion in any point of the grid model (Fig. 8).

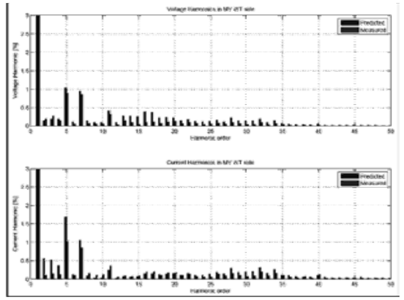

Figure 8. Voltage and current harmonics in the MV WT side.

3 Conclusions

The estimation of the voltage and current distortion on the WF PCC is more realistic by using the voltage harmonics source method coming from the power converter and the grid harmonics background than only forcing an injection of current harmonics which are coming from measurements done in a particular site (WT prototype certification).

The theoretical $Z_h(h)$ get with the DSO data ("PI" modelled sections + transformers) has the same trend to the real $Z_h=V_h/I_h$ get by direct measurements on the MV side. It means the grid could be simulated quite accurately without the real voltage and current harmonics previously measured on the site.

The voltage and current harmonics in the lower range, so the 3^{rd} , 5^{th}, 7^{th}, 11^{th},…, which are normally detected in all the WT power quality assessment are normally coming from the background harmonics already existing in the grid and the power converter has nothing to do with them.

The power converter is usually responsible from the harmonics around the switching frequency and all its multiples.

4 References

[1] Santjer F., Herbrandt J. 2010. Harmonic current emission of wind farms exceeding the limiting values. Dewi Technical Publication.

[2] IEC 61400-21, 2008. Wind Turbine Generator Systems – Measurement and Assessment of Power Quality Characteristics of Grid Connected Wind Turbines.

[3] Hasan K.N., Rauma K., Luna A., Candela J.I., Rodriguez P. 2012. Harmonic Resonance Study for Wind Power Plant. International Conference on Renewable Energies and Power Quality. Santiago de Compostela (Spain).

[4] PTF 11-0098 Proposition Technique et Financière pour le raccordement de l'installation de la Ferme Eolienne du Carnet au Réseau Public de Distribution d'Électricité HTA.

[5] Chung-Wen H, Ruehli A and Brennan P. 1974. The Modified Nodal Approach to Network Analysis. International Symposium on Circuit and Systems. San Francisco (USA).

[6] Wang X, Song Y, Irving M. 2008. Modern Power Systems Analysis: Springer.

[7] IEC 61000-3-3, 2013. Assessment of emission limits for distorting loads in MV and HV power systems.

Symbolic Solution Approach to Wind Turbine based on Doubly Fed Induction Generator Model

M. Cañas–Carretón
E. Gómez–Lázaro
S. Martín–Martínez
Renewable Energy Research Institute[1]
DIEEAC/EIIAb[2]
Universidad de Castilla-La Mancha
Albacete, 02071 Spain
Email: miguel.canas@uclm.es
emilio.gomez@uclm.es
sergio.martin@uclm.es

Weihao Hu
Institute of Energy Technology
Aalborg University
Aalborg, 9220 Denmark
Email: whu@et.aau.dk

A. Molina–García
Dept. of Electrical Eng.
Universidad Politécnica de Cartagena
Cartagena, 30202 Spain
Email: angel.molina@upct.es

***Abstract*—This paper describes an alternative approach based on symbolic computations to simulate wind turbines equipped with Doubly–Fed Induction Generator (DFIG). The actuator disk theory is used to represent the aerodynamic part, and the one-mass model simulates the mechanical part. The 5^{th}–order induction generator is selected to model the electric machine, being this approach suitable to estimate the DFIG performance under transient conditions. The corresponding non–linear integro-differential equation system has been reduced to a linear state-space system by using an ad-hoc local linearization. This novel Symbolic Computation (SYMB) method has been implemented by using two different software-packages, with the purpose of solving simultaneously a remarkable number of individual wind turbines models submitted to different wind speed profiles and/or grid voltage waveforms.**

The obtained results are compared with traditional Finite Difference Discretization (FDD) method, widely proposed for this type of studies. The results offer a good agreement between the proposed SYMB method and the FDD solutions, considering real wind speed profile and electrical transient event.

***Keywords*—Symbolic computation, wind turbine modelling, voltage dip, DFIG**

NOMENCLATURE

H_{eq} Moment of inertia of entire wind turbine.
H_g Moment of inertia of generator.
$\boldsymbol{i_s}, \boldsymbol{i_r}$ Stator and rotor current vectors.
K_{opt} Optimal torque/speed constant.
N_{gb} Gear box ratio.
L_s Stator inductance.
L_r Rotor inductance.
L_m Magnetizing inductance.
L_f Filter inductance.
p Number of pair of poles.
r Turbine blade radius.
R_s Stator resistance.
R_r Rotor resistance.
R_f Filter resistance.
S_b Power base value.
$\boldsymbol{u_s}, \boldsymbol{u_r}$ Stator and rotor voltage vectors.
v Wind speed.
T_e Electromagnetic torque.
T_m Mechanical and electromagnetic torque.
β Blade pitch angle.
λ Stip speed ratio.
ρ Air density.
$\boldsymbol{\psi_s}$ Stator flux linkage vectors.
$\boldsymbol{\psi_r}$ Rotor flux linkage vectors.
ω_{eb} Electrical angular speed base value.
ω_s Synchronous angular speed.
Ω_g Generator rotational speed.
Ω_h Hub mechanical rotational speed.
$_{s,r}$ First subscript indicates stator and rotor.
$_{g,gc}$ First subscript indicates grid and grid-converter.
$_{d,q}$ Second subscript indicates direct and quadrature axes quantities.

[1]DIEEAC / EIIAb. Department of Electrical Engineering, Electronics, Control and Communications / School of Industrial Engineering of Albacete

I. INTRODUCTION

These days, the number of wind turbines connected to power systems requires a special attention from the Transmission and System Operators (TSOs). Advanced models of wind farms are demanded by current TSOs for planning and operating purposes. However, accurate simulations of wind turbines usually imply significant computational efforts. For that reason, most previous contributions have been mainly focused on aggregation techniques by reducing the wind farms to an equivalent wind turbine model, [1], [2], [3], [4] and [5]. In [6], a wind farm of 12 full-converter wind turbines using permanent magnet synchronous machines with a rated power of 5 MW is simulated. In this case, the wind farm is divided into three groups, and each group is formed by the wind turbines receiving a similar wind speed profiles. Consequently, each group is then reduced to an equivalent wind turbine. In [7], the mechanical characteristics of the wind turbine, the electro-mechanical parameters of the generator and the converters are aggregated to represent the equivalent wind farm model. In [8], a wind farm consisting of 68 DFIG wind turbines is modeled and simulated in the same way.

With regard to wind turbine simulations, most commercial software packages proposed for this type of studies are focused on the electrical part, being simplified both aerodynamic and mechanical parts. These software packages usually involve numerical methods, mainly Finite Difference Discretization (FDD) techniques, (PSS/E, Power Factory–DIgSILENT or PSCAD/EMTDC), [9]. However, some drawbacks have been detected when a significant number of individual wind turbines are simultaneously simulated, mainly (i) excessive computational time, (ii) memory requirements or number of variables. For that reason and as was previously discussed, wind turbines are usually aggregated as an equivalent wind turbine, [10], [11]. Analytic techniques are an alternative to the FDD approach, [9]. However, during the last decades their use has been partially discarded, mainly due to the non-linearity of the wind turbine models as well as the computational capacity limitations of the symbolic math software packages. In fact, few contributions can be found in the specific literature regarding these techniques,[12], [13] and [14].

II. WIND TURBINE MODELLING

The basic scheme of a wind turbine equipped with DFIG is represented in Fig. 1. In this configuration, the stator terminals are directly connected to the grid and the rotor terminals are connected through a back-to-back converter, which size is determined for its capacity of handling around 25–30% of the rated power of the wind turbine [15]. The pitch angle β is fixed to zero in all simulations. The wind turbine model proposed in this paper involves the following conditions and assumptions [16]:

- All quantities are referred to the stator-side and taken in per unit, (pu), except ω_{eb} that is in electrical rad/s and t is in seconds.

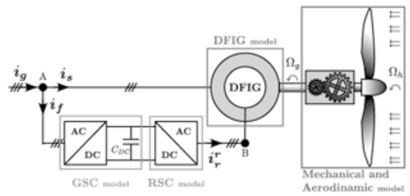

Fig. 1: Basic scheme of a DFIG wind turbine

- The stator current is considered as a positive value when flowing towards the machine, since traditionally the proposed induction machine models have been studied in motor mode [17].
- The q-axis is assumed to be $\pi/2$ ahead of the d-axis with respect to the direction of rotation. Both d and q windings are magnetically decoupled, allowing to control independently active and reactive power variables [18], [19].
- The (d, q) reference system rotates at the same speed value and direction as the stator flux $\boldsymbol{\psi_s}$ (corresponding to the grid frequency speed), becoming the stator parameters (voltage, current and flux) close to their steady-state values.

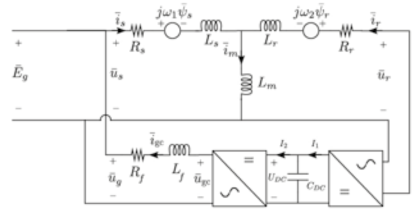

Fig. 2: Wind turbine electrical equivalent circuit (all quantities are referred to the stator-side).

The wind turbine model considered in this work is based on the model developed in [20] with the following additions from [21]: the Grid Side Converter control and 5^{th} order DFIG model have been implemented. In [20] the 3^{rd} order DFIG model was utilized and the GSC control was omitted.

A. Generator

The DFIG model is represented by, [21]:

$$\boldsymbol{u_s} = R_s\boldsymbol{i_s} + j\omega_s\boldsymbol{\psi_s} + \frac{1}{\omega_{eb}}\frac{d}{dt}\boldsymbol{\psi_s} \tag{1}$$

$$\boldsymbol{u_r} = R_r\boldsymbol{i_r} + j(\omega_s - \frac{1}{\omega_{eb}}p\Omega_g)\boldsymbol{\psi_r} + \frac{1}{\omega_{eb}}\frac{d}{dt}\boldsymbol{\psi_r}, \tag{2}$$

where $\omega_{eb} = 2\pi f_s\ rad/s$, $f_s = 50\ Hz$ is the grid frequency, $\omega_s = 1\ pu$ is the synchronous speed, $p = 2$ is the pair of poles and Ω_g is the mechanical speed of the generator in rad/s.

The relation between stator and rotor fluxes and currents is given by the following expressions [22]:

$$\boldsymbol{\psi_s} = L_s \boldsymbol{i_s} + L_m \boldsymbol{i_r} \tag{3}$$

$$\boldsymbol{\psi_r} = L_r \boldsymbol{i_r} + L_m \boldsymbol{i_s}, \tag{4}$$

being $L_s = L_{ls} + L_m$ and $L_r = L_{lr} + L_m$, where L_{ls} is the stator leakage inductance, L_{lr} is the rotor leakage inductance and L_m is the mutual inductance.

With regard to the motion equation of the generator, the following expression is proposed,

$$2H_g \cdot \frac{d}{dt}\omega_g = T_m - T_e, \tag{5}$$

where $\omega_g = \left(\frac{1}{\omega_{eb}/p}\right) \cdot \Omega_g$ is the mechanical speed generator in pu.

B. Grid–Side and Rotor–Side Converter Control Model

DFIG control is usually divided into Grid–Side Control and Rotor–Side Control. Variables are set in a synchronously rotating (d, q) axis frame with the d axis aligned along the stator flux vector position, which ensures decoupling control of stator active and reactive power flows into the grid [18]. This orientation frame leads to $\psi_{sd} \approx |\boldsymbol{\psi_s}|$ and $\psi_{sq} \approx 0$ that means $u_{sd} \approx 0$ and $u_{sq} \approx |\boldsymbol{u_s}|$. It is also usually to neglect R_s, hypothesis affordable for a MW class wind turbine connected to a strong grid [18].

Grid–Side Converter (GSC) is modeled through a current $(\boldsymbol{i_f})$ source. Under these assumptions, the proposed model is suitable for both dynamic simulations and transient stability studies [23], [24], [25]. This current source should be able to maintain constant the DC-bus voltage as well as the power exchange between the rotor and the grid, Fig. 1. Taking into account the stator flux alignment of the control reference frame, and assuming the electrical losses as zero in both converters, $\boldsymbol{i_f}$ dq components can be calculated as follows,[21],

$$\boldsymbol{u_g} = R_f \boldsymbol{i_f} + j\omega_f L_f \boldsymbol{i_{gc}} + \frac{L_f}{\omega_{eb}} \frac{d}{dt} \boldsymbol{i_{gc}} + \boldsymbol{u_{gc}} \tag{6}$$

Rotor–Side Control is modeled according to the following expressions, involving references and controlled variables:

$$i_{rd}^{ref} = \frac{u_{sq}}{\omega_s L_m} - \frac{L_s}{L_m u_{sq}} Q_s^{ref} \tag{7}$$

$$T_e^{ref} = K_{opt} \left(\frac{1}{\omega_{eb}/p} \cdot \Omega_g^m \right)^2 \tag{8}$$

$$i_{rq}^{ref} = -\frac{L_s}{L_m} \frac{\omega_s}{u_{sq}} T_e^{ref} \tag{9}$$

While the Grid–Side Control is modeled as follow:

$$i_{gcd}^{ref} = \frac{Q_s^{ref}}{u_{gq}} \tag{10}$$

$$i_{gcq}^{ref} = f(u_{gq}, v) = k1(v) \cdot u_{gq}. \tag{11}$$

Where i_{gcq}^{ref} is a function of the grid voltage and wind speed. The constant $k1$ is dependent on the parameters of the wind turbine under study and the wind speed.

III. An approach to a linear wind turbine model

The wind turbine model can be divided into two parts: the electrical part and the aerodynamic-mechanical part. In the next two subsections is discussed how to linearize both parts.

1) Linear state–space model for the electrical part: If $\omega_g(t)$ is assumed as constant along a simulation time interval $\tau_j = [t_{0_j}, t_{f_j}]$, the non–linear integro–differential electrical part model defined in section II can be arranged in a linear state–space form. The suitability of this assumption ($\omega_g(t)$ constant) is based on the fact that for power system simulations involving grid disturbances taking time intervals usually lower than 30 seconds, being possible to assume wind speed values as constant [26]. It must be pointed out that this assumption ($\omega_g(t)$ as constant) is only applied for the linearization process of the electrical part, and it is not considered as a constant variable along the whole time interval of the simulation. In fact, the evolution of $\omega_g(t)$ along a $\tau_j = [t_{0_j}, t_{f_j}]$ is obtained by solving the linearized motion equation described in Section III-2.

The equation-system can be transformed into a differential equation system by extending the number of space-state variables. The following change of variables is proposed, [27], [28], in order to adapt the expresions of the Proportional Integral controllers of the Rotor Side Converter and the Grid Side Converter to the state-space form of the model:

$$\epsilon_{rd} = \int (i_{rd}^{ref} - i_{rd}) \tag{12}$$

$$\epsilon_{rq} = \int (i_{rq}^{ref} - i_{rq}) \tag{13}$$

$$\epsilon_{gcd} = \int (i_{gcd}^{ref} - i_{gcd}) \tag{14}$$

$$\epsilon_{gcq} = \int (i_{gcq}^{ref} - i_{gcq}). \tag{15}$$

A first order linear differential equation system can be then deduced and written as:

$$\boldsymbol{M} \cdot \dot{\boldsymbol{X}}(\boldsymbol{t}) = \boldsymbol{N} \cdot \boldsymbol{X}(\boldsymbol{t}) + \boldsymbol{S} \cdot \boldsymbol{U}(\boldsymbol{t}), \tag{16}$$

$$\dot{\boldsymbol{X}}(\boldsymbol{t}) = \boldsymbol{A} \cdot \boldsymbol{X}(\boldsymbol{t}) + \boldsymbol{F}(\boldsymbol{t}), \tag{17}$$

where $\boldsymbol{A} = \boldsymbol{M^{-1}N}$ and $\boldsymbol{F}(\boldsymbol{t}) = \boldsymbol{M^{-1}S} \cdot \boldsymbol{U}(\boldsymbol{t})$. This rearrangement can be carried out due to the existence of $\boldsymbol{M}$ inverse. Further information about the matrix structure of (17) can be found in the Appendix. The state-space variables $\boldsymbol{X}(\boldsymbol{t})$ and the input vector $\boldsymbol{U}(\boldsymbol{t})$ are respectively,

$$\boldsymbol{X}(\boldsymbol{t}) = [i_{sd}, i_{sq}, i_{rd}, i_{rq}, \epsilon_{rd}, \epsilon_{rq}, i_{gcd}, i_{gcq}, \epsilon_{gcd}, \epsilon_{gcq}]^T \tag{18}$$

$$\boldsymbol{U}(\boldsymbol{t}) = [u_{sd}, u_{sq}, u_{gd}, u_{gq}, i_{rd}^{ref}, i_{rq}^{ref}, i_{gcd}^{ref}, i_{gcq}^{ref}]^T. \tag{19}$$

2) Linear model of aerodynamical-mechanical part: To obtain the analytical expression for the rotational generator speed $\omega_g(t)$ along $\tau_j = [t_{0_j}, t_{f_j}]$ time interval, the motion equation defined in (20) has to be linearized.

$$\frac{d\omega_g}{dt} = \frac{1}{2H} \left(T_m(\omega_g, t) - T_e(t) \right), \tag{20}$$

this non-linear differential equation can be locally linearized as:

$$\frac{d\omega_g}{dt} + G(t) \cdot \omega_g = V(t), \tag{21}$$

with $\omega_{g0_j} = \omega_g(t_{0_j})$ and

$$G(t) = -\left.\frac{\partial f}{\partial \omega_s}\right|_{\omega_{g0_j}, t_{0_j}} ; V(t) = f(\omega_{g0_j}, t_{0_j}) + (t - t_{0_j}) \left.\frac{\partial f}{\partial t}\right|_{\omega_{g0_j}, t_{0_j}} - \omega_{g0_j} \left.\frac{\partial f}{\partial \omega_g}\right|_{\omega_{g0_j}, t_{0_j}}.$$

The inputs to the linearized aerodynamic-mechanical model of the wind turbine are: the profile of wind speed $v(t)$ and the stator and rotor currents $i_{sq}(t), i_{rd}(t), i_{sd}(t), i_{rq}(t)$ expressed in function of time t.

A. Proposed wind turbine model solution

Fig. 3 shows schematically the process proposed for symbolic resolution. The simulated global time interval τ is divided into n time intervals to be solved analytically, $\tau = [\tau_1, \ldots, \tau_n]$. In this case, $\boldsymbol{X}(\boldsymbol{t})$ and $\omega_g(t)$ can be determined for each specific time interval $\tau_j = [t_{0_j}, t_{f_j}]$, $\forall t \in [t_{0_j}, t_{f_j}]$. Regarding ω_{g0_j}, $\boldsymbol{X}(\boldsymbol{t_{0_j}})$ and the input variables of the model ($\boldsymbol{U}$ and the wind speed profile v), they have to be updated each τ_j. The value of ω_{g0_j} for a τ_j time interval (with $j > 1$) is equal to the value of ω_g at the end of the previous interval, $\omega_g(t_{0_j}) = \omega_g(t_{f(j-1)})$, to preserve continuity function properties. A similar process is carried out to obtain the initial conditions of the state-space variables, $\boldsymbol{X}(\boldsymbol{t_{0_j}}) = \boldsymbol{X}(\boldsymbol{t_{f_{j-1}}})$. In our case, these values are known before the initialization of the time interval simulation. Nevertheless, contributions focused on solving initial value problems for a system of linear integro–differential equations can be found in [29].

The corresponding state-space system modelling the electrical part, (17), is solved analytically by the method of Variation of Parameters described in [9]. The analytical expression of the solution is:

$$\boldsymbol{X}(\boldsymbol{t}) = \boldsymbol{\phi}(\boldsymbol{t})\boldsymbol{\phi}(\boldsymbol{t_0})^{-1}\boldsymbol{X}(\boldsymbol{t_0}) + \boldsymbol{\phi}(\boldsymbol{t}) \int_{t_0}^{t} \boldsymbol{\phi}^{-1}(\boldsymbol{s})\boldsymbol{F}(\boldsymbol{s}) ds,$$

where $\phi(t)$ is named fundamental matrix of the equation system and it can be determined according to [9].

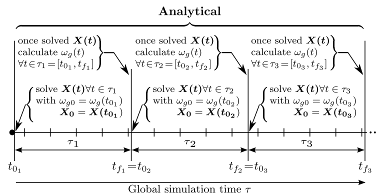

Fig. 3: Scheme of proposed analytical solution considering $\tau = [\tau_1, \tau_2, \tau_3]$

Considering the linearization of the motion equation described in Section III-2, $\omega_g(t)$ can be determined as the analytical solution of (21) given by [9], $\forall t \in [t_{0_j}, t_{f_j}]$,

$$\omega_g(t) = e^{-\int_{t_{0_j}}^{t} G(t)\,dt} \cdot \left[\omega_{g0_j} + \int_{t_{0_j}}^{t} V(t)\,dt \cdot e^{\int_{t_{0_j}}^{t} G(t)\,dt} \right].$$

Finally, the estimation of active and reactive power for stator, rotor and grid side converter (P_s, P_r, P_{gc}, Q_s, Q_r and Q_{gc}) along the whole time interval can be calculated.

IV. Case study description and results

A set of simulations considering real–measured stator voltage waveforms have been carried out to evaluate the proposed symbolic technique based on symbolic solution and FDD solution. For FDD solution, software package MATLAB–Simulink [30] is used to simulate the wind turbine model according to [31]. Software package Mathematica [32] is selected to solve the process involving symbolic operations. For the rest of the paper, the non–linear wind turbine model solved by FDD approach will be labeled as FDD model, and the linearized wind turbine model solved by symbolic form will be referred as SYMB model. The table II contains most relevant parameters of the DFIG wind turbine used in the simulations, [33].

According to Section III-A, both $\boldsymbol{U}(\boldsymbol{t})$ input and wind speed profile must be known *a priori* for the global time interval. The numerical values are fitted through a polynomial structure ($u(t) = c_0 + c_1 t + c_2 t^2 + ... + c_k t^k$) avoiding high-order polynomials ($k > 5$) since their computation is more complex and usually involve a higher number of local maximum and minimum candidates. Moreover, for time intervals where there are not transient events it is recommended ($k <= 2$) for electrical inputs and ($k <= 4$) for wind speed profiles.

The case of study involves a global simulation time of $\tau \approx 30$ seconds. The Grid Side Converter is connected directly to the stator, so $\boldsymbol{u_g} = \boldsymbol{u_s}$. It has been divided into three linearization time intervals with different time durations: $\tau = [14.32, 0.19, 18.99]$. The second time interval involves the voltage dip, [34], that is illustrated in Fig. 4 in instantaneous values. After being filtered and

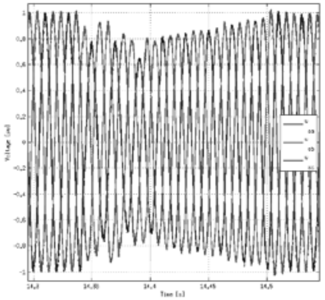

Fig. 4: Stator voltages profile for case of study.

components dq calculated, the voltage dip is assumed to be a three phase balanced voltage dip.

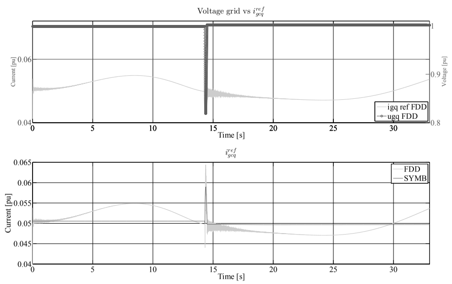

Fig. 5: Voltage grid FDD vs reference current i_{gcq}^{ref} FDD; and i_{gcq}^{ref} FDD vs SYMB comparison

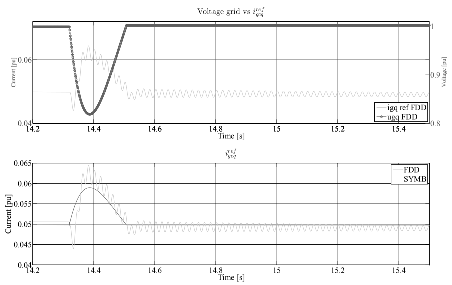

Fig. 6: Voltage grid FDD vs reference current i_{gcq}^{ref} FDD; and i_{gcq}^{ref} FDD vs SYMB comparison detail

The stator currents obtained from FDD and SYMB models are shown in Figs. 7, where the differences along all simulation time between both approaches can be neglected. In Fig. 8, the second time interval along the transient event is depicted in detail. It can be observed how all SYMB values match accurately the FDD values. The rotor currents are shown in Fig. 9 and Fig. 10, for i_{rd} component both methods match accurately but for i_{rq} component there is a small difference. It is due to the assumption of ω_g constant along the the time interval (see (9)).

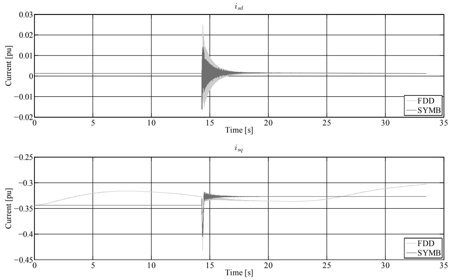

Fig. 7: Stator currents, i_{sd} and i_{sq}, FDD vs SYMB comparison

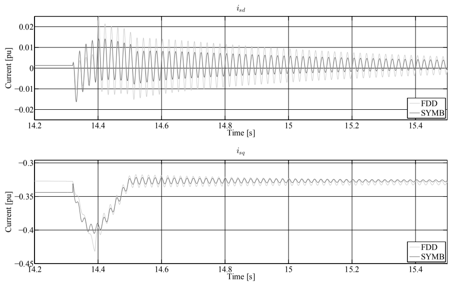

Fig. 8: Stator currents, i_{sd} and i_{sq}, FDD vs SYMB comparison detail

Something similar occurs with the Grid Side Converter currents, Fig. 11 and Fig. 12. For the i_{gcd} component, associated with power reactive control, both methods match correctly but for the i_{gcq} component, associated with DC-bus control, there are some differences. This is caused by how i_{gcq}^{ref} is obtained for to be used as input in the linearized model. As it was pointed out in (11), i_{gcq}^{ref} is obtained from the grid voltage and wind speed. In Fig 5 are depicted the grid voltage and the i_{gcq}^{ref} calculated by the FDD model, it can be appreciated that the behaviour of both variables are related between them. As an initial approach, the i_{gcq}^{ref} for the SYMB model can be obtained multipliying the grid voltage by a constant and making some basic mathematical arrangements. This constant is obtained from the division in one instant of time between the grid voltage and i_{gcq}^{ref} (Fig 5). In Fig 6 is show the comparisson of i_{gcq}^{ref} used by the FDD and SYMB models, paying attention during the voltage dip. In Fig 15 are depicted the error between stator currents, rotor currents and Grid Side Converter currents. It can be observed how the error is maintained below 9%.

For the case of rotational generator speed ω_g (see Fig. 13) the differences between FDD and SYMB models are not significant, considering the small values of the differences in per unit. Regarding the wind speed profile depicted in Fig. 14, the difference observed is due to the trade-off of complexity of the polynomial form and its accuracy respecting the numerical value for the wind speed profile. The wind speed profile is one of the inputs to the model and for the analytical model the input must have a polynomial form, as it was mentioned at the beginning of this section. A high degree polynomial form can lead to instability issues when symbolic solution is applied and increases the computational cost.

With the aim of offering a proper study of the computational cost requirements, the proposed analytical solution has been divided into two computational times: analytical solving for the local linearized differential equation systems (SYMB CALC, independent of the size of time interval and integration step) and the computational time required to evaluate those analytical functions (SYMB EV, that depends on the size of the time vector employed for the evaluation). FDD represents the wind turbine model obtained from blocks and solved with discretized techniques and FDD SS represents the linearized model solved also with discretized tecnhiques. In Fig 16, Fig 17 and Fig 18 are showed the computational costs of FDD and SYMB methods for a different number of wind turbines. It can be observed that SYMB method maintains an appreciable advantage of computational cost respect to FDD method when the number of wind turbines is high, a small time step and long time interval is considered. Moreover, the computational cost is not only related with the speed of calculus, also must be considered the amount of memory necessary to store the results. In Table I is showed the huge difference between the size of the ouput file for the simulation considering solving method and number of wind turbines.

Δt (s)	10^{-3}			10^{-4}		
Number of Wind Turbines	80	160	320	80	160	320
FDD	107	215	434	1100	2170	4376
SYMB	0.6	1.1	2.3	0.6	1.1	2.3

TABLE I: Size in Megabytes of the output file for a simulation time $\tau \approx 30$ [s]

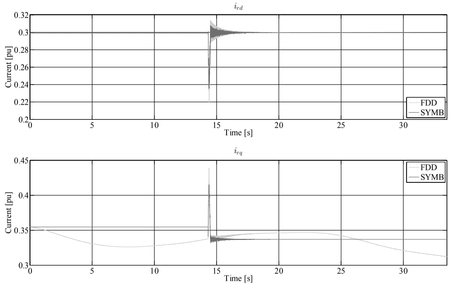

Fig. 9: Rotor currents, i_{rd} and i_{rq}, FDD vs SYMB comparison

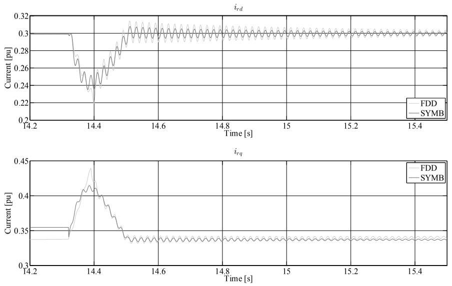

Fig. 10: Rotor currents, i_{rd} and i_{rq}, FDD vs SYMB comparison detail

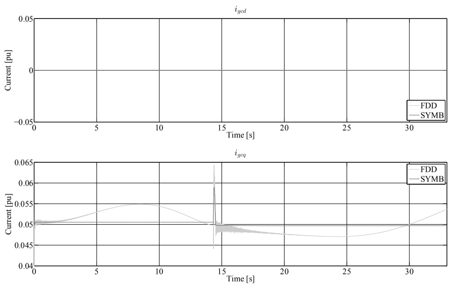

Fig. 11: Grid side converter currents, i_{gcd} and i_{gcq}, FDD vs SYMB comparison

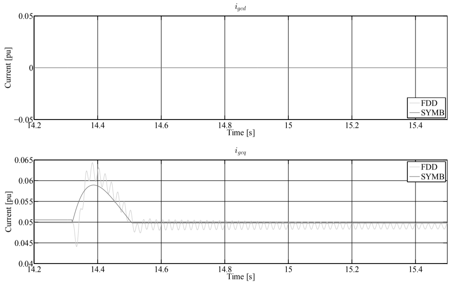

Fig. 12: Grid side converter currents, i_{gcd} and i_{gcq}, FDD vs SYMB comparison detail

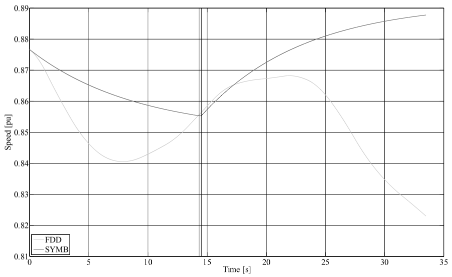

Fig. 13: Generator speed ω_g, FDD vs SYMB comparison

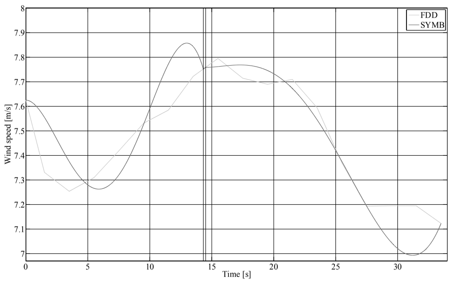

Fig. 14: Wind speed, FDD vs SYMB comparison

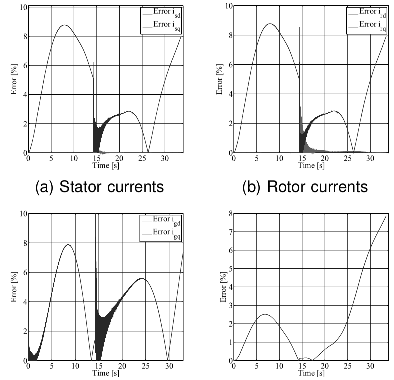

(a) Stator currents (b) Rotor currents

(c) GSC currents (d) Generator speed

Fig. 15: Error FDD vs SYMB for i_s, i_r, i_g and ω_g

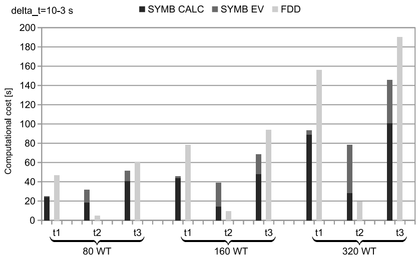

Fig. 16: Computational cost for $\Delta t = 10^{-3}$

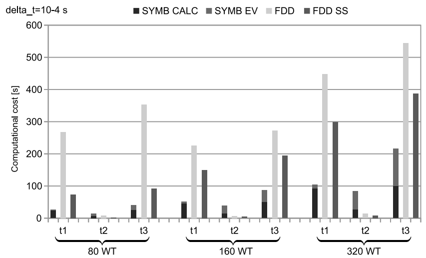

Fig. 17: Computational cost for $\Delta t = 10^{-4}$

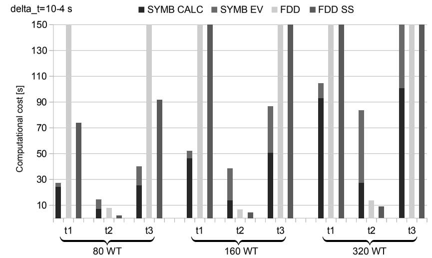

Fig. 18: Computational cost for $\Delta t = 10^{-4}$, detail

V. Conclusion

A symbolic method to solve the model of a wind turbine equipped with DFIG is described and discussed. The aim of this approach is focused on simulating a large number of wind turbines with a lower computational cost in terms of speed and size of memory respect to the traditional method based on discretized techniques.

The symbolic method is compared with classical Finite–Difference Discretization technique for typical time–step values, varying the number of wind turbines considered in the simulation. These comparisons have been carried out under real wind speed conditions and transient disturbance, such as voltage dips. Real wind speed data have been collected at hub height of a Spanish wind farm and filtered through an equivalent wind speed model. The results of the comparisons provide a good agreement between the proposed symbolic method and FDD technique along the whole simulation time. Furthermore, the symbolic method presents clearly advantages in terms of computational time requirements when large time simulation period and small integration-time step are considered. Moreover, the storage capacity necessary for symbolic solutions is very low in comparisson with FDD case, being this difference many orders of magnitude.

Consequently, the proposed symbolic method is highly suitable to simulate individually a substantial number of wind turbines facing different wind speed profiles and under transients events, although more work is needed in order to include pitch control and improve the references signals for the control.

Acknowledgment

This work has been supported by the 'Ministerio de Economía y Competitividad' —ENE2012-34603—, project co-financed with European Union FEDER funds.

Moreover, M. Cañas–Carretón thanks 'Becas CYTEMA-PUENTE' program from University of Castilla-La Mancha to perform stays in foreign research centres.

References

[1] V. Akhmatov and H. Knudsen, "An aggregate model of a grid-connected, large-scale, offshore wind farm for power stability investigations–importance of windmill mechanical system," *International Journal of Electrical Power & Energy Systems*, vol. 24, no. 9, pp. 709–717, Nov. 2002. [Online]. Available: http://dx.doi.org/10.1016/S0142-0615(01)00089-8

[2] A. Shafiu, O. Anaya-Lara, G. Bathurst, and N. Jenkins, "Aggregated wind turbine models for power system dynamic studies," *Wind Engineering*, vol. 30, no. 3, pp. 171–186, 2006.

[3] L. M. Fernández, F. Jurado, and J. R. Saenz, "Aggregated dynamic model for wind farms with doubly fed induction generator wind turbines," *Renewable Energy*, vol. 33, pp. 129–240, 2008.

[4] A. Perdana, S. Uski, O. Carlson, and B. Lemstrom, "Comparison of an aggregated model of a wind farm consisting of fixed-speed wind turbines with field measurements," *Wind Energy*, vol. 11, pp. 13 – 27, 2008.

[5] H. A. Pulgar-Painemal and P. W. Sauer, "Towards a wind farm reduced-order model," *Electric Power Systems Research*, vol. 81, no. 8, pp. 1688–1695, Aug. 2011.

[6] J. Conroy and R. Watson, "Aggregate modelling of wind farms containing full-converter wind turbine generators with permanent magnet synchronous machines: transient stability studies," *IET Renewable Power Generation*, vol. 3, no. 1, pp. 39–52, 2009.

[7] S. Li, Z. Liu, and Y. Jia, "Dynamic aggregation of doubly-fed induction generators (DFIGs) for stability analysis of wind power systems," in *Proc. IEEE Power and Energy Society General Meeting*, 2011, pp. 1–6.

[8] Z. J. Meng, F. Xue, K. Chang, M. Ding, J. Zhang, L. Xiang, J. Shi, and X. Li, "Applications of an improved equivalent wind method for the aggregation of DFIG wind turbines," in *Proc. 4th Int Electric Utility Deregulation and Restructuring and Power Technologies (DRPT) Conf*, 2011, pp. 151–155.

[9] D. G. Zill and W. S. Wright, *Advanced Engineering Mathematics*, 4th ed. Jones and Bartlett publishers, dec 2009, 978-0763779665.

[10] A. B. Morton, "Model aggregation of wind farms and other ensemble systems," in *Proc. Australasian Universities Power Engineering Conf. AUPEC 2007*, Dec. 2007, pp. 1–5.

[11] Y. Yang and X. Zha, "Aggregating wind farm with DFIG in power system online analysis," in *Proc. IEEE 6th Int. Power Electronics and Motion Control Conf. IPEMC '09*, 2009, pp. 2233–2237.

[12] H. M. Power, "Analytical solution of a simulation model for wind turbines," *Applied Energy*, vol. 9, no. 4, pp. 311 – 316, 1981. [Online]. Available: http://dx.doi.org/10.1016/0306-2619(81)90005-2

[13] D. Aguglia, P. Viarouge, R. Wamkeue, and J. Cros, "Analytical determination of steady-state converter control laws for wind turbines equipped with doubly fed induction generators," *IET Renewable Power Generation*, vol. 2, no. 1, pp. 16–25, 2007.

[14] J. Klima, M. Chomat, and L. Schreier, "Analytical closed-form investigation of pwm inverter induction motor drive performance under dc bus voltage pulsation," *IET Electric Power Applications*, vol. 2, no. 6, pp. 341–352, 2008.

[15] A. Petersson, S. Lundberg, and T. Thiringer, "A DFIG wind turbine ride-through system. influence on the energy production," *Wind Energy*, vol. 8, pp. 251–263, July 2005.

[16] J. Ekanayake, L. Holdsworth, and N. Jenkins, "Comparison of 5th order and 3rd order machine models for doubly fed induction generator (DFIG) wind turbines," *Electric Power Systems Research*, vol. 67, pp. 207–215, Apr. 2003.

[17] P. Kundur, *Power System Stability and Control.* McGraw-Hill, 1994.

[18] R. Peña, J. Clare, and G. Asher, "Doubly fed induction generator using back-to-back pwm converters and its application to variable-speed wind-energy generation," *IEE Proceedings-Electric Power Applications*, vol. 143, no. 3, pp. 231–241, 1996.

[19] R. Peña, R. Cardenas, E. Escobar, J. Clare, and P. Wheeler, "Control strategy for a doubly-fed induction generator feeding an unbalanced grid or stand-alone load," *Electric Power Systems Research*, vol. 79, no. 2, pp. 355 – 364, 2009. [Online]. Available: http://dx.doi.org/10.1016/j.epsr.2008.07.005

[20] M. Cañas-Carretón, E. Gómez-Lázaro, S. Amat-Plata, and Ángel Molina-García, "Ad-hoc analytical solution based on local linearisations for doubly-fed induction generator wind turbine electromechanical simulations," *IET Renewable Power Generation*, January 2014. [Online]. Available: http://digital-library.theiet.org/content/journals/10.1049/iet-rpg.2013.0048

[21] T. Sun, "Power quality of grid-connected wind turbines with dfig and their interaction with the grid," Ph.D. dissertation, Institute of Energy Technology. Aalborg University, Aalborg East, Denmark, may 2004.

[22] G. Slemon, "Modelling of induction machines for electric drives," *IEEE Trans. Ind. Appl.*, vol. 25, no. 6, pp. 1126–1131, 1989.

[23] J. B. Ekanayake, L. Holdsworth, X. Wu, and N. Jenkins, "Dynamic modeling of doubly fed induction generator wind turbines," *IEEE Trans. Power Syst.*, vol. 18, no. 2, pp. 803–809, May 2003.

[24] J. G. Slootweg, "Wind power. modelling and impact on power systems dynamics," Ph.D. dissertation, Delft University of Technology, Dec. 2003.

[25] Y. Lei, A. Mullane, G. Lightbody, and R. Yacamini, "Modeling of the wind turbine with a doubly fed induction generator for grid integration studies," *IEEE Trans. Energy Convers.*, vol. 21, no. 1, pp. 257–264, 2006.

[26] W. Price and J. Sanchez-Gasca, "Simplified wind turbine generator aerodynamic models for transient stability studies," in *Power Systems Conference and Exposition, 2006. PSCE '06. 2006 IEEE PES*, nov 2006, pp. 986 –992.

[27] F. Wu, X.-P. Zhang, K. Godfrey, and P. Ju, "Small signal stability analysis and optimal control of a wind turbine with doubly fed induction generator," *IET Generation, Transmission & Distribution*, vol. 1, no. 5, pp. 751–760, 2007.

[28] S. Chondrogiannis and M. Barnes, "Stability of doubly-fed induction generator under stator voltage orientated vector control," *IET Renewable Power Generation*, vol. 2, no. 3, pp. 170–180, 2008.

[29] E. Yusufoğlu, "Numerical solving initial value problem for fredholm type linear integro–differential equation system," *Journal Franklin Institute*, vol. 346, no. 6, pp. 636–649, 2009.

[30] MathWorks®, *MATLAB® & Simulink®*, MathWorks®, 2012, , accessed Dec. 2012. [Online]. Available: http://www.mathworks.com/

[31] F. Iov, A. Hansen, P. Sorensen, and F. Blaabjerg, "Wind turbine blockset in matlab/simulink," Risoe Institute-DTU and Allborg University, Tech. Rep., march 2004.

[32] Wolfram, *Mathematica®*, Wolfram, 2012, , accessed Dec. 2012. [Online]. Available: http://www.wolfram.com/mathematica/

[33] G. Michalke, "Variable speed wind turbines - modelling, control and impact on power systems," Ph.D. dissertation, Risoe-DTU Wind Energy Department, 2008.

[34] M. Bollen, *Understanding Power Quality Problems(Voltage Sags and Interruptions).* New York: Wiley-IEEE Press, 2000.

APPENDIX

TABLE II: 2 MW class DFIG wind turbine parameters

DFIG parameters [pu]	
Stator resistance	$R_s = 0.0130$
Stator leakage inductance	$L_{ls} = 0.1050$
Rotor resistance	$R_r = 0.0094$
Rotor leakage inductance	$L_{lr} = 0.1110$
Magnetisi ng inductance	$L_m = 3.3400$
Filter resistance	$R_f = 0.0235$
Filter inductance	$L_f = 0.3519$
Mechanical values	
Lumped inertia constant	$H_L = 4.510\ [s]$
Mechanical speed rated	$\Omega_s = 1686\ [rpm]$
Pair of poles	$p = 2$
Base values	
Power base	$S_b = 2 \cdot 10^6\ [W]$
Voltage base	$U_b = 563.383\ [V]$
Current base	$I_b = \frac{2}{3}(S_b/U_b)\ [A]$
Frequency base	$f_b = 50\ [Hz]$
Electrical speed base	$\omega_{eb} = 2\pi f_b\ [rad/s]$
Mechanical speed base	$\omega_{mb} = \omega_{eb}/p\ [rad/s]$
Inductance base	$L_b = \frac{U_b}{I_b \omega_{eb}}\ [H]$
Flux base	$\psi_b = U_b/\omega_{eb}\ [Wb]$

Matrix $\boldsymbol{A}$ and matrix $\boldsymbol{F(t)}$ from (17):

$$\boldsymbol{A} = \left(\begin{array}{cccccccccc}
\frac{L_r R_s \omega_{eb}}{L_m^2 - L_r L_s} & \omega_{eb}\left(-\frac{L_m^2 \omega_g}{L_m^2 - L_r L_s} + \omega_s\right) & -\frac{L_m (KP_{rd}+R_r)\omega_{eb}}{L_m^2 - L_r L_s} & \frac{L_m \omega_{eb}\left(-\frac{L_m^2 \omega_g}{L_m^2 - L_r L_s} + \omega_s\right)}{L_s} & \frac{KI_{rd} L_m \omega_{eb}}{L_m^2 - L_r L_s} & 0 & 0 & 0 & 0 & \\
\frac{L_m^2 \omega_{eb}\omega_g}{L_m^2 - L_r L_s} - \omega_{eb}\omega_s & \frac{L_r R_s \omega_{eb}}{L_m^2 - L_r L_s} & \frac{L_m \omega_{eb}\left(\frac{L_m^2 \omega_g}{L_m^2 - L_r L_s} - \omega_s\right)}{L_s} & -\frac{L_m (KP_{rq}+R_r)\omega_{eb}}{L_m^2 - L_r L_s} & 0 & \frac{KI_{rq} L_m \omega_{eb}}{L_m^2 - L_r L_s} & 0 & 0 & 0 & \\
-\frac{L_m R_s \omega_{eb}}{L_m^2 - L_r L_s} & \frac{L_m L_s \omega_{eb}\omega_g}{L_m^2 - L_r L_s} & \frac{L_s (KP_{rd}+R_r)\omega_{eb}}{L_m^2 - L_r L_s} & \frac{L_m^2 \omega_{eb}\omega_g}{L_m^2 - L_r L_s} & \frac{KI_{rd} L_s \omega_{eb}}{-L_m^2 + L_r L_s} & 0 & 0 & 0 & 0 & \\
-\frac{L_m L_s \omega_{eb}\omega_g}{L_m^2 - L_r L_s} & -\frac{L_m R_s \omega_{eb}}{L_m^2 - L_r L_s} & -\frac{L_m^2 \omega_{eb}\omega_g}{L_m^2 - L_r L_s} & \frac{L_s (KP_{rq}+R_r)\omega_{eb}}{L_m^2 - L_r L_s} & 0 & \frac{KI_{rq} L_s \omega_{eb}}{-L_m^2 + L_r L_s} & 0 & 0 & 0 & \\
0 & 0 & -1 & 0 & 0 & 0 & 0 & 0 & 0 & 0 \\
0 & 0 & 0 & -1 & 0 & 0 & 0 & 0 & 0 & 0 \\
0 & 0 & 0 & 0 & 0 & 0 & -\frac{(KP_{gd}+R_f)\omega_{eb}}{L_f} & 0 & \frac{KI_{gd}\omega_{eb}}{L_f} & \\
0 & 0 & 0 & 0 & 0 & 0 & 0 & -\frac{(KP_{gq}+R_f)\omega_{eb}}{L_f} & 0 & \frac{K}{} \\
0 & 0 & 0 & 0 & 0 & 0 & -1 & 0 & 0 & 0 \\
0 & 0 & 0 & 0 & 0 & 0 & 0 & -1 & 0 & 0
\end{array}\right)$$

$$\boldsymbol{F(t)} = \begin{pmatrix}
\frac{(u_5(t) KP_{rd} L_m - L_r u_1(t))\omega_{eb}}{L_m^2 - L_r L_s} \\
\frac{\omega_{eb}\left(u_6(t) KP_{rq} L_m L_s \omega_s - L_r L_s u_2(t)\omega_s + L_m^2 u_2(t)(-\omega_g + \omega_s)\right)}{L_s (L_m^2 - L_r L_s)\omega_s} \\
\frac{-u_5(t) KP_{rd} L_s \omega_{eb} + L_m u_1(t)\omega_{eb}}{L_m^2 - L_r L_s} \\
\frac{L_m u_2(t)\omega_{eb}\omega_g - u_6(t) KP_{rq} L_s \omega_{eb}\omega_s}{L_m^2 \omega_s - L_r L_s \omega_s} \\
u_5(t) \\
u_6(t) \\
\frac{(u_7(t) KP_{gd} + u_3(t))\omega_{eb}}{L_f} \\
\frac{u_8(t) KP_{gq}\omega_{eb}}{L_f} \\
u_7(t) \\
u_8(t)
\end{pmatrix}$$

where $u_1(t) = u_{sd}(t)$, $u_2(t) = u_{sq}(t)$, $u_3(t) = u_{gd}(t)$, $u_4(t) = u_{gq}(t)$, $u_5(t) = i_{rd}^{ref}(t)$, $u_6(t) = i_{rq}^{ref}(t)$, $u_7(t) = i_{gcd}^{ref}(t)$ and $u_8(t) = i_{gcq}^{ref}(t)$.

TURBULENCE INTENSITY WITHIN LARGE OFFSHORE WIND FARMS

Peter Argyle[1], Simon Watson[1], Christiane Montavon[2], Ian Jones[2], Megan Smith[3]
[1] CREST, Holywell Park, Loughborough University, Loughborough, UK
[2]ANSYS UK Ltd, 97 Jubilee Avenue, Milton Park, Abingdon, UK.
[3] The Carbon Trust, 27-45 Stamford Street, London, UK.
p.argyle@lboro.ac.uk, s.j.watson@lboro.ac.uk, christiane.montavon@ansys.com, ian.jones@ansys.com, megan.smith@carbontrust.com

ABSTRACT: The so-called Frandsen model forms the basis for the assessment of wind farm level turbulence intensity (TI) in the IEC standard 61400-1 edition 3. It is used in the choice of turbine suitable for a particular wind farm site. The Frandsen model was developed several years ago using field data when turbines and wind farms were of smaller scale than today. There is now an interest in the accuracy of models such as that of Frandsen when applied to the scale of the largest offshore wind farms. In this paper, we present the results of an analysis of the accuracy of the Frandsen model in predicting TI within the Greater Gabbard offshore wind farm. A comparison is made between measured data and predictions from: 1) the original Frandsen model; 2) a simplified version of the Frandsen model and 3) output from the ANSYS WindModeller CFD model. In general, the Frandsen model was found to perform well in the prediction of mean levels of TI but less well than a simplified model using either a freestream ambient TI or a turbine wake TI regardless of distance. Representative or 90% percentile TI levels are less well predicted under direct wake conditions due to the lack of consideration of turbine generated variance in turbulence and the manner in which the 90% percentile freestream TI is incorporated. ANSYS WindModeller was found to perform well in the prediction of mean TI and has the benefit of not requiring upstream TI data. The CFD model can be used to predict representative TI, when complemented with a model for the variance of turbulence. Predictions from the Frandsen model are more sensitive to the choice of freestream data than those from the CFD model.

1. INTRODUCTION

The fluctuations of the wind speed caused by turbulence affect the fatigue of the turbine blades and tower and consequently the turbine lifetime. As shown in Frandsen [1], wind turbine loads, for a given wind speed, are mostly conditioned by the level of turbulence intensity (TI) in the flow, and more specifically by the longitudinal component σ_u of the velocity fluctuation along the main flow direction. For turbines within a large array, operating in wake conditions, the Frandsen model [1] for TI is used as the basis for the IEC Standard 61400-1 edition 3, amendment 1 [2] to derive an effective TI as a function of wind speed. Turbine suitability is assessed by verifying that the site effective TI is below the turbine design TI for the range of wind speed between 60% of the rated wind speed and the cut-out wind speed.

This paper summarises work carried out as part of the Carbon Trust's Offshore Wind Accelerator's project `*Validation of Frandsen Turbulence Intensity Model and Large Wind Farm Models*` [3]. The objective of this work is to assess the performance of 1) the Frandsen model and 2) a computational fluid dynamics (CFD) code in predicting levels of turbulence intensity within a large wind farm by comparing data from the Greater Gabbard wind farm with model predictions.

2. SITE

The wind farm investigated is that of Greater Gabbard, situated in the North Sea, with a layout as shown in Figure 1. It consists of two sections, one to the North with 102 Siemens 3.6MW turbines ($h_{hub} = 77.5$ m , $D = 107$ m) and one to the South, with 38 turbines. The distance between the southern and northern part of the array is over 70D. For the flow directions with regular spacing, turbines are separated by typically ~9.7D (200˚), ~10D (247˚) and ~8.3D (315˚). The site has two meteorological masts, marked by squares in Figure 1: IGMMX to the south of the Northerly section, 2.5D upstream of a turbine, and IGMMZ embedded within the Northerly section.

SCADA data from each turbine alongside measurements collected at the two masts were made available for the project by the operator SSE. Two turbines, IGH08 and IGK02, are marked as black circles in Figure 1 and were used to validate model predictions in addition to the two met masts.

To provide a representation of the freestream wind conditions, a data set was constructed from a selection of upstream turbines with the freestream wind direction calculated by averaging the yaw position of the six turbines highlighted as open circles in Figure 1, whilst the freestream wind speed values were calculated by averaging the SCADA measurements from these turbines when they were individually considered by direction to be in the freestream flow. Note that the local wind speed for the turbines is derived from nacelle anemometry. The accuracy of using nacelle wind speed to derive turbine upstream conditions was assessed, by correlating the wind speed measured at IGMMX with that measured at IGF10 (2.5D downstream of the mast). For the wind speed, the linear correlation between mast and turbine was good albeit that the slope of the regression line is not exactly 1 (Figure 2). For the wind speed standard deviation, the correlation is less good, and the ratio $\sigma_{IGF10}/\sigma_{mast}$ shows values below 1 at low wind speeds (Figure 3). There are some important caveats to the use of either turbine data or mast data for inferring the freestream wind speed and TI in this study:

- Nacelle anemometers are in the wake of the rotor and their measurements are normally corrected to provide 'freestream' values. This process introduces a degree of uncertainty and is known to lack rigour when trying to measure true freestream wind speed;
- Nacelle anemometers will measure additional turbulent components that result from the blades as well as structures on the nacelle, e.g. hand-rails;
- The limited numbers of pulses per revolution from the anemometers on IGMMX meant that the recording of turbulent fluctuations at low wind speed values (especially below 8m/s) was subject to error.

These factors are discussed later when validating model predictions.

For the comparisons between model and data for the TI by direction in section 4.1, the data were binned by freestream wind speed, and results are shown for the 10m/s (±0.5m/s) bin. The corresponding wind rose at 10 m/s is shown in Figure 4.

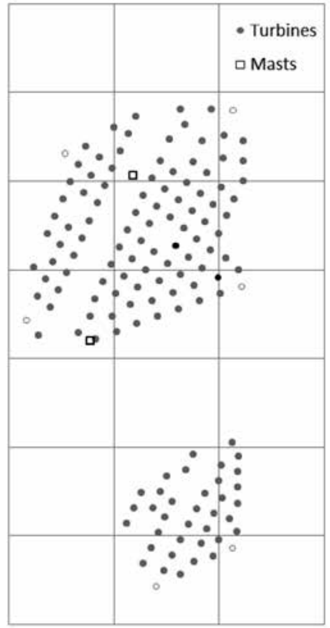

Figure 1: Layout of Greater Gabbard Wind Farm. Turbines marked in black are IGH08 (top left) and IGK02 (bottom right), the met masts are shown as squares and the six turbines used to calculate freestream conditions are shown as open circles.

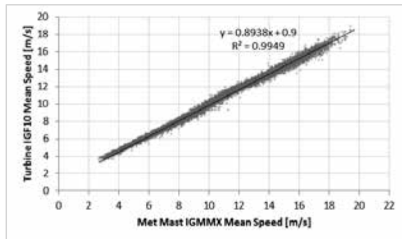

Figure 2: Correlation between wind speed at IGF10 and mast IGMMX, for directions 180°<θ<250° where neither are influenced by upstream turbines.

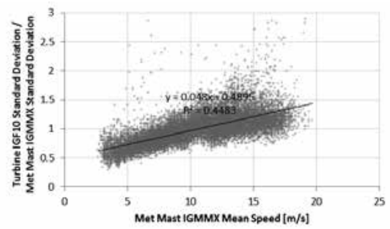

Figure 3: Ratio between wind speed standard deviation at IGF10 and IGMMX against mast wind speed, for directions 180°<θ<250° where neither are influenced by upstream turbines.

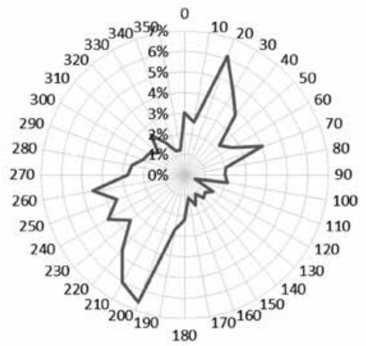

Figure 4. Freestream wind rose for 10m/s wind speed.

With potential problems associated with using nacelle anemometry, a second data set to represent the wind farm upstream conditions was generated by comparing the measurements from mast IGMMX and the wind turbine IGF10 located just 2.5 diameters away. Assuming the systematic bias in mean wind speed measurements between IGMMX and IGF10 is a constant feature of using data from turbine nacelles, the values of nacelle-measured mean wind speed were adjusted to the corresponding values of a mast-measured data set.

3. TURBULENCE INTENSITY

3.1 Frandsen model

The Frandsen model for the effective TI ($I_{eff}(U)$) is providing a local TI at a location within the wind farm, but is specified in terms of wind farm upstream conditions (i.e. conditions which can be measured before the wind farm is operational). It is summarised below, using the representative (i.e. the 90th centile value of the) wind speed standard deviation in the integrand.

$$I_{eff}(U) = \left[\int_{-180}^{180} I^m f_{wd}(\theta|U_0)d\theta\right]^{\frac{1}{m}} \qquad I = \frac{\sigma(\theta,U)}{U} \tag{1}$$

where m is the Wöhler exponent, θ is the wind direction, and U is the wind speed. The value of $\sigma(\theta,U)$ is calculated depending on location within the wind farm with respect to wind direction and assuming a regular turbine layout, via one of the following three equations:

$$\sigma_{repr,0} = \langle\sigma_0\rangle + 1.28stdev(\sigma_0) \tag{2}$$

$$\sigma_{repr,0,wf} = \langle\sigma_{0,wf}\rangle + 1.28stdev(\sigma_0) \tag{3}$$

$$\sigma_{0,wake} = \sqrt{\frac{U_0^2}{\left(1.5 + 0.8\frac{d_i}{\sqrt{C_T}}\right)^2} + \sigma_{repr,0}^2} \tag{4}$$

where $\sigma_{repr,0}$ is the representative wind speed standard deviation of the freestream flow, $\sigma_{repr,0,wf}$ is the representative wind speed standard deviation of the flow within an infinite array, $\sigma_{0,wake}$ is the representative wind speed standard deviation of the flow directly within the wake of an upstream turbine, d_i is the normalised distance to the upstream turbine, C_T is the turbine thrust coefficient. Chevron brackets indicate ensemble averaging. The wind farm ambient (or background) wind speed standard deviation, $\sigma_{0,wf}$, is calculated from the freestream ambient background (σ_0) and wind farm added wind speed standard deviation above the wind farm, $\sigma_{add,wf}$, as follows:

$$\sigma_{0,wf} = \frac{1}{2}\left(\sqrt{\sigma_{add,wf}^2 + \sigma_0^2} + \sigma_0\right) \tag{5}$$

$$\sigma_{add,wf} = \frac{0.36U_0}{1 + 0.2\sqrt{s_f s_r / C_T}} \tag{6}$$

where s_f and s_r are the normalised distances between turbines in a row and between turbine rows respectively. The Frandsen model stipulates that equation (4) shall be used, if the location is in the direct wake of a turbine less than 10 rotor diameters away. For directions with turbines more than 10 diameters away, where there are more than 5 turbines between the selected location and the edge of the wind farm or if the turbine separation is less than 3 diameters, Equation (3) shall be used. For all other directions (no turbine or less than 5 turbines upstream, all of them beyond 10D), the ambient TI calculated via Equation (2) is valid.
Frandsen fitted his model for the direct wake contribution using data from the Vindeby, Andros, Taff Ely and Alsvik wind farms [1] and therefore there may be aspects of the model which are not suitable for modern offshore farms that are much larger. An example of this is the arbitrary 10 diameter cut-off applied to determine whether an individual turbine wake is significant to the TI measured at any particular location. To test the applicability of the 10 diameter cut-off, this work will also investigate a `Simplified` version of the model which does not utilise the infinite array concept. Thus, for the Simplified model, if a turbine exists upstream of a specified location for the wind direction of interest, Equation (4) shall be used, irrespective of its distance, whilst Equation (2) shall be used for all other directions at that location.

3.2 CFD simulations

CFD simulations were carried out using ANSYS WindModeller modelling the wakes with an actuator disk method under neutral atmospheric conditions. Turbulence closure is provided using a *k-ε* model with modified turbulence constants (C_μ = 0.03, turbulence decay rate = 0.6), as successfully validated in earlier work [6]. For the results shown here, only the Northern section was modelled, using a simulation domain with a 17km radius, and 5 km height. Separate simulations for the entire wind farm showed that the effect of the Southern section is only minimal (increasing the TI from 5.8% to 7.1% for mast IGMMX) and only affected the sectors 130˚ to 170˚. The mesh resolution used a background horizontal resolution of 60m. In the vertical, the mesh resolution follows a geometric progression, with a first cell height of 2m, and an expansion factor of 1.16. Simulations have been carried out for 36 equally spaced directions, and 4 reference wind speeds (6, 10, 12 and 14 m/s) at hub height.
When carrying out Reynolds Averaged Navier-Stokes (RANS) simulations, solving for stationary flow conditions, the resulting flow fields are assumed to be representing the mean flow conditions on site. The mean turbulence intensity from the CFD is calculated from:

$$I_{mean} = \frac{\sigma_u}{U} = \frac{\sqrt{\frac{2}{3}k}}{U} \tag{7}$$

When calculating the local TI at mast locations from the model, local values for the turbulence kinetic energy k and the wind speed U are used. For turbine locations, equation (7) is evaluated using the local value for the turbulence kinetic energy k and the turbine upstream wind speed $U_{WT,upstr}$, itself derived from the local wind speed at hub height, using 1D actuator disk theory. The reason for using the turbine upstream wind speed, is an attempt to mimic what is reported in the wind turbine SCADA data, where, via the use of nacelle transfer functions, the turbine wind speed is supposed to be representative of the wind speed upstream of the turbine.

4. COMPARISON WITH DATA

4.1 TI by direction

The results of applying the Frandsen model and the Simplified model are shown for the two met masts in Figure 5 and Figure 6 compared to values of TI measured on each mast, with freestream values indicated. The resulting mean TI from the CFD model is also shown.

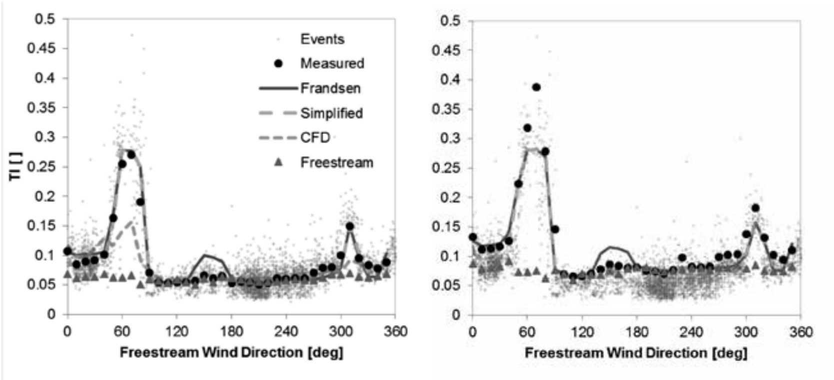

Figure 5: Mean (left) and representative (right) values of TI for the southern met mast IGMMX for a 10 m/s wind farm upstream wind speed.

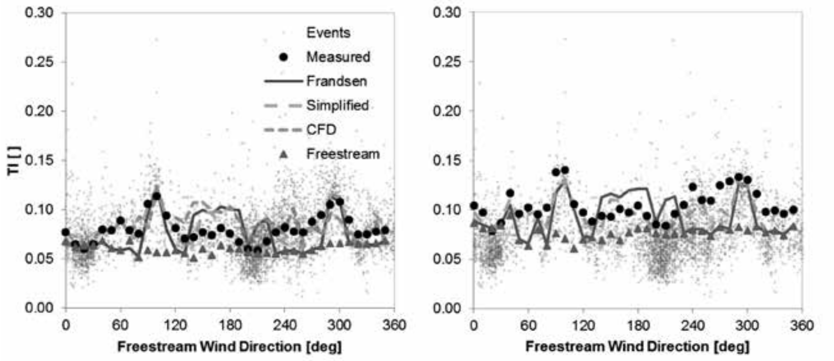

Figure 6: Mean (left) and representative (right) values of TI for the northern met mast IGMMZ.

At mast IGMMX (Figure 5) at the edge of the northern wind farm cluster, the Frandsen model provides a good prediction of the mean turbulence intensity except for the sector 0˚-30˚ and around 150˚. Between 0˚-30˚, the wind farm ambient TI assumed by Frandsen would seem to be an over-estimate. The over-prediction of the TI around sector 150˚ would seem to result from the wind farm ambient TI associated with the Southern section. Arguably, the wind farm ambient TI in the Frandsen model is not intended to cater for the effect of a separate section of the wind farm so far upstream. The Simplified model seems to predict much better the TI in these sectors.

The CFD model provides a reasonably good prediction of the background TI, which affects the majority of directions at mast IGMMX, but tends to underestimate the peak TI in the direct wake (sector 60˚ and 310˚). Additional simulations at a finer horizontal resolution showed that the peak TI in the near wake is not mesh converged. Further refining the mesh allows the capture of the peak in the near wake more accurately (not shown).

For directions in the direct wake of a turbine less than 10D upstream (sectors 60˚ and 310˚), the difference between the mean and representative TI from the Frandsen and Simplified models is small. This may be because the calculation of the representative values in the wake only accounts for fluctuation of the standard deviation in the background flow and not the direct wake. The fact that the model underestimates the representative TI around these sectors may be an indication that the representative TI in the direct wake should be derived in a more sophisticated way. In particular, the inclusion of the standard deviation of the wind speed standard deviation under the square root in equation (4) is questionable. Doing so means that, for a given value of background fluctuation $stdev(\sigma_0)$, the absolute change between σ_{repr} and σ_{mean} in wake conditions, which should be a measure of $1.28\,stdev(\sigma)$ in wake conditions, is smaller than the $1.28\,stdev(\sigma_0)$ that results in freestream conditions. This is in contrast to what we see in the data at IGMMX for example, where $stdev(\sigma)$ for waked sectors tends to be larger than for freestream sectors. It is suggested that the representative σ might be better captured with:

$$\sigma_{0,wake} = \sqrt{\frac{U_0^2}{\left(1.5+0.8\frac{d_i}{\sqrt{C_T}}\right)^2}+\sigma_0^2} \qquad (8)$$

$$+1.28stdev(\sigma_0\ )$$

Figure 6 suggests that deep within the wind farm the Simplified model predicts the mean TI well, except near the sector 260˚ and 330˚. The overestimation around the sector 150˚ was found to be due to reduced availability of turbine IGE06, 11.3D upstream of the mast. The Frandsen model struggles in capturing trends in mean TI with direction at mast IGMMZ, sometimes underestimating where less than five turbines upstream are present, or over-estimating for directions where the wind farm ambient TI over-predicts the actual TI.

The CFD results show a similar trend to the Simplified model, with reasonable agreement with the data, except for an underestimate of the peak around 300˚. Around sector 150˚, the CFD also produces a peak not seen in the data because of the reduced availability of turbine IGE06. Both the Frandsen and Simplified models struggle to capture the amplitude of the standard deviation of the wind speed standard deviation, underestimating the representative TI most likely for the reasons mentioned above.

Figure 7 compares the model outputs against the measured values of TI at the locations of wind turbine IGH08. In general, the Frandsen model captures the fluctuations in TI due to nearby turbines though it struggles for directions where the nearest turbine is more than 10 diameters away. For example, between 270°<θ<300°, due to the farm layout irregularity, the Frandsen model reverts to using the freestream TI value whilst between 40°<θ<120° there are less than the arbitrary 5 turbines required to suggest a wind farm TI has developed. By contrast, the Simplified model which uses the direct wake method in Equation (4) for these sectors, predicts the measured values well.

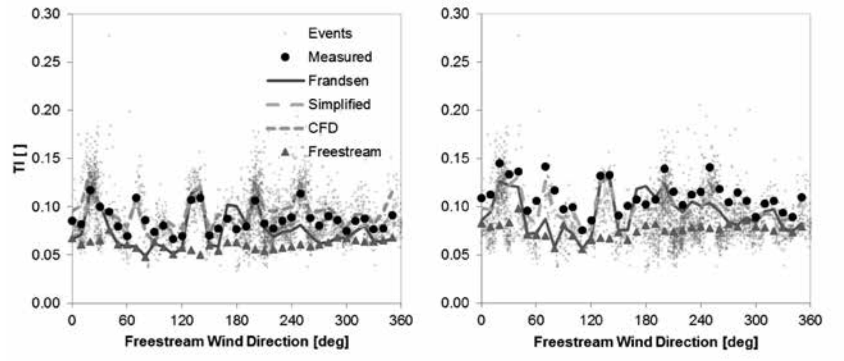

Figure 7: Mean (left) and representative (right) values of TI for the wind turbine IGH08.

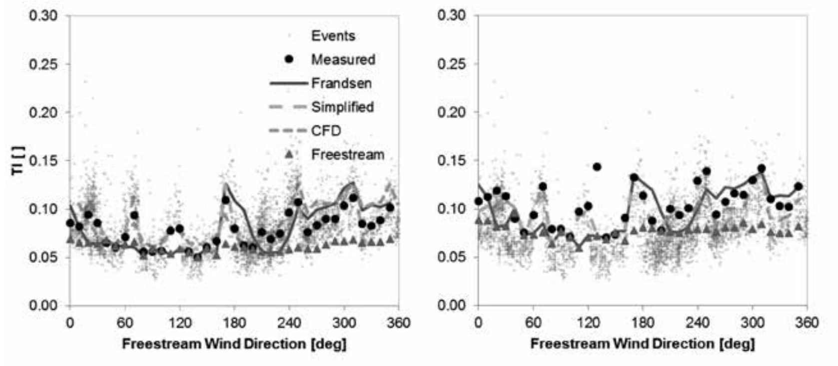

Figure 8: Mean (left) and representative (right) values of TI for the wind turbine IGK02.

Figure 8 shows results from the position of turbine IGK02 and shows similar results to Figure 7, although the proximity of the farm edge is more relevant. This is shown best for directions between 30°<θ<170° where for some directions within this sector, turbine IGK02 experiences the freestream TI values, and there are some directions which are affected by the wakes of other single turbines located further than 10 diameters. For the direction sectors relating to these distant individual turbines, the Frandsen model fails to capture the significant increases in TI whilst the results from the Simplified model agree well with the measured values.

4.2 TI vs wind speed

As would be the case for a turbine suitability assessment, we calculated the effective TI for a range of wind speed between 60% of the rated wind speed and the cut-out wind speed, evaluating equation (1) (using a Wöhler exponent m =1). As data input for this process, when using the Frandsen model, we require a data set representing the wind farm upstream conditions, characterising the ambient TI as well as the frequency distribution at each wind speed. When using a freestream data set derived from the data at mast IGMMX, we obtain the resulting $I_{eff}(U)$ curves at mast IGMMZ, which are shown in Figure 9. The results from the Frandsen and Simplified models are compared to the $I_{eff}(U)$ from the wind data and CFD results, calculated from the local TI and binned by the local wind speed at IGMMZ. When calculating the mean local TI from the CFD results shown in Figure 9, we evaluate TI directly from the solved turbulence kinetic energy, via equation (7). When using this method, the only required wind farm upstream data is the direction distribution at any given reference wind speed. Since the CFD results are stationary solutions, for any given upstream wind speed and direction, they provide a unique value for the wind speed standard deviation, without an associated fluctuation. To derive representative TI values from the CFD, we need to complement it with a model for $stdev(\sigma)$. In the results presented in Figure 9, we used a linear relationship

$$stdev(\sigma) = aU + b$$
$$a = 0.0106, b = 0.0869 \qquad (9)$$

which was derived from correlating $stdev(\sigma)$ with U at mast IGMMX for directions unaffected by wakes. This relationship was also used when evaluating representative I_{eff} using the Frandsen and Simplified models in Figure 9, when working with upstream data derived from mast IGMMX.

When predicting the mean I_{eff}, both the Frandsen and Simplified models provide a very good prediction, between 7 and 25 m/s. Both models are reasonably close to each other, with the Frandsen model producing slightly reduced TI below 13 m/s and slightly increased TI above 13 m/s (compared to the Simplified model). At low wind speeds, the models lead to excessive effective TI values. At this point it is not clear if this is associated with potential measurement problems at mast IGMMZ, as the latter has not been maintained as thoroughly as IGMMX, and anemometers may be suffering from increased bearing friction at low wind speed (P. Housley, private communication). As described above, we also know from our data analysis that wind speed measurements from mast IGMMX seem to be affected by problems when sampling a pulsed anemometer, which leads to artificially increased wind speed standard deviations at low wind speeds. The CFD model also performs very well between the range of wind speeds which were simulated (6-14 m/s). Outside of the simulated range, the CFD model results are not reliable as they depend on an extrapolation of the results which is not physically based.

When calculating the representative I_{eff}, both the Frandsen and Simplified models provide a good match to the measured TI between 7 and 13 m/s. At higher wind speed, these models tend to over-predict the representative I_{eff}.While we noticed from the plots by direction at 10 m/s (Figure 6) that these models tended to under-estimate the peak representative TI in wake situations, it appears that when integrating over the direction, under- and over-estimated predictions cancel out. It should be stressed that this may not be true for all wind farms or indeed for other locations in this wind farm, being dependent on the relative weighting between wake affected, wind farm affected and freestream sectors. The CFD model using the direct method and the linear expression (9) for $stdev(\sigma)$ provides an accurate effective TI for the range of simulated wind speeds.

The sensitivity of the I_{eff} predictions to the assumed wind farm upstream conditions, and in particular to the ambient $I_{eff,0}(U)$ curve, is demonstrated in Figure 10, where the I_{eff} calculations were repeated starting from a wind farm upstream data set derived from nacelle anemometry. As can be seen from these results, the effective TI derived from the Frandsen and Simplified models are very different from those obtained earlier. The predicted mean I_{eff} from these models no longer agree so well with the measured data at IGMMZ. The results from the CFD model using the direct method are unchanged. When deriving I_{eff} from a calibrated CFD model approach, the CFD model results become strongly sensitive to the ambient effective TI too.

In the calibrated approach, the wind farm upstream wind speed standard deviation is transposed to the prediction site by scaling it with the ratio of simulated standard deviation at the prediction site and upstream of the wind farm. The $I_{eff}(U)$ curves derived from the Frandsen and Simplified model, as well as from the CFD model using the calibrated approach, are very sensitive to the assumed ambient effective TI. Their overall trend is strongly reminiscent of the trend seen in the ambient conditions (plotted in Figure 11 for reference).

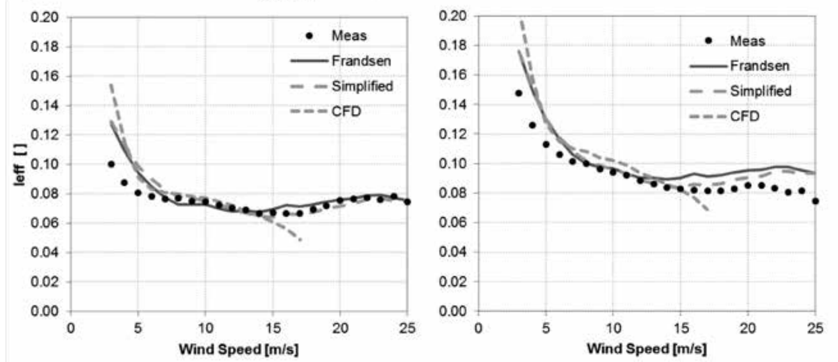

Figure 9: Mean (left) and representative (right) values of TI integrated across all directions, as measured at met mast IGMMZ, *m*=1. TI calculated using wind farm upstream conditions derived from met mast IGMMX.

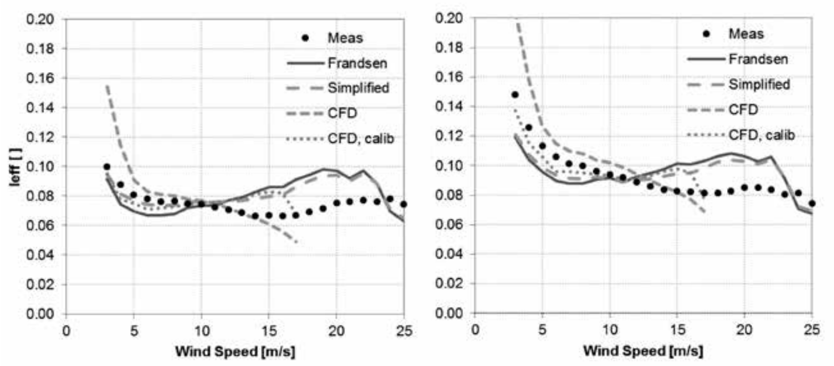

Figure 10: As Figure 9 but using wind farm upstream conditions derived from nacelle anemometry.

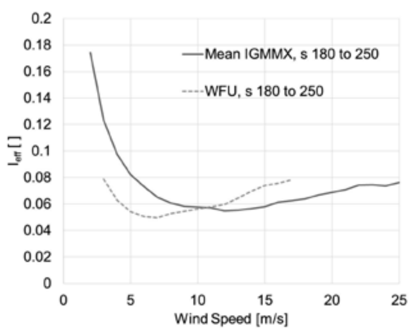

Figure 11. Ambient effective TI vs wind speed for the wind farm upstream (WFU) data set derived from data at IGMMX (continuous curve) and that derived from nacelle anemometry (dashed curve).

5. CONCLUSIONS

From the validation comparing TI vs direction at a constant wind speed of 10 m/s, we conclude that the model proposed by Frandsen for the direct wake turbulence (equation (4)) does a very good job at capturing the mean TI in the wake of a turbine, even at short range such as the 2.5D shortest distance we investigated. The use of a 10D cut-off distance beyond which the direct wake turbulence is not applied is arbitrary, and leads to significant TI peaks being missed when calculating the mean TI vs direction. Using ambient TI for directions where less than 5 turbines are located upstream beyond the 10D cut-off is also questionable as it leads to underestimated TI. Also, when applied, the wind farm background TI, tends to overestimate the measured TI. Because of all of these observations, the Simplified model appears to provide a better agreement to the mean measured values which casts doubt on the use of a wind farm level ambient turbulence intensity.

The change in values between the mean and representative TI seen in the data set is not captured by the Frandsen model when considered by direction, likely because the model only accounts for variability in the wind speed standard deviation as present in the background flow, and no variability associated with the wakes. When averaged over all directions, the Frandsen model does a much better job in predicting this change for the case we have considered, though this is due to underestimation in some sectors and overestimation in others. This may well be wind farm and location specific and we cannot generally assume that the cancellation of errors will always lead to accurate predictions when calculating the directionally averaged value of the representative TI.

The CFD model used here is capable of capturing the key features of mean TI vs direction at the wind speed investigated, although with a tendency to under-estimate the peak TI at short range (2.5D). The derivation of an effective TI from CFD, using the direct method, also showed encouraging results for the range of wind speed simulated (6 to 14 m/s). The stationary CFD model was extended to predict representative TI by assuming a linear correlation between $stdev(\sigma)$ and the wind speed U. While this delivered good results for the site of Greater Gabbard, the applicability of the selected correlation coefficients to other sites needs to be proven.

Effective TI, when derived from the Frandsen or simplified model, as well as from the calibrated CFD model is very sensitive to the assumed freestream conditions and results can change significantly with variations in input data. With these models, to get an accurate prediction of $I_{eff}(U)$ within the wind farm, not only is an accurate wake model required, but an accurate representation of the wind farm upstream conditions will be essential too. The CFD model using the direct method to derive TI has the advantage that it has no sensitivity to the assumed mean upstream standard deviation, instead it relies on the accuracy of the turbulence model itself.

ACKNOWLEDGEMENTS

This work was funded by the OWA project of the Carbon Trust, and data was provided by SSE. The authors would like to thank the OWA partners and the Carbon Trust for many valuable and stimulating discussions on the work, especially DONG Energy and Paul Housley of SSE.

REFERENCES

[1] S. Frandsen, "Turbulence and Turbulence Generated Loading in Wind Turbine Clusters," Risø report R-1188, 2007.

[2] IEC Standard, 61400-1, Edition 3 + Amendment 1, 2010. Wind turbines, Part 1: design Requirements, BS EN 61400-1:2005 + A1:2010.

[3] "Invitation to Tender: 'Validation of Frandsen Turbulence Intensity Model and Large Wind Farm Models' OWA Programme," [Online]. Available: http://www.carbontrust.com/about-us/work-with-us.

[4] C. Montavon, I. Jones, C. Staples, C. Strachan, I. Gutierrez, 2009, Practical issues in the use of CFD for modelling wind farms, EWEC Proceedings, Marseille.

[5] ANSYS CFX – Solver Theory Guide, Release 16.2, July 2015, ANSYS Inc.

[6] C. Montavon, I. Jones, 2013, 'Atmospheric stability and Coriolis effects in the simulation of large array losses', EWEA 2013 conference proceedings, Vienna.

Breakthrough Research EWEA 20-Nov-2015

The benefits and uncertainties of floating lidar

Dr John Slater and Charles Pearce
RWE Innogy UK

Lead author:
Dr John Slater
Wind Resource Manager – Onshore UK
RWE Innogy UK
27 Harmire Enterprise Park,
Barnard Castle,
County Durham. DL12 8BN
UK

Tel: +44 (0) 191 350 4225
Fax: +44 (0) 191 350 4250
Mob: +44 (0) 774 701 7251
Email: John.Slater@rwe.com

Summary

Historically all wind measurements for offshore windfarms have been performed using cup anemometers and stand-alone met masts, usually on monopiles. While these provide excellent datasets, they do so at a high cost and are fixed in location. The development and steady acceptance of lidar technology has opened up the opportunity for potentially cheaper technology particularly offshore. The advantages are explored in this paper and also a quantitative analysis of the errors associated with both sets of measurements is presented.

RWE has managed the deployment of the first UK floating lidar trials. With the financial assistance of the Carbon Trust through the Offshore Accelerator Program, two floating lidar systems have been successfully trialled, for periods of over six months in the last two years.

A summary of the key results are provided in this paper from both trials along with the deployment lessons, learnt from an operators/owner's perspective.

An analysis of results and the production of uncertainty analysis leading to a cost benefit analysis from the owner/developers perspective has been produced.

This demonstrates that while the floating lidars can produce accurate results, there is still a useful primary place for the fixed met mast with cup anemometers for producing data with the lowest uncertainty. This becomes significant when the high capital costs of developing and building offshore wind farms are taken into account and up front additional costs are less significant compared with the greater prediction accuracy leading to potentially lower financing costs.

Breakthrough Research EWEA 2015
Paris 20-Nov-2015

The benefits and uncertainties of floating lidar

Dr John Slater and Charles Pearce
RWE Innogy

1. Abstract

Historically all wind measurements for offshore windfarms have been performed using cup anemometers and stand-alone met masts, usually on monopiles. While these provide excellent datasets, they do so at a high cost and are fixed in location. The development and steady acceptance of lidar technology has opened up the opportunity for potentially cheaper technology particularly offshore. The advantages are explored in this paper and also a quantitative analysis of the errors associated with both sets of measurements is presented.

RWE has managed the deployment of the first UK floating lidar trials. With the financial assistance of the Carbon Trust through the Offshore Accelerator Program, two floating lidar systems have been successfully trialled, for periods of over six months in the last two years.

A summary of the key results are provided in this paper from both trials along with the deployment lessons, learnt from an operators/owner's perspective.

An analysis of results and the production of uncertainty analysis leading to a cost benefit analysis from the owner/developers perspective has been produced.

This demonstrates that while the floating lidars can produce accurate results, there is still a useful primary place for the fixed met mast with cup anemometers for producing data with the lowest uncertainty. This becomes significant when the high capital costs of developing and building offshore wind farms are taken into account and up front additional costs are less significant compared with the greater prediction accuracy leading to potentially lower financing costs.

2. Keywords

Lidar, Floating Lidar, Offshore, met mast, sea trials, cup anemometers, uncertainty, net cost benefit

3. Background

Until recently all RWE offshore wind farms have benefitted from the installation of fixed met masts prior to the full wind farm development. These are given in Table 1.

Plotting the met mast height against the commissioning dates of the wind farms, Fig. 1, it can be seen that there is a steady rise in mast height as would be expected as larger turbines are being developed.

Site	MW	Mast installed	Site commis sioned	Max height
North Hoyle No2	60	2006	2003	70
Rhyl Flats	90	2005	2009	85
Greater Gabbard	504	2005	2012	86
Thornton Bank	325			
Gwynt y Mor	576	2005	2014	90
Nord See Ost	295	2011	2015	96
Development				
Ijmuiden	-	2011	2014	92
Galloper	500	GG mast		
Triton Knoll	900			
Nordsee 1,2&3	1000			
Dogger Bank	7200	2013	2020	110

Table: 1 Details of RWE offshore developments

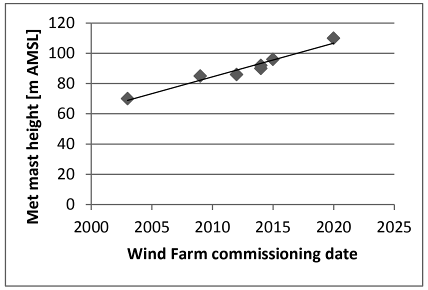

Fig. 1 Change of mast height with commissioning date

The offshore met masts are thus required to be built at ever higher heights to measure the wind speeds at close to the hub height of the wind turbines. In addition most masts have been strategically located so that when the site is commissioned they are in a suitable location to be used for perform power performance measurements at an adjacent wind turbine. For this the top anemometers must be within 5% of the turbine hub height [1]. In some cases (eg Rhyl Flats) this has necessitated the extension of the existing mast. Subsequent masts have been designed to anticipate the hub height variations for a site or with enough design margin to allow a subsequent height extension.

Increased height also brings with it increased cost due to the size of the foundations and mast structure. The effects can also start to affect the wind speed measurements as the larger structures provide more turbulence and blockage effects. So the booms need to be longer to be outside the mast influence zone.

This leads to one of the main drivers – cost. As the mast costs increase and sites are more complex and difficult to develop with certainty, the high multi-million Euro met mast investment a number of years prior to construction is a difficult decision.

Floating lidars are thus seen as potentially providing similar measurements at a reduced cost. There are however advantages and disadvantages to both methods summarised below in Table 2.

	Floating Lidar	Met mast
Design	New designs Design codes not clear.	Known designs, standard design codes.
Deployment	Quick deployment.	Large construction costs.
Location	Moveable	Fixed location
Cost	Lower installation & maintenance costs.	Higher installation and maintenance costs.
Maintenance	Access difficult in all but calm seas. Maintenance of mooring systems required. Little working at height required. Work place usually in contained area. Can be taken to harbours for servicing.	Access generally similar to turbine access. Working at heights required for maintenance. All maintenance to be at sea.
Resilience	Added redundancy can be difficult due to weight and stability issues. Single lidar: when that fails there are no readings.	Redundancy easy to design in: Power systems, instrumentation, navigation aids and additional sensors.
Power	Primary lidar instrumentation have high power consumption.	Primary instrumentation – cup anemometers have very low power consumption and easy redundancy & duplication.
Instrumentation	Measurements to rotor tip height No turbulence measurements. No gust measurements Wind direction can be problematic	All standard measurements and parameters possible Measurements generally to hub height only Lidar systems easily added to give tip measurements.
Accuracy	Lidar verification required. Buoy movements must be accounted for	Known systems with understood accuracies - Boom and mast effects
Versatility	Can be moved Adding extra instruments problematic due to weight, power and stability issues.	Fixed. Addition measurement systems relatively easy to add Provides stable work platform offshore.
Environment	More vulnerable to wave & storm damage. Less visible to shipping.	More vulnerable to lightning strikes.

Table 2. Merits of different measurement systems

3.1. Lidar systems

The lidar works by firing a laser beam into the atmosphere and then analysing the back scatter generated from the beam reflecting off aerosol particles in the air. The change in frequency (Doppler shift) of the back scatter can be used to infer a velocity. The velocity is only measured in the direction of the beam, hence a number of beams are projected outwards at an angles, (at least four usually a cone shape) so that x, y and z velocity components can be derived.

It is worth observing that the beams are generated from the unit on the ground and that any small angular movement will be enhanced at the higher measurement levels. For example a 5° tilt will give a ~±2.5m change in measurement height at 100m with a 30° lidar cone angle. One beam will be above and the other below and the motion of any system in the sea will mean that over a typical 10-minute period, the readings will be averaged out. The question to answer is how much affect does this have on overall accuracy.

3.2. Different systems

Floating lidars fall into two main systems:
Surface buoys and spar buoys
- The surface buoys as the name suggests float in the upper sea surface and are more subject to wave motion. In general they are smaller and easier to deploy. Care needs to be taken with the lidar systems to compensate for this motion either with external gimbals or software motion compensation.

-Spar buoys aim to have minimum movement in the measurement platform, i.e. they try to simulate as much as possible a fixed monopile type foundation. They work in a similar fashion to a fishing float where they are buoyant and are kept vertical by tension in the anchor cables to the seabed. The lidar system is thus most likely to be mounted directly on the platform. In general they will require deeper water to deploy and are larger structures due to their depth.

Hybrid type versions have also been proposed whereby a lidar is co-located with a small met mast. The height of the lidar readings are thus gained and the advantages of cup anemometers also retained for turbulence, gust and low power readings, albeit at a much lower height. Different options are considered in Fig. 3. They are:, clockwise, The Leosphere and Zephir lidar systems. Mojo maritime hybrid mast, Natural Power SeaToc, Babcock floating lidar, Flidar, Axis floating buoy system and Fugro system.

Fig. 3 Different lidar measurement systems

4. Trials

Our approach has been to facilitate the experimental deployment of trial floating lidar at its offshore windfarm sites.
As a company it wants a practical solution at the right cost.

The main aims being:

- To gain practical experience of the development;
- Verify the technology accuracy;
- Get bankability, buy in and bring the cost down.

4.1. Experimental site Gwynt-y-Mor (GYM)

The Gwynt-y-Mor wind farm development site was chosen. It is in the Liverpool Bay area to the West of the UK in the Irish Sea and is approximately 15km from land. The met mast on site was installed in 2005 and has a height of 90m AMSL. The water depth is 10-15m with a high tidal range of just under 10m (i.e MSL is 4.9m above LAT).

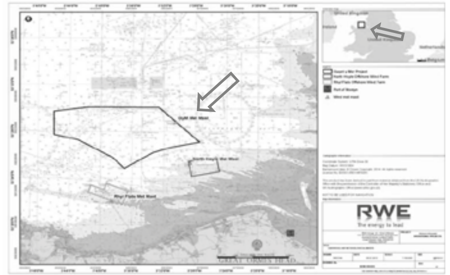

Fig.4 Gwynt y Mor trial site.

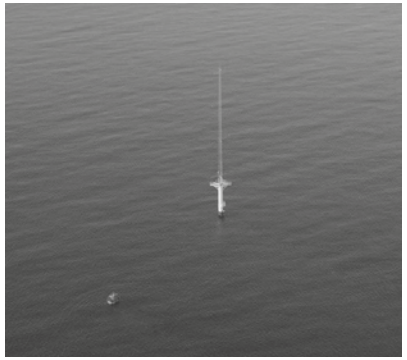

Fig.5 The Flidar buoy on test next to the GYM mast

Fig.6 GYM met mast showing booms

The mast is a lattice structure mounted on a monopile foundation. The main instrumentation comprises Measnet calibrated Vector cup anemometers. Recent additions for the trials have included the addition of wave radars and a Zephir-300 lidar, powered by wind chargers and solar panels. A wavebuoy is also located adjacent to the mast.

Both trials were sponsored by the Carbon Trust through the OWA program. The lidar data and the mast data were collected independently, in such a way that the floating lidar supplier were unable to see the mast results and thus make their results agree. Full details are given in reference [2]. The analysis was also performed by Frazer Nash, an independent company, to ensure impartiality to the results.

4.2. Flidar Trials

The Flidar system, is a surface type buoy, the prototype being made from two marine buoys, attached together with the lidar, a Leosphere wind cube, mounted in Gimbels on a platform, which also carried the power supply and communications systems.

Fig. 7 Flidar system on test at Gwynt y Mor

The unit photographed above was deployed in Oct-2012, the test period being approximately 3 months. The trials were cut short by communications and power supply problems on the prototype unit and re-deployment cancelled as a result of some dockside damage to the system again detailed in [2].

The results were however very good and are summarised below but have been presented in more detail [2]. A scatter plot, Fig. 8, of the Flidar data on the y-axis and the mast data on the x-axis is presented in the graph below. All data is ten-minute mean values. Table 3 includes the line fit labelled X_{mws} which is forced through the origin, for two mast wind speed filters and two instrumentation comparison heights. The column headed "v1" refers to data collected directly from the Flidar by the independent analysers Frazer Nash, whereas the column "v2" represents data with some post processing by Flidar after collection.

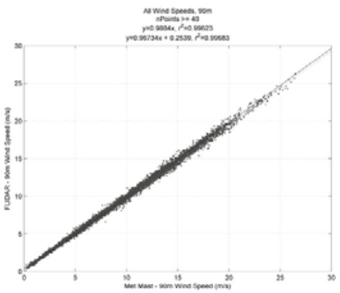

Fig.8 Flidar results: Plot of Flidar wind speed against mast wind speed

	V1 50m	V2 50m	V1 90m	V2 90m
X_{MWS} (MWS > 2 m/s)	0.991	0.992	0.988	0.988
R^2_{MWS} (MWS >2 m/s)	0.991	0.993	0.996	0.996
X_{MWS} (4 m/s < MWS < 16 m/s)	0.995	0.992	0.991	0.996
R^2_{MWS} (4 m/s < MWS <16 m/s)	0.983	0.992	0.993	0.986

Table 3. Flidar wind speed line fit and correlations

Wind direction, Fig.9, also showed a good correlation, though this was after modification to the measurement systems and data processing. The Flidar wind direction is on the y-axis and the mast wind direction on the x-axis.

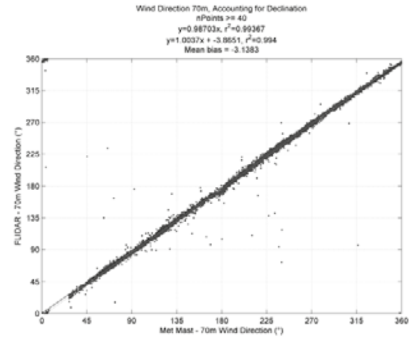

Fig.9 Flidar results: Plot of Flidar wind direction against GYM met mast

The insensitivity of wind speed with wave height is presented in the following figure. The wind speed is on the y-axis presented as a fractional error in the wind speed ratio (Flidar wind speed/mast wind speed) at 90m. The x-axis is the significant wave height in metres.

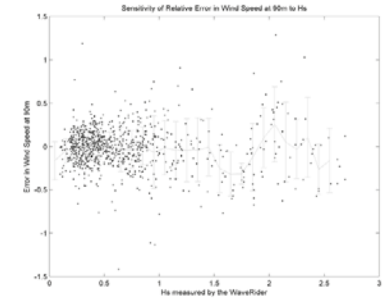

Fig.10 Error in wind speed against wave height

4.3. Babcock floating lidar trials

The Babcock unit is a different buoy design principle being a low motion, low draft spar buoy design. It consists of a large mass at the bottom, followed by the buoyancy chamber and the central tube then links to the platform at the top. The lidar, a Zephir-300 in this case and power systems are mounted on the top platform.

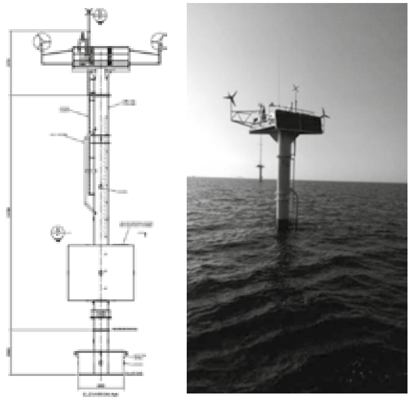

Fig.11 Babcock Floating Lidar

The unit was deployed in July-13 and survived through the winter period though power supply issues meant it was not operational for most of the period. After modification, it was redeployed in April-14 for a period of over 6 months and operated successfully.

The data presented in the following graphs are scatter plots of ten minute mean measurements. The wind speed correlation between met mast and floating lidar was again very good. The y-axis is the Babcock lidar windspeed while the met mast data is on the x-axis. A wind speed filter on the mast wind speed below 2m/s has been applied and is presented below:

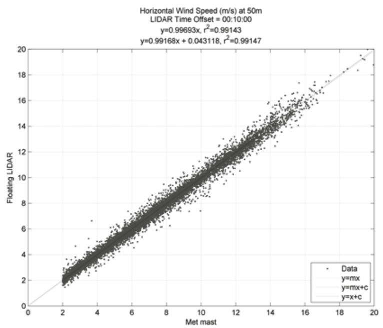

Fig.12 Babcock lidar wind speed comparison against the GYM met mast.

After the application of an offset correction, due to incorrect buoy orientation calibration, direction results showed a good 1 to 1 correlation. The Babcock lidar data is on the y-axis and the mast data again on the x-axis.

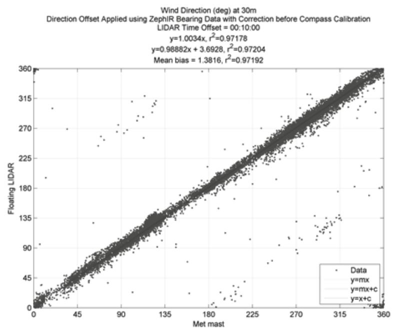

Fig.13 Babcock lidar: Comparison of wind direction lidar against met mast

With the longer deployment of this lidar unit compared with the Flidar, more wave data was obtained over a larger range of significant wave heights and demonstrated that there is no bias with wave height for the range tested. The graph, Fig. 14 below plots the wind speed on the y-axis as a fractional error in the wind speed ratio [Babcock llidar wind speed/mast wind speed] at 90m. The x-axis is the significant wave height in metres.

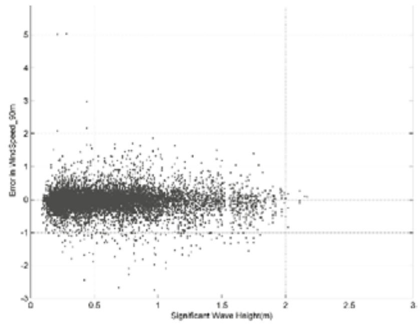

Fig.14 Babcock Lidar: Error in wind speed against wave height

4.4. Results summary

For both units, there were successful sea trials. i.e. they survived 3 months [Flidar] and 6 months [Babcock lidar] at sea with some winter conditions, significant wave heights up to 2.5m and mean wind speeds up to 30m/s (measured at mast hub height)

Correlations with the fixed met mast at a number of heights were performed which demonstrated accuracy in wind speed and wind direction measurements, though both systems required adjustment to ensure good final wind direction measurement accuracy.

The wind speed correlations on both systems appeared to be independent of sea conditions. Availability of the data was also good at all heights, though degradation of signal availability was seen as higher heights which is a normal feature of lidar data.

Correlations between lidar and anemometer turbulence were made and the correlations were found to be poor [2] & [3], as also seen in onshore trials [2] though whether they are worse has not been fully analysed.

Correlations with gust wind speeds were also found to be poor, [2] &[3].

The results were independently verified and both units have reached the commercially acceptable milestones as defined by DNV-GL [5].

4.5. Deployment Lessons

While the trials were successful, there was also a steep learning curve for all participants.

The key lesson is that of robustness, of all parts of the system; power supply and power storage, lidar, data collection and data storage, wiring, communications, buoy design and mooring.

Dockside and sea trials for any unit are essential. The dockside trials of all systems ensure that all systems are working and integrated. Also sea trials against a measurement system of known accuracy is essential.

The sea trials will highlight any design issues in the system. Unfortunately the nature of offshore deployments means that rectification can be a prolonged program. If it is too rough then no access is possible. This is exacerbated by the nature of the units which can generally only be accessed in calm waters of the summer months. The aim of the trials will be to improve reliability to a point where commercial deployments in say the North Sea with a harsher wave climate can be undertaken with confidence.

In particular, attention must be given to the resilience and redundancy of the power supply and power storage systems and also of communication systems. The lidar units have much higher power consumptions than that traditionally associated with solar and wind powered charging systems and this causes additional reliability issues.

Ease of access and maintenance needs also to be considered, boats or crew transfer vessels (CTVs) may vary considerably in different locations and hamper access. Also having easy to lift and replace modular units on the buoys are essential.

There are also different safety standards to be aware of between different companies and different methods of working. That is not to say any are inherently unsafe, but operators will demand compliance to slightly different working methods which can make the initial and subsequent deployments taxing.

4.6. Trials Summary

In Summary as a result of the trials, the following objectives were met.

- Technically:
  - Accurate wind speed correlations
  - Accurate wind direction correlations
  - Reliability proven – after some work.
  - Both at stage 2 of road map [5].
- Sea trials proved both useful and essential
- The results were independently verified
- Planning/permitting issues better understood
- Operational (O&M) and safety issues better understood
- Results going into IEC guidelines.
- Further trials of floating systems undertaken and planned.

Buoy Supplier	Met mast site	Deployed	Removed	Project lead	Independent Data Analyst
Flidar	Gwynt y Môr (RWE)	09/12	01/13	RWE	Frazer Nash
Babcock	Gwynt y Môr (RWE)	07/14	12/14	RWE	Frazer Nash
Fugro Oceanor	Ijmuiden (RWE)	01/14	10/14	Eneco	DNV GL
EOLOS	Ijmuiden (RWE)	01/15	08/15	RWE	ECN
Flidar	Blyth (ORE Catapult)	01/14	04/14	Mainstream	DNV GL
TBA	East Anglia (SPR/ Vattenfall			SPR/ Vattenfall	Natural Power

Table 4 Summary of Floating Lidar deployments in Europe sponsored by OWA

Fig. 15 Photograph of the Fugro Oceanor floating

lidar buoy deployed at RWE Ijmuiden mast – results to be separately reported.

Fig.16 Photograph of the EOLOS floating lidar buoy deployed at RWE Ijmuiden mast – results to be separately reported.

5. Cost Benefit

A way to quantify and justify the benefits of the different measurement systems is to estimate the inherent uncertainties and look at the cost benefits based on a typical/generic offshore wind farm. A standard uncertainty methodology has been used as detailed in Ref: 1.

Assumptions are:

- Offshore wind farm 1000MW, with 140 – 200 turbines.
- Load factor = 37%.
- Gives Energy yield (P50) of 3,200 GWh/yr.
- Revenue of £400M/yr based on £125/MWh ref [4].
- Site life 25 years, discount rate 10%.
- Measurement system(s) installed 5 years prior to generation.

The scenarios analysed are:

1. No mast or lidar, relying only on a Mesoscale Model Prediction.
2. An on-site met mast of traditional construction with hub height cup anemometers – no lidar assumed.
3. On site met mast of traditional construction with hub height cup anemometers and lidar.
4. Floating lidar in early stages of maturity.
5. Floating lidar, mature design with significant testing.
6. Two floating lidars deployed across a site to give reduced spatial uncertainty.

The uncertainties are derived below, based on standard values used within RWE. The uncertainties for the lidar systems are based on values quoted by DNV-GL [4].

Scenario	Wind Speed Measurement / Anemometer Uncertainty	Mesoscale Accuracy	Wind Flow Modelling - Vertical	Wind Flow Modelling - Horizontal	Period Representative of Long-Term		Quality of Correlation	Consistancy of Reference Source	Total Uncertainty in Wind Speed
					Years	Uncertainty			
1		6.0	0.0	0.0	*10.0*	3.2	0.3	3.0	7.4
2	2.2		0.5	0.3	*10.0*	3.2	0.3	3.0	4.9
3	2.1		0.0	0.3	*10.0*	3.2	0.3	3.0	4.9
4	5.0		0.0	0.3	*10.0*	3.2	0.3	3.0	6.6
5	3.0		0.0	0.3	*10.0*	3.2	0.3	3.0	5.3
6	2.8	0.0	0.0	0.0	*10.0*	3.2	0.3	3.0	5.2

Table 5: Uncertainties in wind measurements and modelling

The other energy related uncertainties have also been estimated and presented in the table below. These are combined with the wind uncertainty from above table converted to energy using an internal RWE factor of 1.8.

Scenario	Power Measurments	Array Effects	Substation Meetering	Assumed Technical Losses	Historical period representative of the future	Total Energy Uncertainty (%)	Total Wind Speed Components Converted to Energy	Total Energy Uncertainty (%)
1	3.0	7.0	0.3	1.0	3.2	8.3	13.4	15.7
2	3.0	7.0	0.3	1.0	3.2	8.3	8.9	12.2
3	3.0	7.0	0.3	1.0	3.2	8.3	8.7	12.1
4	3.0	7.0	0.3	1.0	3.2	8.3	12.0	14.6
5	3.0	7.0	0.3	1.0	3.2	8.3	9.5	12.7
6	3.0	7.0	0.3	1.0	3.2	8.3	9.3	12.5

Table 6: Uncertainties in power assumptions

The total uncertainty is then used to generate the P90 figure from the assumed P50 production assuming a Rayleigh wind distribution.

Scenario	Other uncertainties	Total Energy Uncertainty (%)	P50 [GWh/yr]	P90 [GWh/yr]	P90/P50	ΔP90/P50
1	8.3	15.7	3,243	2,589	0.798	0.0%
2	8.3	12.2	3,243	2,737	0.844	-4.6%
3	8.3	12.1	3,243	2,742	0.845	-4.7%
4	8.3	14.6	3,243	2,638	0.813	-1.5%
5	8.3	12.7	3,243	2,717	0.838	-3.9%
6	8.3	12.5	3,243	2,723	0.840	-4.1%

Table 7: Total uncertainties converted to P90

The electricity revenue can then be added and a change in the present value of the various options compared to the base case option 1. The present value at commissioning date and then also at the mast installation date, assumed to be 5 years in advance of commissioning are then presented.

The cost of various installations are assumed as:

Item	Cost [£]	Cost [€]
Mesoscale model prediction	£70k	€97k
Lattice met mast	£6m	€8.3m
Additional lidar & installation	£150k	€200k
Floating lidar & deployment	£1.5m	€2m

The net benefit of the various options compared with Option 1 as the base case is thus given in the last column of table below.

Scenario	P90 Revenue (£ m)	Delta P90 (£ m)	Delta PV at commisioning date (£ m)	Delta PV at metmast installation date (£ m)	Indicitive Costings (£ m)	Net Cost Benefit (£ m)
1	£324 m	£0.0 m	£0 m	£0 m	£0.07 m	£0 m
2	£342 m	-£18.5 m	£168 m	£104 m	£6.07 m	£98 m
3	£343 m	-£19.1 m	£173 m	£108 m	£6.22 m	£101 m
4	£330 m	-£6.1 m	£55 m	£34 m	£1.57 m	£33 m
5	£340 m	-£16.0 m	£145 m	£90 m	£1.57 m	£88 m
6	£340 m	-£16.8 m	£152 m	£95 m	£3.07 m	£92 m

Table 8: Net cost benefit of different measurement scenarios

It should be noted that the figures are indicative and individual uncertainty assumptions are open to discussion. The conclusions do however provide a good indication.

5.1. Conclusions Cost Benefit

- Onsite measurements provide a considerable cost benefit to the project, of the order of €100m. whether they are a fixed lattice mast or a mature floating lidar.
- The fixed lattice mast options (2 & 3) provide the best cost benefit to a project even taking into account the additional installation costs. This is mainly due to the reduced uncertainty due to calibration of the instruments and uncertainties due to the deployment of lidars on a moveable platform offshore.
- The commercialisation or verification of new floating lidars is essential to reduce the uncertainty that can be attributed to their measurements. The uncertainty data is based on that provided by [5].
- The argument that lidar systems provide measurements up to 200–300m and thus cover the whole rotor range is valid when compared to lattice mast measurements. However in practice all current and future offshore masts will also have co-located lidars or at least be "capable" to have one retrofitted. This is the reason scenario 3 has further reduced uncertainty, where the dual systems will provide a reality check to ensure accurate measurements and it is theoretically possible to directly compensate cup measurements for any boom and mast blockage effects.

5.2. Further considerations

A number of other items have not been considered in this analysis.

- Lidar systems cannot at present provide useable turbulence and gust information. This may well result in conservative values being used in particular for flow modelling which will affect wake losses and the array modelling and potentially turbine spacing. On both tests reported, turbulence data was compared but correlations were poor and in the authors opinion unusable at the current time.
- Gust information is not provided by lidar systems though this is arguably less important for offshore structures where extreme loads are dictated by wave loadings.
- Coastal effects are also not considered though some of this will be accounted for by the higher uncertainty applied to mesoscale model prediction results.
- The multiple deployment of floating lidars to provide spatial wind speed data across the site has not been fully explored. This is estimated as scenario 6. It is a very site specific phenomena and will decrease in importance as windfarms are located further offshore out of the coastal region. However the size of these further offshore sites means that spatial measurements would be beneficial to verify the across site variation.
- The accuracies for floating lidar systems are on the basis that verification has been done in sea trials at a site where the sea conditions are similar to the proposed wind farm site. i.e. Sea trials in the Irish Sea, while useful, may not have similar met ocean conditions to those in the North Sea and further offshore, where wave amplitude and frequency will be different (higher and slower respectively).

On the basis of these trials and other work by the OWA and other companies a number of commercial deployments are now underway, which indicates the increasing acceptance of the floating lidar technology.

6. Conclusions

In terms of the trials:

- Successful sea trials have been performed on a number of floating lidar prototypes taking them from the research to pre-commercial and commercial stages.
- The reliability of the systems have been proved, by long trials.
- The accuracy of the measurements is within the roadmap criteria.
- The results have been independently verified
- Operations experience has been gained.
- Cost benefit analysis has demonstrated that mature lidar systems have a net benefit to offshore wind farm projects.
- The same analysis also demonstrates that the fixed lattice type masts still have the best net benefit to a project and their versatility in being able to mount additional instrumentation is still useful.

7. Further research

- Commercial deployments for a unit are valid only where trials have been performed in similar sea conditions. Further trials to provide verification in different sea states will increase utility and start to demonstrate an ocean independent accuracy.
- Verification of directional accuracy needs further work and initial trials showed this was a weakness in the systems.
- Operational issues around maintenance and local communications in the case of no access should be investigated.
- The ability to provide turbulence and gust measurement from the units needs further research. This is more difficult as the platform motion needs to be accounted for and results produced verified.
- The IEA standard needs completing to give guidelines enabling a uniform assessment of the capabilities of different units.

References:

[1]. IEC 61400-12-1 Power Performance Measurement standard 2006.
[2]. Results and Findings of a Floating LIDAR Trial in the Irish Sea. EWEA Offshore, 21 Nov 2013, Frankfurt. Neil Adams and Detlef Stein.
[3]. OWA floating LiDAR campaign: Babcock trial at Gwynt Y Môr. EWEA Offshore 2015, Copenhagen, 11 March 2015 Megan Smith.
[4]. UK Government Renewables CfD strike price results 2014.
[5]. Roadmap to Commercial Acceptance of Floating LiDAR, The Carbon Trust /DNV-GL, 2013
[6]. Benefits of floating Lidars, Wind Resource Assessment Forum 2015, London, John Slater
[7]. Wind Measurement Campaigns Offshore and do they Create Value. Wind Resource Assessment Forum 2014, London, Fergal Darcy, Andrew Henderson.
[8]. The Commercialisation of Floating Lidar Chris McConville , Andy Paterson, EWEA Offshore Poster ID184, Copenhagen 2015.

PRINTED BY ARTOOS
ISO 14001
100% GREEN POWER
CLIMATE NEUTRAL COMPANY
SUSTAINABLE DEVELOPMENT
PRINTED CLIMATE NEUTRALLY
certificate number:53520-1510-1020
www.artoos.be
RECYCLED
Paper made from recycled material
FSC® C007370